PAUL SCHERRER INSTITUT

PSI

SLS 2.0
Beamline Conceptual Design Report

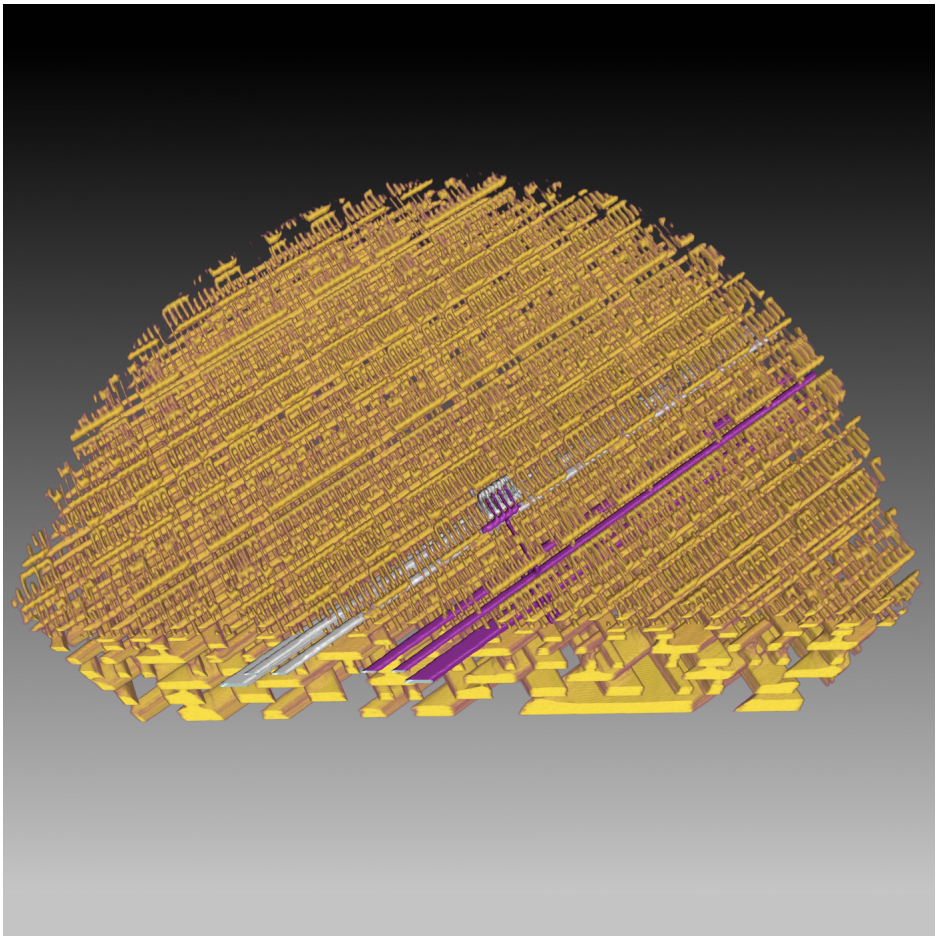

PSI-Bericht 20-01

January 20, 2021

SLS 2.0 Beamline Conceptual Design Report

With contributions from

Luca Artiglia, Patrick Ascher, Alun Ashton, John Beale, Mario Birri, Andras Boedi, Anne Bonnin, Camelia Borca, Christoph Bostedt, Hans Braun, Marc Brügger, Oliver Bunk, Dominik Buntschu, Marco Calvi, Nicola Casati, Adrian Cavalieri, Antonio Cervellino, Adam Clark, Stefan Danner, Ana Diaz, Xavier Donath, Jan Dreiser, Florian Dworkowski, Yasin Ekinci, Sylvain Engilberge, Dario Ferreira Sanchez, Simone Finizio, Uwe Flechsig, Christophe Frieh, Ulrich Frommherz, Wayne Glettig, Daniel Grolimund, Manuel Guizar-Sicairos, Patrick Hemberger, Stephan Hitz, Juri Honegger, Chia-Ying Huang, Lars Huber, Thomas Huthwelker, Thomas Jung, David Just, Jakub Kaminski, Armin Kleibert, Markus Kropf, Michael Lange, Filip Leonarski, Federica Marone, Isabelle Martiel, Katherine McAuley, Nathalie Meier, Dominik Meister, Andreas Menzel, Beat Meyer, Gordan Mikuljan, Iacopo Mochi, Matthias Muntwiler, Maarten Nachtegaal, Frithjof Nolting, Zbynek Novotny, Leonard Nue, Vincent Olieric, Ezequiel Panepucci, Luc Patthey, Anuschka Pauluhn, Andreas Pfister, Cinthia Piamonteze, Nicholas Plumb, Claude Pradervand, Jörg Raabe, Milan Radovic, Sonia Reber, Benedikt Rösner, Olga Safonova, Dario Sanchez, Christian Schlepütz, Marcus Schmidt, Thomas Schmidt, Thorsten Schmitt, Roman Schneider, May Sharpe, Ming Shi, Grigory Smolentsev, Marco Stampanoni, Urs Staub, Vladimir Strocov, Takashi Tomizaki, Roelof van Silfhout, Carlos Vaz, Laura Vera, Urs Vogelsang, Michaela Vockenhuber, Meitian Wang, Xiaoqiang Wang, Benjamin Watts, Reto Wetter, Philip Willmott, Justyna Wojdyla, Elmar Zehnder, Stefan Zeugin, and Philipp Zuppiger

Editors

Phil Willmott, Uwe Flechsig, Thomas Schmidt

PAUL SCHERRER INSTITUT

Paul Scherrer Institut, 5232 Villigen PSI, Switzerland

Tel. +41 56 310 21 11, Fax +41 56 310 2199

www.psi.ch

Foreword

A first request for funding for an upgrade of the SLS was made in January 2014, when a Letter of Intent (LoI) was submitted by PSI (authors: L. Rivkin and F. v. d. Veen) to the State Secretary for Education, Research and Innovation (SERI) in order to place "SLS 2.0" on the roadmap for future Swiss research infrastructures to be financed in the time period 2021 – 2024. This LoI contained a budgetary estimate of MCHF 83 for the upgrade, of which MCHF 63 was reserved for the accelerator. In addition, a request for 2.0 MCHF for preliminary studies in the period 2017-20 was included.

The objectives of the upgrade were reported to the PSI Advisory Board in February 2014, which endorsed the proposal to study the upgrade over the next three years with the SLS machine-physics and dynamics staff.

By 2016, the approximate specifications for the ring performance had been established, promising a horizontal electron-beam emittance of the order of 100 to 150 pm rad; the time had come for a concerted investigation to discover the impact this forty-fold improvement in performance would have on photon science.

The goals of the upgrade of the SLS were prominently featured at the 5th DLSR workshop in Hamburg in March 2016, with both initial machine design features (A. Streun) and scientific drivers (overview, P. Willmott; lensless imaging, A. Diaz; and inelastic x-ray scattering, T. Schmitt) being presented.

Thereafter followed a "Spring Photonics Workshop" in Windisch, Kanton Aargau, in April 2017, assembling external users, SLS staff, and international experts in the fields of imaging, macromolecular crystallography, heterogeneous catalysis, magnetism, and electron spectroscopy. The workshop was summarized in a Synchrotron Radiation News article [1].

Presentations outlining the visions of four of the most prominent scientific disciplines at the SLS (lensless imaging, x-ray computed tomography, resonant inelastic x-ray scattering, and macromolecular crystallography) were given at the Photon-Science Advisory Board (PSAC) meeting in December 2017, prior to submission of the science case for the upgrade to the Research Infrastructure Roadmap of the Swiss National Science Foundation in January 2018. The proposal received the highest rating from the six independent referees and was also approved by the ETH Board in December 2018. In December 2020, funding was approved by the Swiss government, immediately before the formal start

of the project in January 2021.

Detailed discussions between beamline staff, the insertion-device and optics groups, and the SLS 2.0 project leaders (H. Braun, P. Willmott T. Garvey, M. Jörg, R. Kobler, and A. Ashton), plus several smaller topic-specific workshops organized by individual beamlines with their user communities, culminated in an internal workshop in October 2018 in which the immediate and long-term visions of the beamlines were outlined. These ideas were formalized first in "pre-CDR" documents submitted to the project in November 2018 and a presentation to the PSAC in December 2018, and secondly, in two two-day CDR workshops in front of a panel of external experts [2] in April 2019 and September 2020.

The configuration of the lattice was frozen in June 2020. With this in place, a fully developed beamline CDR could be collated. This document details this process.

Phil Willmott, January 2021

Bibliography

[1] P. Willmott, J. Hastings, M. van Daalen, and L. Patthey. Photonics Spring Workshop at the Paul Scherrer Institute. *Synch. Rad. News*, 30:11–12, 2017.

[2] Members included: Jerry Hastings (SLAC, Chair), Edgar Weckert (DESY), Jöel Chavanne (ESRF), Hamed Tarawneh (MAX-IV), Makina Yabashi (SPring8), Gwyndaf Evans (Diamond), Jonathan Lang (APS upgrade), Andreas Scholl (ALS upgrade), Amedeo Perazzo (SLAC).

Contents

Chapter 1

Overview

1.1 Summary

The Swiss Light Source (SLS) has been in operation since early 2001. Since its inception, the SLS has spearheaded groundbreaking research in biomedicine, engineering, and the natural sciences, thanks in large part to the excellent performance of the underpinning electron accelerator and storage ring complex. In addition, it has led the world in industrial exploitation, particularly by the pharmaceutical sector, and spawned numerous new companies, including one of the most successful Swiss-technology spinoffs, Dectris. For much of this time, the SLS has been a benchmark with regards to how closely its performance matched the theoretical limits defined by its machine parameters.

From 2006 (when the PSI DUO database was introduced) to the end of 2019, the SLS has been host to over 45 000 user visits, some 6400 accepted proposals, and approximately 1 100 000 hours of user beamtime, covering areas as diverse as atomic and molecular science, catalysis/surface science, environmental and earth sciences, condensed-matter physics, life- and medical sciences, materials and engineering sciences, and polymeric and soft-matter research. This has culminated in nearly 8000 peer-reviewed publications in the same period, of which well over 30 % have impact factors equal to or above 8.4 (the present impact factor of Physical Review Letters). More than 7000 macromolecular structures solved at the three 'PX' beamlines have, since 2002, been deposited in the Protein Data Bank; in the number of deposited structures per beamline per year, the SLS is the world leader, at 120. A further 16 000 structures of protein/ligand complexes have been determined by industry, many of which have helped the development of drugs under clinical trials to treat ailments such as diabetes, heart disease, and cancer.

The Paul Scherrer Institute (PSI) is the largest research institute in Switzerland for the natural and engineering sciences. Its three central 'grand challenges' are in human health, energy and the environment, and matter and materials. They address urgent societal demands in the 21st century, including clean and low-cost energy generation, delivery, and consumption; affordable, targeted, and personal medicine to cater to an ageing population; and high-capacity and energy-efficient information technology. All these drivers require an understanding of materials, devices, and biomedical systems on a nanoscale- or atomic level. Breakthroughs will depend intimately on the development of novel, tailor-made functional materials designed often at many spatially hierarchical levels down to the atomic

scale. Such ambitious goals can, however, only be achieved if a palette of suitable diagnostics tools is available. The next generation of synchrotrons promise to play a central role in this endeavour.

With the advent of the next generation of quasicontinuous short-wavelength light sources, called diffraction-limited storage-rings, that yield emittances and brightnesses improved by up to two orders of magnitude, it has become imperative to upgrade the SLS (called SLS 2.0) in like manner.

The design of SLS 2.0 addresses two central aspects, namely the photon energy range in which scientific excellence has emerged at the SLS in the last two decades; and the limited real estate of the facility. Originally, the SLS was designed to concentrate on a 'sweet spot' range of energies from 1 to 10 keV, catering for the then known areas of scientific expertize within the Swiss and neighbouring countries' scientific communities. These included, among others, electron spectroscopies, nanoscale magnetism, and macromolecular crystallography. In the two decades since the first users arrived at SLS, several novel and unanticipated techniques have emerged, in particular in the field of nanoscale imaging, that, while yielding cutting-edge and sometimes seminal results within the original 'sweet spot' of energies, would gain significantly if this were extended to photon energies of several tens of keV. An innovation regarding source technology (see Chapter 2), and a simple change in a single storage-ring parameter, namely the ring energy, from 2.4 to 2.7 GeV, will combine to redefine the sweet spot of SLS 2.0 to align with the scientific developments at SLS since 2001.

The second facet, that of limited real estate, has been addressed as follows. Brightness is defined as the spectral flux for a given total emittance (including contributions from both the electron- and photon beams). Diffraction-limited storage rings are characterised by their small electron emittance, provided by the implementation of multibend achromats (MBAs). In turn, MBAs consist of many more magnet elements than traditional double or triple-bend achromats used in third-generation facilities. This increased complexity has only become feasible as a result of miniaturization of the magnet-lattice components. At the SLS, the modest circumference of approximately 290 m has forced the machine design to be aggressive with regards to focussing optics, in particular the sextupoles. Nonetheless, an improvement in brightness of approximately 24 has been achieved from the machine design solely through the reduction in horizontal electron emittance.

SLS 2.0 will also increase the brightness through the increase in storage-ring energy, plus novel developments in undulator technology, increasing the spectral flux in some cases by two orders of magnitude. This is achieved by increasing the undulator lengths and reducing the ID periodicity and minimum gap size, resulting in high-K devices. Importantly, these innovations in source technology apply across the entire photon range of interest, including the VUV and soft x-ray regimes. In this manner, SLS 2.0 can expect significant improvements also for photon energies below that associated with the diffraction limit (see the following section).

Together, the increase in storage-ring energy, the implementation of 7-bend achromats, and these insertion-device innovations will further substantially increase not just the brightness compared to today, but also the flux and coherence. This is summarised in Figure 1.1.

1.2 The diffraction limit

The main limit to the horizontal electron-beam emittance in third-generation storage rings is associated with the spread induced at bending-magnet achromats. The lower limit to the electron emittance of

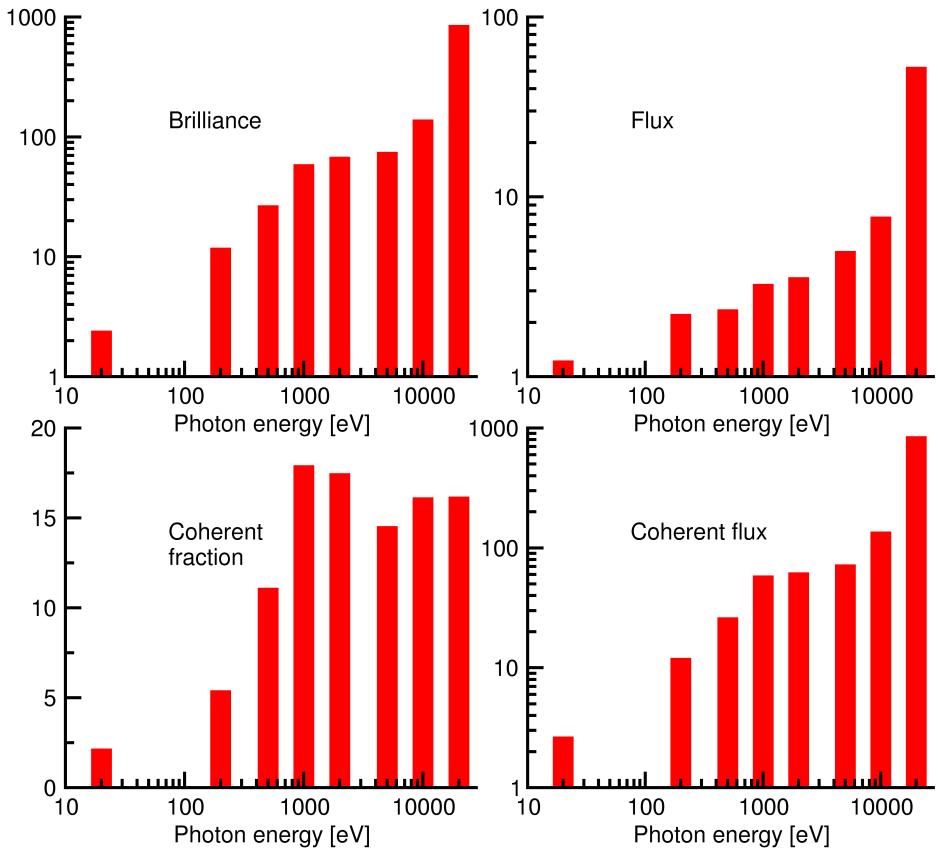

Figure 1.1: Factor improvements in brilliance, flux, coherent fraction, and coherent flux for the SLS 2.0 upgrade, with the new storage-ring energy of 2.7 GeV, for selected photon energies. The undulators assumed in the original SLS are UE212 (8.4 m) for 20 and 200 eV, UE56 (3.6 m) for 500, 1000, and 2000 eV, and U19 (1.8 m) for higher photon energies. The corresponding undulators in SLS 2.0 are UE90 (4.4 m), UE36 (4.4 m), and CPMU15 (3 m).

a multibend achromat in a diffraction-limited storage ring (DLSR) is given by

$$\epsilon^e_{x,\mathrm{MBA}} = \frac{M+1}{3(M-1)} C_{\mathrm{DBA}} \gamma^2 \theta^3, \tag{1.1}$$

whereby M is the number of dipoles in the MBA, $C_{\mathrm{DBA}} = 2.474 \times 10^{-5}$ nm, $\gamma = \mathcal{E}/m_e c^2$ is the Lorentz factor, and θ is the angle swept by a single dipole in the MBA. The theoretical improvement (that is, reduction) in electron emittance between a DBA and MBA is, for a fixed entire swept angle for both achromats, therefore equal to

$$\frac{\epsilon^e_{x,\mathrm{MBA}}}{\epsilon^e_{x,\mathrm{DBA}}} = \frac{M+1}{3(M-1)} \left(\frac{2}{M}\right)^3. \tag{1.2}$$

Thus, for $M = 7$, one can expect a reduction in ϵ^e_x by as much as a factor 0.0104 to values of the order of 100 pm rad.

The total emittance is a convolution of the electron- and photon emittances. The latter is determined solely by diffraction and is given in both the orbital (x-) and y-plane by

$$\epsilon^p\,[\mathrm{pm\,rad}] = \frac{\lambda}{4\pi} = \frac{98.66}{E\,[\mathrm{keV}]}. \tag{1.3}$$

For a facility with an electron emittance of the order of 100 pm rad that is also well phase matched at the undulator straight sectors to the photon beta function, the 'natural' photon emittance therefore begins to dominate below the tender x-ray regime and the storage ring becomes 'diffraction limited'.

The improvement in brightness between third- and fourth-generation facilities is thus most marked for hard x-rays and can be approximately equated to the reciprocal to the improvement in electron emittance [a]. For SLS 2.0, this is predicted to be at approximately $h\nu = 400$ eV.

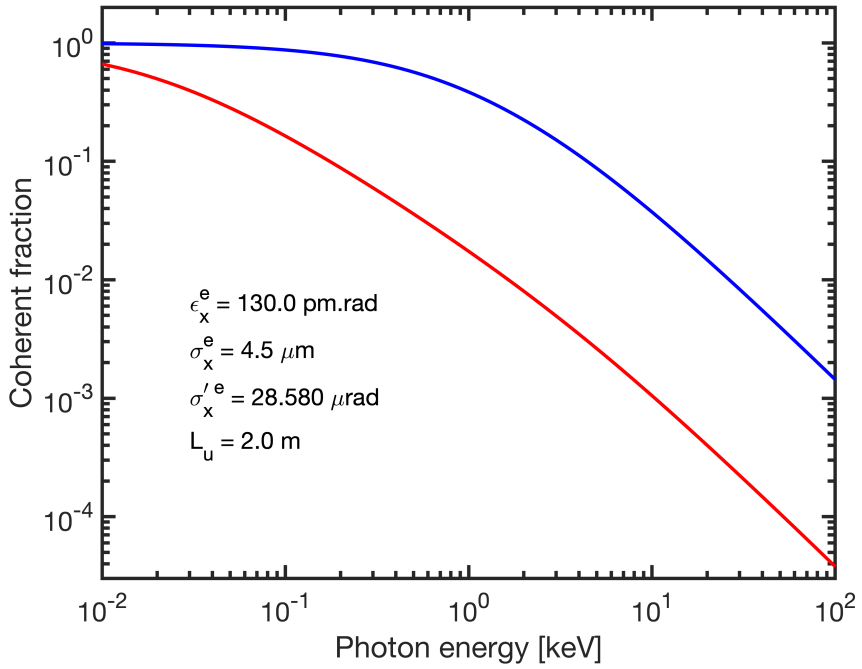

Figure 1.2: The calculated coherent fraction of a 2-m undulator with an ideal beta function of $L/4\pi = 0.159$ for SLS (red curve) and SLS 2.0 (blue curve), assuming an electron emittance of 130 pm rad. Note that at 10 eV, the improvement in f_{coh} is only about a factor of 1.6, while at 10 keV, it is approximately 40, i.e., essentially equal to the improvement in ϵ_x^e.

The reduced total horizontal emittance has a direct impact on the coherent fraction of the emitted radiation. This is given by

$$f_{\mathrm{coh}} = \frac{(\epsilon^p)^2}{\epsilon_x \epsilon_y}, \tag{1.4}$$

[a] This assumes that the 'phase space ellipses' of the electron and photon beams have been well matched. The beta-function associated with the photon emittance is given by $L/4\pi$ and is thus of the order of 20 cm. The electron beta function should ideally have a similar value.

whereby $\epsilon_{x,y}$ is the total emittance in the x- and y-planes. In the hard x-ray regime, ϵ_x is dominated still by the electron emittance, and it is here where the greatest gains are made (see Figure 1.2).

This significant reduction in horizontal electron emittance and similar increase in coherent fraction, has an impact on the performance and technological possibilities at DLSRs that extends beyond a simple enhancement of the brightness. This is summarized in Figure 1.3.

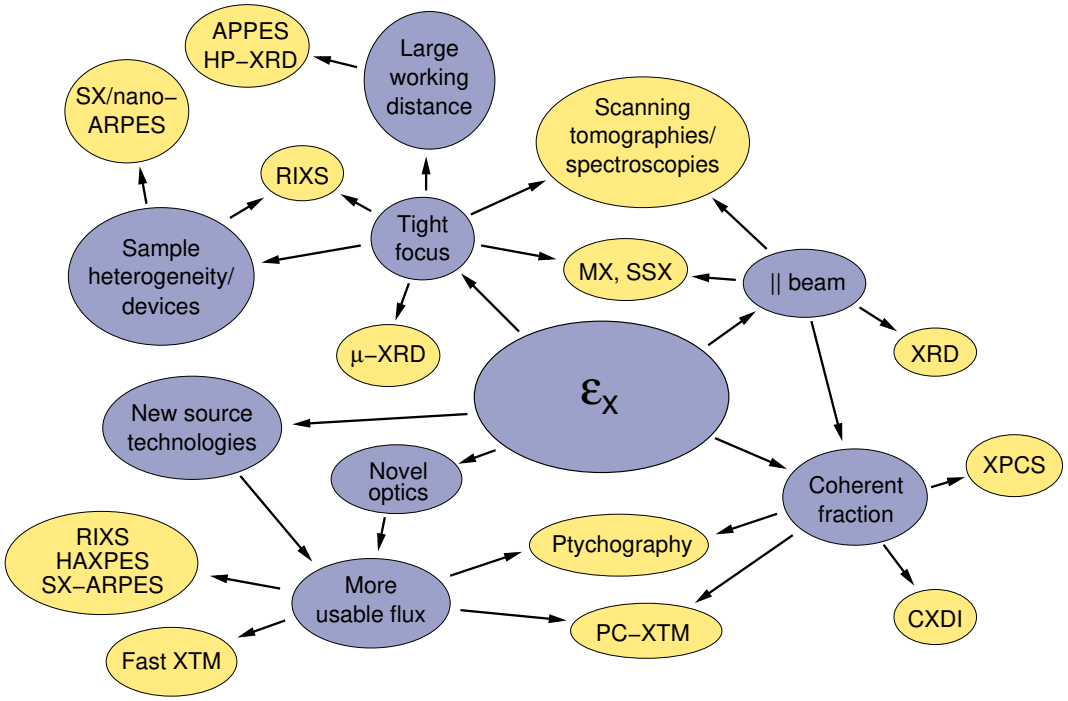

Figure 1.3: Interplay of technology and experimental methods resulting from the upgrade of the SLS. From the reduction of the horizontal electron emittance ϵ_x^e, certain parameters and properties (blue ellipses) directly (or indirectly, through enabling of other technological developments) impact many different experimental methods (yellow ellipses).

1.3 DLSRs worldwide and SLS 2.0

The first DLSR to come online was MAX IV in Lund, Sweden, in 2016. The next fourth-generation facilities to achieve first light are the greenfield facility Sirius, in Campinas, Brazil, and the ESRF-EBS upgrade, which delivered first light at the end of 2019. Several other facilities are either planning or proposing upgrades – the next three facilities expected to achieve DLSR status are the ALS-U (Berkeley), APS-U (Argonne), and SLS 2.0 projects; all of these expect first light between 2024 and 2026. A summary of the performance of both third-generation facilities and DLSRs is shown in the so-called 'Bartolini plot' in Figure 1.4.

The portfolio of beamlines is shown graphically in Figure 1.5. An important aspect compared to the present portfolio is that the two straight sectors 2 and 8 that are not presently exploited will

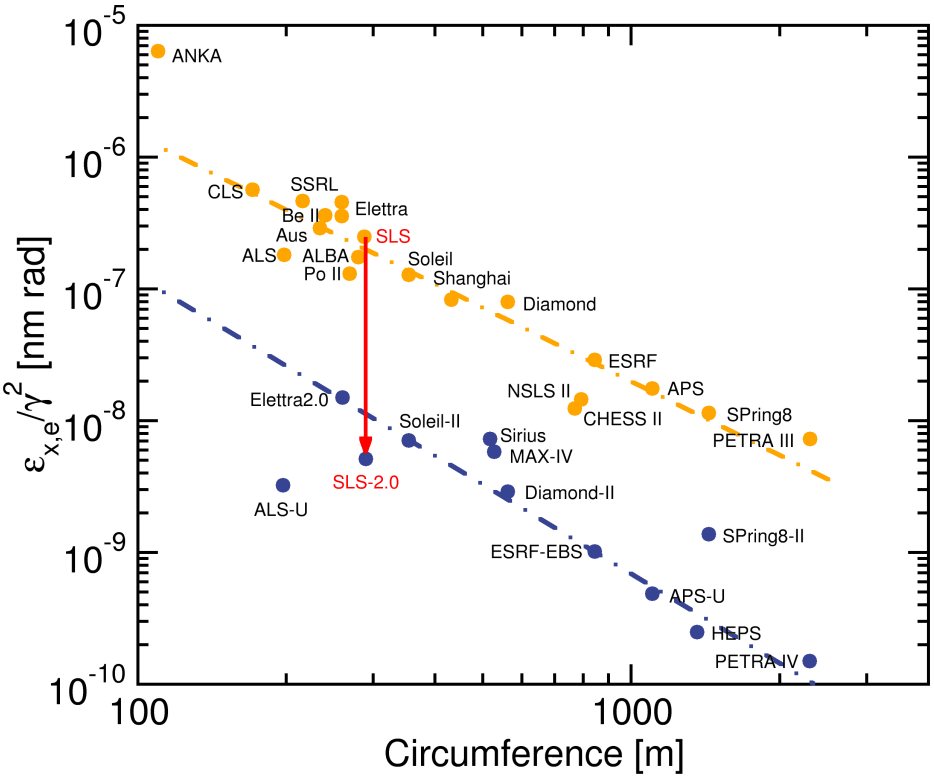

Figure 1.4: Bartolini plot of horizontal electron emittances weighted by the square of the storage-ring energy as a function of ring circumference, for both third- (orange data points) and fourth generation (blue) synchrotrons. Note the approximately twentyfold improvement in emittance for the SLS 2.0 upgrade.

host I-TOMCAT and microXAS 2.0, respectively. Moreover, a fourth superbend beamline, Debye, will be installed in Arc 1, while the PEARL beamline presently served by a bending magnet will be amalgamated with SIS to create the new QUEST beamline in the long straight at Sector 9. XIL will share beamtime with SX-ARPES in Straight 5. If one assumes a beamline which shares a source such as XIL to count as 'half a beamline', the total number of beamlines will increase from 17 today to 19 after the upgrade.

The proposed photon-energy ranges of the SLS 2.0 beamlines detailed in this document are presented in Figure 1.6. They span four orders of magnitude from the vacuum ultraviolet at 7 eV for the VUV and SIS beamlines up to 70 keV or higher for the superbend S-TOMCAT beamline.

1.4 Rollout of the beamline upgrade

The beamline conceptual design reviews, which make up the bulk of this document, assume that sufficient funds and resources are in place so that the upgraded beamlines not only match the enhanced machine performance but also include scientific and technological adventure resulting from the machine

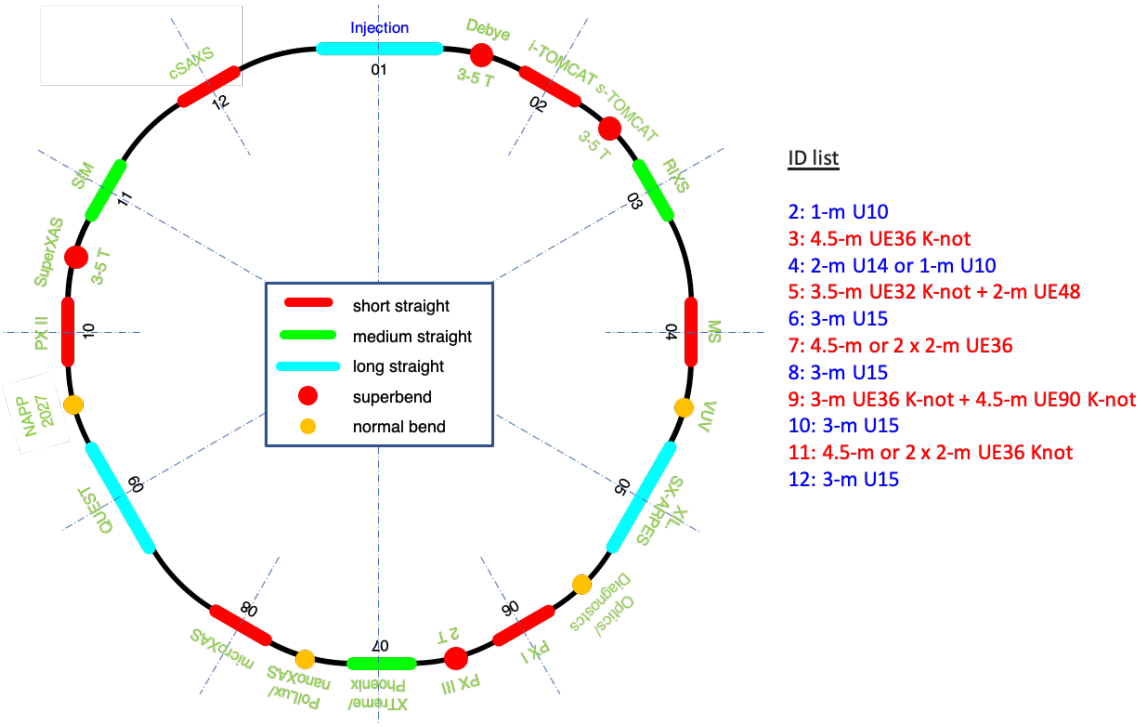

Figure 1.5: Schematic illustration of the beamlines and their locations installed after the SLS 2.0 upgrade.

and optics innovations.

Such a fully-developed beamline upgrade can only be realised through a phased program dictated by resources and funding. The first priority is to resume user operation and maintain the beamlines' user communities as swiftly and efficiently as possible. This first phase will be planned and coordinated to best facilitate further upgrade activities over the first four years after completion of the machine commissioning (2025 to 2028). This has the advantage of gaining experience with handling DLSR radiation on a practical level as a basis for realistic technological innovations in all aspects of beamline infrastructure, from optics, through sample manipulation, to detector technology and IT architecture.

The remainder of this document is concerned with the beamline sources, front end description, and detailed CDRs of the individual beamlines. The order of the beamline chapters roughly follows that of increasing photon energy, attempting also to cluster beamlines with similar scientific and experimental goals.

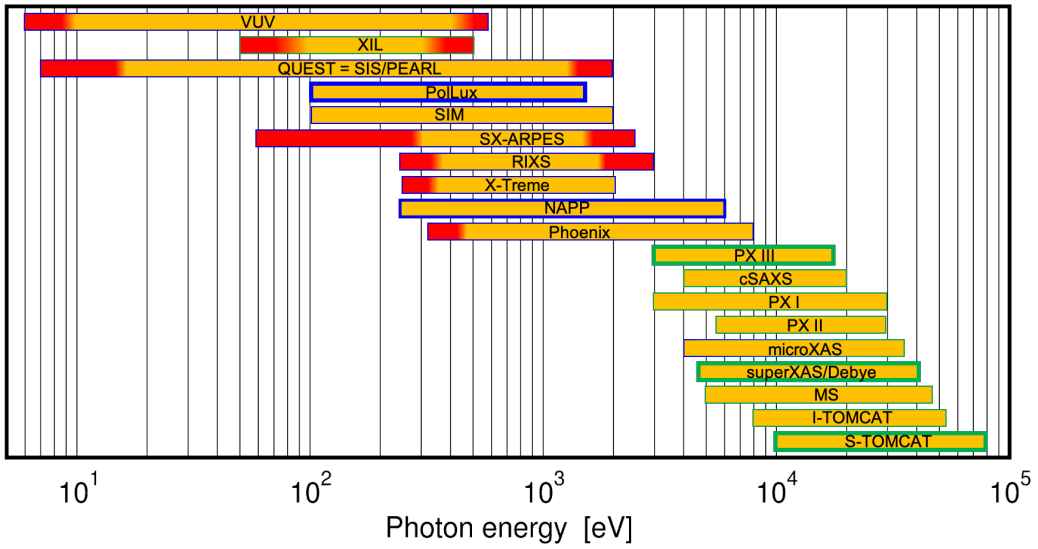

Figure 1.6: Photon energy ranges of the proposed beamlines at SLS 2.0. The values in red represent 'like to have' ranges, while those in yellow are mandatory. Beamlines with a blue border are bending-magnet beamlines, those in green are superbends.

Chapter 2

Sources

Thomas Schmidt, Marco Calvi, Marc Brügger, Steffen Danner, Lars Huber, and Marcus Schmidt

In a nutshell

The increase in brilliance and flux at SLS 2.0 is the result of an interplay between, on the one hand, improvements in electron beam dynamics, including the decrease of the horizontal emittance by a factor of 45, an increase in electron energy from 2.4 GeV to 2.7 GeV, advanced injection schemes, and the concept of antibends, and on the other, implementation of the latest undulator technologies and concepts. Hard x-ray cryogenic in-vacuum undulators with PrFeB permanent magnets allow shorter periods with high fields, which generate an increase in brilliance, depending on the photon energy, by two to three orders of magnitude. The photon-energy range can be extended from 30 keV to 60 keV with high-temperature superconducting undulators. This R&D project promises a factor of two higher fields at very small periods of about 10 mm compared to all other technologies. The concept of using bending magnets which deflect the electrons outwards provide a very small dispersion in the middle of the arcs, so that superconducting dipoles with up to 5 T can be installed without compromising the emittance. The injection concepts allow a small round vacuum chamber in the straight sections with only 8 mm diameter. This enables the use of APPLE X undulators which enclose the vacuum chamber radially. Developed for SwissFEL, they can be also used in SLS 2.0, allowing shorter undulator period lengths. In combination with the higher storage-ring energy, the entire soft x-ray range can be covered on the fundamental. Strategies to reduce the high power densities on-axis will be implemented.

2.1 Overview

A central challenge of the SLS upgrade is to find a new concept for the electron optics compatible with the existing geometry and footprint of the SLS. Based on the planned portfolio of the SLS two decades ago, with beamlines covering a photon range of approximately 7 eV in the VUV to hard x-rays exceeding 40 keV, a threefold symmetry was chosen with six short, three medium, and three long straights.

This low periodicity and the triple-bend-achromatic arcs cannot support small-emittance optics with acceptable lifetimes; consequently, a twelve-fold symmetry with 7-bend achromats has been pursued for SLS 2.0. Moreover, to effectively translate the small electron emittance into an adequate brilliance increase, the focusing of the electron beam into the straights (i.e. the beta function) has to match the undulator lengths.

A solution has been found by the beam-dynamics group which conserves the existing setup of straights with only minor radial shifts of the source points of less than 70 mm. The key aspect in achieving this was to add quadrupoles in the medium and long straights in order to provide identical phase advances in all straights (see Figure 2.1) and thereby preserve a 'pseudo-twelvefold symmetry', even though the physical symmetry remains threefold.

Although SLS has until now run exclusively at 2.4 GeV, the injector is able to provide 2.7 GeV. An increase to this higher storage-ring energy at SLS 2.0 will further boost the brilliance and flux in the soft and hard x-ray regimes; in the VUV the longest wavelength is determined by the diffraction-limited divergence and its extraction through the very compact matching sections of the arcs.

As the large beta functions at the long straights exclude small-gap operation, the 500 MHz RF cavities will be moved from the short straights 2 and 8 into the first part of the long straight 9, making better use of the available space. Hence, two more short straights (with their small β-functions) become available for hard x-ray beamlines, which results in a new imaging beamline (I-TOMCAT) and a higher brilliance for the microXAS beamline, which moves from its present location at the long Straight 5 to Straight 8. All hard x-ray undulators are located in the short (even-numbered) straights with almost unaltered source points, which will facilitate a fast restart after the dark period.

In addition, the third-harmonic cavity will be relocated from Straight 7 to Straight 5, allowing the PHOENIX/X-Treme beamlines to implement a second undulator for fast helicity switching. The relevant parameter for SLS 2.0 are summarized in Table 2.1.

The new lattice of SLS 2.0 reduces the horizontal electron-beam emittance by a factor of 45 (for 2.4 GeV). The corresponding increase in brilliance for an identical undulator would be 24. The increase in storage-ring energy to 2.7 GeV boosts this value to a factor of 59, although due the quadratic scaling of the emittance with energy the win in emittance is reduced to a factor of 36. Taking the U19 in-vacuum undulators of SLS as a reference, new cryogenic undulators with the shorter period of 15 mm and 3 m total length will result in a brilliance increase of 140 at 10 keV and 868 at 20 keV (see Figure 1.1). This will extend the photon energy range for hard x-ray ID beamlines at SLS 2.0 easily to 50 keV and above.

The increase in brilliance and flux for the upgrade of SLS to SLS 2.0 is based not only on improvements in beam dynamics, which result mainly in a reduced horizontal emittance and in optimised injection schemes allowing reduced pole width and round vacuum chambers, but also on enhanced

	$\mathcal{E}$	I	ϵ_x/ϵ_y	$\Delta\mathcal{E}/\mathcal{E}$
	[GeV]	[mA]	[pm rad]	$\times 10^{-3}$
SLS	2.411	400	5630/10	0.878
SLS 2.0	2.7	400	156/10	1.145
SLS 2.0	length	radial shift	long. shift	β-functions
Straight	[mm]	[mm]	[mm]	β_x/β_y/D [m]
Short (2,4,6,8,10,12)	4110	-2.4	0	2.52 / 1.30 / 0
Medium (3,7,11)	4980 + 820	+ 67.3	-685	3.45/2.40/0
Long (5)	5000 + 6560	+ 67.3	-2975/+3755	7.2-12.1/4.0-12.6/0
Long (9)	6560 + 5000	+ 67.3	-3755/2975	7.2-12.1/4.0-12.6/0
Bending magnet		-62.9	$\pm$135 (+ even)	0.1/4.6/0.05

Table 2.1: Main parameters and layout of SLS 2.0. The straights allow for 3 m-long hard x-ray undulators and up to 4.5 m-long soft x-ray undulators, or alternatively 2×2 m-long twin undulators. In the upstream parts of the long straights, four RF cavities (5) and the 3^{rd}-harmonic cavity (9) are located. Undulators will be installed in series in the downstream parts to allow light extraction through the very condensed arc. For the same reason and because of heat load in the undulators themselves, the installation of canted undulators is not possible and beamlines in Straights 5 and 9 will be operated in time-sharing mode. Long Straight 1 is reserved for injection, which also requires 2×1 m in Straight 2. Additional machine components (current monitors, feedback kicker, pinger and scraper) will be located in the 685 mm parts of the medium straights and in the extremities of Straight 4.

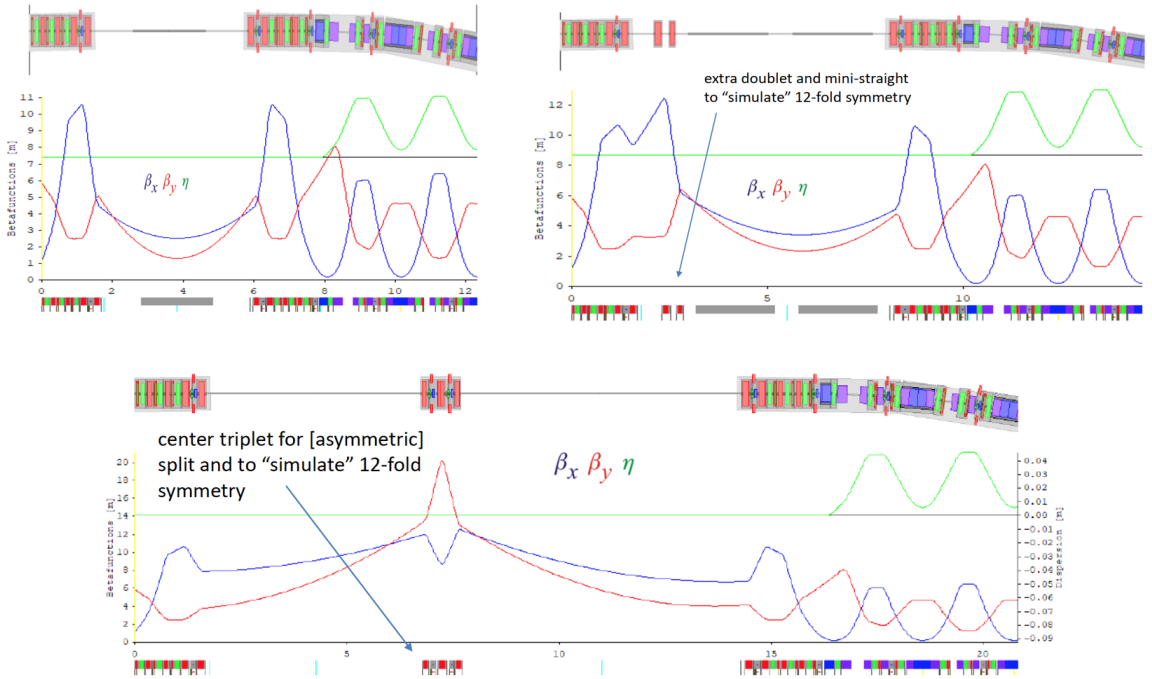

Figure 2.1: Layout of straight sections in SLS 2.0 with six short straights providing small β-functions for high brilliance, three medium straights split with a quadrupole doublet (the short section is reserved for machine diagnostics, the longer section for IDs), and three long straights divided into two similar sections by a quadrupole triplet. This layout produces only minor shifts of the source points compared to today, which thus avoids costly modifications of the tunnel walls.

undulator technologies for soft and hard x-ray undulators (see Figure 1.3). These include:

- New magnetic materials and enhanced manufacturing techniques allowing shorter periods and/or higher fields.
- Cryogenic in-vacuum undulators operating at liquid-nitrogen temperatures with shorter periods are now state of the art in medium-energy storage-ring facilities, replacing room-temperature, in-vacuum undulators.
- A new type of undulator based on high-temperature superconducting material has a high potential for even smaller periods.
- New schemes for soft x-ray undulators have been developed for small, round vacuum chambers in single-pass accelerators like FELs and can be used now also for DLSR facilities with their improved injection schemes.

SLS 2.0 will profit from the large experience gained at PSI with the SLS and SwissFEL projects, both based on cutting-edge undulator technologies [1].

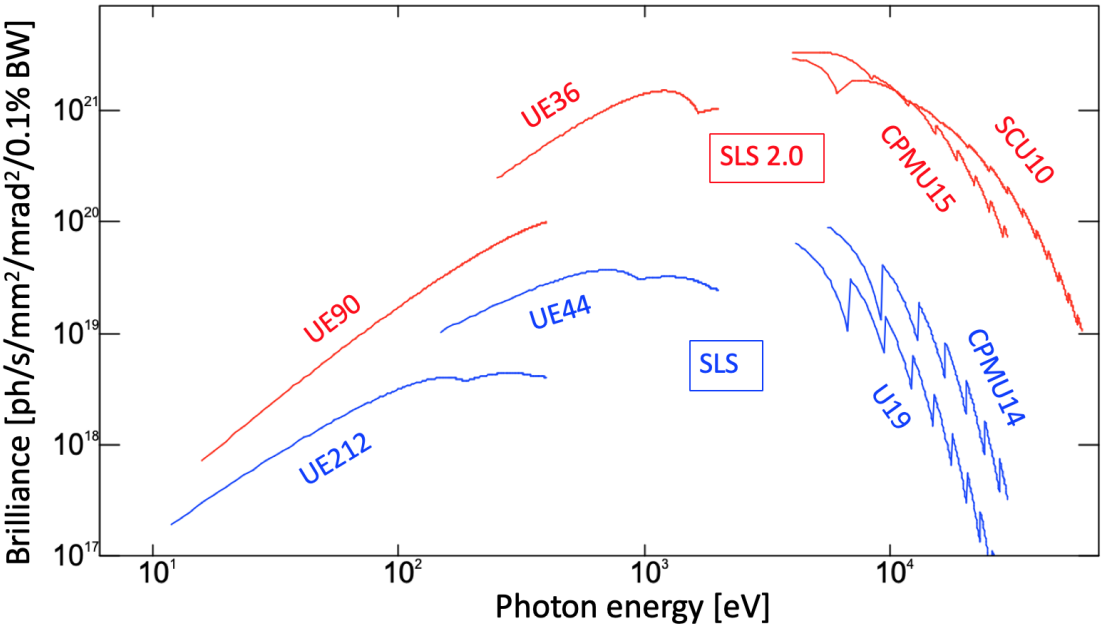

Figure 2.2: Brilliance curves for insertion devices at SLS and SLS 2.0. The increase in brilliance is due to reduced emittance, higher storage-ring energy, longer undulators, and shorter undulator periodicities, while maintaining high K-values. Soft x-ray beamlines profit from shorter periods by covering the entire photon energy range on the fundamental, in contrast to the SLS, for which the 3$^{\text{rd}}$ and 5$^{\text{th}}$ harmonics are needed to cover the desired photon-energy range, with a consequent reduction in the degree of circular polarisation.

2.2 Hard x-ray undulators

To generate hard x-rays using the medium-energy storage ring of the SLS, 2-m long in-vacuum undulators with 19 mm period were originally designed; they operate with small gaps between 4.5 and 7 mm. The third to 13th harmonics cover the photon-energy range from 4 to 20 keV. NdFeB magnets with a remanence of $B_r = 1.15$ T have been used with a high coercivity of $H_{cj} = 2400$ kA/m, a prerequisite to ensure good radiation hardness. No demagnetization resulting from radiation has been observed in the first two decades of operation and these undulators remain the working horses for the hard x-ray beamlines of SLS. For still higher photon energies, SLS began with a minigap wiggler, which remained operational at the Materials Science beamline until 2010.

2.2.1 Cryogenically-cooled permanent-magnet undulators

The W61 minigap wiggler was exchanged in 2010 with a liquid-nitrogen cryogenically cooled in-vacuum undulator (CPMU) with a periodicity of 14 mm (U14). The NdFeB permanent magnets become stronger and significantly more stable when the temperature is decreased. This material has a flat maximum remanence at $T = 135$ K of $B_r = 1.65$ T. A further reduction of the temperature, however, reduces the field strength again, thus requiring an active temperature control (both heating

and cooling) to maintain the optimal temperature of 135 K.

More recently, PrFeB magnets are being employed, which do not show this spin reorientation and associated drop in field strength at lower temperatures [2]. Cooling of these novel magnets is thus more straightforward, although the temperature stability becomes more critical, as the operation point lies on a gradient instead of a plateau.

The existing U19 undulators could be converted for SLS 2.0 into CPMUs with shorter periods down to 14 mm. While The CPMU14 needed a reinforced support structure comapred to the U19 standard, the small horizontal emittance and the improved injection permit a smaller horizontal good-field region such that the pole width can be reduced from 42 mm to 15 mm. This results in smaller magnetic forces, thus allowing a refurbishment of the existing undulator supports. However, based on the experiences in SLS and SwissFEL to build compact systems and as the vacuum chamber in the SLS 2.0 arc is reduced from 32 mm to 18 mm and with the gained experience with the flexible taper in SLS, the undulator length can be increased by 50% while the length of the short straights remains basically unchanged.

This requires new undulators for the PX I, PX II, microXAS and cSAXS beamlines. Inspired by concepts for the Horizon2020 compact light source project and a novel design for the compact HERO modulator for the SwissFEL Athos beamline, a modular undulator design is also envisaged for the cryo undulators. The basic concept is that instead of using a bulky and heavy support structure and a separate welded vacuum chamber, several short modules modules machined with high precision combine the functions of the vacuum chamber and the support unit. These modules will then be put on girders similar to the magnets in the arcs, as shown in Figure 2.3. Each module has its own drive unit which can act independently. The design profits from the smaller forces due to the reduced pole width. This also offers the more advanced possibility to further reduce the magnetic forces by adding side magnets with counterbalancing forces [3]. It is planned to incorporate the compensation for SLS 2.0 into the hybrid structure, so that it has the identical gap dependency and might work over the entire gap range. The drive systems can be either motor driven, or with hydraulic driven posts.

This concept could revolutionise the fabrication of undulators. Because of the modularity, any length can be fabricated without becoming bulkier or using ever stronger drive systems.

For cryogenic undulators, it is known that the shimming procedure to optimise the phase errors can be performed at room temperature [4]. After cooling down to liquid nitrogen temperature, the phase correction settings for the individual magnets are preserved, but the long-range column fixations need to be adjusted. For this, either additional differential screws are implemented or shims have to be added. In the concept proposed here, the long-range column correction can be integrated into the automated magnet correction system, developed by PSI and used with high success for the SwissFEL hard- and soft-x-ray undulator series production [5].

Another benefit to the alternative of refurbishing the existing support structures is that the available time for the work is not limited to the “dark period“. The vacuum system would need to be replaced, the cryo-system integrated, and the drive system replaced as the installed VME based electronics are at their end of life without commercially available spare parts.

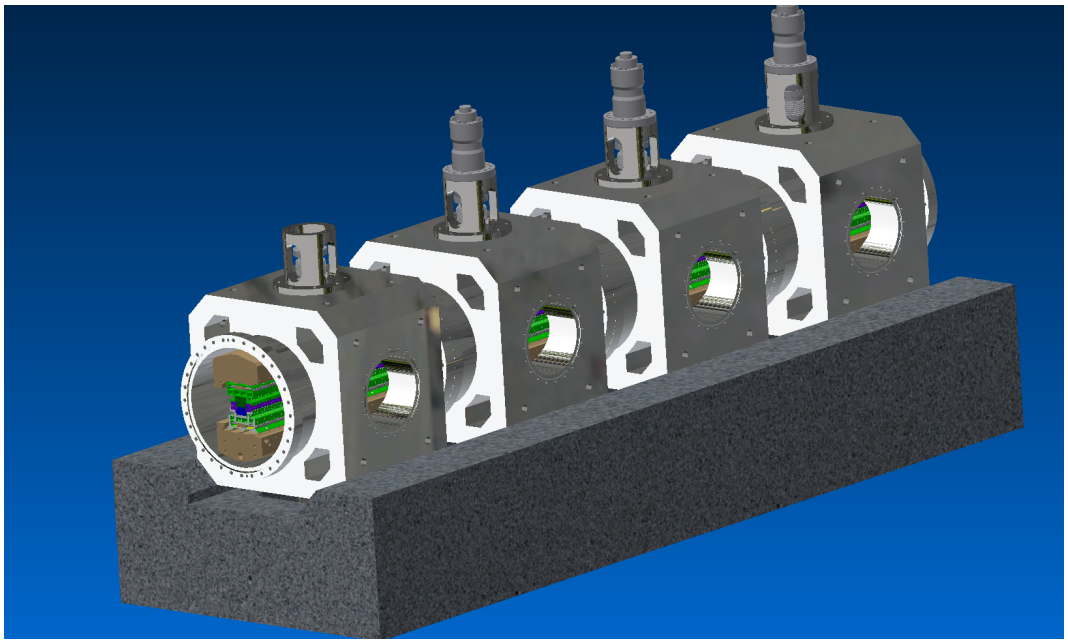

Figure 2.3: Design study for a new compact and modular in-vacuum undulator. The machined modules combine vacuum chamber and support structure. The load will be distributed over several drive units.

2.2.2 High-temperature superconducting undulators

For PrFeB-based CPMUs, period lengths as small as 12 mm might be possible. Even smaller periods could be achieved with high-temperature superconducting undulators (HTSUs), which will also profit from small effective horizontal gaps.

The HTSU is a real R&D project, launched not just for the second hard x-ray undulator line at SwissFEL, but would also be ideal for the extension of the photon-energy range of SLS 2.0, in particular for I-TOMCAT, but possibly also for the Materials Science beamline [6–10].

A first ten-period mock-up was tested in August 2019, and initial results have been extremely encouraging. The principle of the "HTSU10" is a staggered array of high-temperature superconductor (HTS) blocks installed in a cylindrical superconducting solenoid coil (see Figure 2.4). The coil will be able to produce fields of up to 12 T, which can be trapped by the HTS blocks. The electron trajectory is located in the fringe field of these HTS blocks, which can thus assume values of 2 T or even more at gaps of 4 mm. In contrast to CPMUs, a thermal shield is required due to the heat produced by synchrotron radiation and wakefields, so small gaps are also of very high interest.

This R&D project is supported by the CHART (Swiss Accelerator Research & Technology) program. Collaborations with Cambridge University, Fermilab, and SPring-8 have been established. The HTS technology is also part of the LEAPS infrainnov program with close collaboration of ESRF.

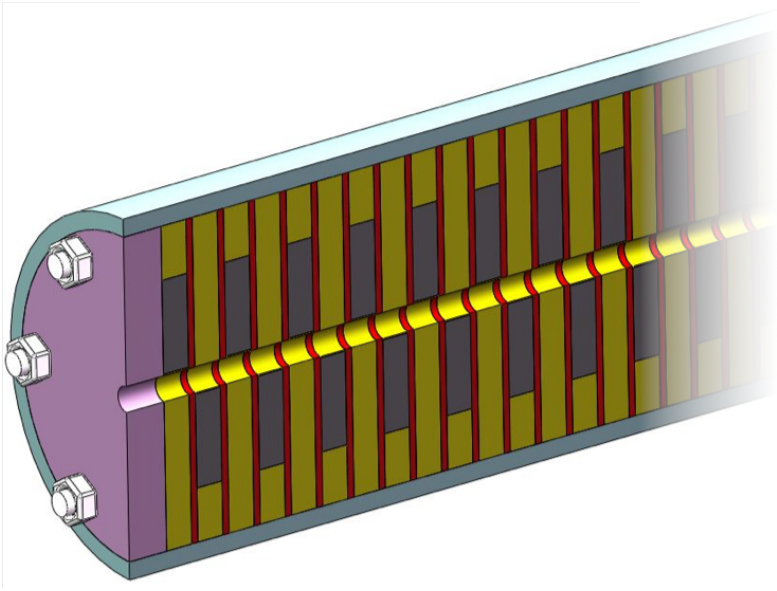

Figure 2.4: Vertical section through the U10 HTSCU prototype planned for the I-TOMCAT beamline and possibly also the Materials Science beamline. The HTSC elements are staggered and shown in grey.

2.2.3 Enhanced spectral profiles at DLSRs

In the hard x-ray regime, the effective source size at DLSRs, while being an order of magnitude smaller than at third-generation facilities, still dominates over the diffraction-limited size associated with single-electron emission.

Figure 2.6 compares the brilliance of the same undulator at SLS with that at SLS 2.0, assuming a 40 times smaller total horizontal emittance. In addition to the expected 40 times increase in peak brilliance, the SLS 2.0-spectrum is substantially cleaner – the off-axis-radiation lobes seen on the low-energy flanks of the spectral peaks for the third-generation source are completely absent in the DLSR spectrum. This is because the order-of-magnitude smaller horizontal width of the electron beam (approximately 10 μm), is slowly approaching the oscillation amplitude A produced by the magnet array. This means that an observer on axis at the SLS 2.0-undulator will see a much smaller contribution from emission from the off-axis electrons which produce the low-energy lobes in the spectra.

Many experiments (such as at I-TOMCAT, the PX beamlines, and cSAXS) do not always require the relative bandwidths of the order of 10^{-4} provided by crystal monochromators, and would profit from using the entire flux from any given harmonic. The relative bandwidth of the mth undulator harmonic is $1/mN$, whereby N is the number of undulator periods. For the lower harmonics this is of the order of 0.005 to 0.01; for higher harmonics, the relative bandwidth does not drop as steeply as $1/m$, as gradually, the off-axis contributions do begin to leak in to the peaks, causing them to broaden marginally. Nonetheless, the spectral quality remains sufficiently high to use the entire flux of any given harmonic for small-period undulators at SLS 2.0. Note, however, spectral filtering is still required

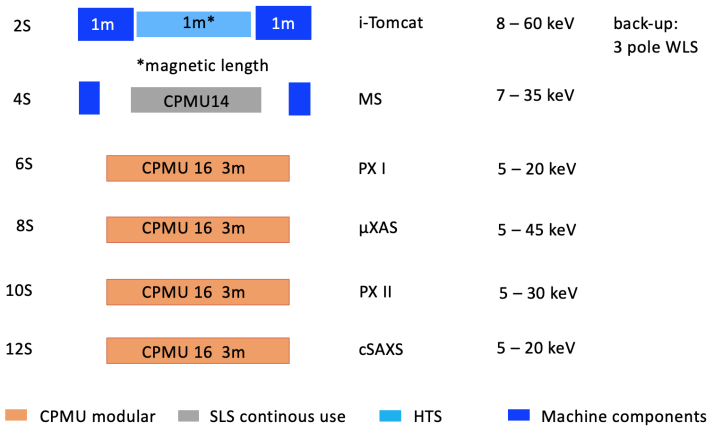

Figure 2.5: While in SLS, Straights 2 and 8 are used to host RF cavities for acceleration, in SLS 2.0 all six short straight sections will be equipped with hard x-ray undulators, which are optimized with small β-functions to effectively convert the small emittance in a high brilliant photon beam. In Straight 2 the HTS undulator with 10 mm period is surrounded by two kicker magnets used for improved injection schemes.

to remove the other harmonics. This can be effectively achieved using multilayer monochromators or, in some instances, refractive optics such as CRLs or prisms.

2.3 Superbends

SLS 2.0 will also be equipped with superbends to generate higher flux and brilliance at higher photon energies. While at SLS, the superbends are normal electromagnets providing a field of 2.9 T, superconducting dipoles will be installed at SLS 2.0, with longitudinal gradient fields with central maximum values of 5 T. Development of the superbends is provided by experts within the Large-Research Facility department's magnet group. In total, three 5-T superbends are foreseen for SuperXAS, Debye, and S-TOMCAT, plus a warm 2-T superbend for PX III.

Compact designs are required and in-vacuum designs with gaps of 34 mm or even smaller are proposed with NbTi wires for a 5-T version. For more challenging higher-field versions, an R&D project based on HTS has been started, which is also supported also by the CHART program. The increase in brilliance with respect to SLS is significant and an energy range potentially up to 100 keV can be covered with these sources.

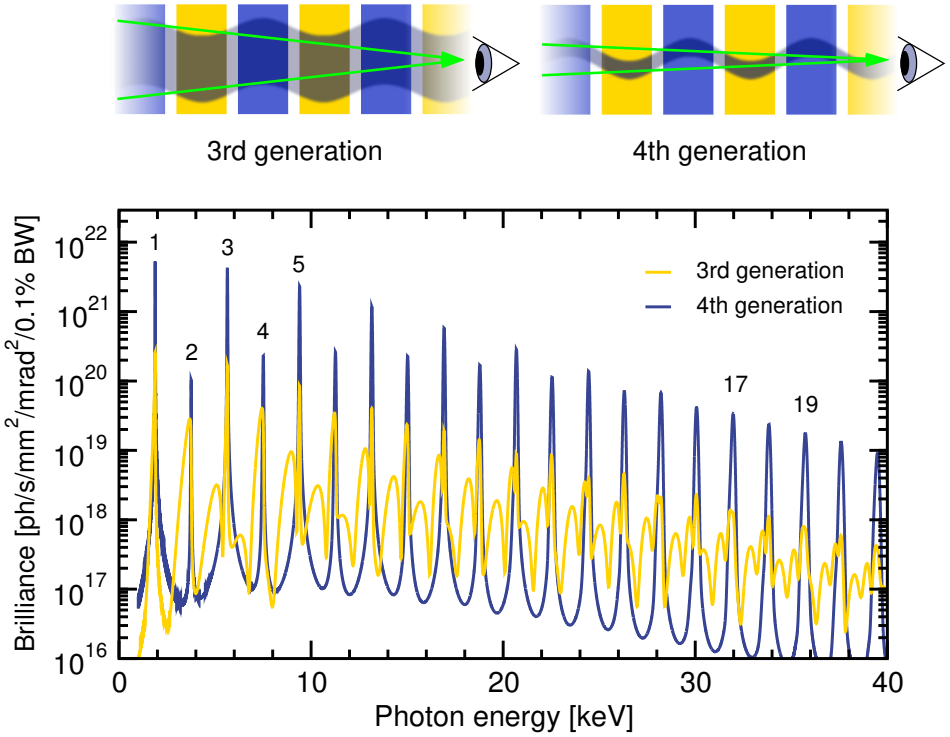

Figure 2.6: Comparison of the brilliance of undulator spectra at SLS and SLS 2.0. Top: the lateral extent of the electron beam passing through an undulator at third-generation facilities is approximately two orders of magnitude larger than the oscillation amplitude A, while at DLSRs, it might only be approximately $10A$ or less. Bottom: as a consequence, an observer on axis will 'see' less off-axis radiation, thereby suppressing the lobes on the low-energy flanks of the main spectral maxima. Note also the enhanced brilliance at the spectral peaks for SLS 2.0. Both simulated spectra were generated for a U12 undulator (that is, $\lambda_u = 12$ mm) containing 120 magnet periods, for $K = 1.6$, 400 mA, and a storage-ring energy of 2.4 GeV.

2.4 Soft x-ray and VUV undulators

A new type of undulator has been developed for the SwissFEL Athos beamline, the APPLE X design, which combines an identical photon-energy range in all major polarization modes, namely LH, LV and circular, with full symmetry over the entire range [11]. This is achieved by using individually controllable radial instead of vertical plus longitudinal movements for all four magnet arrays. The radial design is suited to small, round, vacuum chambers used in FELs or other single-pass accelerators, and also to DLSRs such as SLS 2.0. By exploiting the latest grade of permanent-magnet material, the period length can be significantly reduced *and* the K-value increased, so that the desired photon-energy range can be covered by the fundamental harmonic alone. Undulators with a large number of periods and high K-values are problematic because of the associated high and variable heat load.

With the recent development of the K-not APPLE design with an additional subharmonic field

component (second period 3× longer than that of the main undulator period) it is now possible to shift the higher harmonics from the electron-beam axis to larger angles, which can then be blocked in the front end [12,13]. This K-not design is compatible with the APPLE X design: The two periodicities are implemented within a superperiod of 24 magnets where 8 magnets per period are used for the fundamental period.

A series production of 20 APPLE X undulators, each 2 m long, with period length of 38 mm and, in a modified version, 90 mm is underway for SwissFEL and EUXFEL. This type of undulator is the baseline design also for SLS 2.0. However, as these undulators have a wedge-based drive system, they are not flexible in length. The final layout of the SLS 2.0 medium and long straights allows undulator lengths of 2 m to 4.5 m. Moreover, for the soft x-ray beamlines a modular concept could be beneficial. Figure 2.8 summarizes the possible scenarios. The energy upgrade for SLS 2.0 precludes the continuous use of the existing soft x-ray undulators. Refurbishing the existing undulator supports would also be suboptimal, with several compromises: the two UE56 and the UE54 have only two shift axes which requires different operation modes and they cannot be equipped with remote controlled movers which significantly hinders the commissioning. Only the 3.4 m long fixed gap APPLE II undulator of the ADRESS beamline can be refurbished, which is part of the baseline design for the soft x-ray undulators.

The X-Treme and the SIM beamlines demand fast helicity switching for circular dichroism experiments. SIM uses twin undulators with opposite helicity; with alternating small gap changes a switching rate of about 0.5 Hz is achieved. In an alternative scenario with single undulators, the new hydraulic system will be used for the first time in undulators which combines sub μm precision with high speed and force, so that helicity switching will be comparably fast. The system has been experimentally studied within a master thesis in collaboration with Fachhochschule NordWest Schweiz.

The benefit of the second scenario is higher flux in circular polarization mode because the full undulator length can be exploited. In general, the operation of a single undulator is always preferable because of reduced operating expense for commissioning and the need to periodically recalibrate the two undulator plus phase matcher system.

2.5 Project management

2.5.1 Timeline

Most undulators need to or will be replaced by new devices. This is also of practical considerations, because it allows one to prepare and optimize the undulators before the start of the darktime in Q4, 2023. Three undulators are planned for continued use in SLS 2.0: The CPMU14, the fixed gap APPLE II UE44 and possibly the planar undulator of XIL. The installation of the undulators is foreseen to split into the two shutdowns in 2024 with the back-up wavelength shifter for I-TOMCAT in Straight 2, the reinstallation of CPMU14 for MS in Straight 4, new hard x-ray undulators for PX I, PX II, and cSAXS in Straights 6, 10 and 12, and for the soft x-ray lines and twin undulators for the SIM beamline in Straight 11. In a second shutdown in Q1, 2026 the HTS undulator shall be installed (I-TOMCAT, Straight 2), the μXAS undulator (Straight 8) and the Knot APPLE X undulators for RIXS (3), SX-ARPES (5), and QUEST (9) plus the SLS UE44 (7) and U70 (5).

The high-temperature superconducting undulator will have an elliptical vacuum chamber of rather small dimensions of $3 \times 6\text{mm}^2$. As this is too small to start up the new SLS 2.0 and because the development of the HTS undulator is a high potential but also high risk project, in the first shutdown a wavelength shifter or few period wiggler will be installed instead which allows the I-TOMCAT beamline to start up immediately. The HTS undulator will be installed in the second shutdown.

The development of the four new hard x-ray permanent magnet undulators is planned in two stages. Currently a prototype with two modules of in-vacuum undulators at room temperature is under way. Based on the experience we will decide if we produce the required undulators based on this, continue towards CPMU, or even step back to standard in-vacuum undulator design.

For the soft x-ray undulators, a modular concept shall also be studied. In summer 2021 we have to decide between the 2m long Athos series undulators or the up to 4m long modular supports. For both versions, the Knot scheme will be prototyped for the APPLE X configuration.

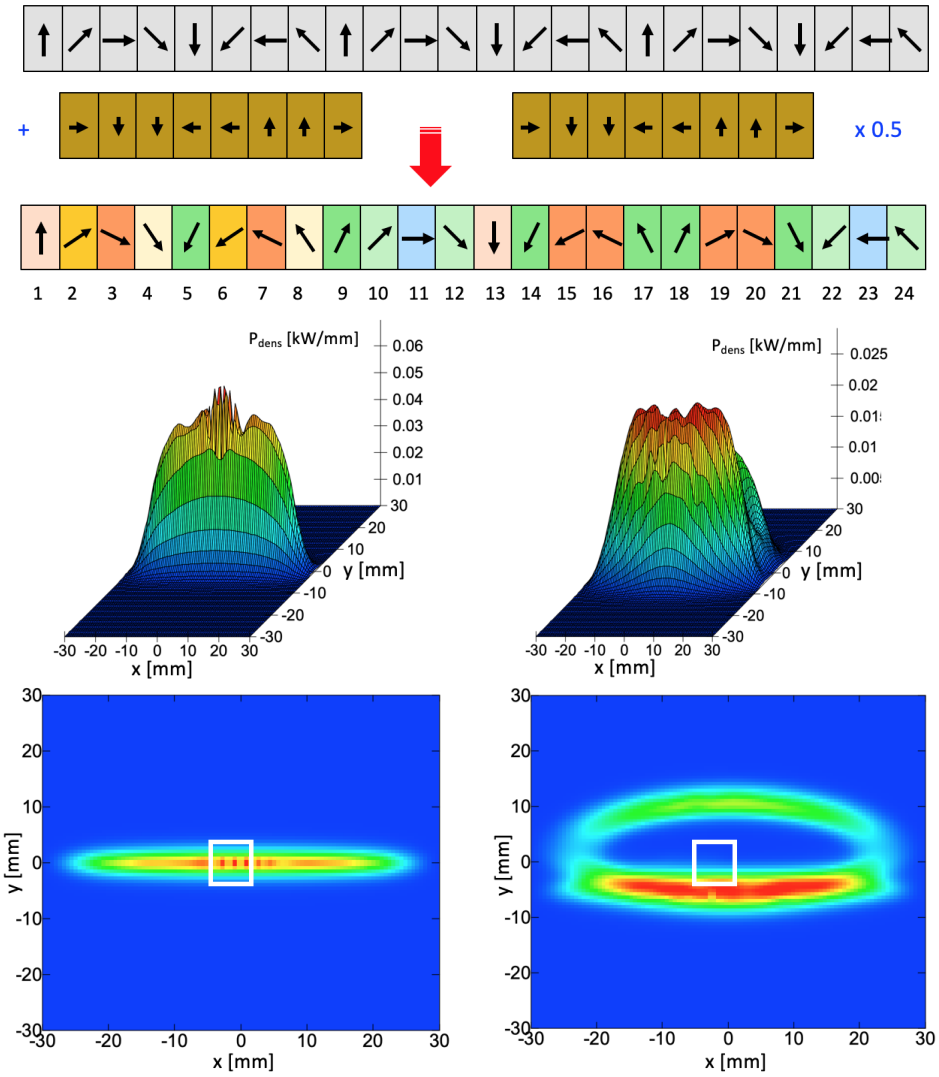

Figure 2.7: Top: Super-period with 24 magnets of a single row in the K-not undulator concept but with a period field from 8 magnets per period. The strength of the superimposed virtual magnets is a free parameter. Best results are found with a 50 % strength of the added field. The colors indicate the 7 different magnetization directions of the magnets. Bottom: Power distribution of the UE90 in periodic and K-not mode at a typical front-end position 13 m away from the source point (i.e. the middle of the undulator). The higher harmonics are emitted off-axis allowing an effective reduction of the heat load within the front-end aperture, marked with the white square. For the VUV undulator the reduction of heat load in K-not mode is a factor of 10, for other soft x-ray undulators the heat load decreases to 60%.

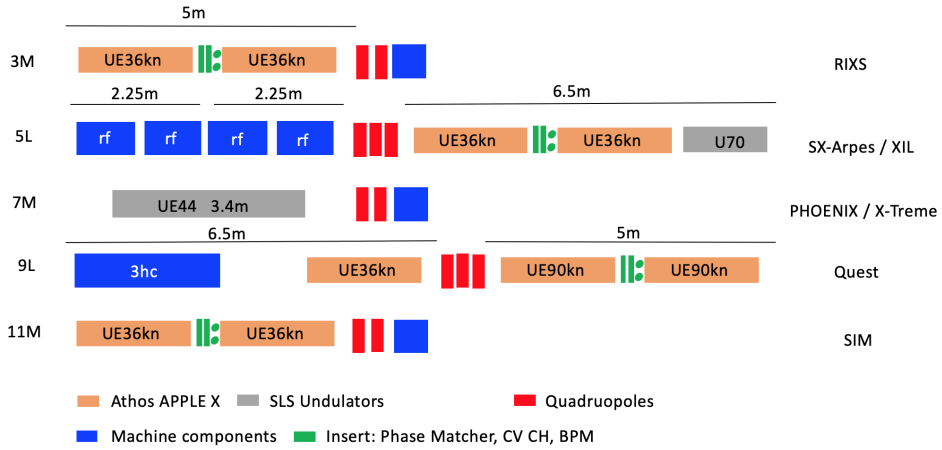

Figure 2.8: Soft x-ray and VUV undulators in SLS 2.0. Medium and long straights are separated by quadrupoles providing length of 5 m and 6.5 m for undulators, respectively. The upstream parts of the long straights cannot be used for undulators and are perfectly used through a rearrangement of the RF acceleration cavities. In the scenario shown here, the 2 m long Athos undulators are used. Knot-type APPLE X undulators will be used with period length of 36 mm and 90 mm, respectively. The fixed gap APPLE II will be used for the combined soft x-ray/tender x-ray beamlines. It is possible that the twin undulators in Straights 3, 5, and 9 are replaced by single units based on a compact and modular concept.

Bibliography

[1] T. Schmidt, M. Calvi, and G. Ingold. Undulators for the PSI light sources. *Synchrotron Radiat. News*, (28(3)):34–38, 2015.

[2] J. C. Huang *et al.* Development of cryogenic permanent magnet undulators at NSRRC. *AIP Conference Proceedings*, (2054):030022, 2019.

[3] R. Kinjo *et al.* T. Tanaka. Insertion devices for spring-8 upgrade project. *Proceedings of IPAC2016*, (IPAC2016):4035–4037, 2016.

[4] M. Calvi, T. Schmidt, A. Anghel, A. Cervellino, S. J. Leake, P. R. Willmott, and T. Tanaka. Commissioning results of the U14 cryogenic undulator at SLS. *Journal of Physics: Conference Series*, 425:032017, 2013.

[5] M. Dalli, M. Calvi, A. Sammut, N. Sammut, and T. Schmidt. Development of a new magnetic measurement bench for in-vacuum undulators. *SN Applied Sciences*, 1:704, 2019.

[6] T. Kii *et al.* Low-temperature operation of a bulk HTSC staggered array undulator. *IEEE Transactions on Applied Superconductivity*, 22(3):4100904–4100904, 2012.

[7] R. Kinjo *et al.* Demonstration of a high-field short-period undulator using bulk high-temperature superconductor. *Appl. Phys. Express*, 6:042701, 2013.

[8] M. Calvi *et al.* A GdBCO bulk staggered array undulator. *Superconductor Science and Technology*, 33(1):014004, 2020.

[9] S. Hellmann, M. Calvi, T. Schmidt, and K. Zhang. Numerical design optimization of short-period HTS staggered array undulators. *IEEE Transactions on Applied Superconductivity*, 30(4):4100705, 2020.

[10] K. Zhang, S. Hellmann, M. Calvi, and T. Schmidt. Magnetization simulation of Rebco tape stack with a large number of layers using the Ansys A-V-A formulation. *IEEE Transactions on Applied Superconductivity*, 30(4):4700805, 2020.

[11] T. Schmidt and M. Calvi. APPLE X undulator for the SwissFEL soft x-ray beamline Athos. *Synchrotron Radiation News*, 31(3):35–40, 2018.

[12] S. Sasaki, A. Miyamoto, and S. Qiao. Design study of KNOT-APPLE undulator for PES-Beamline at SSRF. volume PAC13, pages 1043–1045, 2013.

[13] F. Ji *et al.* Design and performance of the APPLE-Knot undulator. *J Synchrotron Radiat.*, 22(4):901–907, 2015.

Chapter 3

Front ends

David Just and Claude Pradervand

3.1 General strategy

The front-end elements at the SLS have largely been in use for more than a decade and in some instances for about two decades. During this time they have proven to be very reliable and require low-maintenance. It is therefore planned to reuse some of the front-end elements after thorough refurbishment which will include replacement of components subjected to wear, as well as dismounting, cleaning, reassembling and testing all components of each individual front-end element.

The motivation driving this approach is less to reduce costs and effort, rather to stay with a proven, reliable concept. Moreover, it is planned to upgrade some elements which are not subject to a complete redesign. Examples include the use of absolute encoders, which are more user friendly than the currently used incremental encoders; new motor-drive components which will allow better software integration and applications; and new end-switches which fulfil more stringent safety standards.

Nevertheless, many components need to be completely redesigned, due to increased heat load from the new sources associated with higher power densities and smaller beam size. In addition, the footprint of the new lattice differs sufficiently from the original that careful considerations must be made to fit all the needed front-end elements inside the confines defined by the exit ports, the multibend achromats, and the tunnel wall.

3.2 Front-end elements

The front ends at SLS 2.0 vary from beamline to beamline in terms of the implemented elements, desired functionality, and design. However, there is only a limited amount of elements used in the front ends (Figure 3.1), some of which are used for every beamline and others which will be built and tailored to the needs of individual beamlines.

All front ends include one or more water-cooled beam-defining apertures such as beam masks and diaphragms. The main purpose of these elements is to limit the cross-section of the synchrotron beam and to reduce the heat load on subsequent optical elements such as mirrors and monochromators. Additionally, since the outer part of the beam contains lower-energy photons these elements also act

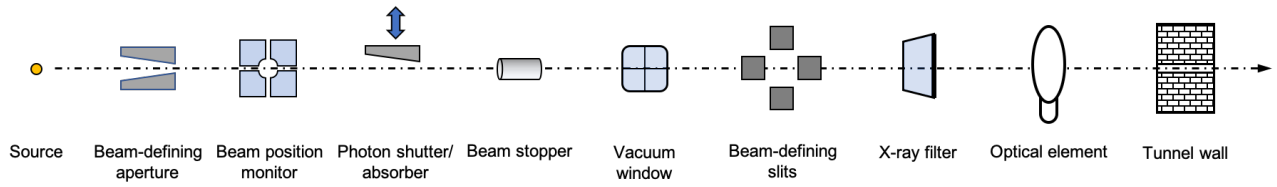

Figure 3.1: Schematic diagram of a typical front end.

as a high pass energy filter for the synchrotron radiation. Since the synchrotron source characteristics and the layout of the beamline (i.e. the distance between the source and first front end elements) change for most beamlines, these water-cooled elements will be completely rebuilt and adapted to the new lattice.

Photon shutters and beam stoppers are used in all beamlines. These two elements work in combination and are, together with the ring wall, the primary safety elements of the front end. In the closed position they absorb the beam to ensure that personnel can safely work in downstream areas outside the ring wall. The photon shutter is water cooled. It absorbs the high-power x-rays emitted by the source. The beam stopper, made from tungsten, absorbs the high-energy Bremsstrahlung radiation. For bending-magnet and superbend beamlines, the two components are combined into one single device, since the power load and power density are much lower than for insertion-device beamlines. These components will be reused from the SLS after refurbishment and upgrade to new safety standards. In some cases we will adapt the design of the photon absorber head to comply with the increased heat load at SLS 2.0.

Currently, for insertion-device beamlines, two tungsten-blade XBPMs (x-ray beam position monitors) are installed in each front end at SLS. For SLS 2.0, we plan to continue to use one of these and to replace the other with a different XBPM technology. The purpose of these XBPMs will be to analyze the x-ray beam position and to provide feedback to the machine in order to optimize the electron-beam stability.

To be able to reuse the tungsten-blade XBPMs, they need to be refurbished and mechanically modified to the new reduced beam sizes, particularly in the horizontal plane. In order to find the best technologies for the second XBPM, a working group was established. Different beamlines will require different solutions: while for hard x-ray beamlines a CVD (chemical vapor deposition) diamond or SiC quadrant XBPM are good options, these elements would absorb too much flux for soft x-ray beamlines. A hybrid concept in which a SiC XBPM has a central opening and only the outside halo of the beam is intercepted (as in tungsten-blade XBPMs) is presently being investigated as a possible solution for the soft x-ray beamlines.

For bending magnet beamlines, it is not planned to install tungsten-blade XBPMs. Where required and where floor space is available, retractable XBPMs can be installed.

For some beamlines CVD diamond or Be-vacuum windows are installed in the front ends. Where the beam size and the energy range of the new beamline at SLS 2.0 allow, we plan to reuse the same windows after refurbishment. The main purpose of these windows is to separate the UHV vacuum of the accelerator ring from the rest of the beamline and to act as vacuum-protection element in the case

of a vacuum breach downstream of the window. These windows absorb low-energy photons. While in many cases this is desired, in some, the reduced flux at lower energies is problematic. For example, in the case of the PX-III superbend beamline, it is planned to work at lower energies for SLS 2.0 than for SLS, down to 3 keV (see Chapter 15). In this case, the CVD diamond window could be replaced with a Be window or the front end must be completely UHV compatible.

Most beamlines are equipped with slits. The purpose of these slits is to reduce the beam size and to scan the beam with a small aperture in order to obtain the beam profile (pinhole scan or edge scan). Currently, three different slit types are in development for SLS 2.0. For bending-magnet and superbend beamlines, a new set of horizontal and vertical slits is under development, which will avoid the need of a separate vacuum chamber. This goal is primarily driven by the limited floor space for the front ends caused by the new footprint of the SLS 2.0 lattice for certain beamlines.

Currently a set of fast horizontal and vertical slits for soft x-ray insertion-device beamlines is being developed. These slits will be mounted in the existing vacuum chambers and will allow one to perform a complete beam scan within a few seconds. While at SLS, this process may take up to 15 minutes, this increase in speed by well over two orders of magnitude will allow a complete scan each time the gap of the undulator is opened or closed at SLS 2.0. Using the monochromator, energy- and spatially resolved beam profiles will be available to the beamline. For some hard x-ray beamlines, we are developing new slits with improved mechanical stability and enhanced thermal management, driven by the need for better stability both mechanically and thermally associated with the extensive use of the coherent beam fraction at SLS 2.0.

Some beamlines use a set of filters in the front end. The purpose of these is to remove the low-energy portion of the beam and to reduce the heat load on optical elements downstream. Where beam sizes and heat loads allow, it is planned to refurbish and reuse the existing components for SLS 2.0.

A few beamlines also include optical elements such as monochromators and x-ray mirrors in the front end before the tunnel wall. Although these elements are not considered as front end elements, their location inside the tunnel raise substantial space-management challenges because of their relatively large size and the limited floor space available. These issues will be addressed on a case-to-case basis.

Chapter 4

Vacuum Ultraviolet Beamline – Valence Photoionization For Reaction Dynamics

Andras Bodi, Patrick Hemberger, Patrick Ascher, and Christoph Bostedt

In a nutshell

The VUV beamline applies valence photoionization to study chemistry in all states and phases. It strives to understand reaction mechanisms and energetics by revealing elusive and highly reactive intermediates, locating rate-determining transition states, and identifying reaction coordinates with the goal of rational reaction design. Since its commissioning, the VUV beamline has been at the forefront of developing and applying double imaging photoelectron photoion coincidence (i^2PEPICO) spectroscopy to deliver accurate energetics data and as a universal, sensitive, selective and multiplexed analytical tool to reveal reaction mechanisms. Data acquisition approaches, coincidence experiments, and beamline components pioneered at the VUV beamline have inspired research programs at synchrotron radiation sources worldwide.

The SLS 2.0 machine upgrade and beamline optics improvements will benefit the enduring methods development efforts at the VUV beamline. The mass resolution and detection limit will increase by up to an order of magnitude, which will allow for more sensitive experiments to understand reaction dynamics and contribute to research fields ranging from catalysis, energy storage and conversion, combustion, pollution abatement, to questions in astrochemistry.

4.1 Overview

Neutrals, ions, aerosols, and clusters are studied at the gas-phase vacuum ultraviolet (VUV) beamline at SLS 1.0 (Figure 4.1). Photoionization, in particular in coincidence with photoelectron spectroscopy, has proven to be a universal, multiplexed, sensitive, and selective detection method for neutral molecules, which interrogates chemical reactions with high fidelity [1]. The photoelectron spectrum belonging to a cation mass channel provides an isomer-specific fingerprint of the species at hand. The research focus at the VUV beamline originally involved the fundamental understanding of photoionization mechanisms and obtaining high-resolution energetics data [2], and was later broadened to include the isomer-resolved characterization of targetedly prepared unstable and fleeting reactive intermediates [3]. A photolysis experiment now allows us to study kinetics on a μs–ms scale [4]. These advances have led to the study of more complex reactive environments to understand bimolecular systems [5] and map catalytic reaction mechanisms (Figure 4.2) [6–8]. Furthermore, molecular dynamics of elusive species at ps to fs timescale has been investigated in our laser laboratory utilizing UV pump and IR multiphoton probe approaches [9–11]. In preparing this report, we have evaluated the opportunities that novel electron modulation schemes and laser light sources offer to expand the science case of the beamline in the future towards time-resolved experiments with high-repetition rate sources (see Section 4.9). However, within the envelope of the SLS 2.0 upgrade we will first focus on rebuilding and upgrading the bending magnet VUV beamline.

4.1.1 Upgrade motivation

A combination of various upgrade factors will allow us to improve the sensitivity of VUV detection by about a factor of 10 in SLS 2.0. The peak magnetic field in the longitudinal gradient bends (LGBs) is going to be 1.35 T, slightly lower than the current 1.4 T, which shifts the bending magnet spectrum to slightly lower energies. Thanks to the increased energy at 2.7 GeV vs. 2.4 GeV now, the bending magnet will deliver a total of 360 W synchrotron radiation vs. 260 W now for the same acceptance. All in all, we expect an increased VUV flux at the experiment by 15%. More importantly and because of the decommissioning of slicing in SLS 2.0, the space of the current FEMTO hutch could be used to accommodate a longer transfer line (see Figure 4.6). By exchanging the focusing mirror for softer focusing optics and building a 5 m longer transfer line, the usable flux could be doubled in experiments requiring a smaller spot size, *e.g.,* when mass resolution is crucial. Because the vertical spot will also be smaller and the mass spectral peaks narrower, the signal-to-noise ratio will improve by an estimated 50%, too. Combined with experimental improvements already on the way, which will double the sensitivity of coincidence detection, these changes could lead to a lower detection limit for reactive intermediates by as much as one order of magnitude, from 1 ppm to 0.1 ppm [12]. This suffices for the VUV beamline to stay competitive with current and planned vacuum ultraviolet bending magnet and insertion device sources worldwide and to maintain its advantage in chemical analysis for the foreseeable future. Furthermore, the endstation will newly be in a laser hutch, which will allow us to explore novel, time-resolved research avenues without much infrastructural overhead.

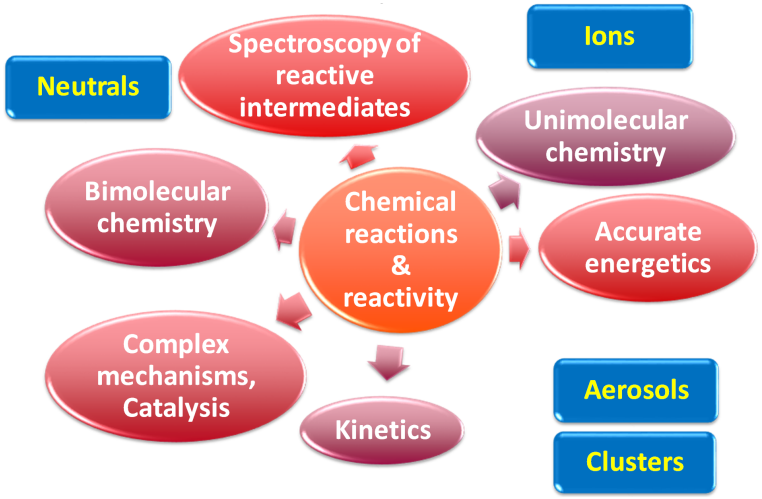

Figure 4.1: Systems (rectangles) and fields (ellipses) of study at the SLS-VUV beamline.

4.1.2 Science impact

The VUV spectral regime corresponds to valence ionization, and as changing valence equals chemical reactions, chemical dynamics is mirrored in this energy range. Valence ionization energies of most stable molecules range between 8 and 15 eV, whereas those of unstable radical intermediates range between 7 and 10 eV. The ionization energy together with the photoelectron spectrum provides an isomer-selective fingerprint for the identification of reactive species in harsh environments [1, 13]. Thanks to the large cross-sections (up to 20 Mb) and collection efficiencies (up to 50%), dilute samples can now be routinely analyzed at our beamline at number densities of less than 10^8 cm^3 (< 1 ppm in a reaction mixture).

The competitive edge of the VUV beamline lies in the development and application of advanced coincidence techniques to enable such endeavors. A limiting factor is sensitivity, which is why crucial reactive intermediates have only recently been detected experimentally [14]. Here, we will benefit from the enhanced flux of the beamline, as well as from the smaller ionization volume. Thus, the detection limit will be ca. 10 times lower than at SLS 1.0 now. This will allow us to broaden the spectrum of chemical processes to study, and unveil the underlying reaction networks in, *e.g.,* catalytic systems [15, 16] at sub-ppm concentrations.

The brilliance of the current BM beamline is slightly above 10^{11} (s mrad^2 0.1% BW)$^{-1}$. In continuous coincidence experiments, a much higher flux and signal rate would inevitably lead to a debilitating false coincidence background, which affirms that the beamline is already well-suited to serve the experimental environment. Looking to the future, pulsed sources, be it harmonic generation by the modulation of the electron beam in the ring or by capitalizing on recent developments in lasers, could lead to a peak brilliance as much as 10 orders of magnitude higher, allowing for new research topics to be pursued at the VUV beamline. As outlined in the outlook in Section 4.9, figures of merit of such a light source would be between synchrotron and free-electron laser sources. The spectral density, the comparatively large average flux, and the peak fluence would enable new, pulsed experiments using

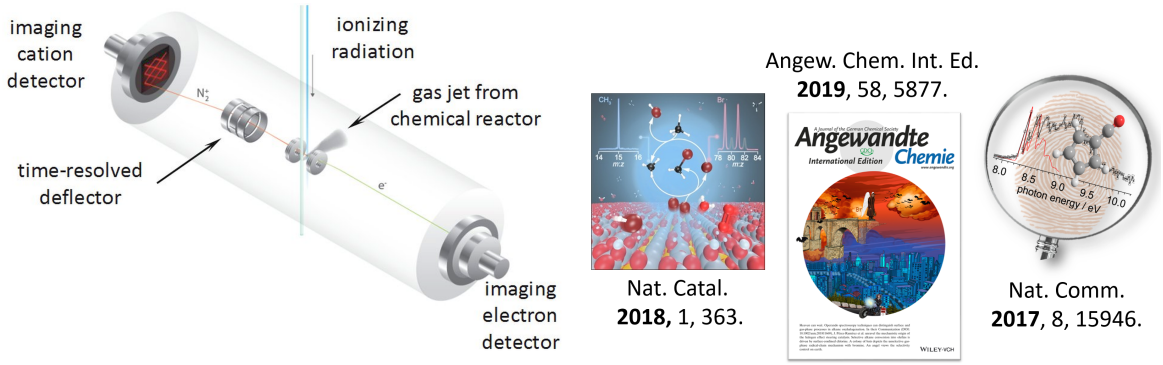

(a) Double imaging coincidence endstation (b) Understanding catalysis

Figure 4.2: Current experimental approach and results at the VUV beamline (see https://www.psi.ch/en/sls/vuv/publications and https://www.psi.ch/en/sls/vuv/scientific-highlights).

the same or slightly modified endstation hardware.

4.1.3 Vacuum ultraviolet sources worldwide

The VUV synchrotron community covers a broad spectrum from analytical and environmental chemistry through astrochemistry, combustion and atmospheric chemistry to the study of fundamental photoionization phenomena in nanoparticles, as well as fragmentation processes in ions and neutrals. Intense ID sources are offered at ALS, Soleil, LNLS, TLS, HLS-II, MAX IV, CLS, and Elettra. Further large-scale VUV sources are available in Japan, India, and Denmark. While a gas-phase coincidence endstation is available at the newly built FinEstBeAMS at MAX IV [17], only Soleil and ALS have capitalized similarly on the analytical capabilities of VUV photoionization as the VUV beamline at SLS so far. Most bending magnet sources focus on absorption studies, whereas ID VUV sources at Elettra or CLS focus on inner valence or core ionization and photoluminescence spectroscopy. The bending magnet VUV beamline at SLS can thus be compared with the undulator-based VUV sources at, *e.g.,* the ALS and Soleil [18]. In general, ID sources profit from higher overall flux and lower divergence. The VUV beamline has attracted users from most continents because of its leading role in the development and application of coincidence techniques. Thus, we will continue pursuing experimental developments to maintain the main competitive advantage of the beamline in the field. Numerous ID sources have emphasized the soft x-ray regime at the expense of tunability towards the soft VUV. A second distinguishing feature of the VUV beamline is therefore the easy tunability to 6–7 eV, which allows us to study the ionization onset energy range of unstable intermediates. Lastly, laboratory-based light sources have become more powerful and versatile recently, as reviewed in Section 4.9. These, normally pulsed sources do not represent direct competition with quasi-continuous synchrotron radiation, but they can be thought of as complementary tools, which we will strive to integrate into the research program at the VUV beamline to further its research program.

4.1.4 Reaction Dynamics Group at SLS

The Reaction Dynamics Group at PSI uses vacuum ultraviolet photoionization (5-30 eV) to study unimolecular and bimolecular reactions relevant in combustion, atmospheric and astrochemistry, catalytic reaction mechanisms, as well as aerosols, clusters and thermochemistry. It develops new reactors and interfaces for the study of free radicals and reactive intermediates with synchrotron radiation and refines spectroscopic methods for isomer-selective detection [19]. A few highlights are given here to illustrate the breadth of systems studied at the VUV beamline.

Reaction mechanisms are driven by free radicals and unstable short-lived intermediates. The in-depth knowledge of their energetics and reactivity are essential when constructing predictive models for reaction networks, but their selective detection is challenging. Intermediates can be generated *in operando* conditions, or specifically and isomer-selectively from carefully chosen precursors using laser photolysis or flash pyrolysis, as is done in ca. 40% of the beamtime at the VUV beamline. The threshold photoelectron spectrum, obtained for a single ion mass channel, reveals the electronic structure, and makes isomer-selective online detection possible in complex reaction mixtures [3].

Aromatic diradicals have a high-spin character and exhibit fascinating properties for a wide range of potential applications from molecular magnets and magnetic organic frameworks through materials science to quantum chemistry. Meta-xylylene is one of the smallest, most interesting, albeit elusive, system. The triplet electronic ground state renders it reactive and called for an innovative approach to prepare it in-situ in a microreactor. Electronic and vibrational insights could then be revealed by measuring its photoelectron spectrum. The results implied that multiplicity change of a meta-xylylene moiety in a substrate could dramatically alter the electronic and magnetic properties of a material without necessarily affecting its structural features [20].

More than a quarter of the proposals for the VUV beamline are catalysis related, thanks to the unique set of interfaces and techniques developed in the group over the years. We must understand reaction mechanisms in detail to move beyond the trial-and-error approach and enable rational catalyst design to improve selectivity and conversion. This is crucial in our quest to convert cheap and abundant biomass, such as lignin, into high value fine chemicals and fuels. Catalysis intermediates in phenol and benzene production were identified using photoionization techniques and by control experiments in lignin catalytic fast pyrolysis [6]. Selective catalytic alkane functionalization to olefins with halogens is a promising avenue for alkane valorization to fully exploit natural gas, a key energy vector in the transition between oil and the renewables era. By measuring radical intermediates and their concentration as a function of reaction conditions, experiments at the VUV beamline have confirmed that surface-confined and gas-phase mechanisms are at play simultaneously [7, 8, 21, 22]. This is fundamentally important when optimizing selectivity and conversion: The choice of the catalyst only affects the surface-confined steps, whereas pressures and temperatures can be used to control the gas-phase processes.

Thus, the research program of the Reaction Dynamics Group is furthering our understanding of fundamental chemical processes in outer space, in the atmosphere as well as in reactive gas-phase environments. By unveiling catalysis mechanisms, it also contributes to applied efforts, *e.g.,* on how to to utilize natural gas as a key energy vector and lignin as a sustainable fine chemical feedstock. Thanks to the increased sensitivity of detection and the new, time-resolved opportunities at SLS 2.0,

the VUV beamline will be able to maintain its cutting-edge chemical dynamics research and expand into new fields.

4.1.5 VUV beamline in the PSI research landscape

The VUV beamline is complementary to the SLS beamline portfolio and unique in terms of its energy range, allowing for valence ionization, and the focus on gas-phase samples. This is also mirrored in the user community, which is quite distinct, thereby expanding the user base of the SLS. A notable exception is the study of heterogeneous catalysis, in which gaseous sampling affords us further insights into the reaction mechanism than attainable by surface-sensitive techniques alone, such as x-ray absorption spectroscopy.

4.2 Source

The increased detection sensitivity is thanks to the new machine, softer focusing optics, which leads to smaller spot size in the ionization volume, and endstation upgrades. First, we will profit from higher VUV flux in the bending magnet spectrum of the upgraded machine. The source characteristics of the SLS 2.0 bending magnets in the VUV are summarized in Figure 4.3. Because of the 300 MeV higher electron energy, we expect an increased heat load on the x-ray absorber. Combined with the slightly lower magnetic field and assuming an unchanged, 8×4 mrad^2 ($h \times v$) acceptance of the beamline, the overall effect is a somewhat higher VUV flux, predominantly in the high-energy range. For most intents and purposes, the BM source characteristics will not change significantly in the VUV range due to the machine upgrade. Currently, the beamline is found on the X04DB port, as the X04DA axis is occupied by the laser incoupling line of the FEMTO slicing project. Because slicing became obsolete after the commissioning of SwissFEL, and its host, the μXAS beamline, is moving out from straight 5, the VUV beamline can move to the central bending magnet in the SLS 2.0 machine, *i.e.,* to X04DA.

4.3 Front end

The front end setup is shown in Figure 4.4. In SLS 2.0, the synchrotron ring will become rounder, which, by definition, decreases the space available upstream the shielding wall. Because of the shift from the X04DB port to X04DA, the distance to the tunnel wall will decrease by ca. further 0.5 m. As shown in Figure 4.5, the space gained by removing the FEMTO laser incoupling helps markedly to accommodate all front end components, but it is probably not sufficient in itself. It is likely that the absorber will have to be redesigned, and we may have to install movable diaphragms in the transfer line to tune the flux instead of the front end slits. These changes will allow us to maintain the large, 8×4 mrad^2 ($h \times v$) acceptance of the beamline while shortening the front end.

Currently, the x-ray blocker (6 in Figure 4.4) blocks ± 0.1 mrad of the beam center vertically and absorbs most of the heat load. If its position is unchanged at the tunnel wall, it will be ca. 10% closer to the source point. In order to maintain the blocked angle, the x-ray blocker will have to be

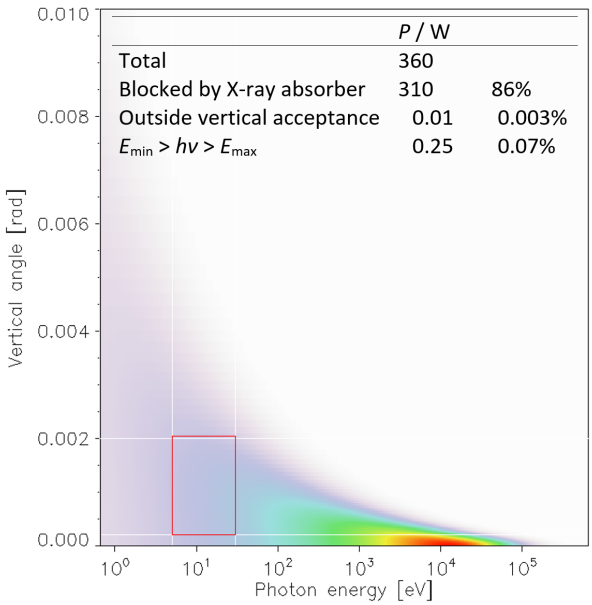

Figure 4.3: Bending magnet spectral characteristics in SLS 2.0 assuming 2.7 GeV energy, 8×4 mrad^2 ($h \times v$) acceptance and 1.35 T magnetic field. The red rectangle indicates the working range of the VUV beamline.

moved downstream or made slimmer. Additionally, it will absorb 70 W more heat load because of the increased ring energy.

4.4 Optics

The current beamline setup is ideally suited to mid-resolution ($\Delta E/E \approx 10^{-3}$) valence photoionization studies from the ionization onset to more than 20 eV. It consists of a collimating mirror, a grazing incidence plane grating monochromator and a focusing mirror [23]. However, the focus is bound to be in the rare gas filter [23], which is used to filter out higher harmonics and relies on multiple stages of differential pumping. The distance from the focus to the ionization volume is difficult to reduce to less than 50 cm in photoionization experiments, and refocusing would entail large losses in photon flux. Before addressing this issue, the beamline will be rebuilt in its current form at its new location X04DA (Phase 1) immediately after the dark period, to serve the user community as quickly as possible.

Afterwards, in Phase 2 of the upgrade, we intend to change the optical characteristics of the beamline to allow for a smaller spot size in the ionization volume. This is the second major contributor to the enhanced experimental capabilities of the VUV beamline in SLS 2.0, as it will improve signal-to-noise ratios while at the same time increasing the useful flux in the experiment. We will exchange the focusing mirror to one with a longer focal length, 12 m to 17 m, to decrease the divergence of the beam. Because of the larger spot size in vertical focus, ca. 400 µm instead of 300 µm, the photon energy resolution is going to be ca. 30% lower. However, this will be compensated by the smaller spot

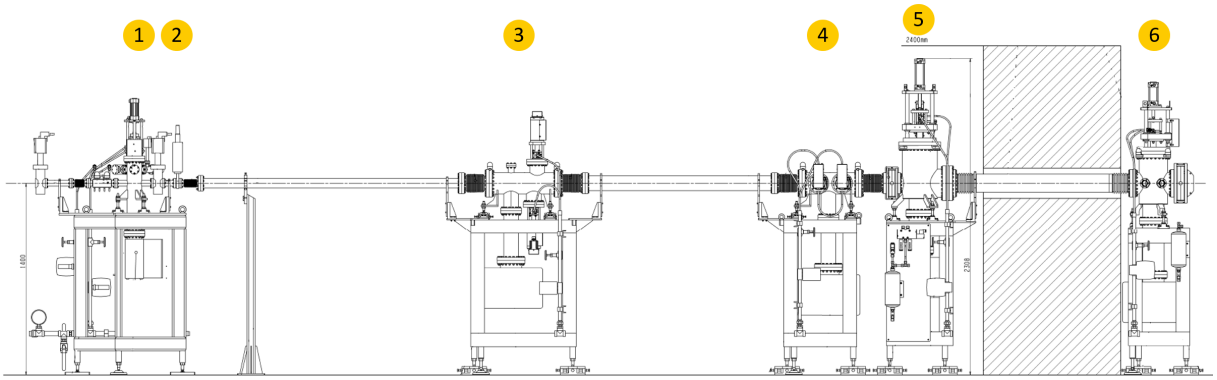

Figure 4.4: Current front end layout: (1) absorber, (2) fast valve, (3) vertical slits, (4) horizontal slits, (5) shutter, (6) x-ray blocker after the shielding wall.

size in the experiment, allowing for a higher dynamic range and mass resolution in mass spectrometry experiments.

4.4.1 Mirrors

The toroidal collimating (M1) and focusing (M2) mirrors have a grazing incidence angle of 12° and a focal distance of 12 m [23]. Their active area is comparable, 218×94 and 270×95 mm^2, respectively. M1 is internally cooled, has Pt reflective coating, a Cr binding layer and is made of Cu. In contrast, M2 is made of Herasil 3. In Phase 2, M2 will be replaced by a softer focusing mirror and the transfer line lengthened to allow for a smaller spot size in photoionization experiments.

4.4.2 Monochromator

We currently use an in-house developed, turntable-style grazing incidence plane grating monochromator [24] with a blazed (150 grooves/mm for high-flux experiments below 12 eV) and two laminar gratings (600 and 1200 grooves/mm for studies in the 7–16 and 11–30 eV ranges, respectively). The grating is the only moving optical element during an energy scan with constant deviation angle of $2\Theta = 130.9°$. The beamline is optimized for the 6–30 eV energy range, but delivers light with varying intensity and a progressively lower resolution up to 100 eV. Normal incidence monochromators offer better higher order suppression, but have a much lower reflectivity. As the gas filter is proven to deliver superior higher order suppression, the monochromator is well-suited to the beamline as is and will be kept unchanged.

4.4.3 Filters

Normal and, in particular, grazing incidence monochromators alone provide insufficient high-harmonic suppression. VUV beamlines operate differentially pumped rare gas filters [25] or employ thin films [26] to remove higher order radiation from the grating. The gas filter at the current bending magnet beamline achieves 10^6 suppression above the rare gas ionization energies with the help of a 10 cm gas

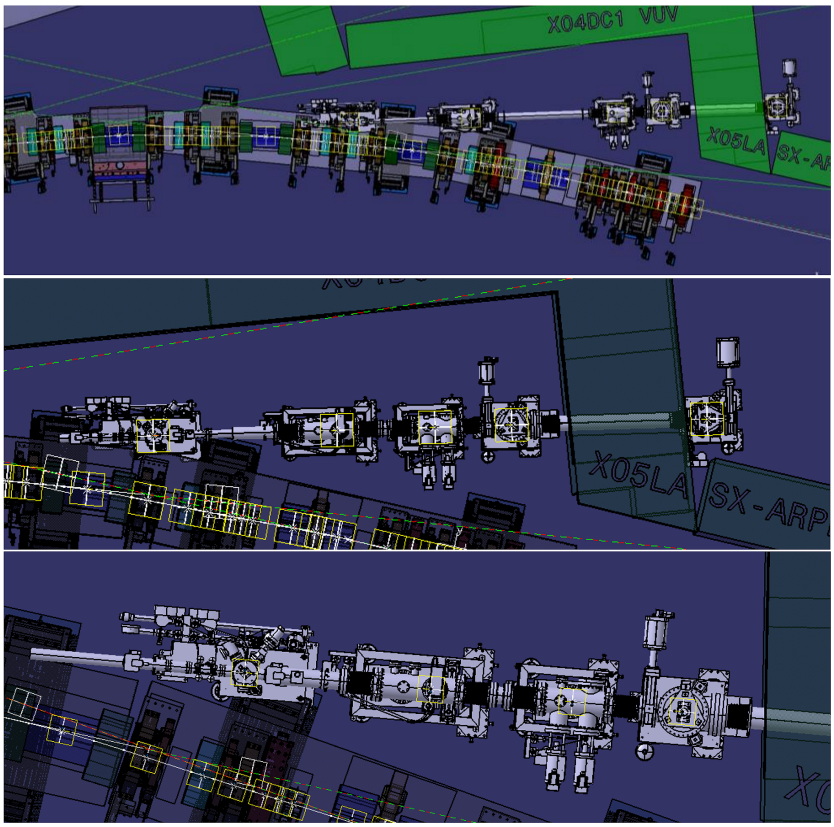

Figure 4.5: Repositioning the current front end components. Top: Shifting all components to X04DA and moving the horizontal slits and the shutter upstream to avoid tunnel wall collisions. Middle and bottom: compacting the front end to minimize collisions using the current components.

cell operated at 10 mbar and allows us to maintain UHV conditions ca. 1 m upstream from there [23]. This was the first rare gas filter with a large acceptance of 8×4 mrad^2 ($h \times v$), which allows for its use at a bending magnet source, and has since been replicated at the Hefei and MAX IV synchrotrons. However, it can only provide monochromatic radiation below 21.5 eV, the ionization energy of neon. Thanks to the higher flux in the EUV range at VUV-SLS 2.0, there may be renewed interest in monochromatized light above 20 eV. If so, we will evaluate and commission thin film filters, similar to those used at the FinEstBeaMS beamline [27].

4.5 Endstations

Together with the higher bending magnet VUV flux and higher useful flux, due to the revised optics and smaller spot size, experimental improvements constitute the third pillar of the VUV beamline upgrade. The setups shown in Figure 4.7 will be used to carry out continuous as well as time-resolved experiments in the isolated phase. The current double velocity map imaging photoelectron photoion coincidence (i^2PEPICO) endstation [4] will be complemented by a pure mass spectromet-

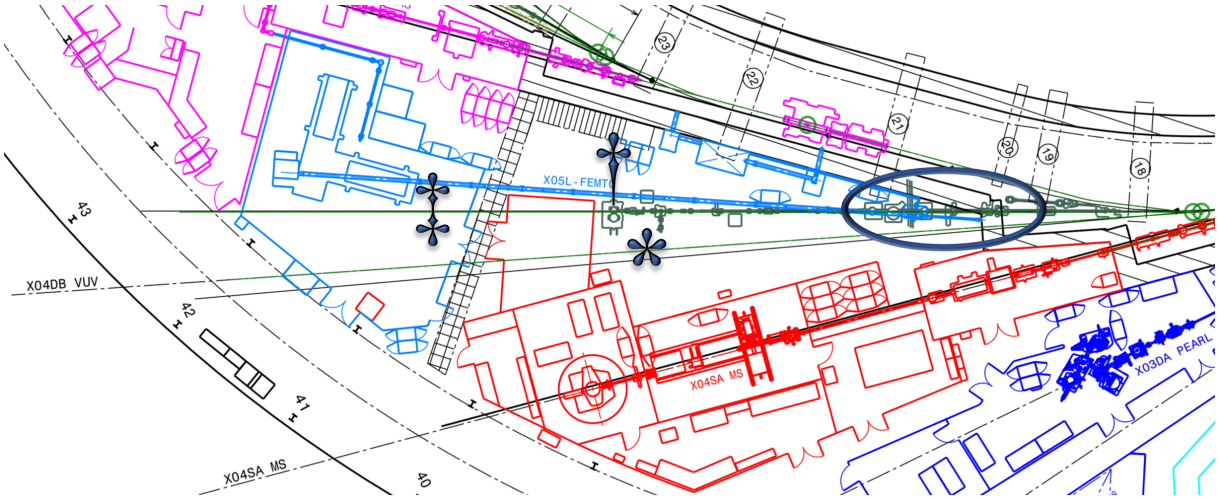

Figure 4.6: The current position of the endstation is marked by a star. The dagger shows the endstation position with the X04DA source. The double dagger shows the endstation position in the current FEMTO hutch after the focusing mirror is swapped for a softer focusing one. The ellipse shows the critical region for tunnel wall collisions.

ric experiment, a multi-hit electron TOF spectrometer, as well as a high mass resolution reflectron coincidence endstation (COREMS). Pure mass spectrometric approaches are neither limited by the false coincidence barrier, nor are they subject to design compromises due to electron imaging. In terms of revealing reaction mechanisms, they will represent a reaction microscope with a much higher magnification than currently available to the user community. These experimental developments are considered and funded independently from the SLS 2.0 upgrade.

4.5.1 Controls and data systems

Off-the-shelf controls and locally developed data acquisition solutions have so far been relied on at the VUV beamline. This is not expected to change. The amount of raw data produced, currently at ca. 4 TB/a is expected to grow by less than an order of magnitude and will remain manageable using standard tools. In the future, we will seek the collaboration with the Laboratory for Non-linear Optics to established pulsed and time-resolved experimental approaches (see Section 4.9).

4.5.2 Sample environment and delivery

The VUV beamline uses a broad set of sample delivery systems and sources stretching from the solid through the liquid to the gas phase. Figure 4.8 summarises the available and future sources.

We utilize established sources to efficiently vaporize solid and liquid samples at temperatures from −20 to 500 °C to produce effusive or supersonic molecular beams with sharp translational energy distributions delivering rovibrational ground state samples into the ionization volume. Reactive and elusive intermediates, such as radicals or carbenes, are routinely produced using hot pyrolysis microreactors

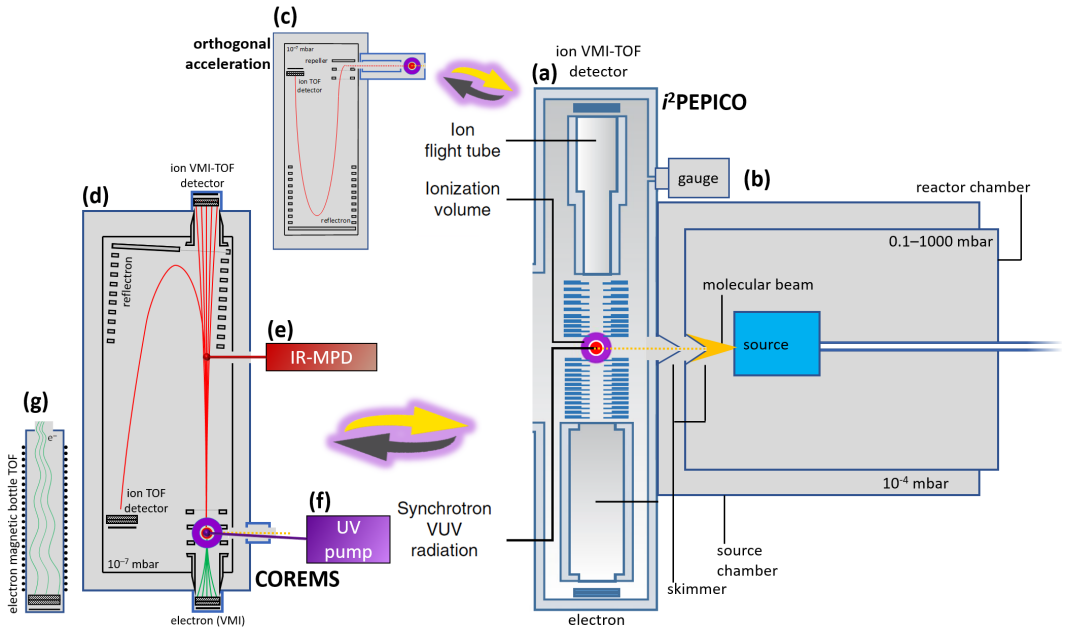

Figure 4.7: Experimental approaches for valence photoionization in the gas phase: (a) PEPICO with ion VMI-TOF for high-resolution studies, (b) versatile source chamber, (c) orthogonal extraction for pure mass spectrometry, (d) coincidence reflectron mass spectrometry approach (COREMS) as ultimate analytical tool with high mass resolution and low energy resolution imaging capabilities. Development opportunities for pulsed experiments include (e) resonance enhanced multiphoton dissociation, (f) UV pump for ps time-resolved experiments, and (g) electron magnetic bottle TOF analyzer for, *e.g.,* multiple ionization.

to obtain spectroscopic fingerprints [28].

Laser photolysis in a quartz glass reactor produces thermally labile species such as peroxy radicals [4]. In addition, their reactivity can be followed on a µs to ms timescale to determine bimolecular rate constants in combustion and catalysis [29]. The reaction networks in nanoparticle flame synthesis can be directly investigated using molecular beam sampling, which minimizes quenching of reactive molecules without disturbing the flame conditions [30]. Recently, we have established pulsed and continuous catalytic reactors to study reaction mechanisms by detecting the key intermediates directly [6]. In time-resolved experiments, these sources may be complemented by laser ablation, which enables efficient production of clusters [31].

Currently we are developing two new sources to address mechanistic questions and intrinsic properties of condensed matter. A vaporisation is being built to sample chemical reactions in the liquid phase directly. This will provide unprecedented insights into industrially relevant chemical transformations. Furthermore, we are planning to commission a sample delivery system to generate an ultrathin free-flowing sheet of water with a thickness of only 10–100 nm. This promising piece of technology will ultimately enable VUV experiments in the liquid phase with applications relevant for biochemistry and biology in the 6–30 eV energy range [32].

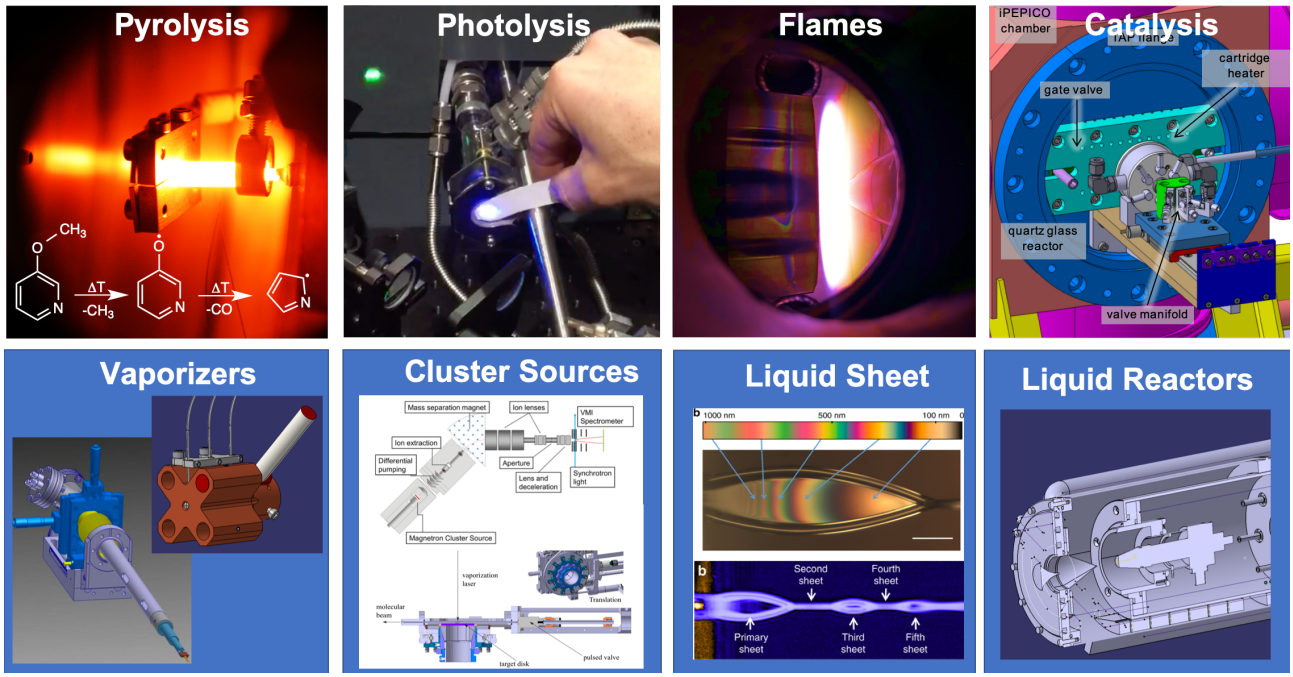

Figure 4.8: Overview of the available and future sources at the (TR-)VUV beamline.

4.5.3 Detectors

We rely on commercially available charged particle time-of-flight and imaging detectors from our suppliers, such as Jordan TOF Products, Inc. and Roentdek Handels GmbH. Photon flux and absorption measurements are performed utilising calibrated IRD photodiodes from Opto Diode. Our current detector portfolio is sufficient for all developments discussed herein.

4.6 IT requirements

Thanks to the increase in flux and also to the possibility of pump–probe experiments in the long run, data acquisition rates are expected to increase by ca. an order of magnitude. However, this will still put the VUV beamline among the less data intensive beamlines at SLS 2.0, and standard approaches will serve IT needs well.

4.7 Timeline

4.7.1 Planning

The VUV beamline will be disassembled and rebuilt in the same overall area in Phase 1, but because of the new source point, it will be shifted downstream by ca. 1 m and 1.2°. Because of the large beam size, the shielding wall will have to be revised. The lead enclosure for the collimating mirror on the outside of the tunnel will have to be enlarged to accommodate the shifted x-ray blocker and collimating

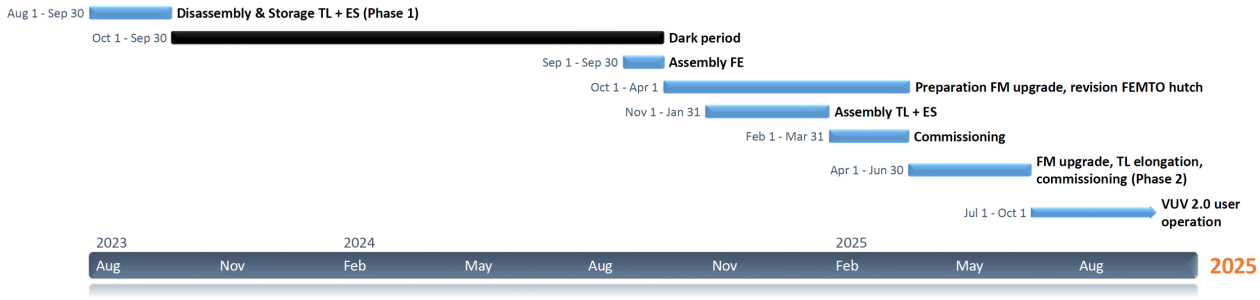

Figure 4.9: Project schedule for the VUV beamline upgrade.

mirror. The remaining beamline components (monochromator, focusing mirror, transfer line) can be moved and reassembled without change. Figure 4.9 summarizes the time line of the construction and assembly of the new VUV beamline in SLS 2.0.

4.8 Risks

Because of the comparable simplicity of the beamline optics and the straightforward albeit sizeable shift in the beamline axis, the VUV beamline upgrade is a low-risk project. Because of the shift in the source point, the front end needs to be shortened significantly. This represents an engineering challenge, with the fallback option of moving the beam defining apertures from the FE to the transfer line.

4.9 Outlook – time-resolved approaches

Although time-resolved studies and (ultra)fast experiments are seldom associated with synchrotron light sources, slicing in the hard x-ray regime was also pioneered at the Swiss Light Source [33]. Seeing how far seeding techniques have evolved recently, innovative time-resolved research could find a home in SLS 2.0 thanks to coherent and echo-enabled harmonic generation. This could be a distinguishing feature of SLS 2.0 among 4^{th} generation light sources, and would contribute to keeping large-scale facilities at Paul Scherrer Institute unique in the world.

Thanks to novel seeding techniques, short and intense light pulses at high repetition rates are now within reach also at synchrotron light sources. We propose to exploit these techniques first in the VUV, then also in the soft x-ray regime to broaden the science case of SLS 2.0 in the long run. Coherent and echo-enabled harmonic generation (CHG and EEHG) produces femtosecond to picosecond pulses at high brightness and repetition rate, putting such light sources between incoherent synchrotron sources and free-electron lasers. Such a light source would allow novel chemical dynamics experiments at all chemically relevant timescales from fs to ms at a new TR-VUV beamline. It would enhance our ability to identify and characterize reactive intermediates and reveal reaction networks far beyond today's state of the art; it would enable the study of molecules and ions with unprecedented spectral resolution, as well as a new class of VUV pump-probe experiments to study molecular dynamics, such

as tautomerization, isomerization, and solvation. A HG-VUV test bed could be conceived for the development of CHG and EEHG at SLS 2.0 and profit from the high spectral intensity; high average flux; and qualitatively higher peak fluence that synchrotron source based harmonic generation offers. Our ultimate goal is to operate a TR-VUV and soft x-ray beamlines in a new EEHG section for chemical and materials science at SLS 2.0.

CHG and EEHG are currently in development at DELTA [34,35]. To our knowledge, the undulator-based VUV beamlines at ALS, SOLEIL and Elettra have not considered harmonic generation related to the upcoming machine upgrades. Thus, a TR-VUV project at SLS 2.0 would likely be a unique light source worldwide, and its competitive edge would be maintained over at least several years because of the intensive machine development needs. Depending on the repetition rate, the TR-VUV beamline could deliver several orders of magnitude more average flux at a far higher peak fluence and spectral density than available elsewhere.

As seen in Table 4.1, commercially available HHG systems as well as laser systems being developed in academia deliver comparable repetition rates and only slightly lower flux than what is available at large scale facilities. We organized a VUV workshop to understand the competitive edge these tabletop systems and free-electron lasers may offer now and in the foreseeable future (see https://www.psi.ch/en/sls/vuv/vuv-workshop-2018 for the program). Large-scale facilities continue to be superior radiation sources overall, as their tuneability, dependability and raw flux are better or higher than that of lab-based alternatives. Nevertheless, there are applications, *e.g.,* in surface sensitive techniques, where laser sources start to be viable alternatives to synchrotrons, particularly at low photon energies. However, even in these areas, the larger tuneability, polarization control, and flexibility of large-scale facilities trump the generally lower funding need for lab-based sources. Furthermore, synchrotrons and free-electron lasers bring researchers together and foster synergies and cross-pollination of ideas in ways that are hard to replicate in laboratories. This was raised as a possible explanation why such light sources may be more productive than tabletop sources even when their specifications are comparable. Furthermore, we could build on synergies among HG projects at PSI from ATHOS to extending HG towards hard x-rays at PORTHOS/SwissFEL.

Alternatively, we could capitalize on the know-how of the Laboratory for Non-linear Optics together with the availability of the FEMTO laser hutch to couple laser-based harmonic generation sources to the experimental environment of the VUV beamline. As shown in Table 4.2, the availability of short VUV pulses would open up new avenues in reaction dynamics research irrespective of the photon source. These developments are foreseen after the SLS 2.0 upgrade has been completed and will ensure that the VUV science at PSI and its application to chemistry problems remain competitive for decades to come.

4.10 Concluding remarks

We would like to acknowledge the contributions of David Just and Andreas Streun regarding the bendling magnet upgrade. Sven Reiche, Eugenio Ferrari, Bernard Riemann, Volker Schlott, Andreas Streun, Thomas Schmidt, Marco Calvi, Terence Garvey, Uwe Flechsig, Ulrich Wagner, Adrian Cavalieri, Yunpei Deng, Adriano Zandonella, Nicholas Plumb, Milan Radovic, Ming Shi, and Phil Willmott helped us explore state-of-the-art time-resolved approaches and contributed to the outlook.

	$h\nu$ / eV	lg (flux / s^{-1})	Rep. rate	Pulse t	FWHM / meV	Pulse E
HHG						
KMLabs RAEA	40	13	25 kHz	15 fs	120	<5 nJ
HP + Xuus[1]	20	13	30 kHz	15 fs	120	3 nJ
CLF Artemis[2]	30	9	1 kHz	30 fs	100	9 pJ
Cavity enhancement[3]	40	11	88 MHz	100 fs	65	20 fJ
High rep. rate OPCPA[4]	22	12	500 kHz	20 fs	110	20 pJ
FEL						
FERMI FEL-1[5]	12.4–65	17	50 Hz	50–100 fs	<100	100 µJ
DCLS[6]	8–24	16	50 Hz	500 fs	<100	40 µJ
ELBE[7]	5–25	21	<5 MHz	200 fs	<100	30 µJ
EEHG S.R.						
long pulses	10	14	10 kHz	1 ps	<2	80 nJ
high rep. rate	100	12	100 kHz	100 fs	<100	1 nJ

Table 4.1: Comparison of table-top HHG, FEL and EEHG synchrotron radiation, in part compiled by Yunpei Deng. [1]Communicated by Nicholas Plumb, [2]https://www.clf.stfc.ac.uk/Pages/XUV-beamlines.aspx, [3]Corder et al. [36], [4]Puppin et al. [37], [5]https://www.fels-of-europe.eu/fel_facilities/x_ray_facilities/fermi/, [6]Qiang Gu, Tenth International Workshop on High-Gradient Acceleration, HG2017, [7]pending proposal, according to private communication with Pavel Evtushenko.

	Spectral intensity	Average flux	Peak fluence
Value	$\frac{\Delta E}{E} \approx 10^{-5}$ @ 20 eV (ps coherent pulse)	10^{13-15} s^{-1} @ 10 eV (1 − 100 kHz rep. rate)	10^{25} $s^{-1}mm^{-2}$ @ 10 eV
Edge	10^3 over SOLEIL	10^{3-4} over SLS 1.0, 10^{1-2} over best available	Same number of photons in one pulse as in 1 s now in a 10^5 smaller focus
Case	Rydberg atoms, molecules, and ions	Dilute systems, chemical dynamics and reaction networks in, *e.g.*, catalysis	VUV-pump–probe experiments; molecular dynamics: isomerization, tautomerization, solvation; excited neutrals

Table 4.2: Three distinguishing features of HG-VUV radiation.

Bibliography

[1] Andras Bodi, Patrick Hemberger, David L. Osborn, and Bálint Sztáray. Mass-resolved isomer-selective chemical analysis with imaging photoelectron photoion coincidence spectroscopy. *J. Phys. Chem. Lett.*, 4(17):2948–2952, 2013.

[2] Andras Bodi, József Csontos, Mihály Kállay, Sampada Borkar, and Bálint Sztáray. On the protonation of water. *Chem. Sci.*, 5(8):3057–3063, 2014.

[3] Engelbert Reusch, Fabian Holzmeier, Philipp Constantinidis, Patrick Hemberger, and Ingo Fischer. Isomer-selective generation and spectroscopic characterization of picolyl radicals. *Angew. Chem. Int. Ed.*, 56(27):8000–8003, 2017.

[4] Bálint Sztáray, Krisztina Voronova, Krisztián G. Torma, Kyle J. Covert, Andras Bodi, Patrick Hemberger, Thomas Gerber, and David L. Osborn. CRF-PEPICO: Double velocity map imaging photoelectron photoion coincidence spectroscopy for reaction kinetics studies. *J. Chem. Phys.*, 147(1):013944, 2017.

[5] Johan I. M. Pastoors, Andras Bodi, Patrick Hemberger, and Jordy Bouwman. Dissociative ionization and thermal decomposition of cyclopentanone. *Chem. Eur. J.*, 23(53):13131–13140, 2017.

[6] Patrick Hemberger, Victoria B. F. Custodis, Andras Bodi, Thomas Gerber, and Jeroen A. van Bokhoven. Understanding the mechanism of catalytic fast pyrolysis by unveiling reactive intermediates in heterogeneous catalysis. *Nat. Commun.*, 8:15946, 2017.

[7] Vladimir Paunović, Patrick Hemberger, Andras Bodi, Núria López, and Javier Pérez-Ramírez. Evidence of radical chemistry in catalytic methane oxybromination. *Nat. Catal.*, 1(5):363–370, 2018.

[8] Guido Zichittella, Matthias Scharfe, Begoña Puértolas, Vladimir Paunović, Patrick Hemberger, Andras Bodi, László Szentmiklósi, Núria López, and Javier Pérez-Ramírez. Halogen-dependent surface confinement governs selective alkane functionalization to olefins. *Angew. Chem. Int. Ed.*, 58(18):5877–5881, 2019.

[9] M. Steglich, G. Knopp, and P. Hemberger. How the methyl group position influences the ultrafast deactivation in aromatic radicals. *Phys. Chem. Chem. Phys.*, 21:581–588, 2019.

[10] Y. Z. Liu, G. Knopp, P. Hemberger, Y. Sych, P. Radi, A. Bodi, and T. Gerber. Ultrafast imaging of electronic relaxation in o-xylene: a new competing intersystem crossing channel. *Phys. Chem. Chem. Phys.*, 15(41):18101–18107, 2013.

[11] P. M. Mayer, D. Staedter, V. Blanchet, P. Hemberger, and A. Bodi. Comparing femtosecond multiphoton dissociative ionization of tetrathiafulvene with imaging photoelectron photoion coincidence spectroscopy. *J. Phys. Chem. A*, 117(13):2753–2759, 2013.

[12] Thomas Bierkandt, Patrick Hemberger, Patrick Oßwald, Markus Köhler, and Tina Kasper. Insights in *m*-xylene decomposition under fuel-rich conditions by imaging photoelectron photoion coincidence spectroscopy. *Proc. Combust. Inst.*, 36(1):1223–1232, 2017.

[13] P. Hemberger and A. Bodi. Photoelectron photoion coincidence spectroscopy to unveil reaction mechanisms by isomer-selective detection of elusive molecules: From combustion to catalysis. *Chimia*, 72:227–232, 2018.

[14] J. D. Savee, E. Papajak, B. Rotavera, H. Huang, A. J. Eskola, O. Welz, L. Sheps, C. A. Taatjes, J. Zador, and D. L. Osborn. Direct observation and kinetics of a hydroperoxyalkyl radical (QOOH). *Science*, 347(6222):643–646, 2015.

[15] Feng Jiao, Jian Li, X. Pan, J. Xiao, H. Li, Hao Ma, Mingming Wei, Yang Pan, Zhongyue Zhou, M. Li, Shu Miao, Jian Li, Yifeng Zhu, Dong Xiao, Ting He, Junhao Yang, Fei Qi, Qiang Fu, and Xinhe Bao. Selective conversion of syngas to light olefins. *Science*, 351(6277):1065–1068, 2016.

[16] Rui You and Weixin Huang. Photoionization mass spectrometry for online detection of reactive and unstable gas-phase intermediates in heterogeneous catalytic reactions. *ChemCatChem*, page cctc.201901639, 2019.

[17] Ivar Kuusik, Mati Kook, Rainer Pärna, Antti Kivimäki, Tanel Käämbre, Liis Reisberg, Arvo Kikas, and Vambola Kisand. The electronic structure of ionic liquids based on the TFSI anion: A gas phase UPS and DFT study. *Journal of Molecular Liquids*, 294:111580, nov 2019.

[18] Daniel Felsmann, Kai Moshammer, Julia Krüger, Alexander Lackner, Andreas Brockhinke, Tina Kasper, Thomas Bierkandt, Erdal Akyildiz, Nils Hansen, Arnas Lucassen, Patrick Oßwald, Markus Köhler, Gustavo A. Garcia, Laurent Nahon, Patrick Hemberger, Andras Bodi, Thomas Gerber, and Katharina Kohse-Höinghaus. electron ionization, photoionization and photoelectron/photoion coincidence spectroscopy in mass-spectrometric investigations of a low-pressure ethylene/oxygen flame. *Proceedings of the Combustion Institute*, (1):779–786.

[19] Patrick Hemberger, Jeroen A. van Bokhoven, Javier Pérez-Ramírez, and Andras Bodi. New analytical tools for advanced mechanistic studies in catalysis: photoionization and photoelectron photoion coincidence spectroscopy. *Catalysis Science & Technology*, 10(7):1975–1990, 2020.

[20] Mathias Steglich, Victoria B. F. Custodis, Adam J. Trevitt, Gabriel DaSilva, Andras Bodi, and Patrick Hemberger. Photoelectron spectrum and energetics of the meta-xylylene diradical. *Journal of the American Chemical Society*, 139(41):14348–14351, 2017.

[21] Vladimir Paunović, Guido Zichittella, Patrick Hemberger, Andras Bodi, and Javier Pérez-Ramírez. Selective methane functionalization via oxyhalogenation over supported noble metal nanoparticles. *ACS Catalysis*, 9(3):1710–1725, 2019.

[22] Guido Zichittella, Patrick Hemberger, Fabian Holzmeier, Andras Bodi, and Javier Pérez-Ramírez. Operando photoelectron photoion coincidence spectroscopy unravels mechanistic fingerprints of propane activation by catalytic oxyhalogenation. *The Journal of Physical Chemistry Letters*, 11(3):856–863, 2020.

[23] Melanie Johnson, Andras Bodi, Lothar Schulz, and Thomas Gerber. Vacuum ultraviolet beamline at the Swiss Light Source for chemical dynamics studies. *Nucl. Instrum. Methods Phys. Res. A*, 610(2):597–603, 2009.

[24] Andras Bodi, Patrick Hemberger, Thomas Gerber, and Bálint Sztáray. A new double imaging velocity focusing coincidence experiment: i^2PEPICO. *Rev. Sci. Instrum.*, 83(8):083105, 2012.

[25] B. Mercier, M. Compin, C. Prevost, G. Bellec, R. Thissen, O. Dutuit, and L. Nahon. Experimental and theoretical study of a differentially pumped absorption gas cell used as a low energy-pass filter in the vacuum ultraviolet photon energy range. *J. Vac. Sci. Technol. A*, 18(5):2533–2541, 2000.

[26] F. M. Quinn, D. Teehan, M. MacDonald, S. Downes, and P. Bailey. Higher-order suppression in diffraction-grating monochromators using thin films. *J. Synchrotron Radiat.*, 5(3):783–785, 1998.

[27] R. Parna, R. Sankari, E. Kukk, E. Nommiste, M. Valden, M. Lastusaari, K. Kooser, K. Kokko, M. Hirsimaki, S. Urpelainen, P. Turunen, A. Kivimaki, V. Pankratov, L. Reisberg, F. Hennies, H. Tarawneh, R. Nyholm, and M. Huttula. FinEstBeaMS - A wide-range Finnish-Estonian Beamline for Materials Science at the 1.5 GeV storage ring at the MAX IV Laboratory. *Nucl. Instrum. Methods Phys. Res. A*, 859:83–89, 2017.

[28] Daniel W. Kohn, Horst Clauberg, and Peter Chen. Flash pyrolysis nozzle for generation of radicals in a supersonic jet expansion. *Rev. Sci. Instrum.*, 63(8):4003–4005, 1992.

[29] D. Schleier, P. Constantinidis, N. Faßheber, I. Fischer, G. Friedrichs, P. Hemberger, E. Reusch, B. Sztaray, and K. Voronova. Kinetics of the a-C_3H_5 + O_2 reaction, investigated by photoionization using synchrotron radiation. *Phys. Chem. Chem. Phys.*, 20:10721–10731, 2018.

[30] P. Osswald, P. Hemberger, T. Bierkandt, E. Akyildiz, M. Kohler, A. Bodi, T. Gerber, and T. Kasper. In situ flame chemistry tracing by imaging photoelectron photoion coincidence spectroscopy. *Rev. Sci. Instrum.*, 85(2):025101, 2014.

[31] B. Visser, M. Beck, P. Bornhauser, G. Knopp, T. Gerber, R. Abela, J. A. van Bokhoven, and P. P. Radi. Unraveling the electronic structure of transition metal dimers using resonant four-wave mixing. *J. Raman Spectrosc.*, 47(4):425–431, 2016.

[32] Jake D. Koralek, Jongjin B. Kim, Petr Bruza, Chandra B. Curry, Zhijiang Chen, Hans A. Bechtel, Amy A. Cordones, Philipp Sperling, Sven Toleikis, Jan F. Kern, Stefan P. Moeller, Siegfried H.

Glenzer, and Daniel P. DePonte. Generation and characterization of ultrathin free-flowing liquid sheets. *Nat. Commun.*, 9(1):1353, 2018.

[33] G. Ingold, P. Beaud, S. L. Johnson, D. Grolimund, V. Schlott, T. Schmidt, and A. Streun. Technical report: FEMTO: A sub-ps tunable hard x-ray undulator source for laser/x-ray pump-probe experiments at the sls. *Synchrotron Radiat. News*, 20(5):35–39, 2007.

[34] Arne Meyer auf der Heide, Shaukat Khan, Gholamreza Shayeganrad, Peter Ungelenk, Carsten Mai, Marc Jebramcik, Nils Lockmann, Mateusz Suski, Raffael Niemczyk, Fabian Götz, Fin Bahnsen, Benedikt Büsing, Svenja Hilbrich, Dennis Zimmermann, and Bernard Riemann. Progress towards an EEHG-based short-pulse source at DELTA. page WEPAB010, 2017.

[35] Shaukat Khan, Claus Schneider, Carsten Mai, Nils Lockmann, Fabian Götz, Gholamreza Shayeganrad, Sven Döring, Stefan Cramm, Arne Meyer auf der Heide, Mathias Gehlmann, Shunhao Xiao, Mateusz Suski, Bernard Riemann, Dennis Zimmermann, Moritz Plötzing, Uwe Bovensiepen, Peter Ungelenk, Marc Jebramcik, Lukasz Plucinski, Benedikt Büsing, Raffael Niemczyk, Andrea Eschenlohr, and Manuel Ligges. Pilot experiments and new developments at the DELTA short-pulse facility. page WEPAB009, 2017.

[36] Christopher Corder, Peng Zhao, Jin Bakalis, Xinlong Li, Matthew D. Kershis, Amanda R. Muraca, Michael G. White, and Thomas K. Allison. Ultrafast extreme ultraviolet photoemission without space charge. *Struct. Dynam.*, 5(5):054301, 2018.

[37] M. Puppin, Y. Deng, C. W. Nicholson, J. Feldl, N. B. M. Schröter, H. Vita, P. S. Kirchmann, C. Monney, L. Rettig, M. Wolf, and R. Ernstorfer. Time- and angle-resolved photoemission spectroscopy of solids in the extreme ultraviolet at 500 kHz repetition rate. *Rev. Sci. Instrum.*, 90(2):023104, 2019.

Chapter 5

QUEST – a cutting-edge toolset for electron spectroscopy of quantum matter

Matthias Muntwiler, Andreas Pfister, Patrick Ascher, Ming Shi, Milan Radović, and Nicholas Plumb

In a nutshell

Quantum materials are characterized by couplings between multiple degrees of freedom, and/or nontrivial band topologies and are of keen interest due to their intriguing fundamental physics, as well as their potential applications in electronics, sensing, data storage, and quantum computing. The QUEST beamline is conceived as an unparalleled facility for comprehensive spectroscopic studies of quantum matter, including size- and dimensionality effects, such as in device-like structures. QUEST will be realized by merging the scientific programs, instrumentation, and expertise of the SIS and PEARL beamlines in Sector 9 of SLS 2.0. It will deliver photons from 15 to 2000 eV to two endstations: (1) ULTRA, optimized for the vacuum ultraviolet range, will specialize in angle-resolved photoemission spectroscopy (ARPES) with ultrahigh energy and momentum resolution, spin resolution, and temperatures down to 4 K; (2) OPERA will be geared toward ARPES and x-ray photoelectron diffraction experiments in the soft x-ray range. It will be equipped for *operando* device studies and spatially-resolved ARPES down to ~ 1 μm. The two endstations will connect to a shared instrument cluster for sample growth and scanning tunneling microscopy. Combined, these techniques will directly probe characteristics such as momentum-space electronic structure and spin texture – correlated with real-space spectroscopic mapping – with extreme performance in systems ranging from single crystals to thin films, molecular networks, and functioning quantum devices. The unique and powerful combination of capabilities will interact synergistically, forging a new scientific program that brings new research opportunities and promises a high scientific return on investment. The quick ramp-up of the beamline, endstations, and scientific program opens the door to 'Phase II' development of novel ARPES stations with an unprecedented combination of ultrahigh energy/momentum/spin/spatial resolution, ultralow temperature, and ultimate possibilities for integrating *operando* measurements and multi-technique spectro-microscopy correlation studies.

5.1 Overview

Quantum materials and novel phases characterized by exotic properties arising from electronic correlations and/or nontrivial band topology are positioned as science and technology drivers of the coming decades [1–4]. A key goal is to elevate quantum materials to the level of miniaturized, integrated technologies via elaborate investigations of contacted, nanoscale device setups. Thus the challenge for research lies not only in revealing and understanding the electronic states responsible for the behavior of these systems, but also in manipulating the materials in order to further explore, fine-tune, and eventually utilize these quantum phenomena in novel electronic devices. This demanding research not only pushes the spectroscopic boundaries of energy-, momentum- and spatial resolution, but also requires a new level of experimental integration, bringing together numerous complementary techniques for sample (micro-/nano-)fabrication, preparation, and spectro-microscopy investigation in an *operando* setup.

The QUEST beamline will synergistically merge the scientific programs, advanced instrumentation, and technical expertise of the former SIS (Surface and Interface Spectroscopy) and PEARL (Photo-Emission and Atomic Resolution Laboratory) beamlines in Sector 9 of SLS 2.0. Undulators in the long straight section will supply photons spanning the vacuum ultraviolet (VUV) and soft x-ray (SXR) range of 15 to 2'000 eV. A pair of cutting-edge endstations, designed to leverage the lower and upper regions of this energy range to maximum advantage, will operate on separate branches while being coupled together via an all-*in-situ* system for sample growth, preparation, and characterization. While ARPES was once used almost exclusively in basic research, recent industrial usage of the SIS, PEARL, and ADRESS beamlines at SLS illustrates how the technique has made the jump to application development. The comprehensive, integrated toolset at QUEST will be aimed at fostering a "lab-to-fab" pipeline that lowers the barriers for bringing quantum materials into the realm of commercial devices.

The scientific benefits of combining the SIS and PEARL via a powerful, broad-range photon source and a sophisticated sample preparation and microscopy/characterization facility will be more than a simple sum of the instrumentation. The resulting scientific program will exploit the highest performance in ARPES energy/momentum resolution and cryogenic temperatures, and also develop the next generation of local *operando* spectro-microscopy experiments. The PEARL beamline has pioneered the use of scanning probe techniques in combination with synchrotron-based photoelectron spectroscopy and providing state-of-the-art *in situ* sample preparation methods [5]. The current scientific focuses of the PEARL beamline are *in-situ* and *operando* spectro-microscopy correlation experiments at the surfaces of novel functional materials, supramolecular architectures [6], micro- and nanostructures [7], and two-dimensional materials for electronic and spintronic device applications [8, 9] in future quantum technologies. Meanwhile the SIS beamline offers world-class performance in high-resolution and spin-resolved ARPES that has placed it at the forefront of research in condensed matter physics and materials science during last 20 years. Highlights have included the experimental realization of helical massless Dirac fermions [10]; identifying the first Weyl nodes and associated topologically non-trivial Fermi arcs in solids [11]; and the full mapping and discovery of the giant spin splitting of the 2-

dimensional electron gas at the surface of $SrTiO_3$ [12, 13], which has opened new pathways for novel devices. In addition, the SIS beamline has established the first successful integration of ARPES and pulsed laser deposition film growth for *in situ* studies of complex heterostructures [14].

With the new QUEST beamline, we aim to address fundamental and technological issues in the forefront of research in condensed matter and to explore/identify exotic physical properties of novel quantum materials. Examples include: the symmetry of electron pairs in unconventional superconductors; the BCS-BEC crossover in pairing behavior; the emergence of superconductivity from two-dimensional systems; the electron correlation effects in 'magic angle' twisted bilayer graphene and other twisted layered systems; electronic states that encode high-order topological invariants; the correlations leading to fractional quantum Hall effects; and massive and massless quasiparticles with and without definitive chirality. These studies will not only significantly advance our knowledge in condensed matter physics, but also lay the scientific groundwork for the application of novel quantum materials in modern industry.

5.1.1 Methods

Angle-resolved photoemission spectroscopy (ARPES) is a key player in quantum-materials research, as it is the most powerful, direct method to probe the E-vs.-k electronic structure of solids, yielding rich information about the symmetries, topologies, and interactions that endow these systems with their astounding characteristics. The instrumentation used for ARPES supports many specialized flavours of PES like chemical analysis (XPS), valence-band spectroscopy and Fermi-surface mapping (ARPES) and photoelectron diffraction (XPD). Offering high photon flux, variable photon energy, small spot size and tunable polarization, synchrotrons have become indispensable radiation sources for ARPES. Tunable photon energy is required in energy-scanned XPD and resonant Auger/photoelectron spectroscopy, and can be used to control the escape depth, the photoemission cross-section, and the perpendicular momentum (k_z) for 3D k-space mapping. Full polarization control furthermore enables experiments based on circular and linear dichroism effects – e.g. to detect the orientation of molecules, electronic and magnetic states, or to probe the orbital characters of electron bands.

As a powerful, direct real-space probe of electron states, scanning tunneling microscopy (STM) is a natural complement to ARPES that allows for quick assessment of sample quality and provides reference topography maps of measured samples. In addition, in spectroscopy mode, the density of states above and below the Fermi level can be probed on specific sites and correlated to corresponding spectral information from ARPES. Important breakthroughs have been achieved in non-contact atomic force microscopy where now, with the same instrument, topographic and electronic structure can be investigated on the atomic level. Spectro-microscopy correlation at present is an increasingly essential prerequisite to solid scientific work as complex materials are often challenged by local degradation and the material characteristic changes at interfaces, and for structures of different topology, dimensions and shape. Ideally it is the goal to determine the electronic and DOS information at the same location of a complex material and within an operated device - at the best resolution of photoelectron spectroscopy and at the position of a single atom.

Photoemission and tunneling techniques are inherently surface sensitive. They need to be performed on fresh, pristine sample surfaces preserved in a UHV environment. While certain surfaces

can be prepared by simple cleaving or ion bombardment and annealing, others need to be synthesized and studied completely *in situ*. Pulsed laser deposition (PLD) and molecular beam epitaxy (MBE) are sophisticated methods for thin film growth with layer-by-layer thickness control. When coupled through a UHV transfer system, these techniques can be used to extend ARPES beyond traditional single-crystal samples in order to perform experiments on non-cleaving (e.g., cubic) systems and heterostructure interfaces, and to manipulate material properties in new ways (e.g. substrate-induced strain).

Therefore the new QUEST beamline at SLS 2.0 will develop and offer to the community:

- ARPES at ultralow temperature to study the electronic structure upon approaching the ground state and to access low-energy scale phases;
- high energy-resolution to unveil various instabilities and to identify novel low-energy excitations;
- high momentum and spin resolution for investigating low-carrier-density systems, e.g. semiconductors, semimetals, topological and quantum well systems;
- angle- and energy-scanned XPD to resolve local atomic structure of electronically and magnetically active sites in three dimensions with chemical specificity;
- complementary photoelectron spectroscopy-based techniques, such as resonant ARPES, core level spectroscopy, and linear/circular photoemission dichroism for probing properties such as chemical composition, orbital character, or time-reversal symmetry;
- STM and transport measurements to study the electronic structure in parallel with ARPES; and
- micro/nano-ARPES to study small and inhomogeneous samples, patterned surfaces, as well as non-local transport effects;
- capabilities for *operando* ARPES studies of working quantum devices (e.g. under applied gate voltage);
- UHV-coupled MBE and PLD growth chambers for synthesizing and engineering novel thin-film and heterostructure systems;

In particular, the beamline will specialize in angle-resolved photoelectron spectroscopy in a wide range of photon energy from vacuum ultraviolet to soft x-rays. It will combine spatially averaged spectroscopic techniques with scanning probe microscopy in a "laboratory" environment where different properties of the sample can be studied and correlated. For instance, spin polarization can be probed by spin-resolved photoelectron spectroscopy as well as magnetic circular dichroism or spin-polarized STM, the chemical composition of a material can be measured and put in correspondence with valence effects, and the structure of the surface can be analyzed for different electronic phases. The wide photon energy range of the QUEST beamline, covering both VUV and SX ranges enables systematic and comprehensive investigations of electronic and atomic structure *in situ* on the same sample.

With this toolset, the new QUEST beamline at SLS 2.0 will unify spectroscopic, sample preparation, and growth methods at a truly world-class level. This will allow scientists at the SLS to not only significantly advance general knowledge in condensed matter physics, but also benefit from the best available experimental infrastructure for the comprehensive study of novel quantum materials in device applications for industry.

Property	Unit	Values
Photon energy	eV	15–2'000
Photon flux	/s/0.1%BW	10^{14}
Energy resolution $E/\Delta E$		10'000
Polarization		LH, LV, C+, C-
Spot size	μm	1–100

Table 5.1: Photon beam specifications of the QUEST beamline. Photon flux refers to the estimated flux on the specimen. The abbreviations are: LH: linear horizontal, LV: linear vertical, C+: right-hand circular, C-: left-hand circular. The stated energy resolution is the nominal target in the core operating range of each branchline.

5.1.2 Uniqueness compared to other present and planned beamlines worldwide

Most competing photoelectron spectroscopy beamlines at other synchrotron facilities focus on one particular aspect in a limited photon energy range or optimized on a specific parameter, such as high resolution, high flux, spot size, or low temperature. To our knowledge, QUEST is currently the only ARPES beamline covering the energy range from 15 to 2000 eV in situ, and thus giving access to valence band and core levels at the flip of a switch. With the auxiliary deposition chambers and the scanning probe microscope the beamline also features a unique combination of sample growth methods, microscopic characterization tools and two world-class ARPES measurement setups. The ARPES endstations' combined performance will be able to go head-to-head against other world-leading instruments in terms of temperature; energy and momentum resolution; operando capabilities; small, high-throughput focusing; and 3D spin resolution.

5.1.3 Impact of the new ring brilliance

While brilliance is not the ultimate benchmark of a photoelectron spectroscopy beamline, QUEST profits in many ways from the advancement of storage ring and insertion device technology in SLS 2.0: As described in Chapter 2 and Section 5.2, the whole photon energy range of QUEST can be covered by two undulators, where each operates on the fundamental line and is fully linearly or circularly polarizable over its respective energy range. The lower aspect ratio of the beam due to the lower horizontal emittance allows for better focusing on the sample. The lower divergence reduces optical aberrations along the beam path, which, in turn, increases energy resolution. Finally, the KNOT undulator design reduces the heat load on the optical elements, which leads to better stability.

5.1.4 Complementarity to other PSI BLs

QUEST will have strong scientific overlap and complementarity with the SX-ARPES (Chapter 12) and RIXS (Chapter 13) beamlines of SLS 2.0, as well as other solid state spectroscopy beamlines, namely X-Treme (Chapter 10), SIM (Chapter 9) and ATHOS (SwissFEL). The SX-ARPES beamline, foreseen to operate in the range of 400 to 1'600 eV, is especially tuned toward the tasks of full

3D k-space mapping and probing buried heterostructure interfaces – quantum materials systems in which QUEST has a mutual interest. These experiments require particularly high photon flux and energy resolution, which calls for specialized tuning of the optics and endstation that the SX-ARPES beamline will deliver. QUEST's core strength, on the other hand, lies in offering a wide range of photon energies, measurement conditions, and preparation techniques. Its highest resolution performance will be concentrated in the VUV regime on the ULTRA endstation, whereas the soft x-ray range will be optimized for efficient core-level spectroscopy, photoelectron diffraction and resonant spectroscopy. Thus, the QUEST and SX-ARPES beamlines will strongly complement each other's spectroscopic abilities and scientific objectives, offering a fully diversified and cutting-edge array of photoemission techniques in the study of quantum materials. The already substantial amount of joint research among the existing SIS, PEARL and ADRESS SX-ARPES facilities may be expected to grow among QUEST and SX-ARPES in SLS 2.0.

RIXS techniques at SLS and SwissFEL are also highly complementary to QUEST's scientific aims. While high-resolution ARPES data from QUEST will be able to see signatures of the totality of interactions affecting electrons in complex systems, soft x-ray RIXS will identify and probe specific lattice, spin, and orbital excitations with energy, momentum, and even (at ATHOS) time resolution. The combined knowledge obtained from these techniques can thus be used to decisively untangle the complex interactions among various degrees of freedom that define many intriguing phases of quantum materials.

Complementarity with the X-Treme and SIM beamlines is also foreseen, for example, in the field of magnetic nanostructures, surface-supported molecular magnets and multiferroics, where these two beamlines can resolve magnetic contrast in the spectroscopic and mesoscopic domain.

5.1.5 Size and impact of community – potential increase through the upgrade

The global ARPES user community is large and has been growing rapidly in recent years. The growth is driven by the convergence of several factors, including: (1) improvements in the capabilities of the ARPES technique such as high-resolution ARPES, nano-ARPES, and spin-resolved ARPES; (2) the critical importance and applicability of ARPES data for the field of quantum materials science, paired with the rising interest in quantum materials in the realms of novel devices and quantum computation; and (3) the surging number of quantum materials research groups, especially in China. The fact that so many quantum materials research groups have set up their own laser-/lamp-based ARPES systems in university labs seems not to have diminished the demand for synchrotron-based ARPES, as synchrotron-based ARPES complements "tabletop" experiments, thanks to its greater flexibility in terms of photon energy range, polarization, and focusing. If anything, the availability of tabletop systems has drawn more attention and users to the technique, who in turn often seek out synchrotron-based ARPES facilities to pair with their own in-house experiments.

Swiss groups that have traditionally relied heavily on ARPES for their research hail from many of the major universities and institutes: University of Zürich, University of Geneva, University of Fribourg, University of Basel, the École Polytechnique Fédérale de Lausanne, and EMPA. The ARPES beamlines at SLS are also utilized by groups from other PSI facilities and research divisions, such as SINQ, SμS, ENE and NES. The existing ARPES user community – both globally and within

Switzerland – stands to benefit enormously from the development of QUEST, which will provide them with access to a cutting-edge facility equipped with an array of sophisticated tools for a holistic approach to investigating complex problems in quantum materials research.

The multi-technique integration and capabilities for more applied research promise to attract new users. For instance, users who have focused on one particular aspect such as electronic structure and need to better understand atomic structure aspects of their samples. Similarly, groups who have spent a lot of effort in growing samples under well-defined conditions will want to complement thei

5.1.6 Industrial potential

The ongoing miniaturization of electronic devices, the incorporation of quantum materials, and the exploitation of quantum phenomena, from spin-based computation to topological effects, is currently pushed not only by basic research but also industrial R&D. Particularly the demonstration of functional quantum computers has spurred development on all aspects from basic research to device integration, where established methods like materials growth, lithography and structural characterization are facing new challenges due to small size and the limits of conventional electronic structure theory.

QUEST will provide a "one-stop-shop" for industrial partners seeking to research novel materials, characterize nanostructures and test device prototypes, where in situ sample preparation, high resolution and micro/operando ARPES, plus complementary real-space techniques are of key importance. This plan is specifically informed and motivated by experience with industrial partners so far, who utilize the full battery of existing SLS photoemission beamlines but frequently suffer from complications related to performing much of their sample preparation and characterization off-site.

5.2 Source

The wide photon energy range from 15 to 2'000 eV required by the scientific methods poses a number of technical challenges. To cover the whole range with the fundamental or 3rd harmonic, two undulators with different period length are necessary. QUEST takes advantage of the fact that the triplet in the long straight can be shifted off-center. This allows the sector to house two undulators of different lengths, so that an optimal performance balance can be struck. The proposed upstream device is an APPLE-X UE36 undulator with 36 mm period length, delivering fundamental radiation in the soft x-ray (SXR) range of 250 to 1'600 eV. The range is extended up to 2'000 eV by use of the 3rd harmonic. The downstream device is a 4.5 m APPLE-Knot UE90kn covering the VUV photon energy range 15 to 600 eV. The undulators are aligned on the same beam axis, so that both beams can be fed into the beamline (though only one of the devices can be active at a time). The device types are described in more detail in Chapter 2.

The VUV source is subject to special constraints/challenges and hence chosen with particular care. While a minimum photon energy as low as 6 to 7 eV would be desirable for enhanced energy and momentum resolution, as well as bridging the gap between laser and synchrotron sources, the low end is limited by the divergence of the outgoing beam and the clearance of the downstream bending magnets. The 90 mm period length can access energies down to 15 eV, which is seen as a reasonable lower limit. The other challenge is the large high-harmonic background radiation, which would normally deposit

several kW of thermal load onto the optical elements. The Knot design mitigates this problem by deflecting the harmonics away from the central axis onto the apertures in the front end.

The combination of UE36 and UE90kn devices thus covers the whole specified photon spectrum from 15 to 2'000 eV. The overlap of energy ranges lowers the number of situations where a switch of insertion device is necessary during a photon-energy scan. AppleX devices are chosen for their flexible control of linear horizontal/vertical and circular left/right polarization.

The calculated photon flux emitted by the insertion devices is plotted in Figure 5.1 and compared with the existing SIS and ADRESS undulators. Notwithstanding the low-energy cutoff being shifted to 15 eV, the choice of undulators is essentially a no-compromise solution: Not only will the combined SXR and VUVX sources cover an exceptionally broad energy range with flexible polarization, but they will also enhance photon flux overall compared to current standards.

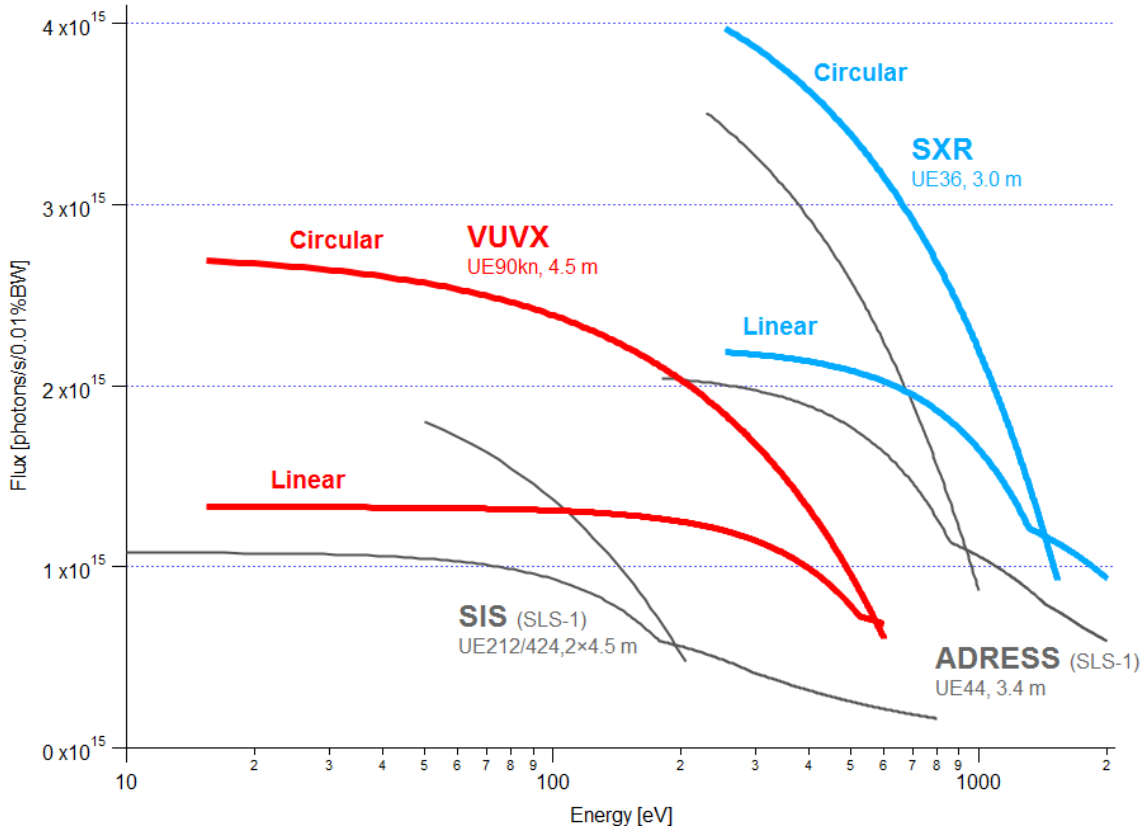

Figure 5.1: Photon flux in the central cone of undulator radiation produced by the UE36 and UE90kn AppleX devices. Linear and circular polarization modes from each device are displayed. Flux curves from the existing undulators used for ARPES at the SIS and ADRESS beamlines are shown for comparison.

5.3 Front end

The QUEST front end will be equipped with a diaphragm, a photon shutter, a four-blade slit system, a beam stopper for radiation safety, and vacuum gate valves (see also Chapter 3). The slit system defines a variable acceptance aperture of the beamline. It is the most important device to restrict the photon flux in the beamline and to limit the detrimental effects of optical aberration on energy resolution and spot size. At the largest aperture, it should accept the full center cone of undulator radiation, given by the divergence of undulator radiation. The divergence is as high as 0.2 mrad (half-width) at the lowest photon energy of 15 eV and decreases to 0.02 mrad at 2000 eV. Depending on the distance to the source, the slit system should thus provide a variable aperture between 0.1 and 4 mm with ≤ 100 μm resolution. Most crucially, the front end must be able to dissipate the off-axis power emitted by the UE90 Knot undulator at low energy.

5.4 Optics

	Mode	ID	M1	FM
I	VUV-ULTRA	UE90kn	1.8°	2.5°
II	SXR-ULTRA	UE36	1.8°	2.5°
III	VUV-OPERA	UE90kn	1.8°	2.5°
IV	SXR-OPERA	UE36	1.5°	1.5°

Table 5.2: Operation modes of the beamline. ID: insertion device; M1: collimating mirror; FM: focusing mirror; L/R: left/right deflection. The angles are grazing angles.

The optics section accepts the beam from either one of the two insertion devices and delivers it to any of the two endstations. The beamline concept in its idealized form calls for each branch to deliver the full available spectrum from the two insertion devices. This will grant each endstation enormous breadth and flexibility in the types of experiments it can perform. The resulting operation modes are summarized in Table 5.2. Thus, the optical design of QUEST must overcome the simultaneous challenges of:

1. delivering the fullest possible spectrum from both the SXR and VUV undulators to each endstation;
2. optimizing resolution and focusing from both undulator source points (separated by roughly 4 m) to the greatest possible extent; and
3. sufficiently branching the beam to provide space for both endstations.

The conceptual design, shown in Figure 5.2, satisfies these demands rather elegantly through the use of a cylindrical first mirror (M1). It manages to do so while offering a number of cost savings compared to other potential designs: There is only a single mirror in the M1 unit and one monochromator shared between both branches; the existing lead optical hutch of X09L can most likely be reused.

Due to design constraints of the diffraction-limited storage ring, it is not possible to cant the undulator sources; hence branching must be handled by the optics section. Due to the grazing reflection

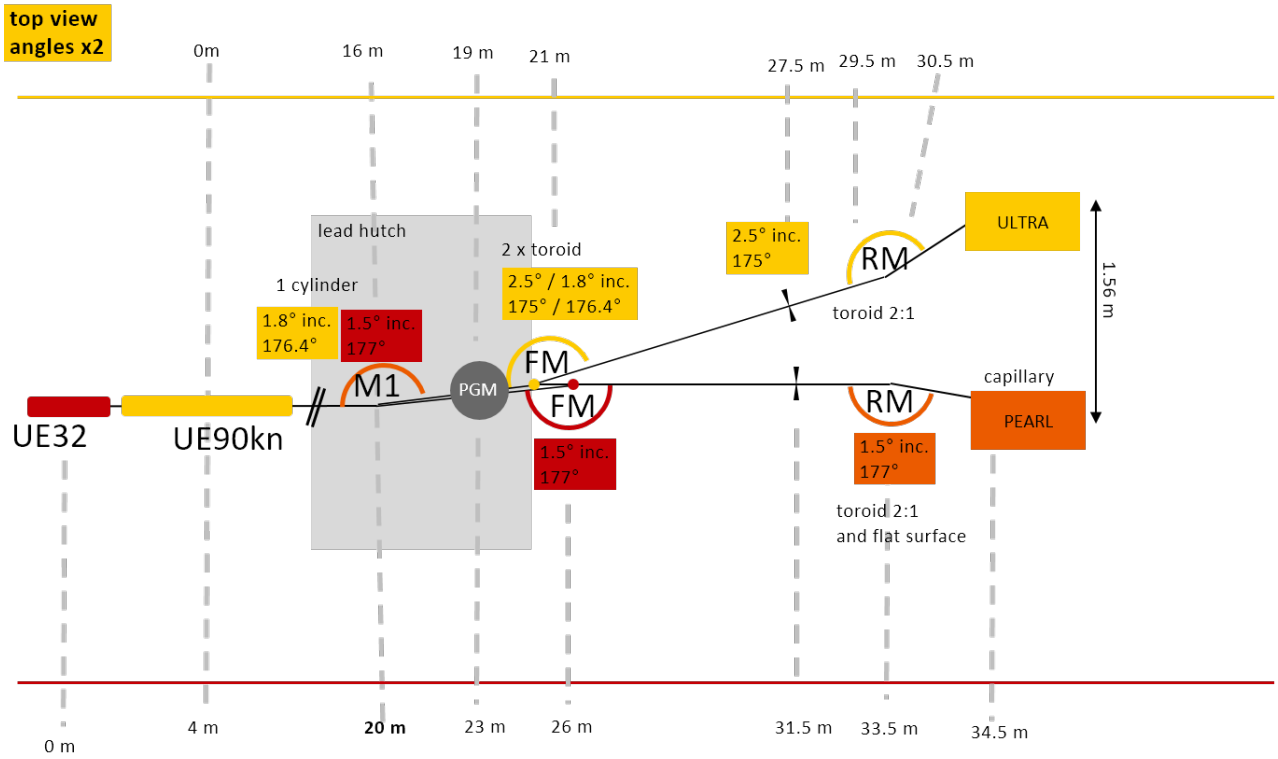

Figure 5.2: Schematic overview of the QUEST optical layout. UE36: periodic APPLE-X undulator (250–2'000 eV); UE90kn: k-not APPLE-X undulator (15–500 eV); M1: collimating mirror; FM: focusing mirror; RM: refocusing mirror; ULTRA/OPERA: endstations.

angles needed in the soft x-ray regime, this separation needs to be generated from the first optical element in order to achieve sufficient spacing between endstations downstream. Branch separation is thus achieved by sagittal focusing of M1 to couple the mirror's focal length to the reflection angle. By adjusting this angle, M1 can be tuned to collimate the beam coming from either source point. Hence there is a distinct beam path associated with each insertion device. The collimated beam from M1 feeds to a plane-grating monochromator (PGM), at which point the separation between the beam paths is about 40 mm. The beam continues separating as it travels to one of two focusing mirrors (FM-VUV or FM-SXR), depending on the path corresponding to the chosen insertion device. On each branch, the beam then travels through an exit slit and refocusing mirror (RM-ULTRA, RM-OPERA) chamber to reach the endstation. In the case of OPERA, the RM element can be switched between a toroidal mirror (for conventional focusing) or a flat surface to be used with a micro-capillary in the endstation (Section 5.4.4).

The beamline concept, as shown in Figure 5.2 achieves a separation of 1.56 m between the two endstations. There is likely some flexibility to increase the separation (e.g. by staggering the endstations) in the final design, if needed.

The monochromator concept is based on the well-established plane-grating monochromator (PGM) scheme [15] consisting of collimating mirror (M1), plane mirror, plane grating, focusing mirror (FM)

and exit slit (SL), as shown schematically in Figure 5.2. This scheme provides the flexibility of trading photon flux versus energy resolution or harmonic suppression by changing the fix-focus constant c_{ff} during operation. High energy resolution ($E/\Delta E \approx 10'000$) is required to resolve gaps in the valence band structured due to electronic correlation effects, or, in the SXR range, to resolve surface shifts and multiplet splittings of the order of 50 meV. Harmonic suppression is typically important in resonant spectroscopy where harmonic lines would otherwise cross the fixed final state photoemission peak and pollute the measured spectrum. The monochromator section is shared by both branchlines.

5.4.1 Filters and slits

The PGM scheme employs a precise horizontal slit in the focal point after the monochromator. The smallest opening is adapted to the monochromatic beam size taking grating resolution, beam divergence and aberrations into account. Precision mechanics allowing for reproducible slit opening in the range 5–500 μm is required. Further four-blade slits to control the photon flux and to block stray light are located at the entrance of the monochromator and the refocusing mirrors, respectively.

No need for filters is foreseen, thanks to the harmonic rejection of the Knot undulator scheme, as well as the tunable fixed-focusing parameter, c_{ff}, of the collimated PGM.

5.4.2 Mirrors

According to Figure 5.2, the beamline employs five mirror units. All mirrors are mounted in UHV chambers that are positioned along two transversal axes and rotated about three perpendicular axes by external motors. Some of the units contain two reflective surfaces that can be switched by a vertical motion, as explained below.

The collimating mirror (M1) is an internally cooled cylindrical mirror shared by both branch lines. Its deflection angle is set according to Table 5.2. In three operating modes, it is matched to the position of the source and produces a vertically collimated beam for the PGM. In the SXR-ULTRA mode, the beam is not collimated but rather slightly focusing with a long exit leg. This can be compensated in the PGM by choice of a particular c_{ff}, as has been done before at the PEARL beamline [16]. The incidence angles are chosen such that the OPERA branch delivers photons up to 2 keV. In the ULTRA branch, the mirrors are optimized for the lowest photon energy and the upper limit is around 1'500 eV.

After the beam passes through the monochromator (Section 5.4.3) one of three toroidal mirrors focuses the beam on the exit slit according to Table 5.2. The two VUV mirrors (yellow in Figure 5.2) are mounted in the same chamber and deflect the beam either to the left or right. A second mirror chamber houses the SXR focusing mirror for the OPERA branch. Note that the SXR-OPERA and the other beams pass through the monochromator at an angle of about half a degree. This and the necessity for three focusing mirrors is a disadvantage of the concept. However, the cost, complexity and possible loss of precision of two internally cooled collimating mirrors outweigh the drawbacks.

The refocusing mirrors provide a demagnification by a factor of two, which results in a spot size between 20–50 μm (depending on the source and photon energy). In the OPERA branch, the refocusing mirror also features a flat surface which can be switched to provide diverging beam to the sample or the micro-focusing unit (c.f. Section 5.4.4.

5.4.3 Monochromator

The monochromator is a plane-mirror plane-grating monochromator as used before. The combination of gratings will be capable of covering the range of 15–2'000 eV. Optical elements will be optimized for high resolving power $\geq 10'000$ in the range below 500 eV, translating to a resolution of 2 meV below 20 eV, or 50 meV in the SXR range. Resolution can be further enhanced by tuning the c_{ff} parameter at the cost of photon flux.

The existing monochromators at SIS and PEARL are equipped with 300, 600 and 1200 l/mm gratings, covering photon energy ranges of 20–2'000 eV, respectively. An upgrade with a 115 l/mm grating is already in progress at the SIS beamline, with installation foreseen during the 2020/21 winter shutdown. The actual number of gratings needed to cover the specifications needs to be addressed in the technical design phase. Due to the wide range of photon energy and the shifted VUV/SXR beams, the number of gratings and/or the angular range may require a new mechanical solution.

5.4.4 Secondary optics

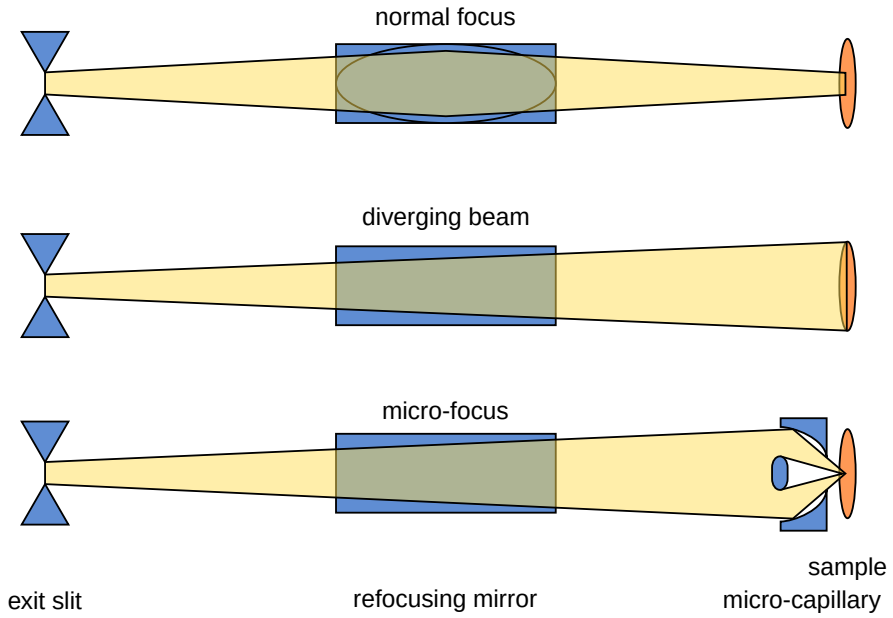

Figure 5.3: Refocusing options of the OPERA branch. (a) 1:1 image of the exit slit, (b) divergent beam, (c) micro-capillary with a demagnification of 10:1. (drawing not to scale.)

The OPERA branch will be equipped with a micro-focusing unit providing a spot size of ≈ 1 μm on the sample for selective excitation of single domains of ferroic materials, separated structural phases or parts of micropatterned devices. The micro-focusing unit consists of a capillary with a coated, elliptical interior shape. The capillary is inserted 3–4 cm in front of the sample and manipulated by in-vacuum piezo-drives. In a 3 m long refocusing section, a demagnification of 100:1 can be realized with a theoretical spot size of 0.2-0.5 μm. Compared to other micro-focusing solutions, the advantages of micro-capillaries are their compact size and achromaticity, i.e. the focal point does not move during

a photon energy scan. Tight spatial constraints in the analysis chambers of ARPES systems typically preclude the use of K-B systems, and zone plates are ruled out because of their chromaticity.

The capillary can be retracted from the beam. Together with the two surfaces of the refocusing mirror unit, three different spot sizes are available, c.f. Figure 5.3: The standard 2:1 mapping by the toroidal mirror produces a spot size of 20–50 μm. For radiation sensitive samples, the unit can be switched to a plane mirror surface which passes the divergent beam to the sample, resulting in a spot size between 200 and 500 μm.

5.5 Endstations

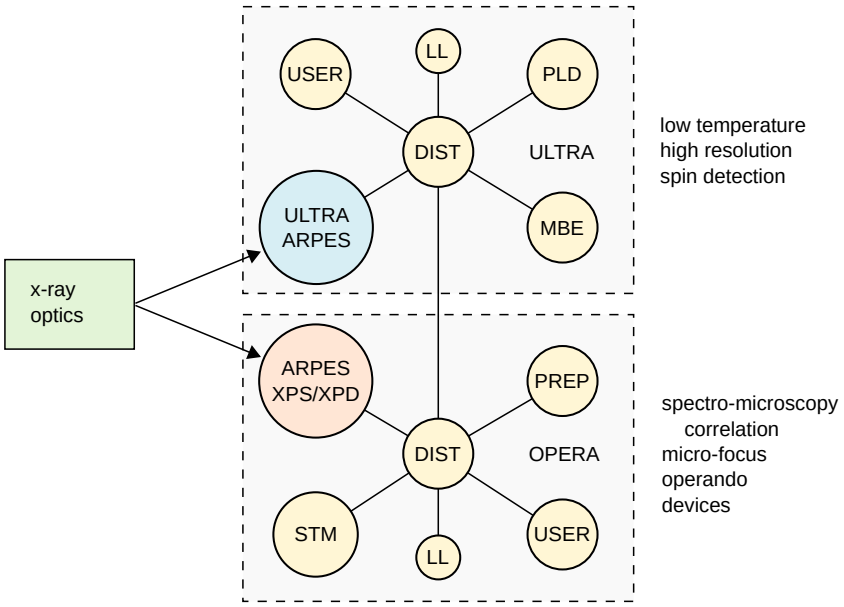

Figure 5.4: Schematic topology of the QUEST endstations ULTRA and OPERA. The ARPES measurements are done in the main analysis chambers connected to the respective optics branch. The analysis chambers are connected to satellite systems for in situ sample preparation (PREP) and characterisation via distribution (DIST) chambers. Samples can be introduced via load locks (LL) and transferred under UHV between the two endstations. Ports for chambers brought by users (USER) are also provided. These may be adapted for specialized sample preparations (e.g., nanotube structures or exfoliated 2D materials).

The QUEST beamline will service a pair of complementary endstations, ULTRA and OPERA, aimed at enabling a broad array of experiments, see Figure 5.4. These endstations are already in operation at the SIS and PEARL beamlines of SLS. Each is equipped with its own set of advanced capabilities for sample preparation and characterization, including thin-film growth, surface cleaning, and scanning-probe stations. ULTRA endstation emphasizes absolute ARPES performance in terms of energy, momentum, and spin resolution at temperatures down to 4 K for the study of single crystals and crystalline films. These are vital features for exploring the fine spectral aspects – such as

band gaps, splittings, spin textures, and self-energies due to collective modes – which define many electronic phases. Meanwhile, OPERA is geared toward soft x-ray ARPES/XPS, photoelectron diffraction (XPD) and spectromicroscopy correlation studies of a broad range of complex surface-supported systems, including molecular networks, two-dimensional materials, nanostructured materials and device prototypes. An ultrahigh-vacuum sample-transfer system linking the two endstations enables the user to take full advantage of all preparation and analysis methods provided. The synergy of the two endstations will allow true multi-technique investigations to be carried out over a wide photon energy range on the same sample. This level of integration and comprehensive study will set a new standard in synchrotron-based photoelectron spectroscopy facilities worldwide.

5.5.1 ULTRA: on the cutting edge

The recently-commissioned ULTRA endstation represents a new standard in synchrotron ARPES instrumentation that combines world-class energy, momentum and (soon) spin resolution, with an advanced cryogenic system and powerful, flexible data acquisition. The core of ULTRA is a PSI-designed 6-axis cryogenic sample manipulator capable of reaching temperatures below 4 K (Figure 5.5). This cutting-edge system is the lowest-temperature true 6-axis ARPES manipulator available at any synchrotron beamline. Cooling is localized at the sample in order to minimize thermal drift during temperature changes or long acquisitions.

The advanced manipulator is paired with a state-of-the-art Scienta Omicron DA30-L hemispherical electron analyzer, which offers an energy resolution better than 1.6 meV, angular resolution of 0.1°, and up to 30° angular acceptance. The analyzer also features deflector-based scanning (so-called "DA mode"), which allows ARPES data to be acquired along both surface-parallel momentum directions, without rotating the sample. While the DA scanning mode is especially useful when dealing with small, difficult-to-align samples or sample regions, traditional mechanical scanning is still of high value thanks its reliability and flexibility.

An approved project co-funded by an SNF R'Equip grant will incorporate a next-generation 3D Mott spin polarimeter onto ULTRA's DA30-L analyzer (see Section 5.5.5), allowing for simultaneous conventional and spin-resolved data acquisition. The detector concept emphasizes high spin polarization sensitivity at the level of 0.1–0.01%, improved efficiency, and rock-solid stability/reliability. ULTRA also features a basic set of on-board preparation/characterization tools: MCP-based low-energy electron diffraction (MCP-LEED), alkali-metal deposition for surface doping, ion sputtering, and sample annealing. The combination of high-precision scanning options, 6-axis manipulation, 3D spin resolution, and 4-Kelvin temperature performance make ULTRA a versatile system for demanding, high-resolution investigations of quantum materials.

5.5.2 OPERA: advanced versatility

The OPERA endstation will be adapted from the PEARL beamline of SLS, which has pioneered the complementary use of scanning tunneling microscopy and photoelectron spectroscopy at a synchrotron facility. The main benefit comes from measuring spectroscopic and microscopic properties on exactly the same sample and from correlating atomic or molecular structure with measurements of electronic valence states. These features, along with flexible sample preparation techniques, will be carried over

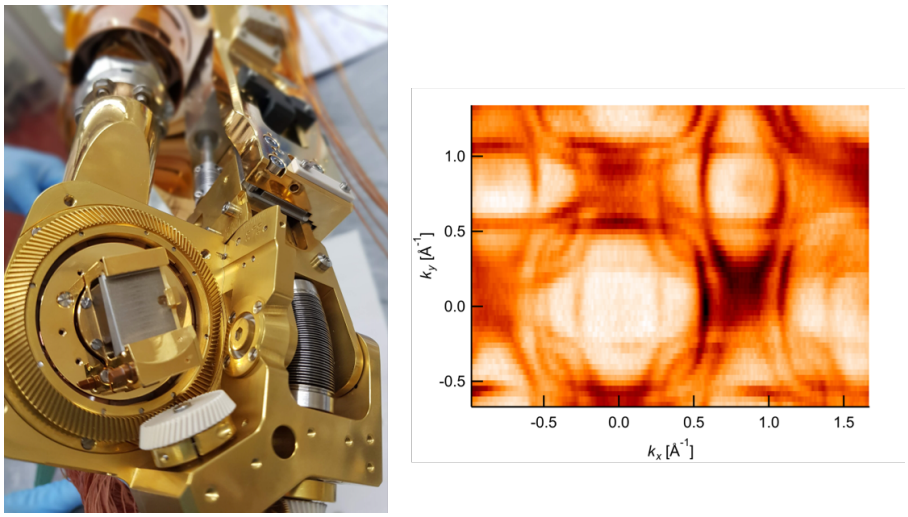

Figure 5.5: Left: The 4-Kelvin, 6-axis manipulator of the ULTRA endstation. Right: Fermi surface of $Sr_3Ru_2O_7$ acquired at 4.4 K.

to SLS 2.0 and complemented with micrometer focusing optics and increased angular resolution in ARPES, in addition to the higher photon flux, wide energy range and flexible polarization options provided by the beamline.

The experimental station is divided into the sub-systems shown in Figure 5.4. The photoelectron spectroscopy system, attached to the high-energy branch of the beamline, is designed as a state-of-the-art ARPES facility with a precise 6-axis manipulator and a hemispherical electron analyser with two-dimensional detection. For working with the micrometer beam size, the existing analyser will be upgraded with an angle-deflection (DA) mode so that mechanical rotation of the manipulator can be avoided. In contrast to ULTRA, this endstation focuses on a versatile sample environment: the sample stage features electrical contacts that permit, e.g. *operando* measurements of device prototypes under applied source-drain and/or gate voltages. Using a specialized sample holder, the manipulator can alternatively provide variable temperature programming from 40 K to 700 K.

The low-temperature STM provides real space sample characterization down to atomic resolution. Standard topography mode allows for quick assessment of the surface quality and reference to measurements at the user's home laboratory, dI/dV spectroscopy and mapping provides an atomically resolved probe of the local electron density of states in the occupied and unoccupied region near the Fermi level. Stable measurements in scanning probe microscopy typically require quiet and vibration-free environments. At the PEARL beamline this was possible by placing the whole endstation in an experimental hutch, separate from noisy vacuum pumps, and by adding active damping units under the frame of the instrument.

5.5.3 Controls and data systems

Controlled devices fall into three categories according to the degree of integration into the beamline control system: (I) beamline optics and diagnostics that are tightly integrated into the distributed

control system, (II) closed commercial instruments that are used in connection with beamline controls, and (III) closed commercial instruments for offline sample preparation and characterization that are not integrated into the control system.

Controls for category I comprise positioners of insertion devices, optical elements, industrial CCD cameras, sample positioning as well as analog input and output signals. For these devices, SLS-wide standards can be used as in the past for optimum synergy.

In category II, most notably, the two electron analysers are controlled by vendor-supplied computer systems. The systems have a programming interface, which enables their seamless integration into the high-level measurement application, either via EPICS or another common protocol, so that the beamline and the detector can be controlled, and data collected within the same user interface. The high-level application is developed in-house and can be built on a common framework shared with other beamlines.

Devices of category III are used for sample preparation and characterization, most notably the STM. These systems are controlled by vendor-supplied, standalone systems and are not integrated into the beamline control system.

Due to the relatively modest data rate of the detectors (≈ 1 MB/s , see Section 5.5.5), data collection and quick analysis can usually be done on regular workstations. For a preview of the collected data, generic data analysis software programs are used. Beamline-specific routines for browsing, loading, and viewing datasets, as well as performing basic analysis are developed and maintained by the beamline staff.

5.5.4 Sample environments and delivery

Engineered surfaces and interfaces are a promising platform where novel electronic phases can be stabilized. Properties of such systems are very responsive to structural distortions and defects, and much of the relevant physics, and potentially new discoveries are highly localized at the surface or interface. Therefore we are further developing the existing unique combination of *in situ* growth, STM and ARPES as a powerful tool for the structural and electronic characterization of ultrathin films down to one or two unit cells thickness. The facility combines oxide molecular beam epitaxy (MBE), pulsed laser deposition (PLD), organic physical vapour deposition (PVD), and chemical vapour deposition (CVD) in the same, interconnected UHV system. Such a cluster of sample growth techniques and characterization methods is new in Switzerland and presently available in very few laboratories around the world. All growth processes take place in ultrahigh vacuum (UHV) chambers at a base pressure below 1×10^{-9} mbar to enable sample preparation in a controlled environment and to prevent contamination of the surfaces. PLD and MBE growth processes are monitored in realtime with layer-by-layer resolution using high-pressure reflection high-energy electron diffraction (RHEED). Samples, substrates and organic powders for evaporation are introduced from ambient or a vacuum suitcase via a fast-entry lock. The transfer system will be designed in such way that samples can be transferred *in situ* between the various preparation, STM and analysis chambers. For more complex, project-specific sample preparation, quick access ports for user chambers and deposition sources are provided. Moreover, the preparation chambers provide standard surface science techniques for cleaning by ion bombardment and annealing by heating up to 1300° C. The grown samples are characterized by low-

energy electron diffraction (LEED), x-ray photoelectron spectroscopy (XPS) for chemical analysis, and scanning tunnelling microscopy for surface mapping down to atomic resolution.

5.5.5 Detectors

Emitted photoelectrons are detected using commercial hemispherical analysers with a two-dimensional detector ($\approx$ 1 megapixel) based on a multi-channel plate/phosphor screen/CCD camera stack that have become standard for ARPES. This setup has advantages in terms of operational simplicity and throughput, but some drawbacks in linearity and maximum count rate. In the future, micro-strip or delay-line type detectors might replace the phosphor/CCD unit. Their main benefit would be better linearity at high count rates. Since the electron yield and resolution is determined by physical processes before the detector, such an upgrade would likely not have a big effect on the data rate on the higher application levels.

In addition to the standard 2D detector, the ULTRA endstation will be equipped with a state-of-the-art 'NextGen' Mott spin polarimeter targeted at highly quantitative momentum- and energy-dependent measurements of 3D spin polarization – so-called 'spin texture'. Key features of the new polarimeter will be extreme polarization sensitivity (better than 0.1%), improved stability, and enhanced efficiency relative to existing Mott detection systems. The system will also utilize a side hole in the exit port of the DA30-L analyzer, allowing both conventional and spin-resolved ARPES data to be acquired simultaneously. This upgrade will consolidate the current spectroscopic activities at the SIS beamline within the single endstation, ULTRA. The existing COPHEE endstation for spin-resolved ARPES will be retired, opening up floor space at X09L for the merger of SIS and PEARL operations. The new Mott polarimeter is co-funded by an SNF R'Equip grant. The upgrade project is already underway and will be completed before SLS goes into shutdown.

5.6 IT requirements

While IT demands for photoemission experiments are presently very modest, the spatially-resolved measurements foreseen in SLS 2.0 could potentially bring a notable increase in storage consumption. Unfortunately, a rough estimation of these demands is difficult, as it will depend heavily on the usage balance of micro-scanning and conventional ARPES techniques. Considering only raw data from 2D angle- and energy-dependent ARPES measurements (ARPES, XPS, XPD, STM techniques), the combined storage demands of ULTRA and OPERA would only be about 1 TB per year. But storage demands would markedly increase for experiments involving spatially-resolved micro-ARPES measurements. For concreteness, a "typical" scan region of 100×100 μm^2 sampled in 1 μm steps could conceivably generate about 160 GB of data in a few hours, and perhaps multiple TB of data over the course of a week-long beamtime.

Concerning data transfer, there is no foreseeable need for high-performance IT hardware, as data is transmitted directly from the CCD cameras to the instrument-control PCs where a first data accumulation/data reduction step is executed. For typical acquisition modes, data processing demands are similarly negligible; users currently analyze data offline on standard PCs using some combination of their own routines and software tools provided by the beamlines. In the future, there could be a

need for more sophisticated data handling software specific to large, spatially-resolved datasets.

5.7 Timeline

During the operation time of SLS (2021-2023) all design for the beamline, general infrastructure and hutches will be finished. The procurement for optical elements will follow this process and should be completed before the dark period. The endstations will be brought into full operation in two phases. During Phase I, both existing endstations (ULTRA and OPERA), upgraded before the dark period, will be attached to the beamline as soon as possible and ready for pilot experiments with a first light from SLS 2.0.

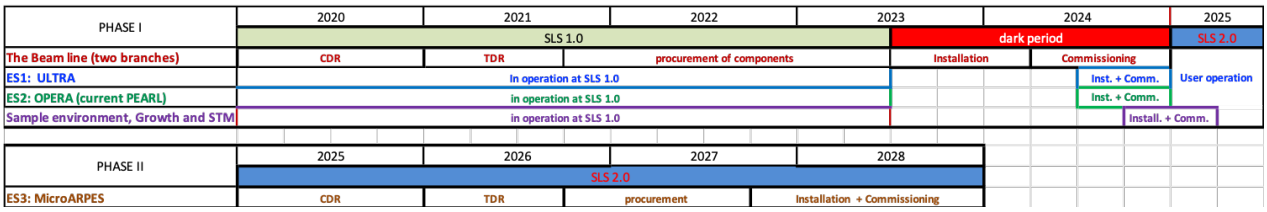

Figure 5.6: Timetable for QUEST beamline. The beamline will be developed and constructed in two phases. Phase I covers the beamline construction and plug in of two existing endstations. Phase II is devoted for a development and a construction of the new ARPES endstation with a high spatial resolution.

5.7.1 Planning

An overview of the planning and the milestones for QUEST beamline project is presented in Table 5.3. The aim is to have both endstations ready to accept photons as soon as SLS 2.0 delivers them. STM and sample growth set-ups will be in operation right after the endstations are commissioned.

5.8 Concluding remarks

The coming decade will see a convergence of basic science – discovering and exploiting novel quantum phenomena – and microtechnology – providing microscopic control over functional materials – which may culminate in the development of new concepts of viable quantum devices for use in information technology. This challenging and comprehensive research demands a new level of experimental integration of various complementary techniques for sample fabrication, characterization, microscopy and spectroscopy. The new QUEST beamline at SLS 2.0 will provide a laboratory where advanced electron spectroscopy methods that require the best tunable synchrotron radiation source are employed to study complex quantum materials and novel device concepts.

The beamline will be realized in two phases:

Phase I A new beamline which operates two insertion devices to cover the VUV and soft x-ray (SX) photon energy ranges from 15 eV to 2000 eV is developed and commissioned. The existing

Time	Milestone
PHASE I	
March 2021	Technical Design (TDR)
December 2022	Procurement of all components finished
July 2024	Infrastructure installed (beamline, hutches, cabling and controls
January 2025	Endstation 1 (ES1) pilot experiment
February 2025	Endstation 2 (ES2) pilot experiment
April 2025	STM and growth chambers in operation
June 2025	Regular user operation at ES1
June 2025	Regular user operation at ES2
PHASE II	
January 2026	CDR of novel ARPES endstation with nanoscale spatial resolution.
June 2026	TDR of novel ARPES endstation with nanoscale spatial resolution.
June 2028	Start commissioning the novel ARPES endstation
September 2029	Pilot experiments at the novel ARPES endstation
January 2029	Regular user operation at the novel ARPES endstation

Table 5.3: Milestones for the new QUEST beamline and instruments.

PEARL and ULTRA endstations will be immediately employed at the start of SLS 2.0 operation to perform experiments and to serve the user community.

Phase II A novel ARPES endstation combining ultrahigh energy, momentum and spin resolution at (sub-)4 K temperature, nanoscale spatial resolution, and *operando* capabilities will be developed to provide the spectroscopic tools for the next decade of condensed matter physics.

The QUEST beamline at SLS 2.0 with advanced photoemission methods (ARPES, XPS, XPD, XAS), scanning electron microscopy (STM), and advanced growth methods, will be a superior experimental laboratory for creation of novel phases and investigation of electronic properties and quantum phenomena in surface, interface, and bulk material systems.

Bibliography

[1] D. N. Basov, R. D. Averitt, and D. Hsieh. Towards properties on demand in quantum materials. *Nature Materials*, (16):1078, 2017.

[2] B. Keimer and J. E. Moore. The physics of quantum materials. *Nature Physics*, (13):10451055, 2017.

[3] M. R. Norman. Materials design for new superconductors. *Rep. Prog. Phys.*, (79):074502, 2016.

[4] H. Boschker and J. Mannhart. Quantum-matter heterostructures. *Annu. Rev. Condens. Matter Phys.*, (8):145–164, 2017.

[5] Matthias Muntwiler, Jun Zhang, Roland Stania, Fumihiko Matsui, Peter Oberta, Uwe Flechsig, Luc Patthey, Christoph Quitmann, Thilo Glatzel, Roland Widmer, Ernst Meyer, Thomas A. Jung, Philipp Aebi, Roman Fasel, and Thomas Greber. Surface science at the PEARL beamline of the Swiss Light Source. *J. Synchrotron Rad.*, 24(1):354–366, Jan 2017.

[6] Res Jöhr, Antoine Hinaut, Rmy Pawlak, Lukasz Zajac, Piotr Olszowski, Bartosz Such aand Thilo Glatzel, Jun Zhang, Matthias Muntwiler, Jesse J. Bergkamp, Luis-Manuel Mateo, Silvio Decurtins, Shi-Xia Liu, and Ernst Meyer. Thermally induced anchoring of a zinc-carboxyphenylporphyrin on rutile TiO_2(110). *J. Chem. Phys.*, 146:184704, 2017.

[7] Marco Di Giovannantonio, Okan Deniz, Jos I. Urgel, Roland Widmer, Thomas Dienel, Samuel Stolz, Carlos Snchez-Snchez, Matthias Muntwiler, Tim Dumslaff, Reinhard Berger, Akimitsu Narita, Xinliang Feng, Klaus Mllen, Pascal Ruffieux, and Roman Fasel. On-surface growth dynamics of graphene nanoribbons: The role of halogen functionalization. *ACS Nano*, 12(1):74, 2018.

[8] J. Seo, D. Y. Kim, E. S. An, K. Kim, Kim. G.-Y., S.-Y. Hwang, D. W. Kim, B.G Jang, H. Kim, G. Eom, S. Y. Seo, R. Stania, M. Muntwiler, J. Lee, K. Watanabe, T. Taniguchi, Y. J. Jo, J. Lee, B. I. Min, M. H. Jo, H. W. Yeom, S.-Y. Choi, J. H. Shim, and J. S. Kim. Nearly room temperature ferromagnetism in a magnetic metal-rich van der Waals metal. *Science Advances*, 6(3):8912, 2020.

[9] Luis Henrique de Lima, Thomas Greber, and Matthias Muntwiler. The true corrugation of a h-BN nanomesh layer. *2D Mater.*, 7(3):035006, mar 2020.

[10] D. Hsieh, Y. Xia, D. Qian, L. Wray, J. H. Dil, F. Meier, J. Osterwalder, L. Patthey, J. G. Checkelsky, N. P. Ong, A. V. Fedorov, H. Lin, A. Bansil, D. Grauer, Y. S. Hor, R. J. Cava, and M. Z. Hasan. A tunable topological insulator in the spin helical Dirac transport regime. *Nature*, 460(7259):1101–1105, August 2009.

[11] B. Q. Lv, N. Xu, H. M. Weng, J. Z. Ma, P. Richard, X. C. Huang, L. X. Zhao, G. F. Chen, C. E. Matt, F. Bisti, V. N. Strocov, J. Mesot, Z. Fang, X. Dai, T. Qian, M. Shi, and H. Ding. Observation of Weyl nodes in TaAs. *Nat. Phys.*, 11(9):724–727, September 2015.

[12] N. C. Plumb, M. Salluzzo, E. Razzoli, M. Mnsson, M. Falub, J. Krempasky, C. E. Matt, J. Chang, M. Schulte, J. Braun, H. Ebert, J. Minr, B. Delley, K.-J. Zhou, T. Schmitt, M. Shi, J. Mesot, L. Patthey, and M. Radovi. Mixed Dimensionality of Confined Conducting Electrons in the Surface Region of $SrTiO_3$. *Phys. Rev. Lett.*, (113):086801, August 2014.

[13] A. F. Santander-Syro, F. Fortuna, C. Bareille, T. C. Rödel, G. Landolt, N. C. Plumb, J. H. Dil, and M. Radović. Giant spin splitting of the two-dimensional electron gas at the surface of $SrTiO_3$. *Nat. Mater.*, 13(12):1085–1090, December 2014.

[14] Y. Sassa, M. Radovi, M. Mnsson, E. Razzoli, X. Y. Cui, S. Pailhs, S. Guerrero, M. Shi, P. R. Willmott, J. Mesot F. Miletto Granozio, M. R. Norman, and L. Patthey. Ortho-ii band folding in $YBa_2Cu_3O_{7-\delta}$ films revealed by angle-resolved photoemission. *Phys. Rev. B*, 83, 140511(R), 2011.

[15] H. Petersen, C. Jung, C. Hellwig, W. B. Peatman, and W. Gudat. Review of plane grating focusing for soft x-ray monochromators. *Rev. Sci. Instrum.*, 66(1):1–14, 1995.

[16] P. Oberta, U. Flechsig, M. Muntwiler, and C. Quitmann. Optical design study of the PEARL beamline at SLS. *Nucl. Instr. and Meth. A*, 635:116–120, 2011.

Chapter 6

EUV Semiconductor Metrology and Interference Lithography Beamline

Iacopo Mochi, Yasin Ekinci, Markus Kropf, Michaela Vockenhuber

In a nutshell

The aim of the XIL beamline is to become a leading infrastructure for advanced semiconductor technology research and to provide the semiconductor manufacturing community with extreme ultraviolet metrology and interference lithography capabilities compatible with the future technology nodes (5 nm and below).
SLS 2.0 will provide a higher brightness which will increase the coherent flux that powers the XIL endstations. This will allow us to reduce the exposure times and thus the effect of mechanical instabilities at the nanoscale which constitute a fundamental limit to the resolution of our platforms. With the upgrade to SLS 2.0, we aim to push the resolution of our metrology endstation to 20 nm and to turn interference lithography fabrication of sub 10-nm structures into a standard capability for our users.
As a long-term vision, we aim to increase the XIL portfolio of semiconductor metrology techniques with an EUV scatterometry endstation to investigate the topography and the material composition of printed silicon wafers and turn the XIL beamline into a metrology facility for all the steps of the semiconductor device fabrication process.

6.1 Overview

The mission of XIL is the study and development of materials and technologies for semiconductor device manufacturing, including extreme ultraviolet (EUV) resist films and EUV photomasks used in the photolithography process. XIL hosts the world most advanced platform for interference lithography

with a record resolution of 6 nm. [1] XIL provides the semiconductor manufacturing community with the ability to test materials for current and future technology nodes. [2] The interference lithography endstation at XIL is also used for the manufacturing of customizable periodic and semi periodic nano-structures that find application in several research fields. [3] RESCAN, the mask metrology endstation, is a test platform for the development of novel inspection techniques for EUV photomasks and pellicles. [1, 4, 5] This tool addresses the fundamental need of the industry to access affordable and reliable metrology of defects that may affect the semiconductor manufacturing process.

The XIL beamline offers a unique capability to address these increasingly difficult challenges, to explore sub-10 nm structures and to provide insights into semiconductor physics, novel devices, quantum systems, catalysis, and material science.

6.1.1 Impact of the new ring brilliance

The SLS upgrade will make it possible to achieve a significant increase in flux, as shown in Section 6.2. This will translate directly into a reduction of the exposure times. This constitutes a major benefit for XIL since it will reduce the effects of thermo-mechanical drifts occurring at the nano scale, one of the main causes of resolution loss in the interference lithography process. The lensless metrology activities will benefit from the increased brightness of the source that will translate directly into a higher coherent flux, which is essential for the performance of coherent diffraction imaging techniques.

6.1.2 Complementarity to other PSI BLs

The XIL beamline at SLS 2.0 will become a facility where the semiconductor manufacturing scientific and industrial community will be able to carry out research on advanced materials and technology for the future photolithography nodes. The beamline will be complementary to cSAXS in the field of metrology of semiconductor devices. While at cSAXS, users are able to inspect the 3D structure of a package device, XIL is designed to characterize the photomask at its design wavelength (EUV). Together, the two beamlines cover the complete range of applications required for advanced research in semiconductor metrology. Moreover, XIL will provide high-resolution and large-area nanostructures for the research on devices physics to characterize nanostructured materials and integrated devices at QUEST and SX-ARPES beamlines. The XIL beamline offers unique capabilities in combination with the PolLuX and SIM beamlines to study the chemical mechanisms due to the EUV light, which is of high importance for the development of EUV resists for future technology nodes in semiconductor manufacturing.

6.1.3 Uniqueness compared to other present and planned beamlines worldwide

EUV lithography: The EUV lithography endstation at XIL is still quite unique. PSIs EUV-IL tool is the leading tool in the world. Shanghai Synchrotron Source has an EUV-IL beamline dedicated to resist testing which PSI contributed with technical and scientific support, however its performance in terms of resolution is still below ours. Currently, the Taiwan National Synchrotron Radiation Research Center and the Australian Synchrotron Source are considering the possibility of building EUV-IL dedicated beamlines and we are advising and helping them in the design of preliminary

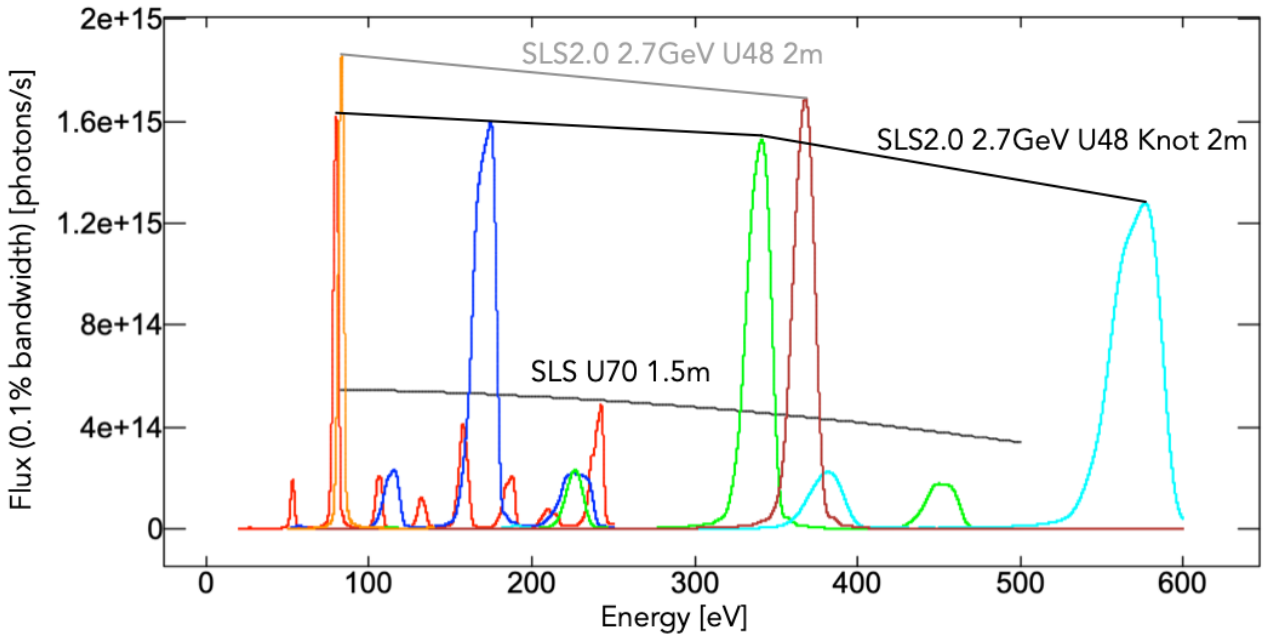

Figure 6.1: The plot shows a comparison between the flux of the new source and the flux of the current XIL source at the SLS. The flux value refers to a bandwidth of 0.1%.

experiments. The only other competitive program for resist testing at a synchrotron facility is the MET5 at the the Advanced Light Source. However, the MET5 is a micro-exposure tool based on projection optics rather than on interference lithography.

EUV mask inspection: The only other synchrotron-based EUV mask inspection program is the SHARP microscope at the Advanced Light Source (bl 11.3.2). SHARP is a FZP-based microscope and is dedicated to mask review (high resolution imaging of selected areas) while RESCAN is being developed for mask inspection (defect detection over the full surface of the sample).

6.2 Source

The XIL beamline will share the long straight of sector 5 with SX-ARPES and both beamlines will have a different insertion device. However, since no canting is possible with the new accelerator design, the beamlines will share the front end and the beam time. The XIL beamline source will be a 2 m Apple *knot* undulator (U48) and will deliver a flux 3 times higher compared to the current insertion device, as shown in Figure 6.1. The *knot* configuration was preferred to the Apple X periodic design, which would have delivered a higher flux, because of the reduced thermal load on the first mirror. The undulator will be configured for optimal performance at 92 eV, but will be able to operate up to $\sim$ 600 eV.

6.3 Optics

The optics conceptual layout of the XIL beamline is illustrated in Figure 6.2. The first mirror, M_1, will be hosted in a dedicated chamber and will deflect the beam by a total included angle of 168° and focus it on a plane where a set of apertures will be installed. The purpose of these apertures is to control the spatial coherence of the beam, remove aberrations and control the flux. In the current XIL configuration we use circular apertures with diameter ranging from 10 to 100 μm. The apertures are mounted on a motorized plate and can be easily substituted to accommodate any experimental need. After the apertures, the beamline is divided into two branches.

6.3.1 Lithography branch

The lithography branch makes use of the pink beam. The interference lithography endstation requires a uniform beam over an area of about 500×500 μm^2. To approximate this condition and ensure an adequate beam intensity stability, a beam diameter of 3 mm is necessary at the entrance of the endstation. To fulfill this requirement a collimation mirror (CM) is added just before the entrance port of the endstation.

6.3.2 Metrology branch

The metrology branch requires a monochromatic beam with $\lambda/\Delta\lambda \geq 1500$. This is achieved by means of a spherical grating monochromator (SGM). The monochromator's grating deflects the beam and focus it horizontally on the exit slit plane. The grating can be moved in and out the beam path to select the beamline operating branch. The exit slits are adjustable in both axis to control the temporal coherence of the beam and the flux level. In this design, the beam horizontal focus is located at the exit slit of the monochromator and the vertical focus lies on the aperture plane before the monochromator. To correct the astigmatism induced by this configuration, a refocusing toroidal mirror, FM_1,is required at the entrance of the endstation.

6.4 Endstations

Preventing the contamination of the samples is a key requirement for the majority of the experiments carried out at the XIL beamline. For this reason, the endstations need to be kept in a cleanroom environment (class $\leq$ 1000), and a sample preparation and processing area (class $\leq$ 100) is also required as shown in Figure 6.3.

6.4.1 XIL

The endstation of XIL is dedicated to extreme ultraviolet (EUV) interference lithography for the evaluation of novel resist materials capable of supporting patterns with critical dimensions lower than 10 nm.

In the interference lithography endstation, a mask with specifically designed diffraction gratings is illuminated by a spatially coherent beam of EUV light (λ = 13.5 nm) [1, 6]. First-order diffraction

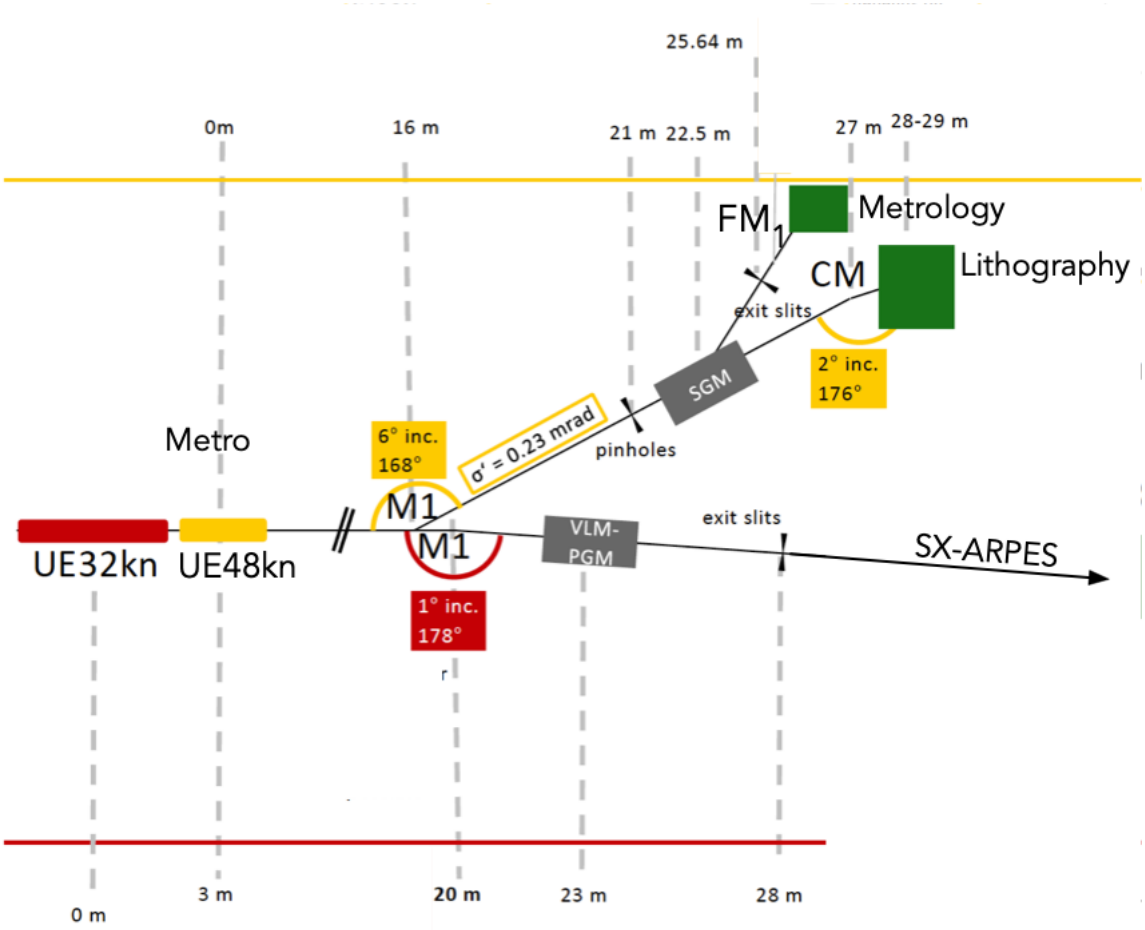

Figure 6.2: XIL optics layout. The XIL beamline is projected towards the wall with the first mirror, M_1, and is divided into a coherent branch, used for the metrology endstations and a branch using the pink beam which serves the lithography endstation. The figure is not to scale.

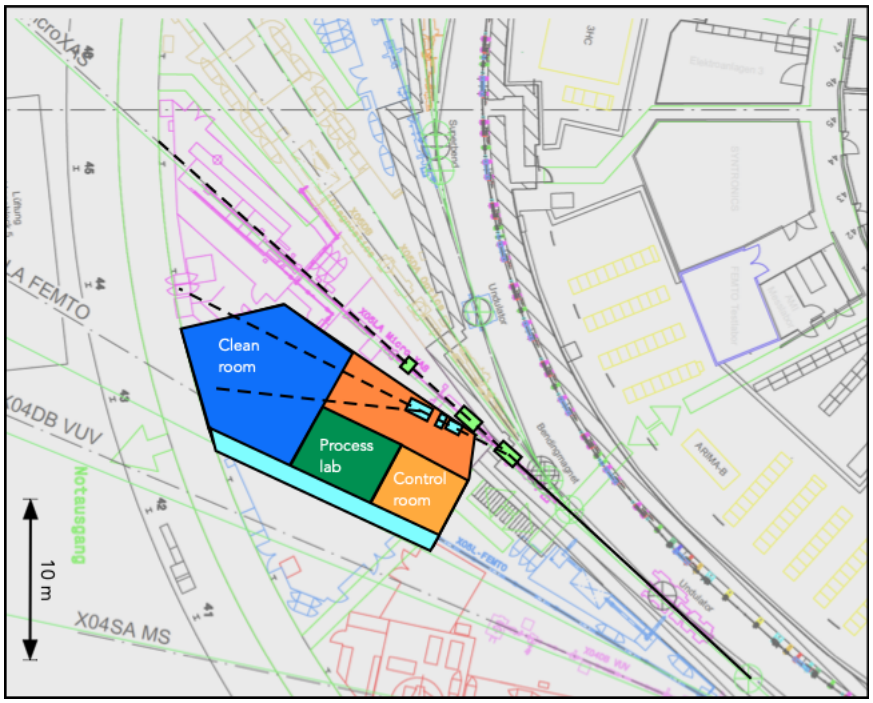

Figure 6.3: Schematic footprint of the XIL beamline at sector 5.

beams overlap and generate an interference pattern on the surface of a coated wafer. The mask mount is equipped with a stepper motor with a resolution of 100 nm to adjust its position along the direction of propagation of the beam in order to control the distance between the mask and the sample. The sample, usually a 4-inch wafer, is installed on 2D stages that move in a plane perpendicular to the beam propagation axis. The sample stage is controlled by stepper motors with a resolution of 50 nm. The endstation is enclosed in a vacuum chamber and operates at a pressure of 10^{-7} mbar. The vacuum chamber is installed on an optical table with a passive vibration insulation system.

EUV-IL generates a well-defined and aberration-free aerial image and is a simple yet powerful method to create high-resolution periodic nanostructures over large areas and for the fast and low-cost characterization of EUV lithography resists. The XIL beamline still holds the world record in resolution in photolithography with 6 nm half-pitch resolution [7] and users routinely expose patterns with 10 nm critical dimension, which makes XIL the world most advanced platform for EUV resist testing. The XIL endstation can also be used with different diffraction masks geometries to print contact arrays or quasi-periodic structures that find application in several nano-fabrication fields.

As part of the transition to SLS 2.0, the endstation will be upgraded to include a load-lock for clean sample handling and a new active vibration-damping system. In addition, the mask and the sample stages will be modified to include interferometers to monitor and correct mechanical and thermal drifts.

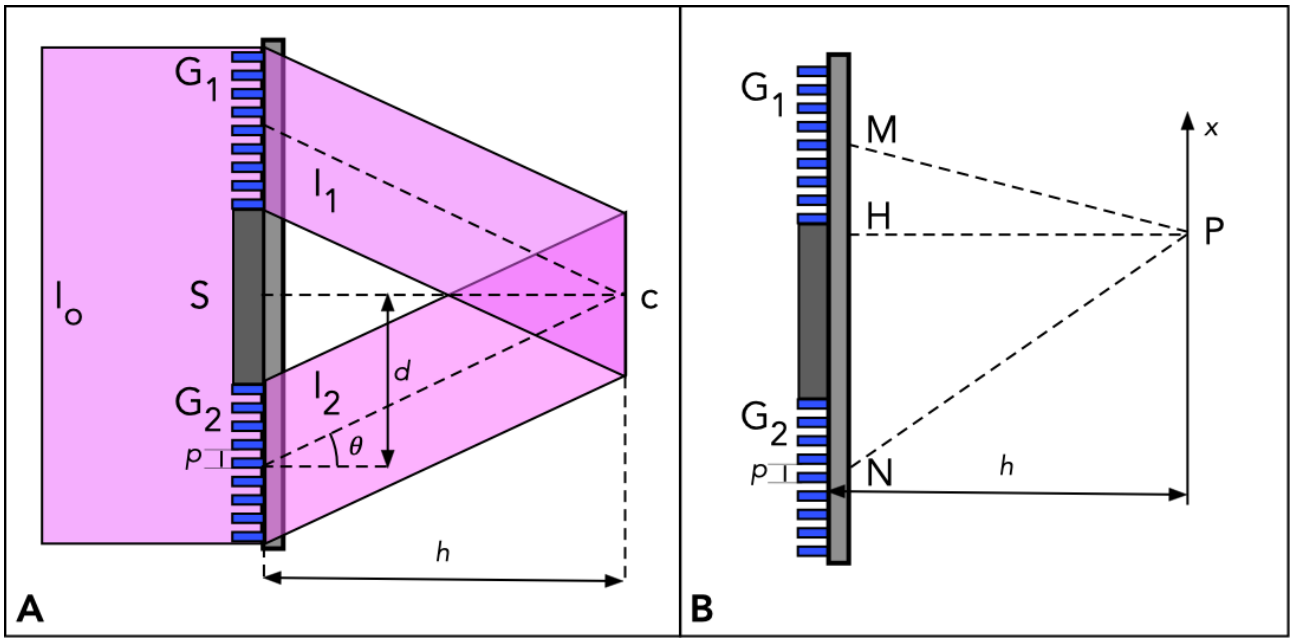

Figure 6.4: Conceptual optical design of the XIL endstation. **A.** The central part of the EUV beam, with intensity I_0, illuminates a Si_3N_4 membrane with a nickel central stop S and two HSQ gratings (G_1 and G_2). The first order diffraction beams I_1 and I_2 overlap at a distance h on the sample plane c. **B.** The intensity of the interference pattern on a point P can be calculated from the optical path difference $MP - NP$ and results in a sinusoidal profile with half the period of the gratings.

6.4.2 XMET1

The XMET1 endstation is the upgraded version of RESCAN, a lensless microscope dedicated to the inspection and review of EUV photomasks. The conceptual drawing of XMET1 is shown in Figure 6.5(b). The endstation will consist of a vacuum chamber installed on a concrete block with a passive vibration insulation system. The pressure in the vacuum chamber is kept at 10^{-7} mbar. XMET1 will be equipped with a Fourier synthesis illuminator, shown in Figure 6.5A, to control the angle of incidence of the beam on the sample without altering its coherence properties. The beam from the exit slit of the monochromator will be focused by a paraboloidal off-axis mirror (M_1) in proximity of the pivot point of M_2, a flat tip-tilt mirror with an angle range of ± 3 deg around the vertical and horizontal axis. The beam will be refocused on the sample by an ellipsoidal mirror (M_3). The foci of M_3 are located on the pivot point of M_2 and on the center of the sample to keep the illumination spot in the same position while changing the illumination angle. All the mirrors will be coated with a gradient multilayer to maximize their reflectance at 13.5 nm.

The diffracted light is collected by an EUV CCD detector. The CCD detector might be substituted with two tiled EUV-compatible JUNGFRAU modules [8] which are still under development and will be able to provide a data acquisition speed improvement of 4 orders of magnitude.

The sample consists in an EUV photomask, a multilayer-coated low TE material plate with a size

of $150 \times 150 \times 6$ mm. The sample is inserted into the vacuum chamber through a lateral load-lock with a robotic arm and is kinematically mounted on a XY stage with 300 mm travel in both directions and an 3-axis interferometer for sub nanometer position control.

XMET1 will be equipped with a visible-light microscope to assist the navigation of the sample as shown in Figure 6.5B.

The current resolution of the RESCAN endstation is 36 nm. The optical system design of XMET1 will bring the resolution of the reconstructed image to < 20 nm and will enable flexible illumination settings to investigate the topography of the sample surface.

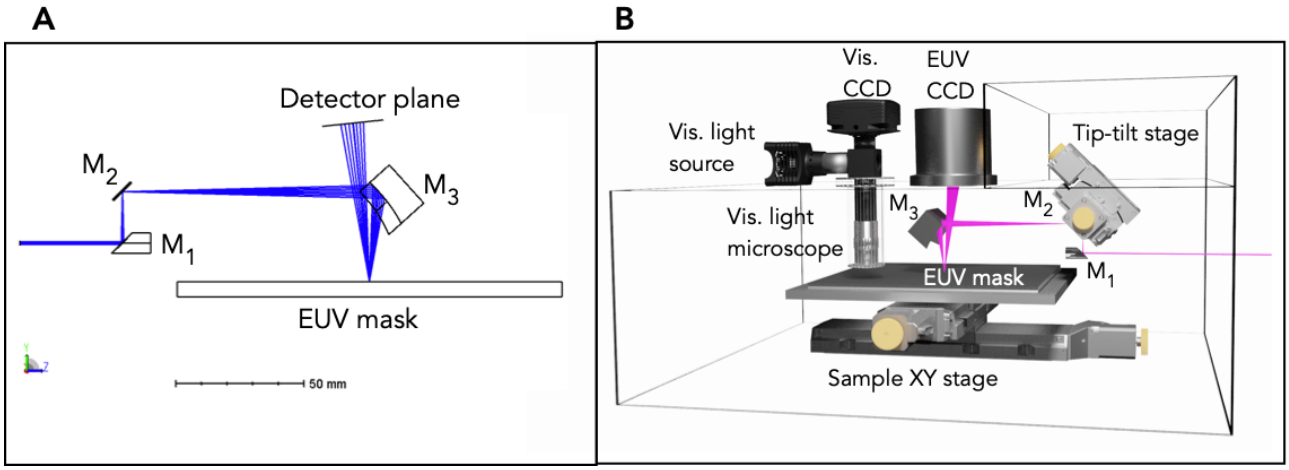

Figure 6.5: A. Optical layout of the XMET1 endstation. B. XMET1 conceptual drawing.

6.4.3 XMET2

The XMET2 endstation is a new soft x-ray scatterometry platform for wafer and generic surfaces metrology that will be swapped with the XMET1 endstation when necessary. Its conceptual design is shown in Figure 6.6. The beam will be focused on the sample with a fixed, compact KB system and will have an energy that can vary between 30 and 250 eV. The sample will be installed on an XY stage with a travel range of 300 mm along both axes. A goniometer will be used to change the incidence angle of the beam on the sample from 0 to 20 degrees and an in-vacuum CCD detector, mounted on a rotation stage, will collect the scattered signal. The system will be installed in a vacuum chamber with a lateral load lock and will operate at pressure of 10^{-7} mbar.

6.5 Timeline

XIL will have to be relocated to Sector 5. This will adds some complexity to the upgrade process and will require a careful effort coordination between all the involved stakeholders. The upgrade process will start with the procurement of the new mirrors M_1, FM_1 and CM and the chambers for two of them. This will start as soon as the funds are available. Starting form the beginning of the dark

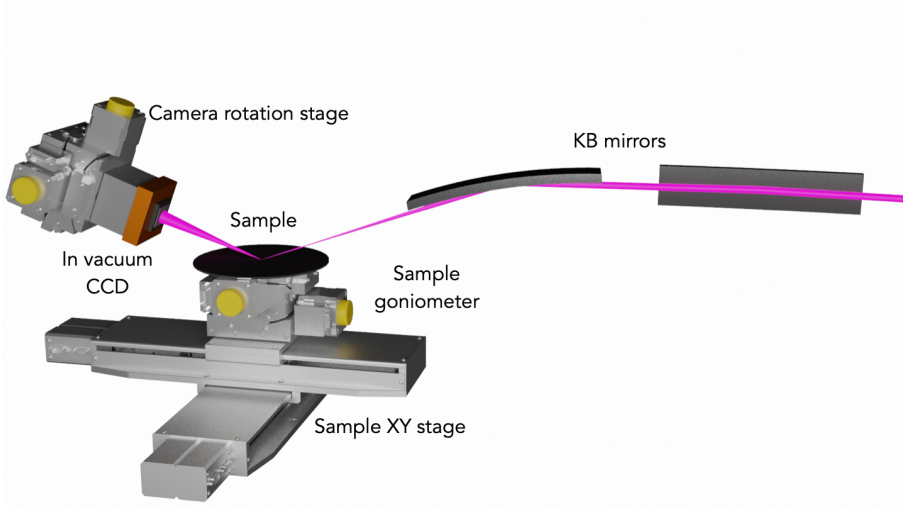

Figure 6.6: Conceptual drawing of the XMET2 endstation.

period, the current beamline will be decommissioned and its components stored. The decommissioning process will be completed in a time-frame compatible with the necessities of the new beamline that will occupy Sector 9. Once the space dedicated to XIL at sector 5 is available the building of the new beamline will start. This process will include several steps from the installation of beamline itself and the building of the new cleanroom area and control hutch, to the installation and commissioning of the new endstations. An ideal timeline for the upgrade of the XIL endstation is shown in Figure 6.7.

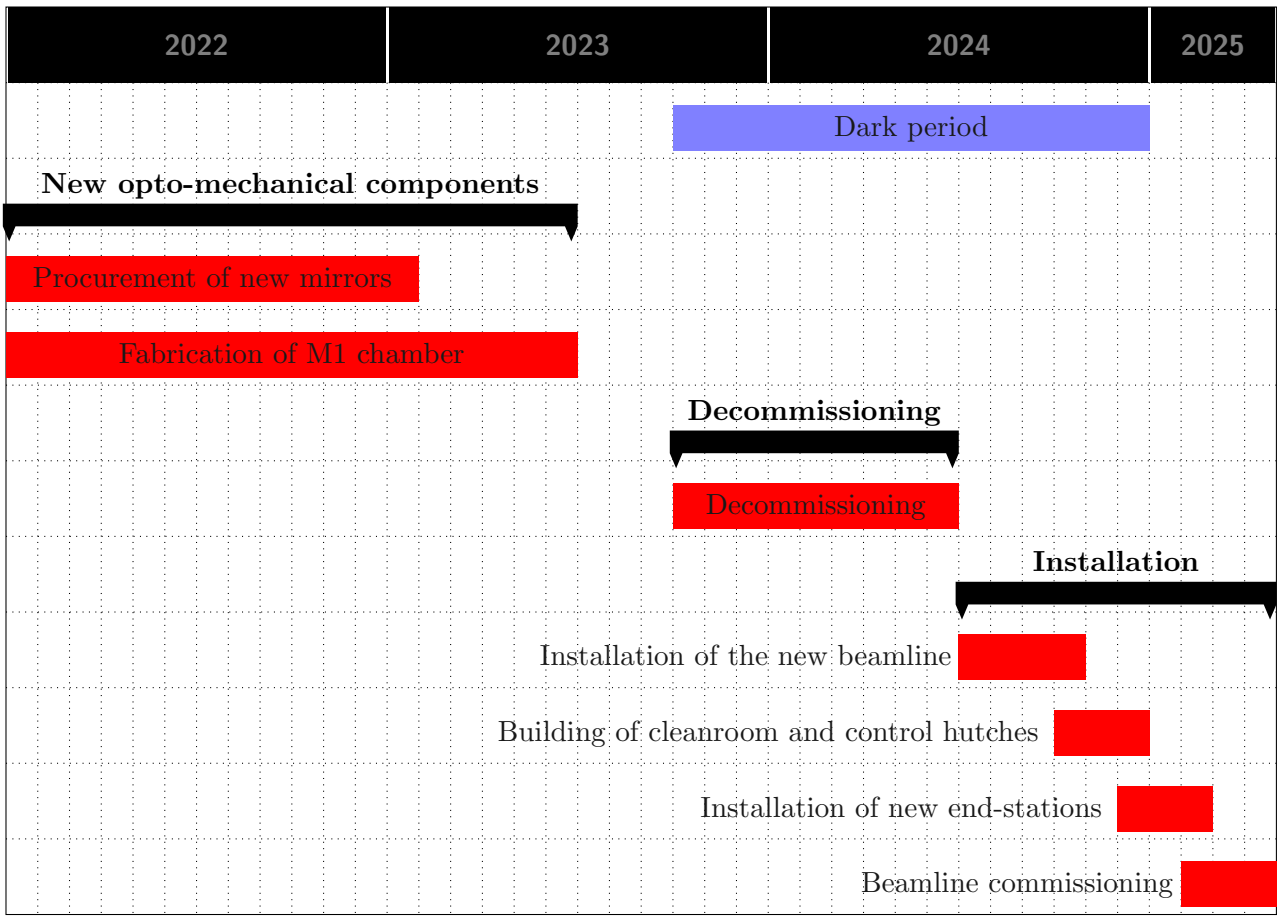

Figure 6.7: Ideal timeline for the upgrade of XIL.

Bibliography

[1] Iacopo Mochi and Yasin Ekinci. Lensless EUV lithography and imaging. *Synchrotron Radiation News*, 32(4):22–27, 2019.

[2] Xiaolong Wang, Li-Ting Tseng, Timothee Allenet, Iacopo Mochi, Michaela Vockenhuber, Chia-Kai Yeh, Lidia van Lent-Protasova, Jara Garcia Santaclara, Rolf Custers, and Yasin Ekinci. Progress in EUV resists status towards high-NA EUV lithography. In Nelson M. Felix and Anna Lio, editors, *Extreme Ultraviolet (EUV) Lithography XI*, volume 11323, pages 42 – 52. International Society for Optics and Photonics, SPIE, 2020.

[3] Steven Gottlieb, Dimitrios Kazazis, Iacopo Mochi, Laura Evangelio, Marta Fernndez-Reglez, Yasin Ekinci, and Francesc Perez-Murano. Nano-confinement of block copolymers in high accuracy topographical guiding patterns: modelling the emergence of defectivity due to incommensurability. *Soft Matter*, 14:6799–6808, 2018.

[4] Iacopo Mochi, Sara Fernandez, Ricarda Nebling, Uldis Locans, Rajendran Rajeev, Atoosa Dejkameh, Dimitrios Kazazis, Li-Ting Tseng, Serhiy Danylyuk, Larissa Juschkin, and Yasin Ekinci. Quantitative characterization of absorber and phase defects on EUV reticles using coherent diffraction imaging. *Journal of Micro/Nanolithography, MEMS, and MOEMS*, 19(1):1 – 11, 2020.

[5] Iacopo Mochi, Marina Y. Timmermans, Emily E. Gallagher, Marina Mariano, Ivan Pollentier, Rajeev Rajendran, Patrick Helfenstein, Sara Fernandez, Dimitrios Kazazis, and Yasin Ekinci. Experimental evaluation of the impact of carbon nanotube EUV pellicles on reticle imaging. *Journal of Micro/Nanolithography, MEMS, and MOEMS*, 18(1):1 – 7, 2019.

[6] Nassir Mojarad, Jens Gobrecht, and Yasin Ekinci. Interference lithography at EUV and soft x-ray wavelengths: Principles, methods, and applications. *Microelectronic Engineering*, 143:55 – 63, 2015. Special Issue on Micro/Nano Lithography with Photons, Electrons & Ions 2014.

[7] Daniel Fan and Yasin Ekinci. Photolithography reaches 6nm half-pitch using extreme ultraviolet light. *Journal of Micro/Nanolithography, MEMS, and MOEMS*, 15(3):1 – 7, 2016.

[8] S. Redford, A. Bergamaschi, M. Brückner, S. Cartier, R. Dinapoli, Y. Ekinci, E. Frjdh, D. Greiffenberg, D. Mayilyan, D. Mezza, A. Mozzanica, R. Rajeev, M. Ramilli, C. Ruder, L. Schdler, B. Schmitt, X. Shi, D. Thattil, G. Tinti, and J. Zhang. Calibration status and plans for the charge integrating JUNGFRAU pixel detector for SwissFEL. *Journal of Instrumentation*, 11(11):C11013–C11013, 2016.

Chapter 7

PolLux – A Scanning Transmission Soft-X-ray Spectro-Microscopy Beamline

Jörg Raabe, Simone Finizio, and Benjamin Watts

In a nutshell

The superior brilliance of SLS 2.0 will directly translate into corresponding performance improvements for the PolLux STXM, allowing higher spatial resolution, energy resolution and image quality. In addition, PolLux 2.0 will utilise a novel *twin source* design that utilises a second bending magnet source to improve spectral purity and extend the photon energy range. This will allow microspectroscopy studies of all elements between Li and Br. Reuse of many existing components minimise the cost and man-hours required to realise these upgrades.
Further detector and electronics upgrades will improve PolLux's capabilities for time-resolved measurements in both time resolution (using methods compatible with normal SLS 2.0 operation) and the range of accessible elements. The SLS 2.0 upgrades will keep PolLux at the forefront of nanoscale materials science.

7.1 Overview

The PolLux beamline performs nanoscale materials science with an emphasis on organic materials [1,2], magnetism dynamics [3,4], *in-situ* environmental cells [5,6], and more recently 3D imaging [7]. To this end, it combines a simple spherical grating monochromator (SGM) with a scanning transmission x-ray microscope (STXM). The reduced emittance of SLS 2.0 will provide a significantly more brilliant bending magnet source that will directly translate into proportionally improved spectroscopy and microscopy performance for PolLux with only minimal changes required to adapt to the new source

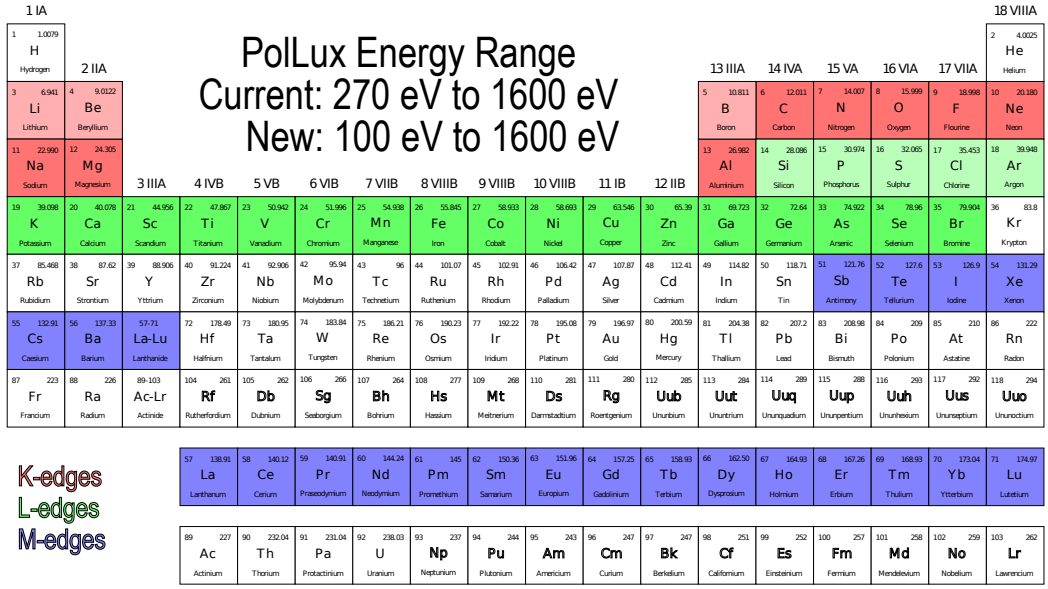

Figure 7.1: X-ray absorption edges of the elements that are accessible in the current PolLux design (saturated colour backgrounds) and that will be accessible in the PolLux 2.0 design (pale backgrounds). Accessible K-edges are indicated with a red background, L-edges with a green background, and M-edges in blue. A white background indicates that the element has no x-ray absorption edges within either the PolLux 1.0 or PolLux 2.0 photon energy range.

position. The two major limits on the current performance of PolLux are the photon flux and the compromise between higher-order suppression and photon energy range. The proposed PolLux 2.0 design addresses these issues through either the addition of a second optical geometry to the SGM monochromator in a novel *twin source* design that utilises a second bending magnet source, or by adopting a PGM monochromator. Both options provide new flexibility for simultaneously improving spectral purity and extension of the photon energy range, which will allow spectromicroscopy studies of Be, B, Si, S, P, Cl and Ar through new access to the corresponding absorption edges (see Figure 7.1).

The reason why the energy resolution limits the performance of the PolLux STXM is interestingly not because of a need for higher resolution spectroscopy, but because the ultra-high resolution Fresnel zone plates (FZP) now available have much stronger temporal coherence requirements to achieve a diffraction limited focus. Since the focal length of a FZP varies with photon energy and the energy resolution of the illumination is finite, the focus can be said to no longer be diffraction limited when the variation in focal length of the illuminating photons exceeds the depth of focus, giving: [8]

$$\frac{E}{\Delta E} \geq N \tag{7.1}$$

where $E/\Delta E$ is the resolving power and N is the total number of zones in the FZP. This means that, for example, a FZP with an outer diameter of 240 microns and a 10 nm outermost zone width would have 6000 zones and requires an equivalent resolving power, which is only achievable at PolLux 1.0 at specific photon energies where the SGM has a good focus on the exit slit. FZPs with even better

spatial resolution and thus stricter resolving power requirements are already available. [9, 10]

7.1.1 Unique points compared to other beamlines

Imaging techniques are one of the core activities of synchrotron light source facilities, as underlined by the strong imaging programs of new and upgrading facilities worldwide. Soft x-ray transmission imaging beamlines are present at several synchrotrons in the world (BESSY II, Elettra, Diamond, ALS, CLS - to name a few examples), and PolLux 1.0 has established itself as a beamline combining record-breaking spatial resolution with time-resolved imaging, and the possibility to combine x-ray imaging with user-specific solutions for *in-situ* and *in-operando* experiments. True to this statement, PolLux 1.0 holds the world record in STXM resolution, with a demonstrated resolution of 7 nm [10], and has pioneered a novel approach to time-resolved imaging. The success of the PolLux 1.0 beamline, spearheaded by its specialization in high-resolution and time-resolved imaging, is documented by a ten-year overbooking ratio of 1.62 and a total of about 200 published papers over the last ten years.

With respect to time-resolved imaging, which is one of the core competencies of PolLux 1.0, only the MAXYMUS beamline at the BESSY II light source in Berlin offers similar performances (time-resolved imaging is planned for the Hermes and SoftiMAX beamlines at Soleil and MAX-IV respectively, but neither is expected to reach temporal resolutions comparable to PolLux and MAXYMUS). Here, a critical difference between SLS (and SLS 2.0) and BESSY II is that BESSY II offers a low-α optics operation, which allows for the achievement of temporal resolutions of 10 ps at the MAXYMUS beamline, compared with a temporal resolution on the order of 50 ps for SLS with normal optics operation. To compensate for this disadvantage, a novel approach to time-resolved imaging, based on time-of-arrival measurements, combined with the use of specialized detectors has been developed (see Section 7.5.2 and Reference [11] for more details). As this method requires high statistics to provide temporal resolutions comparable to the operation of the light source with low-α optics, the upgrade to SLS 2.0 will enable the routine achievement of high temporal resolutions without the disadvantages connected to low-α optics operation, therefore maintaining the competitiveness of PolLux.

Thanks to the collaboration between the PolLux and cSAXS teams, PolLux 1.0 pioneered a novel soft x-ray 3D imaging method [7], that no other STXM beamline worldwide is able to offer. While developments towards this direction are planned in other facilities (e.g. the proposed CSXID beamline for the Diamond-II upgrade), those developments lack the expertise and synergetic effort currently available at PSI. This, combined with the several years of advantage/experience at PSI, guarantees a leading edge of PolLux 2.0 over proposed competitor beamlines.

For the imaging of organic materials at the C K-edge, PolLux is a favoured instrument due to minimisation of carbon contamination on the optics [12] and strong higher-order suppression. The PolLux 2.0 beamline design will result in further improvements in both of these aspects, while also providing access to the L-edges of P, S and Cl, elements that are often critical molecular components, but are only available at a few STXM beamlines such as ALS 11.0.2, Soleil HERMES and CLS 10ID-1. Together, these improvements mean that the imaging of organic materials at PolLux 2.0 will be strongly competitive with undulator-based microscopes.

7.1.2 Synergies and complementarities to other SLS 2.0 beamlines

Similarly to PolLux 1.0, the focus of PolLux 2.0 will be on (spectro-)microscopy imaging combining high spatial and temporal resolutions. Our goal will be to provide a measuring platform compatible with the increasing imaging demands from condensed-matter physics, chemistry, environmental science, and biology, with the possibility to operate *in-situ* and *in-operando* investigations. As mentioned in the previous section, thanks to a well-established collaboration with the x-ray optics group of the Laboratory for Micro- and Nanotechnology of PSI, we currently hold the world record in STXM resolution (7 nm – see Reference [10]), and the upgrade to SLS 2.0 will allow us to expand the user base to which this ultimate resolution imaging can be offered. PolLux 2.0 will offer, similarly to PolLux 1.0, a soft x-ray transmission microscopy technique, which directly complements SIM (where surface-sensitive x-ray microscopy is performed at the PEEM endstation). Furthermore, with the successful commissioning of the soft x-ray laminographic imaging [7], we will be able to offer a complementary measurement method to cSAXS (where a hard x-ray laminography setup is available). Finally, we will be sharing our expertise in transmission x-ray imaging with the SIM beamline, where the development of a soft x-ray ptychographic endstation is proposed (see Chapter 9 for more details).

7.1.3 Impact on the STXM user community

PolLux has operated over the last 10 years with an average overbooking factor of 1.62, rising to about 1.81 since 2016. This performance metric indicates a healthy interest from the user community for the PolLux beamline, which will be further increased by the improvement in the beam performances promised by the SLS 2.0 upgrade. The user community of PolLux can be divided into two macro-areas, given by condensed-matter physics, and chemistry/environmental science/biology, each requesting, on average over the last 10 years, about 50% of the beamtime. In the last five years, the demand for PolLux beamtime has shifted towards condensed-matter physics, with about 60% of the requested beamtime.

The proposed PolLux 2.0 upgrade will benefit both communities through the following impacts:

- Higher statistics due to the brighter SLS 2.0 source will translate to improved imaging and spectroscopy quality as well as an increased rate of measurement.
- The further improvement of the temporal resolution offered by the combination of time-of-arrival imaging will allow for the investigation of faster dynamical processes, which is currently in high demand in the magnetism research community, due to the increasing interest in antiferromagnetic and synthetic antiferromagnetic materials. The upgrade to PolLux 2.0 will therefore enable the investigation of scientific cases otherwise not possible with the current setup.
- Higher coherence of the beam illuminating the Fresnel zone plate (especially due to better energy resolution of the monochromator) will improve microscope performance in high-spatial-resolution measurements.
- Higher throughput of laminography measurements through improvement in imaging times.

7.2 Source

The beamline will continue to use two adjacent standard bend magnets in sector X07D.

7.3 Front end

The beamline needs standard front ends for bend magnets with ±2 mrad in both the horizontal and vertical directions.

7.4 Optics

7.4.1 Geometry

A core design decision of any soft x-ray beamline is the choice of angle through which each mirror should deflect the beam. This is because the angle through which soft x-rays can be efficiently reflected has a strong dependence on the photon energy. So while lower energy photons can be strongly deflected by the beamline mirrors, higher energy photons require low angle deflections for efficient mirror reflectivity and so the upper end of a beamline's photon energy range will be limited by the strongest mirror deflection. Another issue in soft x-ray beamline design is that higher-order diffraction contributions from grating monochromators result in significant spectral contamination that is very detrimental to transmission experiments such as STXM. While strategic materials choices for mirror coatings and transmission filters can significantly improve spectral purity, strategic choice of mirror deflection angle is a far more efficient method for obtaining a pure spectrum. However, altering the mirror deflection angles in order to accommodate a wide photon energy range generally requires additional mirrors and cumbersome realignment efforts every time the energy range is changed, meaning extra construction costs and wasted operation time.

The PolLux 2.0 design uses a novel *twin source* concept whereby a second, adjacent bend magnet source is used to illuminate the monochromator gratings from a steeper angle to provide a second optical geometry, as shown in Figure 7.2. The two beamline geometries can then be separately optimised for lower and higher soft x-rays without the compromises required in a traditional soft x-ray beamline design. Switching between these optical geometries is accomplished simply by opening and closing shutters in the two branches upstream of the grating chamber - with no mirror realignment necessary. A simple simulation of beamline performance for both the current and PolLux 2.0 designs is shown in Figure 7.3 and demonstrates the strong performance improvements expected, especially in the lower photon energies.

7.4.2 Mirrors

The changed source positions and required beam deflections to steer the beam into the grating chamber will necessitate new first mirrors and monochromator gratings with different curvatures. The conceptual design of each branch will remain the same, however, with the toroidal first mirror making a vertical focus on the shared exit slit and a horizontal focus on the corresponding entrance slit.

The higher-order suppressor (HOS) mirrors, with their MgF_2 coating, will be obsolete in the new design, as higher-order suppression in the 250–600 eV photon energy range will be handled by other aspects of the beamline design. The HOS will therefore be repurposed to provide spectral filtering in the very soft energy range by recoating the central mirror with a carbon stripe that can be applied via the existing horizontal translation stage.

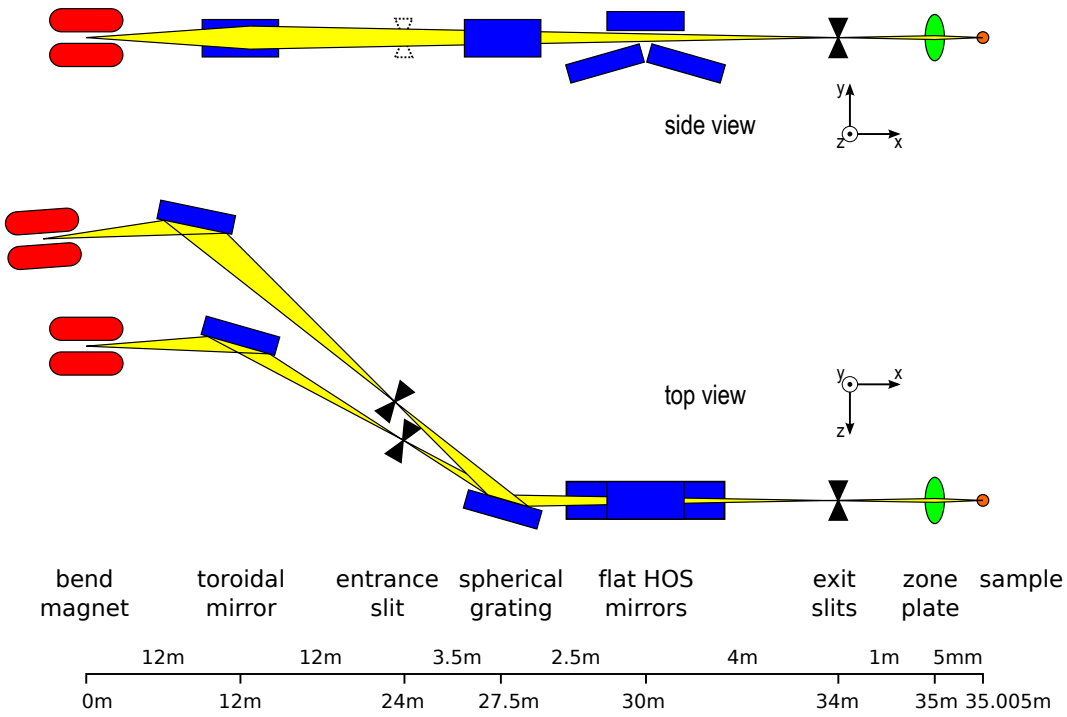

Figure 7.2: Schematic of the PolLux 2.0 beamline layout with the *twin source* branches visible from the top view. The monochromator chamber and all downstream components will remain in the same position, while the first mirrors and entrance slits will reuse components from PolLux 1.0 and NanoXAS beamlines.

7.4.3 Monochromator

The monochromator, a PSI design of a spherical grating monochromator (SGM) can be adapted to fit the SLS 2.0 source position. An SGM design has the advantages of minimising reflections (hence minimising absorption losses) and a reliable photon energy selection that relies on only one mechanical parameter (grating rotational position). A second bending magnet source can be connected (after activities at the neighbouring beamline have moved to a new location) to the SGM to provide better performance in the lower energy ranges. However, extending the photon energy range below 200 eV will require an extra grating that cannot be easily added to the current SGM and so will require a new monochromator. Therefore, we will consider switching to a plane-grating monochromator (PGM) design [13] that will provide similar improvements in spectral purity and extended photon energy range at the cost of reduced photon flux efficiency due to extra mirror reflections.

7.5 Endstation

PolLux will continue to use the existing scanning transmission x-ray microscope (STXM) after the upgrade. The endstation was delivered in 2006, but is kept up to date by continuous upgrades and improvements. For example, PolLux is one of the two beamline worldwide (besides Maxymus, Bessy),

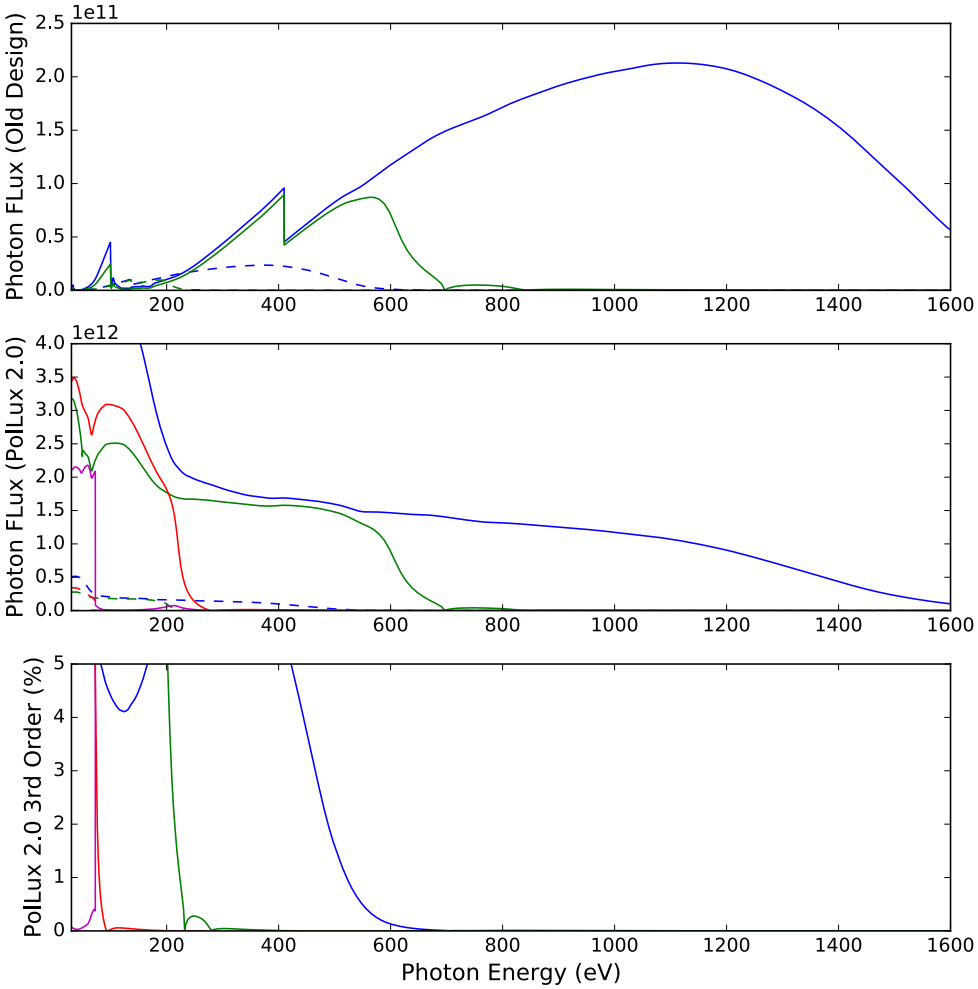

Figure 7.3: Photon flux and spectral contamination at PolLux. Upper panel: flux at the current PolLux design for different mirror and grating configurations, targeting the energy ranges of (blue) 600–1600 eV, (green) 270–600 eV, (red) 90–270 eV and (magenta) 30–75 eV; Middle: flux at PolLux 2.0. Lower panel: Percentage of 3rd order light in the PolLux 2.0 design.

where time-resolved magnetism studies with time resolutions down to ∼100 ps are routinely performed.

7.5.1 Controls and data systems

In 2011 we started to develop, together with an external company, our own STXM control software, called Pixelator. This provides a flexible and extendable solution, also for future scanning instruments. Currently this software is also used by the STXM beamlines at Soleil and at Bessy.

7.5.2 Detectors

Currently, the detection setup employed at the PolLux 1.0 endstation is based on single-photon detection and photon counting. Depending on the energy of the x-ray photons and on whether time-resolved measurements are being performed, the two photon counting detectors are the following:

- **Photomultiplier tube:** This detector can be employed across the entire energy range of PolLux, and consists of a phosphor screen converting the x-ray photons into visible light; the visible light photons are then detected through a photomultiplier tube (PMT). The disadvantage of this setup is that the length of the pulses generated by the PMT does not allow them to be employed for time-resolved measurements.
- **Avalanche Photodiode:** This detector can be employed for x-ray energies above about 500 eV. In this case, the x-ray photon generates a set of electron-hole pairs in the junction, which is then amplified by the avalanche effect in the photodiode (APD). The bandwidth of the APD can be selected to be higher than the repetition rate of the synchrotron, allowing the use of the detector for time-resolved measurements, where the determination of the photon arrival time is critical. A 900 MHz APD is currently in use, and no changes are expected. The disadvantage of the APD is that its low efficiency below photon energies of about 500 eV makes its use impractical in the 270 to 500 eV energy range.

In both cases, a photon is counted if the signal from the detector is above a (selectable) threshold. In the case of time-resolved experiments, where a pump-probe protocol for the detection is employed, a fast field-programmable gate array (FPGA) detection setup is employed to determine the electron bunch from which the detected photon was emitted.

One of the main current limitations in the time-resolved detection setup is given by the assumption that the x-ray photons are generated at the exact center of the electron bunch. This leads to an error in the determined time-of-arrival of the x-ray photon given by the width of the bunch. For SLS, this error is about 70 ps FWHM, and a similar figure is expected for SLS 2.0. This puts a strong limitation on the frequencies for the time-resolved measurements if the current setup is kept, as shown in Figure 7.4(a).

In order to extend the accessible frequency range without resorting to low-α optics operations, a different detection system for measuring the time-of-arrival of the x-ray photons will be implemented. This setup, currently undergoing the first prototype testing at PolLux 1.0, will employ the same APD as before, but the detection will be performed with a fast FPGA-based time-tagging discriminator (from the company QuTools). By performing a software-based constant fraction discrimination of the voltage pulse generated by the APD, the time of arrival of the x-ray photons can be calculated. The main advantage of this setup is that, in contrast to the currently-employed system, the excitation

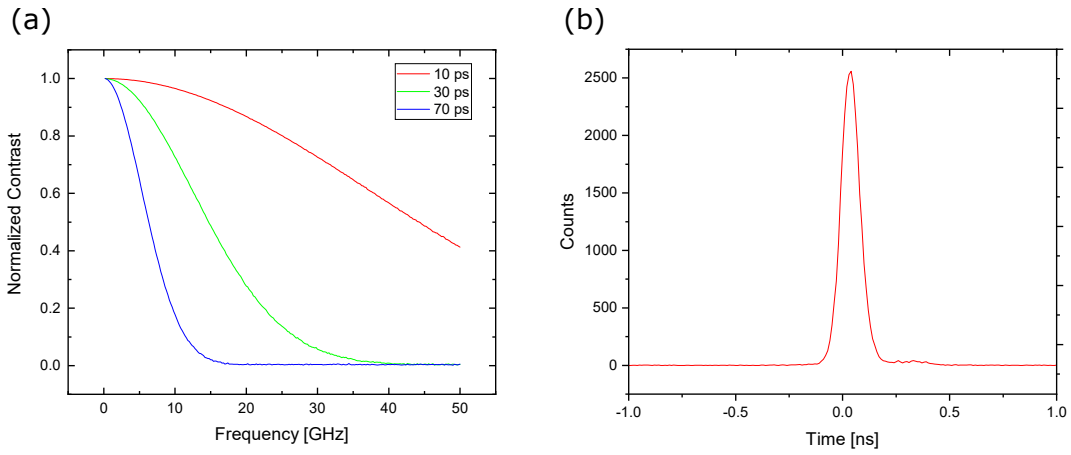

Figure 7.4: (a) Calculation of the influence of the x-ray bunch width on the achievable contrast for a time-resolved measurement as a function of its frequency. For a FWHM of 70 ps, only frequencies below 10 GHz are accessible, while for a FWHM of 10 ps (low-α), frequencies well above 50 GHz are in principle accessible; (b) Measurement of one of the x-ray bunches of the SLS 1.0 filling pattern carried out with a prototype time-tagging discriminator, proving a temporal resolution of better than 30 ps.

signal would not have to be synchronized to the synchrotron master clock [11]. This would allow for the use of arbitrary signals for the excitation of the dynamical processes in the samples.

First test measurements using the SLS filling pattern as a benchmark time-resolved signal [see Figure 7.4(b)] reveal that this setup can achieve temporal resolutions of better than 30 ps, potentially offering performances comparable to the operation with low-α optics without the disadvantages connected with it (and being therefore compatible with the upgrade to SLS 2.0).

Within the upgrade to PolLux 2.0, an extension of the energy range where x-ray detection with an APD is feasible would be desirable. For this, the use of different detector materials and concepts is foreseen.

Finally, the current detectors in use at PolLux 1.0 are point detectors. However, in synergy with the developments planned at the SIM beamline, the possibility of employing 2D photon counting detectors (with a concept similar to the EIGER detector) operating in the soft x-ray energy range, would allow for the full exploitation of the improvements in the photon flux and coherence offered by the upgrade to SLS 2.0. These detectors would be employed primarily for ptychographic imaging. To spur this development, a collaboration with the PSI detector group is underway (see Chapter 9 for more details).

7.6 IT requirements

The detection of the time of arrival of the x-ray photons proposed in Subsection 7.5.2 would allow, in principle, for the measurement and recording of the time of arrival of each individual x-ray photon. For most investigations, a simple binning of the times of arrival based on a synchronization signal

(typically a marker synchronized with the signal employed for the excitation of the sample) would suffice. However, if all of the arrival times were to be recorded and analysed, this would allow one to investigate dynamical processes that are not synchronized with the signal employed to excite the sample under investigation.

For these special situations, where the dynamical process occurs non-synchronously with the excitation signal, the time of arrival of each photon would be recorded. With the predicted photon fluxes for PolLux 2.0, this would result in data production rates of the order of 1-2 GB/min. In order to guarantee that the predicted data rates do not negatively affect the operation of the instrument, access to a fast Ethernet connection and to a suitable multi-TB storage space would be required.

7.7 Timeline

7.7.1 Planning

During the dark period, the front end and the first mirror must be replaced. This minimal adaptation will allow PolLux to restart directly after the dark period, already making use of the improved source properties.

After the current activities of the NanoXAS beamline, the In Situ Spectroscopy/NAPP Project will move to their new beamline at Sector X09D one to two years after the dark period, at which point the second bending magnet port will be available for the low energy branch. The planned schedule is shown in Figure 7.5.

Vorgangsname	Start	Finish
SLS Shutdown	Sun 01.10.23	Tue 31.12.24
PolLux: Replacement of 1st Mirror	Mon 01.07.24	Fri 30.08.24
PolLux 1st Light @SLS 2.0	Mon 03.02.25	Mon 03.02.25
Installation NAPP Beamline @ X09D	Tue 01.07.25	Thu 31.12.26
Installation NAPP Endstation @ X09D	Fri 01.01.27	Sun 31.01.27
1st Light NAPP @X09D	Mon 01.02.27	Mon 01.02.27
Decommissioning NanoXAS BL	Fri 01.01.27	Sun 28.02.27
Installation of PolLux Low-Energy Branch	Mon 01.03.27	Wed 30.06.27

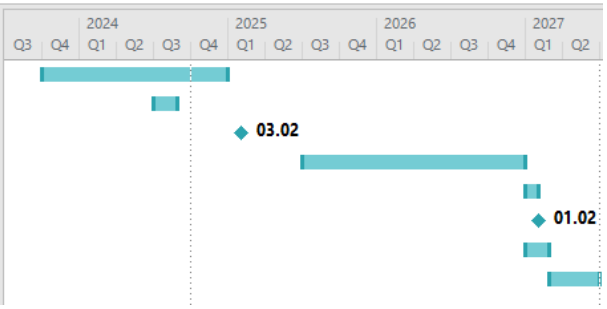

Figure 7.5: Timeline of the PolLux beamline upgrade

7.8 Concluding remarks

The PolLux beamline is currently a very productive STXM beamline at a bending magnet. In the next years, the PolLux STXM will be complemented with a more advanced instrument located at the SIM beamline. The higher flux of an undulator and full polarization control will allow more advanced techniques like ptychography and more sophisticated sample environments. A flexible allocation system of proposals to the two instruments will be implemented.

Bibliography

[1] Chen Xie, Andrej Classen, Andreas Spth, Xiaofeng Tang, Jie Min, Markus Meyer, Chaohong Zhang, Ning Li, Andres Osvet, Rainer H. Fink, and Christoph J. Brabec. Overcoming microstructural limitations in water processed organic solar cells by engineering customized nanoparticulate inks. *Advanced Energy Materials*, 8(13):1702857, 2018.

[2] Robby Janneck, Nicolas Pilet, Satya Prakash Bommanaboyena, Benjamin Watts, Paul Heremans, Jan Genoe, and Cedric Rolin. Highly crystalline C8-BTBT thin-film transistors by lateral homoepitaxial growth on printed templates. *Advanced Materials*, 29(44):1703864, 2017.

[3] Seonghoon Woo, Kyung Mee Song, Xichao Zhang, Yan Zhou, Motohiko Ezawa, Xiaoxi Liu, S. Finizio, J. Raabe, Nyun Jong Lee, Sang-Il Kim, Seung-Young Park, Younghak Kim, Jae-Young Kim, Dongjoon Lee, OukJae Lee, Jun Woo Choi, Byoung-Chul Min, Hyun Cheol Koo, and Joonyeon Chang. Current-driven dynamics and inhibition of the skyrmion hall effect of ferrimagnetic skyrmions in GdFeCo films. *Nature Communications*, 9(1):959, Mar 2018.

[4] Simone Finizio, Sebastian Wintz, Katharina Zeissler, Alexandr V. Sadovnikov, Sina Mayr, Sergey A. Nikitov, Christopher H. Marrows, and Jrg Raabe. Dynamic imaging of the delay- and tilt-free motion of Néel domain walls in perpendicularly magnetized superlattices. *Nano Letters*, 19(1):375–380, 2019.

[5] Abbas Beheshti Askari, Mustafa al Samarai, Bruno Morana, Lukas Tillmann, Norbert Pfnder, Aleksandra Wandzilak, Benjamin Watts, Rachid Belkhou, Martin Muhler, and Serena DeBeer. In situ x-ray microscopy reveals particle dynamics in a nico dry methane reforming catalyst under operating conditions. *ACS Catalysis*, 10(11):6223–6230, 2020.

[6] J.-D. Förster, C. Gurk, M. Lamneck, H. Tong, F. Ditas, S. S. Steimer, P. A. Alpert, M. Ammann, J. Raabe, M. Weigand, B. Watts, U. Pöschl, M. O. Andreae, and C. Pöhlker. Mimix: a multipurpose in situ microreactor system for x-ray microspectroscopy to mimic atmospheric aerosol processing. *Atmospheric Measurement Techniques*, 13(7):3717–3729, 2020.

[7] Katharina Witte, Andreas Spth, Simone Finizio, Claire Donnelly, Benjamin Watts, Blagoj Sarafimov, Michal Odstrcil, Manuel Guizar-Sicairos, Mirko Holler, Rainer H. Fink, and Jörg Raabe. From 2d stxm to 3d imaging: Soft x-ray laminography of thin specimens. *Nano Letters*, 20(2):1305–1314, 2020. PMID: 31951418.

[8] D. Attwood and A. Sakdinawat. *X-rays and Extreme Ultraviolet Radiation*. Cambridge University Press, second edition, 2016.

[9] *Microscopy and Microanalysis*, 24(S2):270271, 2018.

[10] Benedikt Rsner, Simone Finizio, Frieder Koch, Florian Dring, Vitaliy A. Guzenko, Manuel Langer, Eugenie Kirk, Benjamin Watts, Markus Meyer, Joshua L. Ornelas, Andreas Spth, , Stefan Stanescu, Sufal Swaraj, and et al. Soft x-ray microscopy with 7 nm resolution. *Optica*, 7(11):1602, 2020.

[11] Simone Finizio, Sina Mayr, and Jörg Raabe. Time-of-arrival detection for time-resolved scanning transmission x-ray microscopy imaging. *Journal of Synchrotron Radiation*, 27:1320, 2020.

[12] Benjamin Watts, Nicolas Pilet, Blagoj Sarafimov, Katharina Witte, and Jörg Raabe. Controlling optics contamination at the PolLux STXM. *Journal of Instrumentation*, 13(04):C04001–C04001, apr 2018.

[13] P. Oberta, U. Flechsig, M. Muntwiler, and C. Quitmann. Optical design study of the PEARL beamline at SLS. *Nuclear Instruments and Methods in Physics Research Section A: Accelerators, Spectrometers, Detectors and Associated Equipment*, 635(1):116 – 120, 2011.

Chapter 8

NAPP (In Situ Spectroscopy) Beamline

Luca Artiglia, Zbynek Novotny, and Jörg Raabe

In a nutshell

Interfaces play a paramount role in the chemical and physical sciences and modern technologies, yet their characterization has remained challenging. Catalysis, electrochemistry, and environmental chemistry are fundamental in developing a sustainable future, and, for that, specific and novel characterization tools are a necessity. We propose the construction of a new, dedicated bending magnet beamline to carry out ambient pressure x-ray photoelectron spectroscopy at SLS 2.0. The system will be modular, with the possibility to investigate all the relevant interfaces (solid-solid, solid-gas, and solid-liquid) at the atomic level. This will be possible thanks to the extended photon energy range (from 250 to 6000 eV) and a high energy resolution. Due to the versatility of the technique and the unique capabilities offered by our experimental setups, we will be able to build up a large user community of interdisciplinary character, with the possibility to collaborate with industrial partners.

8.1 Overview

8.1.1 Technique

X-ray photoelectron spectroscopy (XPS) is a surface-sensitive technique that can be used to characterize the elemental composition and the chemical nature of a wide range of substrates, from model systems (e.g. single crystals) to real devices. The XPS technique is based on the photoelectric effect, that is, the emission of an electron from a core-level orbital with element-specific binding energy (BE) upon exposure to a photon beam of sufficient energy. Because the chemical environment and the oxidation state of an element affect the BEs of core levels on the eV scale, photoemission spectra

provide important information about the oxidation state and local coordination. The surface sensitivity of XPS is due to the strong interactions of photoelectrons with matter. Indeed, only electrons coming from the near-surface layers can reach the detector without undergoing inelastic scattering events. Historically, to avoid the scattering of photoelectrons in the gas phase and to protect the detector, XPS has been conducted under ultrahigh vacuum (UHV) conditions. This has led to the so-called "pressure gap" in studies of surface chemical reactions and has severely limited the impact of XPS studies, not least in heterogeneous catalysis and environmental chemistry. In turn, model systems (single crystals, metal-supported thin oxide films, etc.), mimicking real samples, have been used to limit the complexity of measurements while still getting useful information about the surface properties (surface science studies) and the interaction between a surface and a specific environment (surface chemistry studies).

In order to reduce the pressure- and the material-gap and allow XPS measurements in the mbar range, differentially pumped electron analyzers have been developed. Such a concept was first introduced in the 1970s by Siegbahn and coworkers [1], and has become more widely applicable in the late 1990s thanks to instrumental developments of electron optics that refocus the photoelectrons passing through differentially pumped pre-lenses [2]. In a typical APXPS setup, the sample is located in a cell where the pressure can be tuned in the millibar range, and x-rays (synchrotron light or laboratory source) enter the measurement cell through a photon-transparent membrane (usually silicon nitride) or a series of differentially-pumped stages. Photoelectrons are collected by a differentially pumped pre-lens nozzle having a diameter (d) in the 0.1 to 1.0 mm range. To minimize the path traveled by photoelectrons through the gas phase, the sample is placed close to the analyzer aperture (typically at a distance ranging from d to $2d$). The factors influencing the pressure limit in an ambient pressure XPS (APXPS) system are the attenuation by scattering of the incident photon beam, reduction of the photoelectron signal through interactions with the gas phase molecules, and the pumping efficiency in the first differential pumping stage. New perspectives in the technology of APXPS electron analyzers include the development of:

1. pre-lenses and differential pumping stages to reach higher pressures (more than 100 mbar) in the analysis cell;
2. new lens operation modes allowing spatially-resolved imaging;
3. new detectors capable of ms time-resolution.

The typical configurations of the Scienta R4000 HiPP-2 photoelectron analyzer employed so far in our endstation allowed us to measure photoemission spectra at pressures up to 50 mbar in the experimental cell using an analyzer aperture of 300 μm diameter. While ambient pressure setups are becoming more common, and many of them have been designed with the main focus of investigating single-crystalline model systems, our approach is to develop a unique endstation with a high throughput for applications in heterogeneous catalysis and environmental chemistry. The technique can be further upgraded by combining it with in-situ photo- and electro-chemistry, making the APXPS capabilities at SLS 2.0 truly unique worldwide. Until 2018, an ambient-pressure photoelectron spectroscopy beamline was not available for external users at the Swiss Light Source. Since the In Situ Spectroscopy beamline has become operative at the X07DB site, it has attracted the interest of several users, generating oversubscription already during the first official call (first semester of 2019). This demonstrates the interest of an international research community toward the technique and toward the potentialities

offered by the setup available at SLS. A portion of the user community includes research groups belonging to the Paul Scherrer Institute, whose main research interests are environmental/surface chemistry, catalysis, and electrochemistry. The reason for this is because, in general, it is difficult to find in situ surface sensitive spectroscopic techniques, and APXPS is suitable to investigate interfaces with a high level of sensitivity regarding the elemental composition and electronic state of selected emitters. The results obtained at the In Situ Spectroscopy beamline at SLS and a new beamline dedicated to APXPS at SLS 2.0 will help to solve relevant open questions related to different research branches, improving the quality of the research output produced at the Paul Scherrer Institute.

8.1.2 Unique points compared to other beamlines

Generally speaking, APXPS is a relatively young technique. There are two synchrotrons that can be considered points of reference for the APXPS technique: BESSY (Berlin, Germany) and the Advanced Light Source (ALS, Berkeley, USA). In the case of ALS, the beamlines hosting APXPS (9.3.2 and 11.0.2) are among the most oversubscribed [3]. The experimental chambers in ALS were developed from ultra-high vacuum setups and allow static experiments, mainly concerning the investigation of the solid-gas interface [4]. Beamline 9.3.1 was the last developed system and offers the possibility to investigate the solid-liquid interface (dip and pull method) with tender x-rays. The design of In Situ Spectroscopy offers advantages because it allows fast dosing of gases in the measurement cell, which allows the investigation of actual samples under various reaction environment. The ISISS station [5], operated in BESSY offers the possibility to explore the solid-gas interface, and the research is mainly focused on catalyst characterization under steady-state conditions due to the lack of fast-exchange gas capabilities of the high-pressure cell. Recently, two new projects focused on the development of APXPS have been financed in Germany: EMIL [6] and BElChem [7], for the in-situ investigation and characterization of energy materials (solid-gas interface), electrochemical interfaces (solid-liquid interface created by the dip-and-pull method) and environmentally relevant interfaces (liquid-jet). During the last ten years, APXPS facilities were developed at other synchrotrons to try to accommodate the increasing request for in situ characterization of interfaces. A complete list can be found in Table 8.1.

Notably, the recently commissioned fourth-generation synchrotron light source in Lund (MAX-IV) offers state-of-the-art beamlines for APXPS. In particular, the HIPPIE[6] beamline offers a new design of the experimental high-pressure cell, limiting its volume to get exceptional performances in terms of fast gas exchange and ultimate pressure, and new-generation photoelectron analyzers. In this respect, the possibility to access tender x-rays and enhanced energy resolution available at SLS 2.0, will allow our beamline to keep competing with HIPPIE at the same level. Most of these dedicated APXPS beamlines offer the possibility to characterize all the relevant interfaces, but their energy range is limited either to the soft or to tender/hard x-rays. Thanks to its unique features, the In-Situ Spectroscopy beamline will be competitive with respect to other state-of-the-art beamlines and versatile enough to offer measurements in both energy ranges. In particular, it will offer the possibility to investigate the solid-gas and the solid-liquid interface up to 50 mbar pressure already with the currently used analyzer.

Beamline	Photon Energy [eV]	Max Pressure [mbar]	Country
BL02B@SSRF	40-2000	30	China
BL8A2 KBSI@PAL	200-2000	10	South Korea
BL13-2@SSRL	150-1300	130	USA
9.3.1@ALS	2300-6000	146	USA
9.3.2@ALS	200-900	7	USA
11.0.2@ALS	160-2000	10	USA
BL P22@DESY	2400-15000	2500	Germany
BL24A@TLS	10-1500	10	Taiwan
BL36XU@SPring-8	5200-37700	30	Japan
HIPPIE@Max IV	250-2200	30	Sweden
CIRCE@ALBA	100-2000	25	Spain
TEMPO@SOLEIL	50-1500	20	France
NAP-XPS endsation@PF-KEK	50-2000	1	Japan
SPECIES@Max IV	30-1500	20	Sweden
VERSOX@Diamond	250-2800	100	UK
ISISS@BESSY	80-2000	20	Germany

Table 8.1: Worldwide APXPS facilities

8.1.3 Dedicated in-situ spectroscopy beamline

The concept for a new beamline at SLS 2.0 foresees two branches being served by x-rays from two adjacent bend magnets and using two different monochromator types. For the low-energy part, a plane grating monochromator (PGM) will be used. The hard x-ray range will be provided by a double crystal monochromator (DCM). Both monochromators introduce a vertical offset allowing one to separate the two branches in height. By using refocusing mirrors, the two beams can be recombined on the sample. This will be a unique feature of this beamline, allowing spectroscopic measurements using soft and hard x-rays as excitation energies on the same sample spot. For instance, hard x-ray photoelectron spectroscopy (HAXPES) and fluorescence-yield x-ray absorption spectroscopy (FY-XAS) in the soft x-ray energy range may be acquired at the same time. Such spectroscopies not only give complementary useful information about the sample, but also allow one to probe different depths. Indeed, the information depth of XPS, even in the tender x-ray energy range, is limited to a few tens of nanometers, whereas FY-XAS is sensitive to the bulk of the sample (penetration depth of x-rays). XAS could be used to check for beam damage and/or for the sample evolution during a measurement.

8.1.4 Impact on the user community

In the long term, we plan to extend our user community and to foster the interplay with industry and with academic partner. This will require two main developments:

1. A control system, with the aim of making the endstation even more user friendly and to allow the possibility to work in remote. We plan to create software controlling both the beamline and the instrumentation available at the endstation (analyzer/detectors, manipulators, dosing lines, etc.).
2. Technical improvement of the experimental cell. The maximum pressure reachable with the current setup, making use of tender x-rays as the excitation source, is 50 mbar. Recent developments in the field showed that, combining tailored technological developments with the use of tender x-rays, it is possible to measure XPS while dosing in situ 1000 mbar of gas and beyond [8], thus completely filling the pressure gap and opening the possibility to investigate high-pressure reactions. Using the tender x-ray photons available in the new beamline at SLS 2.0 (up to 6000 eV) and upgrading the existing setup, we plan to extend the maximum gas pressure to 1000 mbar.

We also plan to develop new experimental approaches to investigate relevant interfaces. As an example, the dip and pull method, currently used to investigate the solid-liquid interface (see the following sections) has several limitations in the analysis of working electrodes under operando conditions. These are mainly due to diffusion in the thin liquid layer created on top of the sample. Such an issue can be overtaken developing new setups working with permanently refreshed liquid layers. Such an improvement will open new research scenarios/collaborations in the fields of electrochemistry, electrocatalysis, and photoelectrocatalysis.

8.2 Source

The beamline will use two adjacent standard bend magnets in Sector X12D or X09D.

8.3 Front end

The beamline needs standard front ends for bend magnets with ±2 mrad in the horizontal and vertical directions.

8.4 Optics

8.4.1 Beamline concept

The beamline concept (Figure 8.1) foresees two branches with x-ray sources from two adjacent bend magnets and using two different monochromator types. For the low energy part, a PGM will be used. The hard x-ray range will be provided by a DCM. Both monochromators introduce a vertical offset allowing to separate the two branches in height. By using refocusing mirrors, the two beams can be combined on the sample.

This will be a unique feature of this beamline allowing spectroscopic measurements using soft and hard x-rays as excitation energies on the same sample spot. For instance, HAXPES and FY-XAS in the soft x-ray energy range may be acquired at the same time. Such spectroscopies not only give complementary useful information about the sample, but also allow probing different depths. Indeed, the information depth of XPS, even in the tender x-ray energy range, is limited to a few tens of nanometers, whereas FY-XAS is sensitive to the bulk of the sample (penetration depth of x-rays). XAS could be used to check for the beam damage and/or for the sample evolution during a measurement.

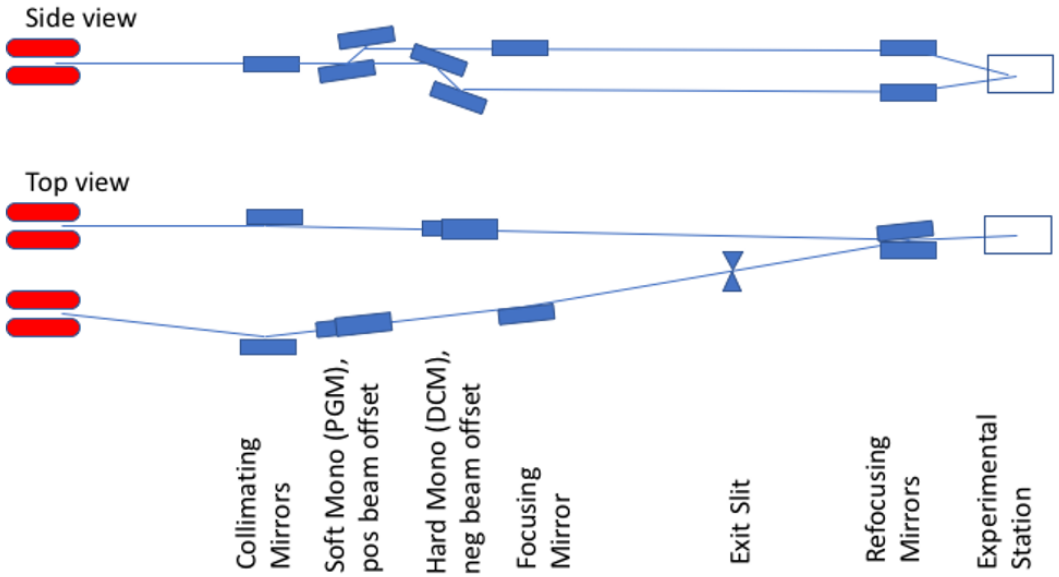

Figure 8.1: Optics concept of the planned In Situ Spectroscopy beamline at X12D or X09D

8.4.2 Monochromators

The concept foresees the use of different monochromator types in the two branches of the beamline. The low energy branch will make use of a PGM providing x-ray in the range of 250-2000 eV. The second monochromator will be a DCM accessing the energy range up to 6 keV.

8.4.3 Floor plan

Currently the bend magnet ports at X12D are not available, due to the design of the local shielding wall of the storage ring tunnel. To make use of the X12D bend magnets, the wall has to be modified during the dark time to provide the necessary outlets. A concept for the modifications is sketched in Figure 8.2. At X09D the same floor plan is possible, without the need of shielding wall modifications.

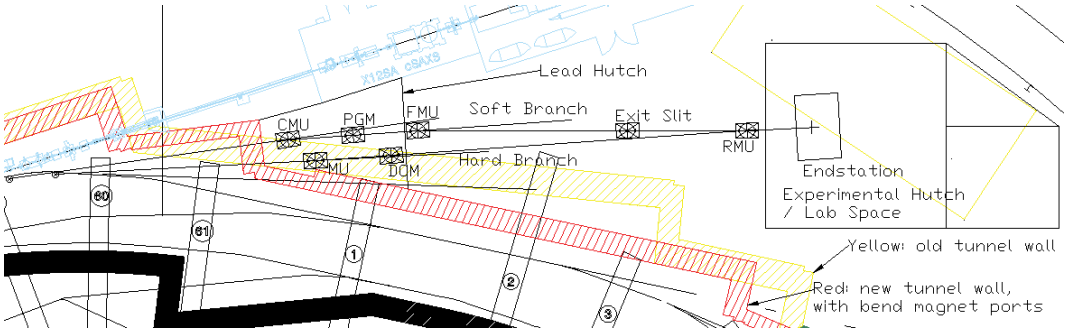

Figure 8.2: Floor Plan concept of the planned In Situ Spectroscopy beamline at X12D, at X09D the same floor plan is possible, without the need of shielding wall modifications

8.5 Endstation

8.5.1 Solid-gas interface chamber (SGIC)

This experimental chamber has been entirely designed and developed at the PSI [9]. It consists of a small-volume, high-pressure cell connected to two vertical tubes having a diameter of 3.0 cm. With the sample placed in the middle of the cell, a gas flow can be created by opening the gas line and pumping the exhaust downstream. Such a configuration mimics a flow tube reactor so that both environmental chemistry and heterogeneous catalysis experiments can be carried out. The design of the setup is unique worldwide thanks to the exceptional control of the sample temperature (160 to 900 K) and working pressure (UHV-50 mbar). The small volume of the experimental cell and the flow tube configuration allows fast gas switching from one mixture to another (on the second timescale), while acquiring photoemission spectra in fast-scan mode. We have recently introduced time-resolved measurements, and could get information about the evolution of real samples (powders) in a specific reaction mixture as a function of time in the second range [10]. Time resolution is one of the next frontiers in in-situ XPS and will enable one to follow dynamic structural changes that typically occur in catalysts. It will also provide previously inaccessible quantitative structure-performance relations. This is extremely difficult to achieve and there are currently no other reports in the literature showing similar performances. Our goal is to further develop time-resolved experiments, so that they will become a distinctive feature of the beamline. Indeed, the gas dosing system will be improved to realize precise pulses of gas while keeping a constant pressure in the cell. We plan to further optimize the experimental cell to reduce its volume. By combining the new cell design with the latest generation electron analyzer, the time resolution can reach the millisecond range.

8.5.2 Solid-liquid interface chamber (SLIC)

SLIC chamber is the latest addition to the APXPS setup available at SLS [11]. This endstation is a versatile system combining a UHV preparation chamber with an ambient-pressure analysis chamber, connected via a fast-entry load lock chamber. The analysis chamber can be operated in UHV or at elevated pressures up to 50 mbar with the existing analyzer. The analysis chamber currently offers the

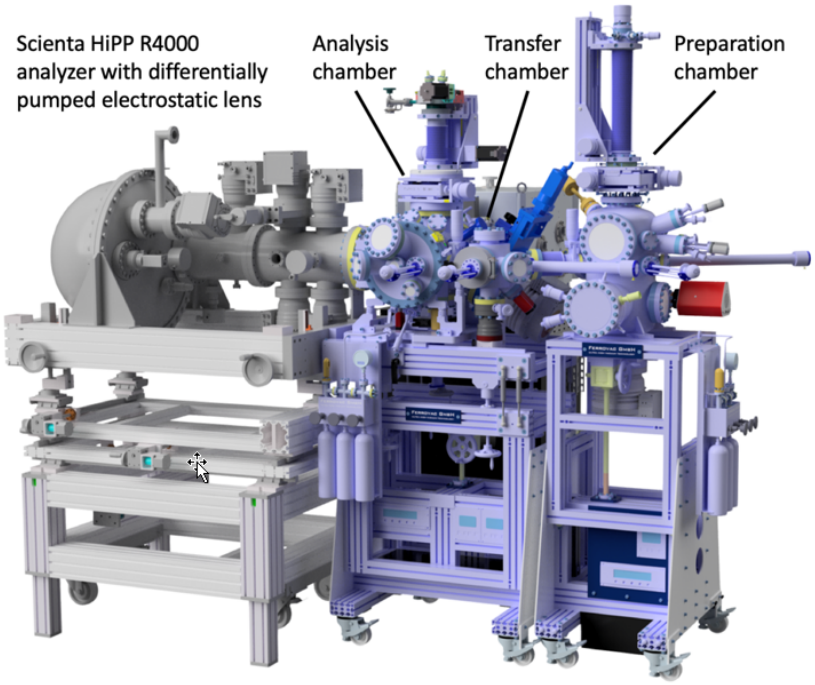

Figure 8.3: Computer-aided design (CAD) rendering of the new endstation for APXPS at solid-liquid interfaces. The left part of the instrument (grey shaded) is a Scienta R4000 HiPP-2 electron analyzer. The right part (blue shaded) shows the new three-chamber SLIC endstation.

possibility to probe the solid-gas interfaces and solid-liquid interfaces created by the "dip-and-pull" method [1]. The capabilities of the analysis chamber can be further extended by designing a dedicated manipulator insert for a specific experiment. Our plans include development of an insert that will offer sample cooling to study solid-ice interfaces, and possibly more inserts in the future based on the needs of us and our users (e.g. heating to high temperatures using a laser diode). The number of different interfaces this endstation will allow to investigate, together with the presence of a UHV preparation chamber (including characterization tools such as low-energy electron diffraction and Auger electron spectroscopy), makes this endstation truly unique.

This chamber represents a highly exclusive tool for the study of solid-liquid interfaces. Solid-liquid interfaces can be stabilized by the "dip-and-pull" method, with the liquid film of 10 to 30 nm thickness in equilibrium with the gas phase. Such experiments require tender x-rays of typically 4 keV photon energy [1]. The high photon energy is necessary to be able to probe the buried liquid-solid interface as well as to get a detectable signal at the high pressures (30 mbar in the case of water) necessary to stabilize the liquid film[a]. This high photon energy, in combination with techniques such as x-ray standing-wave photoemission spectroscopy, will allow us to probe such interfaces with atomic

[a]Commissioning at the NanoXAS beamline demonstrated that the photoelectron signal is completely attenuated at a pressure of 17 mbar when using soft x-rays. Therefore, until the upgrade to SLS 2.0, PHOENIX is the only beamline where experiments at liquid-solid interfaces created by the dip-and-pull method are possible, with severe limits to the amount of available beamtime.

resolution.

The SLIC chamber is an ideal tool to study photoelectrochemical cells, due to its ability to expose the sample (electrode) surface to an artificial sun simulator while performing in-situ electrochemistry, detecting the product formation (H_2, O_2) with a quadrupole mass spectrometer and measuring the intermediate species and changes of the surface chemistry using APXPS under operando conditions. With this chamber, it is possible to probe the fundamental properties of the electrochemical double layer (EDL) at the liquid-solid interface, such as the determination of its capacitance and the potential of zero charge [1, 2]. We have no doubts that this setup will attract a lot of interest from the user communities focused on photoelectrochemical cells, battery research, etc. In addition, this system will be able to perform studies on model systems using single crystals due to its capabilities of UHV sample preparation. This new experimental chamber will benefit greatly from the new beamline since these experiments are highly complex and require ample amounts of beamtime with access to tender x-rays. A bending magnet beamline will be fully sufficient, as prevention of beam damage and x-ray induced chemical reactions ask for limited photon fluxes. The SLIC endstation was installed at SLS in June 2018 and is now fully commissioned [11]. The endstation started hosting first 'friendly' users starting from 2020 and is projected to be open to the user community once the new In Situ Spectroscopy beamline is commissioned.

8.5.3 Controls and data systems

The electron analyzer has four differential pumping stages. The pumps creating the rough and ultra-high vacuum are controlled by means of Labview. The available synoptic panel allows one to turn on and off the pumps and to set their rotation speed. The pressures must be recorded and monitored during the operation of the experimental chamber. A Labview interface reads the pressure gauges in real time and records the values in data files. The analyzer has a dedicated PC where a software developed by the manufacturer (ScientaOmicron) runs and sets the scan parameters and run the measurements. The software generates three formats of data files, containing the main setting of the analyzer. Two file formats are compatible with the software IgorPro, and can be processed by means of dedicated Marcos. The third file format is a general .txt, which can be loaded with many analysis software. The FDA and PShell software are also installed in the same PC, and allow the simultaneous control of the electron analyzer and of the beamline to perform x-ray absorption spectroscopy.

The SGIC is already available for users operation, and can be fully controlled by means of Labview software. The most relevant parameters, namely, sample position, temperature of the sample and of the vapor saturators, pressures inside the measurement cell and in the gas/vapor dosing lines are set, read, recorded and saved in real time by the software. The position of the sample and its temperature can be precisely set and controlled by means of the software.

The SLIC chamber uses the EPICS interface to control the movement of the motors for the manipulator in the analysis chamber (all degrees of freedom: xyz movement and rotation), to read the current position and rotation using absolute optical encoders (Renishaw, Numerik Jena), and to acquire the pressure reading from all eight pressure gauges currently installed to the endstation. Future development and automatization will also use EPICS interface.

The analyzer is located on a frame having adjustable position. This allows an easy connection

of the analyzer to the experimental chambers, thus facilitating the switch from one experiment to another. The motors of the frame are controlled by Labview. The software allows the alignment of the frame setting the positions of the motors and saves the parameters in a data file. The analytical instruments, such as LEED, AES, QMS or potentiostat for electrochemical is currently using a control software provided by the manufactures of the instruments and is controlled using IBM-compatible personal computer.

8.5.4 Sample environments and delivery

The two available experimental chambers allow measurements in a pressure ranging from high vacuum (10^{-6} mbar with the SGIC and 10^{-10} mbar with the SLIC) to the mbar range (50 mbar maximum pressure). Both incondensable gases and vapors can be dosed. In the former case, a pure gas or a gas mixture can be dosed in the analysis chamber by means of either precise mass flow controllers (0.2 to 20 sccm flow range) or leak valves. In the second case, Peltier elements are used to thermalize glass vials containing pure liquids, thus precisely tuning their equilibrium vapor pressure. The vials are connected to a gas line allowing the gas to reach the sample.

In the SGIC, samples are introduced in the analysis chamber by means of manipulator inserts. A heated sample holder controls the temperature of the samples between room temperature and 650 °C (via infrared laser heating), while a cryo-holder allows low temperature experiments down to -100 °C (liquid nitrogen differentially pumped cold finger touching the sample holder). Once supported on the manipulator insert, the samples are connected to a load lock before their introduction into the analysis chamber. The entire procedure to create vacuum in the load lock and to transfer the sample from the load lock to the experimental cell is automated. During an experiment, a sample can be replaced in less than 30 minutes.

Changing the temperature of the samples as well as dosing gas/gas mixtures is possible exclusively when the samples are inside the analysis chamber, i.e. in a confined environment. The exhaust gases are pumped downstream by rough pumping units and are disposed in the SLS exhaust line.

The SLIC endstation uses standard Omicron-type sample holders that are transferred between the chambers (preparation, analysis and transfer chamber) using a combination of wobble sticks and magnetically-coupled transfer arms. The rapid entry load lock, also used as a transfer chamber between ambient pressure conditions in the analysis chamber and UHV conditions in the preparation chamber, allows the introduction or removal of up to two samples simultaneously. This procedure can be achieved within less than 5 minutes, although before transfer to the UHV preparation chamber, a pumping time of at least 60 minutes is recommended to minimize the amount of water transferred to the system. While the SLIC endstation can work under near-ambient pressures of up to some 50 mbar, it can be also used as a UHV chamber with a base pressure in the low 10^{-10} mbar range, which can be obtained after baking out the chamber. The chamber is suited to handle liquids placed into custom-made glass beakers. Gas dosing is performed using backfilling of the chamber. Sample heating is performed via boraelectric heaters heating the back side of the sample holder (both chambers). For samples suited for dip and pull experiments (sample size of 50×10 mm^2, a heating oven capable of heating up to 600 °C is available in the transfer chamber. Furthermore, the preparation chamber is equipped with an electron-bean annealing stage that can heat samples up to 2000 °C.

8.5.5 Detectors

The commercial electron analyzer (Scienta Omicron R4000 HiPP-2) extracts and refocuses photoelectrons emitted from the surface of the sample. The kinetic energy of the photoelectrons is discriminated in the hemisphere region. The detector consists of a 2-dimensional multichannel plate coupled to a phosphor screen. The multiplied photoelectrons hit the phosphor screen and produce an image that is captured by a CCD camera having a maximum time resolution of 40 ms (1 frame). The image of the camera is transferred to the software controlling the analyzer, where it is transduced into a spectrum.

8.6 IT requirements

The endstation can be fully controlled by the dedicated software, installed in the endstation PCs. In this moment, the parameters of the endstations (pressure, sample temperature, pumps settings) are set and recorded by Labview software. The electron spectrometer is controlled by means of the SES software, developed and configured by the manufacturing company ScientaOmicron. The x-ray absorption spectroscopy in electron yield is acquired with the FDA software, developed in PSI. An EPICS channel allows controlling the electron analyzer, in order to scan a precise kinetic energy window as a function of the excitation energy. In the future, we plan to fully control the electron analyzer with the PShell software developed in PSI. This will allow to acquire photoelectron spectroscopy and absorption spectroscopy data and metadata with the same software, making the acquisition even more user friendly. Because the data generated by the software are never exceeding a maximum of 10 MB per single file, network drives and e-accounts will be used to store in-house data and external users data, respectively. The NAPP beamline will be a low data volume beamline, which can be handled with the existing IT infrastructure.

8.7 Timeline

8.7.1 Planning

The SGIC is already fully in operation and we plan to transfer it to the new beamline after the dark period. Commissioning of the SLIC has recently been carried out [11] and the setup will be further developed to become user friendly. In both cases we would like to use EPICS to set and control the system parameters. With the support of IT, we plan to invest on switching from Labview to EPICS control of the SGIC within the next five years, i.e. before and during the dark period. The experimental chambers and the workstation will be placed in a hutch, where an efficient ventilation system is required (air circulation and temperature control). Due to the need to prepare/support samples, a small chemistry laboratory (ideally including a ventilated hood and a table) adjacent to the experimental hutch is added to the project. The solid and liquid chemicals will be safely stored in a ventilated cabinet. Gas cylinders will be stored in an external gas cabinet and will be connected to the endstations by means of non-changeable leak-tested gas lines.

The beamline X07DB (NanoXAS) can be adapted to the new SLS 2.0 layout by replacing the first mirror. This will allow us to restart the soft x-ray user program of the In Situ Spectroscopy soon after

the shutdown and will avoid losing the relatively young user community

The proposed construction of a new beamline, requiring the complete assembly of the setup and of the infrastructure, will require at least 12 to 18 months after the dark period. The planned schedule is shown in Figure 8.4

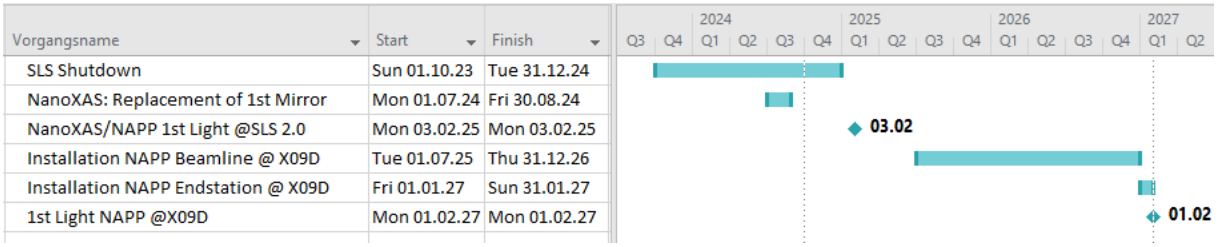

Figure 8.4: Timeline of the NAPP beamline upgrade

8.8 Concluding remarks

After opening the In Situ Spectroscopy beamline to external users, the beamline was already oversubscribed (both in 2019-II and 2020-I). A quick restart of the beamline operation after the dark period, staying at the X07DB site, would permit a prompt restart of the external user operation, thus avoiding a loss of users. In terms of the SLIC endstation, which was originally designed to be compatible with the PHOENIX I beamline, the compatibility with the PHOENIX I beamline after SLS 2.0 upgrade cannot be guaranteed. The PHOENIX I beamline is currently projected to be moved by approximately 300 mm, which will make it impossible to fit the SLIC endstation there, at least not with the UHV preparation chamber attached. Therefore a dedicated bend magnet beamline requested within this proposal is supposed to be a more cost-effective solution, and will be vital for the success of the newly commissioned SLIC endstation.

Bibliography

[1] S. Axnanda, E. J. Crumlin, B. H. Mao, S. Rani, R. Chang, P. G. Karlsson, M. O. M. Edwards, M. Lundqvist, R. Moberg, P. Ross, Z. Hussain, and Z. Liu. Using "tender" x-ray ambient pressure x-ray photoelectron spectroscopy as a direct probe of solid-liquid interface. *Scientific Reports*, 5, 2015.

[2] M. Favaro, B. Jeong, P. N. Ross, J. Yano, Z. Hussain, Z. Liu, and E. J. Crumlin. Unravelling the electrochemical double layer by direct probing of the solid/liquid interface. *Nature Communications*, 7, 2016.

[3] ALS User Statistics.

[4] ALS NAPP Beamlines.

[5] Bessy ISISS Publications.

[6] Bessy EMIL.

[7] Bessy BElChem Publications.

[8] Peter Amann, David Degerman, Ming-Tao Lee, John D. Alexander, Mikhail Shipilin, Hsin-Yi Wang, Filippo Cavalca, Matthew Weston, Jrgen Gladh, Mikael Blom, Mikael Bjrkhage, Patrik Lfgren, Christoph Schlueter, Patrick Loemker, Katrin Ederer, Wolfgang Drube, Heshmat Noei, Johann Zehetner, Henrik Wentzel, John hlund, and Anders Nilsson. A high-pressure x-ray photoelectron spectroscopy instrument for studies of industrially relevant catalytic reactions at pressures of several bars. *Review of Scientific Instruments*, 90(10):103102, 2019.

[9] Fabrizio Orlando, Astrid Waldner, Thorsten Bartels-Rausch, Mario Birrer, Shunsuke Kato, Ming-Tao Lee, Christian Proff, Thomas Huthwelker, Armin Kleibert, Jeroen van Bokhoven, and Markus Ammann. The environmental photochemistry of oxide surfaces and the nature of frozen salt solutions: A new in-situ XPS approach. *Topics in Catalysis*, 59(5):591–604, 2016.

[10] Luca Artiglia, Fabrizio Orlando, Kanak Roy, Rene Kopelent, Olga Safonova, Maarten Nachtegaal, Thomas Huthwelker, and Jeroen A. van Bokhoven. Introducing time resolution to detect Ce^{3+} catalytically active sites at the Pt/CeO_2 interface through ambient pressure X-ray photoelectron spectroscopy. *Journal of Physical Chemistry Letters*, 8(1):102–108, 2017.

[11] Z. Novotny, D. Aegerter, N. Comini, B. Tobler, L. Artiglia, U. Maier, T. Moehl, E. Fabbri, T. Huthwelker, T. J. Schmidt, M. Ammann, J. A. van Bokhoven, J. Raabe, and J. Osterwalder. Probing the solid-liquid interface with tender X-rays: A new ambient-pressure X-ray photoelectron spectroscopy endstation at the Swiss Light Source. *Review of Scientific Instruments*, 91, 2020.

Chapter 9

Surface/Interface: Microscopy (SIM) - Beamline for Advanced Soft X-Ray Spectromicroscopy

C. A. F. Vaz and A. Kleibert

In a nutshell

At the SIM beamline we aim to take full advantage of the new developments and opportunities offered by the SLS 2.0 upgrade, including a much higher brilliance and improved transverse beam coherence compared to SLS, which makes the new light source eminently suitable for coherent scattering-based techniques capable of probing materials and devices down to the nanometer scale and with unprecedented sensitivity. Specifically, we propose to commission a new soft x-ray ptychography nano-spectroscopy imaging microscope with single-digit nm lateral spatial resolution and a unique sample environment and sample excitation capabilities, suitable to addressing scientific questions in a variety of important fields, ranging from spintronics to quantum materials. The new spectromicroscope will be complemented by the existing x-ray photoemission electron microscope (XPEEM) when high surface or interface sensitivity is required. We will also take advantage of the SIM beamline configuration consisting of two elliptical undulators and the incorporation of a highly performing phase shifter to explore new interferometric techniques capable of ultra-high sensitivity. With these developments, we aim to position the SIM beamline at the forefront of coherent soft x-ray nano-spectroscopy worldwide and provide a highly complementary toolbox of techniques within PSI.

The SLS 2.0 upgrade with new insertion devices will offer higher brilliance and improved transverse beam coherence, making the new light source eminently suitable for coherent scattering-based techniques capable of probing materials and devices down to the nanometer scale and with unprecedented sensitivity. Such tools will offer many new insights in a variety of important fields ranging from spintronics to quantum materials. At the SIM beamline we aim to take full advantage of these new developments and opportunities. Specifically, we propose to:

- Install a new soft x-ray ptychography nano-spectroscopy imaging microscope with unique sample environment and sample excitation capabilities. This new development utilises the outstanding in-house resources, synergies, and expertise in hard x-ray ptychography and 2D hybrid x-ray detectors.
- Take advantage of the SIM beamline configuration consisting of two elliptical undulators and the incorporation of a highly performing phase shifter (developed for SwissFEL) to explore new interferometric techniques; the latter offer ultimate sensitivities and could enable the exploration of novel effects in materials when used in combination with the characteristics of synchrotron x-ray light.
- Maintain the operation of the x-ray photoemission electron microscope (XPEEM) for SLS 2.0, also to complement the soft x-ray ptychography microscope when high surface or interface sensitivity is required. Given the high surface sensitivity and spatial resolution of XPEEM, it is predicted that it will remain in high demand by the user community.
- Provide an open port for instrumental developments (for example for the soft x-ray SwissFEL Athos beamline) and for external endstations requiring access to the beam characteristics of the SIM beamline.

To support these developments, a number of modifications in the beamline source and optics are required, as described in detail in this chapter. With these developments, we aim to position the SIM beamline at the forefront of coherent soft x-ray nano-spectroscopy worldwide and provide a highly complementary toolbox of techniques within PSI.

9.1 Overview

The SIM beamline was one of the first operating beamlines at the SLS. It is a soft x-ray beamline dedicated to spatially and non-spatially resolved x-ray absorption spectroscopy (XAS) and scattering of materials, with a focus on condensed-matter physics. It has made a significant impact in fields such as nanomagnetism [1–9], correlated materials [10], interfaces [11, 12], and catalysis [13, 14]. Moreover, the beamline has contributed to important PSI developments such as electron and soft x-ray detectors [15, 16]. It was also crucial for the development of new experimental setups, such as the RESCAN endstation at the XIL beamline [16] or the NAPP endstation presently hosted at the NanoXAS beamline [17]. These successes are based on the concept of operating a permanently installed XPEEM in addition to an open port for variable internal (resonant soft x-ray scattering or RESOXS endstation, and x-ray absorption spectroscopy or XAS endstation) or external (e.g. a dilution cryostat) experimental endstations, together with two Apple-type UE56 undulator sources. Table 9.1 summarises some of the characteristic features of the SIM beamline. Owing to the variety of endstations supported at SIM, the user community of the SIM beamline is versatile and the beamline serves key players in

diverse fields ranging from magnetism and correlated systems to battery research and catalysis. The beamline has a core base of about ten user groups in addition to varying groups from around the world. The research projects carried out at the SIM beamline result in about 20 publications per year with a significant number appearing in high impact journals (IF $>$ 7.2).

	SLS	SLS 2.0
Front end slits	slow scans	fast scans
Focus	astigmatic	stigmatic
Cooling	constant	adaptive
Secondary focus	fixed	adjustable
Secondary slit	none	variable
beam monitors	relative position	absolute position
Sources	2 $\times$ U56	2 $\times$ U56
Energy range [eV]	90 - 2000	90 - 2000
Polarization	linear (0-90°), circular (c+, c–)	linear (0-90°), circular (c+, c–)
Flux (1 keV)	1×10^{15} photons/s/0.1%BW/ 0.4 A	
Focused spot size (H $\times$ V)	52 μm $\times$ 25 μm	48 μm $\times$ 23 μm
Spectral resolution	$>$ 5000	$>$ 5000
Endstations	XPEEM, TR-TEY, RESOXS, others	Ptychography, XPEEM, RESOXS, others

Table 9.1: Present and future characteristics of the SIM beamline.

The high brilliance, increased transverse coherence, and improved beam profile of SLS 2.0 will benefit strongly coherent scattering-based techniques; we aim to take advantage of these new possibilities to develop new soft x-ray spectromicroscopy techniques that are uniquely suited to the characterisation of materials and devices down to the nm-scale with unprecedented sensitivity. While recent years have seen a sizeable increase in the demand for soft x-ray spectromicroscopy using XPEEM, discussions with our user community[a] as well as with members of the Proposal Review Committee show an increasing need and demand for higher spatial resolution beyond the capabilities of current XPEEM technology (of the order of 20-50 nm lateral spatial resolution). This is particularly the case in the magnetism community, where new topics such as topological spin structures, antiferromagnetic spintronics, or complex non-collinear spin structures, e.g. in multiferroic materials, require a spatial resolution in the single digit nanometer range.

Hence, we have embarked on the development of a new, versatile, soft x-ray microscope with a very high-spatial resolution that will take full advantage of the SLS upgrade to a diffraction-limited light source (see Figure 1.2). The upgrade will also make possible the development of ultra-sensitive detection techniques based on interferometry, which we expect will stimulate significant interest in

[a]Breakout session on Magnetism organised by A. Kleibert at the PSI Photonics Workshop held in Windisch (CH) in April 10-12, 2017.

the condensed matter physics community. We describe in the following these new activities at SIM, as well as the current plans for the XPEEM, RESOXS, and the open port capabilities. In addition to these necessary upgrades, we propose several modifications in the optical design to bring the SIM beamline to the state-of-the-art and optimised for scattering-based measurements techniques, such as ptychography and interferometry. Our end goal is to place the SIM beamline at the forefront of soft x-ray nano-spectroscopy imaging and nanoscale scattering worldwide.

9.1.1 Soft x-ray ptychography

In the context of SLS 2.0, we propose to commission and install a soft x-ray ptychographic microscope at SIM for magnetic and spectroscopic characterisation of materials with the highest spatial resolution, down to the x-ray diffraction limit (< 5 nm). The main component parts of the instrument are schematically shown in Figure 9.1. The proposed microscope will combine soft x-ray ptychographic imaging and spectroscopy with laminography to give access to 3D characterisation of samples. The goal is to provide a system that is both user-friendly and capable of a large variety of sample excitations to permit the study of a wide range of material systems and physical phenomena at the nanoscale. Specifically, the microscope will be designed to provide magnetic fields up to 300 mT for studying magnetic systems, sample temperatures down to 10 K for investigating strongly correlated materials, electric and laser excitations for *operando* characterisation of electronic devices and cryo-transfer for vitrified biological tissue. In addition, the instrument will allow for both transmission and reflection measurement geometries, which will enable the investigation of a very wide range of physical systems. With such sample environments, we will probe novel physical phenomena with unprecedented spatial resolution.

The target research areas to be impacted by this new instrument include:

- nanomagnetism, where the single digit nanometer spatial resolution enabled by lensless ptychographic imaging reaches the fundamental exchange length, thus making capable of resolving the smallest spin textures and enabling a full characterisation of the magnetic state of magnetic materials;
- novel materials, including strongly-correlated systems and composites, where low-temperature phase transitions and the correlated state of matter can be investigated at the nanoscale and where individual phases of nanocomposites, such as multiferroics, battery electrodes, and heterogeneous catalysts, can be characterised at the level of the individual components;
- the study of biological vitrified samples, which will benefit from the strongly enhanced contrast in the water window and from spectroscopic analysis at the K-edge of the light elements; and
- electronic nanodevices, where several excitation sources (magnetic, electric field, electric current, and laser light pulses) can be applied *in situ* for *operando* characterisation.

We envisage that the availability of such an instrument will enable disruptive research work in various fields of science, including physics, chemistry, materials science, and biology. The proposed instrument has received strong support from key players of our user community (R'EQUIP grant proposal submitted to the Swiss National Science Foundation, no. 206021_198177, *New soft x-ray ptychographic spectromicroscopy endstation*) and, based on our experience with hard x-ray ptychography, is expected to develop into a full fledged research program. The proposed microscope will be unique

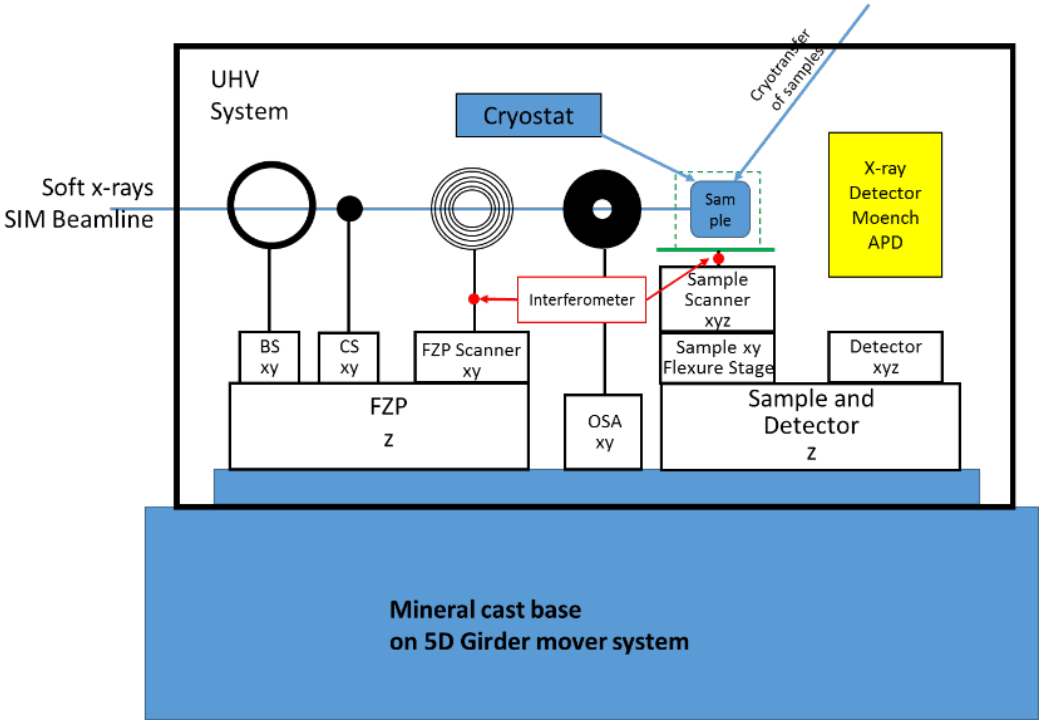

Figure 9.1: Schematic diagram of the planned soft x-ray ptychographic microscope instrument to be commissioned at the SIM beamline, showing the main components, as labeled.

not only in Switzerland but also worldwide and will undoubtedly generate wide interest in the international user community. It will take full advantage of the coming upgrade of the SLS to a diffraction limited light source and will further contribute to the high visibility of the SLS.

9.1.2 New interferometric techniques

SLS 2.0 will be equipped with a new phase matcher between the two Apple-type undulators used to provide increased flux in tandem operation at SIM. We propose to take advantage of the new phase matcher to generate two coherent beams with a well-defined, controllable phase shift for measuring ultrasmall changes in the optical response of the sample via x-ray interferometry, analogous to Rayleigh or Mach-Zehnder interferometers. A 2D detector for soft x-rays (e.g. MÖNCH) will be used to image the interference pattern and detect differential changes therein, as illustrated in Figure 9.2(a,b). Such a scheme may allow x-ray holography with diffraction-limited spatial resolution. In addition, heterodyne detection schemes could be envisaged for ultrasensitive measurements, for instance for energy-loss spectroscopy [c.f. Figure 9.2(c)]. These developments require a configuration with two undulators providing two coherent beams with a narrow spectrum. If successful, interferometric techniques could surpass the sensitivity of current soft x-ray spectroscopy approaches by orders of magnitude and could be used to measure changes of a spin state in quantum dots or molecular devices, to directly determine the polar moment of ferroelectrics, or to measure the chirality of single-molecule enantiomorphs, for

example.

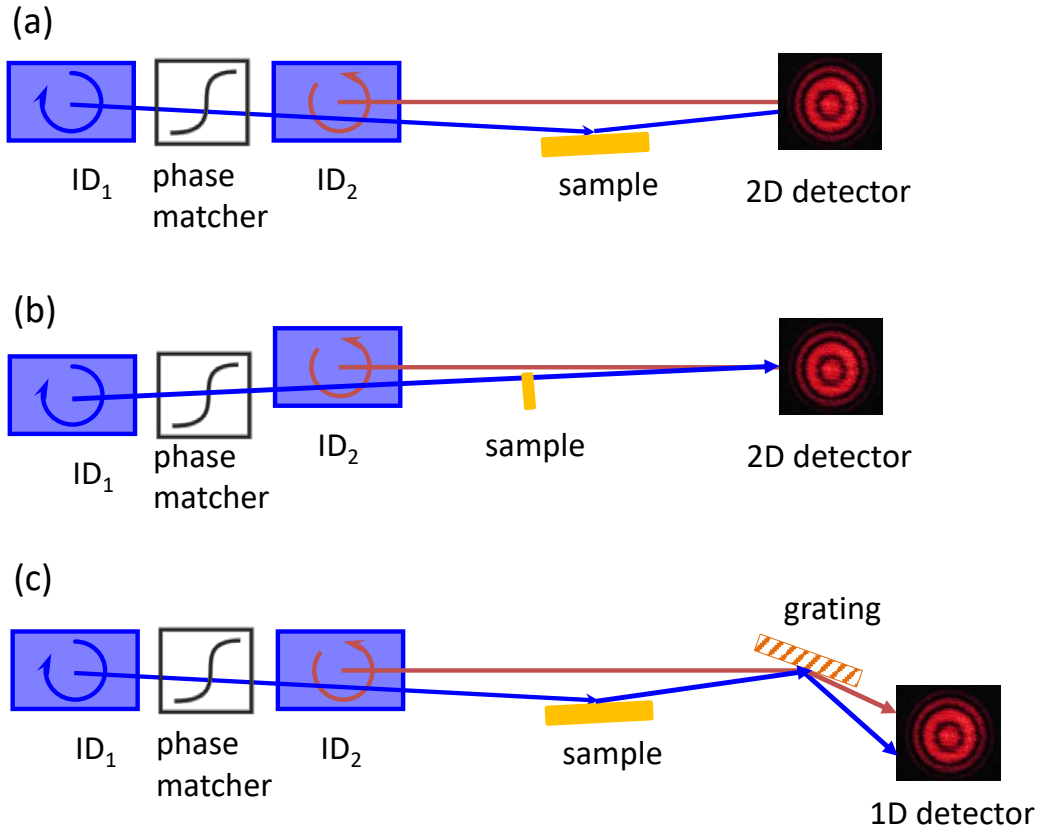

Figure 9.2: Schematic setup for interferometric detection at the SIM beamline: (a) reflection and (b) transmission geometries. (c) Use of interferometry for heterodyne detection.

9.1.3 XPEEM endstation

The XPEEM enables investigations of a wide range of physical phenomena, from magnetism to catalysis, to novel materials systems, and is in high demand by the user community [18]. In recent years, newer XPEEM models have become available, in particular, aberration-corrected microscopes with improved spatial resolution and higher transmittance. However, it is our opinion that presently they are not suitable for user operation, due to the complexity involved with their usage. Also, the gain in spatial resolution is well below a factor of 10 from the standard models, i.e., not sufficiently technically "disruptive". Our approach, in view of the proposed ptychographic endstation, is to allow such aberration-correction microscopes to further develop until they are mature for routine user operation. To keep the XPEEM competitive, we propose to (i) replace the current MCP imaging detector by a gatable EIGER II detector for direct electron detection, (ii) upgrade the electronics rack to allow mounting electronic controllers for tailored sample excitations, (iii) motorize the sample stage, and (iv) upgrade the XPEEM control software to a Linux-based solution for integration with the beamline

software.

9.1.4 Open port

The concept of an open port will be maintained both for the development of novel x-ray based techniques, including for the exploration of interferometric detection, and development of components for the ATHOS beamline at SwissFEL. In addition, it will be used to continue our research activities in x-ray spectroscopy and scattering using the x-ray absorption spectroscopy system and the RESOXS endstation.

9.1.5 Long-term vision

The high brilliance and improved transverse coherence of SLS 2.0 will enable us to develop techniques with unprecedented spatial resolution and sensitivity in imaging and spectroscopy, including ptychography and novel x-ray interference techniques. In combination with advanced surface and interface sensitive techniques, such as XPEEM and soft x-ray resonant scattering (RESOXS), we aim at placing the SIM beamline at the forefront of soft x-ray nano-spectroscopy imaging and nanoscale scattering. The aim is to address both fundamental problems in physics, chemistry, and biology as well as to reach out to technological relevant materials systems and to industry.

Our long-term vision is that of providing access to electronic and magnetic information at increasingly smaller lenghtscales and with higher sensitivity, as illustrated in Figure 9.3: from the current submicrometer lengthscales, the goal is to reach nanometer sized devices comprised of single-molecule elements. Such schematic illustrates the current trend for a continuing demand for ever smaller, efficient, and sustainable data storage and processing technologies that will require research tools with sufficient spatial resolution and sensitivity to study material properties and novel phenomena at the nanometer scale.

More generally, we envisage that a number of fields in science will be impacted strongly by soft x-ray ptychographic spectromicroscopy, such as nanomagnetism, novel materials and devices, in the characterisation of biological samples, and in nanotechnology research.

In magnetism, a lateral spatial resolution in the single nm digit is in the range of the characteristic exchange length of magnetic materials (2-10 nm) [19], making it possible to resolve the smallest spin structures. Of high interest in this context is the imaging of the magnetic configuration of skyrmionic spin textures, in particular in materials where the presence of a Dzyaloshinskii-Moriya interaction (DMI) leads to the presence of chirality and chiral spin textures. The latter can develop in non-centrosymmetric magnetic materials, such as FeGe [20], MnSi [21], (Mn,Fe)Ge [22] and Cu_2OSeO_3 [23]. In these systems, nanometer-sized skyrmion lattices at specific points of the temperature–magnetic-field phase diagram have been identified [24], which are amongst the smallest spin structures that are possible to envisage in nature [25]. The proposed instrument provides the magnetic field and temperature range required to explore large parts of the phase diagram of such materials. In addition to single-phase materials, also multilayer structures composed of asymmetric interfaces, such as Pt/Co/Ir multilayers with perpendicular magnetic anisotropy, develop skyrmionic structures as a result of the presence of a strong net DMI from the strong spin-orbit interaction of the heavy metals [25–27] or

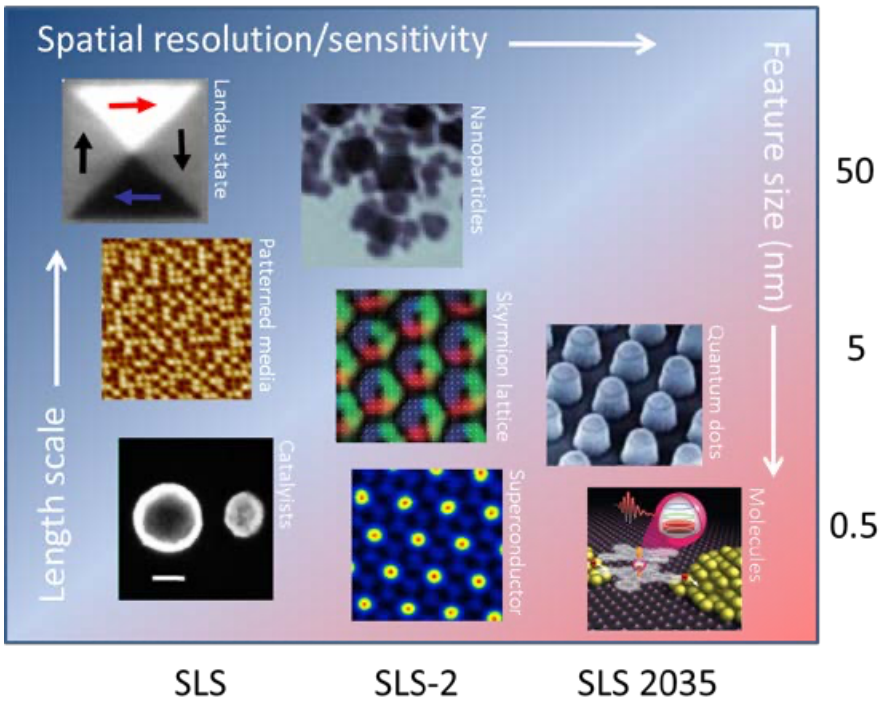

Figure 9.3: With the reduction in dimension, novel material properties and new fundamental phenomena may arise. For example, one can envisage that, in 2035, quantum computation will be the norm and that the SIM beamline will have contributed to such development through the exploration of new quantum variables of state, such as topological superconductors, topologically protected states in novel materials, correlated states of matter, Majorana fermions, or entangled nuclear states of supported single molecules.

due to the Rashba effect at the graphene/3d transition metals interface and the break of centrosymmetric symmetry [28]. Such phenomena can be employed to create new nanoscaled devices based on DMI-induced chiral coupling [9]. New physical phenomena induced by spin-orbit coupling and charge transfer at surfaces and interfaces may lead to the emergence of new electronic and magnetic phases [29–31] that will require high sensitivity and high-resolution spectroscopy techniques with the capability of measuring under external stimuli, such as electric currents, magnetic and electric fields, variable temperature, and optical excitations [32]. Additionally, the 3D imaging capabilities of the proposed instrument will also enable the discovery of novel topological spin structures such as the long sought-after magnetic hopfions in solids consisting of three-dimensional nanometre-sized particle-like spin structures (solitons), which are candidates for spintronic devices in truly three-dimensional architectures [33].

Another important topic is the manipulation, control, and understanding of ferri- and antiferromagnetically ordered systems [34–36]. Antiferromagnets possess interesting properties when compared to their ferromagnetic counterparts: (i) they are virtually insensitive to external magnetic fields; (ii) neighbouring elements do not interact via dipolar interaction; and (iii) the absence of a macroscopic

magnetization makes spin manipulation in antiferromagnets much faster when compared to ferromagnets [37]. Yet, they can be manipulated by currents and photons. However, in many antiferromagnetic systems the antiferromagnetic domains are very small (below 100 nm), and therefore difficult to probe. Moreover, for nanosized antiferromagnets, little is known about their thermal stability [38]. The proposed instrument will significantly contribute to the understanding of these systems by combining the high spatial resolution of soft x-ray ptychography with the x-ray magnetic linear dichroism (XMLD) effect and the various excitation sources to be made available.

Another class of materials that will benefit tremendously from a higher spatial resolution are nanoparticle systems. Although extensively investigated to date, most measurements tend to be carried out in ensembles of particles, yielding average properties. However, it has become evident more recently that individual nanoparticles can exhibit an electronic and magnetic behaviour that deviates strongly not only from bulk properties but also from each other. Soft x-ray ptychography can provide the required lateral spatial resolution combined with magnetic contrast information through the XMCD effect, for example, to directly identify and measure the impact of defects on the internal spin configuration of the nanoparticle or the effect of the magnetic interactions of dense nanoparticle arrays in detail. Due to their importance for catalysis, the local investigation of chemical reactivity could be carried out, where variations in chemical activity across the nanoparticle surface and facets could be identified.

In biological samples, a drastic increase in contrast occurs in the *water window* (x-ray energies between the C and O K edges) where water is transparent to x-rays but organic material is absorbing. Soft x-ray ptychography is therefore ideal for high-resolution imaging of individual cells or of thin sections of tissue, bone or teeth, and for high-resolution spectroscopic mapping to obtain information about the molecular environment of particular elements. Absorption edges of light elements such as C, N, O, Ca and K, become accessible in the soft x-ray regime and can provide information not accessible by other methods, enabling new possibilities in nano-biology and nano-medicine.

Of increasing importance is the optimisation of composite material structures where nanoscopic individual components are brought together to create artificially novel properties. The range of materials taking advantage of this approach is vast, from multiferroic composites, where magnetic and ferroelectric components are brought together to create a novel magnetoelectric coupling between the magnetic and ferroelectric order parameters [39, 40], to battery electrodes, where a mixture of active material, conductive carbon, binder and electrolyte are brought together to enable both ionic and electron charge transport that are required for battery performance [41, 42]. Critical to the performance of composite materials is the interface between the different phases, where the interaction processes take place. Tools that permit the investigation of the interface region of composite materials at the level of individual components, such as XPEEM and x-ray resonant reflectivity (using RESOXS), are of extreme importance to better understand the often complex processes that take place at this region of the system, in particular, in *operando* conditions [43–49]. Strongly-correlated materials exhibiting competing ordered ground states are of particular interest, for example in the perovskite oxides such as in the doped manganites [50] and in $NiNdO_3$ [51, 52]. Likewise, the development of new variables of computation for post-CMOS technologies will require access to novel electronic states in nanoscale devices. One example is quantum entanglement using Majorana fermions for Qbit applications in quantum computing, where high-resolution spectromicroscopy is needed to characterise

the heterostructures that can host such quasi-particle states. In this context, the direct probing of reciprocal space by resonant x-ray scattering using RESOXS offers unique insights into the electronic, magnetic, and structural order of materials with atomic scale accuracy, providing a unique complement to both ptychography and XPEEM techniques. The integration of an x-ray detector, such as MÖNCH, by providing a much higher dynamic range, lower noise and single photon sensitivity, will further expand the capabilities of the RESOXS endstation for studying strongly-correlated materials, interfaces, and order parameters in the solid state.

We therefore anticipate that the range of techniques and of probes into matter offered at the SIM beamline will enable the user community to tackle emergent problems in science and technology with potential for fundamental breakthroughs in science and technology.

9.1.6 Impact of SLS 2.0 on the SIM beamline

The high brilliance and improved transverse coherence of SLS 2.0 will enable us to develop techniques with unprecedented spatial resolution and sensitivity in imaging and spectroscopy, including ptychography and novel x-ray interference techniques. In combination with advanced surface and interface sensitive techniques, such as XPEEM and soft x-ray resonant scattering (RESOXS), we aim at placing the SIM beamline at the forefront of soft x-ray nano-spectroscopy imaging and nanoscale scattering. The aim is to address both fundamental problems in physics, chemistry, and biology as well as to reach out to technological relevant materials systems and to industry.

The new ring brilliance will have the following impact on the SIM beamline: (i) The higher flux, round shape, and higher lateral coherence will be beneficial for scattering-based techniques, such as ptychography and RESOXS. (ii) XPEEM: the higher brilliance may result in stronger space-charging effects and illumination inhomogeneities. We envisage working slightly off the focal point position to avoid such problems. (iii) The combination of the two undulators with the new phase matcher provided by SLS 2.0 will enable the development of new high-sensitivity interferometric techniques.

As a major upgrade in our source, the existing phase matcher will be replaced by an improved design, both to enable an optimal phase match between the two undulators for increased flux and to enable us to explore x-ray interferometry approaches to probe matter. Another significant impact of SLS 2.0 is the replacement of the current design by fast slits with absolute position motor encoders, which would reduce significantly the time required for the beamline initialisation (by reducing beam-profile scans times by a factor of ten) and provide error-free operation. For the SIM beamline upgrade, we propose to carry out a number of modifications to the beamline optics aiming at simplifying the beam path and to optimise it for diffractive optics downstream. The simpler optical design aims at providing a cleaner wavefront for scattering and dispersive optical elements at the endstations.

9.1.7 Uniqueness compared to present and planned other BLs worldwide

The planned beamline concept design combining two elliptical undulators, a new phase matcher, the XPEEM and soft x-ray ptychography spectromicroscopes, and an open port allowing for the further development of novel instrumentation, makes the SIM beamline setup unique compared to other soft x-ray beamlines worldwide. For the soft x-ray ptychography endstation we plan to realize a mature instrument, easy to use and available to a broad user community. No such instrument is

available at any other beamline yet. We foresee that, based on the existing experience with similar instrumentation at the SLS (e.g. OMNY, FLOMNY, etc.), we will be at the forefront of the field. Soft x-ray interferometric detection schemes based on coherent light generated by two phase-matched undulators would be a unique feature, as yet unexplored.

9.1.8 Complementarity to other instruments at PSI

The SIM beamline will complement other beamlines at SLS by adding new tools for high resolution imaging in the soft x-ray range with unique spatial resolution and capabilities such as 5 K and up to 2 T magnetic field. The open port will be available to explore interferometric techniques and will support developments for other beamlines of PSI, e.g. ATHOS.

9.1.9 Impact on the international and local Swiss community

Owing to the variety of endstations, the user community of the SIM beamline is versatile and the beamline serves key players in diverse fields ranging from magnetism, to correlated systems, to battery research and catalysis. The beamline has a base of about ten core user groups in addition to varying groups from around the world. The research projects carried out at the SIM beamline result in about 20 publications per year with a significant number appearing in high impact journals (IP $>$ 7.2). In the recent years we have seen a sizeable increase in the demand for soft x-ray spectromicroscopy using XPEEM. Discussions with users as well as with members of the proposal review committee show an increasing demand for higher spatial resolution beyond the capabilities of current XPEEM technology. This is particularly the case in the magnetism community, where new topics such as topological spin structures, antiferromagnetic spintronics, or complex non-colinear spin structures, e.g. in multiferroic materials, require a spatial resolution in the single digit nanometer range. By providing a new versatile soft x-ray microscope with a very high-spatial resolution, we expect to expand the interest of the magnetism community for our future capabilities at SLS 2.0. Similarly, we expect that providing ultra-sensitive detection techniques based on interferometry will raise significant interest in the condensed matter physics community.

Industrial users could benefit from the future facilities through the availability of a highly advanced microscopy technique that enables one the nanoscopic characterisation of materials with technological relevance, including composite materials and nanoscale electronic devices in operando conditions. Inteferometric techniques could find applications in metrology.

9.2 Source

A large proportion of the activities at the SIM beamline is devoted to the study of magnetic phenomena, hence, it is important that we keep a dual undulator configuration where two elliptical undulators can be operated independently. This makes possible fast switching between different light polarisations and the accurate and reliable measurement of magnetic signals based on dichroic effects. The two undulators UE56 will be replaced with two new APPLE-X type UE36 and, as another major upgrade in our source, the existing phase matcher will be replaced by an improved design, both to enable an optimal phase match between the two undulators for increased flux and to enable us to explore x-ray

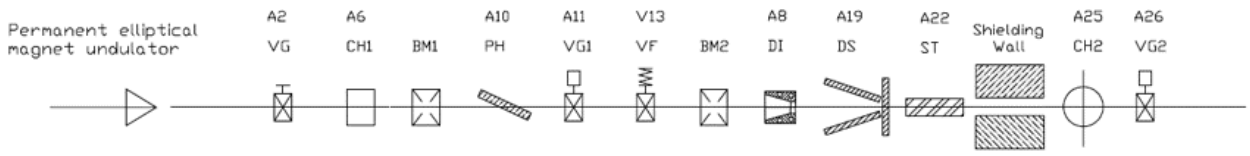

Figure 9.4: Front end components of the SIM beamline. CH1, CH2: (empty) vacuum chambers; BM1, BM2: beam monitors; PH: photon shutter; VF: fast shutting valve; DS, DI: front end slits; ST: beam stopper for Bremstrahlung. (Courtesy D. Just.)

interferometry approaches to probe matter. The new phase matcher benefits from the developments made at SwissFEL and should not require major development work.

The new ring brilliance will have several impacts on the SIM beamline:

- The higher flux, round shape, and higher lateral coherence will be beneficial for scattering-based techniques, such as ptychography and RESOXS.
- XPEEM: the higher brilliance may result in stronger space-charging effects and illumination inhomogeneities. We envisage working slightly off the focal point position to avoid such problems.
- The combination of the two undulators with the new phase matcher provided by SLS 2.0 will enable the development of new high-sensitivity interferometric techniques.

9.3 Front end

The front end components of the SIM beamline, schematically shown in Figure 9.4, comprise a number of elements placed between the source and the SLS exit wall (including front end slits, beam monitors, beam shutter and beam stopper) will be the target of some modifications and upgrades for SLS 2.0.[b] The current length of the front end section is 6.2 m, which will be reduced to 6.1 m for SLS 2.0, a modification that is not problematic. As part of the upgrade, the second set of beam monitors, which can only provide a relative position of the beam, will be replaced by a new type that will provide an absolute position of the beam (still under development). The beam stopper and beam shutter will not require major modifications, given that the power density of the SLS 2.0 beam will not increase significantly (by about 20%). Another critical component in the front end is the front end slits, which are used for controlling the beam size and beam intensity for the experiments and for beam profiling during the beamline initialisation. A significant upgrade here is the replacement of the current design by fast slits with absolute position motor encoders, which would reduce significantly the time required for the beamline initialisation (by reducing beam profile scans times by a factor of 10) and provide error-free operation [53].

[b] This section takes into account discussions with David Just from the Photonics Instrumentation group.

9.4 Optics

For the SIM beamline upgrade, we propose to carry out a number of modifications to the beamline optics aiming at simplifying the beam path and to optimise it for diffractive optics downstream.[c] A drawing of the old and new optical path is given in Figure 9.5 calculated using x-ray tracing. In particular, we propose the replacement of the astcmatic focal points of the beam by a single focal point, to be located at the position of the exit slit. The simpler optical design aims at providing a cleaner wavefront for scattering and dispersive optical elements at the endstations. With the current SLS beam profile, the new layout provides a similar focus (calculated spot size H $\times$ V of 48 μm $\times$ 23 μm for the new design at the PEEM position compared to 52 μm $\times$ 25 μm for the current layout with the SLS beam), which is strongly limited by slope errors of the optical components. The impact of the x-ray source (ID1, ID2 and phase shifter) on the focus is small and here again, the system performance will be limited by slope errors. Upgrades in the optical elements will also be carried out to bring the system to the state-of-the-art. Cleaning of the existing x-ray optics components will also be carried out. In addition, we intend to implement an adaptive cooling scheme for the x-ray optics elements in order to minimise noise through vibrations.

9.4.1 Filters and slits

The SIM beamline requires no filters and the exit slit will stay as at present.

9.4.2 Mirrors

We propose the replacement of the following mirrors at the beamline:

- Replacement of the collimating mirror M1 from an internally cooled GlidCop mirror to an internally cooled silicon mirror with improved properties;
- Replacement of the flat mirror in the monochromator from an internally cooled GlidCop mirror to an internally cooled silicon mirror;
- Removal of the current intermediate focus to achieve stigmatic focusing; this entails the replacement of the focusing (M2) and refocusing (M3) mirrors.

Full motorisation of the mirrors will be implemented. The new configuration with a stigmatic focus will allow a cleaner wavefront and better control of the beam conditioning (shape and focus), which will be beneficial for scattering-based experiments. The new beam optics will have a first focal point at the exit slit position and a variable second focal point at the XPEEM position or at the exit slits for the ptychography station, selectable by means of a double toroidal mirror (M3), as shown in Figure 9.5.

9.4.3 Monochromators

For the monochromator, we propose the replacement of the 300 and 1200 l/mm grating by blazed gratings for improved performance.

[c] The proposed changes have been discussed with Uwe Flechsig and Benedikt Rösner from the Optics group.

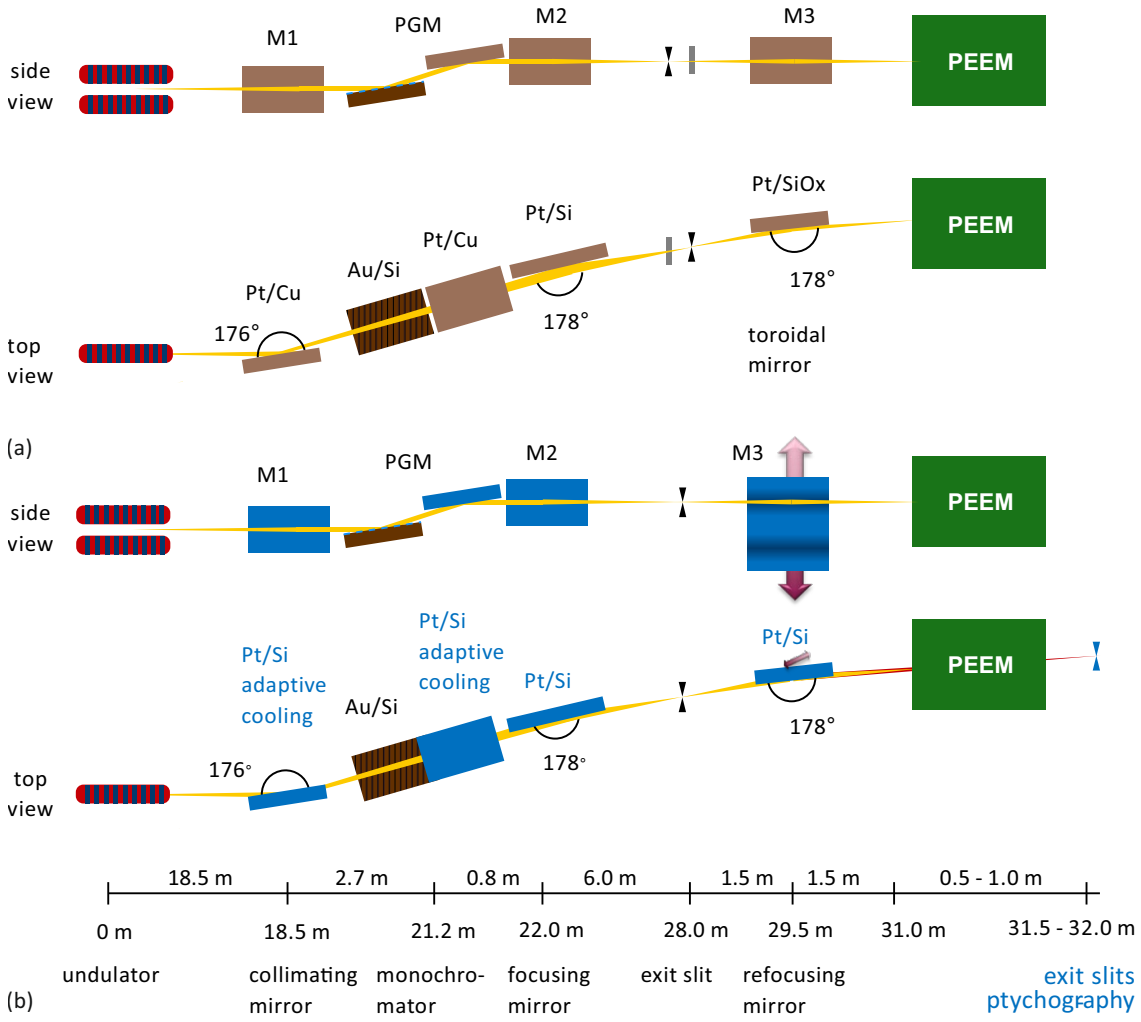

Figure 9.5: (a) Current optical layout of the beamline. (b) Proposed optical upgrade. (Courtesy B. Rösner.)

9.4.4 Secondary optics

In addition to the change of the mirrors discussed above, we will implement new diagnostic components for a more efficient beamline alignment and beamline performance. This will include new beam monitors and the installation of cameras and beam sensors for beam profiling and focal adjustment. We will also replace the fast shutter (situated just before the exit slit) support stage by a more reliable and accurate automated stage to allow the correct positioning of the shutter.

For the ptychography endstation an additional set of slits will be installed (1 μm accuracy, in vacuum) at the secondary focal point for accurate control of the beam size and beam lateral coherence, see Figure 9.5.

9.5 Endstation

The SIM beamline will support various endstations, including:

1. **A permanently installed XPEEM endstation**. The instrument will be the one currently installed at the beamline, with upgrades to the electronic controllers and to the sample stage, and installation of a 2D electron detector (EIGER). This technique, due to its high surface sensitivity, is still highly demanded by the condensed matter and materials science community and will complement other techniques that are being developed at the SIM beamline. The increased light flux of SLS 2.0 could become a problem for XPEEM, in that space charging may start to affect imaging conditions. Illumination with a slightly defocused beam can mitigate excessive flux at the sample without affecting strongly the beam energy spread (using the beam focused downstream at the ptychography exit slit position).
2. **A movable soft x-ray ptychography spectromicroscope**, currently being developed and commissioned. This instrument aims at taking full advantage of SLS 2.0, since it relies on sample scattering and high lateral beam coherence. It further uses diffractive optical elements (Fresnel zone plates) to focus the beam to the sample. For this new endstation, we propose a new beam focal point downstream from the PEEM endstation; a set of high precision slits will be available at this position for shaping the beam and for increasing the beam lateral coherence for the ptychography endstation.
3. **A generic open port**, to allow the attachment of the internal RESOXS and XAS endstations, external user endstations and the further development of new instruments. The required beamline monitoring elements are already available in the present set-up.

9.5.1 Controls and data systems

We will transition from a hybrid Windows-Linux platform to a Linux-only platform. This will be accomplished with the installation of the PEEM EIGER detector. The software for the ptychography endstation will be Linux based. Modifications in the controls will be carried out to incorporate the optics modifications to the beamline, including the new mirror motors and diagnostics tools.

9.5.2 Detectors

At the SIM beamline, a suite of new x-ray and electron 2D detectors will begin operation before the SLS upgrade. For the XPEEM microscope, we are presently commissioning the installation of a quad EIGER detector to be acquired from PSI's detector group, to be upgraded to an EIGERII detector, currently under development. The soft x-ray ptychography spectromicroscope and the RESOXS endstation will use MÖNCH detectors.

9.6 IT requirements

The IT infrastructure required for operating the soft x-ray ptychography spectromicroscope, including the resources for analysing and storing the high volume of data acquired in ptychography, are currently being developed and are expected to be ready before the SLS upgrade (the SIM beamline has already

4 fiber cables, i.e., 2 connections, to the server room). Our estimate is that at the start of SLS 2.0, we will be generating about 70 TB of raw data per year mostly generated by the MÖNCH detector of the soft x-ray ptychography spectromicroscope and a derived data of about 70 GB per year resulting from data analysis. At the start of SLS 2.0, we will need in addition about 150 online controlling processor unit (CPU) cores for fast feedback and about 400 online cores for offline data processing. Five years after start of SLS 2.0, we anticipate to generate 140 TB per year and the need for available online cores will remain at 150 for fast feedback and will increase to 800 for offline data analysis. These numbers have been communicated to the IT division and will be considered in the upgrade of the IT infrastructure for SLS 2.0.

9.7 Timeline

The preferred starting date (commissioning, pilot users) is 2024 and we anticipate that the beamline upgrade will be carried out within the 12 months of the dark period. The time plan for the beamline upgrade until the commissioning phase is provided in Table 9.2. Our goal is to start part of the beamline upgrade before the SLS shutdown, by replacing the focusing (M1) and refocussing (M3) mirrors by 2021 with the goal of obtaining a single focus at the exit slit position. This would directly contribute to increased performance of the beamline and benefit particularly the soft x-ray ptychography endstation, with the added benefit of efficient procurement of the optical elements SLS-wide, since they may have a two-year lead time for delivery. We plan also to carry out the commissioning of the ptychography endstation, the installation of the EIGER detector in the PEEM endstation, and put in place several of the beamline diagnostic tools before the dark period. An upgrade of the front end is also anticipated, and will happen independently of the final optical design. In the following period, the drawing of the final optics layout for SLS 2.0, in collaboration with the Optics group will be carried out, including the CAD design, followed by order placement and construction of the outstanding optical components, such that the parts can be made available before the dark period. The SIM light sources will be shifted 67.3 mm outwards and 540 mm longitudinally downstream. This will require adjustment of all optical components and modifications in the lead-hutch, which however, should not require major construction work. This will be carried out in the dark period, together with installation of the new phase shifter in the ring and modification of the cooling system in the lead hutch to an adaptive cooling system. In the commissioning period, we will need to fully characterise the beamline optics and assess the new beam characteristics, after which we expect to be ready for user operation with both XPEEM and ptychography endstations. The open port will also be available for the other endstations.

9.7.1 Planning

The planning of the SIM beamline upgrade is envisaged to take place at four different stages. The first, current stage involves the commissioning of the ptychography endstation, the funding for which is being sought through an R'Equip grant from the Swiss National Science Foundation (CHF1.05M).

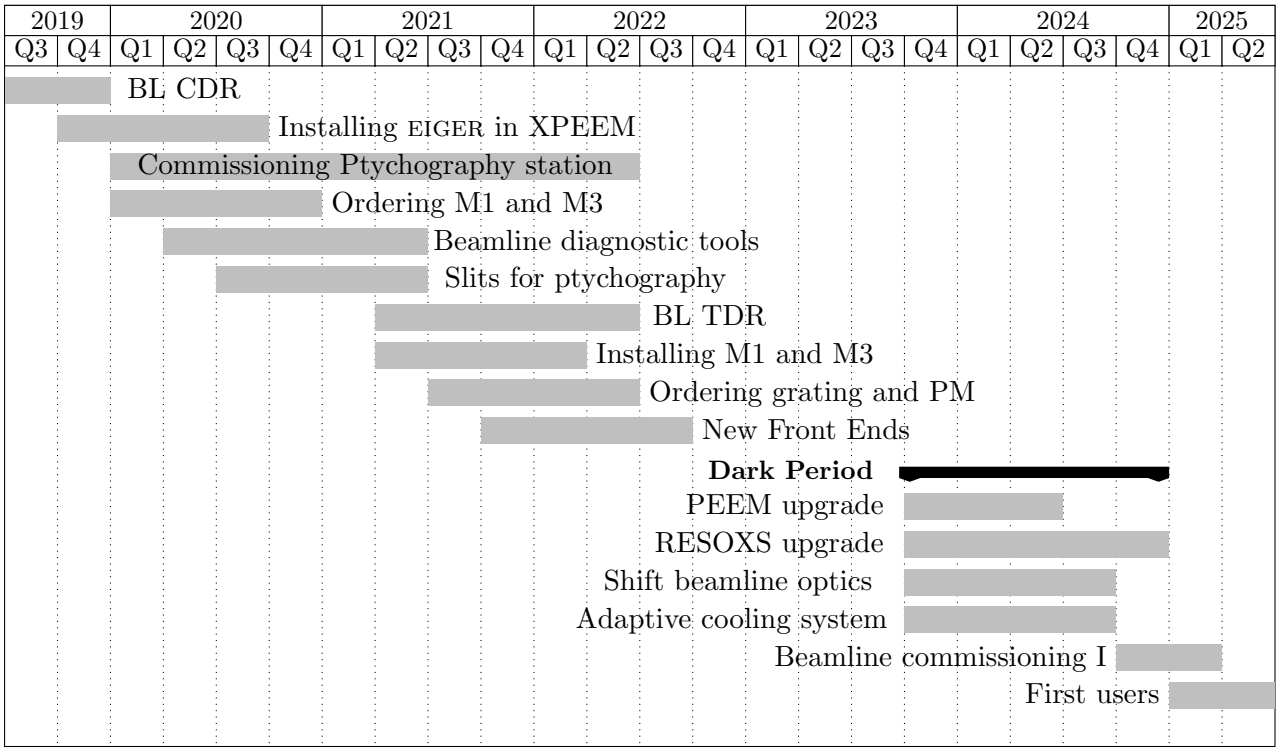

Table 9.2: Detailed time plan for the beamline upgrades.

If granted, design and construction of the endstation will start immediately with the goal of having the instrument fully commissioned and in operation by end of 2021, well before the dark period.

A second stage refers to optics upgrade to be carried out before the SLS shutdown, including the transition from an astigmatic optics to stigmatic. Funds for purchasing the requisite optical components have been requested from the PSD budget for 2020. The procurement of those optical components in 2020 would ease the load on the suppliers, given the lead-time for delivery (2 years) and the likely overload resulting from a simultaneous SLS-wide procurement process (a solution preconised by the Optics group). Upgrades in the front end slits are also envisaged at this stage. During this period, the CAD design of the beamline will be carried out, although we anticipate this will require a minor effort in view of the modest changes that are required for the SIM beamline upgrade.

A third stage will involve the required changes in the optical components to accommodate the new source points of SIM at the SLS 2.0. This will comprise the displacement of the undulators, the installation of a new phase shifter, the necessary modifications in the front end area and of the endstations. Also during this period, the remaining modifications to the optics components will be carried out, including cleaning of the optical components, change of the cooling system to an adaptive system (i.e., dependent on heat load) and the replacement of the 300 and 1200 l/mm monochromator gratings.

A fourth stage will correspond to the full commissioning of the beamline with the SLS 2.0 beam. We anticipate that with the new diagnostic tools, the availability of a fast front end, in combination with the relatively minor overall changes to the SIM beamline, this process will be accomplished within

three months of beam availability.

9.8 Concluding remarks

One major technical adventure of the proposed SIM beamline concept lies in the development of a new soft x-ray ptychography endstation. The planned instrument is highly innovative and benefits fully from the increased coherence of SLS 2.0 and of the leading role of PSI in ptychographic measurement and reconstruction. Another exciting perspective is that of taking advantage of the two undulators and the new phase matcher for SLS 2.0 for devising new schemes for ultra-sensitive detection of changes in the optical signal of materials or in nanosized samples via interferometry. Soft x-ray interferometric detection schemes based on coherent light generated by two phase-matched undulators would be a unique feature, as yet unexplored.

The planned beamline concept design combining two elliptical undulators, a new phase matcher, the XPEEM and soft x-ray ptychography spectro-microscopes, and an open port allowing for the further development of novel instrumentation, makes the SIM beamline set-up unique compared to other soft x-ray beamlines worldwide. For the soft x-ray ptychography endstation we plan to realize a mature instrument, user-friendly, and available to a broad user community. No such instrument is available at any other beamline yet and we anticipate that the capabilities provided by this instrument will place us at the forefront of the field. The proposed upgrades to the SIM beamline are an important step in reaching these goals and in pushing the SIM beamline to the vanguard of soft x-ray nano-spectroscopy imaging and nanoscale scattering worldwide.

Bibliography

[1] M. Kläui, C. A. F. Vaz, J. A. C. Bland, W. Wernsdorfer, G. Faini, E. Cambril, L. J. Heyderman, F. Nolting, and U. Rüdiger. Controlled and reproducible domain wall displacement by current pulses injected into ferromagnetic ring structures. *Phys. Rev. Lett.*, 94:106601, 2005.

[2] M. Mannini, F. Pineider, P. Sainctavit, C. Danieli, E. Otero, C. Sciancalepore, A. M. Talarico, M. A. Arrio, A. Cornia, D. Gatteschi, and R. Sessoli. Magnetic memory of a single-molecule quantum magnet wired to a gold surface. *Nat. Mater.*, 8:194, 2009.

[3] S. Javaid, M. Bowen, S. Boukari, L. Joly, J.-B. Beaufrand, Xi Chen, Y. J. Dappe, F. Scheurer, J.-P. Kappler, J. Arabski, W. Wulfhekel, M. Alouani, and E. Beaurepaire. Impact on interface spin polarization of molecular bonding to metallic surfaces. *Phys. Rev. Lett.*, 105:077201, 2010.

[4] E. Mengotti, L. J. Heyderman, A. Fraile Rodríguez, F. Nolting, R.V. Hügli, and H. B. Braun. Real-space observation of emergent magnetic monopoles and associated Dirac strings in artificial kagome spin ice. *Nature Phys.*, 7:68, 2011.

[5] T. A. Ostler, J. Barker, R. F. L. Evans, R. Chantrell, U. Atxitia, O. Chubykalo-Fesenko, S. El Moussaoui, L. Le Guyader, E. Mengotti, L. J. Heyderman, F. Nolting, A. Tsukamoto, A. Itoh, D. Afanasiev, B. A. Ivanov, A. M. Kalashnikova, K. Vahaplar, J. Mentink, A. Kirilyuk, Th. Rasing, and A. V. Kimel. Ultrafast heating as a sufficient stimulus for magnetization reversal in a ferrimagnet. *Nat. Commun.*, 3:666, 2012.

[6] M. Buzzi, R. V. Chopdekar, J. L. Hockel, A. Bur, T. Wu, N. Pilet, P. Warnicke, G. P. Carman, L. J. Heyderman, and F. Nolting. Single domain spin manipulation by electric fields in strain coupled artificial multiferroic nanostructures. *Phys. Rev. Lett.*, 111:027204, 2013.

[7] A. Farhan, P. M. Derlet, A. Kleibert, A. Balan, R. V. Chopdekar, M. Wyss, L. Anghinolfi, F. Nolting, and L. J. Heyderman. Exploring hyper-cubic energy landscapes in thermally active finite artificial spin-ice systems. *Nature Physics*, 9:375, 2013.

[8] S. Gliga, G. Hrkac, C. Donnelly, J. Büchi, A. Kleibert, J. Cui, A. Farhan, E. Kirk, R. V. Chopdekar, Y. Masaki, N. S. Bingham, A. Scholl, R. L. Stamps, and L. J. Heyderman. Emergent dynamic chirality in a thermally driven artificial spin ratchet. *Nature Materials*, 16:1106, 2017.

[9] Z. Luo, T. P. Dao, A. Hrabec, J. Vijayakumar, A. Kleibert, M. Baumgartner, E. Kirk, J. Cui, T. Savchenko, G. Krishnaswamy, L. J. Heyderman, and P. Gambardella. Chirally coupled nanomagnets. *Science*, 363:1435, 2019.

[10] V. Scagnoli, U. Staub, Y. Bodenthin, R. A. de Souza, M. Garcia-Fernandez, M. Garganourakis, A. T. Boothroyd, D. Prabhakaran, and S. W. Lovesey. Observation of orbital currents in CuO. *Science*, 332:696, 2011.

[11] C. Wäckerlin, D. Chylarecka, A. Kleibert, K. Müller, C. Iacovita, F. Nolting, T. A. Jung, and N. Ballav. Controlling spins in adsorbed molecules by a chemical switch. *Nat. Comm.*, 1:61, 2010.

[12] M. A. Brown, Z. Abbas, A. Kleibert, R. G. Green, A. Goel, S. May, and T. M. Squires. Determination of surface potential and electrical double-layer structure at the aqueous electrolyte-nanoparticle interface. *Physical Review X*, 6:11007, 2016.

[13] L. Artiglia, J. Edebeli, F. Orlando, S. Chen, M.-T. Lee, P. C. Arroyo, A. Gilgen, T. Bartels-Rausch, A. Kleibert, M. Vazdar, M. A. Carignano, J. S. Francisco, P. B. Shepson, I. Gladich, and M. Ammann. A surface-stabilized ozonide triggers bromide oxidation at the aqueous solution-vapor interface. *Nature Communications*, 8:700, 2017.

[14] W. Karim, C. Spreafico, A. Kleibert, J. Gobrecht, J. VandeVondele, Y. Ekinci, and J. A. van Bokhoven. Catalyst support effects on hydrogen spillover. *Nature*, 541:68, 2017.

[15] G. Tinti, H. Marchetto, C. A. F. Vaz, A. Kleibert, M. Andrä, R. Barten, A. Bergamaschi, M. Brückner, S. Cartier, R. Dinapoli, E. Fröjdh, D. Greiffenberg, C. Lopez-Cuenca, D. Mezza, A. Mozzanica, F. Nolting, M. Ramilli, S. Redford, M. Ruat, Ch. Ruder, L. Schädler, Th. Schmidt, B. Schmitt, F. Schütz, X. Shi, D. Thattil, S. Vetter, and J. Zhang. The EIGER detector for low-energy electron microscopy and photoemission electron microscopy. *J. Synchrotron Rad.*, 24:963, 2017.

[16] P. Helfenstein, R. Rajeev, I. Mochi, A. Kleibert, C. A. F. Vaz, and Y. Ekinci. Beam drift and partial probe coherence effects in euv reflective-mode coherent diffractive imaging. *Optics Express*, 26:325789, 2018.

[17] M. A. Brown, A. B. Redondo, I. Jordan, N. Duyckaerts, M.-T. Lee, M. Ammann, F. Nolting, A. Kleibert, T. Huthwelker, J.-P. Mächler, M. Birrer, J. Honegger, R. Wetter, H. J. Wörner, and J. A. van Bokhoven. A new endstation at the Swiss Light Source for ultraviolet photoelectron spectroscopy, x-ray photoelectron spectroscopy, and x-ray absorption spectroscopy measurements of liquid solutions. *Rev. Sci. Instrum.*, 84:073904, 2013.

[18] C. A. F. Vaz, A. Kleibert, and M. El Kazzi. Nanoscale xpeem spectromicroscopy. In K. D. Sattler, editor, *21st CENTURY NANOSCIENCE A HANDBOOK*, chapter 17. Taylor & Francis (CRC Press), 2020.

[19] C. A. F. Vaz, J. A. C. Bland, and G. Lauhoff. Magnetism in ultrathin film structures. *Rep. Prog. Phys.*, 71:056501, 2008.

[20] X. Yu, D. Morikawa, T. Yokouchi, K. Shibata, N. Kanazawa, F. Kagawa, T. Arima, and Y. Tokura. Aggregation and collapse dynamics of skyrmions in a non-equilibrium state. *Nature Physics*, 14:832, 2018.

[21] F. Jonietz, S. Mühlbauer, C. Pfleiderer, A. Neubauer, W. Münzer, A. Bauer, T. Adams, R. Georgii, P. Böni, R. A. Duine, K. Everschor, M. Garst, and A. Rosch. Spin transfer torques in MnSi at ultralow current densities. *Science*, 330:1648, 2010.

[22] X. Z. Yu, N. Kanazawa, Y. Onose, K. Kimoto, W. Z. Zhang, S. Ishiwata, Y. Matsui, and Y. Tokura. Near room-temperature formation of a skyrmion crystal in thin-films of the helimagnet FeGe. *Nature Materials*, 10:106, 2011.

[23] S. Seki, X. Z. Yu, S. Ishiwata, and Y. Tokura. Observation of skyrmions in a multiferroic material. *Science*, 336:198, 2012.

[24] A. Fert, N. Reyren, and V. Cros. Magnetic skyrmions: advances in physics and potential applications. *Nature Reviews Materials*, 2:1, 2017.

[25] C. Moreau-Luchaire, C. Moutafis, N. Reyren, J. Sampaio, C. A. F. Vaz, N. Van Horne, K. Bouzehouane, K. Garcia, C. Deranlot, P. Warnicke, P. Wohlhueter, J.-M. George, M. Weigand, J. Raabe, V. Cros, and A. Fert. Additive interfacial chiral interaction in multilayers for stabilization of small individual skyrmions at room temperature. *Nature Nanotechnology*, 11:444, 2016.

[26] J. Sampaio, V. Cros, S. Rohart, A. Thiaville, and A. Fert. Nucleation, stability and current-induced motion of isolated magnetic skyrmions in nanostructures. *Nature Nanotechnology*, 8:839, 2013.

[27] D. Cortées-Ortuño, N. Romming, M. Beg, K. von Bergmann, A. Kubetzka, O. Hovorka, H. Fangohr, and R. Wiesendanger. Nano-scale magnetic skyrmions and target states in confined geometries. *ArXiv*, 1901.06999v1, 2019.

[28] H. Yang, G. Chen, A. A. C. Cotta, A. T. N'Diaye, S. A. Nikolaev, E. A. Soares, W. A. A. Macedo, K. Liu, A. K. Schmid, A. Fert, and M. Chshiev. Significant Dzyaloshinskii-Moriya interaction at graphene-ferromagnet interfaces due to the Rashba effect. *Nature Materials*, 17:605, 2018.

[29] W. Jiang, P. Upadhyaya, W. Zhang, G. Yu, M. B. Jungfleisch, F. Y. Fradin, J. E. Pearson, Y. Tserkovnyak, K. L. Wang, O. Heinonen, S. G. E. te Velthuis, and A. Hoffmann. Blowing magnetic skyrmion bubbles. *Science*, 349:283, 2015.

[30] C. A. F. Vaz, F. J. Walker, C. H. Ahn, and S. S. Ismail-Beigi. Intrinsic interfacial phenomena in manganite heterostructures. *J. Phys.: Condens. Matter*, 27:123001, 2015.

[31] A. Soumyanarayanan, N. Reyren, A. Fert, and C. Panagopoulos. Emergent phenomena induced by spin-orbit coupling at surfaces and interfaces. *Nature*, 539:509, 2016.

[32] M. Baumgartner, K. Garello, J. Mendil, C. O. Avci, E. Grimaldi, C. Murer, J. Feng, M. Gabureac, C. Stamm, Y. Acremann, S. Finizio, S. Wintz, J. Raabe, and P. Gambardella. Spatially and time-resolved magnetization dynamics driven by spin-orbit torques. *Nature Nanotechnology*, 12:980, 2017.

[33] F. N. Rybakov, N. S. Kiselev, A. B. Borisov, L. Dring, C. Melcher, and S. Blgel. Magnetic hopfions in solids, 2019.

[34] P. Wadley, B. Howells, J. Železný, C. Andrews, V. Hills, R. P. Campion, V. Novák, K. Olejník, F. Maccherozzi, S. S. Dhesi, S. Y. Martin, T.Wagner, J. Wunderlich, F. Freimuth, Y. Mokrousov, J. Kuneš, J. S. Chauhan, M. J. Grzybowski, A. W. Rushforth, K.W. Edmonds, B. L. Gallagher, and T. Jungwirth. Electrical switching of an antiferromagnet. *Science*, 351:587, 2016.

[35] P. Wadley, S. Reimers, M. J. Grzybowski, C. Andrews, M. Wang, J. S. Chauhan, B. L. Gallagher, R. P. Campion, K. W. Edmonds, S. S. Dhesi, F. Maccherozzi, V. Novak, J. Wunderlich, and T. Jungwirth. Current polarity-dependent manipulation of antiferromagnetic domains. *Nature Nanotechnology*, 13:362, 2018.

[36] M. B. Jungfleisch, W. Zhang, and A. Hoffmann. Perspectives of antiferromagnetic spintronics. *Physics Letters A*, 382:865, 2018.

[37] P. Němec, M. Fiebig, T. Kampfrath, and A. V. Kimel. Antiferromagnetic opto-spintronics. *Nature Physics*, 14:229, 2018.

[38] U. Atxitia, L. Rózsa, T. Birk, S. Selzer, and U. Nowak. Reduced thermal stability of antiferromagnetic nanostructures. *Phys. Rev. B*, 100:064422, 2019.

[39] C. A. F. Vaz, J. Hoffman, C. H. Ahn, and R. Ramesh. Magnetoelectric coupling effects in multiferroic complex oxide composite structures. *Adv. Mater.*, 22:2900, 2010.

[40] C. A. F. Vaz. Electric field control of magnetism in multiferroic heterostructures. *J. Phys.: Condens. Matter*, 24:333201, 2012.

[41] K. Xu. Electrolytes and interphases in Li-ion batteries and beyond. *Chem. Rev.*, 114:11503, 2014.

[42] R. Hausbrand, G. Cherkashinin, H. Ehrenberg, M. Gröting, K. Albe, C. Hess, and W. Jaegermann. Fundamental degradation mechanisms of layered oxide Li-ion battery cathode materials: Methodology, insights and novel approaches. *Materials Science and Engineering B*, 192:3, 2015.

[43] D. A. Shapiro, Y.-S. Yu, T. Tyliszczak, J. Cabana, R. Celestre, W. Chao, K. Kaznatcheev, A. L. D. Kilcoyne, F. Maia, S. Marchesini, Y. S. Meng, T. Warwick, L. L. Yang, and H. A. Padmore. Chemical composition mapping with nanometre resolution by soft x-ray microscopy. *Nature Photonics*, 8:765, 2014.

[44] G. Kourousias, B. Bozzini, A. Gianoncelli, M. W. M. Jones, M. Junker, G. van Riessen, and M. Kiskinova. Shedding light on electrodeposition dynamics tracked in situ via soft x-ray coherent diffraction imaging. *Nano Research*, 9:2046, 2016.

[45] F. Meier and B. M. Weckhuysen. Spatial and temporal exploration of heterogeneous catalysts with synchrotron radiation. *Nature Reviews Materials*, 3:324, 2018.

[46] G. Kourousias, B. Bozzini, M. W. M. Jones, G. van Riessen, M. Kiskinova, and A. Gianoncelli. Monitoring dynamic electrochemical processes with in situ ptychography. *Applied Nanoscience*, 8:627, 2018.

[47] D. Leanza, C. A. F. Vaz, I. Czekaj, P. Novák, and M. El Kazzi. Solving the puzzle of $Li_4Ti_5O_{12}$ surface reactivity in aprotic electrolytes in Li-ion batteries by nanoscale XPEEM spectromicroscopy. *J. Mater. Chem. A*, 6:3534, 2018.

[48] D. Leanza, C. A. F. Vaz, G. Melinte, X. Mu, P. Novák, and M. El Kazzi. Revealing the dual surface reaction on a HE-NCM Li-ion battery cathode and their impact on the counter electrode. *ACS Applied Materials & Interfaces*, 11:6054, 2019.

[49] D. Leanza, M. Mirolo, C. A. F. Vaz, P. Novák, and M. El Kazzi. Surface degradation and chemical electrolyte oxidation induced by the oxygen released from layered oxide cathodes in Li-ion batteries. *Batteries & Supercaps*, 2:482, 2019.

[50] M. Fäth, S. Freisem, A. A. Menovsky, Y. Tomioka, J. Aarts, and J. A. Mydosh. Spatially inhomogeneous metal-insulator transition in doped manganites. *Science*, 285:1540, 1999.

[51] G. Mattoni, P. Zubko, F. Maccherozzi, A. J. H. an der Torren, D. B. Boltje, M. Hadjimichael, N. Manca, S. Catalano, M. Gibert, Y. Liu, J. Aarts, J.-M. Triscone, S. S. Dhesi, and A. D. Caviglia. Striped nanoscale phase separation at the metal-insulator transition of heteroepitaxial nickelates. *Nature Communications*, 7:13141, 2016.

[52] D. Preziosi, L.Lopez-Mir, X. Li, T. Cornelissen, J. H. Lee, F. Trier, K. Bouzehouane, S. Valencia, A. Gloter, A. Barthélémy, and M. Bibes. Direct mapping of phase separation across the metal-insulator transition of $NdNiO_3$. *Nano Lett.*, 18:2226, 2018.

[53] D. Just. Speed optimized fast front-end slits prototype for SLS 2.0.

Chapter 10

X-Treme - XMCD at high fields and low temperatures

Jan Dreiser, Cinthia Piamonteze, and Stefan Zeugin

In a nutshell

The X-Treme beamline is dedicated for the use of polarized soft x-rays to investigate magnetic systems at high magnetic fields and low temperatures. The provided sample environment of 7 T and 2 K together with *in-situ* sample preparation, a variety of detection methods, and the beam stability render the beamline highly competitive in a worldwide level. A wide breadth of systems are probed at X-Treme, ranging from a few atoms or molecules covering only fractions of a monolayer up to complex heterostructures.
With the advent of SLS 2.0, we propose to modify the beamline optics in order to provide a much smaller focus size, of the order of tens of microns which will greatly increase the current spatial resolution. This will open up possibilities to measure small samples and prototype devices. In addition, we propose a flexible optical layout where a lower beam density is also available, allowing one to measure radiation-sensitive samples. A new undulator is proposed which will extend the energy range in the first harmonic (where full circular polarization with full flux is available) and in addition provide ten times faster polarization switching. The faster polarization switching will enable a much more precise and stable one-shot measurement of the element-specific magnetic hysteresis curves. A new endstation, for which funding was granted by the Swiss National Science Foundation, will provide two times higher magnetic fields and faster ramping sweep rates, providing sample-environment conditions complementary to other endstations around the world, which will keep X-Treme unique and highly competitive.
In summary, the new X-Treme beamline will allow the exploration of magnetic properties in greater magnetic fields, with higher spatial resolution and more precise one-shot measurements of magnetization curves, provided by fast polarization switching.

10.1 Overview

Soft x-ray absorption spectroscopy (XAS) and x-ray magnetic circular dichroism (XMCD) [1] probe element-specific spin and orbital magnetic moments with ultrahigh sensitivity reaching down to sub-monolayers of materials. X-Treme is specialized in XAS/XMCD at low temperature (2 K) and high magnetic field (7 T) [2]. Among these features which render the beamline competitive on a worldwide level, the sample-preparation system is of high importance, allowing one to prepare samples and to measure them *in situ* without breaking the ultrahigh vacuum. These features allow one to perform research on a large breadth of possible systems, including surface magnetism with adsorbed atoms or molecular magnets, as well as complex oxide heterostructures. The X-Treme beamline shares a UE54 undulator with the Phoenix I beamline. Furthermore, from time to time, the Phoenix II endstation is installed a few meters behind the X-Treme endstation, allowing the soft x-rays of X-Treme to be used in chemical spectroscopy experiments.

The X-Treme beamline was constructed by a collaborative effort between the Laboratory of Nanostructures at Surfaces (LNS), lead by Prof. Harald Brune at EPFL and the Microscopy and Magnetism group in the Photoscience Division (PSD) at PSI. This collaboration concerns both joining the complementary expertise of the different researchers involved as well as a shared funding scheme. While PSI has financed the beamline components, the endstation was funded by SNSF through a proposal from LNS with matching funds from EPFL. This collaboration scheme will continue in our upgrade plans here proposed.

In the context of the SLS upgrade, we propose here to perform major modifications of the elements of the X-Treme beamline while leaving the basic scientific method unchanged. This will allow us to attract new users while also maintaining the current established and highly successful user community. We are convinced that the proposed changes will render the beamline competitive for the following decade.

The proposed changes comprise (a) the installation of a new UE44 undulator with fast (ca. 2 s) helicity switching time (see Chapter 2), important for the XMCD measurements. This undulator will deliver both circularly and linearly polarized x-rays. So far, fast helicity switching was only possible either using two undulators with tune-detune [3] or kicker-magnet schemes [4], or by employing an electromagnetic undulator (such as the EMPHU-65 device used at the DEIMOS beamline at Soleil [5], which can, however, only produce circular polarization). Furthermore, we propose (b) the replacement of the beamline optics and (c) of the superconducting magnet endstation (SNF R'Equip proposal accepted in November 2019), as well as (d) an upgrade of the sample-preparation system. Item (b) will allow one to perform simple microscopy experiments that do not require the high spatial resolution as, e.g. in a scanning transmission x-ray microscope (STXM); however, as an advantage, the flux is not reduced by additional optical elements such as zone plates. The optical upgrade will also provide the choice to use a large beam which is important for the measurement of radiation-sensitive systems. Regarding point (c), besides increasing the available magnetic field, we are currently working on x-ray

detected pulsed electron paramagnetic resonance experiments at low temperature to measure the spin coherence times of magnetic quantum bits (PSI internal CROSS project started in October 2019). This method will be a forerunner and become available as a worldwide unique user experiment at the X-Treme station. In the following these upgrades will be discussed in more detail.

In the current design of the SLS 2.0 optics, a transverse shift of all beamline elements of $\Delta R = 67.3$ mm toward the outer wall is foreseen, following the source point shift imposed by the new machine design. The implications in costs and manpower of this beamline relocation are not taken into account in this chapter.

10.1.1 Gains from beamline and ring upgrade

The smaller divergence and spot size of SLS 2.0 has allowed us to rethink the optical design to optimize the beam focus. The proposed new optics, together with the higher SLS 2.0 brilliance will enable us to reach nearly a one order of magnitude smaller spot size at the sample position. The smaller spot size will allow us to study, e.g., lithographically prepared samples (as prototype devices) and spatially inhomogeneous samples keeping a similar integrated photon flux compared to the present case. Furthermore, the new proposed undulator matches better the operation energy of X-Treme allowing to extend the first harmonic range towards higher energies. This will give a one order of magnitude higher total flux for circular polarization in part of the lanthanides' $M_{4,5}$ edges. The new undulator is planned to provide ten times faster polarization switching. The endstation will also be upgraded, (SNSF R'Equip granted), which will allow us to reach two times larger magnetic field (from 7T to 14T) with a sweep rate which is more than twice faster than we have now (from 2T/min to 5T/min, for fields up to 10T).

10.1.2 Uniqueness of X-Treme in the international milieu

Among the several soft x-ray MCD beamlines worldwide, X-Treme is one of the very few which provides low temperatures and high magnetic fields in combination with *in-situ* sample preparation including advanced tools like scanning tunneling microscopy. The upgraded X-Treme endstation will provide magnetic fields of up to 14 T with a fast sweep rate. The new endstation will render X-Treme a worldwide unique beamline in combination with the *in-situ* sample preparation facility.

In addition, the new endstation will be compatible with a future optional upgrade to incorporate a ^{3}He insert, which will allow also to reach sample temperatures below 1 K.

10.1.3 Complementarity to other SLS beamlines

X-Treme serves predominantly communities working on thin film magnetism, surface and interface science and dilute paramagnetic systems. Several other SLS beamlines are also overlapping science-wise with these fields. These include (SLS 1.0) mainly SIS, PEARL, SIM, ADRESS.

In terms of sample environment X-Treme is unique in SLS. It complements very well the soft x-ray microscopy endstations in SLS (as the STXM at Pollux, the PEEM at SIM and the new planned ptychography endstation at the SIM). While these endstations offer high spatial resolution with mild magnetic fields and standard low temperatures, X-Treme pushes the limit in the sample environment.

This will be even more the case with the new endstation. In addition, the new optimized spot size, will allow X-Treme to study systems in the micrometer range, being also complementary in terms of spatial resolution to the soft x-ray microscopy beamlines in SLS.

10.1.4 Impact on the international and local Swiss community

The overbooking of the X-Treme beamline ranges between 2.0 and 2.8, since it has been open to external users. In the last few years, approximately 30-50% of the proposals were submitted by local, Swiss, groups, while 40-60% came from European, non-Swiss facilities and about 10% were submitted by other, international researchers. The upgrade of the X-Treme beamline is planned to still serve the current user community, but in addition it will provide more features (higher magnetic field, smaller spot size in the focused case, x-ray detected pulsed electron paramagnetic resonance) which will appeal to a larger range of scientific cases. Therefore, we expect that the X-Treme beamline will be able to attract an even larger user community than it does at present.

10.2 Source

Concerning the undulator source [item (a) of the previous paragraph], the key features of the proposed new undulator are summarized in Table 10.1. The most important change is the fast helicity switching, which will allow for a radically new measurement scheme. Currently, in order to obtain a magnetic (XMCD) hysteresis loop, two full loops have to be measured between which the x-ray helicity is switched. The validity of this approach is predicated on the assumption that the magnetic properties do not change over time. In the current state, it is impossible to verify whether this assumption is correct or not. Certainly, this assumption is problematic for radiation-sensitive systems, which represent a good fraction of the investigated samples.

The new undulator will allow one to measure directly the XMCD in one field sweep scan, that is, a single magnetic loop, instead of measuring one field sweep per x-ray polarization, as done currently. Furthermore, the energy range will be shifted with respect to the current undulator, which will allow to access part of the lanthanide $M_{4,5}$ edges with the first harmonic, resulting in one order of magnitude higher flux in the circular polarization mode compared to the third harmonic currently used for the lanthanides.

10.3 Front end

The current front end includes two x-ray beam position monitors (XBPMs) as well as movable vertical and horizontal blades which allow one to set the position and size of the accepted radiation cone from the insertion device.

For the SLS upgrade, it is planned to reuse major components of the existing front end. Currently, the following modifications of the front end are planned: (a) the movement of the front end elements according to the new SLS 2.0 lattice; (b) introducing a fast scanning option (ca. 3 s timescale) of the vertical and horizontal blades in order to obtain a detailed beam profile within a reasonable time; (c)

Description	Current	Proposed for SLS 2.0
ID type	UE54	UE44
Available polarization (linear)	0^o - 90^o	0^o - 180^o
Available polarization (circular)	circular left/right	circular left/right
1^{st} harmonic energy range [eV]	185-950	260-1300
Time to switch between circular polarization helicities [s]	30	2
Period length [mm]	54	44
Number of periods	32	∼75

Table 10.1: Comparison between the current and the proposed insertion devices. The UE44 is the fixed gap APPLE II undulator of the current ADRESS beamline. The undulator will be updated by exchanging the drive system with a hyndraulic drive system to allow fast helicity switching with a single device and adding the 5-axis cam-shaft movers which allow a precise remote adjustment of the undulator with respect to the beamline axis.

the removal of the second XBPM located at the front end slit position if (and only if) item (b) can be successfully established. See also Chapter 3.

10.4 Optics

10.4.1 Filters and slits

Currently there is one filter (attenuator) located before the exit slit. It consists of a 3 μm thick aluminum foil, which can be moved into the beam by a translation stage. It has the function of reducing the flux to protect radiation-sensitive samples. Currently the flux reduction is a factor of $\sim$ 10 at a photon energy of 700 eV. For the SLS upgrade, it is foreseen to include more filters with varying thicknesses on the same linear stage to have different choices of flux-reduction factors.

The beamline is equipped with a vertical exit slit after the monochromator which defines the vertical focus size at the endstation and the energy resolution. We plan to replace this exit slit by double slits with vertical and horizontal openings (Layout 3 discussed in Section 10.4.2) to be able to control the spot size at the sample position.

10.4.2 Mirrors

The optics layout of X-Treme is illustrated in Figure 10.1(a). It includes three standalone mirrors and another one implemented in the plane grating monochromator. The first, collimating, mirror (CMU, collimating mirror unit) performs a collimation in the vertical plane and focuses in the horizontal. The focusing mirror (FMU, focusing mirror unit) then focuses the beam vertically after the monochromator onto the exit slit. Finally, the refocusing mirror (RMU, refocusing mirror unit) focuses the beam onto the sample. The RMU can be moved out of the beam, which allows one to choose between a focused and a defocused beam mode. Given that SLS 2.0 will allow for a smaller horizontal focus, we will

take advantage of that and improve the optical scheme to obtain a significantly smaller focused spot size. This will be complementary to the microscopy endstations at SLS and SLS 2.0, allowing the measurements of samples in the range of ≈ 30 μm in a high-field and low-temperature environment. It should also be noted that the horizontal defocused spot size will decrease by 60% in SLS 2.0 compared to the current spot size. This will pose problems for systems suffering from x-ray induced demagnetization, radiation damage, or electrical charging. Therefore, the proposed optical upgrade will recover a larger defocused beam to allow the measurement of radiation sensitive samples, and will also provide significantly smaller spot size, when operating with focused beams.

The current optical scheme in X-Treme with the horizontal focusing at the first mirror was chosen during the beamline construction to allow acceptance of the full beam by the FMU. With SLS 2.0, the smaller horizontal divergence enables a different optical layout [Figure 10.1(c)], which we discuss below.

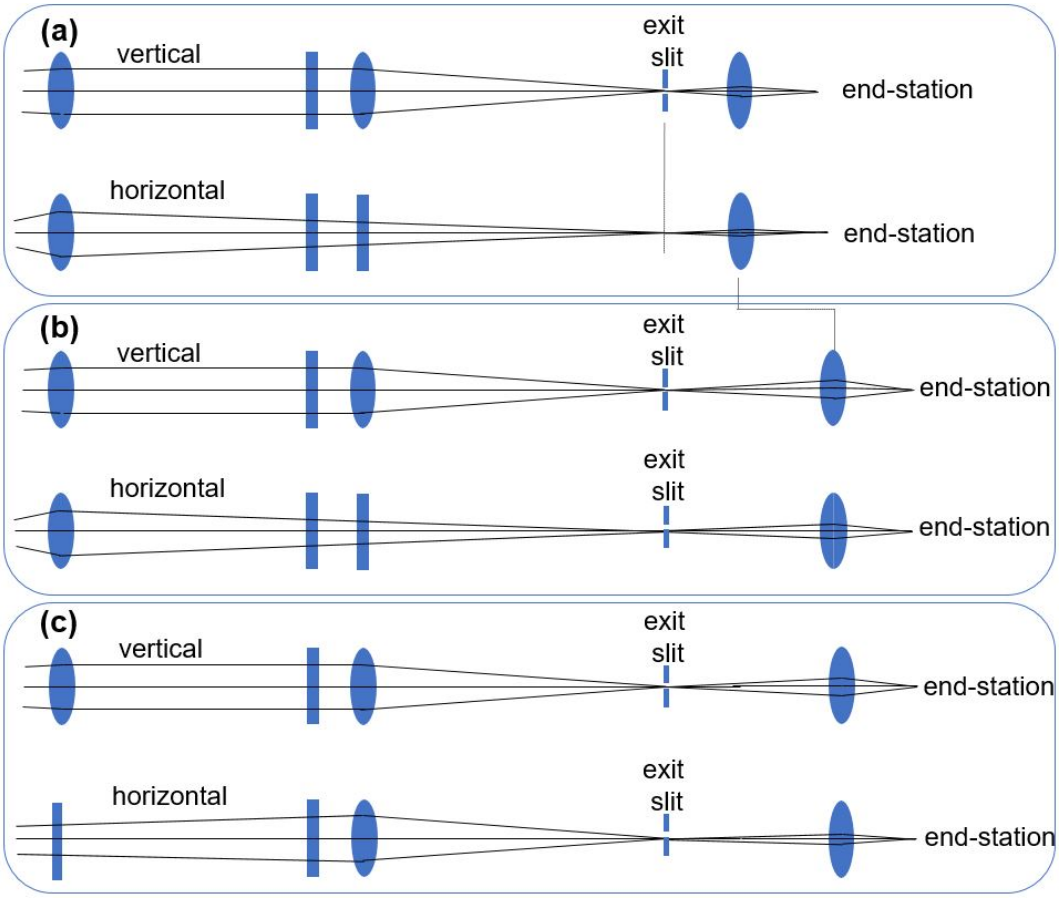

Figure 10.1: (a): Layout 1: current optics scheme of the X-Treme beamline. (b) Layout 2: same optical layout with new RMU and double exit slits. (c) Layout 3: optimal layout, with change of horizontal focusing from CMU to FMU.

Two upgrade options are shown in Figures 10.1(b) and 10.1(c). The trade-off between these options

lies in the flux performance and the size of the focal spot versus the total cost.

In Layout 2 [Figure 10.1(b)], the CMU and FMU mirrors are kept, which is possible initially at SLS 2.0, anticipating an upgrade at a later time. This solution would imply a temporary trade-off between focus size and flux until the focusing scheme is adapted. If the source point moves significantly upstream (>800 mm), CMU and FMU have to be upgraded together with the machine upgrade to keep X-Treme operational. The larger defocused spot size is achieved by a convex mirror at the RMU. The RMU is planned to have three polished surfaces for different uses: for focusing, for defocusing, and a flat surface for deflecting the beam to the Phoenix-II endstation. In Layout 2, the small focused beam is achieved at the cost of flux, by including a horizontal exit slit in addition to the current vertical slit.

The strongly preferred and optimal design is given by Layout 3 in Figure 10.1(c). In this design the horizontal focusing will no longer be performed at the initial collimating mirror, but at the focusing mirror. This allows a higher demagnification factor of the source which at the same time decreases the focused spot size and increases the defocused spot size. Therefore the change in optical layout achieves the two main goals for X-Treme in SLS 2.0, with full flux.

Also here, the RMU is planned to have three polished surfaces for different uses: for focusing, for defocusing, and a flat surface for deflecting the beam to the Phoenix-II endstation.

In Table 10.2, the anticipated beam spot sizes and transmission resulting from the different scenarios are summarized. Layouts 2 and 3 are the ones outlined in Figures 10.1(b) and (c), respectively, and described above. Versions (a), (b) and (c) in Table 10.2 correspond to keeping the RMU at the same position or moving the RMU and the endstation downstream by 1 or 2 meters, respectively. The amount of movement of the RMU and endstation downstream will depend on the final geometries of the Phoenix beamline and auxiliary elements. The calculations were done with the current source distance. For ring lattice B062 the ID position in sector 7 will move by 540 mm upstream which can be compensated by changing the mirror angles in case we decide to start with Layout 2. There is another mirror-symmetric position for the ID which would involve a movement of 1800 mm of the source compared to the current position. This will make the spot sizes in Table 10.2, Layout 3, smaller by about 10%.

Table 10.2 illustrates the differences in performance between Layouts 2 and 3. Layout 3 delivers larger defocused spot sizes compared to Layout 2. The horizontal focused spot size in Layout 2 is at least a factor of two larger than in Layout 3. A similar focused spot size in Layout 3 compared to 2, is obtained by reducing the beam with the newly proposed horizontal exit slit in which case the flux is decreased to half, as pointed out in Table 10.2.

10.4.3 Monochromator

The beamline includes a plane-grating monochromator (PGM) with three gratings having different line spacings, which allow one to optimize either the photon flux or the energy resolution. Because of the highly reliable operation and excellent performance of the present monochromator, this item is foreseen to be further utilized for the SLS upgrade, other than some minor maintenance work.

	Layout 2a	Layout 2b	Layout 2c	Layout 3a	Layout 3b	Layout 3c
Defocused [mm]	1 × 1	1 × 1	1 × 1	0.8 ×1.2	1.0×1.6	1.2×2.0
Focused [μm]	65 × 23	43 × 14	33 × 8	80 × 23	49 × 14	37 × 10
Transmittance [%]	43	47	47	100	100	100

Table 10.2: Spot sizes (H × V) FWHM at the sample position for different beamline optical layouts as explained in the main text. Calculated transmittance normalized to the values of Layout 3, which are expected to be close to those of the present Layout 1, is given for the focused spot size.

10.5 Endstation

In Table 10.3, the key properties of the envisioned, upgraded endstation are summarized. It will include an increase of the maximum available field by a factor of 2, resulting in 14 T, while leaving the sample base temperature unchanged. The options for the acquisition of an ultralow temperature (^{3}He) insert in combination with the 14-T upgrade, which will allow one to reach sample temperatures below 500 mK, are currently under evaluation. Figure 10.2 depicts the proposed modified layout with the RMU and the endstation moved downstream by 2 meters, according to the Layouts 2c or 3c mentioned in Table 10.2. Regardless of this translation, the 14-T magnet produces a stray field which does not allow one to operate the current sample-preparation chamber behind the endstation. This is because of the magnetic field limits of the necessary turbo pumps. Moreover the interference of the Ar^+ ion gun operation with the stray field, prohibits *in-situ* sample preparation while the field is in use, which corresponds to most of the measurement time.

	Current	Proposed for new endstation
Maximum field (T)	7.0	14.0
Maximum sweep rate (T/min)	2.0	6.0
Lowest temperature (K)	2.0	2.0

Table 10.3: Key features of the proposed upgraded endstation.

In order to allow simultaneous measurement and sample preparation, which is mandatory for an optimal use of the x-ray beam, certain measures have to be taken. These include (a) vibrational decoupling between preparation and measurement chambers, and (b) a spatial separation between preparation system and magnet chamber. (a) will suppress the spreading of mechanical vibrations caused by operating the preparation system close to the measurement chamber where the vibrations will result in electrical noise spoiling the x-ray absorption measurements. (b) means that the preparation system is exposed to a smaller magnetic stray field still compatible with the operation of turbo pumps. Taking these issues into account, we propose to set up the preparation system laterally, as shown in Figure 10.2. The spatial separation will be achieved via a cylindrical sample storage and transfer chamber having a radial telescopic transfer arm. With this arm, different neighboring chambers can be accessed for the surface preparation as well as for materials deposition (metals or

molecules) onto the cleaned surfaces. In this context, it would be clearly advantageous to have more space available toward the neighboring beamline (which now is NAPP/NanoXAS). In lattice B062 the the 7M and 7D source points move radially in opposite directions which means only a minor increase of the distance between the two beamlines. As can be seen in Figure 10.2, with the new proposed preparation system, there would be only $\approx$ 1 m of free space left between the X-Treme preparation system and NanoXAS beamline pipe.

The small spot sizes in the focused mode, as listed in Table 10.2, will require improved sample positioning and stabilization. Currently, different options are being evaluated in order to allow a positioning accuracy of the order of $\sim$ 15 μm.

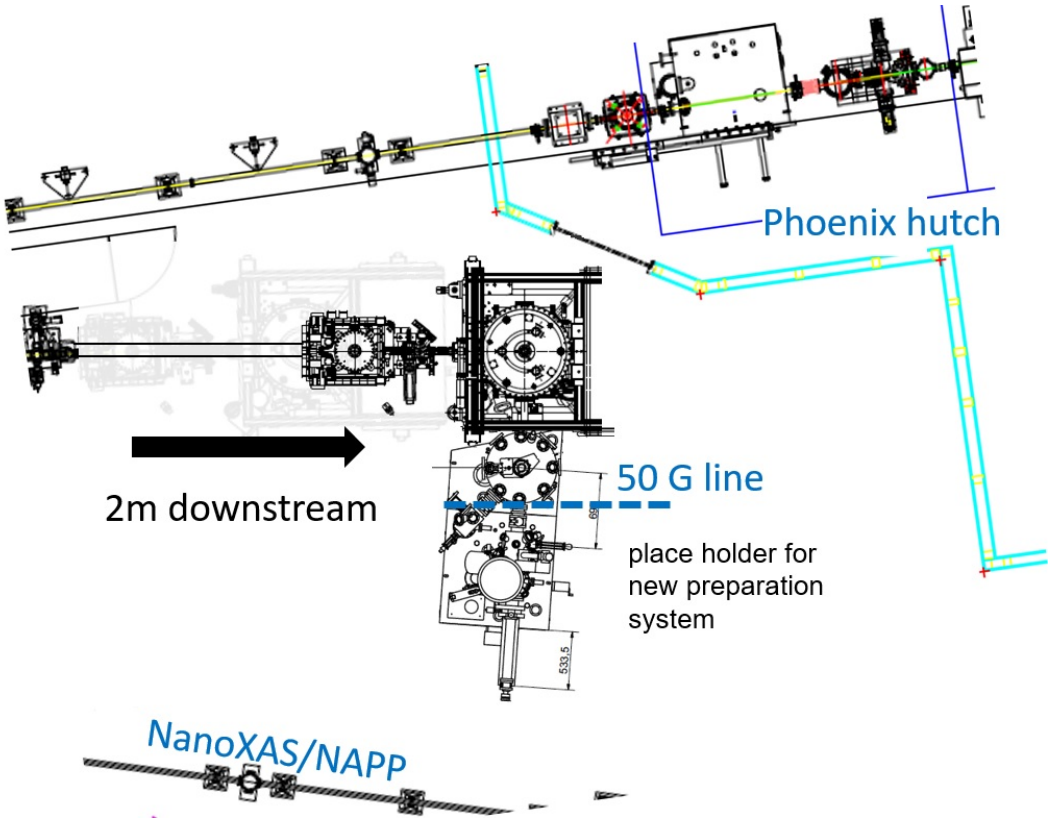

Figure 10.2: Proposed modified layout of the endstation environment with the refocusing mirror unit (RMU) and the X-Treme endstation moved 2 m downstream. The sample-preparation system is now located laterally (it is currently behind the endstation). If it is decided to keep the NanoXAS/NAPP beamline at its current location, the X-Treme preparation system can be adjusted in order to accommodate sufficient room for potential escape paths between the two beamlines.

10.5.1 Controls and data systems

The energy scans of the beamline are performed "on-the-fly" (otf), which means that the monochromator moves continuously, allowing the routine measurement of a 50-eV-wide energy scan in two to

three minutes. During the otf scans, the monochromator acts as a "master" and moves continuously while the insertion device is moving in steps following the monochromator energy readback. The implementation was done this way because the motion-control system does not allow a fully synchronous movement of both devices. This non-synchronous movement can lead to undesired artefacts in the photon-energy scans under certain circumstances. Therefore, in SLS 2.0, such otf scans will benefit from a motion-control system that enables the true synchronous movement of both the monochromator and the insertion device. Currently our otf scans are performed with the PGM moving linearly and the ID moving in steps. In some cases this can induce additional noise in the scan since we are not always at the top of the harmonic. Moreover, the PGM is composed of two moving components: plane mirror and plane grating. Currently they are not moving synchronously, which could also lead to small distortions in the scan since the c_{ff} value of the monochromator (ratio of the cosines of PM and PG angles) changes through the scan.

10.5.2 Sample environments and delivery

At X-Treme, the sample environment is combined with the magnet endstation, as discussed already in Section 10.5. In order to receive funding for the new measurement station, a R'Equip proposal was submitted to the Swiss National Science Foundation, which was accepted in November 2019.

10.5.3 Detectors

There are four detection modes which are routinely used at the X-Treme beamline. These include (a) the total electron yield detection, (b) total fluorescence yield detection, (c) transmission detection and (d) x-ray excited optical luminescence detection. These four detection modes will be available after the upgrade.

Furthermore, as mentioned in the Introduction, we are currently developing a novel detection scheme based on x-ray detected pulsed electron paramagnetic resonance. This will allow one to selectively address different species of the same element (e.g. different sites of Cu(II) in a given crystal structure) in order to disentangle the superposing XMCD response of each species. Furthermore, it will enable the measurement of the spin coherence times of surface-adsorbed spin carriers such as molecular magnets or paramagnetic atoms.

10.6 IT requirements

The rate of measured experimental data is of the order of $\sim$ 10 to 50 MB/day. We anticipate that this rate will not increase significantly after the SLS upgrade. Therefore, the requirements for data storage and transfer are modest. The data rate may increase moderately once the x-ray detected pulsed electron paramagnetic resonance experiment will be in routine operation. The expected rate is still under evaluation.

10.7 Timeline

The foreseen timeline for the X-Treme upgrade, including the endstation upgrade (which is not directly connected to the SLS 2.0 upgrade) are outlined in Table 10.4.

Table 10.4: Envisioned timeline of the X-Treme beamline and the endstation (ES) upgrade.

Milestones	2020	2021	2022	2023	2024	2025
Order endstation						
Order UE34 undulator						
Design and order sample-prep. system						
Commission new ES						
Order optics						
Install undulator						
Install optics						
Pilot proposals						
User operation						

10.8 Concluding remarks

In this chapter we have described the envisioned upgrades of the different elements of the X-Treme beamline in the framework of the SLS 2.0 upgrade. New features include the fast (2-3 s) helicity switching, a very high (14 T) magnetic field combined with a base temperature of 2 K, the choice between a large and a tightly focused spot size, and an enhanced *in-situ* sample-preparation system. The midterm option of acquiring an ultralow temperature setup ($\leq$ 500 mK) is still under evaluation.

The changes, which will require a moderate investment, are of extreme importance for the beamline to remain at the forefront of nano-magnetism research on a worldwide level in this highly competitive environment.

Bibliography

[1] G. van der Laan and A. I. Figueroa. X-ray magnetic circular dichroism - A versatile tool to study magnetism. *Coord. Chem. Rev.*, 277–278.

[2] C. Piamonteze, U. Flechsig, S. Rusponi, J. Dreiser, J. Heidler, M. Schmidt, R. Wetter, M. Calvi, T. Schmidt, H. Pruchova, J. Krempasky, C. Quitmann, H. Brune, and F. Nolting. X-Treme beamline at SLS: X-ray magnetic circular and linear dichroism at high field and low temperature. *J. Synchrotron Rad.*, 19:661–674, 2012.

[3] U. Flechsig, F. Nolting, A. Fraile Rodriguez, J. Krempasky, C. Quitmann, T. Schmidt, S. Spielmann, and D. Zimoch. Performance measurements at the SLS SIM beamline. *Am. Inst. Phys. - Conf. Proc.*, 1234:319–322, 2009.

[4] T. Hara, K. Shirasawa, M. Takeuchi, T. Seike, Y. Saito, T. Muro, and H. Kitamura. Helicity switching of circularly polarized undulator radiation by local orbit bumps. *Nucl. Instrum. Methods Phys. Res. A*, 498(1).

[5] P. Ohresser, E. Otero, F. Choueikani, K. Chen, S. Stanescu, F. Deschamps, T. Moreno, F. Polack, B. Lagarde, J.-P. Daguerre, F. Marteau, F. Scheurer, L. Joly, J.-P. Kappler, B. Muller, O. Bunau, and Ph. Sainctavit. DEIMOS: A beamline dedicated to dichroism measurements in the 350 - 2500 eV energy range. *Rev. Sci. Instrum.*, 85(1).

Chapter 11

PHOENIX: XAS, XES and coherence for energy and environmental research

Thomas Huthwelker, Camelia Borca, Christoph Bostedt, Christophe Frieh, and Reto Wetter

In a nutshell

The PHOENIX beamline will be one of the few undulator beamlines worldwide which offer x-ray microspectroscopy for both soft x-rays and the rarely served tender energy range. The scientific goal of the beamline is the *in situ* characterization of crystalline and amorphous materials in terms of morphology, atomic composition, local order, ligand coordination, and electronic structure covering time scales from hours to picoseconds and length scales from mm to $\sim$ 100 nm. The energy range ($0.3 - 8$ keV) covers the K-absorption edges of low Z-element (O to Fe) and important L-edges (K to La), which places PHOENIX in a unique position to address important questions related to catalysis, energy research, earth science, biology, geochemistry and the design of new functional materials.

The SLS 2.0 upgrade will enhance the photon flux by up to a factor of 10. Most notably, the particularly strong gain in coherence for tender x-rays opens a new avenue for coherent imaging and scattering. PHOENIX will maximally exploit the SLS 2.0 upgrade by offering flux-hungry techniques, in particular x-ray emission microspectroscopy (XAS and XES), time-resolved studies pump and probe studies with micro- and picosecond resolution, scanning fluorescence microscopy, small-angle x-ray scattering (SAXS) and coherent diffraction imaging (CDI).

The envisioned combination of techniques in one single experiment, will allow the characterization of physico-chemical processes *in situ* on both a molecular level by spectroscopy, and simultaneously on a nanometer scale by CDI and SAXS. Such experiments can be crucial to decipher complex multiphase chemical processes, as it often occur in batteries, catalysis or geochemistry.

11.1 Overview

11.1.1 Scientific method

Unraveling the complex interplay between a material's chemical and physical properties, its electronic structure, and its morphology on the micro- and nanoscale is key to understanding modern functional materials. Tackling such questions requires techniques covering a wide range of lengths (atomic scale to mm) and timescales (ps to s). Examples may include nanostructured battery materials, catalysts, biominerals, or multiphase atmospheric aerosols, which are relevant to energy research, catalysis, environmental sciences, climate research, geology and biology. Key elements in these fields are the low-Z elements (Na-Fe), and also transition metals, which have K- and L-absorption edges in the energy range $0.3 - 8$ keV, which includes both soft x-rays and the traditionally under-represented tender x-ray range ($2 - 5$ keV).

Typical research goals are the identification and mapping of oxidation states on a micrometre scale, characterization of ligands in complex systems, deciphering the electronic structure and the nature of chemical bonding and coordination, or the elucidation of the role and location of trace impurities in chemical reactions. Here, x-ray absorption and emission microspectroscopies (XAS and XES) are key techniques, as they provide information about the local atomic order, coordination, and electronic structure in both crystalline and amorphous matter. As an undulator beamline, PHOENIX (PHOtons for the Exploration of Nature by Imaging and XAFS) offers advanced techniques for x-ray microspectroscopy and imaging with tender x-rays. It covers the complete soft and tender x-ray regime (0.3 to 8 keV), providing access to the K-edges of most light elements (N-Fe), and also to the L-edges of transition metals (Zr-Sn, Sb-Cs).

11.1.2 User community

The quite diverse user community addresses many topics including catalysis [1–4], energy research [5], electrochemistry [6, 7], biology [8], studies on solution structure [9, 10], structural studies on light elements [11–14], instrument and detector development [15–17], cultural heritage [18,19], earth sciences [20, 21], time-resolved studies with picosecond time resolution [22, 23], and XPS studies using an external user station [24–28], hosting Swiss and international users. Figure 11.1 illustrates typical examples. Electrochemistry is an emerging field for research using low-Z materials, as it is driven by the need to manufacture novel batteries of abundant elements (e.g. Na, Al, Mg, S, P, see [6,7,29–36]).

The PHOENIX beamline, which operates time-shared with the X-Treme beamline, had a healthy average overbooking factor of 1.8 during the last decade, which rose to above 2.0 since 2019. We expect a swift continuation of our intense collaboration with the existing user community, based on a few important new future research directions. There will be a growing demand to investigate both morphological changes on a submicron-scale and chemical coordination changes that take place in an *in situ* reaction. Examples include cyclic heterogeneous chemical processes, which occur in battery

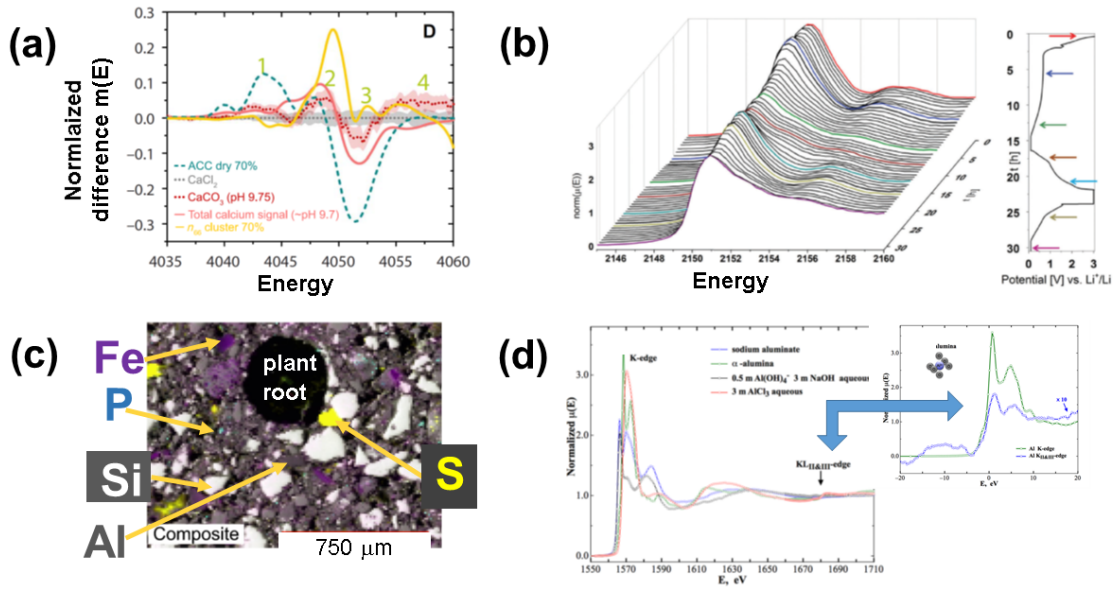

Figure 11.1: Examples for research performed at the PHOENIX beamline. (a) Spectroscopic study of supersaturated carbonate solutions using a liquid microjet disproves the existence of calcium carbonate clusters in solution [10]; (b) Time-dependent P K-edge XANES spectra follow the charging/decharging of a novel phosphorus-based battery, insert shows loading state of battery [7]; (c) Elemental mapping of light elements in soil surrounding a plant root; [37] (d) Al K-edge spectra of various solid and dissolved compounds and as a comparison Al K- and L-multielectron excitation (insert) [38].

charging/discharging cycles or in mineral-based carbon capture technologies. Our goal is to study both types of changes simultaneously by combining XAS and XES with coherent imaging and (anomalous) scattering, which could become a unique approach. Anomalous scattering and diffraction can play a key role to elucidate the specific role of light elements, which is impossible at other scattering beamlines, which typically operate at higher energies compared to PHOENIX. In the last one to two years, a new user community is emerging at PHOENIX, which uses emission spectroscopy at tender x-rays to investigate various topics from research on solar cell perovskites to ion-pairing in aqueous solutions. Finally, there is a growing request from international users to implement pump and probe studies in the micro-second to picosecond ranges This development is particular important, as it directly connects the user communities of PHOENIX and Alvra at SwissFEL.

11.1.3 Impact of SLS 2.0 on PHOENIX

The horizontal electron beam divergence at SLS 2.0 is reduced by about a factor of 7 compared to the present performance. This will enhance the beamline transmission by about a factor of 2 to 5 in the tender x-ray range depending on energy and beamline configuration. The source area will be reduced

by about a factor of 8.5, pushing the achievable spot size into the 1 μm range, if the mirrors of the KB system are replaced with higher-quality mirrors. If the UE44 undulator will be used, the total photon flux into the beamline would rise by a factor 3 to 10 for energies between 0.5 and 8 keV. This increase in total flux would be extremely beneficial for systems with low concentration and for photon-hungry techniques, such as emission spectroscopy and pump-probe experiments. The most important benefit in the tender x-ray range will be the dramatic increase in horizontal coherence by a factor of 10. This will open fundamentally new opportunities for scattering and imaging techniques in the tender x-ray range. For further details, see Section 11.2.

11.1.4 Uniqueness compared to other beamlines worldwide

PHOENIX is an insertion-device beamline, which offers a microfocus for the combined soft and tender x-ray ranges ($\sim 0.3 - 8$ keV). To minimize scattering and absorption in the gas phase, samples are kept in a vacuum chamber, which is devoted to *in situ* experiments. To ensure maximum energy resolution of the incoming photons, PHOENIX uses a planar grating monochromator (PGM) for soft x-rays and a double crystal monochromator (DCM) for tender x-rays. In Europe, only LUCIA (Soleil, 0.6-8keV) and ID21 (2-10keV) are comparable insertion-device beamlines with similar specifications in terms of focal size and the possibility to host samples in a vacuum chamber. These complementary beamlines offer a different scientific focus than PHOENIX. ID21 and LUCIA specialize in scanning microscopy, microspectroscopy, and XAS. PHOENIX offers XAS and micro-spectroscopy as well, but has a stronger focus on additional options for complex *in situ* studies (catalysis, electrochemistry, liquid microjet). Although this is partially driven by the local Swiss chemical community, PHOENIX also hosts a steadily increasing number of international users in the field. The ongoing implementation of novel pump-probe schemes in the pico- to microsecond time domains and the implementation of micro-emission spectroscopy represent unique features of the PHOENIX beamline, which further illustrate the different scope of PHOENIX. The emission spectrometer recently developed at ID26 (ESRF, TXES endstation), is an in-vacuum emission spectrometer, similar to the new instrument proposed here. The main difference is that we will integrate the spectrometer fully in the scanning microscope and scattering experiments, providing an extended scope of the instrumentation. There are other European facilities which operate either on a bending magnet, rendering flux-hungry measurement difficult, or do not provide a vacuum chamber, which is essential in the tender x-ray energy range. At the APS, beamline 13-ID-E is an insertion device beamline covering the range of 2.4 to 28 keV, but without a vacuum endstation, which puts the focus of this beamline towards heavier elements. Emission spectrometers for the tender x-ray range have been used as temporary installations or are dedicated instruments, such as the one-crystal Johansson spectrometer at beamline 6.2a at the SSRL. To the best of our knowledge, currently other beamlines worldwide are either bending magnet beamlines or provide XAS in the tender x-ray range as an add-on to higher energies in non-vacuum environments.

Hence, PHOENIX offers the full soft and tender energy ranges for x-ray microscopy, *in situ*, and pump-probe experiments in various research fields. Furthermore, the integration of high-resolution emission spectroscopy and anomalous scattering into the general imaging capability of the beamline would be another important asset to the PHOENIX beamline. The overall goal is to offer μ-XAS, μ-XES, CDI and/or SAXS, in a special setup for complex *in situ* studies, which would make PHOENIX

a worldwide unique facility.

11.1.5 Complementarity to other PSI beamlines

Due to its special tender x-ray energy range, PHOENIX is complementary to other SLS beamlines, as further detailed in the main text. X-ray absorption and emission spectroscopy is offered at SuperXAS for energies above 4.5 keV, while PHOENIX covers lower energies (XES: $2-5$ keV, XAS 0.3 to 8 keV). The cSAXS beamline offers SAXS and CDI at energies above ~ 5 keV, SIM plans CDI for energies below 2 keV, making PHOENIX complementary by covering the intermediate energies. Similarly, due to its energy range, PHOENIX complements scanning x-ray absorption microscopy at PolLux (< 1.6 keV) and μ-XAS (> 4 keV). Finally, the Alvra beamline at SwissFEL covers similar energies and instrumentation for pump and probe experiments on a femtosecond timescale, while PHOENIX covers longer timescales from some ~ 100 ps to μs.

11.1.6 Strategy for the PHOENIX beamline at SLS 2.0

The long-term strategy for PHOENIX has three interconnected goals:

1. Use the dramatically enhanced coherence in the tender x-ray range to add new options for coherent and anomalous scattering.
2. Exploit the significantly enhanced flux to further develop new unique capabilities for x-ray emission spectroscopy in the tender x-ray range.
3. Add capabilities for time-resolved studies in the second to picosecond time domain.

Maintaining beamline capabilities and use of coherence. A basic upgrade ('maintain and coherence', Section 11.7.1) preserves the beamline's functionality and prepares for future upgrades by modest investments (stabilization of relevant elements by mounting on granite blocks, adding high-quality pinholes, slits and detectors). These actions are only possible during the dark period of the SLS upgrade, as they involve significant civil engineering, which would otherwise hamper user operation. It will enable new options for scattering [small angle x-ray scattering (SAXS), coherent diffraction imaging (CDI), and ptychography] using the existing infrastructure. This strategic approach ensures that the benefits of the dramatically enhanced coherence of SLS 2.0 in the tender x-ray range (see Section 11.2) will be available directly after the dark period. These activities will be carried out in close collaboration with the coherent scattering group (Dr. A. Menzel), combining the expertise for imaging applications at cSAXS with the spectroscopic and chemical expertise of the PHOENIX team, thereby generating powerful synergies. Within SLS 2.0, PHOENIX will be complementary to imaging and scattering activities at cSAXS (> 5 keV), and SIM (< 2 keV), with PHOENIX covering the range between 2 and 5 keV for scattering and coherent diffraction imaging (CDI).

Optics. An important further step is to replace the existing focusing unit (KB1, see below, Figure 11.4) by a new system with improved optical quality and a movable focal plane. This upgrade secures the long-term beamline operation, reduces the focal size, and eases the operation of external endstations.

State-of-the-art x-ray emission spectroscopy. The current options for emission spectroscopy are based on a simple von Hamos spectrometer in the existing endstation. To keep the beamline

competitive for x-ray spectroscopy, we want to replace the existing endstation, thus offering a state-of-the-art *in-vacuum* Johansson type emission spectrometer (5 to 7 crystals, $\sim 2-5$ keV, $\Delta E \sim 0.4-0.5$ eV), scattering (SAXS, CDI), pump-and probe studies and *in-situ* experiments. These activities are complementary to the SuperXAS beamline, which covers higher photon energies (above 4.5 keV).

Time-resolved studies. With the advent of new 2-D detectors for the tender x-ray range [16], both scattering and emission spectroscopy becomes possible in the time domain of seconds to milliseconds. Here, a new air-bearing monochromator would be a game changer, as it would allow one to record XAS spectra in the time domain of some 10 seconds, significantly faster compared to the currently available system. Furthermore, pump-probe experiments serving the milli- to picosecond time domain, which are currently being developed within the LSF laboratory, will be integrated into the general PHOENIX endstation environment for routine user operation. These experiments are complementary to the LSF/SwissFEL beamlines ALVRA and ATHOS, which provide similar techniques and energy ranges as PHOENIX, but with femtosecond time-resolution.

Scientific benefits. With these upgrades, the PHOENIX beamline will be one of the few places where both electronic structure (XAS, XES) and morphological changes (SAXS, CDI) can be probed with state-of-the-art techniques in a single *in-situ* experiment with tender x-rays. This multiscale approach opens a new avenue for research in real systems, which are often governed by the interplay of electronic processes (e.g. chemical reactions, electronic transitions) with morphological changes on a nm to μm-scale (e.g. precipitation, phase transitions, transport, core-shell structures), as frequently observed in (porous) catalysts, geological material, or new functional materials. Another highly relevant example, involving chemical reaction and morphological changes are cyclic processes, as typical for the charging of batteries, or in carbon capture technologies. The ability to study such processes *in situ* on several scales will provide fundamentally new insights into these micro-chemical processes.

It is important that PHOENIX covers the full energy range from 0.3 to 8 keV, as only then are all the relevant low-Z elements from O to Fe covered; this helps secure a stable scientific user community for the beamline. Finally, it should be noted that by offering x-ray emission spectroscopy, (coherent) scattering, and capabilities for pump-probe studies, PHOENIX will be complementary to the planned TENDER beamline at the ALS, the new bending-magnet TES beamline at the NSLS II, the LUCIA beamline at Soleil, and the TXES endstation at the ESRF.

11.1.7 Layout of the current PHOENIX beamline

The PHOENIX and the X-Treme beamlines share a common undulator, front end and optics hutch. Figure (11.2) shows the experimental hutches, the laboratory space and the layout of the two branchlines. Switching between the branchlines can easily be achieved by choosing a mirror which either guides the light into the X-Treme or the PHOENIX I branchline. The PHOENIX I beamline uses a double crystal monochromator (DCM) to cover the energy range of 0.8 to 8 keV, while X-Treme offers the range of 0.3 to 2 keV using a planar grating monochromator (PGM). At the exit of the X-Treme beamline, the PHOENIX team operates an endstation (PHOENIX II) for complex *in situ* experiments, which can easily be moved between the two PHOENIX branches. Both branches offer either a microfocus of about 3 to 5 μm, or a large beam of 1×2 mm. The availability of the two

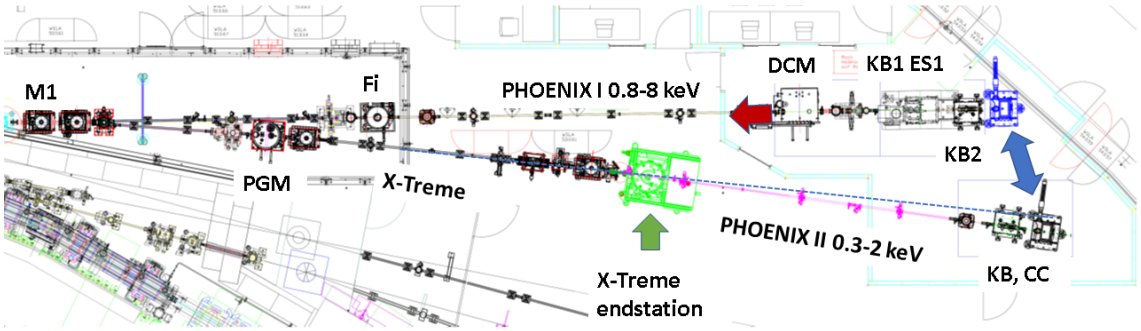

Figure 11.2: Overview Image of PHOENIX/X-Treme beamlines with current optical elements and endstations. M1: first spherical mirror, Fi: filter for high harmonic suppression, DCM: double crystal monochromator, KB: KB system, ES1: main PHOENIX endstation (XAS, XES, microscopy, imaging), CC: mobile 'chemistry chamber' for *in situ* experiments, PGM: planar grating monochromator. The technical drawing shows the beamline shifted sideways as required for SLS 2.0. Also, the deflection of the beam, if an additional planar mirror (green arrow) is added to the X-Treme branchline and is considered (See also Chapter 10 and Figure 10.2). The blue arrow indicates the two positions for the chemistry chamber (CC). The red arrow indicates the relocation of the current monochromator to create space if a 4-bounce monochromator is added at a later time (See Section 11.5.3)

branches with different monochromators is critical for the PHOENIX user community, as it allows one to cover research on all low-Z elements, with the best possible monochromators in terms of flux and energy resolution.

11.2 Source

	Size X	Size Y	Divergence X	Divergence Y
	$\sigma_x[\mu\text{m}]$	$\sigma_y[\mu\text{m}]$	$\sigma'_x[\mu\text{rad}]$	$\sigma'_y[\mu\text{rad}]$
SLS	120	8	54	3.2
SLS 2.0	23	4.9	6.8	2.1

Table 11.1: Electron beam parameters for SLS vs. SLS 2.0.

The PHOENIX beamline is located in a medium length Straight 7 and currently uses an elliptical undulator UE54. The source parameters for SLS 2.0 and SLS are summarized in Table 11.1. The electron source size is reduced from 121×8 μm to 23×5 μm ($h \times v$), effectively decreasing the source area by a factor of 8.5. The horizontal divergence is reduced by about a factor of 7, while in the vertical direction, it is reduced by about 30%. Replacing the current undulator by a longer elliptical undulator (e.g. UE44) would have many benefits for both PHOENIX and X-Treme (See Chapter 10)

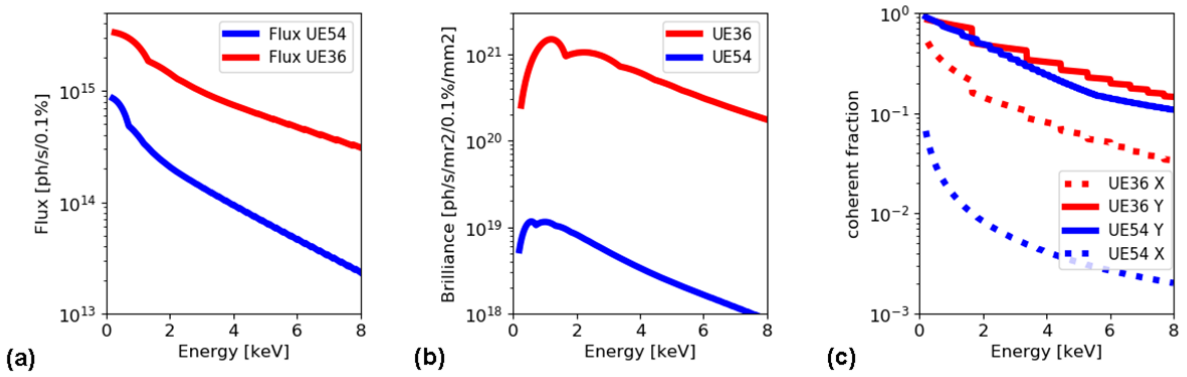

Figure 11.3: Comparison of insertion device characteristics for SLS vs. SLS 2.0. Blue: current undulator (UE54) at SLS, red: envisioned undulator (UE36) at SLS 2.0. (a) total flux, (b) brilliance, (c) coherent fraction horizontally (x), and vertically (y).

in terms for flux, brilliance and coherence (see Figure 11.3). One essential benefit [Figure 11.3(a)] of the new device is an increase in total photon flux for energies from 0.5 to 8 keV by a factor of 3 to 10. For SLS 2.0, the brilliance increases by about two orders of magnitude compared to the current situation. [Figure 11.3(b)]. The key benefit at SLS 2.0 will be the dramatic increase in horizontal coherence [Figure 11.3(c)] from less than a percent to some 10% for energies below 3 keV and to more than 5% for energies in the range 3 to 8 keV. This dramatically enhanced coherence in the tender x-ray range presents a new avenue for coherent scattering and imaging techniques.

11.3 Front end

The front end is shared between PHOENIX and X-Treme. The source axis needs to be moved 67 mm radially outwards. This shift can be accommodated within the current walls of all hutches. For the activities concerning coherent scattering, a very important requirement is that the front end slits are of high mechanical stability and positioning accuracy in the micrometer range. The blade quality must be sufficient to shape the beam at energies below 8 keV, and the cooling needs to ensure spatial stability of the blades over extended periods of time. Although the space in the front end is limited, beam position monitors are needed to facilitate the beamline alignment, while the front end should be optimized for maximum beam coherence.

11.4 Optics

11.4.1 Optical concept for PHOENIX I

Figure 11.4 depicts the current optical setup of the PHOENIX I branchline. The first spherical mirror (M1) reflects the beam by 0.8° horizontally and creates an intermediate horizontal focus at the slit

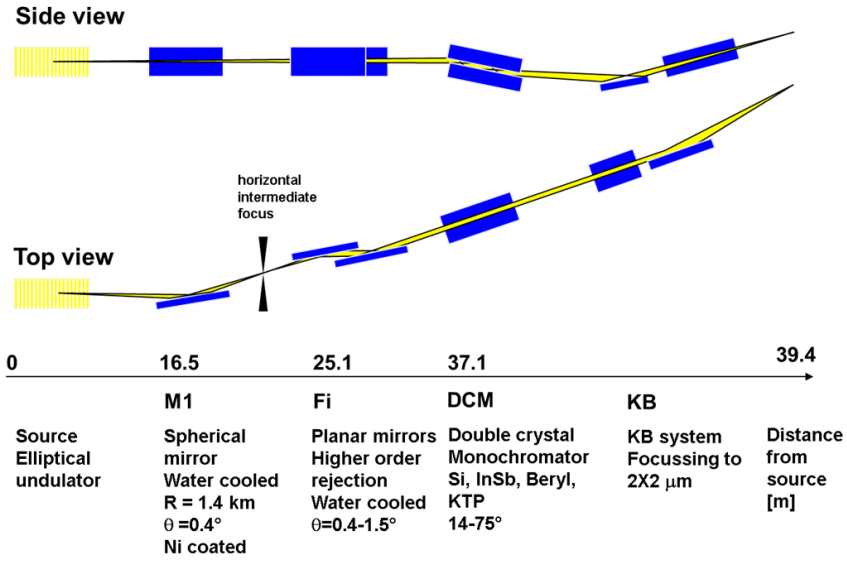

Figure 11.4: Optical layout of the PHOENIX I branchline.

SL1. The second optical element is a high-order suppressor with two planar mirrors, which can be rotated between $0.4 - 1.7°$ to vary the cut-off energy. The third element is the DCM, which covers the energy range from 0.8 to 8 keV. Finally, a Kirkpatrick-Baez (KB) system with two bendable mirrors generates the microfocus. All mirrors at the PHOENIX I branchline are silicon substrates with a coating of 50 nm of nickel, as the Ni absorption edges (K-edges at 8333 eV, the weak L1-edge at 1008 eV, and a L2 edge at 870 eV) are outside of the range interest, i.e. below the Na K-edge and above 8 keV.

11.4.2 Monochromator

Current system. Currently, a DCM (manufacturer Bruker/ACCEL) with fixed exit is used. A goniometer holds the first, water cooled, crystal in its center, while the second crystal is positioned by two perpendicular translation stages, which are also mounted on the goniometer. This construction covers the large range of Bragg angles (14 to 75°) as required to access the full energy range from 0.8 to 8 keV using a set of four crystals (Si, InSb, KTP, and beryl).

Scanning operation modes and beam stability. The monochromator operates in step-scan mode; it cannot use faster on-the-fly schemes. Its physical beam stability for a typical XAS scan is in the order of some 5 to 50 μrad. With a programmed correction of roll and pitch the beam stability can be reduced to the order of 1 to 2 μm at the sample. There is no online beam stabilization system due to the inherent difficulties in measuring the beam position with acceptable loss of intensity in the tender x-ray range.

Proposed monochromator upgrade. For SLS 2.0, we intend to replace this monochromator by a commercially available airbearing-based system, which would provide beam stability of the order of

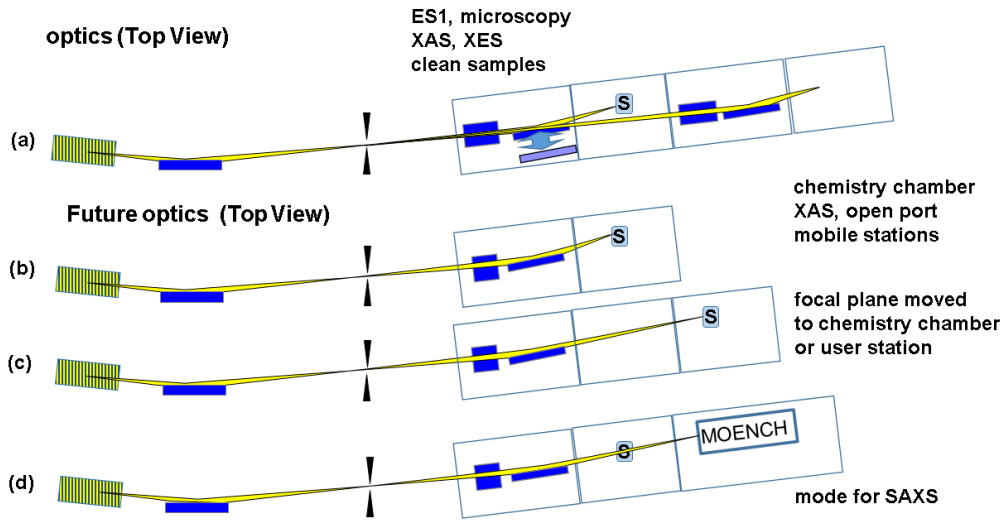

Figure 11.5: Optical scenarios for the PHOENIX I branchline. (a) Current setup with two KB systems, the first one serving the standard station ES1 and the second one serving user endstations or the PHOENIX chemistry chamber for *in situ* experiments. (b-d) Future modes of operation using a single KB system with a movable focal plane. (b) Focal plane in microscopy and XES chamber with best possible focus. (c) Focal plane moved to external endstation (PHOENIX chemistry chamber or user supplied chambers). (d) Focal plane set to 2D detector for SAXS measurements in first chamber. Not shown: focal plane can be moved to a position where it serves as an intermediate focus for endstations with diffractive optics for very high resolution imaging experiments. The envisioned minimal focal length is about 30 to 45 cm, the maximum is about ca. 120 to 150 cm.

54 nrad [39] over a typical XANES scan. The beam stability of the current system is sufficient for μ-XANES scans, if the beam size is larger than the stabilized beam movement, which thus limits μ-XANES to spot sizes and most important to sample structures of the order of $\sim 5\mu$m. The significantly improved beam stability of an air-bearing monochromator would greatly enhance the performance of the beamline for microspectroscopy.

Moreover, this monochromator would also deliver a faster scanning speed, as it allows on-the-fly scanning with speeds as fast as 20°/s, compared to the current value of $\sim$ 0.5°/s, reducing current scanning times from 5 to 10 min per XANES to some 10 s, providing a new avenue for time-resolved measurements, as further discussed in Section 11.5.4. Hence, this upgrade would be a true game changer, as it would enable XAS, XES and scattering techniques for the study of dynamic systems with a time resolution of the order of seconds to minutes, all in the tender x-ray regime.

11.4.3 Focussing KB units

KB Systems at PHOENIX I branchline. The KB1 system for the endstation ES1 uses two

pre-bent elliptical mirrors with additional motorized benders to fine-tune to the ideal elliptical shape without the option to move the focal plane significantly downstream. The slope error of the current KB mirrors limits the achievable spot size to 3 to 4 μm, which could only be reduced to less than 1×1 μm^2 if mirrors with a slope error below 0.3 μrad rms were used. **Hence, with the current KB mirrors, we could only take very limited advantage of the SLS 2.0 machine upgrade**.

The PHOENIX I branchline also hosts a second KB system (KB2, spotsize $\sim$ 6 μm), located downstream of the main endstation, which was added to the existing beamline due to user requests to provide a microfocus for external user endstations.

For SLS 2.0, we plan to simplify the setup and want to replace the first KB system with a system with motorized benders, which allows adjustment of the focal length from $\sim$ 30 to 45 cm to about 1.2 to 1.5 m. This would allow us to remove the second KB system, while keeping all existing functionalities. This approach would have major advantages for the beamline performance:

1. Only with improved mirror quality of a new system would we fully benefit from the smaller source size at SLS 2.0.
2. Due to the smaller slope error of currently available optics, the focal distance in the first chamber could be relaxed from 30 to 45 cm without loss of performance.
3. The system would provide a microfocus in both the existing chamber and in any added user station and the chemistry chamber (see Figure 11.2), while freeing space in the endstation region, simplifying operation of the beamline and allowing one to mount flight tubes needed for scattering and coherent-diffraction experiments.
4. For SAXS experiments (see Section 11.5.2), the focal plane could be moved to the plane of the detector, which would significantly enhance the quality of the scattering patterns compared to patterns taken with an unfocussed beam.
5. An intermediate focus can be generated, which can be a source point for the high-resolution ptychography station planned by Drs. J. Raabe and A. Kleibert (SIM beamline, see Chapter 9), which would also be available for other external endstations such as the near-ambient-pressure photoelectron spectroscopy endstation, (NAPP).
6. The manufacturer of the current system (KB1) has discontinued the product and no replacement parts are available. This poses a significant risk to the beamline operation, and emphasizes the urgent need to replace the existing optics with a new system.

11.4.4 Optics of PHOENIX II branchline

The PHOENIX II branchline operates an endstation dedicated to chemical *in situ* experiments at the exit of the X-Treme beamline ([40], see Chapter 10), which covers the soft x-ray energy range ($0.3-2$ keV). The exit slit of the X-Treme beamline serves as the source point of a KB system, located $\sim$ 12 m downstream of the entry slit. This system generates a focal size of about $5-8$ μm.

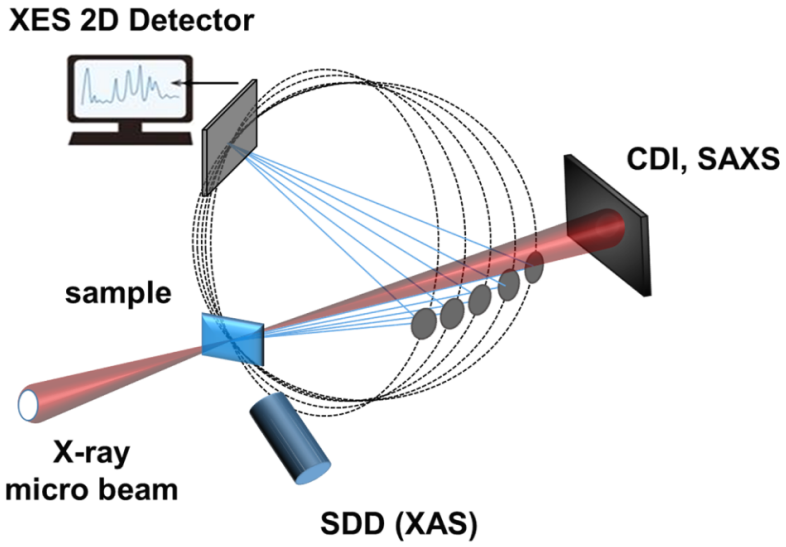

Figure 11.6: Conceptual overview of techniques available in upgraded vacuum endstation.

11.5 Endstation

11.5.1 Current situation

PHOENIX offers two permanent endstations, one located at PHOENIX I (ES1), and the other [the chemistry chamber (CC), see Figure 11.2], which can be moved between the two branchlines. The current main endstation offers a microfocus (focal size $\sim$ 2 to 3 μm). The routine detection modes are total electron yield (TEY), transmission, total and partial fluorescence, and x-ray emission spectroscopy using a compact Hamos spectrometer (2.1 to 4.9 keV, energy resolution of about 0.4 eV). While the main endstation focuses on microscopy and x-ray emission spectroscopy, the chemistry chamber offers flexible 'dirty' environments, including options for a liquid microjet, for pump-probe experiments, and for user-supplied *in situ* experiments. The chemistry chamber can be easily moved between the two PHOENIX branchlines, thus effectively covering the full range from 0.3 to 8 keV for *in situ* experiments.

11.5.2 New options for scattering at PHOENIX.

Coherent Scattering. The highest gain for the PHOENIX beamline at SLS 2.0 is the large increase in coherent fraction (see Section 11.2). To maximally exploit the coherence, new options for both (coherent) scattering and SAXS will be implemented. Essentially, a 2D detector (larger version of the MOENCH 2D detector) will be located downstream of the sample to record the scattering pattern (see Figure 11.6) with appropriate adaptations of the entry slits and pinholes. These activities will offer several new options, including ptychography, holography, and SAXS.

SAXS using tender x-rays. Most setups for SAXS typically operate at higher energies (i.e. above

8 keV) to detect the smallest possible structures. However, using SAXS in the tender x-ray range offers interesting new opportunities: Using the energies from 2 to 7.5 keV will cover the Q-range from $\sim 10^{-4}$ to 1 $Å^{-1}$, which can characterize particles in the size class from 5 to a few hundred 100 nm, bridging the gap between light-scattering techniques and SAXS at higher energies. Most importantly, exploiting the elemental absorption edges will introduce elemental sensitivity to low-Z elements in scattering experiments (anomalous SAXS). The new endstation would provide flight tubes with different lengths (up to 160 cm) equipped with a 2D MOENCH detector.

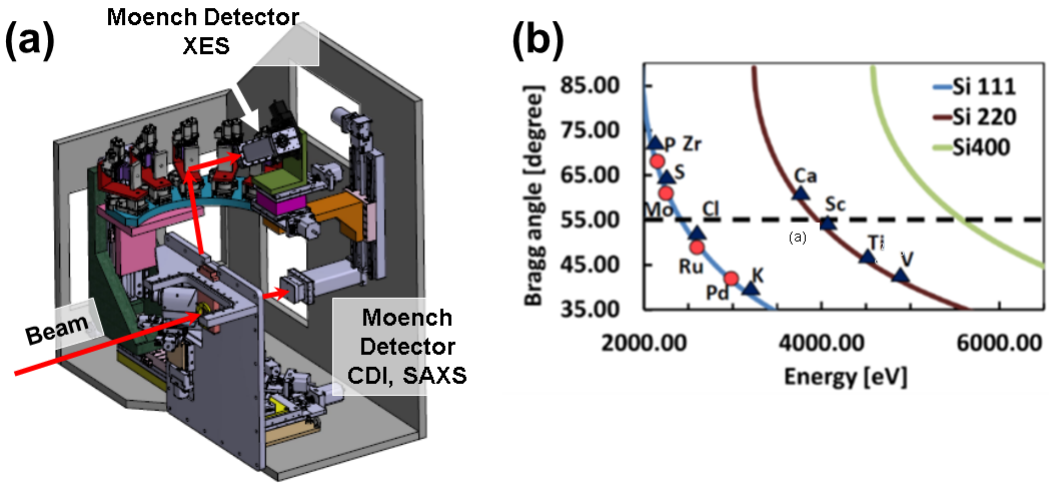

Figure 11.7: Implementation of an *in-vacuum* emission spectrometer at the PHOENIX beamline. (a) Concept study of spectrometer in vacuum chamber with Rowland radius of 30 cm, front plate shows existing sample microscope, crystals reflect fluorescence light on MOENCH 2D Detector, large MOENCH detector at chamber exit collects scattering pattern for SAXS or CDI, not shown: load lock for sample transfer into the endstation and a fluorescence silicon drift detector (SDD) (several single Ketek SDD Detectors) for complementary total fluorescence XAS. (b) Required Bragg angles for the spectrometer as function of energy and some of the important elements (triangles: K-edges, circles: L-edges, dashed line indicates maximum Bragg angle, where Johann crystal could be used. For larger Bragg angles, Johansson crystals are required).

11.5.3 Emission spectrometer

The proposed emission spectrometer (Johansson type, 5 to 8 crystals) for tender x-rays will operate in a new experimental chamber as depicted in Figure 11.7(a). A set of three crystals [Si(111), Si(220), Si(400)] used at Bragg angles from 35 to 85°, will cover the energy range from 2 to 6 keV. Because cylindrical Johansson crystals image a point source (sample) onto a line, a 2D detector is required, as has been demonstrated by Kavcic and co-workers [41] for which a MOENCH detector will be used (see Section 11.5.6). Independent manipulators for both detector and crystal assembly (see Figure 11.7(a))

allow flexible implementation of different spectrometer geometries in both scanning mode or energy-dispersive modes. A selection of accessible elements are shown in Figure 11.7(b). For a Rowland radius of 0.3 m, the estimated energy resolution is of the order of 0.3 to 0.5 eV, taking into account the bandwidth of the incoming photons ($\sim$ 0.3 eV) and contributions from crystal bending (0.2 to 0.4 eV) [42, 43]. The size of the spectrometer is dimensioned for higher energy resolution, which could be implemented once better-quality crystals, (e.g. segmented Johansson crystals) become available. As the bandwidth of the incoming photons is a limiting factor, the location of the current monochromator will be moved upstream to provide space to add at a later time a 4-bounce monochromator to reduce the energy bandwidth of the photon source (See Figure 11.2).

11.5.4 Time-resolved experiments in the milli- to picosecond domain.

For the PHOENIX beamline, implementation of new techniques for time-resolved studies at different timescales is a core aim. Using the time resolution of the new 2-D detectors (MOENCH, frame rate 1 kHz), will allow time-resolved studies using SAXS and XES in the second and sub-second domains. Coupled with new on-the-fly modes of an upgraded monochromator, XAS measurements in the tender x-ray domain can also be pushed into time domains of some seconds. Furthermore, employing laser driven pump-probe schemes, XAS and XES signals can be recorded in the milli- to picosecond domain, using concepts which were already tested at the PHOENIX beamline [22]. These activities, which also include in-house developed detector solutions, will be supported within the LSF laboratory as an element of the general LSF strategy.

11.5.5 Sample environments and delivery

Various sample environments are currently provided and will be further enhanced and extended. Firstly, all experiments can be performed either in vacuum or in a helium environment. Both end-stations will routinely provide cooling to liquid nitrogen temperature (to reduce radiation damage), and resistive heating to at least $\sim$ 500°C for any standard solid sample (pellets, powders, etc.). The beamline will also offer various *in situ* cells for studies in liquid environments, including different microfluidics cells, manufactured in house. They will be made from polymer and silicon and can be tailored to the user's needs, for example by integration of sensors for pH, temperature, or electrical connections. Figure 11.8 illustrates a selection of typical cells. We will also offer optical Raman spectroscopy as an optional complementary technique in the main endstation. Finally, as routine instrumentation for windowless studies of solutions, a liquid microjet (ca. 30 to 100 μm diameter) is available. The jet will also be used in a pump-probe setup taking advantage of the 70 ps bunch length at SLS 2.0, which is operated within the LSF laboratory in scientific collaboration with the users. Furthermore, we will continue to develop new dedicated sample-delivery systems in close collaboration with users.

11.5.6 Detectors

The beamline uses SDDs for energy dispersive photon detection. Currently, a four-element detector (Hitachi) and a one-element detector (Ketek) are available, both equipped with thin Moxtec windows

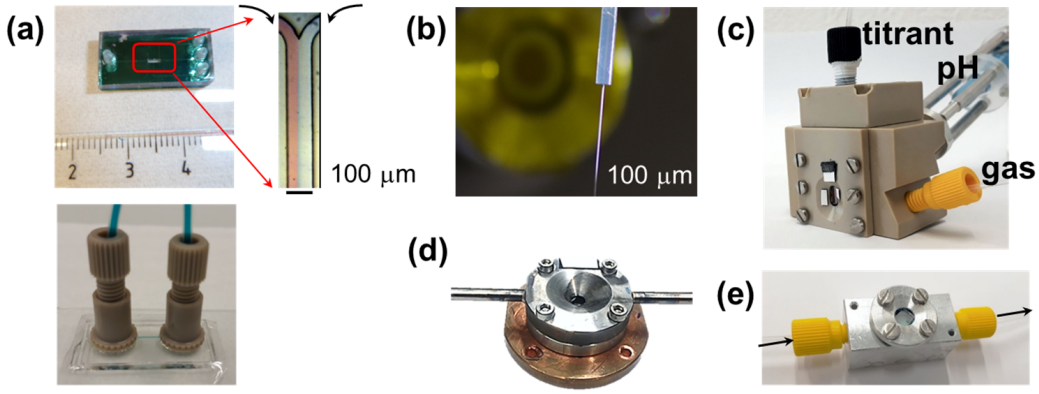

Figure 11.8: Sample environments available for work in liquid environments at the PHOENIX beamline: (a) microfluidics device for mixing of two liquids in laminar flow; (b) liquid microjet sized 30 to 100 μm; (c) environmental cell to study materials under controlled gas phase; (d) liquid flow through cell, where the sample is only in contact with PEEK and Teflon; (e) titration cell, allows titration of a solution, bubbling gas through solution while stirring and measurement of solution pH. The cells in Figures (a, c-e) are designed for measurements in fluorescence mode and in a vacuum chamber (10^{-5} mbar).

for operation at tender x-rays. These detectors, located on a long re-entrant nose, have ultra-high rate readout electronics outside of the vacuum chamber. We plan to replace these detector types by newer, smaller SDD detectors, which can operate in vacuum, providing more flexibility to optimize the solid angle. Furthermore, a diode located downstream of the sample detects the transmitted light, and the total current to the sample provides the TEY signal.

For scattering experiments and the emission spectrometer, the MOENCH detector [16], will be used. This hybrid detector is based on charge-integration readout and works well in the tender x-ray range. It is a unique PSI in-house development, and an invaluable asset for the beamline, as it is one of the first detectors worldwide to cover this energy range. Currently tested to energies as low as 800 eV, the detector will be further developed and optimized for future use at SwissFEL, and tuned towards low energies. We will have access to prototypes of this detector, meaning that PHOENIX will be at the forefront of these developments. The currently available MOENCH detector provides single photon counting on an active area of 1×1 cm, 800×800 interpolated pixels of 12.5 μm, 1 kHz frame rate. With expected developments for SwissFEL, larger modules will become available, and we plan to enlarge the detector surface area by using up to six modules of the larger 3×6 cm^2 MOENCH detector.

11.5.7 Controls and data systems

The control system will be based on EPICS, as implemented at the SLS. The main tool for scanning will be the PSI developed fda and pshell software, and also python-based scripting.

Figure 11.9: Different packages for the beamline upgrade in relation to the beamline elements. Different colors represent different work packages. Grey: unchanged elements, light green: package 'maintain and coherence', green: replaced monochomator, red: added Johansson emission spectrometer. Upgrade of KB system (KB) and new endstation (XES) are not completely independent, as both elements are located on the same granite block, and use interconnected vacuum chambers. M1: first mirror, SL1: slit at intermediate focus, Fi: filter for high harmonics suppression, SLS: entry slit for KB system, CC: existing mobile chemistry chamber, which is also operated at PHOENIX II, PTY: potential mobile high resolution ptychography endstation

Currently, all motorized motions are made in a step-scanning mode. For XRF mapping using micro-beam, continuous scanning (on-the-fly) will be implemented. Secondly, the motion control for the envisioned emission spectrometer requires complex concerted motions of several motors. Finally, a new monochromator will run in an on-the-fly scheme, which requires one to couple the movement of the insertion device and monochromator in real-time.

11.6 IT requirements

The addition of the MOENCH 2D pixel detectors will require significant IT resources in terms of both, on-the-fly data processing and data storage. A large MOENCH detector with several modules and high repetition read-out will require a dedicated server and a large storage capacity of the order of several 100 TB for detector operation and on-the-fly reconstruction of images (i.e. for ptychography experiments).

11.7 Timeline

11.7.1 Work packages

The upgrade for the PHOENIX beamline consists of several almost independent packages, as illustrated in Figure 11.9.

Work package 'Maintain and coherence'

The work package, 'Maintain and coherence' will implement the beamline with its current functionality at SLS 2.0 and uses the SLS shutdown 2023/2024 to prepare for future upgrades by performing all required civil-engineering changes, which would be difficult once the beamline is back to user operation. This includes relocating the beamline to its new position, and the required refurbishments of the lead

hutches and the local infrastructure. Any upgrade to enhance the imaging capabilities and to enable scattering experiments requires excellent stability of all slits and the endstation. Therefore, all slits will be mounted on granite blocks. Also, the entire endstation will be placed on a granite block, which can be positioned by a girder. Finally, slight repositioning of the monochromator (Figure 11.2) will generate space for an additional four-bounce monochromator, which would generate a narrower bandwidth of the incoming photons to extend the limits of emission spectroscopy, as required, for example, for applications in solid-state physics. This package also anticipates measures for additional radiation protection, which might become necessary if the new undulator provides a significantly higher fraction of high-energy photons compared to the current one. Implementing this package will enable us to take advantage of the enhanced coherence of SLS 2.0, and to implement ptychography, CDI and SAXS at PHOENIX. For these activities, a larger MOENCH detector is required. The timeline is summarized in Figure 11.10.

Work package 'Mirror recoating'

The current mirrors consist of nickel-coated silicon substrates. During the last years, traces of silicon have diffused into the coating layer, leaving a silicon signature in the flux curve, hampering spectroscopy of dilute samples at the Si-edge. To resolve this issue, the existing mirrors need to be recoated with an additional interlayer of B_4C [44].

Work package 'KB System' (KB)

As detailed in Section 11.4.3, replacement of the existing KB system by a system with an adjustable focal plane is **highly critical to secure the beamline operation** (discontinuation of the current system by the manufacturer). It also provides major advantages in terms of focal size, beamline operation for SAXS, and additional flexibility to host further endstations (e.g. NAPP). This work package includes the design of a new vacuum chamber for the KB system, which needs to be adapted to the endstation vacuum chamber.

Work package 'Endstation' (XES)

This work package will implement a new *in vacuum* Johansson type emission spectrometer, including a new endstation, as described in Section 11.5. We plan to finance the new endstation by an SNF R'Equip proposal. The design and manufacturing will take about two years, as outlined in Figure 11.10. We aim to begin pilot experiments directly after the SLS 'dark period'. Although the work packages 'KB System' and 'Emission Spectroscopy' can be implemented independently, **the implementation of both packages is interconnected because the vacuum chambers for the two packages depend on each other**.

Work package 'Monochromator'

This work package will involve the replacement of the current monochromator by a new air bearing system to allow for improved beam stability and on-the-fly operation. It can be added to the beamline at any time.

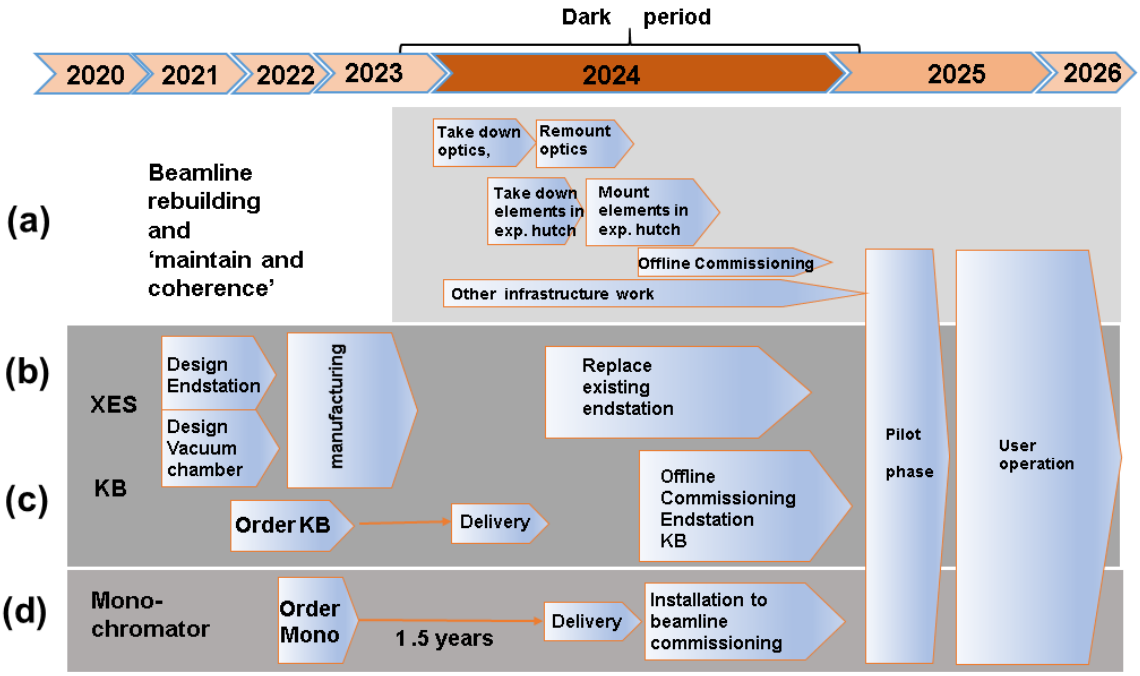

Figure 11.10: Time line for different work packages: (a) for base package 'maintain and coherence', (b) for new endstation 'XES', (c) for new KB system, (d) for a new monochromator.

11.7.2 Planning

The implementation of the beamline for SLS 2.0 will follow the timeline shown in Figure 11.10. Row (a) shows the timeline of the basic work package 'maintain and coherence', which has two aims: First, it returns the beamline to user operation directly after the dark period and secondly, it takes all preparatory action needed for the envisioned future upgrades. Rows (b,c,d) show the timelines for the additional work packages, 'XES', 'KB' and 'monochromator'.

To adapt the beamline to SLS 2.0, the beamline needs to move by 67 mm radially outwards. This requires a dismounting of the beamline in order to move all concrete blocks and stands sideways. Once the dark period has started, the beamline will likely be moved in a stepwise approach. Current planning assumes that the radial shift by 67 mm does not imply major rebuilding of the existing infrastructure (cables, cooling water). The main remounting should be finished by the middle of 2024, leaving about six months to commission all motion-control issues.

11.8 Concluding remarks

SLS 2.0 will open new scientific and technical opportunities for PHOENIX. The dramatically enhanced coherent fraction in the tender x-ray regime will enable new options for coherent scattering experiments in particular for nanometer-scale samples and structures. The strong increase in flux will allow to develop new and unique capabilities for x-ray emission spectroscopy. Both aspects will make PHOENIX a unique and world-wide leading beamline for the investigation of electronic structure and morphological changes of chemical systems or environmental samples in situ and in a single experiment.

The PHOENIX beamline can be returned to operation without changes of the optical setup. The work package 'maintain and coherence' includes all civil engineering, including the engineering required for future upgrades. It would allow us to continue the existing spectroscopy program and start a efforts on coherent diffraction imaging. A fundamental benefit to the beamline and scientific program would come from the upgrade package 'KB-system' which is **highly critical** for PHOENIX for two reasons: (1) Only the upgraded mirror quality will allow us to take full advantage of the improved performance of SLS 2.0, including the additional endstation capabilities and flexibility. (2) The current system is discontinued by the manufacturer introducing a large risk for the endstation operations. The package 'endstation (XES)' will implement a new endstation with unique capabilities for emission spectroscopy, scattering, and imaging in the tender x-ray range, making PHOENIX competitive for many years to come.

Bibliography

[1] J. Ihli, D. Ferreira Sanchez, R. R. Jacob, V. Cuartero, O. Mathon, F. Krumeich, C. Borca, T. Huthwelker, W. C. Cheng, Y. Shu, S. Pascarelli, D. Grolimund, A. Menzel, and J. A. van Bokhoven. Localization and speciation of iron impurities within a fluid catalytic cracking catalyst. *Angew. Chem. Int. Edit.*, 56(45):14031–14035, 2017.

[2] M. W. Tew, M. Janousch, T. Huthwelker, and J. A. van Bokhoven. The roles of carbide and hydride in oxide-supported palladium nanoparticles for alkyne hydrogenation. *J. Catal.*, 283(1):45–54, 2011.

[3] Min Wei Tew, Maarten Nachtegaal, Markus Janousch, Thomas Huthwelker, and Jeroen A. van Bokhoven. The irreversible formation of palladium carbide during hydrogenation of 1-pentyne over silica-supported palladium nanoparticles: in situ Pd K and L-3 edge XAS. *Phys. Chem. Chem. Phys.*, 14(16):5761–5768, 2012.

[4] A. Vjunov, M. Wang, N. Govind, T. Huthwelker, H. Shi, D. H. Mei, J. L. Fulton, and J. A. Lercher. Tracking the chemical transformations at the Bronsted acid site upon water-induced deprotonation in a zeolite pore. *Chem. Mat.*, 29(21):9030–9042, 2017.

[5] G. Nurk, T. Huthwelker, A. Braun, C. Ludwig, E. Lust, and R. P. W. J. Struis. Redox dynamics of sulphur with Ni/GDC anode during SOFC operation at mid- and low-range temperatures: An operando S K-edge XANES study. *J. Power Sources*, 240:448–457, 2013.

[6] Yelena Gorlin, Armin Siebel, Michele Piana, Thomas Huthwelker, Himendra Jha, Georg Monsch, Florian Kraus, Hubert A. Gasteiger, and Moniek Tromp. Operando characterization of intermediates produced in a lithium-sulfur battery. *J. Electrochem. Soc.*, 162(7):A1146–A1155, 2015.

[7] Sebastian Schmidt, Sebastien Sallard, Camelia Borca, Thomas Huthwelker, Petr Novak, and Claire Villevieille. Phosphorus anionic redox activity revealed by operando P K-edge X-ray absorption spectroscopy on diphosphonate-based conversion materials in Li-ion batteries. *Chem. Commun.*, 54(39):4939–4942, 2018.

[8] J. Czapla-Masztafiak, W. Kwiatek, J. Lekki, K. Okon, M. Galka, J. Dulinska-Litewka, R. Steininger, J. Gottlicher, and T. Huthwelker. The determination of chemical forms of sulfur in prostate cancer cells and tissue. *AIP Conf. Proc.*, 22:38, 2013.

[9] M. Galib, M. D. Baer, L. B. Skinner, C. J. Mundy, T. Huthwelker, G. K. Schenter, C. J. Benmore, N. Govind, and J. L. Fulton. Revisiting the hydration structure of aqueous Na^+. *J. Chem. Phys.*, 146(8):084504, 2017.

[10] K. Henzler, E. O. Fetisov, M. Galib, M. D. Baer, B. A. Legg, C. Borca, J. M. Xto, S. Pin, J. L. Fulton, G. K. Schenter, N. Govind, J. I. Siepmann, C. J. Mundy, T. Huthwelker, and J. J. De Yoreo. Supersaturated calcium carbonate solutions are classical. *Sci. Adv.*, 4(1):eaao6283, 2018.

[11] Daniel Hiller, Jorg Gottlicher, Ralph Steininger, Thomas Huthwelker, Jaakko Julin, Frans Munnik, Michael Wahl, Wolfgang Bock, Ben Schoenaers, Andre Stesmans, and Dirk Konig. Structural properties of Al-O monolayers in SiO_2 on silicon and the maximization of their negative fixed charge density. *ACS Appl. Mater. Inter.*, 10(36):30495–30505, 2018.

[12] M. Vespa, R. Dahn, T. Huthwelker, and E. Wieland. Soft X-ray absorption near-edge investigations of Mg-containing mineral phases relevant for cementitious materials. *Phys. Chem. Earth*, 99:168–174, 2017.

[13] M. Vespa, B. Lothenbach, R. Dahn, T. Huthwelker, and E. Wieland. Characterisation of magnesium silicate hydrate phases (M-S-H): A combined approach using synchrotron-based absorption-spectroscopy and ab initio calculations. *Cement and Concrete Res.*, 109:175–183, 2018.

[14] A. Vjunov, J. L. Fulton, T. Huthwelker, S. Pin, D. H. Mei, G. Schenter, N. Govind, D. M. Camaioni, J. Z. Hu, and J. A. Lercher. Distribution of $Al3^+$ in HBEA zeolite. *Abstr. Pap. Am. Chem. Soc.*, 247, 2014.

[15] J. H. Jungmann-Smith, A. Bergamaschi, M. Bruckner, S. Cartier, R. Dinapoli, D. Greiffenberg, T. Huthwelker, D. Maliakal, D. Mayilyan, K. Medjoubi, D. Mezza, A. Mozzanica, M. Ramilli, Ch Ruder, L. Schadler, B. Schmitt, X. Shi, and G. Tinti. Towards hybrid pixel detectors for energy-dispersive or soft X-ray photon science. *J. Synchroton Radiat.*, 23(2):385–394, 2016.

[16] M. Ramilli, A. Bergamaschi, M. Andrae, M. Bruckner, S. Cartier, R. Dinapoli, E. Frojdh, D. Greiffenberg, T. Hutwelker, C. Lopez-Cuenca, D. Mezza, A. Mozzanica, M. Ruat, S. Redford, B. Schmitt, X. Shi, G. Tinti, and J. Zhang. Measurements with MOENCH, a 25 μm pixel pitch hybrid pixel detector. *J. Instrum.*, 12, 2017.

[17] J. Rehanek, C. J. Milne, J. Szlachetko, J. Czapla-Masztafiak, J. Schneider, T. Huthwelker, C. N. Borca, R. Wetter, L. Patthey, and P. Juranic. A compact and versatile tender X-ray single-shot spectrometer for online XFEL diagnostics. *J. Synchroton Radiat.*, 25:16–19, 2018.

[18] E. Cato, C. Borca, T. Huthwelker, and E. S. B. Ferreira. Aluminium X-ray absorption near-edge spectroscopy analysis of discoloured ultramarine blue in 20th century oil paintings. *Microchem. J.*, 126:18–24, 2016.

[19] M. Meyer, C. N. Borca, T. Huthwelker, M. Bieber, K. Messlinger, R. H. Fink, and A. Spath. μ-XRF Studies on the Colour Brilliance in Ancient Wool Carpets. *Scanning*, 2017.

[20] V. Fichtner, H. Strauss, V. Mavromatis, M. Dietzel, T. Huthwelker, C. N. Borca, P. Guagliardo, M. R. Kilburn, J. Gottlicher, C. L. Pederson, E. Griesshaber, W. W. Schmahl, and A. Immenhauser. Incorporation and subsequent diagenetic alteration of sulfur in Arctica islandica. *Chem. Geol.*, 482:72–90, 2018.

[21] M. V. Merkulova, M. Munoz, F. Brunet, O. Vidal, K. Hattori, D. Vantelon, N. Trcera, and T. Huthwelker. Experimental insight into redox transfer by iron- and sulfur-bearing serpentinite dehydration in subduction zones. *Earth Planet. Sc. Lett.*, 479:133–143, 2017.

[22] F. A. Lima, C. J. Milne, D. C. Amarasinghe, M. H. Rittmann-Frank, R. M. van der Veen, M. Reinhard, V. T. Pham, S. Karlsson, S. L. Johnson, D. Grolimund, C. Borca, T. Huthwelker, M. Janousch, F. van Mourik, R. Abela, and M. Chergui. A high-repetition rate scheme for synchrotron-based picosecond laser pump/x-ray probe experiments on chemical and biological systems in solution. *Rev. Sci. Instrum.*, 82(6):063111, 2011.

[23] M. Hannelore Rittmann-Frank, Chris J. Milne, Jochen Rittmann, Marco Reinhard, Thomas J. Penfold, and Majed Chergui. Mapping of the photoinduced electron traps in TiO_2 by picosecond x-ray absorption spectroscopy. *Angew. Chem. Int. Edit.*, 53(23):5858–5862, 2014.

[24] L. Artiglia, F. Orlando, K. Roy, R. Kopelent, O. Safonova, M. Nachtegaal, T. Huthwelker, and J. A. van Bokhoven. Introducing time resolution to detect $Ce3^+$ catalytically active sites at the Pt/CeO_2 interface through ambient pressure x-ray photoelectron spectroscopy. *J. Phys. Chem. Lett.*, 8(1):102–108, 2017.

[25] M. A. Brown, A. B. Redondo, I. Jordan, N. Duyckaerts, M. T. Lee, M. Ammann, F. Nolting, A. Kleibert, T. Huthwelker, J. P. Muachler, M. Birrer, J. Honegger, R. Wetter, H. J. Worner, and J. A. van Bokhoven. A new endstation at the Swiss Light Source for ultraviolet photoelectron spectroscopy, X-ray photoelectron spectroscopy, and X-ray absorption spectroscopy measurements of liquid solutions. *Rev Sci Instrum*, 84(7):073904, 2013.

[26] S. Kato, M. Ammann, T. Huthwelker, C. Paun, M. Lampimaki, M. T. Lee, M. Rothensteiner, and J. A. van Bokhoven. Quantitative depth profiling of $Ce^{(3+)}$ in Pt/CeO_2 by in situ high-energy XPS in a hydrogen atmosphere. *Phys Chem Chem Phys*, 17(7):5078–5083, 2015.

[27] Xiangrui Kong, Astrid Waldner, Fabrizio Orlando, Luca Artiglia, Thomas Huthwelker, Markus Ammann, and Thorsten Bartels-Rausch. Coexistence of physisorbed and solvated HCl at warm ice surfaces. *J. Phys. Chem. Lett.*, 8(19):4757–4762, 2017.

[28] Astrid Waldner, Luca Artiglia, Xiangrui Kong, Fabrizio Orlando, Thomas Huthwelker, Markus Ammann, and Thorsten Bartels-Rausch. Pre-melting and the adsorption of formic acid at the air-ice interface at 253 K as seen by NEXAFS and XPS. *Phys. Chem. Chem. Phys.*, 2018.

[29] L. Duchene, R. S. Kuhnel, D. Rentsch, A. Remhof, H. Hagemann, and C. Battaglia. A highly stable sodium solid-state electrolyte based on a dodeca/deca-borate equimolar mixture. *Chem. Commun.*, 53(30):4195–4198, 2017.

[30] W. Luo, F. Shen, C. Bommier, H. L. Zhu, X. L. Ji, and L. B. Hu. Na-ion battery anodes: Materials and electrochemistry. *Accounts Chem. Res.*, 49(2):231–240, 2016.

[31] C. G. Li, X. D. Zhang, and W. He. Design and modification of cathode materials for high energy density aluminum-ion batteries: a review. *J. Matter Sci.-Mater. El.*, 29(16):14353–14370, 2018.

[32] Z. A. Zafar, S. Imtiaz, R. Razaq, S. N. Ji, T. Z. Huang, Z. L. Zhang, Y. H. Huang, and J. A. Anderson. Cathode materials for rechargeable aluminum batteries: current status and progress. *J. Mater. Chem. A*, 5(12):5646–5660, 2017.

[33] D. Aurbach, Z. Lu, A. Schechter, Y. Gofer, H. Gizbar, R. Turgeman, Y. Cohen, M. Moshkovich, and E. Levi. Prototype systems for rechargeable magnesium batteries. *Nature*, 407(6805):724–727, 2000.

[34] E. Roedern, R. S. Kuhnel, A. Remhof, and C. Battaglia. Magnesium ethylenediamine borohydride as solid-state electrolyte for magnesium batteries. *Sci. Rep.-UK*, 7, 2017.

[35] H. S. Kim, T.S. Arthur, G.D. Allred, J. Zajicek, J. G. Newman, A. E. Rodnyansky, A. G. Oliver, W. C. Boggess, and J. Muldoon. Structure and compatibility of a magnesium electrolyte with a sulphur cathode. *Nat. Commun.*, 2, 2011.

[36] Z. W. Seh, Y. M. Sun, Q. F. Zhang, and Y. Cui. Designing high-energy lithium-sulfur batteries. *Chem. Soc. Rev.*, 45(20):5605–5634, 2016.

[37] A. van Veelen, N. Koebernick, C. S. Scotson, D. McKay-Fletcher, T. Huthwelker, C.N. Borca, J.F. W. Mosselmans, and T. Roose. Root-induced soil deformation influences Fe, S and P: rhizosphere chemistry investigated using synchrotron XRF and XANES. *New Phytol.*, 2019.

[38] J.L. Fulton, N. Govind, T. Huthwelker, E.J. Bylaska, A. Vjunov, S. Pin, and T.D. Smurthwaite. Electronic and chemical state of aluminum from the single-(K) and double-electron excitation (KLII and III, KLI) x-ray absorption near-edge spectra of α-alumina, sodium aluminate, aqueous $Al^{3+}.H_2O_6$, and aqueous $Al(OH)_4$. *J. Phys. Chem. B*, 119:8380–8388, 2015.

[39] http://www.idtnet.co.uk/air_bearing_dcm.html.

[40] C. Piamonteze, U. Flechsig, S. Rusponi, J. Dreiser, J. Heidler, M. Schmidt, R. Wetter, M. Calvi, T. Schmidt, H. Pruchova, J. Krempasky, Ch. Quitmann, H. Brune, and F. Nolting. X-Treme beamline at SLS: X-ray magnetic circular and linear dichroism at high field and low temperature. *J. Synchroton Radiat.*, 19:661–674, 2012.

[41] M. Kavcic, M. Zitnik, K. Bucar, A. Mihelic, and R. Bohinc. Resonant inelastic X-ray scattering on atoms and simple molecules in the tender X-ray region. *J. Electron. Spectrosc.*, 188:47–52, 2013.

[42] U. Bergmann and S. P. Cramer. *A high-resolution large-acceptance analyzer for X-ray fluorescence and Raman spectroscopy*, volume 3448 of *P. Soc. Photo-Opt. Ins.*, pages 198–209. 1998.

[43] M. Kavcic, M. Budnar, A. Muhleisen, F. Gasser, M. Zitnik, K. Bucar, and R. Bohinc. Design and performance of a versatile curved-crystal spectrometer for high-resolution spectroscopy in the tender x-ray range. *Rev. Sci. Instrum.*, 83(3):033113, 2012.

[44] D. Vantelon, N. Trcera, D. , Roy, T. Moreno, D. Mailly, S. Guilet, E. Metchalkov, F. Delmotte, B. Lassalle, P. Lagarde, and A. M. Flanka. The LUCIA beamline at SOLEIL. *J. Synchrotron Rad.*, 23:635–640, 2016.

Chapter 12

Soft-x-ray ARPES beamline – electronic structure of complex materials, heterostructures, and devices

Vladimir N. Strocov, Thorsten Schmitt, Leonard Nue, and Xiaoqiang Wang

In a nutshell

Angle-resolved photoelectron spectroscopy (ARPES) informs momentum-resolved electronic structure of solid-state systems, which is the most fundamental property determining a whole host of their optical, transport, and other properties. Soft-x-ray ARPES (SX-ARPES), operating in a photon-energy range around 1 keV, benefits from enhanced probing depths and chemical specificity achieved with resonant photoemission. This extends its spectroscopic potential from the conventional crystalline systems to buried heterostructures and impurity systems, which are at the heart of electronic and spintronic devices. The upgrade of the present SX-ARPES facility at SLS 2.0 will improve its detection efficiency and energy resolution by a factor of 2 and 5, respectively, extending experimental capabilities to new unexplored fields such as electron-boson interactions, in-situ field effects in functional heterostructures, etc. Furthermore, provisions for sub-micron focusing will open spectroscopic studies on microstructured materials and devices; moreover, a revolutionary multichannel spin analyzer 'iMott' will allow previously unthinkable access to spin textures of buried systems. The SX-SARPES facility at SLS 2.0 will be at the frontier of experimental physics in a multitude of hot fields, including topological matter, buried semiconductor- and oxide-heterostructures, magnetic doping of semiconductors and topological insulators, and many other systems that pave the way towards novel quantum materials and devices.

12.1 Overview

Crucial virtues of soft-x-ray ARPES (SX-ARPES), operating in the photon energy ($h\nu$) range of a few hundreds of eV include its probing depth increasing by a factor of three to five compared to conventional ARPES in the VUV energy range, and elemental and chemical-state specificity achieved with resonant photoemission at the *L*-edges of the transition and *M*-edges of the rare-earth metals. These advantages extend the unique momentum-resolving capabilities of ARPES from conventional crystalline solid-state systems to buried heterostructures and impurity systems, which are at the heart of modern quantum electronics. The spectroscopic potential of SX-ARPES can be illustrated by a plethora of pioneering scientific results, including quantum-well states in buried high-electron-mobility transistor heterostructures, the polaronic nature of charge carriers in oxide heterostructures, magnetic impurities in semiconductors and topological materials, and many more besides (see recent reviews [1, 2]).

The main challenge of SX-ARPES is the valence-band photoexcitation cross-section, which typically drops by a few orders of magnitude compared to the UV energy range. A breakthrough in the practical application of this technique has been demonstrated at the ADRESS beamline of the SLS, where a combination of high photon flux [3] with the pioneering grazing-incidence endstation geometry [4] has not only overcome the cross-section problem, but also allowed one to extend SX-ARPES to the most photon-hungry cases of buried heterostructures and impurities. At present, the SX-ARPES beamtime is shared in roughly equal measure between the investigation of the electronic structure of 3D materials (including topological systems, see [5]), buried heterostructures (including semiconductor [6], oxide systems [7]), impurity systems (mostly magnetic impurities in semiconductors [8]), and topological insulators [9]. The overall scientific output of the SX-ARPES facility, achieved within approximately 50% of the total beamtime at the ADRESS beamline, has reached now about 20 papers/year, whereby 40% of these are high-rank publications.

Since coming online in 2011, the SX-ARPES facility at SLS still remains worldwide the most advanced facility of this kind in terms of photon flux, energy resolution and data-acquisition efficiency, It is widely recognized in the international community as a reference SX-ARPES facility. The instrumental advance and user demand of the ADRESS beamline can be characterized by its massive overbooking factor of 4 to 5. To stay at the frontiers of SX-ARPES science for years to come, we propose here upgrades of the present facility to utilize the low emittance of the SLS 2.0 ring and exploit the recent availability of beamline optics elements with ultralow slope errors. These upgrades should result in a dramatic improvement of the energy resolution and detection efficiency of the SX-ARPES facility as well as allowing the incorporation of sub-micron focusing, crucial for device spectroscopy. The upgrades will also invite totally unexplored scientific domains such as, for example, order parameters and electron-boson interactions in quantum devices tuned through the in-situ field effect.

12.1.1 Uniqueness compared to other present and planned beamlines worldwide

SX-ARPES has been pioneered by S. Suga and A. Sekiyama at the beamline BL25SU of SPRing-8 already in 2004. It was however not before the advent of the ADRESS beamline of SLS with its extremely high photon flux that the notorious photoexcitation cross-section problem would be overcome

and, moreover, SX-ARPES expanded to the buried heterostructure and impurity systems for devices. Since then, several new dedicated SX-ARPES beamlines (DIAMOND, PETRA-III, BESSY) and those where SX-ARPES is optional (SOLEIL, ALBA, SSRF, NSLS-II, TPS) have been constructed. However, the SX-ARPES facility at the SLS still remains the worldwide best regarding the combination of the photon flux, detection efficiency, and energy resolution. In a perspective of a year, this advantage will yet increase with an installation of gratings with ultralow slope errors, pushing the beamline resolving power to 50K. However, other facilities are chasing us with sub-micron focusing (BLSU25 at SPRing-8, ESM at NSLS-II), **k**-microscope (ESM at NSLS-II and P04 at PETRA-III) and multichannel spin-resolving spectrometers (P04 at PETRA-III). Based on the advantages of SLS 2.0, the proposed upgrade of the SX-ARPES facility at the SLS (sub-micron focusing, multichannel spin detector, etc.) will allow us to catch up with and even outperform these new instrumental developments.

12.1.2 Impact of the new ring brilliance

The main advantage of the boosted brilliance of the SLS 2.0 diffraction-limited source for spectroscopic experiments is a dramatic reduction of its horizontal emittance, whereby both horizontal spot size and beam divergence reduce by a factor of about 6. As we explain below, first of all, the much smaller horizontal source size proportionally reduces the horizontal spot size on the sample. In addition, the smaller horizontal divergence allows the design of the refocusing optics with larger demagnification. When combined, these two effects can reduce the horizontal spot size on the sample by a factor of more than 10 compared to the existing ring, allowing experiments on micro-structured samples. Finally, the rounder beam divergence will facilitate even illumination of the round aperture of the capillary and zone-plate sub-micron focusing optics to increase its transmission. These improvements coming with the SLS 2.0 source will be pushing the SX-ARPES experiment to new classes of micro- and nanostructured materials and devices such as cleaved crystals with domains, heterostructures of layered materials, nanowires and nanowhiskers, microelectronics devices, and many more.

12.1.3 Complementarity to other PSI BLs

All materials properties like electrical transport, ferroelectricity, magnetism, colossal magnetoresistance, superconductivity, etc. boil down essentially to a combination of the single-particle spectrum (quasi-particles) and two-particle response function (collective excitations). The main momentum-resolved spectroscopies probing these two aspects of the electron-boson interacting system in solids are ARPES and RIXS, respectively. Thus the SX-ARPES facility at SLS 2.0 will ideally complement RIXS. On the other hand, the ability of SX-ARPES to access 3D materials and buried heterostructures with energy resolution of a few tens of meV will ideally match the ability of VUV-ARPES at the QUEST beamline of SLS 2.0, accessing only surface properties but with a better resolution of few meV. These two complementary modes of ARPES experiment can serve for multimodal investigations of the electronic structure of quantum materials and devices. Furthermore, SX-ARPES and particularly its spin-resolved version employing the iMott multichannel spin detector will counterpart the XMCD studies at XTREME beamline. The new SX-ARPES instrument will thus naturally complement all spectroscopic facilities of SLS 2.0 and, when fitted with sub-micron probing capabilities, will also naturally complement the imaging and x-ray diffraction beamlines of SLS 2.0.

12.1.4 Industrial potential

The advantages of SX-ARPES, including enhanced probing depth and resonance photoexcitation, make this spectroscopic technique particularly suitable for the heterostructure and impurity materials which are at the heart of modern electronics, spintronics and quantum technologies. The SX-ARPES experiments yield the fundamental electronic structure characteristics of these materials such as the interfacial band offsets, the shape of the interfacial quantum well embedding the quantized electron states, electronic band dispersions, effective mass, Fermi surface, electron-boson interaction, electron-impurity scattering, etc., which are of utmost importance for the design of novel quantum devices [2]. Presently, the SX-ARPES facility at the ADRESS beamline is involved in a large-scale project with industry to design materials for quantum computers. Such materials include, in particular, A3B5 semiconductors with strong spin-orbit interaction (InAs, InSb) which are interfaced with superconductors (Al, Pb). Such heterostructures are conceived as a prototype of one-dimensional systems which can host zero-energy excitations (so-called Majorana fermions) to be used in topologically protected qubits of quantum computers. Other active fields of research include nitride-semiconductor heterostructures, constituting the barebone of the 5G telecom [6], semiconductor interfaces with ferromagnetic materials (EuO, EuS) [10], magnetic impurities in topological materials for spintronics [9], etc. The SX-ARPES facility is equipped with provisions for spectroscopically controlled in-situ deposition of thin films, field-effect studies, off-line control of the sample preparation with AES, etc. which are important ingredients of the industrial research.

12.2 Optics

The ADRESS beamline is presently shared by two advanced spectroscopic techniques, SX-ARPES and RIXS. The beamline is heavily overbooked (up to a factor of ~ 4.5). Furthermore, a significant beamtime fraction is distributed to industrial research (up to 45 shifts/semester). Budget permitting, we propose to split the ADRESS beamline in two separate SX-ARPES and RIXS beamlines that will allow full realization of the scientific and industrial potential of SLS 2.0. The two ADRESS2.0 beamlines will be essentially identical, as described below, and the only difference between them will be somewhat different refocusing distances. This will much simplify their design and commissioning, and minimize the total cost. The beamlines (hereon in referred to as ADRESS2.0) will go through a major optics upgrade, in which the present collimated-light plane-grating monochromator (CL-PGM) optical scheme [3, 11] will be replaced by a variable-line-spacing plane grating monochromator (VLS-PGM) [12] discussed below. Two upgrade plans of the ADRESS2.0 are considered, a medium-upgrade beamline having a total length of 38 m (floorspace of the present ADRESS beamline) and an ultimate-upgrade, having a length of 98 m (requiring an extension of the SLS hall) to achieve the best energy resolution/flux parameters. More space available at each beamline in the ultimate-upgrade plan will allow higher demagnification of the source and thus higher energy resolving power $E/\Delta E$; higher demagnification at the refocusing stage will further squeeze the spot size on the sample. Furthermore, a second endstation can in future be installed in the available space. Within the context of the medium-upgrade scenario, the SX-ARPES beamline may be installed in the long straight section X05LA shared with the x-ray interference lithography (XIL) beamline.

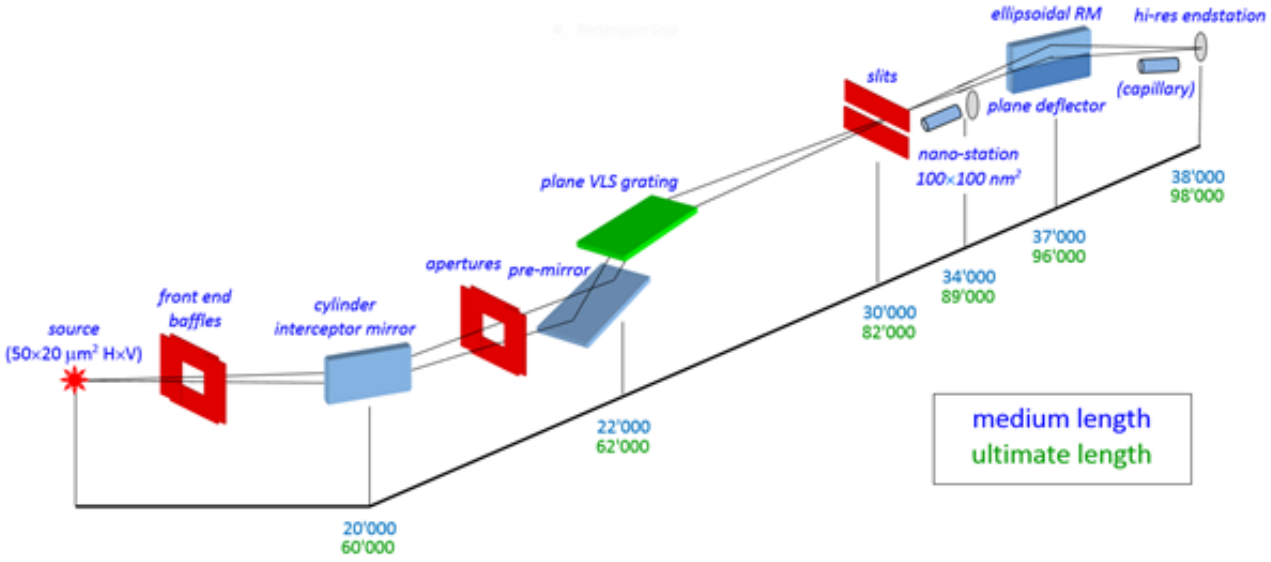

Figure 12.1: VLS-PGM optical scheme of the ADRESS2.0 beamline for the medium and ultimate-upgrade programs.

12.2.1 Source

A minimal heat load originating from the undulator is a prerequisite for high energy resolution, which is otherwise impeded by inevitable vibrations associated with turbulent flow of cooling water. This can be achieved with the APPLE-Knot undulator scheme, whereby a certain magnetic-field configuration shapes electron trajectories in such a way that the higher-harmonic radiation stays outside the central cone. Preliminary calculations show that this undulator can cover the photon-energy range from 400 to 1600 eV. Because of extremely high photon-flux requirements of the SX-ARPES experiment, the beamline should use undulators with maximal length, optimally two standard 2-m sections. The envisaged installation in the section X05LA should allow such an undulator length. Details of the beamline source and front end are described in more detail in Chapter 2.

12.2.2 General principles of high-resolution VLS-PGMs

The VLS-PGM optical scheme of the ADRESS2.0 monochromator for the medium- and ultimate-upgrade plans is presented in Figure 12.1. The use of only the sagitally plane optics ensures minimal slope errors resulting in the highest $E/\Delta E$. The horizontally focussing plane-cylinder interceptor mirror produces a stigmatic focus at the exit slit. The beamline dispersion length is increased by ~5 m compared to the present ADRESS beamline to allow operation of the VLS gratings in a wide energy range without significant aberrations. The absence of the focussing mirror, necessary in the CL-PGM scheme, simplifies the optics alignment, and marginally increases the beamline transmission and resolution.

The main factor which has so far limited energy resolution of the PGMs has been the root-mean-

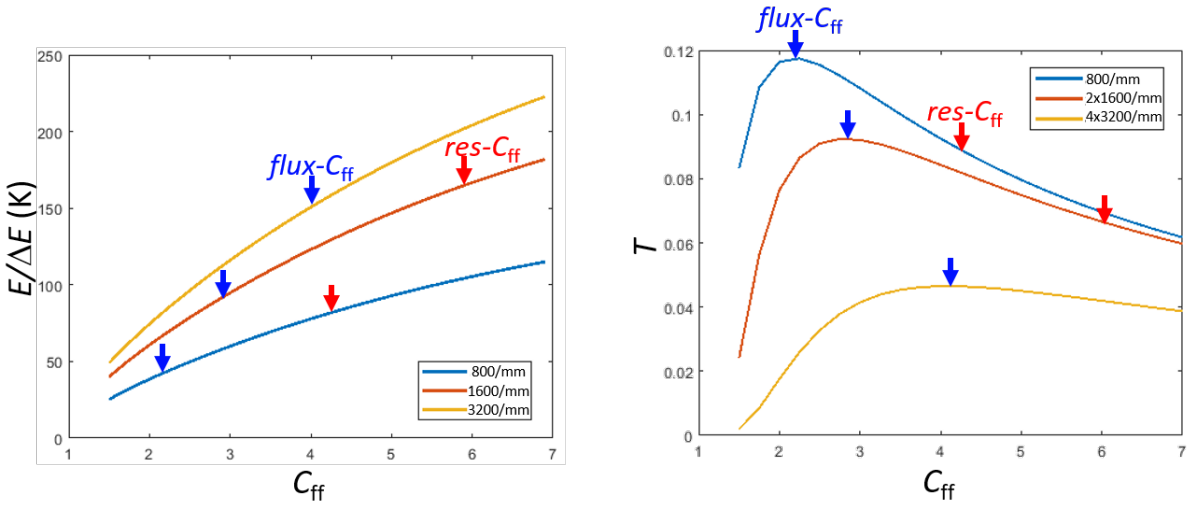

Figure 12.2: Total $E/\Delta E$ (a) and the grating reflectivity T (b) in the photon-energy range from 500 to 1300 eV for the medium-upgrade VLS-PGM with $\sigma_s = 0.1$ μrad. A doubling of C_{ff} from flux-C_{ff} to res-C_{ff} nearly doubles the total $E/\Delta E$ but results in a beamline transmission loss of ~ 30 %.

square (rms) slope errors σ_s of the plane gratings. However, recent developments in the manufacturing of the optical elements (most remarkably at JTEC) have allowed a reduction of σ_s by a factor of up to ten towards 0.05 to 0.1 μrad for both plane and curved optics, with a proportional increase of the corresponding $E/\Delta E$ contributions. With this obstacle removed, the next limiting factor is the vertical size of the synchrotron beam.

One way to reduce the source contribution is to increase the operational C_{ff}-value, thereby proportionally demagnifying the source. Figure 12.2(a) shows the total $E/\Delta E$ as a function of C_{ff} calculated for three gratings. Doubling of the C_{ff} relative to its flux-value increases $E/\Delta E$ by a factor of $\sim$2. The associated reduction of the grating reflectivity ($\sim$30% with the grating profile parameters following the C_{ff} variation) can be considered a fair compromise for the achieved $E/\Delta E$ increase. The alternative (noncompromised) way to achieve this resolution improvement without intensity loss is, however, the doubling of the grating distance from the source, incorporated into the ultimate-upgrade plan described below.

12.2.3 Monochromator optics

In order to improve $E/\Delta E$ and the photon flux on the sample compared to the present ADRESS beamline, the optics of the ADRESS2.0 will undergo the following upgrades:

Interceptor mirror

Thanks to a much reduced heat load from the APPLE-Knot undulator, water cooling and thus associated vibrations of the intercepting mirror can be much reduced. Furthermore, small SLS 2.0's

horizontal divergence will allow a more aggressive grazing incident angle of about 0.7°, spreading the heat load along the mirror surface and increasing the beamline transmission by ∼20%. The mirror will be installed in a high-precision hexapod mechanics from FMB-Oxford, which has demonstrated its excellent performance at the present ADRESS beamline.

Monochromator mechanics

The present monochromator from JENOPTIC has major mechanical-design drawbacks, making its setability, stability and reproducibility insufficient for a modern high-resolution beamline. It will be replaced by a monochromator from BESTEC, which not only solves the above problems, but also offers higher immunity of the angular settings of the optical elements to any cooling-water turbulence. Furthermore, it will accept grating lengths extended from the present 100 mm to 150 mm, allowing operation at high C_{ff} values necessary for effective demagnification of the source (see below). For the SX-ARPES beamline, this monochromator has already been funded through the R'Equip project cofunded by the Swiss National Science Foundation and PSI, and is presently in production at BESTEC.

Premirror

The above $E/\Delta E$ improvement will mean that the slope error of the monochromator's premirror must be accordingly matched. We propose to replace it by a new one from JTEC with $\sigma_s \sim 0.1$ μrad. The main intensity loss in the beamline is presently due to the premirror working at a less grazing x-ray incidence angle. We propose to increase its width to ∼100 mm and deposit stripes of multilayer coating optimized for a sequence of important edges from 460 eV (Ti L-edge) to 1270 eV (La M-edge) which will be selected by transversal translation of the premirror. This simple measure will increase the beamline transmission up to a factor of ∼5 at these energies.

Gratings

The main factor limiting $E/\Delta E$ at the present ADRESS beamline is the gratings' $\sigma_s \sim 0.3$ μrad. We propose to fit the monochromator with new gratings on substrates by JTEC with $\sigma_s \sim 0.1$ μrad. Three gratings will be ruled with a groove density of 800, 1600 and 3200 grooves/mm. According to the data in Table 12.1, their operational C_{ff} values will be chosen as the high-flux value 2, intermediate value 4, and high-resolution value 8, respectively. The two first gratings will be blazed to increase their reflectivity by ∼70% and 50%, respectively, compared to a laminar profile. Larger high-order contamination of the monochromatic x-ray beam from these gratings will be much reduced thanks to the use of the APPLE-Knot undulator and to relatively high photon energies.

Groove densities, C_{ff} values, and corresponding $E/\Delta E$ values at $h\nu = 1$ keV for the two upgrade plans and various σ_s-values of the optical elements are presented in Table 12.1. The ultimate resolving power achieved with a realistic $\sigma_s \sim 0.1$ μrad is ∼130 000 for both the medium and ultimate-upgrade options. Thanks to small state-of-art σ_s values and optimization of the beamline parameters, this value supersedes that of the present ADRESS beamline by a factor of about 4. Also given in Table 12.1 are the $E/\Delta E$ values for the ideal case of $\sigma_s = 0$, and for $\sigma_s \sim 0.15$ μrad as the most conservative

case for the medium upgrade plan and $\sigma_s \sim 0.05$ μrad as the most optimistic case for the ultimate-upgrade plan. The corresponding energy dependence of $E/\Delta E$ is shown in Figure 12.3. The maximal $E/\Delta E = 200\,000$ delivered by the SX-ARPES endstation (see below) would require ADRESS2.0 to adopt the ultimate-upgrade plan, where the maximal $E/\Delta E$ is achieved without compromising the photon flux.

BL length [m]	Grating, C_{ff}	Slope error σ_s [μrad]			
		0	0.05	0.1	0.15
38 (medium)	800/mm, 2.2	$E/\Delta E = 32'000$		26′800	22′900
		H×V = 3.6 × 0.7 μm^2		3.7 × 0.8	3.8 × 1.0
	1600/mm, 4	89′500		65′500	52′100
		3.6 × 0.4		3.7 × 0.5	3.8 × 0.7
	3200/mm, 8	259′200		137′900	100′100
		3.6 × 0.2		3.7 × 0.4	3.8 × 0.5
98 (ultimate)	800/mm, 2.2	90′200	66′400	43′100	
		2.6 × 0.6	2.8 × 0.9	3.2 × 1.3	
	1600/mm, 2.8	170′200	117′700	73′500	
		2.6 × 0.5	2.8 × 0.7	3.2 × 1.1	
	3200/mm, 4	356′500	216′300	127′100	
		2.6 × 0.3	2.8 × 0.6	3.2 × 1.0	

Table 12.1: $E/\Delta E$ (zero-slit limit) at $h\nu = 1$ keV for different upgrade programs, gratings and σ_s of the optical element. The two programs should be compared for the same $\sigma_s \sim 0.1$ μrad.

12.2.4 Refocusing optics

The grazing-incidence geometry of the SX-ARPES experiment (see below) requires tight vertical focusing of the photon beam in order to restrict its footprint on the sample surface. Due to a limited length of SX-ARPES' refocusing stage and aberrations introduced by the toroidal mirror, the beam cross-section cannot presently be reduced below 75 × 10 μm^2 (H × V). In early 2021, the toroidal mirror will be replaced by an ellipsoid with ultralow $\sigma_s \sim 5.0$ μrad in the sagittal direction and 1.0 in the meridional direction, produced by JTEC (funded through the R'Equip project co-funded by SNF and PSI). This upgrade will squeeze the beam cross-section to $\sim 60 \times 5$ μm^2 (H × V), allowing a twofold reduction of the grazing angle with a proportional increase of the photoelectron yield. The ellipsoidal surface of the refocusing mirror will be complemented by a plane surface, exchangeable by a vertical mirror translation, which will deliver light to the microfocusing optics. Within the medium-upgrade plan, this refocusing stage will be directly transferred to SLS 2.0, where the reduced horizontal emittance will squeeze the focused beam cross-section to $\sim 12 \times 5$ μm^2 (H × V).

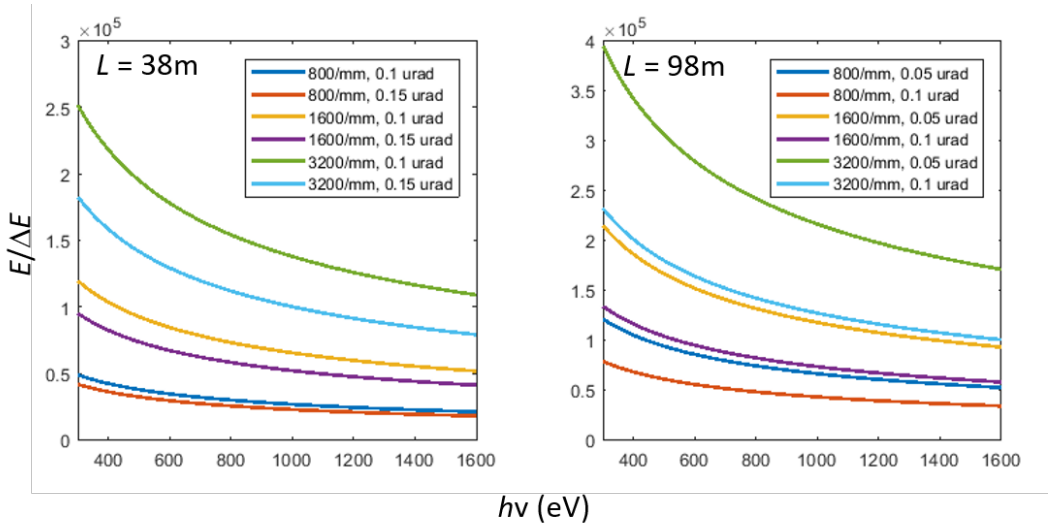

Figure 12.3: $E/\Delta E$ (zero-slit limit) as a function of $h\nu$ for different upgrade programs, gratings and σ_s values from Figure 12.1.

Sub-micron focusing

Reduction of the focused beam size to below 1 μm (sub-micron focusing) will dramatically expand the spectroscopic vista to samples with small domains and even polycrystalline samples. Ideally, such a small spot size could be achieved by a KB-pair of plane-elliptical mirrors. However, this solution requires a large refocusing distance of >20 m, which is available only within the ultimate-upgrade plan. Within the confines of the medium upgrade, our options are either capillary optics or zone plates, which can be accommodated in a refocusing stage of few metres. Our preliminary study shows that the capillary optics, having recently demonstrated a spatial resolution of 250 nm [13], has a number of advantages over zone plates: (1) achromaticity, particularly important for the SX-ARPES experiment where $h\nu$ is always highly dynamic; the necessity to translate zone plates as a function of photon energy practically excludes that the focal point stays at the same point on the sample; (2) high transmission of 30 to 40%, which is at least 2 orders of magnitude larger than that of the zone plates; and (3) the absence of an overwhelming stray intensity beyond the central peak. An advantage of the capillary optics over KBs, apart from the smaller refocusing distance, is the annular shape of the defocused spot (Figure 12.4), allowing a convenient trade-off between the focal size and photon damage. The sub-micron focusing optics can be implemented on a miniature hexapod installed in an oversized light-in flange of the SX-ARPES analysis chamber. The capillary optics can be produced by SIGRAY Inc. who have already demonstrated a focused spot size of 250 nm. We stress that a number of facilities worldwide (ALS, HiSOR, ASTRID, PETRA-III, SOLEIL, etc) are currently using or constructing capillary-based microfocusing beamlines. The SLS should urgently adopt this trend, extending the spectroscopic potential of ARPES to real devices with lateral structure on the sub-micron scale.

The main idea of the ultimate-upgrade plan is the extension of the beamline length to 98 m (Fig-

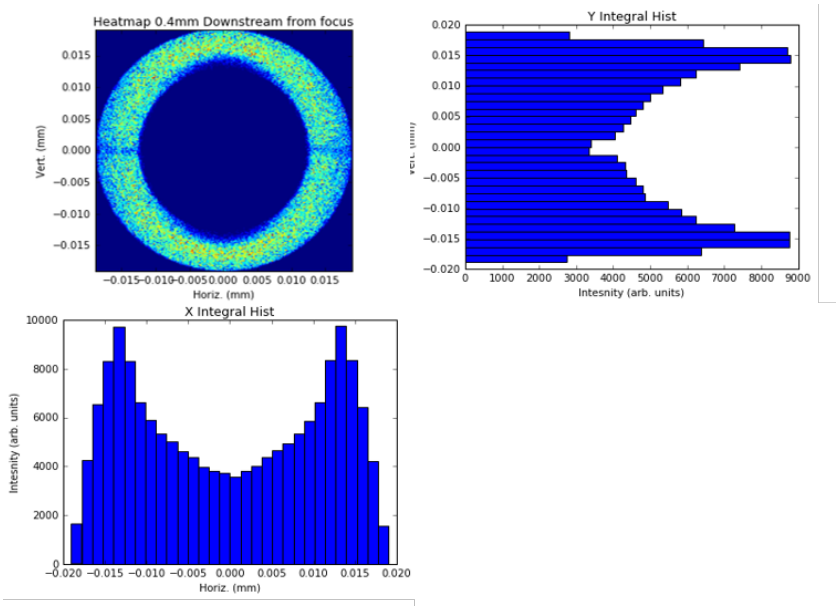

Figure 12.4: The spot profile produced by a capillary optics under defocusing (courtesy B. Stripe, SIGRAY Inc).

ure 12.1). The increase of the available refocusing distance will allow (1) the replacement of the capillaries with their practical transmission of about 30% by elliptic-hyperbolic imaging optics with its twice larger transmission and focused spot size down to 0.1 μm, and (2) larger working distance between the refocusing optics and the sample. The latter will allow the realization of more sophisticated sample environments such as high magnetic fields for RIXS experiments, differential pumping for gas exposure in operando conditions and sample re-magnetization for SX-ARPES experiments.

12.3 Endstation

12.3.1 General principles

A key factor to increase the ARPES signal in the soft-x-ray energy range, dictated by an interplay of the large x-ray penetration depth with much smaller photoelectron escape depth, is the grazing-incidence experimental geometry [14]. When going towards more grazing angle α, the photon yield gradually scales up proportional to $\sin\alpha^{-1}$ and then blows up near the critical angle α_c at which the electromagnetic field concentrates in the near-surface region (for a detailed discussion see Ref. [14]. The grazing x-ray incidence dictates the experimental geometry sketched in Figure 12.5(a). The sample is rotated to the grazing incidence around the horizontal axis: In this case, the x-ray footprint on the sample blows up in the vertical plane where the synchrotron beam has much smaller size than in the horizontal. The analyzer is rotatable around the lens axis, and normally works with the slit oriented within the measurement plane (MP) which enables symmetry analysis of the valence states by switching the x-ray polarization between horizontal and vertical (s- and p-polarizations, respectively).

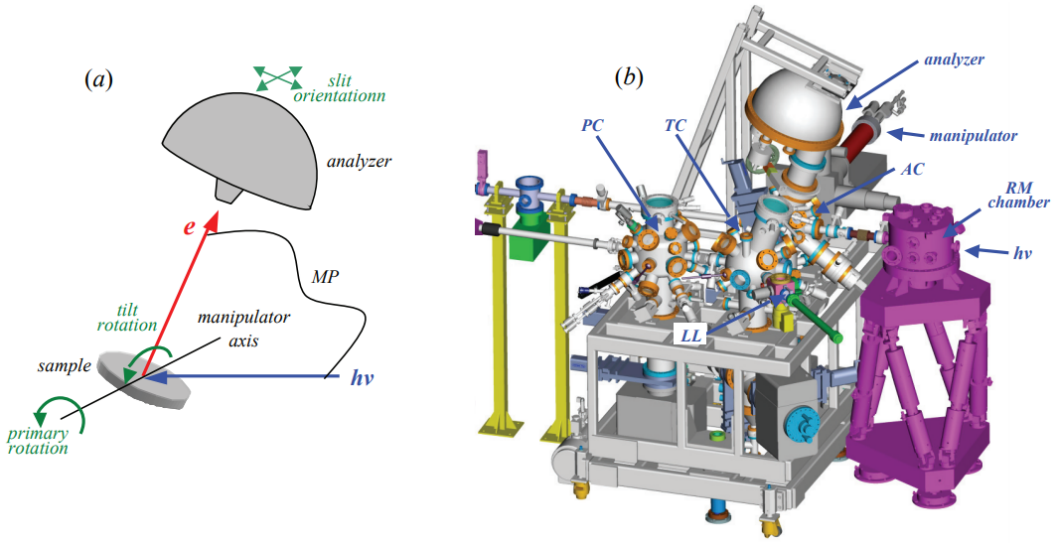

Figure 12.5: SX-ARPES endstation: (a) Experimental geometry featuring grazing x-ray incidence and vertical measurement plane (MP); (b) Technical layout. The endstation includes an analysis chamber (AC) with the photoelectron analyzer, transfer chamber (TC) to distribute samples between other chambers and cleave them at low temperatures, preparation chamber (PC) providing ion bombardment, annealing, and deposition of thin films, and load lock (LL) for the sample introduction.

A technical sketch of the endstation is shown in Figure 12.5 (b). The x-ray beam is focused on the sample with a refocusing mirror driven by high-precision hexapod mechanics. The radial layout of the vacuum chambers around the transfer chamber (TC) enables efficient sample manipulation. The endstation is equipped with the CARVING manipulator providing with three translational and three angular degrees of freedom (primary, tilt and azimuthal rotations) A helium-flow cryostat with thermal shielding allows routine measurements at sample temperatures around 11 K, which suffices to quench the destructive electron-phonon scattering effects even for materials with low Debye temperatures. The photoelectron analyzer offers an angular resolution of $\sim 0.1^\circ$ FWHM, which is in fact better than typical planarity errors of cleaved surfaces. We note that high angular resolution is particularly important for SX-ARPES because the corresponding momentum uncertainty is magnified by high kinetic energy E_k. Concepts and technical realization of our SX-ARPES endstation is described in detail in Ref. [4].

12.3.2 Ongoing upgrade

The endstation is presently undergoing a major upgrade funded mainly from funds granted by SNF within the R'Equip scheme and matched by PSI funds, and partially from industrial funds of SX-ARPES. The upgrade includes: (1) Adaptation of the sample environment for in-situ field-effect measurements, relevant for the characterization of operative electronic devices; (2) Installation of a new ARPES analyzer PHOIBOS-225 from SPECS GmbH, which improves energy resolution/transmission

by 50% and includes electrostatic deflection of the emission angle in the lens. The latter, allowing mapping of electronic structure in 2D k-space without movement of the sample, is mandatory for microfocusing experiments; (3) New analysis chamber adopting an aggressive grazing-incidence experimental geometry with the grazing angle reduced from the present 20° to 9°. This increases the photoyield gain compared to the standard incident angle of 45° from the present factor of 2 to 4 at 1 keV. Although the aggressive grazing incidence will magnify the x-ray footprint on the sample, the latter will stay the same due to the retrofitting of the present toroidal RM by the ellipsoidal one from JTEC (see above); (4) Motorized optical table for precise endstation positioning in the beamline; (5) A number of off-line sample-characterization tools such as a compact raster Auger spectrometer in the PC. The upgraded endstation, being at the forefront of ARPES instrumentation, will be transferred to SLS 2.0 without change (no additional costs). The only weak element of the endstation is the present CARVING manipulator, whose practical mechanical accuracy is limited to $\sim$ 10 μm. We propose to replace it by a high-precision manipulator with the accuracy improved to $\sim$ 1 μm as required for the microfocusing functionality of the endstation. Furthermore, the working temperature should be reduced from the present $\sim$15 K to 7 K.

The endstation energy-resolving power $E/\Delta E$, determined by the PHOBOS-225 analyzer, is sketched in Figure 12.6 as a function of the entrance-slit and angular-mode settings. Calculated at the maximal retarding ratio $RR = E_k/E_{\text{pass}}$ accessible for the two modes, $RR_{\text{max}} = 20$ for medium-angle mode (MAM) and 30 for large-angular dispersion (LAD) mode, it does not depend on E_k. Among other ARPES analyzers on the market, PHOIBOS-225 allows the maximal RR and thus maximal $E/\Delta E$ in the angle-resolving modes. The analyzer's $E/\Delta E$ far supersedes that of the beamline. This fact calls for pushing the beamline towards yet higher resolution, which can be achieved by increasing its length in order to achieve larger demagnification of the source (see above).

12.3.3 Spin-resolved SX-ARPES

Another ongoing instrumental project, running in collaboration with V. N. Petrov (St. Petersburg Technical University) and J.-H. Dil (PSI/EPFL), is the development of a multichannel electron spin detector based on optical imaging principles and Mott scattering, nicknamed iMott [15]. Its working principle is presented in Figure 12.7. A multichannel electron image produced by a standard angle-resolving (photo)electron analyzer or microscope is re-imaged by an electrostatic lens at an accelerating voltage of 40 kV onto a gold target. Quasielastic electrons bearing spin asymmetry of the Mott scattering are imaged by magnetic lenses onto position-sensitive electron CCDs whose differential signals yield the multichannel spin asymmetry image. Fundamental advantages of this concept include acceptance of inherently divergent electron sources from the electron analyzer or microscope focal plane as well as small aberrations achieved by virtue of high accelerating voltages, as demonstrated by extensive ray-tracing analysis. The efficiency gain compared with the single-channel Mott detector can be a factor of more than 104 which opens new prospects of spin-resolved spectroscopies applied not only to standard bulk and surface systems (Rashba effect, topological insulators, etc.) but also to the totally unexplored area of buried heterostructures and impurities, the methodological focus of SX-ARPES.

Having demonstrated the imaging working principle of iMott in late 2018 (manuscript in prepara-

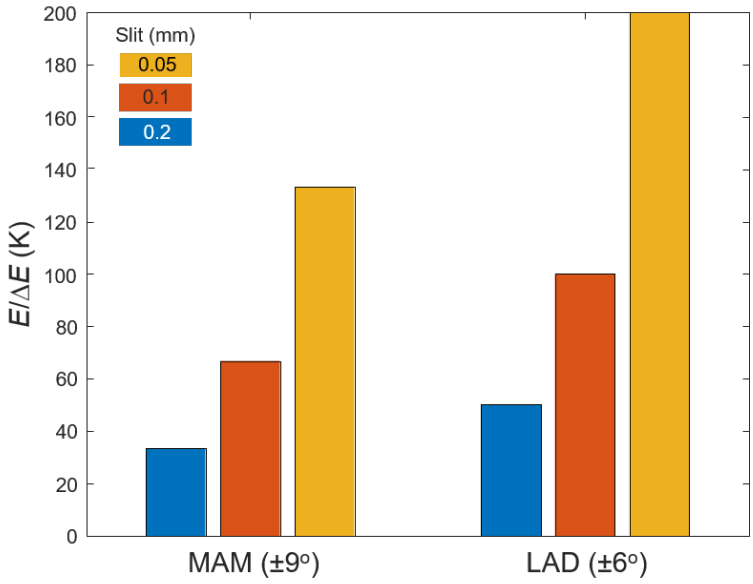

Figure 12.6: $E/\Delta E$ of the PHOBOS-225 analyzer as a function of the entrance-slit and angular-mode settings, calculated at the maximal accessible retarding ratio $RR_{\max}$. The analyzer's $E/\Delta E$ far supersedes that of the beamline.

tion) we are now constructing a serial version of this instrument. This will be fitted to the PHOIBOS-150 analyzer installed at a separate mobile enstation, and extensively tested at the SIS beamline. Afterwards, we will construct a scaled-up high-efficiency version of iMott which will be fit to the PHOIBOS-225 analyzer at the actual SX-ARPES endstation for user operation. The iMott project is funded by PSI funds and industrial funds of SX-ARPES. A commercial version of iMott is being designed to retrofit virtually any commercial ARPES analyzer. The simultaneous spin detection combined with fast CCD readout enables efficient use of the iMott detectors at x-ray free electron laser facilities.

12.3.4 Prospects

Based on our experience with this microfocusing stage, we foresee the second endstation for nanoscale experiments, where a zone-plate or advanced refractive optics will deliver a spot size below 100 nm. To realize such spatial resolution, the nanoscale endstations will use granite baseblocks and high-stability (possibly hexapod-based) manipulators with temperature control and nano-resolution piezo-stages similar to those used in the OMNI project now developing towards full UHV compatibility. The nanoscale photon beam resolution will be complemented by a **k**-microscope such as KREOS-150 from SPECS GmbH, which combines the hemispherical analyzer with a PEEM lens to produce in one shot iso-energetic cuts of electronic structure over a large **k**-space area covering a few Brillouin zones. The ultimate energy resolving power and angle resolution of this instrument are presently 5 K and 0.1°, respectively. In addition, it can operate in a PEEM mode with a spatial resolution of $\sim$ 50 nm and

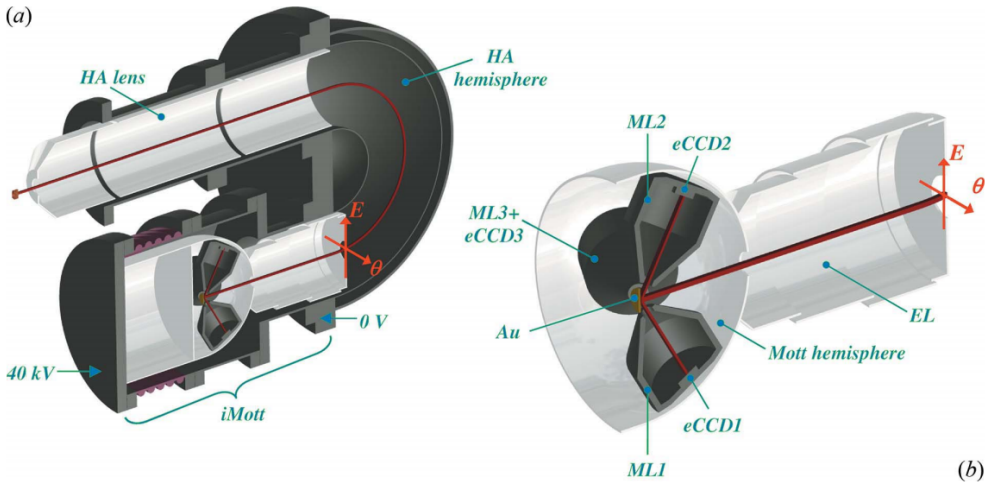

Figure 12.7: (a) Schematics of the iMott detector attached to the standard angle- and energy-resolving HSA. (b) Detail of the iMott, which includes the imaging electron lens EL, Au target, four magnetic lenses MLs and electron-sensitive CCD-detectors eCCDs. Differential images between the opposite eCCDs yield a multichannel image of the spin asymmetry. The use of imaging principles allows iMott to work with divergent electron beams.

a micro-ARPES mode with resolution < 2 μm. This instrument is obviously ideal to investigate the electronic structure of nanoscale electronic and spintronic devices.

12.4 Project management

12.4.1 Timeline

- Conceptual design: January - December 2019
- Technical design: January - June 2021
- Procurement and in-house manufacturing: July 2021 - September 2023
- Installation of new beamline and endstations: October 2023 - September 2024
- Commissioning phase: October 2024 - June 2025
- Pilot user phase: July 2025 - October 2025
- Regular user operation: November 2025

12.4.2 Resources

The realization of the medium and ultimate upgrades will require 18 months of engineering and 24 months of technicians (including the beamline technicians and help of external manpower) plus one additional staff beamline scientist. The minimal upgrade will require three months of engineering and 18 months of technicians.

12.5 Concluding remarks

To summarize, we have presented a program to upgrade the SX-ARPES facility for its most efficient operation at the SLS 2.0 diffraction-limited source. It describes a dramatic improvement of the energy resolution and detection efficiency of the SX-ARPES facility as well as incorporation of microfocusing, crucial for device spectroscopy. We have outlined two upgrade programs, the medium upgrade restricted by the present beamline length, and an ultimate upgrade that involves an extension of the beamline length to $\sim$ 98 m to further increase its energy resolution/transmission. We stress that the heavy overbooking of the present ADRESS beamline (overbooking factor up to $\sim$ 4.5) and its excellent scientific output ($\sim$ 40 papers per year delivered jointly by SX-ARPES and RIXS) strongly favour an endeavor to build two separate beamlines for SX-ARPES and RIXS. This is supported by a significant investment of 1.5 MCHF already made to the SX-ARPES facility (including a new analyzer with angular deflection) and ADRESS beamline (high-precision monochromator mechanics).

The small horizontal emittance of SLS 2.0 is of vital importance for the above upgrades. In addition to an increase of the beamline transmission by $\sim$ 20% due to more glancing incidence angles on the sagittal optical elements, the reduction of both horizontal spot size and beam divergence will allow one to squeeze the horizontal spot size on the sample by a factor of more than 10 compared to the existing ring. Furthermore, the rounder beam divergence facilitate even illumination of the capillary and zone-plate nano-focusing optics to increase their transmission. These improvements will push the SX-ARPES experiment to new classes of the micro- and nanostuctured materials and devices, including cleaved crystals with domains, heterostructures of layered materials, nanowires and nanowhiskers, microelectronics devices with electrodes and active areas, and many more.

The proposed upgrades of the SX-ARPES facility will keep the PSI and Swiss science in general at the frontiers of many current and highly competitive scientific fields, including topological matter, buried semiconductor and oxide heterostructures, magnetic doping of semiconductors and topological insulators, and other promising systems for future quantum devices.

Bibliography

[1] V.N. Strocov, M. Kobayashi, X. Wang, L.L. Lev, J. Krempasky, V.A. Rogalev, T. Schmitt, C. Cancellieri, and M.L. Reinle-Schmitt. Soft-X-ray ARPES at the Swiss Light Source: From 3D materials to buried interfaces and impurities. *Synchr. Rad. News*, 27:31–38, 2014.

[2] V.N. Strocov, L.L. Lev, M. Kobayashi, C. Cancellieri, M.-A. Husanu, A. Chikina, N.B.M. Schrter, X. Wang, J.A. Krieger, and Z. Salman. **k**-resolved electronic structure of buried heterostructure and impurity systems by soft-X-ray ARPES. *J. Electron Spectrosc. and Relat. Phenom.*, 236:1–15, 2019.

[3] R. Follath and F. Senf. High-resolution soft X-ray beamline ADRESS at the Swiss Light Source for resonant inelastic X-ray scattering and angle-resolved photoelectron spectroscopies. *J. Synchrotron Rad.*, 17:631–645, 2010.

[4] V.N. Strocov, X. Wang, M. Shi, M. Kobayashi, J. Krempasky, C. Hess, T. Schmitt, and L. Patthey. Soft-X-ray ARPES facility at the ADRESS beamline of the SLS: Concepts, technical realisation and scientific applications. *J. Synchrotron Rad.*, 21:32–45, 2014.

[5] N.B.M. Schroeter, D. Pei, M.G. Vergniory, Y. Sun, K. Manna, F. de Juan, J.A. Krieger, V. Sss, M. Schmidt, P. Dudin, B. Bradlyn, T.K. Kim, T. Schmitt, C. Cacho, C. Felser, V.N. Strocov, and Y. Chen. Chiral topological semimetal with multifold band crossings and long Fermi arcs. *Nature Physics*, 15:759–765, 2019.

[6] L.L. Lev, I.O. Maiboroda, M.-A. Husanu, E.S. Grichuk, N.K. Chumakov, I.S. Ezubchenko, X. Wang, T. Schmitt, M.L. Zanaveskin, V.G. Valeyev, and V.N. Strocov. k-space imaging of anisotropic two-dimensional electron gas in GaN-based high-electron-mobility transistor heterostructures. *Nature Communications*, 9:2653–2659, 2018.

[7] C. Cancellieri, A.S. Mishchenko, U. Aschauer, A. Filippetti, C. Faber, O.S. Barisic, V.A. Rogalev, T. Schmitt, N. Nagaosa, and V.N. Strocov. Polaronic metal state at the $LaAlO_3/SrTiO_3$ interface. *Nature Communications*, 7:10386–10392, 2016.

[8] M. Kobayashi, I. Muneta, Y. Takeda, Y. Harada, A. Fujimori, J. Krempasky, T. Schmitt, S. Ohya, M. Tanaka, M. Oshima, and V.N. Strocov. Unveiling the impurity band induced ferromagnetism in the magnetic semiconductor (Ga,Mn)As. *Phys. Rev. B*, 89:205204–205211, 2014.

[9] J.A. Krieger, C.-Z. Chang, M.-A. Husanu, D. Sostina, A. Ernst, M.M. Otrokov, T. Prokscha, T. Schmitt, A. Suter, M.G. Vergniory, E.V. Chulkov, J.S. Moodera, V.N. Strocov, and Z. Salman. Spectroscopic perspective on the interplay between electronic and magnetic properties of magnetically doped topological insulators. *Physical Review B*, 96:184402–184412, 2017.

[10] Y. Liu, A. Luchini, S. Mart-Snchez, C. Koch, S. Schuwalow, S. A. Khan, T. Stankevi, S. Francoual, J. R. L. Mardegan, J. A. Krieger, V. N. Strocov, J. Stahn, C. A. F. Vaz, M. Ramakrishnan, U. Staub, K. Lefmann, G. Aeppli, J. Arbiol, and P. Krogstrup. Coherent Epitaxial Semiconductor - Ferromagnetic Insulator InAs/EuS Interfaces: Band Alignment and Magnetic Structure. *ACS Applied Materials & Interfaces*, 12:8780–8787, 2019.

[11] R. Follath and F. Senf. New plane-grating monochromators for third generation synchrotron radiation light sources. *Nucl. Instr. and Meth. in Phys. Res. A*, 390:388–393, 1997.

[12] R. Reininger. The in-focus variable line spacing plane grating monochromator. *Nucl. Instr. and Meth. in Phys. Res. A*, 649:139–143, 2011.

[13] R.J. Koch, C. Jozwiak, A. Bostwick, B. Stripe, M. Cordier, Z. Hussain, W. Yun, and E. Rotenberg. Nano focusing of soft X-rays by a new capillary mirror optic. *Synchrotron Radiation News*, 31:50–52, 2018.

[14] V.N. Strocov. Optimization of the X-ray incidence angle in photoelectron spectrometers. *J. Synchrotron Rad.*, 20:517–521, 2013.

[15] V.N. Strocov, V.N. Petrov, and J.H. Dil. Concept of multichannel spin-resolving electron analyzer based on Mott scattering. *J. Synchrotron Rad.*, 22:708–718, 2015.

Chapter 13

Soft x-ray RIXS facility at SLS 2.0 - Elementary excitations of emerging quantum materials and devices

Thorsten Schmitt, Vladimir N. Strocov, Xiaoqiang Wang, and Leonard Nue

In a nutshell

Resonant Inelastic X-ray Scattering (RIXS) directly measures the elementary excitations within lattice, charge, orbital, and spin degrees of freedom of quantum materials as a function of momentum and energy transfer. The goal of the new soft x-ray RIXS facility at SLS 2.0 is to develop and provide new instrumentation with vastly superior performance that will enable new science by revealing the low-energy properties of new quantum materials and their application potential in future electronic and spintronic devices, as well as for information technology. For this purpose a new soft x-ray RIXS beamline will be build employing optical elements with ultralow slope errors and taking full advantage of the low-horizontal emittance of SLS 2.0 by increasing the beamline entrance arm, thereby pushing the achievable energy resolution. The new soft x-ray RIXS facility at SLS 2.0 will comprise also an ultra-high energy resolution RIXS spectrometer of 10 to 15 meters length with at least a factor of five increased energy resolution and a continuous rotation chamber that can be extended with sub-micron focusing optics, as well as a polarimeter for the polarization analysis of the emitted x-rays. The capabilities of this instrument will place PSI again at the forefront of RIXS spectroscopy and provide the Swiss RIXS user community with a highly competitive facility for years to come. It will allow the study of quantum many-body phenomena that enable emergent functions like Mottronics, magnetoelectrics, topological electronics, spintronics, or quantum computing.

13.1 Overview

Resonant Inelastic X-ray Scattering (RIXS) is a powerful probe of excitations from the electronic ground state of quantum materials involving lattice, charge, orbital and spin degrees of freedom. RIXS gives direct information as a function of momentum and energy transfer, on the elementary excitations within these degrees of freedom of transition metal oxides and related strongly-correlated materials. These excitations are sensitive to many-body and collective effects in the solid-state and are directly related to the correlated materials properties as well as low-temperature phenomena in the energy scale of magnetic exchange and lattice vibrations. Soft x-ray RIXS at the SLS has been utilized in scientific problems associated with superconductivity [1–9], metal-insulator transitions [10–12], charge order [8], magnetic order [5], and low-dimensional magnetism [13–16], as well as in molecular physics and organic transition-metal complexes.

The ADRESS beamline of the SLS, which began operation in 2007, was the premier worldwide RIXS facility for about a decade. Still today it is one of the leading facilities, but faces strong competition from upcoming new high-resolution RIXS projects at other synchrotrons. In order to stay at the forefront of RIXS for years to come, we propose here to upgrade the present RIXS facility, utilizing the low emittance of SLS 2.0 and beamline optical elements with ultralow slope errors. Such instrumental upgrades are vital to significantly improve the energy resolution of RIXS in order to reveal the low-energy properties of new quantum materials and their application potential in future electronic devices, as well as for information technology.

We describe the conceptual design (CD) of two upgrade scenarios for the soft x-ray RIXS facility at ADRESS, both employing optical elements with ultralow slope errors for beamline and spectrometer. Both CD versions presented here assume splitting of the ADRESS beamline into separated and dedicated SX-ARPES and RIXS beamlines. The SX-ARPES CD is described in Chapter 12. For RIXS, we plan to build for SLS 2.0 a new state-of-the-art beamline with a triple-axis variable-line-spacing (VLS) spectrometer and continuous rotation chamber, as well as a polarimeter for the polarization analysis of the emitted x-rays. We divide the CD in two possible phases/stages for realizing such a facility: (a) a medium upgrade with an approximtely 38 meter long VLS-PGM beamline inside the SLS building with a 10 meter spectrometer; and (b) an ultimate upgrade with an approximately 98 m long VLS-PGM beamline with a 15 m spectrometer in an extension hall outside of the SLS building. These scenarios can be extended by submicron to 100-nm focusing options to enable spatially resolved RIXS on inhomogeneous quantum materials and devices. In the longer term, towards 2035, we propose a combination of this ultimate resolution facility with an echo enabled harmonic generation (EEHG) source for soft x-rays, enabling an additional operation mode for time-resolved RIXS with 1-ps time resolution and ultimate energy resolution from the source equating to a resolving power of 3×10^5.

Table 13.1 summarizes key performance parameters of the suggested new RIXS facility within the medium upgrade scenario (a) with an approximately 38 meter long VLS-PGM beamline and a 10 meter spectrometer compared to the current SAXES spectrometer at the ADRESS beamline. A

Key performance parameters	Current SAXES/ADRESS	SLS 2.0 RIXS facility
Spectrometer length	5 m	10 m
Beam spot size (v × h)	4 μm × 55 μm	$<$ 1 μm × 4 μm
Grating slope errors	0.35 μrad	0.05 μrad
Resolving power	12'800 (1500 lines/mm)	47'600 (800 lines/mm)
@ 1 keV	23'300 (3000 lines/mm)	83'300 (1500 lines/mm)
		125'000 (2500 lines/mm)
Energy resolution	78 meV (1500 lines/mm)	21 meV (800 lines/mm)
@ 1 keV	43 meV (3000 lines/mm)	12 meV (1500 lines/mm)
		8 meV (2500 lines/mm)
Polarisation analysis	Only incident beam	Incident and outgoing beam
Scattering angle	Discrete: 30°, 50°, 70°,	Continuous 0° − 150°
rotation	90°, 110°, and 130°	

Table 13.1: Comparison of key performance parameters of the current SAXES spectrometer at the ADRESS beamline with the spectrometer proposed in upgrading scenario (a) for the new SLS 2.0 RIXS facility. Resolving power and energy resolution are given for VLS gratings of different central line densities. For this new facility, ultimate low slope errors of 0.05 μrad are assumed. How these performance values change for more moderate effectively achieved slope errors is discussed in detail in Section 13.5.1

detailed analysis of both upgrading scenarios is given in Section 13.5.1.

13.1.1 Uniqueness compared to other present and planned beamlines worldwide

PSI is one of the leaders of new instrumental developments in the RIXS technique and has been operating since 2007 the ADRESS-beamline optimized for soft x-ray RIXS and SX-ARPES experiments. ADRESS is highly recognized in the international community of synchrotron radiation research and has stimulated new developments of similar projects at other synchrotron radiation facilities. Such new beamlines similarly optimized for RIXS in the soft x-ray range have in recent years come into operation or are close to the construction phase at nearly all synchrotron sources (ESRF, Diamond, Sirius, SOLEIL, ALS, CLS, BESSY II, NSLS-II, TPS, MAX-IV, PETRA III at DESY, SLiT-J etc.). The ADRESS beamline is recognized as the role model for developing RIXS projects at the forefront of synchrotron radiation research. With the upcoming RIXS projects elsewhere, the RIXS project at ADRESS beamline is entering into a competitive situation with other synchrotrons. We therefore propose to construct a new RIXS facilities at SLS 2.0 in order to assure that PSI will stay at the front in this research field. Improvements connected to state-of-the art optical quality of mirrors and gratings, detector technology (begun already with the development of an EM-CCD for RIXS at ADRESS that is operational since 2016), a RIXS beamline with a larger entrance arm of the monochromator and the employment of an at least 10 m long spectrometer arm, are expected to reestablish PSI as

the world leader in RIXS by the time of the SLS 2.0 upgrade. The proposal comprises the addition of nano-focusing capabilities to the new RIXS instrument which would open opportunities to investigate intrinsic or artificially manipulated nano-scale inhomogeneity and future electronic devices based on quantum materials. The SLS 2.0 RIXS facility could be the first facility worldwide adding such performance capabilities to their portfolio.

13.1.2 Impact of the new ring brilliance

The main advantage of the boosted brilliance of the SLS 2.0 diffraction-limited synchrotron source for spectroscopic experiments is a dramatic reduction of its horizontal emittance, whereby both horizontal spot size and beam divergence reduce by a factor of about 6. As we explain below, first of all, the much smaller horizontal source size proportionally reduces the horizontal spot size on the sample. In addition, the smaller horizontal divergence allows the design of the refocusing optics with larger demagnification. When combined, these two effects can reduce the horizontal spot size on the sample by a factor of more than 10 compared to the existing ring, allowing experiments on micro-structured samples. Finally, the rounder beam divergence will facilitate even illumination of the round aperture of capillary and zone-plate sub-micron focusing optics to increase its transmission. These improvements, in combination with the SLS 2.0 source, will open new opportunities for RIXS spectroscopy to investigate new classes of micro- and nanostructured materials and devices, as well as cleaved crystals with domains, heterostructures of layered materials, nano-materials, microelectronics devices, and many more.

13.1.3 Complementarity to other PSI BLs

The basic origin of all materials properties like electrical transport, ferroelectricity, magnetism, colossal magnetoresistance or superconductivity can be understood from the single particle spectrum (quasi-particles) and the two-particle response function (collective excitations), which together give a complete description of the electronic system. The main momentum-resolved spectroscopies probing the quasi-particle response and collective excitations are Angle-Resolved Photoemission Spectroscopy (ARPES) and Resonant Inelastic X-ray Scattering (RIXS), respectively. Thus the proposed SLS 2.0 RIXS facility will be ideally complementary to the SX-ARPES facility and the VUV-ARPES instrument at the QUEST beamline, which together can serve for multimodal investigations of the electronic structure of quantum materials and devices. The new RIXS instrument will naturally be complementary to all spectroscopic facilities at the SLS 2.0 like, e.g., the XTreme beamline for x-ray absorption XMCD studies, and with the enhancement through nano-probing capabilities be also a natural extension of the imaging and diffraction beamlines of the SLS 2.0Ṫhere will be particular important synergies of static RIXS at SLS 2.0 with time resolved RIXS opportunities at the Furka station at the Athos line of SwissFEL.

13.1.4 Size and impact of community – potential increase through the upgrade

There will be many research groups both within Switzerland and from abroad who will be interested to use the new RIXS beamline and instrument at SLS 2.0Åfter the ADRESS beamline was built, many

groups worldwide immediately applied to obtain beamtime, which led to a situation that ADRESS has still today an overbooking factor of above 4. We expect a similar situation once the new SLS 2.0 RIXS facility goes online. Switzerland hosts many world-recognized research groups in quantum materials, including the following groups who have expressed strong direct support for a R'Equip proposal by sharing their scientific cases and having provided a letter of support in the initial beamline suggestion phase for the SLS 2.0 facility: Prof. Johan Chang and Prof. Marta Gibert Gutierrez (Zuerich University), Prof. Claude Monney, Prof. Christian Bernhard, Prof. Philipp Werner and Prof. Ana Akrap (Fribourg University), Prof. Henrik M. Roennow (EPFL), Prof. Jean-Marc Triscone (University of Geneva), Dr. Eugenio Paris, Dr. Cristian Svetina, Dr. Elia Razzoli, Dr. Marc Janoschek, Dr. Simon Gerber, and Dr. Daniel Mazzone (PSI). Due to the high overbooking (> 4) the RIXS station at the ADRESS beamline could during the last years not serve its user community sufficiently. It is expected that the user community has large potential of growing as many very good user proposals had to be turned down due to this large overbooking, which leads to some fluctuations of the user community and eventual dropping out of promising user groups. Increased capacity, if splitting the soft x-ray RIXS and SX-ARPES in two separate beamlines, is expected to extend the user community, tapping into interested users from neighboring experimental fields like ARPES, neutron scattering, and optical spectroscopy. In particular the nano-probing extension of the RIXS capabilities could motivate users that were traditionally using imaging beamlines to begin using RIXS in their projects.

13.1.5 Industrial potential

Modern quantum materials with entangled degrees of freedom of charge, orbital, spin, and lattice, as well as topological properties, are very promising for future electronic and information technology devices. The application of these materials is based on the quantum many-body phenomena that enable emergent functions like Mottronics, magnetoelectrics, topological electronics, spintronics or quantum computing. The detailed analysis of the elementary excitations in these quantum materials will help in understanding the electronic structure origin and manipulation potential of their emergent functionalities. The new RIXS instrument with its significantly improved resolution, field-effect and nano-probing capabilities will open enormous opportunities to unlock the future application potential of quantum materials in future electronic and spintronic devices, as well as for information technology. With such improved capabilities it is expected that the new RIXS instrument at SLS 2.0 will also get attractive for industry as currently already the case for the SX-ARPES station of ADRESS.

13.1.6 Spectroscopic method

Resonant Inelastic X-ray Scattering (RIXS) is a powerful photon-in/photon-out spectroscopic probe of the electronic structure [17]. RIXS is extremely sensitive to electronic excitations within charge, orbital, spin and lattice degrees of freedom of quantum materials. In a RIXS experiment the photon energy of incident x-rays is tuned close to an absorption edge of an atomic species in the material of interest, thereby initiating an electron transition between a core level and an unoccupied valence band state. The created energetic disturbance in the intermediate core-excited state gives rise to a multitude of elementary excitations, which are probed after a valence electron has recombined with a core-hole after typically femtoseconds and a photon of corresponding energy is re-emitted. The

characteristic atomic absorption edges involved in the initiating step of the RIXS process make RIXS an element-selective probe that, depending on the detailed fine-structure of the absorption spectrum, can often differentiate between inequivalent chemical sites of a material.

Charge, orbital, magnetic, and phonon excitations are characterized by their characteristic energy, being determined as the energy difference between incident and re-emitted photons. Furthermore, knowledge of the wavevectors of the incident and detected photon beam enables RIXS to infer the momentum-transfer dependence of such collective electronic excitations, from which the energetic dynamics can be extracted in the form of dispersion relations that can be connected to the basic electronic interactions. Choosing the polarization of the incident x-rays as either linearly horizontally polarized in the scattering plane, vertically polarized out of the scattering plane, or circularly polarized, reveals the symmetry of the involved electronic states in the RIXS process, which allows one to selectively suppress or enhance particular modes in the RIXS spectra.

13.1.7 New research opportunities emerging from increased energy resolution and nano-focusing

Modern quantum materials with entangled degrees of freedom of charge, orbital, spin, and lattice, as well as topological properties, are very promising for future electronic and information technology devices. The application of these materials is based on the quantum many-body phenomena that enable emergent functions like Mottronics, magnetoelectrics, topological electronics, or quantum computing [18]. Significantly improving the energy resolution of soft x-ray RIXS will be crucial in accessing the low-energy excitation energy scales for many classes of quantum materials. The detailed analysis of these elementary excitations will help in understanding the electronic structure origin and manipulation potential of the emergent functionalities of quantum materials. With such improvements of the energy resolution it will, for instance, be able to study topological spin excitations [19] or Higgs modes, i.e. the amplitude modes of the spin-orbit condensate [9, 20]. Together with the polarization analysis of the emitted x-rays [21, 22], this will allow one to characterize the spin and charge dynamic structure factor at the superconducting gap [23], from which the pairing-symmetry of the superconducting order parameter can be determined in a bulk-sensitive manner.

With regards to developing a better understanding of the decisive criteria that govern high-temperature superconductivity, it will be essential to resolve the intrinsic heterogeneities between the competing or interlinked orders, i.e. in the antiferromagnetic, superconducting, charge-ordered, pseudo-gap, or strange metal phase, in terms of their elementary excitations [24, 25]. This can be achieved by adding nano-probing capabilities to the RIXS technique. Ideally, one would like to perform spatially resolved RIXS mapping of the elementary excitations with a spatial resolution of below 20 nm and an energy resolution around the superconducting gap size or below. An intermediate step towards 100 to 250 nm would be very promising for spatially separating the low-energy response of these phases. For elucidating the percolative behavior of many phase transitions like metal-insulator transitions (MIT) [26] or magnetic transitions, much of the underlying physics connected to phase separation can already be investigated with a submicron spatial resolution. Submicron focusing will also allow one to perform operando RIXS studies of the material components of electronic or magnetoelectric devices.

13.2 Source

A minimal heat load coming from the undulator is a prerequisite for high energy resolution, which is otherwise impeded by vibrations inevitably coming with turbulent flow of cooling water. This can be achieved with the APPLE-Knot undulator scheme, whereby a certain magnetic-field configuration shapes the electron trajectories in such a way that the higher-harmonic radiation stays outside the central cone and can easily be filtered out by the front end slits. This will mean that a lower cooling capacity would suffice and thereby avoid or diminish vibrations of the beamline optics. Preliminary calculations show that this undulator can cover the photon energy range from 200 to 1600 eV. Because of extremely high photon-flux requirements of the RIXS experiment, the beamline should use undulators with maximal length, optimally covering the complete section of $4 - 4.5m$. Details of the beamline source are described in more detail in Chapter 2.

13.3 Front end

The front end of the new SLS 2.0 RIXS beamline will be developed as an extension of the current ADRESS front end (see Figure 13.1). It will be adapted for the newly developed APPLE-Knot undulators that are expected to deliver a total power of 8.4 kW and a power density of 12 kW/mrad^2 (see Chapter 2). The CD description of the front end, applying to both versions of new SLS 2.0 soft x-ray RIXS facilities, are described in detail in Chapter 2.

13.4 Optics

Developing and constructing a beamline and RIXS spectrometer for a facility with a resolving power towards 100 000 will require ultimate performing optics with 0.05 to 0.1 μrad rms slope errors. Such instruments will furthermore require the best possible thermal (down to 0.1 K) and vibrational stabilities.

The small horizontal source size of SLS 2.0 will result in a reduction of the horizontal spot size at the sample by a factor of at least 5. Furthermore, the small horizontal divergence of the beam will result in small beam footprints at the optical elements that have their sagittal plane in the plane of the electron orbit. This will enable (1) more grazing angles at the sagittal elements (interceptor and refocusing mirrors) and thus a beamline transmission increase of ca. 20 %; (2) It will allow increasing the entrance arm of the monochromator, resulting in higher demagnification of the source and an increase of the resolving power $E/\Delta E$. (3) This in turn means that the extremely small slope errors need to be met only within a smaller optical surface, which is beneficial for very high-resolution beamlines. (4) Finally, the rounder source will facilitate even illumination of the round aperture of a capillary and zone-plate nano-focusing optics that will increase its transmission.

In the following we describe the CD of the beamline optics of both upgrading scenarios: (a) a "medium upgrade" replacing ADRESS with a new ca. 38-m long beamline optimized for the reduced emittance of SLS 2.0, fitting inside of the SLS building, and (b) an "ultimate upgrade" consisting of a new ca. 98-m long beamline with an extension hall outside of the SLS building. Groove densities, C_{ff} values and corresponding $E/\Delta E$ values at $h\nu = 1$ keV for the two upgrade plans and various slope

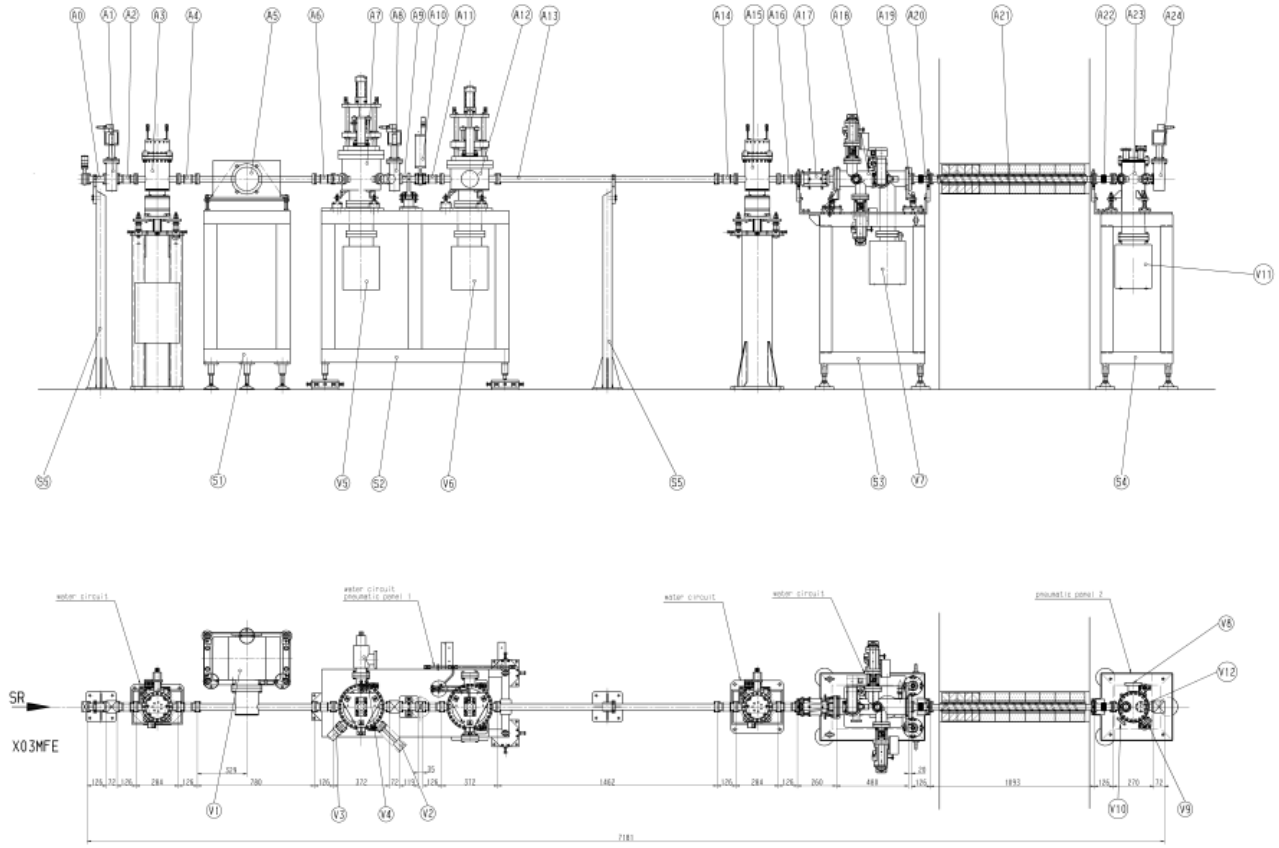

Figure 13.1: 2D component layout of the existing ADRESS front end.

errors σ_s of the optical elements are presented in Table 13.2. The ultimate resolving power achieved with a realistic $\sigma_s = 0.1$ μrad is ca. 130 000 for both the medium and ultimate upgrade options. Also given in Table 13.2 are the $E/\Delta E$ values for the ideal case of $\sigma_s = 0$, and for $\sigma_s = 0.15$ μrad as the most conservative case for the medium-upgrade plan and $\sigma_s = 0.05$ μrad as the most optimistic case for the ultimate-upgrade plan. The corresponding energy dependence of $E/\Delta E$ is shown in Figure 13.3.

13.4.1 Beamline optics of the medium upgrade

The SLS 2.0 soft x-ray RIXS beamline described in this CD report can be implemented in Sector 3, where the existing infrastructure can be fully used (also suitable for a later length extension and building of an extension hall outside of the SLS building). The optics of the new beamline would be based on the proven variable-line-spacing plane grating monochromator (VLS-PGM) [22, 27] sketched in Figure 13.2. The use of only sagitally plane optics, ensuring minimal slope errors σ_s, will result in the highest resolution. The horizontally focusing plane-cylindrical interceptor mirror produces a stigmatic focus at the exit slit. The absence of the focusing mirror in a VLS-PGM beamline, necessary in the present collimated-light PGM (CL-PGM) scheme at ADRESS [28], will increase the resolving power $E/\Delta E$ by $\approx$ 10% and simplify the optics alignment compared to a CL-PGM beamline. Increased

BL length [m]	Grating, C_{ff}	Slope error σ_s [μrad]			
		0	0.05	0.1	0.15
38 (medium)	800/mm, 2.2	$E/\Delta E = 32'000$		$26'800$	$22'900$
		H×V = 3.6×0.7 μm^2		3.7×0.8	3.8×1.0
	1600/mm, 4	$89'500$		$65'500$	$52'100$
		3.6×0.4		3.7×0.5	3.8×0.7
	3200/mm, 8	$259'200$		$137'900$	$100'100$
		3.6×0.2		3.7×0.4	3.8×0.5
98 (ultimate)	800/mm, 2.2	$90'200$	$66'400$	$43'100$	
		2.6×0.6	2.8×0.9	3.2×1.3	
	1600/mm, 2.8	$170'200$	$117'700$	$73'500$	
		2.6×0.5	2.8×0.7	3.2×1.1	
	3200/mm, 4	$356'500$	$216'300$	$127'100$	
		2.6×0.3	2.8×0.6	3.2×1.0	

Table 13.2: $E/\Delta E$ resolving power and FWHM spot size at the sample for $h\nu = 1$ keV with ellipsoidal refocusing optics for different grating configurations assuming different effective rms slope errors for the medium and ultimate beamline upgrade options. Note that the $E/\Delta E$ values are given for the zero-slit limit.

space available at the dedicated SLS 2.0 RIXS beamline will allow higher demagnification of the source by using an approximately 2 m longer entrance arm and thus higher $E/\Delta E$ balanced with higher demagnification at the refocusing stage and thus smaller spot size on the sample. Furthermore, the endstation space freed when having SX-ARPES placed at a separate beamline would allow the installation of two RIXS endstations, a high-resolution and nano-focusing endstation.

Interceptor mirror

The smaller heat load from the APPLE Knot undulator source will allow a reduction of the cooling water flow through the interceptor mirror, minimizing its vibrations, and thus the small horizontal spot size and angular divergence will allow a more aggressive grazing incidence angle of about 0.7°, increasing the beamline transmission by $\approx 20\%$.

Mirror mechanics

We propose to employ high-precision hexapod mechanics from e.g. FMB-Oxford for both the interceptor and the refocusing mirrors. These mechanics, presently used for the two refocusing mirrors at ADRESS, have performed excellently.

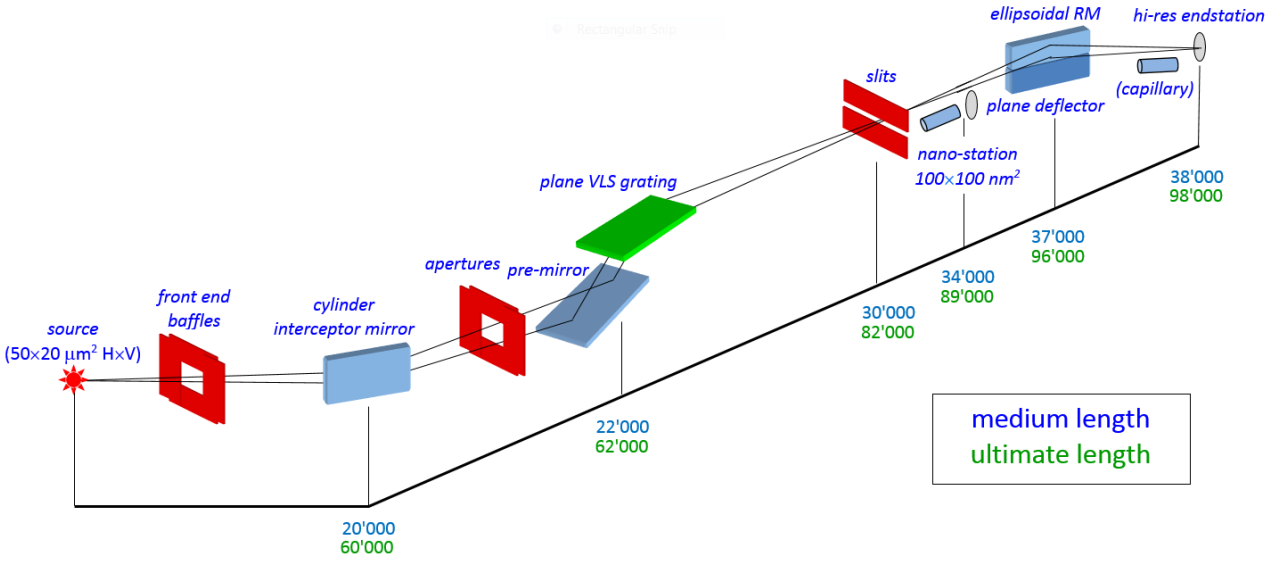

Figure 13.2: VLS-PGM optical scheme of the new SLS 2.0 RIXS beamline for the medium-upgrade and ultimate-upgrade options.

Monochromator

The grating length of the present ADRESS monochromator from JENOPTIC is limited to 100 mm, which does not allow operation at high C_{ff}-values for effective demagnification of the source. The planned increase of $E/\Delta E$ by employing higher C_{ff} values requires a monochromator with increased mechanical stability with grating holders allowing gratings of up to 200 mm length to be mounted (e.g. from BESTEC).

Gratings

New state-of-the-art plane VLS gratings (e.g. substrates by JTEC and ruling by SHIMADZU) will have $\sigma_s \approx 0.05$ to 0.1 μrad rms. The next limiting factor is the vertical source size. We will reduce this contribution by a factor of ≈ 2 by a proportional increase of the operational C_{ff}-values and consequently the lengths of the gratings. Their profiles will be re-optimized for large C_{ff}-values, which will keep the corresponding decrease of the grating efficiency within $\approx 30\%$ (for details see Section 12.2). Three gratings will be ruled with a groove density of 800, 1600, and 3200 grooves/mm. Their operational C_{ff}-values will be chosen as 2.2 for the high-flux value, 4 for the intermediate value, and 8 for the high-resolution value. The two first gratings will be blazed to increase their reflectivity by $\approx 70\%$ and 50%, respectively, compared to laminar profiles.

Premirror

The improvement originating from doubling of the demagnification also requires the reduction of the slope errors of the monochromator's premirror that contribute significantly to increasing $E/\Delta E$. With an expected SLS 2.0 source size of 50 $\times$ 20 μm^2 (H$\times$V), the calculated $E/\Delta E$ at $h\nu = 1$ keV is about 140 000 for $\sigma_s \approx 0.1$ μrad rms (grating 3200 line/mm, $C_{ff} = 8$), see Table 13.2 and Figure 13.3.

Multilayer coating of the premirror

The main intensity loss in the beamline is presently at the premirror with a less grazing light incidence angle of a few degrees . We propose to increase the premirror width to approximately 100 mm and deposit stripes of multilayer coatings optimized for a sequence of important edges from 450 eV (Ti L-edge) to 1270 eV (La M-edge) which will be selected by transverse translation of the premirror. This measure will increase the beamline transmission up to a factor of approximately 5 at these energies, but will, however, require significant Research and Development. It could also be added at a later stage after the SLS 2.0 upgrade.

Refocusing optics and Microfocusing

New ellipsoidal refocusing optics will deliver to the new high-resolution RIXS endstation a spot of 3.7 $\times$ 0.4 μm^2 H$\times$V assuming effective slope errors of the optical elements of 0.1 μrad rms with a 1 m refocusing exit arm (see Table 13.2). The ellipsoidal surface of the refocusing mirror will be complemented by a plane one, exchangeable by a vertical mirror translation, which will deliver light to a microfocusing optics. In order to switch between normal refocusing with the ellipsoid and microfocusing, we plan to engage retractable capillary optics from e.g. SIGRAY, whose benefits compared to zone plates include (1) achromaticity, (2) absence of shape distortion when changing the focal distance allowing convenient trade-off between the focal size and photon damage, and (3) a high transmission of 30 to 40%, which at least exceeds that of zone plates by 2 orders of magnitude. With this capillary lens, one can expect submicron focusing to 0.25 $\times$ 0.25 μm^2 H$\times$V. The capillary optics are discussed in greater detail in Section 12.2 of the SX-ARPES CDR.

13.4.2 Beamline optics of ultimate upgrade

The ultimate-upgrade plan aims to achieve uncompromised resolution and photon flux parameters of the SLS 2.0 RIXS beamline via an extension of the beamline length to $\approx$ 98 m (see Figure 13.2). This will allow one to increase the beamline entrance arm to 60 m, thereby (1) maximizing the energy resolution owing to the practical elimination of the source size contribution, and (2) enabling the operation of the monochromator at smaller C_{ff}-values, resulting in $\approx$ 30% increase of the beamline transmission in comparison to the medium upgrade scenario. Assuming that an ultimate $\sigma_s \approx 0.05$ μrad rms will be achieved, the ultimate $E/\Delta E$ at $h\nu = 1$ keV will in this case reach 220 000 with a grating of 3200 line/mm and $C_{ff} = 4$, see Table 13.2 and Figure 13.3. Figure 13.3 compares the achievable resolving power of the two upgrade scenarios for different grating configurations and effectively achieved slope errors. New ellipsoidal refocusing optics will deliver to the new high-resolution RIXS endstation a spot of 2.8 $\times$ 0.6μm^2 H$\times$V, assuming effective slope errors of the optical elements of 0.05 μrad rms

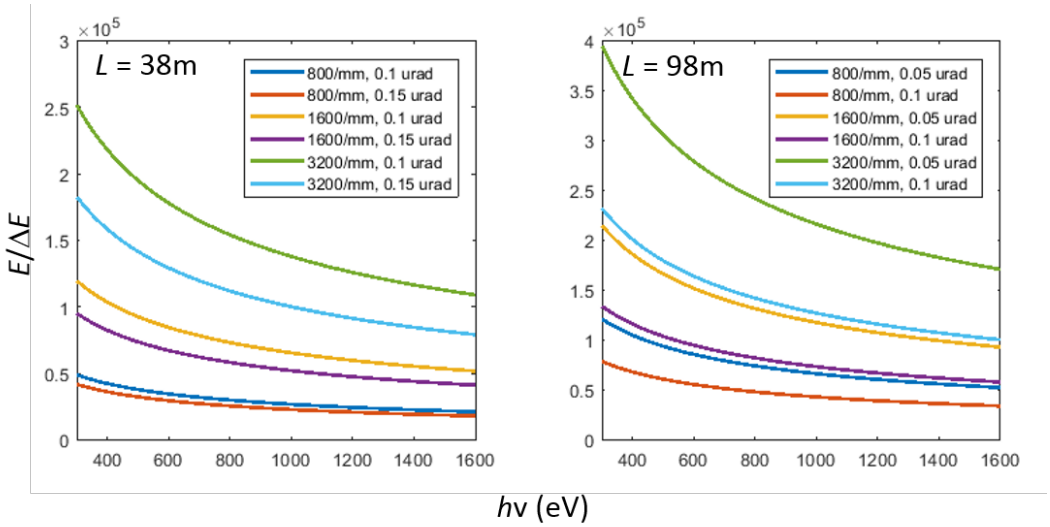

Figure 13.3: $E/\Delta E$ resolving power as a function of photon energy for different grating configurations, assuming different effective slope errors for the medium and ultimate beamline upgrade options. Note that the $E/\Delta E$ values are given for the zero-slit limit.

at a relaxed refocusing exit arm of 2 m (see Table 13.2). A major advantage of the larger refocusing distance is that it (1) allows the replacement at a later stage of the capillary with transmission of about 30% by elliptic-hyperbolic imaging optics with twice larger transmission, and (2) results in a larger working distance between the refocusing optics and the sample. The latter will in the future for instance allow the realization of more sophisticated sample environments, such as high magnetic fields for RIXS experiments.

13.5 RIXS Endstations

13.5.1 High-resolution RIXS spectrometer

Our group has large experience with optimizing and building VLS-type spectrometers [11,29,30]. For SLS 2.0, we suggest to build an extreme high-resolution VLS-type RIXS spectrometer [22,31] of a total length of 10 to 15 m (see Figure 13.4 for a concept sketch). Such long spectrometers will be needed to match $E/\Delta E$ of the spectrometer to that of the beamline (see Table 13.2 and Figure 13.3). Too high line densities would limit the efficiency of the RIXS spectrometer and thereby increase the acquisition times. Assuming a cylindrical VLS grating with slope errors of 0.1 μrad rms, a spectrometer entrance arm of 2 m, an ultimate spatial resolution of the CCD of 2 μm, and conservatively a 1μm vertical source size, one obtains $E/\Delta E$ values of the 10 m spectrometer (see Figure 13.5, left panel) at 1 keV of: 35 000 for a grating of average line density of 800 line/mm, 62 000 for 1500 line/mm and 93 000 for 2500 line/mm. The spectrometer will employ a horizontal collimating mirror to increase the horizontal acceptance up to a factor of 3 [22,31]. It will also engage sub-μm focusing with capillary optics, as described above.

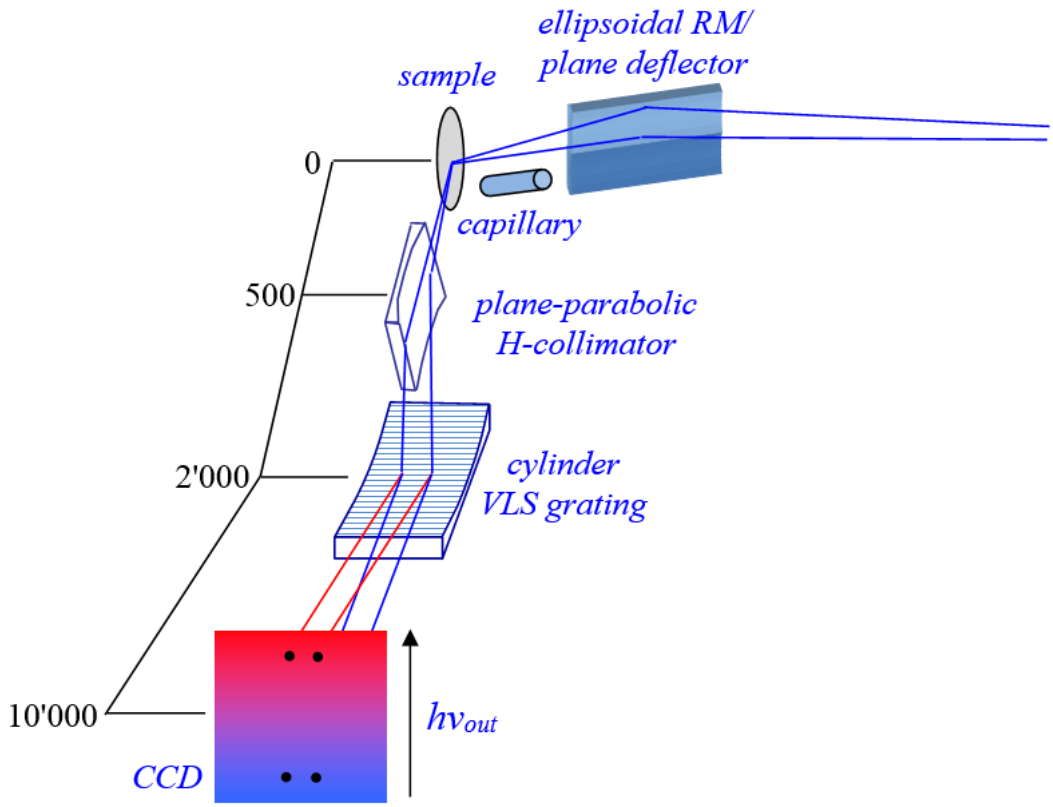

Figure 13.4: Concept of high-resolution VLS type RIXS spectrometer with horizontal plane-parabolic collimating mirror and cylindrical gratings.

A 15 m spherical grating VLS spectrometer would match the resolution of the ultimate SLS 2.0 RIXS beamline upgrade. Assuming a cylindrical VLS grating with slope errors of 0.05 μrad rms, a spectrometer entrance arm of 2 m, an ultimate spatial resolution of the CCD of 2 μm, and conservatively a 1 μm vertical source size, one obtains $E/\Delta E$ values of the 15 m spectrometer at 1 keV of: 52 000 for a grating of average line density of 800 line/mm, 88 000 for 1500 line/mm, and 136 000 for 2500 line/mm (see Figure 13.5, right panel), slightly better than the beamline values in Table 13.2 and Figure 13.3. This is thereby compatible with the EEHG upgrade scenario (see below). Figure 13.5 compares the resolving power performance of the two spectrometer versions for gratings of different central line densities and different effectively achieved slope errors.

The CCD camera for the high-resolution endstation has already been developed in a collaboration between PSI, the Open University in UK, and XCAM Ltd., and is since 2017 in use at the current RIXS instrument at the ADRESS beamline. It is based on electron-multiplying (EM) CCD chips optimized for sub-pixel resolution with read–out frame rates of above 1 Hz enabling analysis of the photon events with centroiding algorithms. With a pixel size of 16 μm this camera has an effective spatial resolution of 2 μm in single–photon counting mode. As can be seen in Figure 13.6, clustering of 3 CCD-chips in this camera triples the horizontal acceptance.

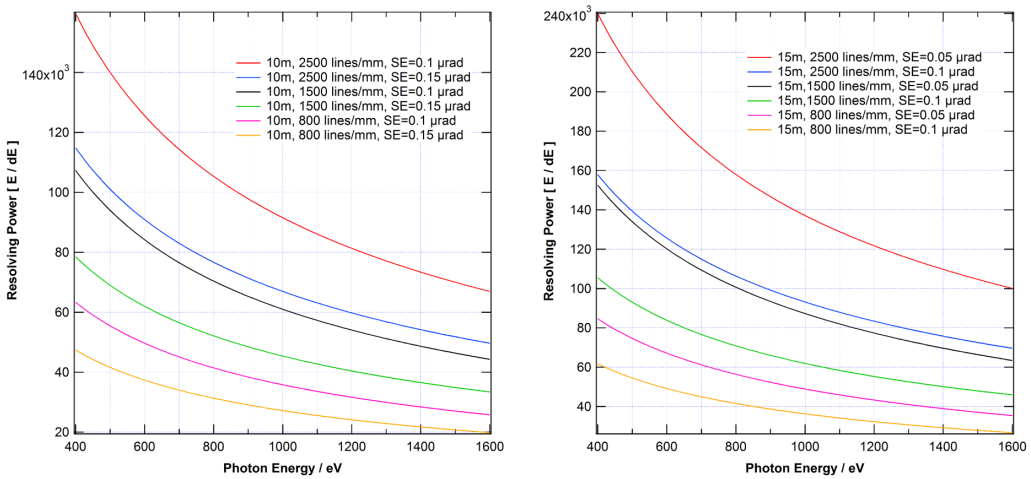

Figure 13.5: $E/\Delta E$ resolving power as a function of photon energy for different grating configurations, assuming different effective slope errors for the 10 m and 15 m versions of the spherical VLS-type RIXS spectrometer. Both spectrometers assume a 2 m entrance arm, a vertical spot size at the sample of 1 μm and an effective detector spatial resolution of 2 μm.

The sample manipulator for the high-resolution RIXS instrument depicted in Figure 13.7 will be a 6-axis manipulator with 3 translational and 3 rotational degrees-of-freedom. This manipulator is already in use since 2016 at the current ADRESS RIXS instrument and is based on the series of Carving manipulators developed and manufactured by PSI. All rotations and translations are decoupled in this manipulator concept, which allows all rotations of the sample to pass through the sample surface without any parasitic movements. It is equipped with a liquid helium cryostat that can cool down the sample to 10 K, reducing thermal drifts to below 20 μm.

The sensitivity of RIXS experiments can also be enhanced by tuning the polarization of the incident and detected x-rays. The polarization of the incident photons can be selected with a polarized APPLE II undulator source as linearly polarized horizontally (π-polarization) or vertically out of the plane (σ-polarization) of the synchrotron as well as rotated light in between these, or circularly polarized light of positive or negative helicity. The polarization of the detected x-ray beam after the interaction with the sample has so far only been implemented at ID-32 at ESRF [21,22]. As the polarization of the photons may be modified in the intermediate state of the RIXS process, valuable information can be gained about the symmetry and type of the detected low-energy excitations. Scattering processes leading to the creation of phonon or charge-transfer excitations leave the polarization of the light as unchanged as elastic scattering ($\pi-\pi$ or $\sigma-\sigma$ scattering). On the contrary, for single spin and orbital excitations the incident linearly polarized light is rotated by 90 degrees ($\pi-\sigma$ or $\sigma-\pi$ scattering). Polarization analysis is achieved in such instruments with graded multilayers. Such a polarimetric RIXS set-up will also need a second CCD camera or a mechanical arrangement that allows displacing the CCD camera accordingly. Implementation of the RIXS polarimeter tools will enable one to separate various overlapping spectral contributions in the low-energy excitation spectra. With this, we will for instance be able to discriminate between single magnon excitations and multimagnon or phonon excitations

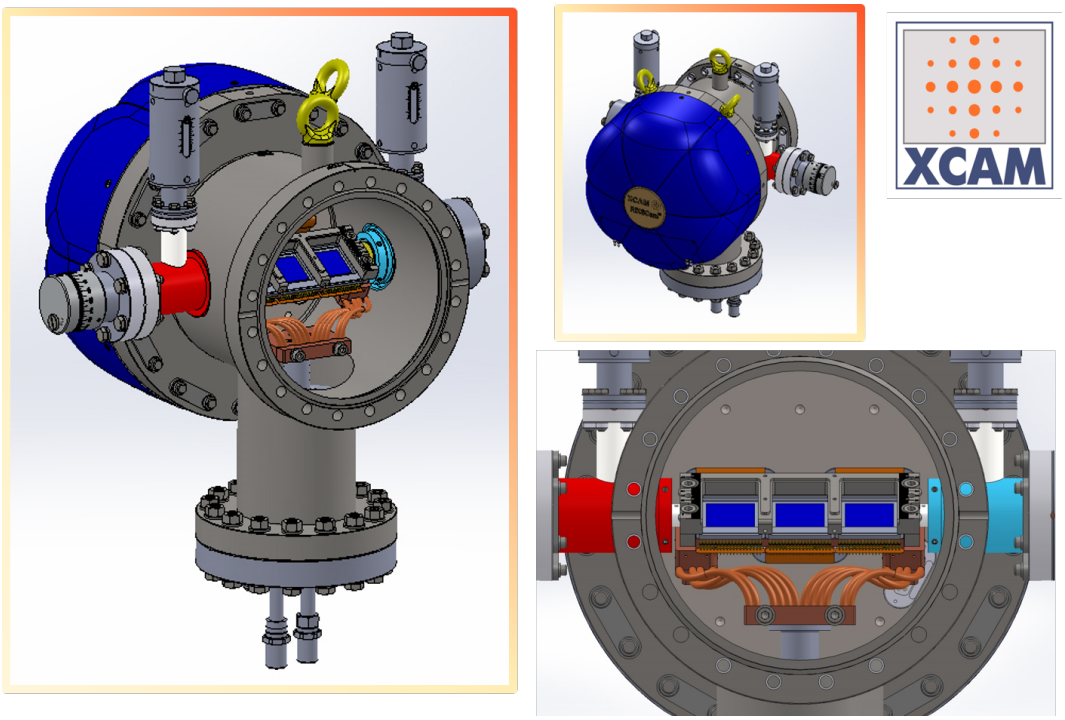

Figure 13.6: RIXCcam (from XCAM Ltd.) EM-CCD camera with three CCD chips optimized for RIXS spectrometers requiring high spatial resolution through photon event centroiding algorithms.

when analyzing the magnetic fluctuations in superconductors. This will also allow the discrimination between charge and orbital excitations.

The new SLS 2.0 RIXS facility will also include a scattering chamber for continuous rotation according to the triple-axis spectrometer concept, allowing one to independently vary the incident angle on the sample, and the scattering angle. The possibility to continuously change the scattering angle will allow the study of momentum-transfer (q) dependent RIXS spectra perpendicular to the sample surface and thereby also in three-dimensional materials with prevoskite like crystal structures.

13.5.2 Nano RIXS spectrometer

As a further upgrading option, we foresee installation of a second endstation for nanoscale experiments, where a zone-plate or advanced refractive optics will deliver a spot size below 100 nm. To realize such spatial resolution, the nanoscale RIXS endstation will use a granite baseblock and a high-stability (possibly hexapod-based) manipulator with temperature control and nano-resolution piezo-stages or a further development of the OMNI manipulator towards full UHV compatibility. Such nano-focusing capabilities of a dedicated Nano-RIXS instrument would open opportunities to investigate intrinsic or artificially manipulated nano-scale inhomogeneities and future electronic devices based on quantum materials.

Furthermore, the imaging properties of the zone plates will allow the realization of the so-called

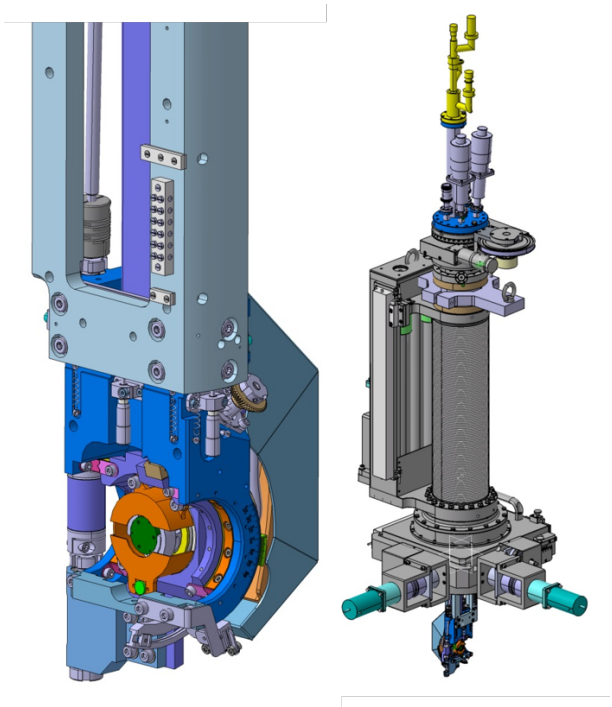

Figure 13.7: Liquid helium sample manipulator with 3 translational and 3 rotational decoupled degrees–of–freedom.

$h\nu^2$-spectrometer [32], delivering a full two-dimensional map of RIXS intensity as a function of incoming $h\nu_{\mathrm{in}}$ and outgoing $h\nu_{\mathrm{out}}$ photon energies (see the concept sketch of such an imaging spectrometer in Figure 13.8). In this case, the monochromator slit can be opened to large values, with the monochromator producing in its focal plane a line image extending in $h\nu_{\mathrm{in}}$. The zone plate re-images this into a demagnified line on the sample. It becomes a source for the RIXS spectrometer combining imaging action in the vertical (imaging) plane with dispersion action in the horizontal (dispersion) plane. In the imaging plane a Wolter-type imaging optics, combining plane-hyperbolic and plane-elliptic shapes [33], deflects the light scattered from the sample into a magnified image on the two-dimensional detector extending in $h\nu_{\mathrm{in}}$. In the dispersion plane, simultaneously, a spherical VLS grating disperses the scattered light and brings it into focus on the detector extending in $h\nu_{\mathrm{out}}$. The combination of the imaging and dispersion actions forms a two-dimensional map of RIXS intensity as a function $h\nu_{\mathrm{in}}$ and $h\nu_{\mathrm{out}}$. The zone plate in this scheme can be replaced by another Wolter-type imaging optics, whose transmission much exceeds that of the zone plate.

By utilizing an extended $h\nu_{in}$-range, such a $h\nu^2$-spectrometer increases the detection efficiency by a factor of a few tens, remarkably, without any sacrifice in the energy resolution. This is particularly useful for dilute samples and cases where the incident number of photons onto the sample within the narrow $h\nu_{\mathrm{in}}$-bandwidth is not large enough to acquire RIXS spectra with sufficient signal statistics. The spectrometer in an $h\nu^2$ concept intercepts all $h\nu_{\mathrm{in}}$ within the energy width of the inverse core-hole lifetime, over which the RIXS spectra are identical. Therefore, this concept allows one to compensate

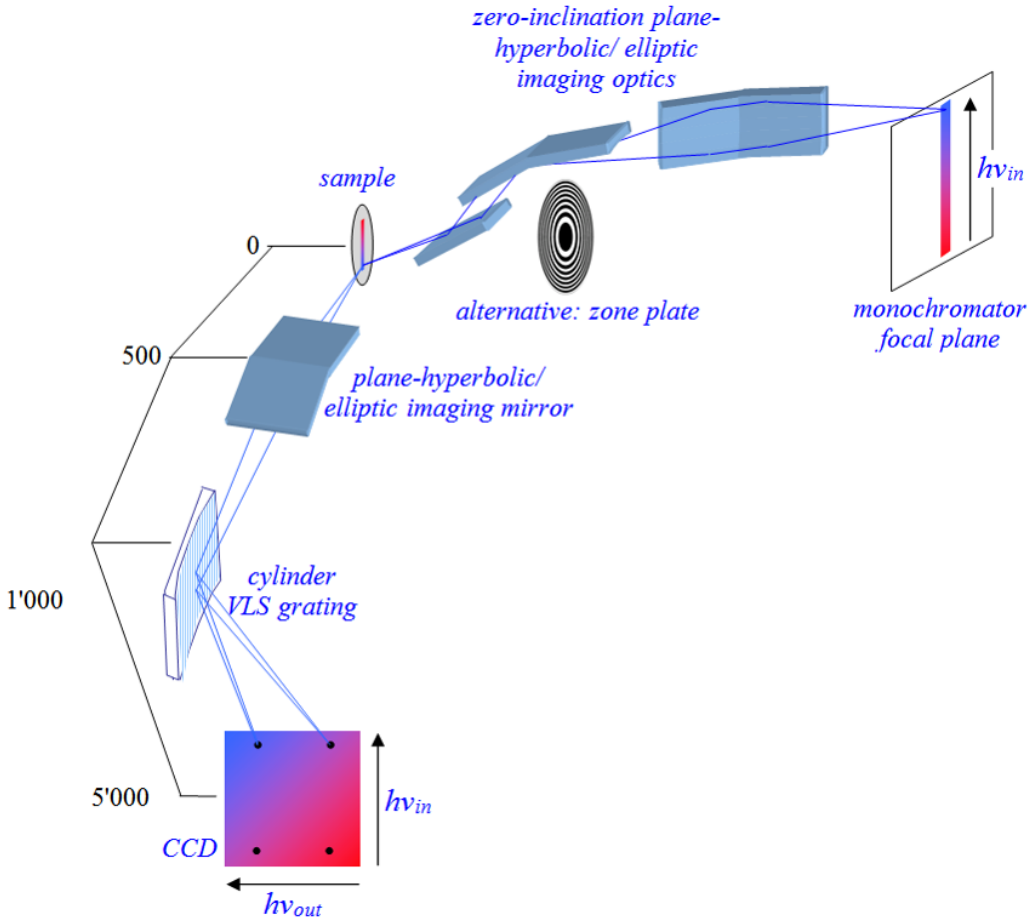

Figure 13.8: Concept of an imaging type $h\nu^2$ VLS-RIXS spectrometer with cylindrical gratings and horizontal plane-hyperbolic/elliptic imaging mirror and different refocusing options.

the intensity loss when pushing RIXS to higher energy resolution. However, it is important to consider that the momentum scanning and the projection of the horizontal image size at the sample, determining the energy resolution of the spectrometer, are coupled in the $h\nu^2$ spectrometer, which is a practical limitation of this concept for momentum-resolved RIXS. It should be noted that all non-momentum resolved RIXS applications would not suffer from such limitations as those would be operated mostly in fixed angular geometries between the incident and scattered beam. However, the realization of such a $h\nu^2$ RIXS instrument would require a significant research and development effort stretching well beyond the SLS 2.0 upgrade period.

13.5.3 EEHG upgrade option

Echo Enabled Harmonic Generation (EEHG) is a scheme to produce coherent radiation by converting a short laser pulse to high harmonics of the laser wavelength. This technique has been demonstrated at FELs and studies for its use in storage rings have already been performed. The implementation

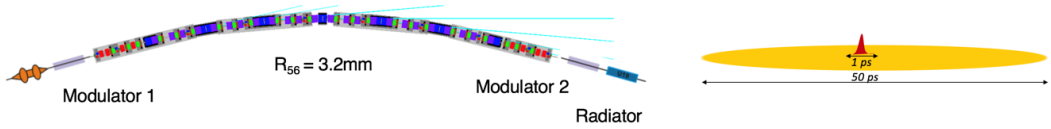

Figure 13.9: Left: EEHG scheme at SLS 2.0. The first modulator is located in Straight 1, i.e. together with a cavity. The second modulator and the radiator are located in the second straight. Right: The electrons are modulated only in the small fraction of the electron bunch that overlaps in time with the optical laser, allowing time-resolved measurements.

of EEHG requires two modulators (modulator 1 and 2 in left panel of Figure 13.9) for the energy modulation of the electrons with an external laser, each followed by a dispersive section, which rotates the phase space. The last element of this EEHG configuration is the radiator, which is an undulator matched to the photon energies to be emitted (see Figure 13.9). Unique for SLS 2.0 is that one can take the arc between the two straight sections as the first strong dispersive section, which avoids emittance blowup inherent to an additional chicane. It also saves significant space, because its R56 matches nicely the operating range of the EEHG scheme in the soft x-ray regime. The second chicane can be weak, which makes a phase-matcher between modulator 2 and the radiator a viable option.

The result of such an EEHG scheme would be a modulation of the electron density inside the bunch of about 5% at the resonant undulator wavelength which results in an increase in peak brilliance by 5 to 6 orders of magnitude. The pulse length of the laser and that of the coherent radiation has to be 1 ps or less to achieve repetition rates of up to 1 MHz needed to keep the increase of the overall energy spread in the beam reasonably low (see right panel of Figure 13.9). Therefore, EEHG at the proposed SLS 2.0 RIXS beamline would enable time-resolved measurements in the 1 ps range, being thus nicely complementary to the SwissFEL ATHOS beamline. For a 266 nm seed laser, the number of photons per pulse (1 ps) at the central photon energy of 1.24 keV will be about 2.4×10^7. Moreover, as the energy bandwidth will be in the range of 3.2×10^{-6}, the monochromator could be bypassed for experiments in EEHG operation mode.

In the longer perspective towards 2035, it is envisioned to extend the new SLS 2.0 RIXS beamline with such an EEHG source. This would allow time-resolved RIXS experiments with 1 ps to ultimately 100 fs time resolution. It would also operate at a resolving power of 3×10^5, i.e. the monochromator could be equipped with bypassing mirrors with very high transmission when having the EEHG mode switched on, thereby preserving the very high peak brilliance of the source. This would uniquely enable pump-probe soft x-ray RIXS experiments at a synchrotron and would be ideally complementary to time-resolved RIXS at the Furka station of the Athos line of Swiss-FEL with 1 to 10 fs time resolution. Such a source would need to be switchable between normal undulator mode for static experiments and EEHG mode for time-resolved RIXS experiments.

13.6 IT, controls, and data system

The beamline instruments will be interfaced to EPICS, through drivers developed by the community or in-house. This allows us to deploy generic utility programs during beamline commissioning, as well

as in operation. The addition of various surveillance/diagnostic cameras and fast updating EPICS data has imposed higher network throughput requirements. It is thus desirable to have all PCs with 10 GBit capable Ethernet connections.

It is important that the EPICS drivers/tools are maintained for the future. The current detector system consists of 3 CCD chips, which typically produce data at 3-4 MB/s. If this data is saved, it requires more than 250 GB per day. Because we perform online analysis of the 2D images, in which we record the event positions instead of saving complete images and directly produce 1D RIXS spectra, the amount of storage required is dramatically reduced. The current analysis is able to explore the full CPU power using multi-thread techniques. Towards SLS 2.0, it is initially not foreseen to change the detector system. However, future detector systems are envisioned to take similar advantage of data reduction strategies. Nevertheless from our experience, a file server with improved throughput and reliability would be beneficial.

13.7 Timeline

Time period	Main Activities
January 2020 - June 2021	Technical design and CAD
July 2021 - September 2023	Procurement and in-house manufacturing
October 2023 - September 2024	Installation of modified infrastructure, new beamline and endstation
October 2024 - March 2025	Commissioning phase
April 2025 - June 2025	Pilot user phase
July 2025	Regular user operation

Table 13.3: Planning and installation phases of the new SLS 2.0 RIXS beamline.

13.8 Concluding remarks

In summary, we have described the CD of two upgrade scenarios for the future soft x-ray RIXS facility at SLS 2.0. Both upgrade paths employ optical elements with ultralow slope errors for beamline and spectrometer, and take full advantage of the low horizontal emittance of SLS 2.0, enabling the construction of beamlines with significantly increased entrance arms, thereby pushing the achievable energy resolution. Such instrumental upgrades are vital for PSI to stay at the forefront of RIXS for years to come, and will significantly improve the energy resolution of RIXS in order to reveal the low-energy properties of new quantum materials and their application potential in future electronic devices as well as for information technology. The priority suggested is to build a new state-of-the-art RIXS beamline with a triple-axis VLS spectrometer and continuous rotation chamber as well as a polarimeter for the polarization analysis of the emitted x-rays. The stages for realizing such a facility are: a medium upgrade (a) with a ca. 38 meter long VLS-PGM beamline inside the SLS building with a 10 meter spectrometer and an ultimate upgrade (b) with a ca. 98 meter long VLS-PGM beamline

with a 15 meter spectrometer in an extension hall outside of the SLS building. These scenarios can be extended by submicron to 100 nm focusing options in an additional endstation to enable spatially resolved RIXS on inhomogeneous quantum materials and devices. In the perspective towards 2035, we suggest to combine this ultimate resolution facility with an EEHG source for soft x-rays, enabling an additional operation mode for time-resolved RIXS with 1 ps time resolution and ultimate energy resolution from the source of up to a resolving power of 3×10^5.

Bibliography

[1] M. Le Tacon, G. Ghiringhelli, J. Chaloupka, M. Moretti Sala, V. Hinkov, M. W. Haverkort, M. Minola, M. Bakr, K. J. Zhou, S. Blanco-Canosa, C. Monney, Y. T. Song, G. L. Sun, C. T. Lin, G. M. De Luca, M. Salluzzo, G. Khaliullin, T. Schmitt, L. Braicovich, and B. Keimer. Intense paramagnon excitations in a large family of high–temperature superconductors. *Nat. Phys.*, 7:725–730, 2011.

[2] Ke-Jin Zhou, Yao-Bo Huang, Claude Monney, Xi Dai, Vladimir N. Strocov, Nan-Lin Wang, Zhi-Guo Chen, Chenglin Zhang, Pengcheng Dai, Luc Patthey, Jeroen van den Brink, Hong Ding, and Thorsten Schmitt. Persistent high–energy spin excitations in iron pnictide superconductors. *Nat. Comm.*, 4:1470, 2013.

[3] Jonathan Pelliciari, Kenji Ishii, Yaobo Huang, Marcus Dantz, Xingye Lu, Paul Olalde-Velasco, Vladimir N. Strocov, Shigeru Kasahara, Lingyi Xing, Xiancheng Wang, Changqing Jin, Yuji Matsuda, Takasada Shibauchi, Tanmoy Das, and Thorsten Schmitt. Reciprocity between local moments and collective magnetic excitations in the phase diagram of $BaFe_2(As_{1x}P_x)_2$. *Commun. Phys.*, 2:139, 2019.

[4] O. Ivashko, M. Horio, W. Wan, N.B. Christensen, D.E. McNally, E. Paris, Y. Tseng, N.E. Shaik, H.M. Rnnow, H.I. Wei, C. Adamo, C. Lichtensteiger, M. Gibert, M.R. Beasley, K.M. Shen, J.M. Tomczak, T. Schmitt, and J. Chang. Strain-engineering Mott-insulating La_2CuO_4. *Nat. Comm.*, 10:786, 2019.

[5] M. P. M. Dean, R. S. Springell, C. Monney, K. J. Zhou, J. Pereiro, I. Boovic, B. Dalla Piazza, H. M. Roennow, E. Morenzoni, J. van den Brink, T. Schmitt, and J. P. Hill. Spin excitations in a single La_2CuO_4 layer. *Nat. Mat.*, 11:850–854, 2012.

[6] L. Braicovich, J. van den Brink, V. Bisogni, M. Moretti Sala, L. J. P. Ament, N. B. Brookes, G. M. De Luca, M. Salluzzo, T. Schmitt, V.N. Strocov, and G. Ghiringhelli. Magnetic excitations and phase separation in the underdoped $la_{2-x}sr_xcuo_4$ superconductor measured by resonant inelastic x–ray scattering. *Phys. Rev. Lett.*, 104:077002, 2010.

[7] W. S. Lee, J. J. Lee, E. A. Nowadnick, W. Tabis, S. W. Huang, V.N. Strocov, E. M. Motoyama, G. Yu, B. Moritz, M. Greven, T. Schmitt, Z. X. Shen, and T. P. Devereaux. Asymmetry of collective excitations in electron and hole doped cuprate superconductors. *Nat. Phys.*, 10:883–889, 2014.

[8] G. Ghiringhelli, M. Le Tacon, M. Minola, S. Blanco-Canosa, C. Mazzoli, N. B. Brookes, G. M. De Luca, A. Frano, D. G. Hawthorn, F. He, T. Loew, M. Moretti Sala, D. C. Peets, M. Salluzzo, E. Schierle, R. Sutarto, G. A. Sawatzky, E. Weschke, B. Keimer, and L. Braicovich. Long-range incommensurate charge fluctuations in (y,nd)$ba_2cu_3o_{6+x}$. *Science*, 337:821–825, 2012.

[9] L. Das, F. Forte, R. Fittipaldi, C.G. Fatuzzo, V. Granata, O. Ivashko, M. Horio, F. Schindler, M. Dantz, Yi Tseng, D.E. McNally, H.M. Roennow, W. Wan, N.B. Christensen, J. Pelliciari, P. Olalde-Velasco, N. Kikugawa, T. Neupert, A. Vecchione, T. Schmitt, M. Cuoco, and J. Chang. Spin–orbital excitations in ca_2ruo_4 revealed by resonant inelastic x–ray scattering. *Phys. Rev. X*, 8:011048, 2018.

[10] Daniel E. McNally, Xingye Lu, Jonathan Pelliciari, Sophie Beck, Marcus Dantz, Muntaser Naamneh, Tian Shang, Marisa Medarde, Christof W. Schneider, Vladimir N. Strocov, Ekaterina V. Pomjakushina, Claude Ederer, Milan Radovic, and Thorsten Schmitt. Electronic localization in $CaVO_3$ films via bandwidth control. *npj Quant. Mater.*, 4:6, 2019.

[11] Thorsten Schmitt, Vladimir N. Strocov, Ke-Jin Zhou, Justine Schlappa, Claude Monney, Uwe Flechsig, and Luc Patthey. High-resolution resonant inelastic X-ray scattering with soft X-rays at the ADRESS beamline of the Swiss Light Source: Instrumental developments and scientific highlights. *Journal of Electron Spectroscopy and Related Phenomena*, 188:38–46, 2013.

[12] Valentina Bisogni, Sara Catalano, Robert J. Green, Marta Gibert, Raoul Scherwitzl, Yaobo Huang, Vladimir N. Strocov, Pavlo Zubko, Shadi Balandeh, Jean-Marc Triscone, George Sawatzky, and Thorsten Schmitt. Ground–state oxygen holes and the metal-insulator transition in the negative charge-transfer rare–earth nickelates. *Nat. Comm.*, 7:13017, 2016.

[13] J. Schlappa, T. Schmitt, F. Vernay, V.N. Strocov, V. Ilakovac, B. Thielemann, H.M. Roennow, Vanishri S, A. Piazzalunga, X. Wang, L. Braicovich, G. Ghiringhelli, C. Marin, J. Mesot, B. Delley, and L. Patthey. Collective magnetic excitations in the spin ladder $sr_{14}cu_{24}o_{41}$ measured using high-resolution resonant inelastic x–ray scattering. *Phys. Rev. Lett.*, 103:047401, 2009.

[14] J. Schlappa, K. Wohlfeld, K. J. Zhou, M. Mourigal, M. W. Haverkort, V. N. Strocov, L. Hozoi, C. Monney, S. Nishimoto, S. Singh, A. Revcolevschi, J.-S. Caux, L. Patthey, H. M. Roennow, J. van den Brink, and T. Schmitt. Spin-orbital separation in the quasi–one–dimensional Mott insulator Sr_2CuO_3. *Nature*, 485:82–85, 2012.

[15] J. Schlappa, U. Kumar, K. J. Zhou, S. Singh, M. Mourigal, V.N. Strocov, A. Revcolevschi, L. Patthey, H. M. Roennow, S. Johnston, and T. Schmitt. Probing multi-spinon excitations outside of the two-spinon continuum in the antiferromagnetic spin chain cuprate sr_2cuo_3. *Nat. Comm.*, 9:5394, 2018.

[16] Claude Monney, Valentina Bisogni, Ke-Jin Zhou, Roberto Kraus, Vladimir N. Strocov, Guenter Behr, Jiri Malek, Roman Kuzian, Stefan-Ludwig Drechsler, Steve Johnston, Alexandre Revcolevschi, Bernd Bchner, Henrik M. Roennow, Jeroen van den Brink, Jochen Geck, and Thorsten Schmitt. Determining the short–range spin correlations in the spin–chain

li$_2$cuo$_2$ and cugeo$_3$ compounds using resonant inelastic x–ray scattering. *Phys. Rev. Lett.*, 110:087403, 2013.

[17] Luuk J. P. Ament, Michel van Veenendaal, Thomas P. Devereaux, John P. Hill, and Jeroen van den Brink. Resonant inelastic x-ray scattering studies of elementary excitations. *Rev. Mod. Phys.*, 83:705, 2011.

[18] Yoshinori Tokura, Masashi Kawasaki, and Naoto Nagaosa. Emergent functions of quantum materials. *Nat. Phys.*, 13:1056–1068, 2017.

[19] Weiliang Yao, Chenyuan Li, Lichen Wang, Shangjie Xue, Yang Dan, Kazuki Iida, Kazuya Kamazawa, Kangkang Li, Chen Fang, and Yuan Li. Topological spin excitations in a three-dimensional antiferromagnet. *Nat. Phys.*, 14:1011–1015, 2018.

[20] A. Jain, M. Krautloher, J. Porras, G. H. Ryu, D. P. Chen, D. L. Abernathy, J. T. Park, A. Ivanov, J. Chaloupka, G. Khaliullin, B. Keimer, and B. J. Kim. Higgs mode and its decay in a two–dimensional antiferromagnet. *Nat. Phys.*, 13:633–637, 2017.

[21] L. Braicovich, M. Minola, G. Dellea, M. Le Tacon, M. Moretti Sala, C. Morawe, J.-Ch. Peffen, R. Supruangnet, F. Yakhou, G. Ghiringhelli, and N. B. Brookes. The simultaneous measurement of energy and linear polarization of the scattered radiation in resonant inelastic soft x–ray scattering. *Review of Scientific Instruments*, 85:115104, 2014.

[22] N.B. Brookes, F. Yakhou-Harris, K. Kummer, A. Fondacaroa, J.C. Cezara, D. Betto, E. Velez-Fort, A. Amorese, G. Ghiringhelli, L. Braicovich, R. Barretta, G. Berruyer, F. Cianciosi, L. Eybert, P. Marion, P. van der Linden, and L. Zhang. The beamline ID32 at the ESRF for soft X-ray high energy resolution resonant inelastic X–ray scattering and polarisation dependent X-ray absorption spectroscopy. *Nuclear Inst. and Methods in Physics Research A*, 903:175–192, 2018.

[23] Pasquale Marra, Steffen Sykora, Krzysztof Wohlfeld, and Jeroen van den Brink. Resonant inelastic x–ray scattering as a probe of the phase and excitations of the order parameter of superconductors. *Phys. Rev. Lett.*, 110:117005, 2013.

[24] K. M. Lang, V. Madhavan, J. E. Hoffman, E. W. Hudson, H. Eisaki, S. Uchida, and J. C. Davis. Imaging the granular structure of high-Tc superconductivity in underdoped $Bi_2Sr_2CaCu_2O_{8+\delta}$. *Nature*, 415:412–416, 2002.

[25] G. Campi, A. Bianconi, N. Poccia, G. Bianconi, L. Barba, G. Arrighetti, D. Innocenti, J. Karpinski, N. D. Zhigadlo, S. M. Kazakov, M. Burghammer, M. v. Zimmermann, M. Sprung, and A. Ricci. Inhomogeneity of charge-density-wave order and quenched disorder in a high-Tc superconductor. *Nature*, 525:359–362, 2015.

[26] S. Lupi, L. Baldassarre, B. Mansart, A. Perucchi, A. Barinov, P. Dudin, E. Papalazarou, F. Rodolakis, J. P. Rueff, J. P. Iti, S. Ravy, D. Nicoletti, P. Postorino, P. Hansmann, N. Parragh, A. Toschi, T. Saha-Dasgupta, O. K. Andersen, G. Sangiovanni, K. Held, and M. Marsi. A

microscopic view on the Mott transition in chromium–doped V_2O_3. *Nat. Comm.*, 1:1056–1068, 2010.

[27] R. Reininger. The in-focus variable line spacing plane grating monochromator. *Nuclear Inst. and Methods in Physics Research A*, 649:139–143, 2011.

[28] V.N. Strocov, T. Schmitt, U. Flechsig, T. Schmidt, A. Imhof, Q. Chen, J. Raabe, R. Betemps, D. Zimoch, J. Krempasky, X. Wang, M. Grioni, A. Piazzalunga, and L. Patthey. High-resolution soft-X-ray beamline ADRESS at Swiss Light Source for resonant inelastic X-ray scattering and angle-resolved photoelectron spectroscopies. *J. Synchrotron Rad.*, 17:631, 2010.

[29] G. Ghiringhelli, A. Piazzalunga, C. Dallera, G. Trezzi, L. Braicovich, T. Schmitt, V. N. Strocov, R. Betemps, L. Patthey, X. Wang, and M. Grioni. SAXES, a high resolution spectrometer for resonant x-ray emission in the 400 eV to 1600 eV energy range. *Rev. Sci. Instrum.*, 77:113108, 2006.

[30] V.N. Strocov, T. Schmitt, U. Flechsig, L. Patthey, and S. G. Chiuzbaian. Numerical optimization of spherical variable-line-spacing grating x-ray spectrometers. *J. Synchrotron Rad.*, 18:134, 2011.

[31] Joseph Dvorak, Ignace Jarrige, Valentina Bisogni, Scott Coburn, and William Leonhardt. Towards 10 meV resolution: The design of an ultrahigh resolution soft X–ray RIXS spectrometer. *Review of Scientific Instruments*, 87:115109, 2016.

[32] V. N. Strocov. Concept of a spectrometer for resonant inelastic X-ray scattering with parallel detection in incoming and outgoing photon energies. *J. Synchrotron Rad.*, 17:103–106, 2010.

[33] T. Warwick, Y.-D. Chuang, D. L. Voronov, and H. A. Padmore. A multiplexed high-resolution imaging spectrometer for resonant inelastic soft X-ray scattering spectroscopy. *J. Synchrotron Rad.*, 21:736–743, 2014.

Chapter 14

Operando x-ray spectroscopy and scattering for chemistry beamline suite

Adam Clark, Stephan Hitz, Maarten Nachtegaal, Olga Safonova, Roelof van Silfhout, Grigory Smolentsev, and Urs Vogelsang

In a nutshell

In the last decade, the SuperXAS beamline team has been providing and further developing x-ray spectroscopic methods, which provide insights in the time-resolved local geometric, as well as the full electronic structure-function/performance relationships of functional materials under their true operating (operando) conditions. The SuperXAS beamline is world leading in QEXAFS, which allows the continuous collection of full EXAFS spectra within 10 ms and is one of the drivers in the developments of new x-ray emission spectrometers as well as laser pumpprobe XAS spectroscopy in the nano- to millisecond regime.
To maintain our leading role in the field and serve the needs of a large (Swiss) chemistry user community (both academic and industrial), two hard x-ray beamlines for operando studies will be available at SLS 2.0. The SuperXAS beamline will keep its leading position in QEXAFS and be further upgraded with the development of a new x-ray emission spectrometer allowing pump-probe XES experiments. An additional beamline, the Debye beamline, recently funded by the ETH domain, will already be added to the SLS 2.0 portfolio before the upgrade. This beamline will combine high-throughput QEXAFS with XRD and total-scattering experiments in the forward direction on the same sample. With this newly designed instrument, to be operated under a new rapid-access user model, and the upgraded SuperXAS beamline, a unique x-ray tool-set for chemical research will be available at SLS 2.0. Both beamlines capitalize on the developments of a new tunable superconducting bending magnet, which will allow experiments up to 50 keV. With these two unique hard x-ray beamlines, PSI will remain at the forefront of operando studies for the chemistry community.

14.1 Overview

Chemistry is an enabling foundation of modern society, directly contributing to economic growth and life quality. Despite only ranking 99$^{\text{th}}$ in terms of world population, Switzerland is the 8$^{\text{th}}$ largest chemical supplier. However, the chemical industry is undergoing a sea change, as it needs to simultaneously adapt to the shifting global economy, a complete change in availability and efficient use of resources, massively reducing the effects on the environment, and swiftly evolving advanced healthcare needs. Furthermore, the Swiss Federal Council has launched the Energy Strategy 2050 [1], which aims to develop new technologies for efficient production, storage, and use of renewable energy sources (replacing both fossil fuels and nuclear sources) while at the same time reducing the environmental impact. Catalysis is a powerful facilitator in overcoming these emerging pressures. Several initiatives have been launched by the ETH domain to provide the knowledge basis for this. The operando spectroscopy team is involved in these initiatives; one is the national competence center of research (NCCR) 'Sustainable Chemical Processes Through Catalysis, which will run for the next 12 years. Another initiative is the 'Catalysis Hub, which together with SLS 2.0, was successfully funded this year.

The SuperXAS beamline, in operation since 2008, is dedicated to hard x-ray absorption and emission spectroscopy (XAS and XES). At SuperXAS, XAS and XES have proven to be particularly suitable for uncovering structure-activity relationships in energy materials, such as (photo-), (electro-) catalysts and batteries [2–4]. Importantly, structural features of these materials can be revealed under real working conditions (so-called operando): under electrical potential, during charging, and/or during a catalytic reaction. This knowledge is essential to rationally design new materials and processes [5]. In such studies, both enhanced chemical sensitivity (achieved by better resolving x-ray emission spectrometers) and time resolution are crucial. Tunable time resolution is required to probe each material or process at time scales relevant to the specific application, ranging from slow degradation processes (for example, in batteries) to fast photo-activation of photo-catalysts.

The SuperXAS beamline hosts a unique combination of standard and in-house developed methods, including x-ray absorption near-edge structure (XANES), extended x-ray absorption fine structure (EXAFS), non-resonant and resonant XES, hard x-ray resonant inelastic x-ray scattering (RIXS) and a technique we put on the map: high energy resolution off-resonance spectroscopy (HEROS) [6]. XAS provides information on the projected empty density of states of the element of interest and identifies the type of nearest-neighbour atoms, their number, symmetry and bond distances. XES provides insights into the occupied density of states, where especially the weak valence-to-core transitions (vtc-XES) provide essential chemical information about the nature of nearest neighbors and their coordination. Hard x-ray RIXS (alternatively called resonance XES or RXES) combines XAS with XES at resonance energy, thus providing a complete picture of the projected density of states. The ability of SuperXAS to collect XAS spectra in a few milliseconds (quickXAS) is world leading and allows one to follow rates of chemical reactions (including identification of the structure of reaction intermediates). Finally, the laser-lab (hosting a femtosecond laser and an optical parametric amplifier, OPA) in combination with a unique data-acquisition system enables laser-pump-x-ray-probe XAS experiments in the ns to μs time range, complementary to the fs to ps range available at SwissFEL.

To remain at the forefront of hard x-ray spectroscopy beamlines after the SLS 2.0 upgrade, Su-

perXAS plans to make x-ray emission spectroscopy available for pump-probe studies, thereby enhancing the chemical sensitivity of time-resolved studies. After the upgrade, pump-probe non-resonant XES will become available in the ns to μs time range, providing additional insights in the time-evolution of occupied density of states. QuickRIXS with ms time resolution will be developed to obtain a complete picture of the electronic structure of the element of interest during a chemical process. The time required for the measurements of weak vtc-XES spectra will decrease by a factor of 100. Developing these methods requires a high-field bending magnet, a reduction of the focal spot on the sample down to 30×30 μm^2, implementation of a high-bandwidth multilayer monochromator, installation of a continuously scanning four-bounce monochromator, and an upgrade of the laser infrastructure.

To address the increasing need for operando studies by the chemistry community, we recently obtained funding (period 2021-2023) from the ETH domain to build an additional beamline for x-ray absorption spectroscopy combined with high-energy scattering experiments (XRD and PDF in the forward direction) on a superbend port. This beamline will experiment with providing a regular and rapid access model to serve the chemistry community with standardized operando x-ray analysis methods in a timely matter. The technical design work, including ray-tracing studies, have just started for this beamline. In general a large commonality in optical layout between both beamlines is anticipated.

14.1.1 Uniqueness compared to other present and planned beamlines worldwide

Quick XAS (with a sub-second time resolution) became for the first time worldwide permanently integrated at the SuperXAS beamline more than a decade ago. This technique is now implemented at other synchrotron facilities (TPS 44A, PETRA III P64, SOLEIL ROCK), with the SuperXAS still offering the best reported time-resolution. The SuperXAS beamline is currently being upgraded with a newly developed monochromator that will uniquely allow the possibility to scan simultaneously multiple absorption edges, while keeping the same spatial position on the sample (thanks to the recent development of a direct drive quick-scanning four-bounce monochromator, including a modern regulated driving control concept). Additionally, recent advancements in time-resolved quick fluorescence XAS have been demonstrated recently at the SuperXAS beamline, uniquely providing sub-second time resolution on dilute chemical systems, a particular advantage for the studies of batteries, fuel cells, electrolyzers and catalysts. With these pioneering developments, the SuperXAS beamline will remain worldwide leading for Quick XAS studies.

We will maintain our capabilities for XAS-based techniques which currently form the core of our activities and output and for which we have highly-optimized setups: steady-state XAS, pump-probe XAS in the nanosecond-microsecond time range, and quick XAS under in-situ or in-operando conditions.

X-ray emission spectroscopy (XES) is complementary to XAS and has been implemented at many synchrotron facilities in the last decade, with the von Hamos geometry (allowing single shot XES) being introduced by the SuperXAS beamline team. Nevertheless, instruments for XES at energies above 15 keV are not currently available at synchrotrons. We are currently developing such a spectrometer and have the first version of it established at the SuperXAS beamline. For time-resolved non-resonance XES, the lower incident beam flux in comparison to undulator beamlines can be compensated by using

the high flux of pink beam or broadband beam (with approximately 5% bandwidth) from a multilayer crystal. The development of a cylindrical XES spectrometer, which increases the solid angle by a factor 15 will give access to sub-second XES as well as pump-probe XES in the ns to ms time range.

Pump-probe XES experiments with $\sim$ 100 ps resolution have been demonstrated at 7ID of APS and ID26 of ESRF by experienced users bringing their own hardware (lasers or XES spectrometers); such experiments are also under development at ID09 of ESRF, but experiments in the microsecond range have not been demonstrated so far. Only pump-probe XAS in the microsecond range is performed regularly at SuperXAS and at 11ID-D of APS. Pump-probe XES with microsecond delays has been demonstrated at the LCLS x-ray free electron laser. At first glance the boost of the repetition rate of XFELs (up to 4.5 MHz within the burst for European XFEL, 1 MHz for LCLS-II-HE and SHINE XFEL (after 2025)) will make experiments in the microsecond time range efficient using a sequence of pulses to measure kinetics. Nevertheless, experiments at existing XFELs show that short pulses of XFELs disturb the sample so much that it is impossible to irradiate the same sample volume with multiple x-ray pulses and ultrafast sample replacement between two x-ray pulses is needed. Therefore, we do not expect a revolution for experiments in the microsecond time range induced by the development of high repetition rate XFELs. Consequently, SuperXAS will be a leading beamline for pump-probe XES and XAS in the microsecond time-range.

Finally, the combination of the new cylindrical XES spectrometer with quick XAS will allow quick resonant x-ray emission spectroscopy (quick RXES): a potential powerful techniques for which we will have unique capabilities at SLS 2.0 and which has not been demonstrated at any other synchrotron. For quick RXES only few beamlines worldwide have capabilities to perform quick energy scans and at the same time have (or still developing) emission spectrometers in dispersive geometry. These are P64 at PETRAIII, CLAESS at ALBA and Balder at MAX IV. Besides these two components, Quick RXES requires a fast detector (with readout at MHz frequency or with event-based readout) and a data acquisition system, which synchronize monochromator and detector. To the best of our knowledge, none of these beamlines plan to implement fast 2D detectors to realize QuickRXES with sub-second resolution.

14.1.2 Complementarity to other PSI BLs

SuperXAS is complementary to other x-ray spectroscopy beamlines at SLS 2.0, including Phoenix (XAS and XES in the tender x-ray range) and microXAS (chemical imaging). The scheme developed for pump-probe XAS and XES at SuperXAS (including lasers) is spread out to the Phoenix and microXAS beamlines and is complementary to the Alvra facility at SwissFEL. This allows detection of XAS and XES in a complementary time regime as offered at SwissFEL.

The SuperXAS team collaborates with a large number of chemistry research groups from Swiss Universities, Industries and the ETH domain, and is matrixed with the Energy and Environment research division at PSI. This led to the development of world-wide unique operando setups for studying catalysts, batteries, fuel cells and electrolyzes by spectroscopic, scattering and imaging methods. Moreover, large research initiatives in energy and sustainable chemistry research on the national level, including the newly funded Catalysis Hub at ETH and EPFL, NCCR Catalysis, and SynFuel at PSI and EMPA require the use of the SuperXAS (and Debye) beamlines and will further increase the user

base and demand for beamtime.

14.1.3 Size and impact of community – potential increase through the upgrade

SuperXASs 10 year average overbooking factor is about 2.1 and has an average of 38 accepted proposals per year. We expect that this overbooking factor will only increase, considering the steady growth we observed in the last five years of the chemistry and energy research communities in Switzerland and worldwide. Accordingly, even with our continued push towards shortening XAS and XES acquisition times, new software tools for online data analysis, remote operation and efficient setups at both the Debye and SuperXAS beamlines, leading to significantly more beamtimes per year, this will not lead to a reduction of the overbooking factor.

14.2 Source

The 2.9 T superbend source, which was first introduced at SLS, has been the feature that made the SuperXAS beamline super, by providing a continuous flux over a large energy range (critical energy 11.9 keV). A continuous source is needed for an x-ray spectroscopy beamline where fast (in the ms-regime) scans through several keV are routinely performed to cover two to three absorption edges (3 to 5 keV) in a given scan. Thanks to the small source size, this resulted in a photon flux of 10^{11} - 10^{12} ph/s in a 100 × 100 μm^2 spot at the sample. At SLS 2.0, we will install a novel superbend, which is semi-tunable (between shutdowns one is able to switch between field strengths of 2.8 T up to 5 T). This source means that at low energies there is a reduction of the vertical divergence and thus an increase in the total acceptance; while at high energies the flux will increase by a factor of five (Figure 14.1).

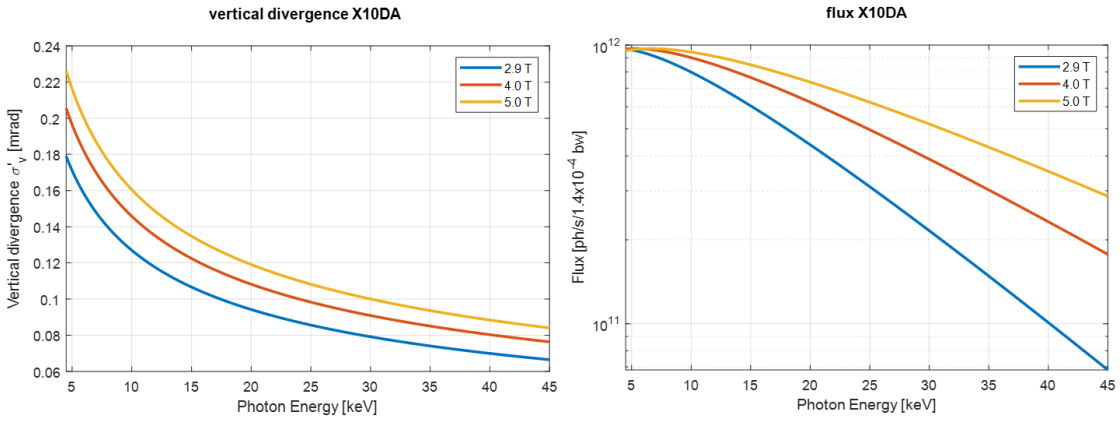

Figure 14.1: Comparison of integrated flux of the superbend dipole source for different field strengths before and after the upgrade for photon energies between 4 and 45 keV with a Si(111) monochromator and acceptance of 2 mrad horizontally. [7]

14.3 Front end

Currently, the SuperXAS front end uses a 0.1 mm thick CVD diamond window placed in the machine tunnel (5 m from the source), which seals the machine vacuum from that of the SuperXAS beamline. This low-Z material creates an attenuation of the beam at the lower energy part of the spectrum, as shown in Figure 14.2. Alternatively, one could use a Be window for better transmission at lower x-ray energies. This is currently being looked into. The use of a water-cooled filter rack is very helpful in various circumstances and it is a relatively simple device to install. Together with the use of x-ray mirrors with different coatings a very effective energy filter is created that helps to keep the heat load down on optical components and prevent higher harmonics from reaching the sample. Ideally, the filters are made of different materials and thicknesses so that the beam can be attenuated by well-known factors. Materials suitable for filters include: aluminium, graphite, glassy carbon (Sigradur K & G – http://www.htw-germany.com), and CVD diamond (http://www.diamond-materials.com).

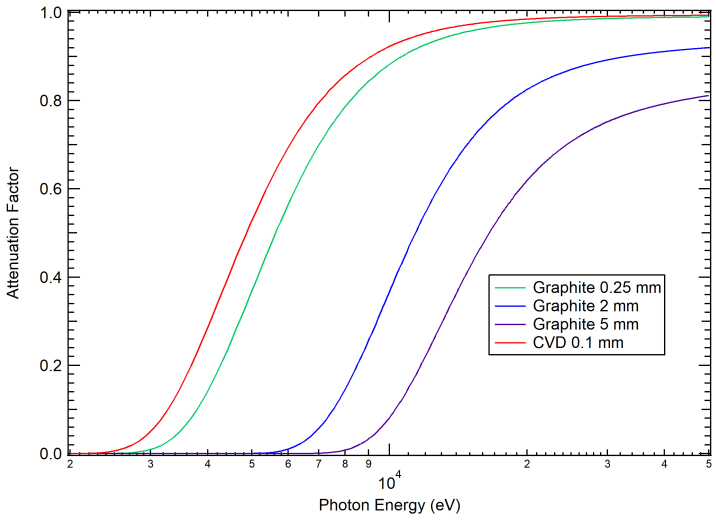

Figure 14.2: The attenuation factor from several elements used in the beamline in the form of vacuum windows and filters as a function of photon energy. Aluminium is only used if photon energies above 20 keV are required.

Particularly for the high-energy side of the spectrum in which the mirrors become less useful, the filters take on the job of effectively reducing the heat load on the monochromator. Also for alignment purposes, the ability to reduce beam intensity is quite helpful, especially when working with either white or pink beam.

In the new front end design of the SuperXAS II and Debye beamlines, which mimics the one from the PX III beamline now and at SLS 2.0, the mirror tank and mirror will be replaced by an overall smaller version. Also, a novel design to define the beam size of two movable apertures will be used instead of the current slit system. These changes will lead to a more compact front end, which would fit better with the new SLS 2.0 lattice.

Table 14.1 shows a comparison of the heat load of each subsequent element under the conditions

	SuperXAS (2.9 T)	SuperXAS II (4 T)
Max. Power Density [W.mm^{-2}]	7	9
Total Power Through Fixed Aperture [W]	187	258
Absorption CVD Window [W]	69	71
Absorption Graphite [W]	11	14
Removed by slits (4.8×0.8 mm^2) [W]	90	147
Collimating Mirror Exposed [W]	17	26
Collimating Mirror Absorbed [W]	8	16
Incident on Monochromator [W]	9	10

Table 14.1: Power loads of front end beamline components that are exposed to the white beam shown before and after the SLS upgrade. The power loads were determined by XRT.

in which the collimating mirror was set at an angle of 3 mrad with a rhodium coating. The existing 0.3 mm thick CVD window will absorb about 70 W of power and removes from the beamline most x-rays with an energy below 4 keV. The white beam slits take the brunt of the power loading when set at their regular setting as indicated.

The slit setting chosen to calculate the power loading of the collimating mirror and monochromator corresponds to a transmitted fan of radiation measuring 0.75×0.125 (h $\times$ v) mrad^2 and is currently a default setting at SuperXAS. The optical system downstream of the slits is capable of accepting a larger fan of up to 1×0.5 (h $\times$ v) mrad^2. Although the collimating mirror can collect the full horizontal fan of 2.8 mrad, the limit of about 1 mrad is determined by the existing toroidal mirror (see Section 14.4.3). In Table 14.1 the expected power loading and resulting flux at the sample are given for a set of white beam slit settings, as derived from ray tracing calculations [8].

Slit settings [h $\times$ v mrad^2]	0.75×0.125	0.75×0.25	0.75×0.32	1×0.32	2×0.32
Exposing collimating mirror [W]	26	39	44	57	112
Absorbed by mirror [W]	16	21	23	30	59
Absorbed by monochromator [W]	10	18	20	27	53
Flux at 12 keV [ph s^{-1}]	5x10^{11}	7x10^{11}	9x10^{11}	1.0x10^{12}	1.2x10^{12}

Table 14.2: Power loads after the SLS upgrade for different white beam slit settings. The power loads were determined by XRT. The flux shown is measured at the sample position where the monochromatic beam (12 keV) is focused by the existing toroidal mirror. The mirrors are set at 3 mrad and are coated with Rh. Note that because the toroidal mirror can only handle horizontal fans up to 1 mrad, there is no linear increase in flux at the sample for the largest horizontal slit setting.

14.4 Optics

The different experiments envisioned at SuperXAS II require a flexible but stable optical layout. SuperXAS features a tried and tested, traditional collimating and toroidal mirror pair in a non-dispersive configuration, such that the monochromatic exit beam travels parallel to the floor. In order to cover a wide range of photon energies without harmonic contamination, the collimating and toroidal mirrors have sets of different coatings. The collimating mirror for an x-ray spectroscopy beamline is essential in order to make full use of the photon flux from the source using a double crystal monochromator with high energy resolution. The toroidal mirror allows for both horizontal and vertical focusing of the monochromatic beam at the sample position using a single optical element with a minimum of controls, thus providing easy operation of the beamline. Any modification in the existing setup will have to fit into the current footprint of the existing hutches.

An overview of the proposed SuperXAS II beamline and its main components is shown in Figure 14.3. For clarity, filters, beam shutters, beam diagnostics, sample environments and potential upgrades are not presented. The proposed design features ease of operation across the full energy range whilst taking full advantage of the expected increase of brilliance without compromising the high-energy resolution necessary for spectroscopy. The layout shown matches that of the existing SuperXAS facility with the addition of a KB micro-focusing setup. This has been added to provide the option to attain the focal spot size required for pump-probe experiments of 30×30 μm^2 or smaller. The choice for an optional KB system is guided by the requirement that such post-focusing optics are achromatic and feature a reasonable numerical aperture.

The configuration shown has an up-up-down-down deflection geometry that provides an effective way of blocking Bremsstrahlung using a beam stop downstream of the first monochromator crystal. A detailed description of each beamline component is given in the following sections. The sample position is variable to lend flexibility in the sample environments and additional equipment. When using the toroidal mirror, the focus will be located at about 23 m, which is between a 1:1 and 2:1 demagnification of the source.

The general layout requires two lead-lined hutches: one optical hutch (10 - 18 m) and one experimental hutch downstream of the optical hutch (18 - 30 m) with space for control cabins and sample preparation at the back of the experimental hutch (30 - 40 m). Currently it is assumed that the old hutches will remain at SLS 2.0.

14.4.1 Vertically collimating mirror (VCM)

The first optical element that is exposed to the pink beam is a vertically collimating mirror (VCM), which is capable of collecting the white beam cone as transmitted through the front-end mask. The VCM has three functions:

- Removing high-energy photons (harmonics) which adversely affect spectroscopy measurements;
- Reducing the heat load on the monochromator with a low-pass filter;
- Collimating the incident beam to provide a better energy resolution.

For Si(111) monochromator crystals, the strongest harmonics are the third order ones. Therefore, starting at 4 keV photon energy, the first cut-off energy should be set below 12 keV (less than triple

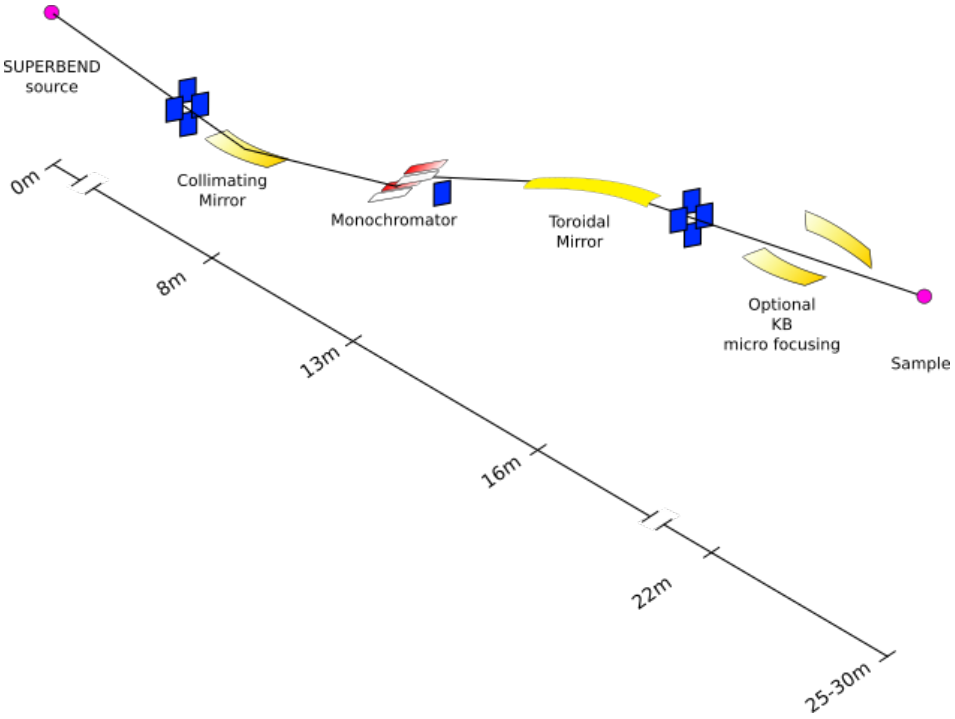

Figure 14.3: Proposed spectroscopy beamline layout, only key optical components are shown (not to scale). A KB micro-focusing system would be placed in the experimental hutch. Various slit systems and a white beam stop are shown in blue.

the desired photon energy). A second cut-off set below 30 keV is then required for higher energy x-ray edges. Matching these cut-offs with suitable mirror coatings and usable incident angles of the beam with the mirror, one can identify three energy ranges: Si: 4 - 10 keV, Rh: 10 - 20 keV, and Pt $>\sim$ 20 keV. In order to cover the full energy range, one can readily distinguish three sub-ranges for which a different mirror coating or angle of incidence must be chosen (see Table 14.3).

For experiments with radiation at the upper end of the usable energy range (30 - 45 keV), the Pt-coating must be used at a reduced angle of 2 mrad. The angular change from 3 to 2 mrad results in height changes of monochromator, toroidal mirror/sample of 15.7 and 8.2 mm, respectively. Alternatively, it would also be possible to operate without the use of the toroidal mirror (denoted by - in Table 14.3) for high-energy experiments.

Figure 14.4 shows the reflectance of a single reflection of a coated mirror with suitable angles of incidences for each coating type in order to achieve the above listed three photon energy ranges. Besides Si and Rh coatings, a Pt coating would be required for the higher range of energies. A compromise with this choice is that Pt absorption edges appear in the reflected beam around 11 keV causing an effective reduction in the reflectivity of the mirror at higher energies. Note that the calculation represents the reflectivity for one mirror only. With a second (focusing) mirror, the reflectivity for a Pt coating would be approx. $0.85^2 = 0.72$.

Capturing the full horizontal divergence (limited to 2.8 mrad by a white beam aperture) with

Photon Energy (keV)	VCM Coating	Angle of Incidence (mrad)
4 - 10	Si	3
10 - 20	Rh	3
20 - 30	Pt	2.5
> 30	-/Pt	2

Table 14.3: Mirror coating selection and angle of incidence used for the different energy regions that are measured at the beamline.

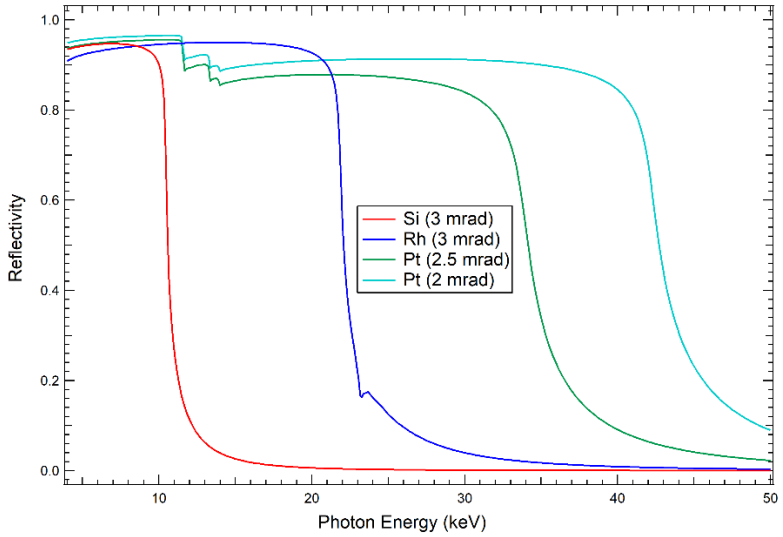

Figure 14.4: Mirror coating and angle of incidence for creating energy cut-offs at 10, 20 and >30 keV. The calculated reflectivity of each coating is for a single reflection, whereas the beamline generally will use two mirrors.

the VCM located at approximately 7.7 m from the source requires coating strips with a width of approximately 25 mm.

14.4.2 Two-bounce or four-bounce channel-cut monochromator

The monochromator is the heart of any spectroscopy beamline and therefore deserves special attention. Most hard x-ray spectroscopy monochromators use a non-dispersive two crystal arrangement as shown in Figure 14.5(a). Such a setup is non-dispersive because an incoming ray, which deviates from the central ray at angle θ by $\Delta\theta$ on the first crystal, will also deviate by $\Delta\theta$ on the second. Thus, every ray passing the first crystal passes the second. The energy resolution achieved by such a setup is determined by two factors: the range of $\Delta\theta$ allowed to strike the first crystal, and the intrinsic resolution of the crystal measured by its rocking curve width.

For a dispersive arrangement shown in Figure 14.5(b) the situation is different. If a ray deviates by

$\Delta\theta$ on the first crystal, it will strike the second crystal displaced by $-\Delta\theta$. Therefore, if $\Delta\theta$ is greater than the rocking curve width, the ray will not be transmitted. In effect, the first crystal acts as a slit for the second crystal and the energy resolution is solely set by the crystal properties. The two-crystal dispersive geometry shown in Figure 14.5(b) is not practical since the exit beam will deflect strongly as the photon energy is scanned. A more practical variant with four crystals is shown in Figure 14.5(c). Here, the second and third crystal are in a dispersive arrangement.

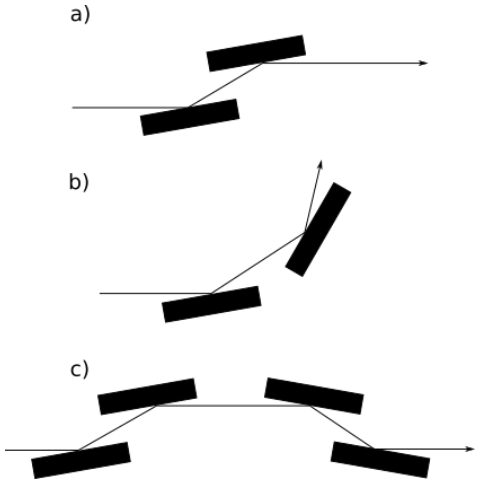

Figure 14.5: Monochromator crystal geometry for three different configurations: a) non-dispersive (+ -), b) dispersive (+ +) and c) four crystal dispersive (+ - - +)

The four-crystal variant has a further, significant advantage. If the two Bragg angle rotations are located on the surface of the first and fourth crystal, respectively, the incident white beam and exit monochromatic beam are perfectly aligned at any energy setting (true fixed-exit). This is a big benefit as long as the line of sight can be blocked between the two sets of crystals with a white beam stop made of a dense material such as tungsten or lead. The intrinsic suppression of the tails of the reflectivity curve by the multi-bounce arrangement further improves the energy resolution offered by such a solution.

So far, relatively few x-ray spectroscopy beamlines use a four-bounce crystal monochromator setup, although this arrangement was already suggested in 1937 by DuMond [9] and several interesting implementations have been published [10–13]. The reason for the modest uptake is due to the added complexity to keep the two sets of crystals perfectly aligned during energy scans. Modern precision motor control and high precision encoders have significantly simplified such tasks and the use of two channel-cut crystal sets further reduces the complexity.

The precise distance or gap between the crystal sets, photon energy range required, position and length of each crystal are interrelated. The width of the crystals is determined by the horizontal size of the beam at the position of the monochromator. A typical gap between the crystals would typically be larger than 5 mm, simply because the vertical extent of the incident beam would be similar in size.

For a channel-cut monochromator in which the crystal gap is fixed, a gap size between 6 and 8 mm is recommended. For this choice, the gap between white beam and monochromatic of 12 to 16 mm is

sufficient and can be blocked easily with a substantial beam stop. The vertical deviation of the beam height over the full energy range is limited to 1 - 1.5 mm, respectively (10.9 - 12 mm for 6 mm gap and 14.5 - 16 mm for 8 mm gap).

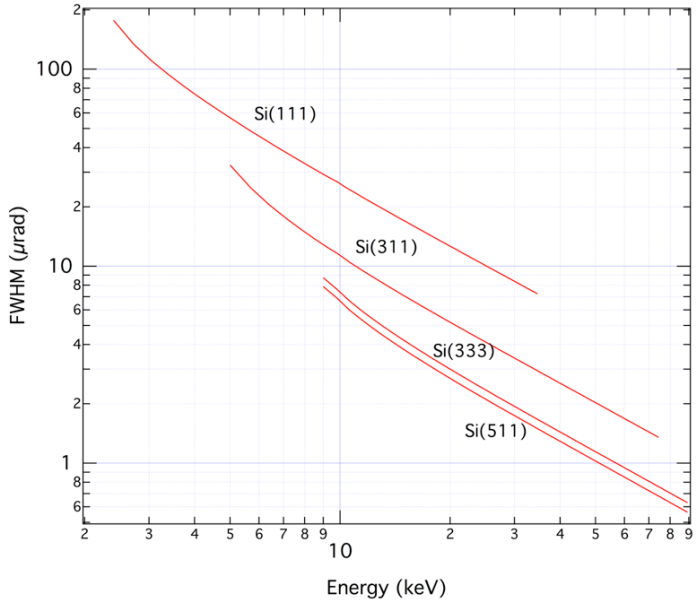

Figure 14.6: Angular Darwin width of a single silicon crystal with different orientations.

An important aspect for spectroscopy is the energy resolution of the monochromatic radiation selected by the monochromator. The inherent energy resolution of a crystal monochromator is dictated by its acceptance angle, also called the angular Darwin width. With Si(111) and Si(311) crystals available side by side in the monochromator chamber, one has access to the Si(111), Si(311) and Si(333) reflections. The Darwin width (ζ) of each reflection is shown in Figure 14.6 together with that of the Si (511) reflection for comparison. To cover the large energy range, at least two different reflections must be used. For all cases the Si(111)/Si(333) and Si(311) crystals suffice and give access to the full energy range of 4 to 50 keV. A Si(220) crystal set with a resolution between Si(111) and Si(311) was considered, but the strong second harmonic would require frequent mirror adjustments.

The Si(111) and Si(311) crystal sets provide an energy resolution of 1.3×10^{-4} and 0.5×10^{-4}, respectively. One can also opt for Si(333) without changing crystals by filtering the first harmonic of the Si(111) reflection using attenuators. For Si(333) the energy resolution is 0.3×10^{-4}. The trade-off for the higher energy resolution is a lower flux.

Stability is critical. The best performing monochromator systems have a pointing stability of about $50 - 100$ nrad. At a distance of 10 m from the monochromator, these movements would result in beam changes that are significantly smaller than the beam size. The best commercially available double crystal monochromator system reports an angular stability figure of 54 nrad and relies on an air bearing Bragg rotation axis. The SuperXAS beamline uses a channel-cut monochromator, which inherently features an excellent level of stability with high resonance frequencies due to a much reduced

complexity alignment system which consists of a single (Bragg) axis to set the photon energy.

A four-bounce liquid nitrogen cooled system consisting of two channel monochromators with synchronised Bragg motors is currently being installed at the SuperXAS beamline and will be fully compatible with SLS 2.0 space requirements and power densities. This monochromator can also be used as a conventional two bounce channel-cut monochromator where the second channel cut monochromator is moved out of the beam.

Due to the fact that it is impossible to operate the beamline with a single, fixed setting of the reflecting angle of the collimating mirror, it will be necessary to equip the monochromator with a precise, remotely controlled vertical positioning system. This system would also be of use to allow the reflected white (or pink) beam to pass the monochromator undisturbed by lowering the crystals out of the beam.

14.4.3 Focusing mirror optics

The collimated and monochromatic beam emerging from the monochromator is rather large and focusing optics are required to provide an intense beam at the sample position. Several schemes can be employed to do so, each with specific issues that merit some discussion. Due to the choice of mirror optics, several modes may be selected depending on the required beam size, energy resolution, and selection of a large coherent fraction. The options combined provide a rich palette of beamline setups that will cater for a wide variety of experiments in addition to standard spectroscopy setups that do not necessarily require a tightly focused beam. The preferred optical setup offers a variety of measurement options providing for a wide range of experiments, namely:

- Toroidal mirror focusing only
- KB focusing only
- Compound focusing

Figure 14.7 shows the various focusing options, two of which use an additional KB micro-focusing system either in combination with a toroidal mirror and a secondary source aperture, or alone.

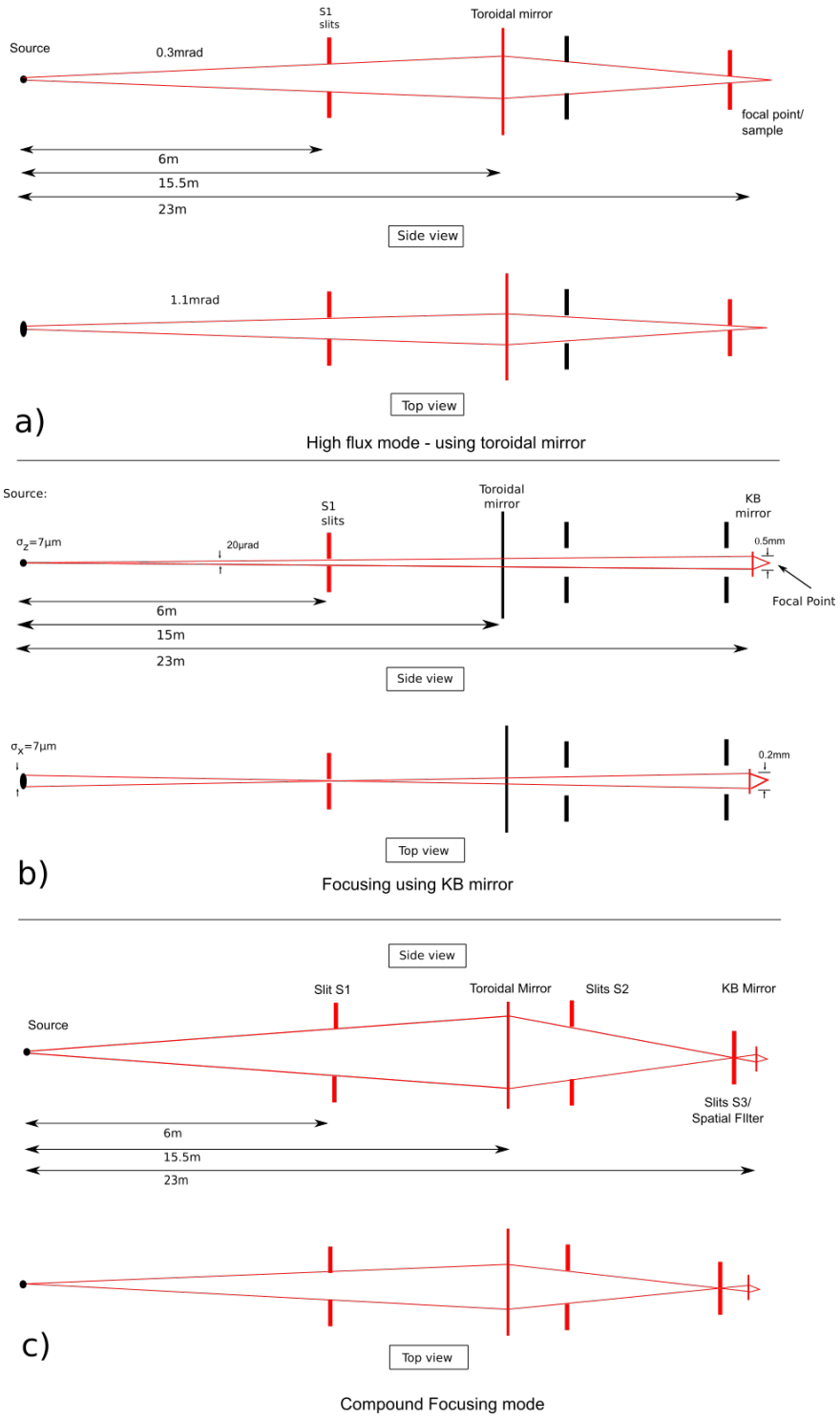

Figure 14.7: The three focusing options for SuperXAS with the optional KB mirror system. Only the focusing elements and slits systems are shown. a) shows the situation in which only the toroidal mirror is inserted; b) depicts the KB-only focusing option and c) represents a compound focusing system using a secondary source arrangement

The use of curved reflecting surfaces is a well-established method of creating both horizontal and vertical focused beams and this type of focusing optics needs no adjustments over a range of photon energies, for which it is setup in terms of incident angle and mirror coating. There are three options to consider: a single toroidal mirror which is able to focus the beam both horizontally and vertically with a single reflection, a KB mirror set where horizontal and vertical focusing is done with two separate mirrors (two reflections) and a combination of these two types of mirrors (three reflections). Note that the use of the KB mirror system is optional and only of use if the focal spot size provided by the toroidal mirror is too large.

In principle, a sagittal focusing monochromator can also be used to focus the beam in the horizontal direction. This solution is not advisable. Such a device is not achromatic and would require constant adjustments as photon energy is scanned. As such, it is not compatible with a fast scanning monochromator. It is also adding to the complexity of a monochromator, making it less user friendly.

Toroidal mirrors are convenient from the point of operation. By bending a long toroidal mirror, a finely focused beam is obtained at the sample position. Small adjustments to the mechanical bender and/or angle of incidence with the beam allow precise control of the focal spot size at the sample. The choice for a toroidal mirror fixes the position of the sample and the angle of incidence that should be used. Use of the toroidal mirror at different angles than the design angle will lead to defocusing which could be beneficial if a larger sample area must be probed.

As shown by MacDowell *et al.* [14] an optical system consisting of a collimating mirror and toroidal focusing mirror with a 2:1 horizontal demagnification has the benefit of eliminating astigmatic coma. At SuperXAS, the toroidal mirror is located at a distance of 15.5 m from the source, whereas the sample position is at about 23 m resulting in a demagnification close to 2:1.

There are several situations where a fixed sample position and the implicit use of horizontal focusing would be problematic. For example, when dealing with larger, beam-sensitive, or inhomogeneous samples, a user might prefer to probe a larger area with a larger defocused beam. The requirement for a fixed sample location can be problematic with larger sample environments or in experiments where the sample is placed further downstream.

Typically, the meridional curvature (R_m) is large and the sagittal curvature (R_s) is small, as described by:

$$R_s = 2 \sin \alpha \left(\frac{pq}{p+q} \right) \tag{14.1}$$

$$R_m = \frac{2q}{\sin \alpha} \tag{14.2}$$

Here p is the source-to-mirror distance and q is the mirror-to-focal-spot distance. For the SuperXAS beamline layout ($q = 7.7$ m; $\alpha = 3$ mrad), $R_s = 30.9$ mm and $R_m = 5.1$ km. For $\alpha = 2$ mrad, these numbers change to: $R_2 = 20.6$ mm and $R_m = 7.66$ km. Note that we have assumed that the incoming beam is perfectly collimated in the vertical direction so that effectively the mirror-to-source distance (p) is infinite.

For the SuperXAS geometry, the sagittal radius is rather small and will limit the horizontal acceptance of the optical system as a whole because not the whole diameter can be exposed to the beam.

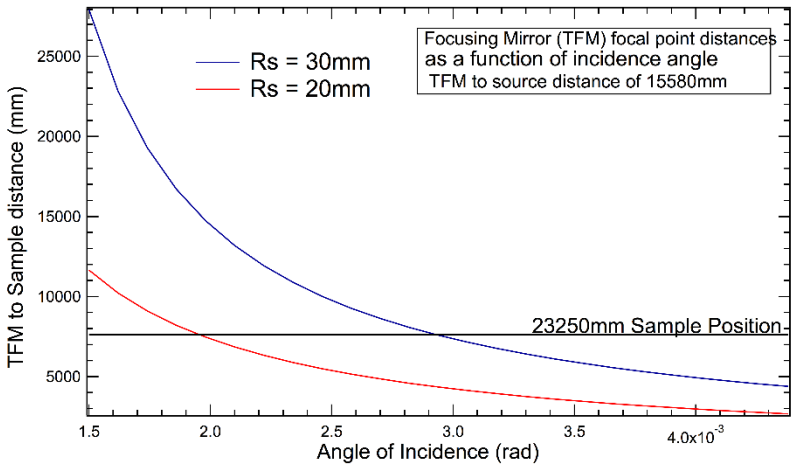

Figure 14.8: Position of focal spot for a toroidal mirror with two cylindrical grooves with radii of R_s = 20 mm and 30 mm, corresponding to the angular range of mirror angles. The nominal sample position is indicated.

To provide the user with a more flexible arrangement, it is proposed to use the combination of a flat and toroidal mirrors that has a cross-section with two toroidal central sections (Rh- and Pt-coated) and three flats, one each to either side and one in the middle, that are coated with different materials (Si, Rh, Pt) to allow for a wide energy range with vertical only focusing properties (see Figure 14.9).

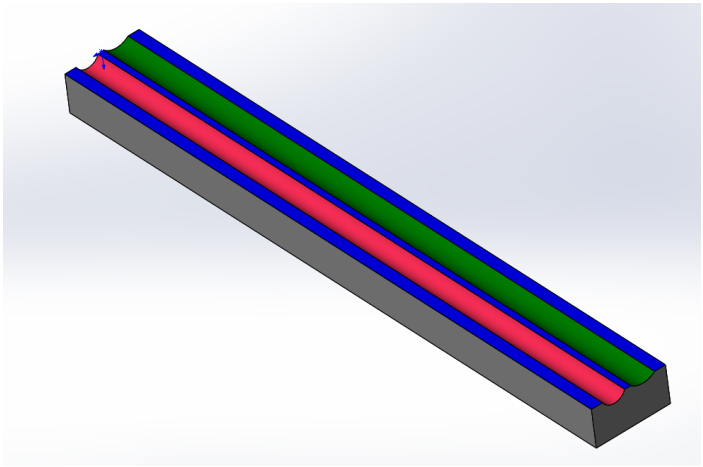

Figure 14.9: Cross-section of proposed toroidal mirror (not to scale). Green and red surfaces indicate different surface coatings and radii for the two polished cylinders cut into a common substrate. The substrate is bent using a single mechanical bender to provide the correct meridional radius for vertical focusing of the x-ray beam. The blue areas, which are about 10 mm wide, could also be coated and used for applications in which vertical-only focusing suffices (large horizontal beam).

By horizontal movement of the mirror blank, one of the two toroids can be selected giving the user a choice in cut-off energy and focusing conditions. In order to capture most of the vertical extent of the beam, a mirror of at least 1 m length would be used with a width of 120 mm.

The effective width of the toroidal parts of the mirror is smaller than that of a flat mirror. This reduction is a consequence of the small radius of curvature of the toroidal mirror. Thus, even though the mirror at the position of either toroidal part would be wider (as measured in the horizontal direction) than 20 mm, they will not be able to focus a beam with a horizontal divergence of more than 1 mrad without incurring losses. Figure 14.10 highlights this issue by showing the footprint of a 1.0×0.32 mrad^2 fan of monochromatic radiation on a mirror of 1 m length set at an incidence angle of 3 mrad. This particular part of the mirror has a 30 mm sagittal radius cut into its surface. About 3.5% of the generated rays miss the mirror surface. Increasing the horizontal fan size will quickly lead to larger losses.

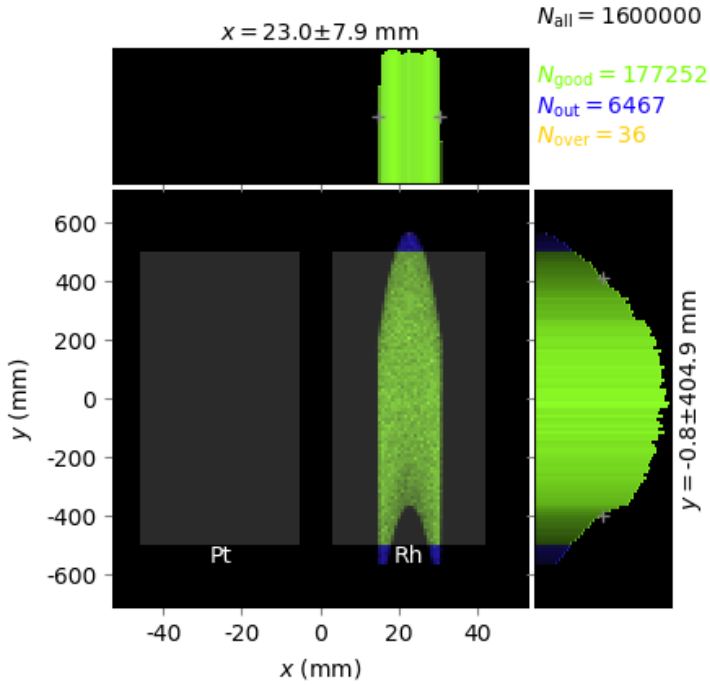

Figure 14.10: Top view of a dual toroidal mirror with two coatings, Rh and Pt set at an angle of 3 mrad and exposed by a 1×0.32 mrad^2 fan of radiation. Ray tracing has indicated rays that undergo a reflection (green) or that miss the toroidal mirror (blue).

Ray tracing calculations were performed using the new source parameters for SLS 2.0 with a 4 T dipole. Both collimating and toroidal mirrors were given their respective meridional radii to provide a vertically collimated beam at the monochromator and a vertically focused beam at the sample position. Similar ray trace calculations were performed for the existing SuperXAS facility with the existing source parameters as a comparison. In order to mimic a realistic mirror surface, we generated four different surfaces with RMS slope errors varying between 0.5 and 1.6 μrad. For these calculations the complete optical path was used which includes the collimating mirror, a Si(111)

two-crystal monochromator and a toroidal mirror. From these calculations, it was concluded that the existing mirrors feature RMS slope errors larger than 1.6 μrad. With this information, we proceeded to simulate what one can expect by reusing the SuperXAS optics at SLS 2.0. All components are located at their current positions at SuperXAS.

The RMS profile error of the polished mirrors should follow the Marechal criterion, taking into account that there are N reflections and that the mirror is exposed at a grazing angle:

$$\sigma \leq \frac{\lambda}{14\sqrt{N}2\alpha} \tag{14.3}$$

With four reflecting surfaces, a grazing incidence angle of 3 mrad, and a design wavelength of less than 0.1 nm, the RMS profile error should be smaller than 0.6 nm.

Due to the increase of beam brilliance, the quality of the mirrors used becomes a very important parameter. Particularly, the size of the vertical focus that can be obtained is a function of the RMS slope error of the mirror. To preserve the small source size, it is important to study the effect of slope error on focal spot size. To this end, we have performed ray trace calculations with mirrors of varying slope error to avoid introducing significant losses in source brilliance. In order to perform realistic simulations of beamline performance, we have contrasted perfect mirrors with real mirrors that have roughness and slope errors. To focus the superbend dipole source without significant distortions, mirror slope errors must be smaller than the angular size of the source or 7 μm/15.5 m = 0.45 μrad.

Unfortunately, this figure is difficult to achieve for a toroidal mirror of sufficient length. For mirrors with RMS slope errors of 0.65 μrad, preliminary ray trace calculations with XRT result in a 28×46 μm^2 (h $\times$ v) FWHM spot size (see Figure 14.10). This calculation was performed for an energy of 12 keV without VCM inserted into the beamline, thus providing a worst-case scenario.

A set of results obtained for different mirror surface qualities is given in Table 14.4. From these results, it is clear that a focal spot size of 30 μm is not easy to achieve.

RMS Slope Error (μrad)	Horizontal FWHM (μm)	Vertical FWHM (μm)
0.33	22	32
0.5	24	38
0.67	28	46
1.65	90	100

Table 14.4: Ray trace results for the complete beamline, showing the focal spot size at the sample for mirrors of four different surface qualities. The calculation was performed for a photon energy of 12 keV accepting a 0.75×0.125 mrad^2 fan of white beam. Affordable mirrors typically feature RMS slope errors above 0.5 μrad RMS.

For ideal focusing conditions, one should be able to perform a 2:1 imaging of the source, which would mean a focal spot size a factor two smaller than that of the cross-section of the electron beam distribution in the synchrotron.

The Kirkpatrick-Baez (KB) focusing mirrors are achromatic and are, therefore, ideal for energy-scanning applications, and can operate over the full beamline energy range using two metal coating

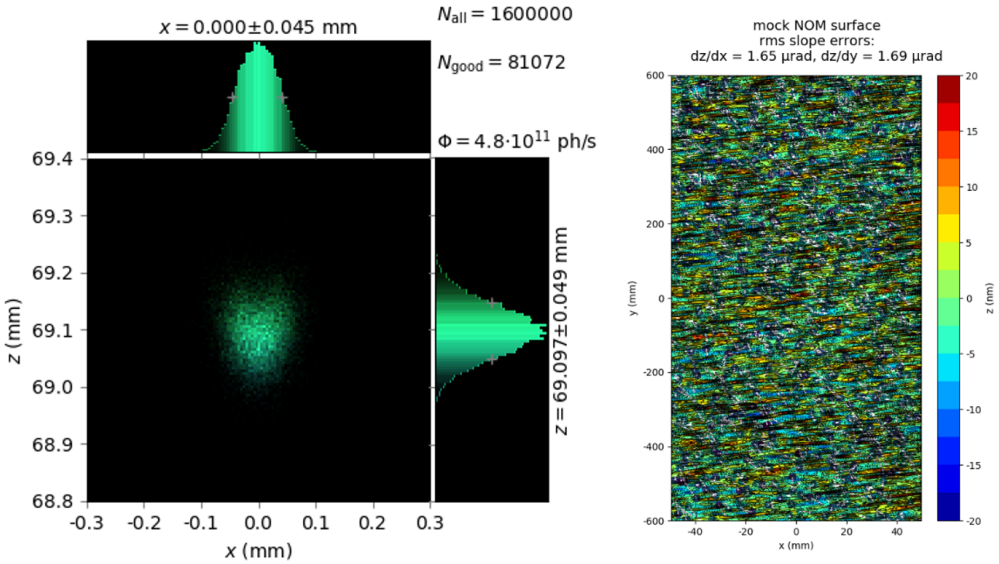

Figure 14.11: Ray trace calculations (left) for the toroidal mirror in the 2:1 geometry. An RMS slope error of 1.65 μrad of the mirrors is used in the calculations (mirror surface shown on the right).

stripes, if necessary. Using a relatively large demagnification (as compared to that of the toroidal mirror), this device allows a significant reduction in focal spot size needed by experiments that require better resolution, i.e. pump-probe experiments. The device will be fully integrated into the beamline design and motorized such that it can be remotely inserted into the beam path. The geometry of a KB mirror produces a finely focused beam, which is both laterally and vertically shifted compared to the incoming beam path due to the horizontal and vertical reflection of the beam in the device. This shift, however, will typically be of the order of 10 mm and should be within the range of any sample positioning equipment.

Separating horizontal and vertical focusing elements using two orthogonally placed mirrors (KB arrangement) is problematic due to the large horizontal fan of radiation. Typically, the two mirrors are placed in series making the device longer compared to a single reflection device.

KB mirrors operate with a high demagnification ratio of 100:1 or higher; as a consequence they are placed close to the sample – typically at a distance of 0.2 to 1 m. For the SuperXAS beamline with the sample at approximately 23 m from the source, a demagnification ratio of up to 100:1 is possible. A portable ESRF KB focusing optics (System 1) can collect a (h × v) 0.2×0.5 mm^2 cross-section of radiation when operating at 3 mrad angle of incidence.

Due to the short sample-to-KB-mirror distance, this setup would be placed in the experimental hutch. Because the horizontal size of the beam is larger than the vertical one the horizontal focusing mirror should be the one closest to the sample allowing a higher demagnification than for the vertical direction.

Other types of KB mirror systems that feature larger acceptance angles or have the sample closer to the exit of the mirrors with the aim of increasing photon flux or decreasing spot size could be also

considered. Whatever system is chosen, it will have to be placed close to the sample and best be located in the experimental hutch. Large KB systems consisting of mirrors of 500 mm become rather large and are more difficult to control with the high precision that is needed to shape the mirrors.

Commercial suppliers of x-ray mirrors list their capability for long mirrors ($\geq$ 1 m) generally with RMS slope errors and often also with a roughness parameter. The last decade has seen a significant reduction in the RMS slope errors due to a research effort in the polishing methods. For example, slope errors for medium-sized mirrors (600 mm) of 0.1 μrad (J-TEC) or 0.2 μrad (SESO) are available. Mirrors with these specifications are, however, extremely expensive. Even if such mirrors were affordable they should not be considered by themselves, but as part of a mirror system that consists of mirror, its mount and the mechanical bender. Judging from the results listed in Table 14.4, it seems beneficial to aim for an RMS slope error of 0.6 μrad or better.

Equally important is the quality of the mirror bender. For the collimating mirror, the radius of curvature is large and adjustment must be made for gravity sagging of the mirror. Fortunately, good commercial solutions are available.

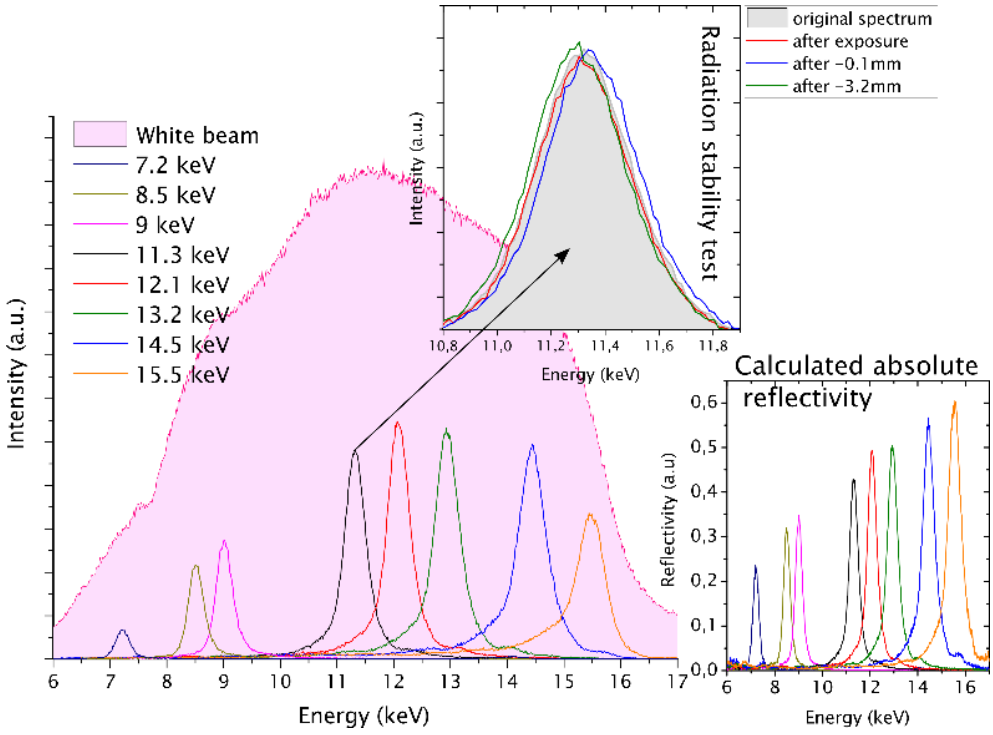

Figure 14.12: Energy spectra from a Mo/Si multilayer compared with the white beam (and absolute reflectivity). Radiation stability tests were realized at 11.3 keV with an exposure time of 8 hours and are shown within the upper inset figure. The different curves correspond to different, horizontally perpendicular translated to the incident x-ray beam, positions on the Mo/Si multilayer.

Finally, for new applications, such as pump-probe non-resonant XES, we need to work with large energy bandwidths. For this purpose both mirrors are put at 4.5 mrad so that the monochromator is bypassed (Figure 14.12). This can produce a significant heat load on the toroidal mirror, which is

presently not cooled. Calculations are currently being performed by the optics group to check if the mirror can withstand such operation on a routine basis, or if the mirror needs to be upgraded to a water-cooled mirror. Multilayer operation (located in the experimental hutch after both mirrors) is possible using a Mo/Si multilayer (developed by the Immanuel Kant Baltic Federal University). First tests on bandwidth (4%) and reflectivity are shown above. Stability tests were also performed over an 8 hour period (Figure 14.12 inset).

14.5 Endstation

Experiments at the SuperXAS beamline can be relatively short (sometimes a day or less), which means that the experimental hutch should support quick changeover between experiments so that a minimum amount of time is lost preparing the beamline for new users. With beamline alignment and beam energy changes quick and smooth, the hutch layout should allow for co-existence of two or more measurement setups. This approach could be combined with one in which several setups are in parallel sitting on a common slide. Any switchover would, therefore, be quick by removing the need for lengthy re-alignment cycles. Particularly in the case of experiments that use complex post-focusing and detector setups this approach using two large platforms will provide significant gains. Flexible sample positioning and the integration of a variety of sample environments (cryostats, ovens, gas cells, etc.) has already been addressed in the existing SuperXAS setup. Basic requirements for the experiments hutch are:

- Lifting tables
- X-ray optics (e.g. harmonics-rejecting mirror system and/or KB)
- Three ionisation chambers, gas system, HV supplies and programmable low-noise amplifiers
- Gas infrastructure for reactive and toxic gases. Mass spectrometry, micro gas chromatography for gas analysis
- State-of-the-art fluorescence detectors and electronics
- He-cryostat and LN2 cryostream
- High-precision sample stages
- Optical spectroscopy (confocal Raman system, IR, visible)
- Crane (500 kg)

The key detectors for EXAFS and quick EXAFS are a set of three ionization chambers with characteristics that permit one to collect spectra quickly and with a minimum of noise. The current set of gridded ion chambers from Ionitech GmbH (ionitech.de) feature a response time below 10 μs and can easily be filled with a gas mixture/pressure to suit optimal behavior for a transmission x-ray spectroscopy experiment.

For fluorescence-mode spectroscopy measurements, a 5-element silicon drift detector and a silicon drift detector with a 1 mm thick sensor are available. It would be advantageous to add a multi-element germanium detector, which would replace the existing silicon drift detector for photon energies above 15 keV where silicon becomes transparent. Multi-element germanium fluorescence detectors from Mirion, for example, allow experimenters to improve signal-to-noise ratios by collecting fluorescence radiation over a larger solid angle. Such a detector should be combined with the latest generation of read-out systems capable of capturing high event rates. Currently a six-channel FalconX readout

is available. Integrating these photon-counting systems within the quick EXAFS (QEXAFS) data acquisition will require an extension of the current data acquisition system. Improved low-energy germanium-detector systems combines electric cooling with up to 18 discrete sensors that feature a much improved energy resolution at significant count rates for a range of energies starting at 3 keV. These systems operate without LN2 cooling, which brings benefits in terms of maintenance and infrastructure.

Performing total scattering experiments complementary to XAS and XES will require a 2D detector featuring small pixels and an excellent signal-to-noise ratio capable of detecting photons at high photon energies. Hybrid photon counters such the EIGER family equipped with a CdTe sensing layer would be a good choice.

The beamline is currently equipped with wavelength dispersive setups either in von Hamos (3 crystal setup with a 25 cm diameter Rowland circle) or Johann geometries (5 crystal setup with a 1 m diameter Rowland circle) combined with a Pilatus 100k or Mythen strip detector. This allows one to measure non-resonant XES spectra, including valence to core (using the Johann spectrometer) and resonant XES (RXES or alternatively called hard x-ray RIXS) time resolved using the von Hamos spectrometer. For sulphur XES experiments, a dedicated vacuum von Hamos spectrometer (15 cm diameter Rowland circle) with a CCD camera and reactor cell that allows one to pass reactive gases and heat the sample is available. Non-resonant experiment sulphur XES measurements can be performed, where the sample is excited at 6.9 keV (the third harmonic of the S K-alpha emission line) that gets reflected by the Si(111) crystal.

14.5.1 XES spectrometers post upgrade

To enhance the sensitivity of x-ray spectroscopic methods to small spectral changes, we plan to develop a full-cylinder von Hamos type x-ray emission spectrometer (Figure 14.13). The efficiency of the new spectrometer will be 15 times higher compared to the current spectrometer at SuperXAS, due to the design of full-cylinder analyzer crystals covering a larger solid angle. With this configuration and profiting from the smaller x-ray spot size on the sample (30×30 μm^2 achievable at SLS 2.0 using KB optics compared to 100×100 μm^2 currently) the energy resolution of the x-ray emission spectrometer will remain better than 1 eV.

Furthermore, with the financial support of PSD investments and SNF we have developed and commissioned a spectrometer in the DuMond geometry that allows XES studies in the 15 to 30 keV range. This spectrometer will profit from the smaller spot size achievable at SLS 2.0 and the higher flux from a 5 T superbend.

14.5.2 QuickRIXS post upgrade

QuickRIXS with millisecond time resolution will be developed to obtain a complete picture of the electronic structure of the element of interest during a reaction. RIXS requires the measurement of the fluorescence intensity as a function of the incident and emitted energies. At SLS 2.0, we aim to combine our unique quickXAS monochromator with a new efficient energy-dispersive XES spectrometer (Figure 14.13) and with the newest generation of 2D single-photon-counting detectors with fast readout (currently we are in the process of commissioning a TimePIX detector).

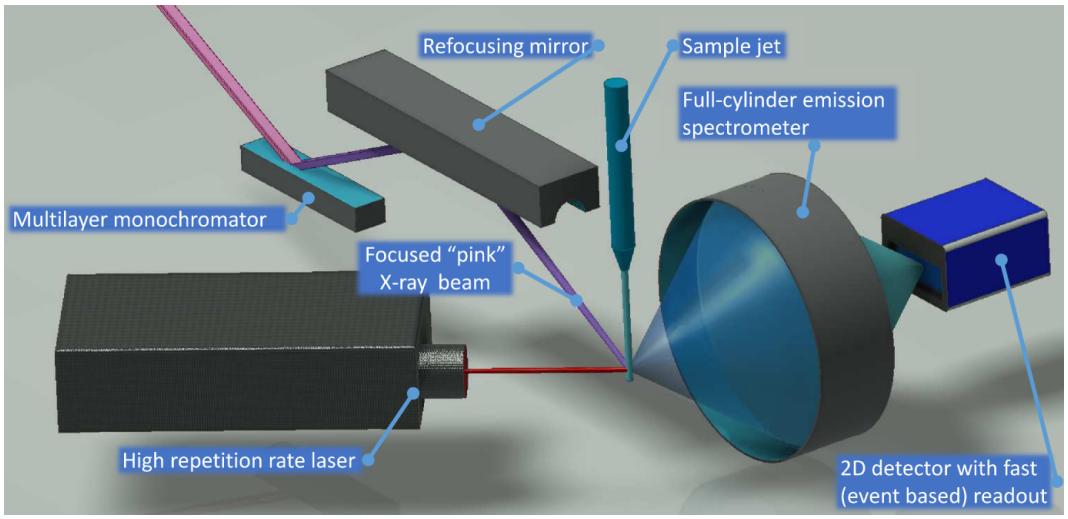

Figure 14.13: Scheme of pump-probe XES setup including multilayer monochromator, full-cylinder x-ray emission spectrometer and 2D detector with fast (event based) readout.

14.5.3 Lasers and laser infrastructure post upgrade

The smaller horizontal source size at SLS 2.0 will allow better focusing of x-rays (down to 30×30 μm^2) by using a KB mirror system and, therefore, the laser beam size (which has to be larger than the x-ray beam size for pump-probe studies) can also be significantly reduced. This will enable laser pump-x-ray probe experiments in the ns time range using lasers with higher repetition rate (1 MHz), which will increase the efficiency of pump-probe experiments in the nanosecond time range by a factor 10. The technology for wavelength tuning for high-power, high-repetition-rate lasers is developing rapidly and we expect the availability of such a commercially available flexible laser by the time of the SLS 2.0 upgrade. In particular it would be desirable to have a laser system that can operate with an output power of approximately 5 W with a repetition rate of 50 - 500 kHz and wavelength range between 250 - 2500 nm. Currently, at SuperXAS we have such output power only at certain wavelengths (harmonics of the laser fundamental wavelength, which we presently use) and after optical parametric amplifier (OPA), providing the wavelength tunability, the power is low, of the order of 10 mW. Taking into account the limited efficiency of optical parametric amplifiers, a high-power high-repetition-rate pump laser for OPA will be needed. Thin disk laser technology is a promising recent development in this direction [15]. All laser infrastructure (including climate controlled laser hutch) is already available at the SuperXAS beamline.

Furthermore, this new laser will be used to develop new reaction triggering schemes. In order to obtain insights into the structure of catalytically active sites and reaction intermediates, the active site needs to be triggered with a certain modulation frequency so that the response of the catalytic system can be filtered out from spectator species by the excitation frequency. This is currently only done for solid catalysts using repeated gas pulses. However, gas pulses cannot be performed faster than in 1 Hz, making studies of sub-second processes inaccessible. With the newest generation of laser sources, we envision that triggering of nonphotocatalytic reactions becomes possible by lasers,

either by initiating fast temperature jumps (tens of degrees), pH jumps (produced by photo-acids), or concentration jumps (released by caged compounds) relevant for the studied reaction. Corresponding reaction steps typically occur in the μs to ms time scale. Therefore, kHz lasers with IR radiation (for temperature jumps), UV radiation (for photo-acids and caged compounds), and even THz radiation might be used as better alternatives to study faster reaction steps.

14.6 IT requirements

The most demanding experiments from the point of view of IT requirements will be time-resolved measurements using the TimePix3 detector. For these experiments the detector is running in an event-driven mode, streaming the data (arrival time, coordinates and energy) about each photon that hits the detector. Therefore, the data rate will strongly depend on the count rate and can be as high as 7 GByte/s. Taking into account that on average the data rate will not be maximal, this type of experiment can still generate 100 TByte/day and we expect such investigations will be running a few weeks per semester. We plan to reduce the amount of data that have to be saved by a factor of 100 or more implementing on-the-fly processing of data. This will include binning (to extract time dependence), azimuthal integration (to extract energy-dependence), and clustering (to use events induced by one photon but observed at a few pixels). All these algorithms are not very demanding for CPU time and challenges from an IT perspective are related mostly to the high bandwidth of input data. Therefore a solution based on small server at the beamline for on the fly processing of data which will reduce the amount of data for centralized storage and simultaneously give the feedback to the users about the running experiment will be developed.

For the majority of user experiments, QEXAFS is the standard mode of operation. In such cases, we currently produce data at approximately 200 GByte/day at maximum throughput. With the upgrade of the monochromator system at the SuperXAS beamline we expect this figure to quadruple due to an increased angular resolution of the monochromator crystals and including on-the-fly calculation of statistical information. However, the size of the data produced is highly dependent on the energy at which QEXAFS data is being collected. Higher energies involve a smaller oscillation angle of the monochromator crystals and as such lead to vastly reduced data sizes. in an average user operation, we expect to produce approximately 30 TByte/annum. Considering the storage of user data we expect to need in the region of a total of 200 TByte of storage space to meet long-term data storage requirements.

14.7 Timeline

Preferred start date (commissioning, pilot users):

Due to its unique portfolio of time-resolved and energy-resolved methods, the SuperXAS beamline is a partner in several large Swiss and international initiatives (including the NCCR Sustainable Chemical Processes Through Catalysis, which is currently at the final stage of evaluation, and the Catalysis Hub). A shutdown significantly longer than the SLS 2.0 ring upgrade will be critical for these collaborative projects strongly counting on the availability of the SuperXAS beamline. We understand the difficulty of including several superbends in the SLS 2.0 lattice simultaneously, but

trust SLS management is doing all it can to ensure that all superbends deliver beam within 3 months after the ring upgrade. About half of the science and research output of the beamline is done with x-rays in the 15 to 30 keV range. This will not be possible with a normal bend at PSI.

The SuperXAS beamline at SLS was commissioned in two months; we do not envision longer commissioning at SLS 2.0. Our project plan suggests that the complete upgrade is possible within six months (depending on the availability of the crane).

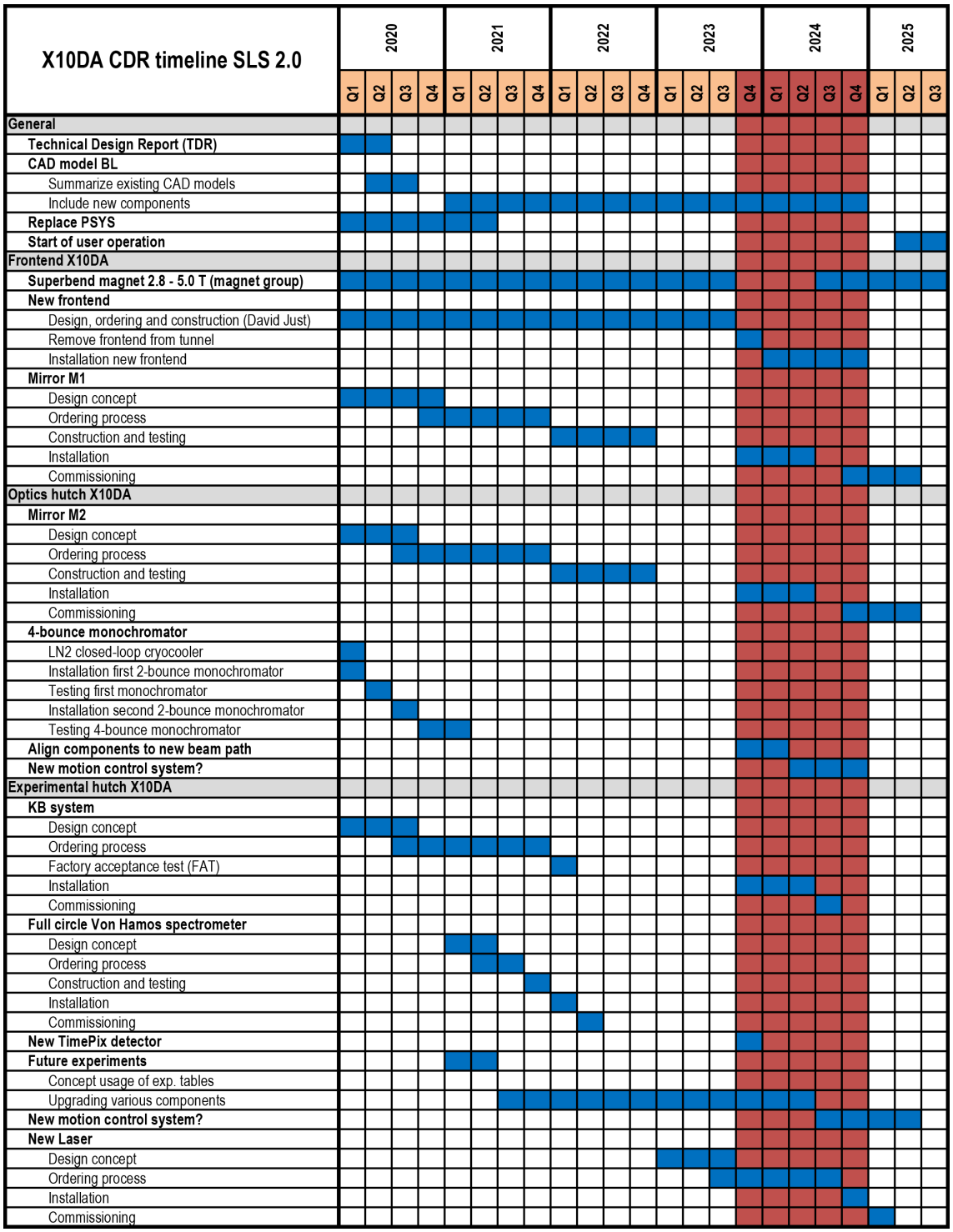

Figure 14.14: Timeline of the development plan for SuperXAS II with the upgrade of SLS

14.7.1 Manpower timeline

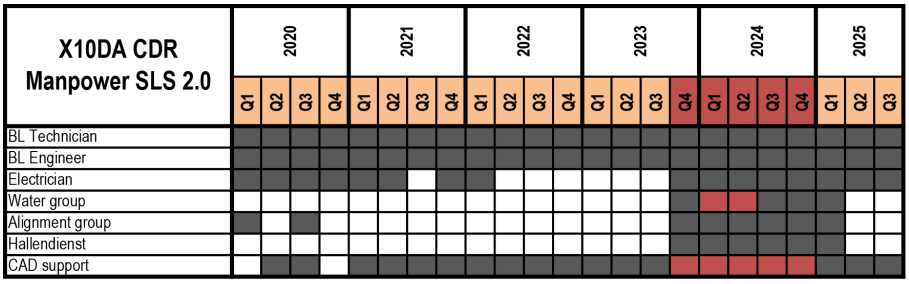

Man-months expected:

	Before shutdown	Shutdown	After Shutdown	Sum
BL Technician	36	18	15	69
BL Engineer	36	18	15	69
Electrician	4	3	1	8
Water group	0	1	0	1
Alignment group	0.5	0.5	0	1
Hallendienst	0	0.5	0	0.5
CAD support	0.5	0	0.5	1

Figure 14.15: Timeline of expected manpower requirements

14.8 Concluding remarks

The presented beamline layout for both the SuperXAS II beamline and the envisioned new high-throughput XAS and scattering beamline, consists of a well-proven concept in which focusing elements are separated from elements that select photon energy. Through the use of a collimating mirror and selected filter materials, the full source spectrum can be restricted such that the monochromator heat load is minimized. The proposed design makes the best use of the energy range and expected photon flux available at a variable superbend source 2.8 to 5 T) at SLS 2.0 and is tailored for giving users a wider range of photon energies at higher photon energies with a flexible approach to focusing such that it is easy to go from large to micro-focused beam size. As such, the proposed upgrade to SuperXAS II has the same layout as its predecessor, such that the existing infrastructure can be used with little change.

Ray trace studies have highlighted the requirement for sub-microradian slope errors for collimating and focusing mirrors, if focal spot sizes are to be obtained comparable to the requirement of 30×30 μm^2. Also, mirror bending mechanisms and gravity compensating mirror mounts are important in order to maintain source brilliance. The existing mirrors have large slope errors and should be repolished/recoated. Furthermore, the front-end mirror tank needs to be replaced by a smaller tank such that it will fit in the ring tunnel after the SLS 2.0 upgrade. Therefore the optics group will take the lead in the design of a new front-end mirror, which is also essential for the PXIII beamline (and the new high-throughput Debye beamline) post SLS 2.0 upgrade. Finally, by changing the cylindrical approximation of the parabolic/ellipsoidal shape of the toroidal mirror to a true parabolic/ellipsoidal shape would further reduce artefacts on the focal spot. By also replacing the current focusing toroidal mirror in the optics hutch by a new toroidal mirror with a true ellipsoidal shape as well as several coated flats around the two toroids would allow one to work both with large defocused beams (needed for radiation-sensitive samples) as well as tightly focused beams. An additional KB system is still needed in the experimental hutch to reach a spot size of 30×30 μm^2 for pump-probe applications.

With the upgrade of the QEXAFS monochromator to a continuously scanning 4-bounce, liquid-nitrogen cooled mono, the thermal bump with a maximum slope error of approximately 10 μrad on the monochromator crystal will be removed, which helps the focusing of the beam and throughput. Furthermore, the fixed-exit, which is now guaranteed by the 4-bounce monochromator, is essential for pump-probe experiments and allows the development of a full-circle XES spectrometer, which has an increased solid angle by a factor of 15 without any loss of energy resolution. This spectrometer will be essential for pump-probe XES as well as quickRIXS experiments.

Finally, the similarity of the proposed beamline concept with the existing SuperXAS beamline will allow the reuse of the current hutches and many components such as slits, vacuum vessels, support structures and vacuum pumps.

Bibliography

[1] Swiss Federal Office of Energy SFOE. Energy Strategy 2050, https://www.bfe.admin.ch/bfe/en/home/policy/energy-strategy-2050.html, Accessed [01-Oct-2019], 2014.

[2] E. Fabbri, M. Nachtegaal, T. Binninger, X. Cheng, B. J. Kim, J. Durst, F.o Bozza, T. Graule, R. Schäublin, L. Wiles, M. Pertoso, N. Danilovic, K. E. Ayers, and T. J. Schmidt. Dynamic surface self-reconstruction is the key of highly active perovskite nano-electrocatalysts for water splitting. *Nature Materials*, 16(9):925–931, 2017.

[3] A. Marberger, A. W. Petrov, P. Steiger, M. Elsener, O. Kröcher, M. Nachtegaal, and D. Ferri. Time-resolved copper speciation during selective catalytic reduction of NO on Cu-SSZ-13. *Nature Catalysis*, 1(3):221–227, 2018.

[4] G. Smolentsev, B. Cecconi, A. Guda, M. Chavarot-Kerlidou, J. A. Van Bokhoven, M. Nachtegaal, and V. Artero. Microsecond x-ray absorption spectroscopy identification of CoI intermediates in cobaloxime-catalyzed hydrogen evolution. *Chemistry - A European Journal*, 21(43):15158–15162, 2015.

[5] S. Biollaz, M. D. Kaufman Rechulski, C. F. J. König, M. Nachtegaal, and T. J. Schildhauer. A method for methanation of gasification derived producer gas on metal catalysts in the presence of sulfur, EP2870125A1, WO2014009146A1, 2014.

[6] J. Szlachetko, M. Nachtegaal, J. Sá, J. C. Dousse, J. Hoszowska, E. Kleymenov, M. Janousch, O. V. Safonova, C. König, and J. A. Van Bokhoven. High energy resolution off-resonant spectroscopy at sub-second time resolution: (Pt(acac) 2) decomposition. *Chemical Communications*, 48(88):10898–10900, 2012.

[7] T. Tanaka and H. Kitamura. SPECTRA: A synchrotron radiation calculation code. *Journal of Synchrotron Radiation*, 8(6):1221–1228, 2001.

[8] K. Klementiev and R. Chernikov. Powerful scriptable ray tracing package xrt. In Manuel Sanchez del Rio and Oleg Chubar, editors, *Advances in Computational Methods for X-Ray Optics III*, volume 9209, page 92090A, 2014.

[9] J. W. M. DuMond. Theory of the use of more than two successive x-ray crystal reflections to obtain increased resolving power. *Physical Review*, 52(8):872–883, 1937.

[10] M. Krumrey. Design of a four-crystal monochromator beamline for radiometry at BESSY II. *Journal of Synchrotron Radiation*, 5(1):6–9, 1998.

[11] W. J. Bartels. Characterization of thin layers on perfect crystals with a multipurpose high resolution X-ray diffractometer. In *Journal of Vacuum Science and Technology B: Microelectronics and Nanometer Structures*, volume 1, pages 338–345, 1982.

[12] M. Servidori. X-ray monochromator combining high resolution with high intensity. *Journal of Applied Crystallography*, 35(1):41–48, 2002.

[13] S. M. Heald. Focusing X-ray monochromator for EXAFS studies in the energy range 4-30 keV. *Nuclear Instruments and Methods In Physics Research*, 222(1-2):160–163, 1984.

[14] A. A. MacDowell, R. S. Celestre, M. Howells, W. McKinney, J. Krupnick, D. Cambie, E. E. Domning, R. M. Duarte, N. Kelez, D. W. Plate, C. W. Cork, T. N. Earnest, J. Dickert, G. Meigs, C. Ralston, J. M. Holton, T. Alber, J. M. Berger, D. A. Agard, and H. A. Padmore. Suite of three protein crystallography beamlines with single superconducting bend magnet as the source. *Journal of Synchrotron Radiation*, 11(6):447–455, 2004.

[15] Ultrafast Laser Physics, ETHZ. Thin Disk Lasers, https://ulp.ethz.ch/research/thin-disk-laser-tdl.html, Accessed [27-Feb-2020], 2020.

Chapter 15

Macromolecular Crystallography Beamlines

John Beale, Dominik Buntschu, Florian Dworkowski, Sylvain Engilberge, Wayne Glettig, Chia-Ying Huang, Jakub Kaminski, Filip Leonarski, Isabelle Martiel, Katherine McAuley, Nathalie Meier, Vincent Olieric, Ezequiel Panepucci, Anuschka Pauluhn, Sonia Reber, Roman Schneider, May Sharpe, Takashi Tomizaki, Justyna Wojdyla, David Just, Benedikt Roesner, and Meitian Wang

In a nutshell

Third-generation synchrotron facilities have been a major driving force in the development of macromolecular crystallography (MX) in the past two decades. The SLS 2.0 upgrade to a fourth-generation facility provides unprecedented opportunities for MX – complete data sets in one-second exposures; high-quality x-ray diffraction from a single micron-sized crystal; de novo structure determination of native protein; time-resolved crystallography down to microsecond resolution. To realize this fully, we envisage a paradigm shift in the development and user operation of MX beamlines, where self-driven MX beamlines, powered by intelligent beamline devices, kHz frame-rate x-ray detectors, and hardware-assisted real-time data analysis, will enable autonomous data collection for routine and advanced MX applications. We propose a comprehensive upgrade of three MX beamlines to increase flux density by factors of 10^3 and 10^2 at undulator beamlines (PXI, PXII) and superbend beamline (PXIII), respectively. The high flux-density is essential for improving beamline throughput further and eliminates the need to grow large crystals. Also, the energy range and bandwidth of x-rays will be extended. The lower energy x-rays (3-5 keV) help solve the crystallographic phase problem, one remaining hurdle in MX; the higher energy x-rays (25-30 keV) allow even submicron-sized crystals to be studied. A data-driven approach will be developed to integrate beamline control system, experiment, and data analysis. The three beamlines are complementary; collectively they provide a wide range of MX methods to deliver high-resolution 3D structure and associated dynamics to biology user communities.

15.1 Overview

15.1.1 Trends in macromolecular crystallography

Macromolecular crystallography (MX) at third-generation synchrotron light sources has been the dominant method for high-resolution structure determination for the last two decades. Collectively, 30 synchrotron facilities worldwide have produced 120 000 x-ray structures. Since the completion of X06SA-PXI in 2001 at the Swiss Light Source (SLS) [1], the MX group at PSI has been at the forefront of both MX hardware and software development. Of the ten most productive beamlines in the world [2], X06SA-PXI was the first European beamline to reach 2 000 depositions in the Protein Data Bank (http://biosync.sbkb.org). Built in 2004, X10SA-PXII was the first micro-focus beamline dedicated for proprietary and drug-discovery research and also features a unique on-axis *in crystallo* spectroscopy setup [3]. The superbend magnet beamline X06DA-PXIII, built in 2007, was designed with a strong focus on automation and stability, which better allowed for *in situ* diffraction screening [4] and experimental phasing experiments, particularly native-SAD [5]. More importantly, the MX group at SLS has pioneered over the years some key technologies now in place at modern MX beamlines, such as adaptive micro-focusing optics [6], hybrid pixel-array x-ray detectors [7,8], multi-axis goniometry [9], in-situ diffraction screening [10], as well as fast diffraction scanning [11] with real-time analysis [5, 12] for serial crystallography experiments [13].

The dominant position of MX within the field of structural biology has now begun to be challenged by the tremendous technical advances of cryo-electron microscopy (cryo-EM) [14]. However, while some targets, such as large molecular complexes and poor expressing membranes proteins are perhaps better address by cryo-EM, MX remains the method of choice for high-resolution and high-throughput applications. MX uniquely allows for the atomic details of protein-protein interactions to be probed or the ligand-space of a potential drug binding site to be investigated, in a relatively simple and time efficient experiment which cryo-EM currently cannot match [15]. One prominent example is COVID-19 related research - hundreds of high-resolution x-ray structures of viral enzymes and their complexes with potential drug-like molecules have been determined at synchrotron MX beamlines within six months (https://www.rcsb.org/news?year=2020&article=5e74d55d2d410731e9944f52&feature=true). Although MX is a mature and well established field, its capability keeps expanding at an increasing pace thanks to continued developments in micro-focusing capability [16], hybrid pixel-array detectors [17], and novel sample delivery methods [18]. These developments have enabled many emerging methods in the last five years, see Figure 15.1.

These methods include the implementation of automated pipelines at synchrotrons to expedite large-scale fragment screening campaigns to explore the chemical space for biomolecular binding [19], methods to collect from weakly diffracting microcrystals at both 100 K and room-temperature [20–22], and time-resolved crystallography to study protein dynamics in the milli- to micro-second time scale [23, 24]. In addition, low-energy MX has the potential to fully exploit the anomalous scattering of lighter elements which not only facilitates *de novo* structure determination, but also enables the

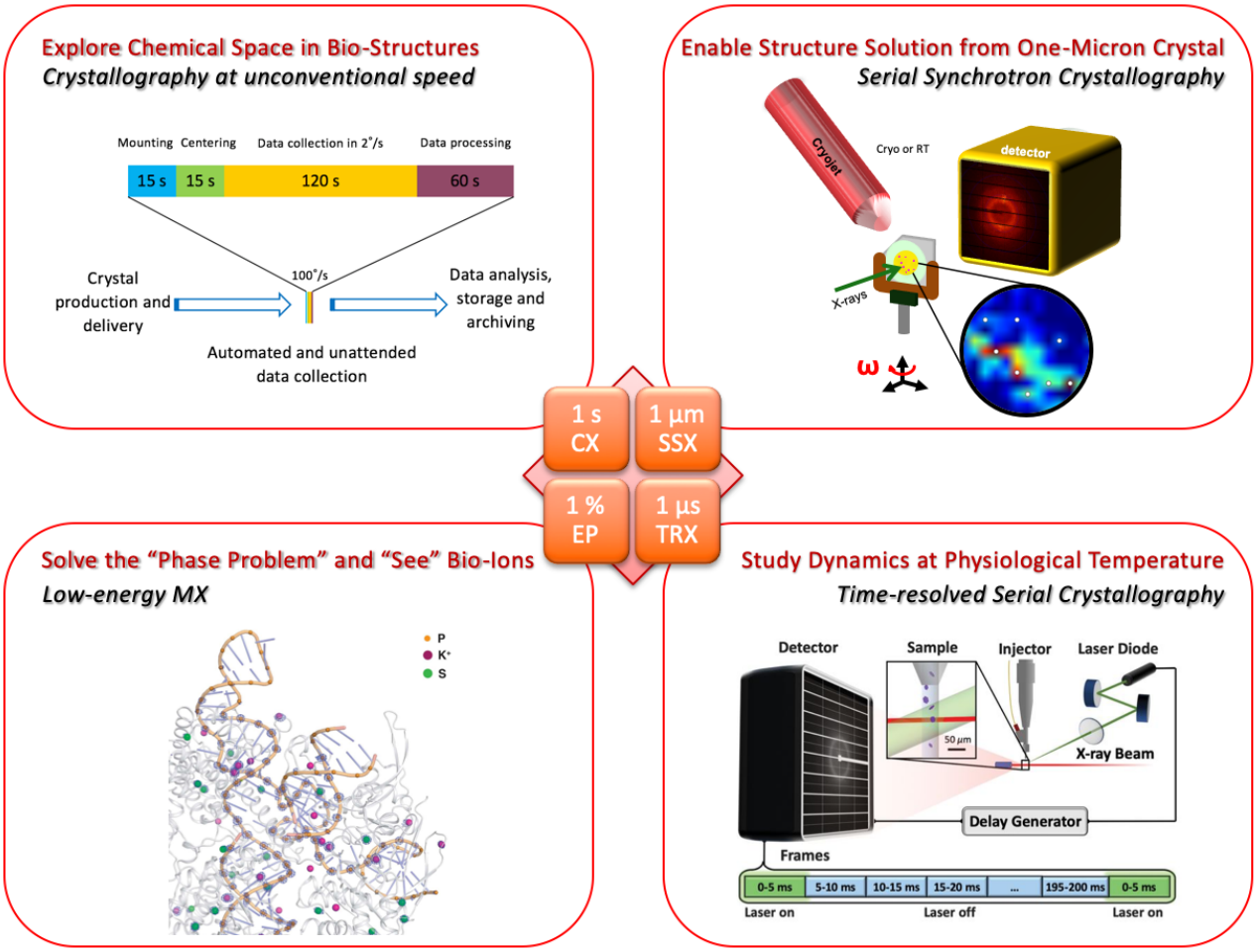

Figure 15.1: Emerging MX applications. High-throughput exploration of the "chemical space" inside bio-structures (top-left); structural determination from micron-sized crystals with serial approaches (top-right); "phase problem" problem solution and resolving bio-ions with low-energy MX (bottom-left); and probing protein dynamics at biologically relevant time-scales (bottom-right).

functional identification of biological ions such as Cl, K^+, Ca^{2+}, and potentially Mg^{2+} and Na^+ as well [5, 25, 26]. Such developments also hold unique opportunities in reaching a new and potentially broader user communities in biology and chemistry.

The arrival of fourth-generation synchrotrons like the SLS 2.0 [27] is an unprecedented opportunity to push the frontiers of MX still further in the coming decades [28]. A routine experiment can be carried out in seconds instead of minutes or hours previously required [29]. It is now possible to realise the theoretical limit of data collection from micron sized crystals [5, 30], and protein dynamics can be studied at micro-second time resolution (Figure 15.1). Advances in serial crystallography also hold the prospect of matching the efficiency of traditional cryo-data collection from large crystals but at more physiological temperatures. All of these exciting opportunities will add stringent demands in

both upstream and downstream data collection processes. For example, on-site sample preparation during beamtime is indispensable for experiments utilizing room temperature samples, which includes samples used for time-resolved experiments [31]. These experiments currently require a close to real-time interplay between sample preparation, data collection and analysis and produce large volumes of data. Therefore, to ensure the continued success of experiments like this in the future, a dedicated IT infrastructure with innovative and sustainable solutions will be essential for receiving and analyzing large amounts of diffraction data and providing real-time feedback to those preparing samples. In what follows, we will present:

1. our concept of the next generation MX beamlines;
2. the main design principles for MX beamlines at SLS 2.0;
3. the implementation ideas and practical considerations for each of three beamlines;
4. challenges and opportunities in MX data science;
5. development of sample preparation laboratory.

15.1.2 Uniqueness compared to present and planned other BLs worldwide

X06SA-PXI At present, the capacity and performance of X06SA are hardly surpassed by any MX beamline worldwide. However, future beamlines at DLS, MAX IV, ESRF-EBS, and APS-U plan one-micron or half-micron beams with an extended energy range of 25 keV to 35 keV and wider bandwidth (Table 15.1). Most of them are exclusively designed for microfocusing applications with a maximum beam size of 10 microns. The proposed X06SA upgrade offers a wider range of beam size (1 μm to 50 μm) with an extended energy range [4 keV to 18(30) keV] and variable bandwidths. We will exploit advanced detector technologies (e.g., JUNGFRAU) and emerging sample delivery methods as well. We believe that the X06SA upgrade will address the foreseeable needs in MX applications and provide a comprehensive environment for its evolution.

X10SA-PXII X10SA is a unique beamline in the macromolecular crystallography community. The only comparable beamline is IMCA-CAT at the APS. Both beamlines cater predominantly for pharmaceutical companies and have strong financial commitment from industrial partners (Table 15.2). They both focus on high-throughput crystallography experiments for drug discovery, while keeping microfocusing capability and a flexible setup. Their productivities are among the best in the MX beamline world. The X10SA upgrade will make it to the top league of MX beamlines while maintaining its leading industry beamline position.

X06DA-PXIII X06DA is one of the two most productive bending-magnet MX beamlines in the world. For low-energy crystallography, there are two beamlines in operation dedicated to experiments at energies < 6 keV, namely I23 at Diamond Light Source, United Kingdom and BL-1A at the Photon Factory, KEK, Japan (Table 15.3). The X06DA upgrade will make low-energy MX routine, while keeping high performance for standard MX.

Beamline	Energy [keV]	Bandwidth	Beam size [μm]	Flux [ph s^{-1}]	Operation status	PDB entries (Dec. 19)
X06SA SLS	5.7 - 18	10^{-4}, mono	5 - 100 (1 - 2)	2×10^{12} (2×10^{11})	2001 (2015)	2766
X06SA SLS 2.0	3 - 30	10^{-4}, mono 10^{-2}, pink	1 - 50 1 - 50	10^{13} 10^{15}	in design	
I24 DLS	6.4 - 20	10^{-4}, mono	7 - 50	3×10^{12}	2009	803
VMXm DLS	7 - 25	10^{-4}, mono	0.5 - 10	1×10^{12}	Commis.	
P14 PETRAIII	6 - 20	10^{-4}, mono	5 - 300	5×10^{12}	2011	266
ID29 ESRF	6 - 20	10^{-4}, mono	60×30 (10×10)	5×10^{12} (1×10^{11})	2000	2541
EBSL8 **ESRF-EBS**	10-20(30)	10^{-3}, ML 10^{-2}, pink	0.5 - 10 0.5 - 10	10^{14} 10^{16}	in design	
MicroMAX **MAX IV**	5 - 30	10^{-4}, mono 10^{-2}, pink	1 - 10	10^{13} 10^{15}	in design	
GA/CA APS	5 - 20	10^{-4}, mono	25 - 70 (5 - 5)	3×10^{12} (2×10^{11})	2005	1350
17ID2 NSLS-II	5 - 30	10^{-4}, mono	1 - 10	3×10^{12}	2017	40
BL32XU **SPring-8**	8.5 - 20	10^{-4}, mono	1 - 10	2×10^{12}	2011	187

Table 15.1: Comparison of MX micro-focusing beamlines worldwide.

Beamline	Energy [keV]	Bandwidth	Beam size [μm]	Flux [ph s^{-1}]	Operation status	PDB entries (Dec. 19)
X10SA SLS	5.7 - 20	10^{-4}, mono	20 - 70 (2 - 7)	2×10^{12} 5×10^{10}	2004 2017	2392
X10SA SLS 2.0	5.0 - 30	10^{-4}, mono (10^{-2}, pink)	1 - 50	1×10^{13}	in design	-
IMCA-CAT **APS**	6.0 - 20	10^{-4}, mono	70×30	8×10^{11}	1997	1887

Table 15.2: Comparison of MX industry beamlines worldwide.

Beamline	Energy [keV]	Beam size [μm]	Flux [ph s^{-1}]	Detector	Environ.	Operation status	PDB entries (Dec. 19)
X06DA SLS	5 - 17.5	90×45	4×10^{11}	P2M-F	Air	2009	1545
X06DA SLS 2.0	3 - 18	10 - 100	2×10^{12}	JF10M	Helium	in design	-
BL8.3.1 ALS	5 - 17	60 - 80	1×10^{12}	P6M	Air	2002	1565
I23 DLS	2 - 10	100	-	P12M	Vacuum	2015	15
BL-1A PF KEK	3.7 - 12.8	13 - 50	1×10^{12}	2×Eiger4M	Helium	2011	206

Table 15.3: Comparison of superbend beamlines and low-energy phasing beamlines.

15.1.3 Impact of SLS 2.0 on the MX beamlines

A 10× greater flux from the SLS 2.0 upgrade, will deliver an unprecedented rise in throughput for conventional MX experiments at X06SA and X10SA, enabling effective probing of chemical space for both mechanistic study and fragment-based drug discovery. In addition, the beamlines will benefit from the improved horizontal emittance. The lower emittance enables the beam to be focused down to 1 μm while maintaining an acceptable divergence (<2 mrad) for MX experiments. The increased brilliance of SLS 2.0 will equate to an increase in flux to $> 10^{13}$ ph/s, in a 1×1 μm spot, which will then have 100× higher flux density than is current achieved (10^{11} ph/s in a 1×1 μm beam at X06SA). Such parameters are highly competitive for micro-focusing MX see Table 15.1). Furthermore, we expect that advanced beamline technology will foster room-temperature measurements to access the dynamic dimension of MX.

For X06DA, which will utilise a warm 2-T superbend, the reduced source size and improved horizontal emittance will have a significant effect on the resulting beam size at the sample. The current beam size is $\sim 90 \times 45$ μm (FWHM), but after the upgrade, this could decrease to $\sim 15 \times 10$ μm beam with a flux of 2×10^{12} ph/s. As a result, X06DA will be the first high-flux micro-beam bending MX beamline with a performance that is comparable to current undulator beamlines.

15.1.4 Impact of SLS 2.0 and beamline upgrades for the MX community

While the SLS 2.0 machine upgrade will benefit the MX beamlines by enabling higher flux densities and a greater energy range across all three beamlines and in turn decrease experiment times and increase throughput, this is not the only important consideration for the MX community. It is essential that the suite of beamlines can meet all the different needs of macromolecular crystallographers in the near future and in the coming years. For this reason, each beamline will have a different capability profile but together they will allow MX users to carry out a wide range of experiments at SLS 2.0: from standard cryocrystallography experiments, still essential to many research groups and pharmaceutical

companies; through to room-temperature, serial crystallography experiments; phasing experiments at low energy; and drug discovery via fragment-based screening approaches.

These capabilities will satisfy the needs of the existing industrial and academic SLS MX user community. But there is an opportunity to expand the community to include laboratories that currently do not use MX beamlines due to a lack of crystallographic expertise. Autonomous data collection on highly-reliable beamlines, combined with auto-processing and automated data analysis, will make the crystallographic experiment accessible to the non-expert. Automation of the data collection process also allows the beamlines to operate with much higher efficiency for standard cryocrystallography experiments. Consequently, more time is available to schedule non-standard experiments, thus attracting new users and projects to the beamlines.

15.2 Development of the next generation MX beamline

During the active beamline development at 3rd generation synchrotron facilities in the last two decades, tremendous improvements have been made in each of the principal components of a beamline: the x-ray optics, the beamline control systems, data acquisition systems, and data analysis [32]. Each component of this pipeline to a large extent has been designed and developed in a modular and sequential way as illustrated in Figure 15.2. These tools have also been optimised with an underlying assumption: that the beamline will be operated and experiment will be carried out primarily by a human being. It is the user's responsibility to supervise the whole experiment and to make appropriate decisions in the complex environment of beamline. However, this approach, on the eve of the development of the 4th generation synchrotrons, needs to be re-examined. Technological improvements such as, shorter data acquisition times, real-time monitoring and adjustment of the beamline, automated data collection and processing, and subsequent structure determination have pushed the automation of the experiment such that the user's decision making ability is now the rate-limiting step of the process. Given the shortening of crystallography user beamtime and the ever widening scope of the technique to people with little or no crystallographic experience, these improvements in beamline technology have all added increasing pressure on the user. The MX beamlines of the future must aim to reduce this burden on the user and develop methods that allow all aspects of the experiment to be fully automated, but still retaining the ability to perform specialised experiments. The SLS 2.0 upgrade presents an ideal opportunity for the MX beamlines at the SLS. Firstly, to shift from the divide-and-rule paradigm of the 3rd generation synchrotrons to a more integrated approach, and to move towards fully automated data collection and analysis.

This vision presents a significant challenge to the MX group amd beamline developer in general. To overcome these hurdles, we aim to exploit modern engineering and computing technologies in the upgraded beamline design for SLS 2.0. To date, x-ray tracing of beamline optics [33], simulated diffraction [34–36], and structure solution propensity [37–39], have been studied separately. However, an approach that based on the internet of things (IoT) ideology with intelligent devices and utilises machine learning (ML) technologies could start to integrate all aspect of an MX experiment. Specifically, metadata from each component of the beamline could start to be collected and analysed by ML for their influence upon the data acquisition process. Correlations between the results of the experiment and the device metadata could be utilised to build a complete simulation of the experiment from

source to diffraction spot. Such a system will allow us to identify the critical beam parameters (*e.g.* flux, size, divergence, profile, energy, energy bandwidth) and the dominating experimental errors (*e.g.* beam stability, goniometer precision, detector noise, crystal imperfection, background scattering) for the entire beamline and experiment. These data can then by combined with the knowledge of the sample that is already available such that appropriate data collection strategies can be advised to meet the requirement of each experiment in an automated or specific manner, *e.g.* a single crystal dataset, a multi-orientation dataset, or a serial dataset. Embedded in an innovative environment at PSI where development requiring high complexity is well supported, the MX group is in a unique position to develop such enabling technologies for self-driving beamlines and self-learning experiments. Such developments will keep our competitive edge over other facilities and make a far-reaching impact on MX.

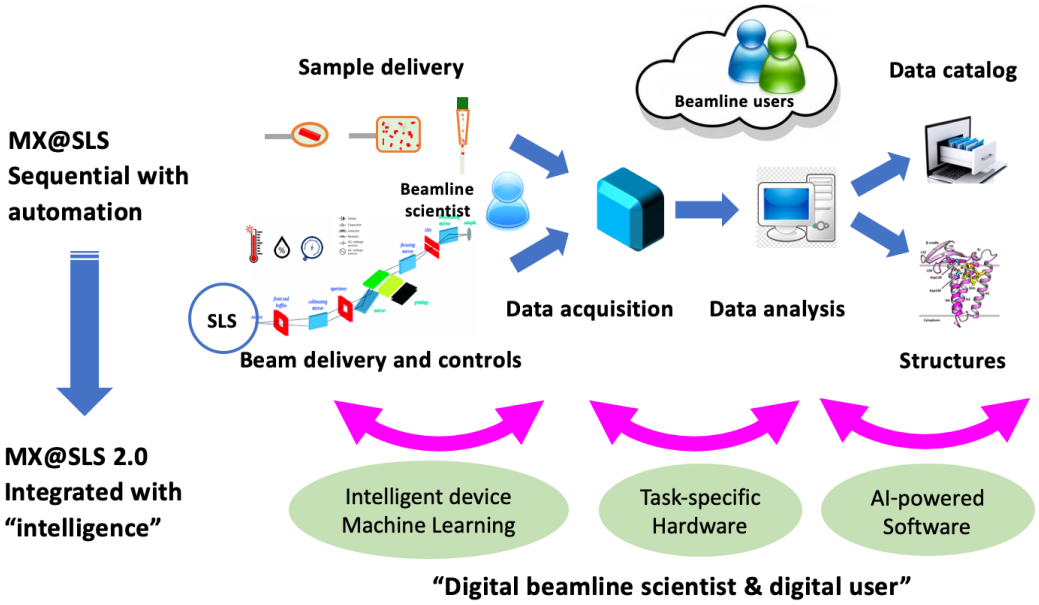

Figure 15.2: The main components and their interactions in the next generation MX beamline.

15.3 Design principles of MX beamline upgrades for SLS 2.0

15.3.1 Source

The upgrade of the three MX beamlines is envisioned to realise the full potential of emerging MX methods by capitalising the unique source properties from the SLS 2.0. One challenge is how to translate the improvement in source brilliance (Figure 2.2) to beamline performance effectively. The small circumference of the SLS ring is challenging for machine design, but it does allow us to build short beamlines (< 30 m), where the first optics element can be positioned close to the source to collect the full radiation cone from the undulators and to increase the acceptance from bending magnets. The reduced source size and divergence allow bringing the full flux into a one-micron focused spot with low divergence at the sample position for an undulator beamline. At a bending magnet beamline, a micro-beam of 10-micron with acceptable beam divergence can be achieved with a moderate focusing (Figure 15.3).

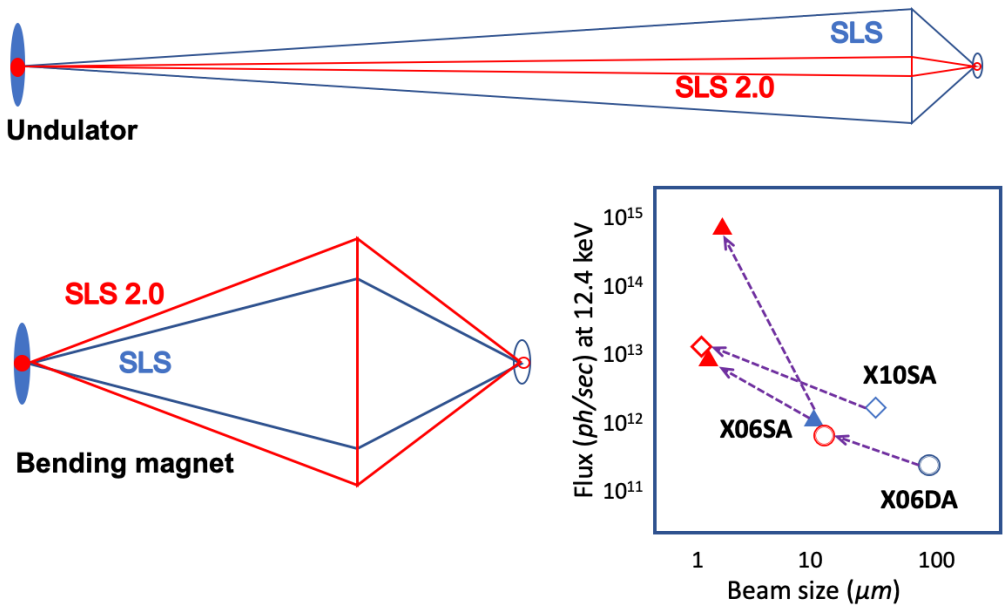

Figure 15.3: The expected improvement in beam size and divergence of MX beamlines at SLS 2.0.

15.3.2 Beam delivery, diagnostics, control, and experiment

To have full control of the x-ray beam to micrometre precision at the sample position, a comprehensive diagnostics and beam feedback system from the electron beam in the SLS 2.0 storage ring to the photon beam at the beamline is mandatory. Firstly, we plan to have x-ray beam position monitors (XBPMs) for both white beam and mono/pink-beam [40]. They will be positioned before and after each major optical element to track both the spatial and angular beam movement to micron-precision at 100 Hz. In addition to the beam position, the beam profile will be recorded by either x-ray cameras or beam

profile monitors. Secondly, all devices should have absolute encoders and additional sensors. Extra computing should be embedded into devices and sensors via system on chip or system on module to allow self-calibration, data preprocessing and potentially device-to-device communication to reduce latency. Thirdly, we would like to exploit the Big Data and machine learning methodologies to integrate and jointly analyse data collected throughout the beamline to assist in autonomous beam alignment and optimisation, to detect anomalies in hardware performance, and to monitor device health for preventive maintenance.

On top of the precise and real-time control system, we plan to build two intelligent systems - smart digital beamline scientist (SDB) and smart digital user (SDU) to assist bemaline staff and beamline user, respectively. The SDB will integrate hardware monitoring, anomalies detection, real-time feedback, and beamline setup and control to ensure best beamline performance for user's experiment, which is in turn operated by SDU for fully automated data collection and analysis (Figure 15.4).

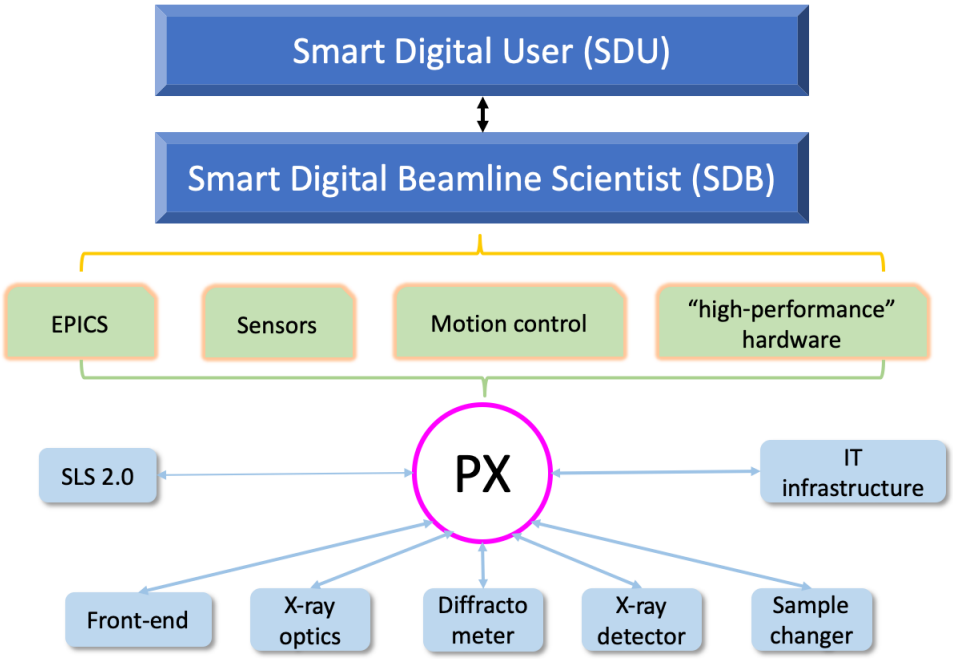

Figure 15.4: Illustration of intelligent systems for beamline control and user operation.

15.3.3 Energy range and energy resolution (bandwidth)

The majority of MX beamlines at third-generation synchrotron facilities have been designed to have an energy range of between 6 keV and 18 keV. This range covers the absorption edges of heavy elements commonly used for experimental phasing. Recently, there are compelling new scientific applications that could benefit from the access of both lower and higher energies. For example, *de novo* structure determination by experimental phasing with naturally present light elements could become routine at 3 keV to 5 keV; at the other end of the energy range, radiation damage could be mitigated effectively

from micron-sized crystals at 25 keV to 30 keV. Therefore, the design of monochromators for the next generation of beamlines should cover 3 keV to 30 keV.

MX data collection by rotation methods with monochromatic beam have been well established over nearly a century [41]. By moving reflections through the thin surface of the Ewald sphere, the reflections are measured precisely and reciprocal space can be sampled completely. The high energy resolution (10^{-4}) of *Si(111)* monochromators with low beam divergence at synchrotrons is required for multi-wavelength anomalous diffraction (MAD) phasing because the peak and inflection points are only a few electronvolts apart [42]. However, for the vast majority of the MX experiments, an energy resolution of 10^{-3} would be sufficient. We have simulated standard MX experiments with both Bragg reflections and background scattering at various bandwidths and found that the impact on the overall data quality is negligible with bandwidths up to 10^{-3}. The $10\times$ larger bandwidth will broaden the Ewald sphere to match the angular width of the diffraction spots in typical rotation cryo-crystallography. Therefore, one could gain $10\times$ more usable photons without loss of data quality. Even a wider bandwidth of 10^{-2}, which is comparable to the natural bandpass of single undulator harmonics for SLS 2.0, could be advantageous for the so-called "still" data collection methods, where reflections are not rotated through the Ewald sphere, but are covered by the width of the Ewald sphere instead [43]. Such still methods are attractive for the emerging method of serial synchrotron crystallography (SSX) at room-temperature, particularly for time-resolved studies, but are currently hampered at synchrotrons due to the narrow bandwidth of the current *Si(111)* monochromator. Any diffraction-spot smearing and the additional scattering background from the much wider bandwidth can be compensated by accumulating diffraction signal from hundreds to thousands of crystals measured by SSX.

Therefore, the tunability in energy bandwidth will be important for MX development in the coming decades [44]. The traditional *Si(111)* monochromator still remains the default choice for narrow bandwidths of 10^{-4} due to silicon's high crystallographic quality and excellent thermal conductivity at cryogenic temperature. However, cryo-cooling often introduces mechanical instabilities that can result in visible beam shaking. Measures need to be taken in the mechanical design in order to achieve sub-micron beam stability at the sample position. For slightly larger bandwidths, an asymmetric cut of *Si(111)* crystals can be exploited that can reach bandwidths between 10^{-4} and 10^{-3} with higher flux [45]. For the range of 10^{-3} to 10^{-2}, multilayer technology could also be used, in which various materials in a numbers of layers are available for the fine tuning of the bandwidth and reflectivity of the monochromater [46]. The achievable bandwidth with different approaches is illustrated in Figure 15.5.

15.3.4 X-ray focusing optics

The beam size and divergence are among the most important parameters for MX data collection. Ideally, one would like to match beam size and crystal size while keeping the beam divergence low. Data collection at the SLS is currently possible from crystals of 10 μm to 100 μm in size. However, data collection from one micron or even submicron crystals is now possible at BL32XU at SPring-8, Japan and VMXm at the Diamond Light Source, UK. Therefore, ideally one would like to vary the beam size from 1 μm to 100 μm in a fast and reliable manner. The most common method to

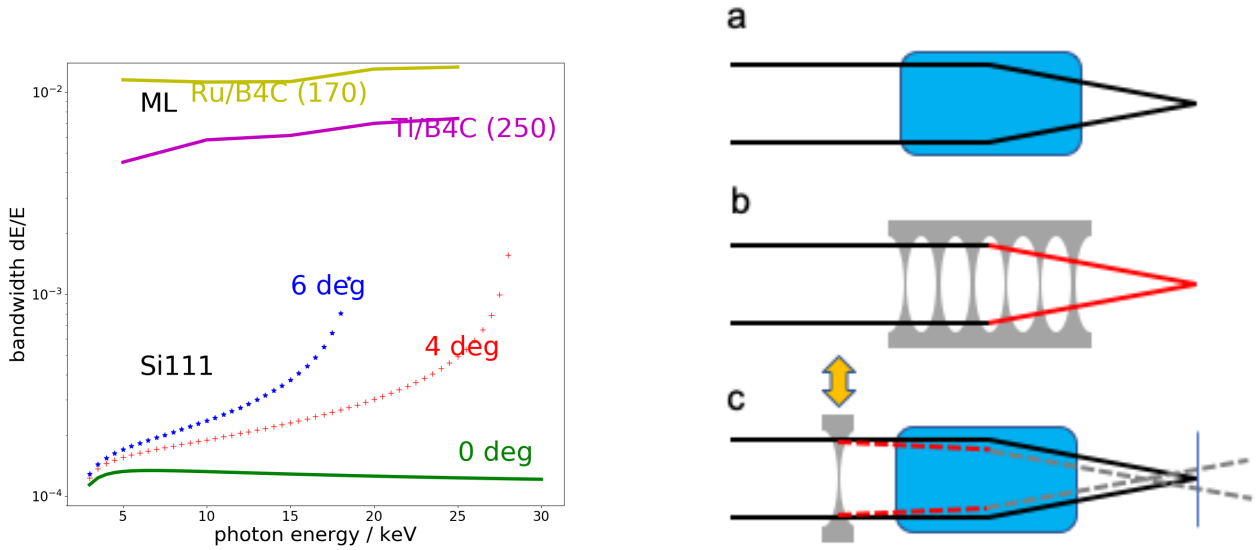

Figure 15.5: Left: control of the energy resolution (bandwidth) by different monochromators. The higher resolutions are achieved with the *Si(111)* monochromators in symmetric (0°) and asymmetric cuts (shown for tilt angles of 4° and 6°). The data for the multilayer optics (Ru/B_4C, 170 layers, period length of $d = 2.83$ nm and Ti/B_4C, 250 layers, period length of $d = 4.01$ nm) have been taken from [46]. Right: illustration of x-ray focusing methods (a) Mirror optics; (b) CRLs; (c) Combination of mirrors and CRLs for fast and reliable change of beam size at sample position.

manipulate beam size and divergence is using dynamically bendable or fixed curvature x-ray reflecting mirrors [Figure 15.5(a)] [44]; moreover, by selecting the appropriate coatings, such mirrors can be used as low-pass filters to remove high-energy radiation, in particular, unwanted harmonics. Mirror optics offer distinct advantages such as high achromatic efficiency (> 90 %). Moreover, mirrors can be bent for adaptive focusing, i.e., varying focal length. Since x-ray mirrors are operated at very low incidence beam angles, the stability and repeatability of beam positioning and focusing depend strongly on the mechanical system of the whole mirror and bending assembly. This could be challenging for autonomous user operation, particularly for strong focusing down to one micron. Alternatively, refractive optics like compound refractive lenses (CRLs) are easier to align and operate because they are used in a normal geometry [47]. They have been used successfully at a few fixed-energy MX beamlines dedicated to full data collection automation [48]. However, they are chromatic, and a transfocator assembly with many sets of lenses is needed to cover a wide energy range [49]. The beam acceptance (<500 μm) and efficiency (10 % to 40 %) of such systems are relatively low when used for strong focusing [Figure 15.5(b)].

In order to obtain the highest-possible flux in a micron-focused beam and at the same time offer fast and reliable beam resizing, we propose a combined approach for the undulator beamlines: to use mirrors as the primary focusing optics for the flux-hungry applications and augment them with CRLs with moderate focusing at selected energies for applications that benefit from fast beam size changing but do not require the highest flux [Figure 15.5(c)]. However, for the superbend beamline,

x-ray mirrors will be used exclusively because the limited numerical aperture of the CRLs does not match the relative large beam divergence.

15.3.5 Endstation

An x-ray diffractometer must be equipped with beam and sample visualisation tools. It brings the crystal into the x-ray beam and manipulates the crystal orientations to cover the reciprocal lattice during data collection. MX data collection methods have been evolved substantially from single rotation to multi-rotation, serial wedge-rotation, helical scan along single crystal or over many crystals, still scan, and in situ screening in the last decade (Figure 15.6) [50,51]. They require a concerted motion of rotation and translation with high precision and high speed. Based on our in-house developed PRIGo goniometer [9], we are developing the next generation multi-axis goniometer (SwissGO) (Figure 15.11). SwissGO has a sphere of confusion of less than 1 micron in all axes and can perform standard rotation and multi-orientation data collection for single crystals, as well as helical and 2-dimensional scans for serial crystallography. Alternative sample delivery methods, like LCP extruders for time-resolved crystallography [52], will be available as well. The sample environment will be in air with extra care taken to reduce background scattering in order to capture signals from weakly diffracting micro-crystals at PXI and PXII. The direct beam path will be reduced to a minimum by a scattering guard and a capillary beamstop [53]. The capillary beamstop will also have an integrated diode for active intensity monitoring. A helium sample enclosure will be developed for low-energy applications at PXIII. The in-house developed TELL sample changer will be adapted to meet sample loading demands at SLS 2.0. The detectors will be based on EIGER and JUNGFRAU technology [54, 55]. Dectris EIGER2 re-triggering technology and CdTe sensors can handle high photon-rates at high energy. JUNGFRAU integrating technology is not photon-rate limited and performs better for high-flux and low energy MX applications. A JUNGFRAU 10M detector with central flat 4M and three 2M wings is currently under development at PSI. The central 4M can be operated independently at 2.3 kHz, which should be sufficient for most high-throughput applications with sustainable data rate. The entire 10M detector will enable the recording of the higher-resolution reflections for low-energy macromolecular crystallography and high-energy chemical crystallography.

15.3.6 Increasing cryo-sample handling capacity

With the advances in crystal harvesting technologies [56, 57] and the surge in interest in fragment screening approaches for drug discovery projects, it follows that the number of samples being sent to MX beamlines will greatly increase over the next few years. Automated data collection procedures will enable faster and more efficient recording of experimental data, however, to fully maximise beamline usage we need to address the shutter-closed time associated with the changeover of sample containers inside the experimental hutch. Previously, sample containers would be loaded and removed from the hutch by the user, but with more remote experiments being scheduled, it is now the beamline staff who are responsible for this and for ensuring that information about the sample identity and location is stored correctly and is available to the user and to the data collection software. A multi-pronged approach will be required to facilitate efficient sample handling at the synchrotron. Procedures for sample shipping, tracking, storage on site, and the possibility of pre-sorting samples for each beamline

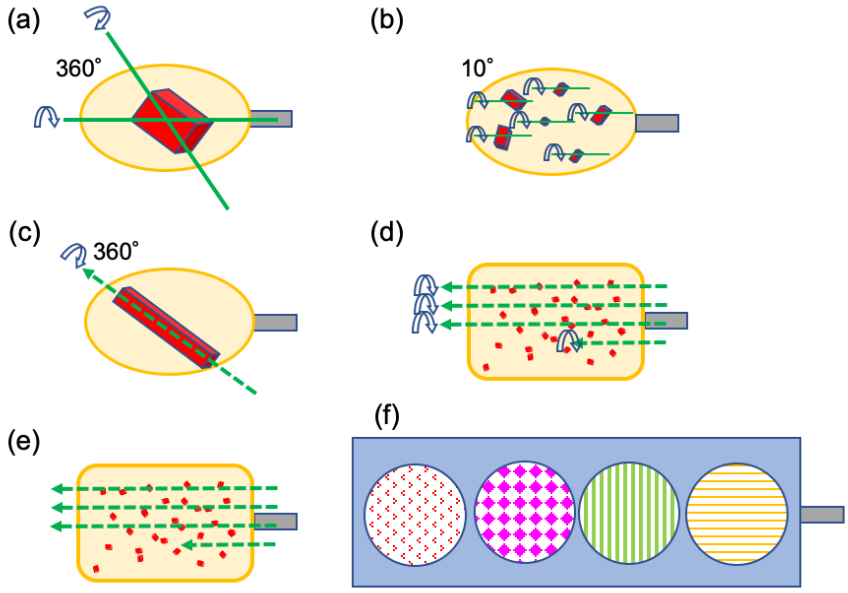

Figure 15.6: MX data collection methods with goniometer. (a) Rotation with multi-orientation, (b) serial small-wedge data collection, (c) helical scan along single crystal, (d) helical scan over many crystals, (e) "still" 2D-scan, (f) in-situ screening at room temperature.

session will be reviewed. Software solutions will be deployed and where needed developed to facilitate the recording of sample location information and status of data collection queues and to give advance warning of when the next sample container changeover is required. New automatous solutions to physically manage the movement of dewars and samples containers will be investigated. Finally, the format of the traditional SPINE3 sample holder will be revised, with a view to increase the number of crystals held on one sample holder. This has the benefits of increasing sample capacity whilst maintaining the format of the currently used sample containers, transport dewars and robot storage dewars. In addition to increasing capacity, the experimental throughput is increased by reducing the number of sample transfer steps required. Combining these steps will produce an efficiently-managed sample to data workflow and increase the productivity of the beamlines.

15.3.7 Complementary upgrades of three MX beamlines

Each of the three MX beamlines will be optimised for one or two of the main MX applications; collectively they will offer a complete portfolio for any kind of MX application in the future (Figure 15.7). X06SA (PXI) has been our main research and method development beamline since 2001, thanks to its versatile design. To this, we will add pink-beam capabilities for time-resolved crystallography. X10SA (PXII) is our main industry beamline, which offers high-throughput MX for ligand screening and serial synchrotron crystallography (SSX) for structure-based drug discovery. Naturally, its upgrade will focus on one-second routine MX and one-micron SSX application with an extended energy

range to 30 keV. X06DA (PXIII) has had an unrivaled impact on experimental phasing, most notably native-SAD, thanks to its stable source and unique multi-axis goniometer. Its upgrade will focus on exploiting lower x-ray-energy native-SAD phasing and unambiguous detection of biologically relevant light ions, taking advantage of the in-house multi-axis goniometer and x-ray detector developments. We believe that the proposed upgrades will make the three MX beamlines at SLS 2.0 among the best in their class. The main targeted design parameters of each beamline compared with its current capacity are summarised in Table 15.4. A comparison between them and their peer beamlines at other synchrotron facilities is presented in the appendix.

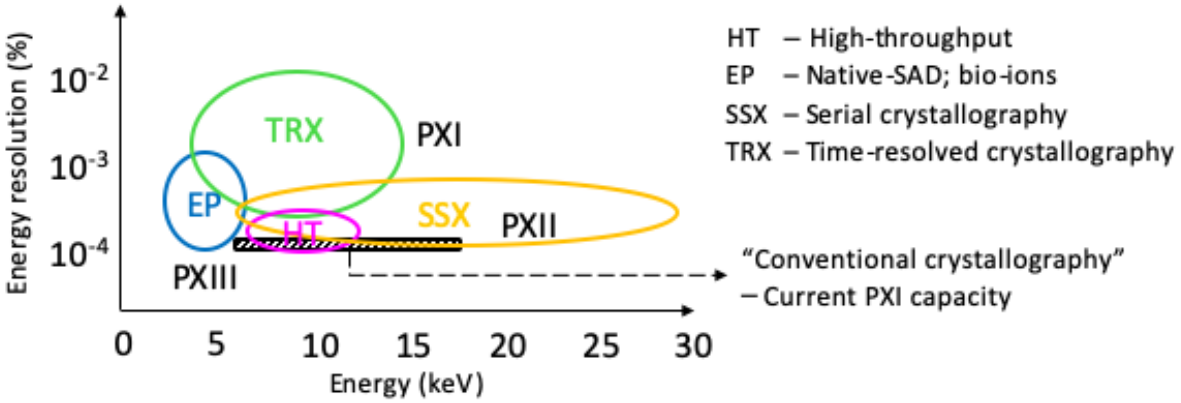

Figure 15.7: Expanding space in MX beamline characteristics and applications.

	X06SA		X10SA		X06DA	
	SLS 2.4 GeV	**SLS 2.0 2.7 GeV**	**SLS 2.4 GeV**	**SLS 2.0 2.7 GeV**	**SLS 2.4 GeV**	**SLS 2.0 2.7 GeV**
Source	U19 @ RT	U15 @ 77 K	U19 @ RT	U15 @ 77 K	SB 2.9 T	SB 2 T
Energy [keV]	6 to 17.5	4 to 18(30)	6 to 20	5 to 30	5 to 17.5	2.5 to 15
Energy res.	10^{-4}	10^{-4} to 10^{-2} †	10^{-4}	10^{-4}	10^{-4}	10^{-4}
Beam size [μm]	5 to 100	1 to 50	15 to 100	1 to 50	90 × 45	10 to 100
Flux [ph/s]	10^{12} (10^{11})‡	10^{13}	10^{12} (10^{11})‡	10^{13}	5×10^{11}	2×10^{12}
Goniometer	single-axis	multi-axis	single-axis	multi-axis	multi-axis	multi-axis
Detector	EIGER 16M	JF 10M/4M	EIGER2 16M	EIGER2 16M	PILATUS 2M	JF 10M

Table 15.4: Main design parameters for the upgrades of the three MX beamlines at SLS 2.0. (†) 10^{-2} to 10^{-3} resolution when using pink beam. (‡) Beam flux for beam sizes of 5 μm and 15 μm, at X06SA and X10SA, respectively.

15.4 X06SA (PXI): A versatile beamline for MX development

The X06SA has been instrumental in the development of MX beamlines at the SLS and has pushed the frontiers of MX over the last two decades [8,13,23,29,58–60]. To keep its leading position in an increasingly competitive field, the proposed upgrade will further expand the X06SA capacity with regards to all the important parameters, from the beam size and flux to energy range and bandwidth, with finer controls so that experiments can be tailored to each individual crystal. The upgrade will enhance the performance significantly for high-throughput and serial crystallography using monochromatic x-rays (see Section 15.5 for details), e.g. a complete data set can be obtained with one-second exposure (Figure 15.8). In addition, the endstation will be equipped with a ns-laser and spectrometer to widen MX applications from static structures to mechanistic and dynamic studies. Coupled with broader bandwidth and high-flux of pink x-rays, more diffraction data can be measured from "still" diffraction pattern; redox states of metalloproteins can be tracked, and biologically relevant dynamics can be studied in the milli- to microsecond time scale at SLS 2.0 (Figure 15.8). These developments will be complementary to the sister facility at SwissFEL, which allows for nano-crystallography, damage-free structure determination of metalloproteins, and fs to ns time-resolved crystallography. Furthermore, machine learning will be exploited for intelligent automation of beamline operations, data acquisition, and data analysis. This is especially critical for X06SA, because this beamline will host a variety of experiments at two endstations.

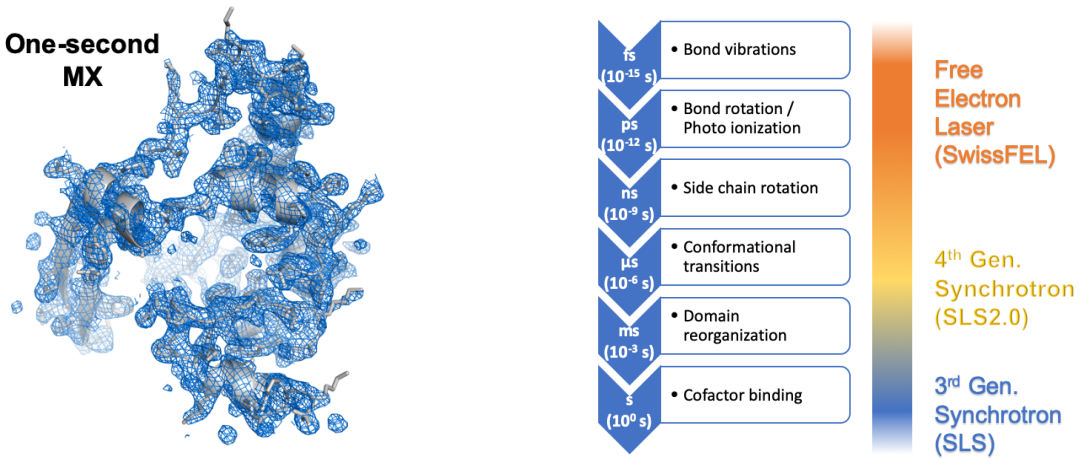

Figure 15.8: (left) Structure of nucleocapsid phosphoprotein from SARS-CoV-2 solved with 1 second x-ray exposure using a JUNGFRAU 4M detector operated at 2 kHz at SLS. (right) time scales of dynamics in biology and their accessibility at synchrotron and x-ray free-electron laser facilities.

15.4.1 Source

Referring to Chapter 2, a cryogenic permanent magnet undulator U15 (CPMU15) at SLS 2.0 (2.7 GeV) will boost the source brilliance 140 times compared with the current room-temperature undulator

U19 at the SLS (2.4 GeV). The SLS 2.0 machine design also allows further brilliance increase by accommodating longer undulator, and we plan to replace the 1.8 m U19 by a 3 m CPMU15. The CPMU15 will have an energy gap from about 4.6 keV to 5.1 keV between its first and third harmonics. Therefore, the second harmonic needs to be used to cover the energy gap. The reduced brilliance of even harmonics will be partially compensated by the gain in diffraction efficiency at low energy, which is proportional to $(1/E)^2$.

15.4.2 Front end

The beam acceptance should be 100 μrad $\times$100 μrad to collect the full beam. We would like to have two white-beam position monitors with 1 μm resolution and positioned metres apart for the accurate measurement of both spatial and angular beam position at kHz frequencies [40]. Such measurements will be essential for both the upstream feedback of the machine orbit and also the automated alignment and fine-tuning of the downstream beamline optics. A high-pass filter (e.g., a beryllium window) will be used to remove the low-energy radiation. An optional low-pass filter could be considered to remove higher harmonics.

15.4.3 Optics

The main technical challenge is to actively support specialised experiments and the development of emerging methods in MX while at the same time maintaining high-throughput routine user operation. Therefore, we designed a versatile x-ray optics system to deliver both monochromatic and pink beam in a broad energy range, feeding two endstations in one experimental hutch. A double multilayer monochromator (DMM) will be used for pink-beam applications with a targeted bandwidth of 0.5 % to 1 %. Multi-striped DMMs with different multilayer coatings will be used for different bandwidths, e.g., 200 layers of Ru/B4C for 1 % and 400 layers of Ti/B4C for 0.5 %. The monochromatic beam will be obtained with a *Si(111)* double crystal monochromator (DCM). The design should allow the use of each monochromator independently with the same beam offset (Figure 15.9). Both monochromators will be cooled to handle the high thermal load. Special care is needed to minimise the potential vibrations induced by cooling. The angular pointing accuracy should be smaller than 100 nrad. Given the limited space in the optics hutch, two monochromators could be hosted in one chamber. A microsecond x-ray chopper will be installed after monochromator for precised timing control for studying protein dynamics.

The x-ray beam focusing will be controlled by two pairs of Kirkpatrick-Baez mirrors (KB) or one pair of KBs and a set of compound-refractive lenses (CRLs) as transfocators via an intermediate focusing point (the secondary source). The secondary source allows convenient control of the beam size and divergence. The upstream KBs are bendable for adjusting the beam size at both the pink-beam station and the secondary source positions. For the scheme with the downstream pair of KBs, additional beam-size controls will be implemented by CRLs positioned upstream of the KB-mirrors. Alternatively, the focusing in the mono-beam station could be achieved with CRL transfocators, with reduced efficiency. To get the best of both focusing technologies, we propose a combined usage of both to offer the required performance for different applications. The overall x-ray optics scheme is depicted in Figure 15.10. The x-ray tracing study shows that one-micron (FWHM) focusing can be

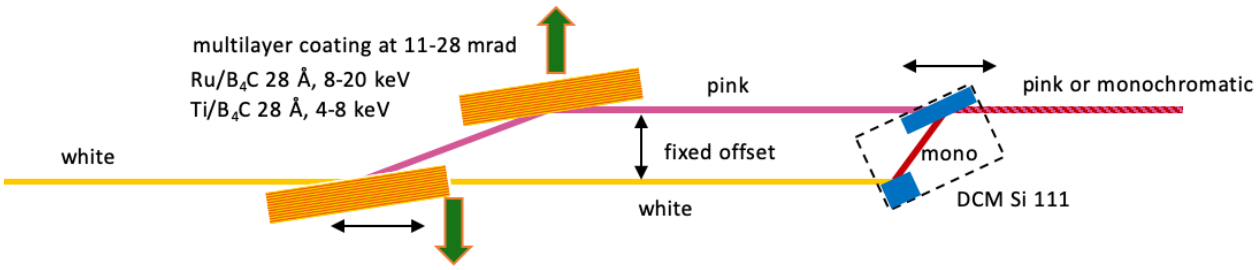

Figure 15.9: Monochromator concept of the X06SA beamline upgrade.

reached with state-of-the-art x-ray mirror technology. The mirrors will have three coatings, Si, Rh, Pt, to cover the entire energy range. No cooling is needed for the KB mirrors for the monochromatic beam. However, the heat load will be increased significantly when the DMM is operated in 1 % bandwidth, which is nearly the natural bandwidth of one single harmonics at SLS 2.0. The power density on the mirror surface will be studied. In order to reduce unnecessary radiation damage for room temperature data collection and to reach the microsecond scale in time-resolved crystallography, a x-ray beam chopper will be of great advantage. If the chopper can be installed immediately after the monochromator, it can be used to reduce the heat load on the mirrors in the pink beam mode.

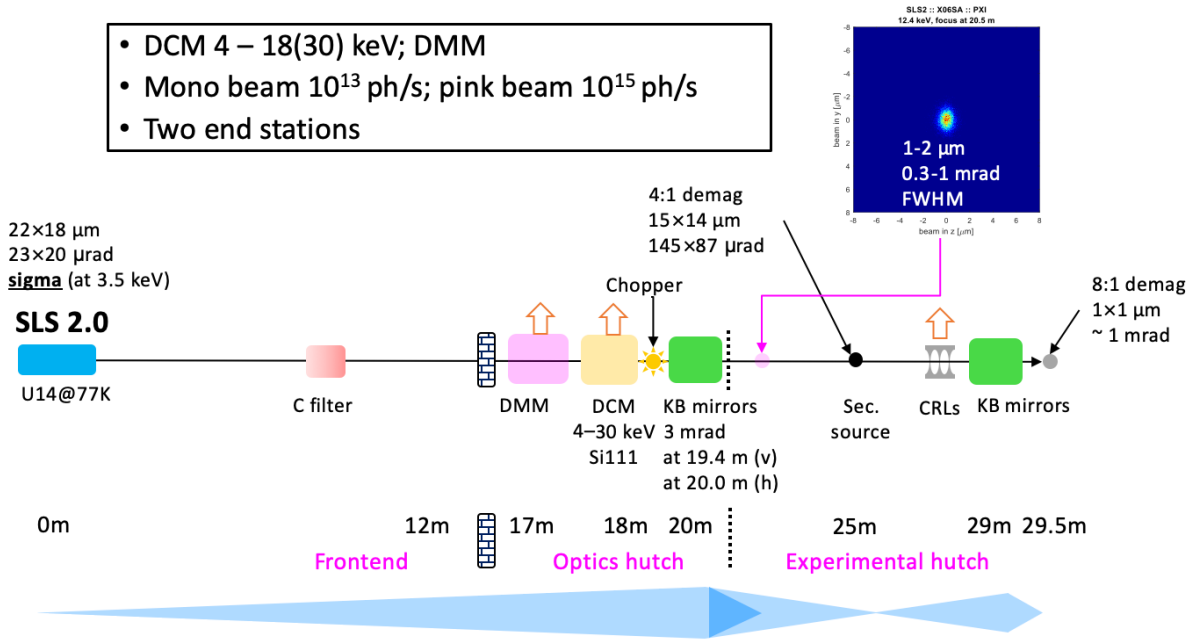

Figure 15.10: Schematic view of the X06SA beamline design for SLS 2.0.

15.4.4 Endstation

The two-stage focusing scheme also provides an opportunity for two "independent" endstations. One endstation will operate with monochromatic x-rays primarily (mono-station). This station will be equipped with the next-generation multi-axis goniometer (SwissGO), integrated sample environment, and a large-format JUNGFRAU detector with custom-shaped geometry (Figure 15.11). The standard serial crystallography experiment with both fixed-target and injector will be carried out at this station as well. The second station is designed for time-resolved crystallography with variable bandwidth (pink-station). It is positioned upstream of the secondary source point and capable of supporting varieties of sample delivery methods including injectors, mixing devices, acoustic droplet injector and levitator, microfluidics chips, and more. The station will also be equipped with a tunable nanosecond laser and spectrometers (Figure 15.11).

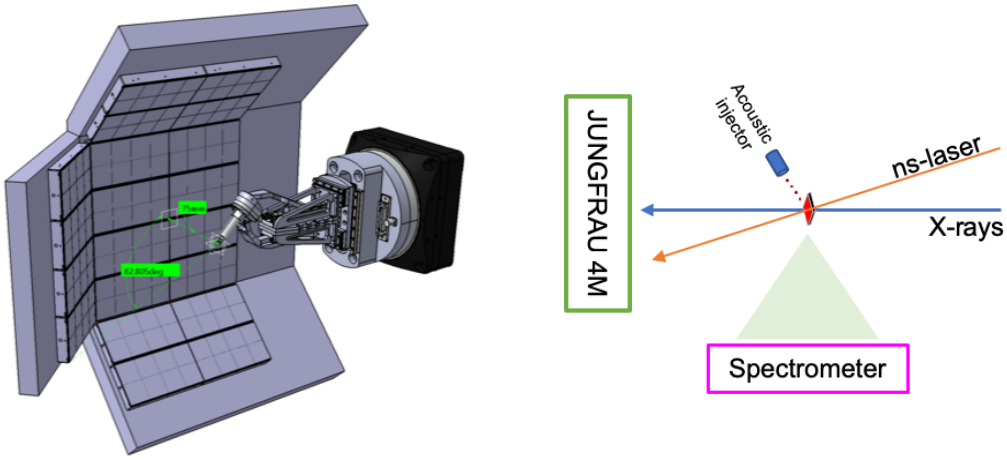

Figure 15.11: (left) Models of multi-axis goniometer (SwissGo) and JUNGFRAU 10M detector at the mono-station of X06SA. (right) Schematic view of the experimental setup at the pink-station of X06SA.

15.4.5 Timeline

We plan to install and commission the instruments for both mono- and pink-applications in parallel. For the day-one experiment, however, we would like to ensure the mono-station with standard MX experiments is in operation so that X06SA can serve most of its academic users after SLS 2.0 upgrade immediately. The pink-station commissioning can be completed during the regular shutdowns.

Time period	Main activities
Jan 2019 - Dec 2020	Conceptual design
Jan 2021 - Dec 2021	Technical design
Jan 2022 - Jun 2023	Procurement and manufacturing
Jun 2023 - Sep 2023	Commissioning at lab
Oct 2023 - Dec 2024	Installation
Jan 2025 - Jun 2025	Commissioning at beamline
Jul 2025 - Dec 2025	Pilot users
Jan 2026	Regular user operation

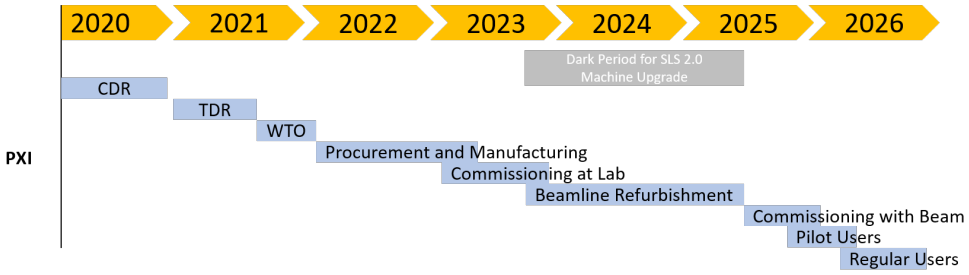

15.5 X10SA (PXII): A one-micron, high-flux MX beamline

X10SA is the second macromolecular crystallography beamline at Swiss Light Source. It is 100 % financed externally, mainly through partnership with industry. The partners currently comprise nine international pharmaceutical companies, including the three founding partners Max-Planck Gesellschaft, Novartis, and Roche. Structural-based drug development heavily relies on a large amount of protein structures solved from hundreds to thousands of ligand-bound protein crystals generated from fragment-based drug discovery campaigns. A significant increase in throughput, reducing the average data acquisition time per crystal from minutes to seconds, as will be possible with SLS 2.0, is clearly of great interest to our industry partners (Figure 15.12). With such throughput, the role of the beamline operator and user will be changed from collecting individual samples to supervising autonomous experiments as a whole. The associated workflow from sample delivery to data acquisition, analysis, and finally reporting needs to be developed with a suitable information-management system.

There is strong and increasing interest in membrane protein drug-targets that however tend to be more difficult to crystallise and that generate only weakly-diffracting crystals in the micrometre range. The proposed beamline upgrade with direct focusing is designed to collect the full flux into

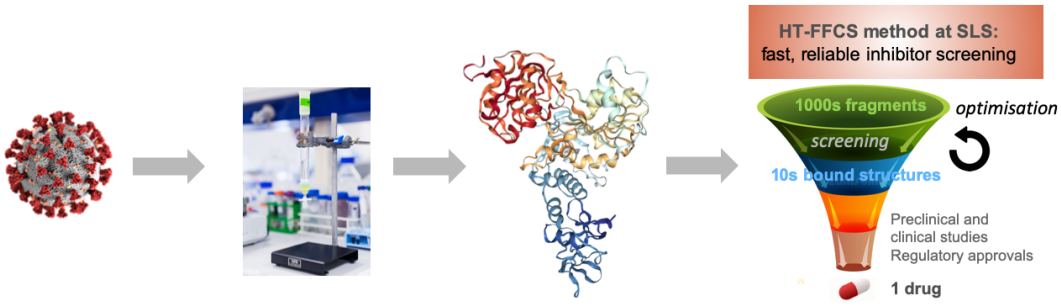

Figure 15.12: An illustration of fast fragment and ligand screening for structure-based drug discovery.

a one-micron spot with a flux density of 10^{13} ph s^{-1} μm^{-2}. With such a tightly-focused beam, the radiation damage could be reduced by the photoelectron escape effect. Moreover, the effect is more pronounced for micron-sized crystals at high energy (20 keV to 30 keV) ([61], see also Figure 15.13). To make best use of these facts, the beamline optics will have an upper energy limit of 30 keV, and a detector upgrade with CdTe sensors will be considered.

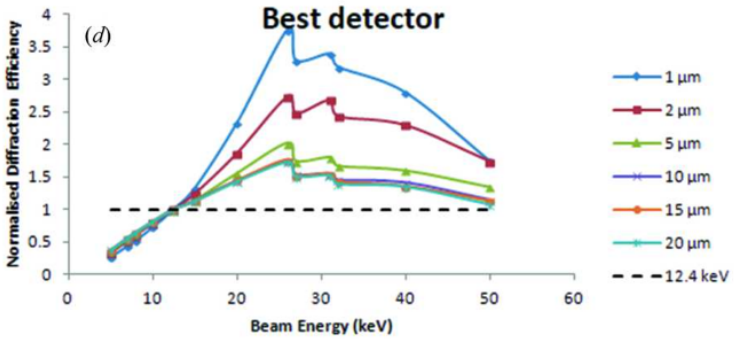

Figure 15.13: Diffraction efficiency as functions of x-ray beam energy and crystal size [61].

15.5.1 Source

The same cryogenic permanent magnet undulator (CPMU15) as planned for X06SA will be used. The brilliance increase is two to three order of magnitude in the designed energy range of 5 to 30 keV.

15.5.2 Front end

The front end will have the same design as beamline X06SA.

15.5.3 Optics

The optics design is optimised for the highest attainable flux in the energy range of 5 keV to 30 keV at the SLS 2.0. This can be achieved by a simple optics scheme with direct focusing using a *Si(111)* monochromator and a pair of KB mirrors, which can produce a 1 μm $\times$1 μm focused beam with $> 10^{13}$ ph s^{-1} at 12.4 keV and acceptable divergence. We will also reserve space for the possible addition of a DMM in the future. The *Si(111)* monochromator will have the same design as that at X06SA, with both symmetrically and asymmetrically cut *Si(111)* crystals. The KB mirrors will be bendable for adjusting the beam size from 1 μm to 50 μm while preserving the flux, and they will be positioned in the current experimental hutch. Three coatings (Pt, Rh, Si) on the KB mirrors will allow for high reflectivity and harmonics rejection (Figure 15.14). Additional sets of CRLs could be

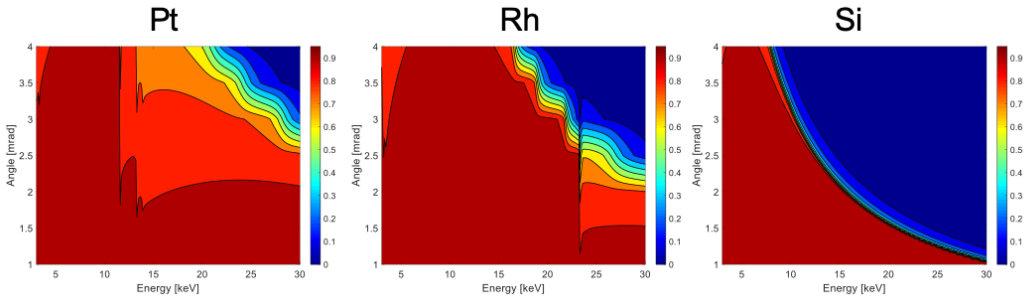

Figure 15.14: Mirror reflectivity as a function of x-ray beam energy and angle of incidence.

inserted before the mirrors for applications that need fast and robust beam size changing but do not need the highest flux. The optics concept is depicted in Figure 15.15.

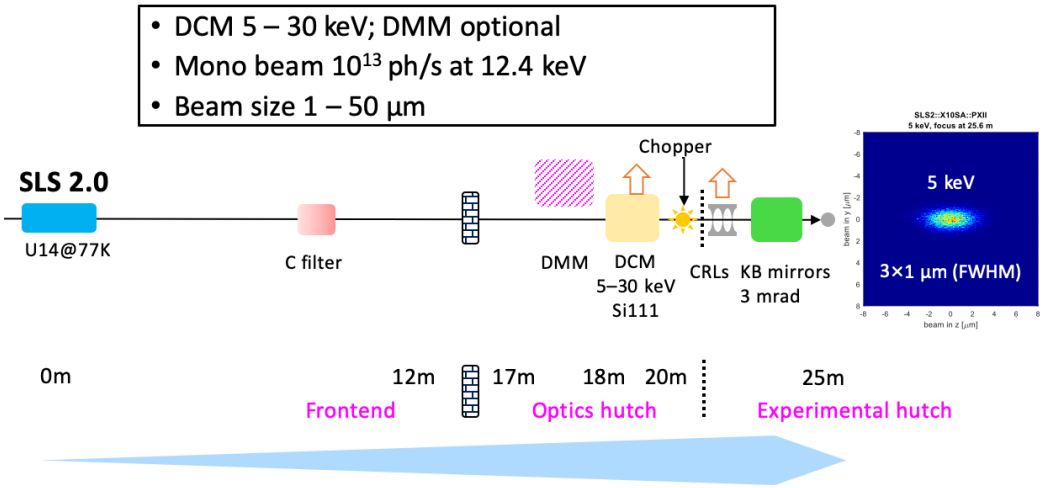

Figure 15.15: Schematic view of the X10SA beamline design for SLS 2.0.

15.5.4 Endstation

The endstation will have a very similar design as the mono endstation at X06SA. It will be equipped with the next-generation multi-axis goniometer (SwissGO). Instead of a JUNGFRAU detector, the current EIGER2 16M detector will remain for the upgrade. In fact, the re-triggering technology in EIGER2 will help in handling the increased photon-rate after the upgrade. To utilise the higher-energy photons (>20 keV) efficiently, a high-Z detector could be added as a phase-II upgrade.

15.5.5 Timeline

Since X10SA is funded 100 % by external beamline partners, we are obliged to provide our partners with the possibility to carry out experiments as early as possible. Considering the current planning for SLS 2.0, we intend to restart beamline operation with limited users in May 2025 and ramp up to full user operation in January 2025. Hence we plan to start rebuilding the beamline as soon as the dark period for the SLS 2.0 upgrade begins, with an estimated duration of 9 to 12 months. If possible, sub-projects of the upgrade project will be developed and commissioned well in advance to minimise the workload on both PSI support groups as well as the MX group itself.

Time period	Main activities
Jan 2019 - Dec 2020	Conceptual design
Jan 2021 - Jun 2021	Technical design
Jun 2021 - Dec 2022	Procurement and manufacturing
Jan 2023 - Sep 2023	Commissioning at lab
Oct 2023 - Dec 2024	Installation
Jan 2025 - Apr 2025	Commissioning at beamline
May 2025 - Sep 2025	Resume limited user operation and ramp up
Oct 2025	Regular user operation

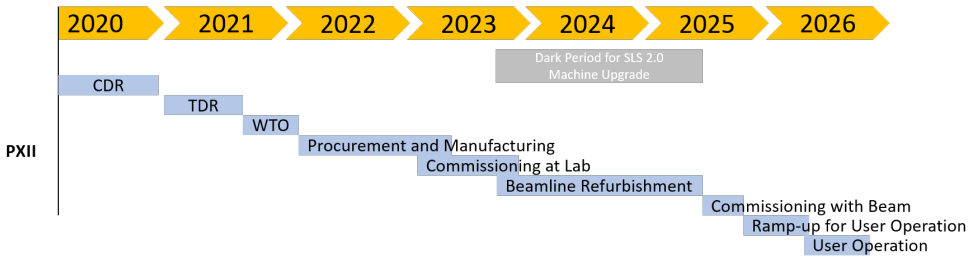

15.6 X06DA (PXIII): A microbeam superbend MX beamline

X06DA is currently the best-performing bending magnet MX beamline in the world. Its capacity to very accurately extract the anomalous scattering signal of low-Z elements intrinsically present in native macromolecular crystals (native SAD) places X06DA at the forefront of *de novo* structure determination. In the SLS 2.0 upgrade, X06DA will benefit from the much-improved horizontal

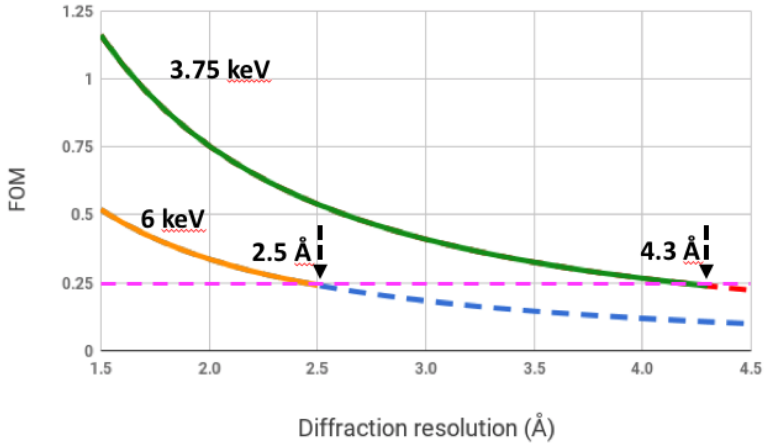

Figure 15.16: The expected phasing power gain in low-energy native SAD. The phasing power (FOM $= f''(1/d)^{3/2}$, where f'' is the anomalous scattering factor of sulfur and d is the diffraction resolution) is plotted as a function of diffraction resolution for two energies – orange for 6 keV and green for 3.75 keV. According to recent research on native SAD using 6-keV x-rays, a resolution of 2.5 Å or better is needed, which provides an estimation of the structure solvability threshold – 0.25 in the FOM scale (magenta dashed line). Applying the same threshold, 4.3 Å or better resolution is accessible for native SAD using 3.75-keV x-rays.

emittance, and it will become the first microbeam bending-magnet MX beamline with a performance comparable to micro-focus undulator beamlines at third-generation synchrotron sources. At the same time, it will preserve its excellent stability across the full energy range. The upgrade of X06DA will be focused on low-energy MX applications down to 3.0 keV, while maintaining high performance and user friendliness at the "standard" x-ray energy of 12.4 keV.

Amongst approximately 10 000 structures deposited in the protein data bank (PDB) per year, about 10 % are novel structures, the majority of which were phased with SeMet or heavy-metal derivatisation methods. These experimental phasing methods pose challenges along the path to successful macromolecular structure solutions, which are impossible to overcome in many cases. This notorious "phase problem" can potentially be solved with truly routine and effective native-SAD. The increase of phasing power which is predicted to occur with utilisation of low-energy MX native-SAD is quite substantial, as shown in Figure 15.16. In practice, however, there are still many considerable experimental difficulties that have to be resolved to achieve the ideal outcome. The X06DA upgrade combines multiple technological advances with the aim of overcoming the main challenges of low-energy measurements. The helium sample environment aims to eliminate air absorption; a multi-axis goniometer samples diffraction geometry comprehensively, while the JUNGFRAU detector with a custom-made shape provides high efficiency at low energy.

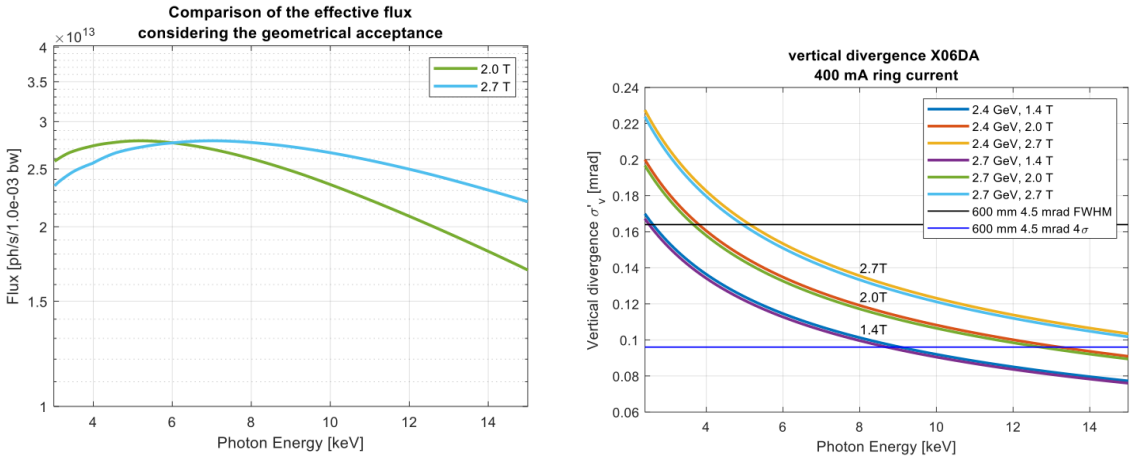

Figure 15.17: Flux (left) and vertical beam divergence (right) as a function of photon energy for different magnetic fields.

15.6.1 Source

A bending magnet emits a broad spectrum of light, so-called "white beam", from which the desired energy can be simply selected by a monochromator. In fact, this intrinsic characteristic of bending magnets is advantageous regarding beamline design and operation as, unlike for example for undulators, no mechanical manipulations like gap-size changes are required for a certain energy set. Thanks to the increased machine energy of 2.7 GeV at SLS 2.0, a 2 T superbend will have similar performance as a 2.7-T superbend in the energy range of 3 to 15 keV [Figure 15.17(a)] because of the reduced vertical source divergence [Figure 15.17(b)]. This allows a simpler magnet design by a modification of normal magnet for SLS 2.0 storage ring.

15.6.2 Front end

In order to maximise the acceptance of a broad horizontal radiation fan, it is critical to position the first x-ray mirror as close to the source point as possible. This means that the mirror must be located in the front end, which adds stringent space constraints to the front end design. A new front end concept has thus been developed, which reduces the footprints of all components and optimises their spatial arrangement. It includes a beam mask, a diaphragm/slits assembly, an absorber, a Beryllium window, a white beam BPM, and the first x-ray mirror. The horizontal acceptance has been increased up to 2 mrad to further increase the flux delivered at sample position.

15.6.3 Optics

The main optics system consists of a toroidal mirror, a Si(111) double channel cut monochromator (DCCM), and a KB-focusing system (Figure 15.18). The toroidal mirror is positioned 7 m from the source in the front end, it provides beam collimation in vertical direction and creates a secondary

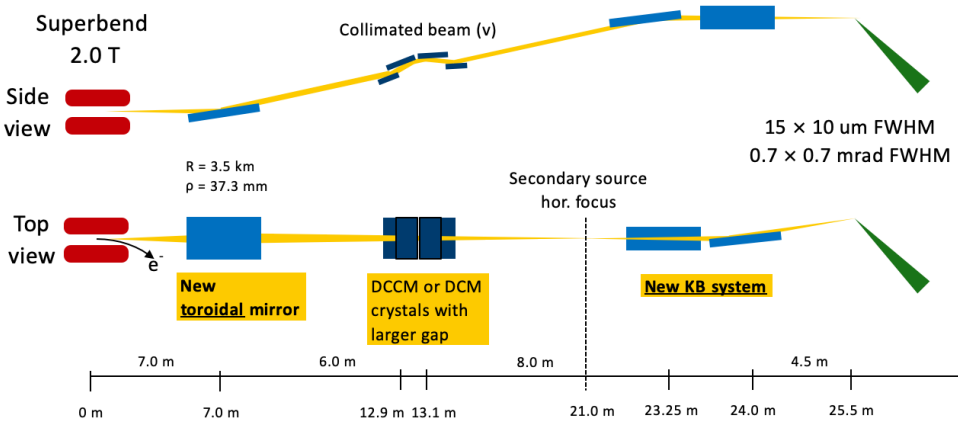

Figure 15.18: Schematic layouts of the X06DA x-ray optics design for SLS 2.0.

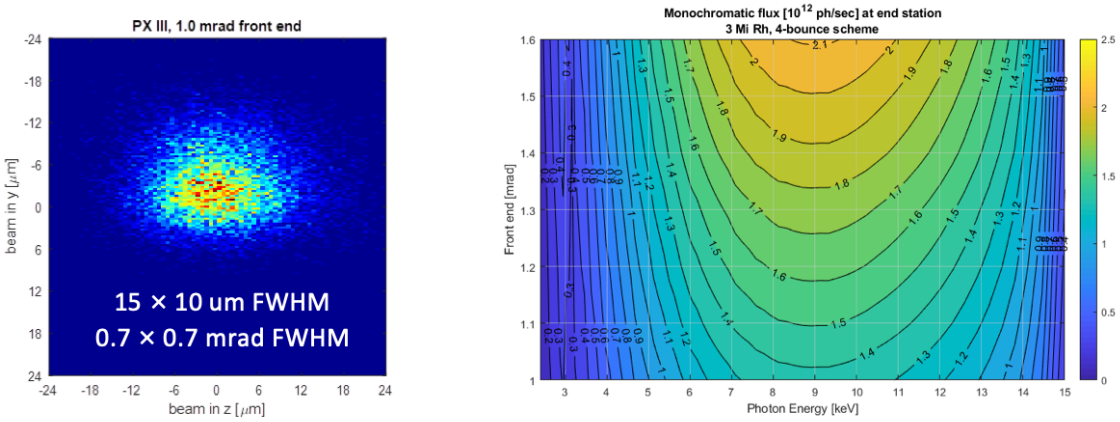

Figure 15.19: Preliminary ray-tracing results for the X06DA upgrade.

source at 21 metres in horizontal direction. The combination of the collimation and 1:2 magnification minimises the beam aberration from the toroidal mirror and allows micro-focusing by the downstream KB mirrors. All mirrors will have a beam incidence angle of 4.5 mrad. The toroidal mirror and one of the KB mirrors will be rhodium coated with $>$ 90 % reflectivity up to 15 keV. The other KB mirror will have both rhodium and silicon coatings. The silicon surface will be used to remove the higher energy passing through the Si(111) monochromator when operating at low energy. The double channel-cut monochromator (DCCM) with silicon (111) crystal will allow full tunability within energy range from 3.0 keV to 15 keV. The ray-tracing study confirmed that 10 μm to 20 μm focused beam with 2×10^{12} ph/sec is achievable at the sample position (25.5 m from the source) as shown in Figure 15.19. The design will keep the current optics hutch, but will require a new experimental hutch because of the new sample position further downstream from the current compact experimental hutch (Figure 15.18).

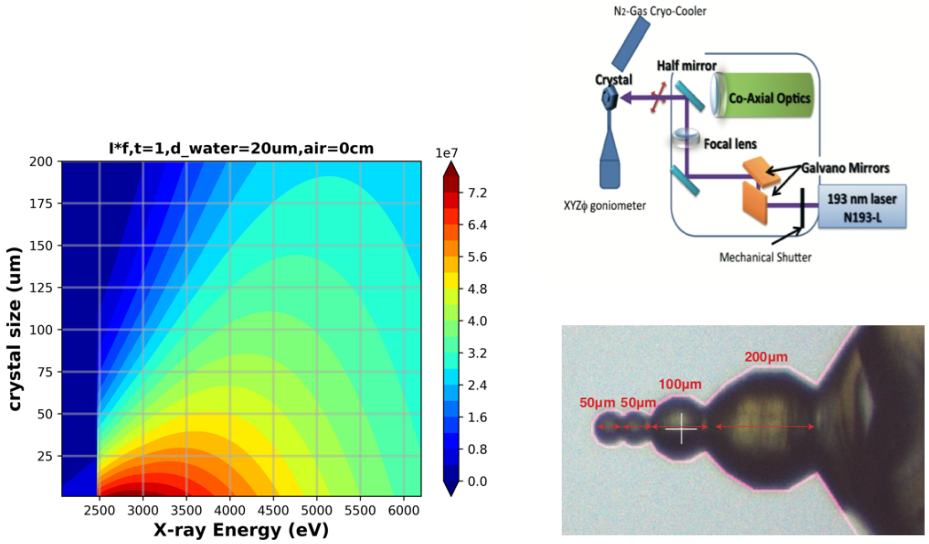

Figure 15.20: (left) 2D contour plot of theoretical anomalous diffraction efficiency for S atoms as a function of x-ray energy and crystal thickness. (right) Deep-UV laser machine setup and example of shaped crystal.

15.6.4 Endstation

At lower photon energies (< 6 keV) air absorption and scattering of the x-rays becomes a significantly limiting factor. Both effects attenuate the diffracted x-rays and adversely affect the measurements of the reflection intensities. Distinct approaches have been employed at different beamlines around the world to overcome this obstacle. A prominent example is beamline I23 at Diamond Light Source with its unique PILATUS 12M curved detector and entire sample environment enclosed in a vacuum chamber [30]. Alternatively, the sample environment can be flooded or purged with helium gas or part of it can be sealed off to provide a localised helium environment (an example being beamline BL-1A at the Photon Factory [62]).

Apart from air absorption, low-energy measurements suffer from absorption by the sample itself (Figure 15.20). In general, an absorption correction is empirically applied at the data processing level but this method is rather inefficient at energies < 6 keV. In this regard, the use of UV laser ablation technology promises a novel solution (Figure 15.20). It allows controlled trimming and shaping of large crystals to achieve stacked spherical shapes for homogeneous x-ray absorption [63]. In addition, it enables the removal of undesired contributions of non-diffracting materials, such as loop and solvent surrounding the crystal. We plan to acquire additional funding for a UV laser ablation system and integrate it into the X06DA beamline.

We plan to design a new sample environment optimised for low-energy MX without compromising routine user operation at higher energy. The setup is enclosed in a helium chamber, which contains a sample camera, a multi-axis goniometer, and a JUNGFRAU 10M detector. The goniometer (SwissGO) will be a successor of our in-house developed PRIGo and the commercialised SmarGon goniometer. The

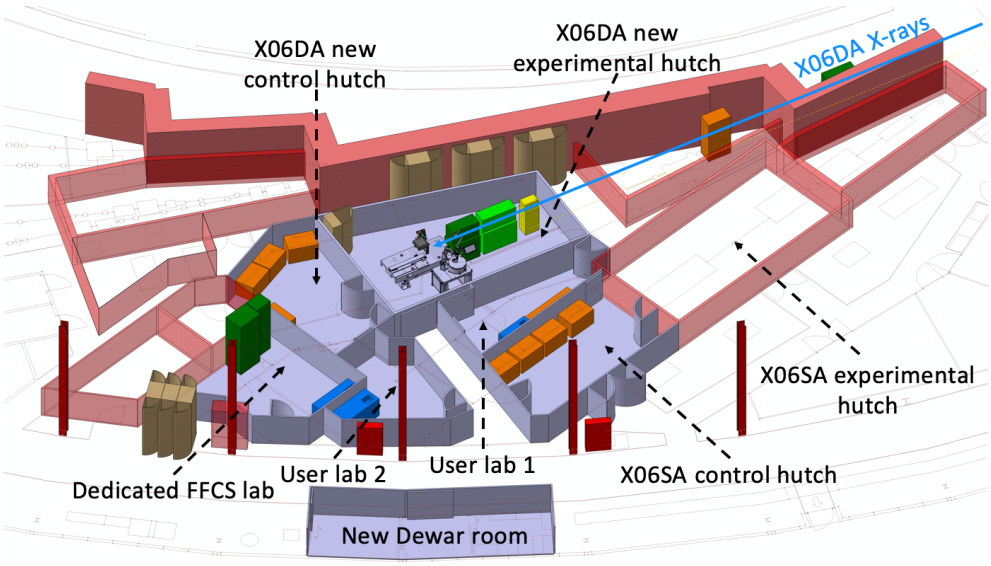

Figure 15.21: X06DA beamline layout with new experimental hutch and associated laboratories.

SwissGO will have improved functionalities such as dynamic positioning, allowing the synchronisation of grid scans, helical scans, and other complex motions with time-critical components such as a shutter, a detector trigger, or possibly a laser system. The JUNGFRAU 10M detector will be custom-shaped with an inclined geometry for capturing high-angle diffraction. Because it is an integrating detector, JUNGFRAU offers distinct advantages in measuring accurate diffraction data at low energies, as demonstrated recently [29].

15.6.5 Beamline layout

The x-ray optics upgrade moves the sample position 4.5 m downstream, which is outside of the current experimental hutch. Therefore, a new experimental hutch and control hutch are needed. Also we take this opportunity to rearrange beamline laboratories for better serving the needs of both X06DA and X06SA. There will be two user labs for standard and special (e.g. in dark) sample preparations and one crystallization lab dedicated to fast fragement and compound screening (FFCS). The new layout are shown in Figure 15.21

15.6.6 Timeline

We plan to start the upgrade of beamline X06DA prior to the SLS 2.0 shutdown. As the MX group is in charge of three beamlines, this allows the distribution of the resources over a longer period of time. In the first phase, pre-dark-time, the collimating mirror in the front end, the KB mirrors, as well as the new experimental hutch and associated labs shall be upgraded. Then, in a second phase, during the dark-time, upgrades for the sample environment and for the monochromator to access 3 keV can take place. This pre-dark-time upgrade provides a head-start in developing and prototyping some key

technologies for SLS 2.0, which on one hand provide a solid basis for further customisation at the other two MX beamlines, but also, on a larger scale, serves as a test bed for key technologies to be used at other beamlines at SLS 2.0. In particular, Beamline Controls, Motion Control and IT infrastructure, are areas where new technologies shall replace the aging old ones, and we offer that these be employed in conjunction with the upgrades at PXIII.

Time period	Main activities
Jan 2019 - Jun 2020	Conceptual design
Apr 2020 - Dec 2020	Technical design
Sep 2020 - Apr 2021	Procurement and manufacturing
Jan 2022 - Jun 2022	Commissioning at lab
Jul 2022 - Oct 2022	Installation of FE, x-ray optics, new hutch and labs
Nov 2022 - Jan 2023	Commissioning at beamline
Feb 2023 - Sep 2023	User operation / commissioning
Oct 2023 - Dec 2024	installation of new endstation
Jan 2025 - Apr 2025	Commissioning at beamline
May 2025 - Sep 2025	Resume limited user operation and ramp up
Oct 2025	Regular user operation

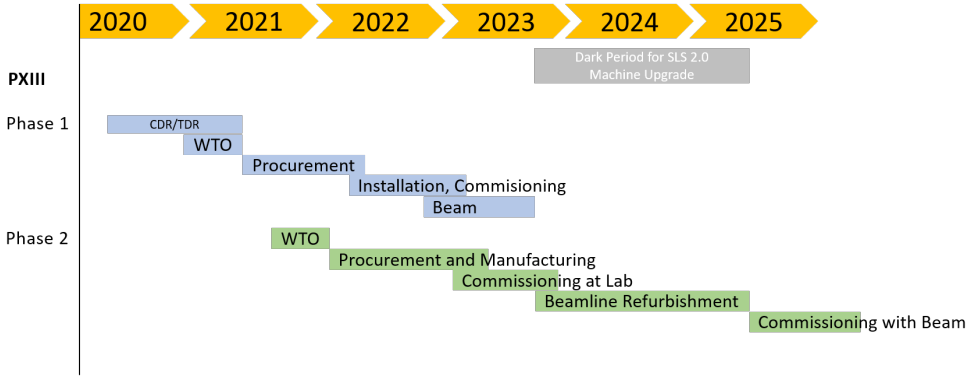

15.7 MX IT and data science plan for SLS 2.0

Increases in source brightness, as well as advances in detector technology and sample delivery methods, lead to an increase in both throughput and time resolution of the MX measurements. This requires preparing IT infrastructure to handle at least a 10-fold increase in both the peak rate and yearly total data volume. The simplest solution would be to scale up existing computing systems to handle increases in data rates. This is, however, a very costly solution and not sustainable.

In the past, two paradigms existed in the semiconductor industry, both a continuous increase in the frequencies at which integrated circuits operate (Dennard scaling) and an increase in the numbers of transistors per units of space (Moores law). All resulting in an exponential growth in computational power with time. If the problem was too computationally demanding for current resources, it was

sufficient to wait for the next generation of CPUs. Due to increasing difficulty in removing heat from silicon chips, CPU frequencies have already stalled for a few years at around 5 GHz, while increasing complexity and core count is also slowly hitting the limit [64,65]. The importance of computing for the economy has resulted in an increase of alternative solutions to CPUs, i.e. task specific accelerators. For example, high-performance computing routinely uses general-purpose graphic processing units (GPGPUs) to perform highly parallel floating-point calculations, as these chips exceed the capabilities of CPUs by orders of magnitudes. While applying task-specific architectures is the only suitable solution to handle the increase in data rates at SLS 2.0, it also carries the risk of fragmentation, with the presence of too many computing architectures being costly to program and maintain. Ideally, single task-specific architecture should be chosen, that will cover the majority of the most intensive workflows.

The MX beamline computing use case requires solutions that are optimized primarily for maximal data throughput, while computational performance is of secondary importance. Tasks like spot-finding and integration that take most of the MX computing resources usually require few CPU instructions per byte of data, which results in a situation where execution time is dependent on the speed that data can be delivered to CPU (or other accelerator) and not on pure performance. In addition, as many tasks are envisioned as part of online analysis and closed-loop feedback, real-time capabilities are also critical. While there are also tasks done by MX computing that are performance limited, i.e., merging of intensities, phasing and structure refinement, these can still be covered by general-purpose computing clusters or outsourced for supercomputing resources at, for example, the Swiss Supercomputer Center (CSCS).

However, data-intensive real-time applications require new solutions. Based on the research of the IT market, we have identified a combination of IBM POWER architecture, NVidia GPUs, and Xilinx FPGAs, as the most promising solution [66]. FPGAs provide moderate performance, but with the benefit of real-time guarantee and with a high level of parallelism. Xilinx High-Level Synthesis, which allows the compiling of existing C/C++ code into register transfer language, significantly simplifies the development of FPGA software. However, FPGAs need a server system to orchestrate the transfer of data to/from storage and flow control. Here POWER architecture comes in handy. Thanks to the Coherent Accelerator Processor Interface (OpenCAPI), data exchange between the FPGA and CPU is simplified, and higher throughput is possible. The implementation of a similar solution on a x86 platform would be more troublesome.

In this regard, the MX Group, in collaboration with the Detector Group, Science IT at PSI, and the IBM CAPI Enablement team, is evaluating a new POWER9 server IC922 with FPGA boards. As of 2020 we have demonstrated the capabilities of these technologies for data acquisition from the JUNGFRAU detector, including GPU implementation of spot-finding COLSPOT algorithms. Spot-intensity integration, in its simplest form, could be already carried out efficiently for real-time evaluation of data strength and completeness. The final intensity integration is the most complex one and probably needs to remain implemented in classical hardware. While this requires extra effort in learning new architecture and hardware/software development, it will be less expensive and more sustainable, than a tenfold scale-up of the IT budget.

The benefits of FPGA go beyond the data-analysis pipeline. FPGAs are already used for machine learning inferencing (i.e., in applying trained models to data of interest). As image recognition with

convolutional neural networks is currently high in the agenda of economic giants, it is expected that the focus of task-specific accelerators in the upcoming year will be mostly in that direction [67]. For SLS 2.0, machine learning could provide viable alternatives for deterministic spot-finding algorithms [68]. Machine learning could be equally applied to other sensors, as explained in more details later below. All inferencing tasks would also be implemented on POWER machines, similar to data-acquisition systems, although GPGPUs could be used in combination with FPGAs, as most machine learning software (for example Tensorflow and Caffe) are currently optimized for GPGPUs and there are solutions to export trained models to FPGA (e.g. Xilinx Vitis AI). POWER systems also have a significant advantage in that regard, with NVLink allowing 6x faster data transfer between CPU and GPGPU, as compared to the Intel platform.

Implementing machine learning also requires training resources to generate models used later for inferencing. This task is computationally much more demanding, and currently, GPGPUs are the best tool for that task. The most efficient way to train models would be through using CSCS supercomputing resources, which could use large volumes of previously collected data. As it might be needed, in some instances, to continuously optimize the machine learning model based on images and processing results, a small-scale machine learning training system is envisioned on site. This training system could either be a dedicated part of the facility computing cluster (with x86) or a dedicated system. In the latter case, the choice would be a 2-3 node cluster of IBM POWER servers with GPGPUs (e.g. AC922).

One additional necessary component will be a storage system that can handle JUNGFRAU peak data rates. As JUNGFRAU 10M can produce 12 GB/s when operated at full frame rate (48 GB/s raw with 4x compression) and EIGER2 16M XE can produce 2 GB/s (16 GB/s raw with 8x compression), the file system needs to be capable of handling 25 GB/s peak rate. Currently, the peak rate for the new GPFS file system is roughly 16 GB/s shared over the whole SLS. In order to obtain the required bandwidth, an SSD cache is necessary. Three options for the buffer are currently under evaluation (a combination of these options is the most likely possibility) and include the placing of extra SSDs inside the data acquisition system, the use of additional IBM POWER servers for buffering, and the use of a GPFS integrated SSD buffer (e.g. IBM ESS 3000).

The design of the online processing cluster depends on efforts in implementing data processing tasks on task-specific architectures. If these tasks are highly successful, and it is possible to implement all current functionalities in an innovative architecture (i.e., CPU+GPGPU or CPU+FPGA), then the new computing cluster could be entirely built of such components. If, however, achieving this goal becomes too complicated, the use of a standard x86 cluster would remain the only possible option. Currently, other synchrotrons (e.g., ESRF with POWER9 and GPGPUs) are also experimenting with task-specific architectures, so it is expected that there will be further community development in this direction.

Changes to the hardware architecture require changes in data flow. Currently, online data processing flow is file-based, i.e., the detector provides an HDF5 file that is written to the beamline file system, and data processing is then executed on the cluster with the file path as an input. In the SLS 2.0 flow, processing would need to be modified to operate directly on streams, i.e., the detector image would be packed into a queue protocol and transferred directly to the data processing node, which would reduce the transfer overhead, while files would be in parallel written to storage. For the

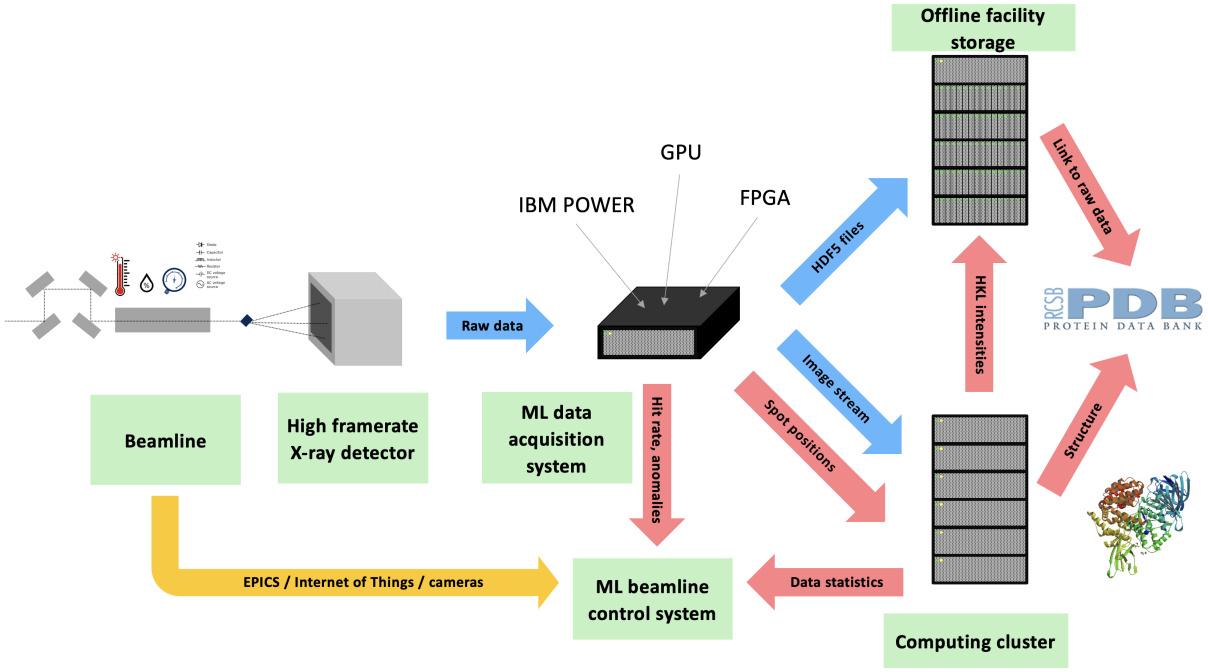

Figure 15.22: Data flow of the MX beamline at SLS 2.0. Blue arrows represent the flow of x-ray images (the most throughput critical), red arrows the flow of metadata, and the yellow arrow the flow of sensor information. [66]

best performance, it would be necessary to move the data-intensive and the straightforward steps of processing closer to the hardware. For example, data acquisition systems would calculate background standard deviation and spot positions, and online processing cluster would be only responsible for spot intensity integration and scaling. An expected flow is presented in Figure 15.22.

In parallel to hardware development, continuous improvement in algorithms is necessary. One of the key issues for efficient storage and data transfer is compression. X-ray images require fast algorithms, so that compression is not limiting data analysis throughput, but also gives good compression factors. Although a combination of bit shuffling filter and LZ4 gives good results, it is envisioned to test new developments in the compression community continuously. While lossy compression algorithms are currently not used in the MX community, they might become necessary for sustainable operation. Currently, we have started to evaluate the SZ algorithm [69] to verify how a lossy scheme affects data quality.

X-ray images are not the only data relevant to the beamline staff. Numerous sensors produce a significant amount of information about the beamline environment. There are also cameras to monitor the hutch and motor encoder read-outs. Currently, analysis of these streams is done by human scientists and using simple scripts. However, for SLS 2.0, we would like to implement more robust ways to use these extra information channels. We would like to follow the example of industry, where sensor data are used for example to decide on maintenance efforts (preventive maintenance), to trace conditions leading to equipment malfunction or to make data-driven operational decisions.

The foundation of such an approach would be a robust repository of all sensor data and software logs, stored in a modern time-series database (e.g. Elastic Search or InfluxDB), allowing the data to be efficiently queried and visualized, both by human scientists and software. The next layer would be big data analytics, to extract trends and time correlations from the stored data (e.g. Apache Spark and Hadoop). When a sufficient amount of data is collected, these could be used to train machine learning models (e.g. with Tensorflow) to automate beamline operation tasks or to detect anomalies and errors creating a digital beamline scientist. An interesting application would be also applying machine learned models for hutch cameras. These cameras could be directly connected to single board computers like Nvidia Jetson or Google Coral, allowing for immediate reduction of video stream for example to tag misplaced equipment - such solutions can be built around e.g. OpenCV and Tensorflow Lite, but also with commercial tools like IBM PowerAI Vision.

Lastly, but still very important, are data management strategies. If a tenfold increase in beamline throughput is realised, the tracking of experimental samples and generated datasets will likely become difficult for the human scientist. Therefore, database solutions are being developed to track samples from their arrival at the SLS to data production. This solution would be linked to the data catalogue, which lists all the datasets collected at the SLS by academic users. Such data would be available to the community according to the data policy. On request, a data catalogue DOI identifier could be provided, allowing the referencing of diffraction images along with the PDB record or in a publication. To ensure data collected at SLS 2.0 serve best the structural biology community, we want to conform with FAIR principles (Findable, Accessible, Interoperable and Reusable) [70,71]. Here the most crucial task for the facility is to ensure proper metadata for all the measurements are recorded, both regarding sample (taken from the database) and instrumentation. PSI is actively taking part in defining the NXmx "gold standard" [72] for macromolecular diffraction data and it is expected all MX detectors will produce compliant data by SLS 2.0.

To summarise, the main tasks for data science for SLS MX 2.0 are: (a) implementation of data acquisition and processing on task-specific architectures with spotlight on POWER architecture and FPGA acceleration, (b) development of machine learning models for image analysis, efficient maintenance and experiment control, (c) research on best compression practice for x-ray diffraction data, and (d) implementation of sample and data management systems to suit the best interests of both users and the whole community. We do expect, that outcome of these developments will benefit not only MX beamlines, but also other beamlines at the SLS 2.0 and in the broader synchrotron community.

15.8 Development of the sample preparation facility at SLS 2.0

15.8.1 Overview

The PSI crystallisation facility (CF) at the SLS is a hub for structural biology research at the PSI and is run by the MX Samples group. This provides crystallography support for groups in the BIO department and sample support at the SLS and SwissFEL, conducts research into new methods of crystallisation and sample delivery for both soluble and membrane proteins, and provides a variety of support and expertise to external users and industrial partners (e.g. LeadXpro, Idorsia). A final routine but important role of the group is to supply a range of crystalline samples of very high

diffraction quality and consistency for beamline testing and method development by the wider MX group.

15.8.2 Current situation

Since the reconfiguration of the CF in 2014, it has been transformed better to serve the needs of local users, focusing on proven and pragmatic technologies, good crystallisation practice, and method development. This approach has seen a dramatic increase in use, and integration of the CF in many SLS, LBR and SwissFEL projects.

15.8.3 Opportunities

The situation of the CF at the SLS provides unique opportunities for diffraction-guided optimisation of crystallisation, facilitates the provision of samples for beamline testing, and is of particular importance in supporting the preparation of samples for which timing, consistency of environment, and minimal disruption by transport and handling are important. These factors will remain unchanged for projects at SLS 2.0.

In addition, the provision of lab space for the CF at SLS 2.0 is essential for the continued development and implementation of two projects of prime strategic importance for the future of macromolecular crystallography at the PSI, namely fragment-based drug discovery for industrial partners (FFCS pipeline) and serial crystallography and its time-resolved variants using solid supports or liquid jets (SSX and SFX). These demands and constraints placed upon beamline properties by these projects are discussed elsewhere, but the consequences for the future space requirements of the CF are as follows:

FFCS: In a fragment screen, every soaked crystal is an independent and unique assay of binding for a particular fragment, and both positive and negative results have meaning. To ensure that reliable information is gathered in every case, consistency, precision, and traceability are required at each stage of the project: crystal growth, fragment dispensing, crystal soaking, crystal harvesting, crystal storage, data collection and data analysis. All of the preparative steps (from crystal growth to storage) are performed in the CF.

Storage of the fragment library, robotic dispensing of fragment screens, and robot-assisted high-throughput crystal harvesting employ sensitive and expensive equipment and materials, placing particular demands on space. At present, the equipment is located in an adapted section of the X06DA_3 lab. However, this is a sub-optimal arrangement because the lab is a frequently-used communal space, with conflicting experimental and environmental demands. In the future, provision of a dedicated space for the FFCS equipment would best ensure consistency and continuity of performance for these instruments. Since FFCS campaigns require frequent diffraction-guided optimisation and will be closely integrated with industrial beamtime and data collection, it is sensible for this space to be at the SLS.

SSX and SFX: Experiments using solid supports or liquid jets to introduce crystals into the beam are regularly employed by Structural Biologists at the SwissFEL and SLS. These methods facilitate data collection for samples that are particularly susceptible to radiation damage, samples that are unstable

in traditional cryo-crystallography, samples where room-temperature data collection is required, and samples where rapid-mixing or photo-triggering is to be used for time-resolved experiments. The MX Sample staff are developing methods for growing crystals suitable for SSX and are involved in the development and testing of new delivery methods at the SLS and SwissFEL.

SSX places exquisite spatial and temporal requirements on sample preparation. The experiments often require large volumes of samples that are fragile and evanescent in nature, demanding careful environmental control, and rapid and specialist handling. It is therefore crucial for success to have space for sample preparation in close proximity to the beamline.

15.8.4 Current lab configuration

The changing nature of the facility has created quite different demands and constraints on physical space and location. The facility space has grown and been reshaped in recent years, in an organic fashion contingent on the vacation of rooms by other users. The facility presently occupies two rooms:

X06DA_3: A 38 m^2 temperature-controlled lab space adjacent to X06DA, which houses crystallisation robotics, crystal-plate imaging equipment, a preparative wet-lab, and the recently-installed equipment for the fragment-based drug discovery pipeline (FFCS).

WSLA/026: A 44 m^2 lab space containing additional crystallisation robotics and a preparative wet-lab, a 9 m^2 cold room with a crystallisation robot and a crystal-plate imager, and various small instruments and storage.

15.8.5 Planned lab configuration for SLS 2.0

This configuration is not optimal, as it requires users regularly to cross the storage ring to access some instruments, and necessitates duplication of wet-lab resources. In particular, the X06DA_3 lab space is overcrowded following the addition of FFCS equipment. SLS 2.0 provides an opportunity to reconfigure the CF space, to retain current capabilities and improve operation for the future. We have planned a rearrangement of the facility space that would allow for beamline expansion, be more efficient and ergonomic for CF users, and provide dedicated space for FFCS and SSX. A floor plan showing the planned labs for FFCS and SSX is shown in Figure 15.21.

The CF will consist of a suite of rooms:

1. A general access CF lab space situated in the centre of the ring in labs WSLA /026 and 028. This will house the preparative lab equipment (centrifuges, pH meters, spectrometers, de-ionised water supply etc.) and the current cold-room crystallisation facility currently located in WSLA/026. In addition the space will be used for the crystallisation robotics, crystal-imaging and crystal-handling instruments currently located in the X06DA_3 lab. Location at the centre of the ring will also enable CF activities to continue during the SLS upgrade.
2. A separate, restricted-access, temperature-controlled room (or compartment) to house the library-storage, dispensing and sample storage equipment for the FFCS project.

3. Two small temperature-controlled wet-lab located between beamlines X06SA and X06DA with equipment for manual sample preparation. To be used where samples need to be prepared during the beamtime.

15.9 Concluding remarks

Large research infrastructure like SLS 2.0 provides a unique environment to foster cutting-edge instrumentation and methods development for MX. The upgrade of three MX beamlines will exploit both the source property of SLS 2.0 and the latest technology in intelligent devices, x-ray optics, goniometers, x-ray detectors, and integrated data analysis to push MX frontiers and offer a data-driven approach in beamline operation. Autonomous user operation supported by self-driving beamline will make MX more accessible and enable new sciences from a broader user community.

Bibliography

[1] Clemens Schulze-Briese, Gerd Heidenreich, Harry Auderset, Detlef Vermeulen, and Andreas K. Freund. Novel monochromator concept for sagittal micro-focusing of undulator radiation. volume 3448, page 156. International Society for Optics and Photonics, 1998.

[2] Heping Zheng, Jing Hou, Matthew D Zimmerman, Alexander Wlodawer, and Wladek Minor. The future of crystallography in drug discovery. *Expert opinion on drug discovery*, 9(2):125–37, 2014.

[3] Guillaume Pompidor, Florian S N Dworkowski, Vincent Thominet, Clemens Schulze-Briese, and Martin R Fuchs. A new on-axis micro-spectrophotometer for combining Raman, fluorescence and UV/Vis absorption spectroscopy with macromolecular crystallography at the Swiss Light Source. *Journal of synchrotron radiation*, 20(Pt 5):765–76, 2013.

[4] R. Bingel-Erlenmeyer, V. Olieric, J. P. A. Grimshaw, J. Gabadinho, X. Wang, S. G. Ebner, A. Isenegger, R. Schneider, J. Schneider, W. Glettig, C. Pradervand, E. H. Panepucci, T. Tomizaki, M. Wang, and C. Schulze-Briese. SLS Crystallization Platform at Beamline X06DAA Fully Automated Pipeline Enabling in Situ X-ray Diffraction Screening. *Crystal Growth & Design*, 11(4):916–923, 2011.

[5] Shibom Basu, Vincent Olieric, Filip Leonarski, Naohiro Matsugaki, Yoshiaki Kawano, Tomizaki Takashi, Chia-Ying Huang, Yusuke Yamada, Laura Vera, Natacha Olieric, Jerome Basquin, Justyna A Wojdyla, Oliver Bunk, Kay Diederichs, Masaki Yamamoto, and Meitian Wang. Long-wavelength native-SAD phasing: opportunities and challenges. *IUCrJ*, 6(Pt 3):373–386, 2019.

[6] Daniel Rossetti, Ulrich Lienert, Claude Pradervand, Roman Schneider, Ming Shi, Sasa Zelenika, Michel Rossat, Olivier Hignette, Amparo Rommeveaux, and Clemens Schulze-Briese. Design and performance of the flexural-hinge-based mirror bender at the SLS protein crystallography beamline X06SA. volume 4782, page 86. International Society for Optics and Photonics, 2002.

[7] Marcus Mueller, Meitian Wang, and Clemens Schulze-Briese. *Acta crystallographica. Section D, Biological crystallography.*

[8] Arnau Casanas, Rangana Warshamanage, Aaron D. Finke, Ezequiel Panepucci, Vincent Olieric, Anne Nöll, Robert Tampé, Stefan Brandstetter, Andreas Förster, Marcus Mueller, Clemens

Schulze-Briese, Oliver Bunk, Meitian Wang, and IUCr. EIGER detector: application in macromolecular crystallography. *Acta Crystallographica Section D Structural Biology*, 72(9):1036–1048, 2016.

[9] Sandro Waltersperger, Vincent Olieric, Claude Pradervand, Wayne Glettig, Marco Salathe, Martin R. Fuchs, Adrian Curtin, Xiaoqiang Wang, Simon Ebner, Ezequiel Panepucci, Tobias Weinert, Clemens Schulze-Briese, and Meitian Wang. PRIGo: a new multi-axis goniometer for macromolecular crystallography. *Journal of Synchrotron Radiation*, 22(4):895–900, 2015.

[10] Isabelle Martiel, Vincent Olieric, Martin Caffrey, and Meitian Wang. Practical approaches for in situ x-ray crystallography: from high-throughput screening to serial data collection. In *Protein Crystallography*, pages 1–27. 2018.

[11] Justyna Aleksandra Wojdyla, Ezequiel Panepucci, Isabelle Martiel, Simon Ebner, Chia-Ying Huang, Martin Caffrey, Oliver Bunk, and Meitian Wang. Fast two-dimensional grid and transmission X-ray microscopy scanning methods for visualizing and characterizing protein crystals. *Journal of applied crystallography*, 49(Pt 3):944–952, 2016.

[12] Justyna Aleksandra Wojdyla, Jakub W. Kaminski, Ezequiel Panepucci, Simon Ebner, Xiaoqiang Wang, Jose Gabadinho, and Meitian Wang. *DA+* data acquisition and analysis software at the swiss light source macromolecular crystallography beamlines. *Journal of Synchrotron Radiation*, (1):293–303.

[13] Kay Diederichs and Meitian Wang. Serial synchrotron X-Ray crystallography (SSX). *Methods Mol. Biol.*, 1607:239–272, 2017.

[14] Jana Ognjenović, Reinhard Grisshammer, and Sriram Subramaniam. Frontiers in Cryo Electron Microscopy of Complex Macromolecular Assemblies. *Annual Review of Biomedical Engineering*, 21(1):395–415, 2019.

[15] Matthew K Higgins and Susan M Lea. On the state of crystallography at the dawn of the electron microscopy revolution. *Current opinion in structural biology*, 46:95–101, 2017.

[16] Janet L Smith, Robert F Fischetti, and Masaki Yamamoto. Micro-crystallography comes of age. *Current opinion in structural biology*, 22(5):602–12, 2012.

[17] Andreas Förster, Stefan Brandstetter, and Clemens Schulze-Briese. Transforming X-ray detection with hybrid photon counting detectors. *Philosophical transactions. Series A, Mathematical, physical, and engineering sciences*, 377(2147):20180241, 2019.

[18] Raymond G. Sierra, Uwe Weierstall, Dominik Oberthuer, Michihiro Sugahara, Eriko Nango, So Iwata, and Alke Meents. Sample Delivery Techniques for Serial Crystallography. In *X-ray Free Electron Lasers*, pages 109–184. Springer International Publishing, Cham, 2018.

[19] Patrick M. Collins, Alice Douangamath, Romain Talon, Alexandre Dias, Jose Brandao-Neto, Tobias Krojer, and Frank von Delft. Achieving a Good Crystal System for Crystallographic X-Ray Fragment Screening. *Methods in Enzymology*, 610:251–264, 2018.

[20] Cornelius Gati, Gleb Bourenkov, Marco Klinge, Dirk Rehders, Francesco Stellato, Dominik Oberthür, Oleksandr Yefanov, Benjamin P Sommer, Stefan Mogk, Michael Duszenko, Christian Betzel, Thomas R Schneider, Henry N Chapman, and Lars Redecke. Serial crystallography on in vivo grown microcrystals using synchrotron radiation. *IUCrJ*, 1(Pt 2):87–94, 2014.

[21] Chia-Ying Huang, Vincent Olieric, Nicole Howe, Rangana Warshamanage, Tobias Weinert, Ezequiel Panepucci, Lutz Vogeley, Shibom Basu, Kay Diederichs, Martin Caffrey, and Meitian Wang. In situ serial crystallography for rapid de novo membrane protein structure determination. *Communications biology*, 1:124, 2018.

[22] Tobias Weinert, Natacha Olieric, Robert Cheng, Steffen Brünle, Daniel James, Dmitry Ozerov, Dardan Gashi, Laura Vera, May Marsh, Kathrin Jaeger, Florian Dworkowski, Ezequiel Panepucci, Shibom Basu, Petr Skopintsev, Andrew S. Doré, Tian Geng, Robert M. Cooke, Mengning Liang, Andrea E. Prota, Valerie Panneels, Przemyslaw Nogly, Ulrich Ermler, Gebhard Schertler, Michael Hennig, Michel O. Steinmetz, Meitian Wang, and Jörg Standfuss. Serial millisecond crystallography for routine room-temperature structure determination at synchrotrons. *Nature Communications*, 8(1):542, 2017.

[23] Tobias Weinert, Petr Skopintsev, Daniel James, Florian Dworkowski, Ezequiel Panepucci, Demet Kekilli, Antonia Furrer, Steffen Brünle, Sandra Mous, Dmitry Ozerov, Przemyslaw Nogly, Meitian Wang, and Jörg Standfuss. Proton uptake mechanism in bacteriorhodopsin captured by serial synchrotron crystallography. *Science (New York, N.Y.)*, 365(6448):61–65, 2019.

[24] Pedram Mehrabi, Eike C Schulz, Raison Dsouza, Henrike M Müller-Werkmeister, Friedjof Tellkamp, R J Dwayne Miller, and Emil F Pai. Time-resolved crystallography reveals allosteric communication aligned with molecular breathing. *Science (New York, N.Y.)*, 365(6458):1167–1170, 2019.

[25] Qun Liu and Wayne A Hendrickson. Crystallographic phasing from weak anomalous signals. *Current Opinion in Structural Biology*, 34:99–107, 2015.

[26] Patricia S Langan, Venu Gopal Vandavasi, Kevin L Weiss, Pavel V Afonine, Kamel El Omari, Ramona Duman, Armin Wagner, and Leighton Coates. Anomalous X-ray diffraction studies of ion transport in K+ channels. *Nature communications*, 9(1):4540, 2018.

[27] Andreas Streun, Terence Garvey, Lenny Rivkin, Volker Schlott, Thomas Schmidt, Philip Willmott, and Albin Wrulich. SLS-2 the upgrade of the Swiss Light Source. *Journal of Synchrotron Radiation*, 25(Pt 3):631, 2018.

[28] Sol M. Gruner and Eaton E. Lattman. Biostructural Science Inspired by Next-Generation X-Ray Sources. *Annual Review of Biophysics*, 44(1):33–51, 2015.

[29] Filip Leonarski, Sophie Redford, Aldo Mozzanica, Carlos Lopez-Cuenca, Ezequiel Panepucci, Karol Nass, Dmitry Ozerov, Laura Vera, Vincent Olieric, Dominik Buntschu, Roman Schneider, Gemma Tinti, Erik Froejdh, Kay Diederichs, Oliver Bunk, Bernd Schmitt, and Meitian Wang.

Fast and accurate data collection for macromolecular crystallography using the JUNGFRAU detector. *Nature Methods*, 15(10):799–804, 2018.

[30] Armin Wagner, Ramona Duman, Keith Henderson, and Vitaliy Mykhaylyk. In-vacuum long-wavelength macromolecular crystallography. *Acta crystallographica. Section D, Structural biology*, 72(Pt 3):430–9, 2016.

[31] Isabelle Martiel, Henrike M Müller-Werkmeister, and Aina E Cohen. Strategies for sample delivery for femtosecond crystallography. *Acta crystallographica. Section D, Structural biology*, 75(Pt 2):160–177, 2019.

[32] E. M. H. Duke and L. N. Johnson. Macromolecular crystallography at synchrotron radiation sources: current status and future developments. *Proceedings of the Royal Society A: Mathematical, Physical and Engineering Sciences*, 466(2124):3421–3452, 2010.

[33] Manuel Sanchez del Rio, Niccolo Canestrari, Fan Jiang, Franco Cerrina, and IUCr. SHADOW3 : a new version of the synchrotron X-ray optics modelling package. *Journal of Synchrotron Radiation*, 18(5):708–716, 2011.

[34] James M Holton, Scott Classen, Kenneth A Frankel, and John A Tainer. The R-factor gap in macromolecular crystallography: an untapped potential for insights on accurate structures. *The FEBS journal*, 281(18):4046–60, 2014.

[35] Kay Diederichs and IUCr. Quantifying instrument errors in macromolecular X-ray data sets. *Acta Crystallographica Section D Biological Crystallography*, 66(6):733–740, 2010.

[36] Kay Diederichs and IUCr. Simulation of X-ray frames from macromolecular crystals using a ray-tracing approach. *Acta Crystallographica Section D Biological Crystallography*, 65(6):535–542, 2009.

[37] James M Holton. A beginner's guide to radiation damage. *Journal of synchrotron radiation*, 16(2):133–142, 2009.

[38] Thomas C. Terwilliger, Gábor Bunkóczi, Li-Wei Hung, Peter H. Zwart, Janet L. Smith, David L. Akey, Paul D. Adams, and IUCr. Can I solve my structure by SAD phasing? Anomalous signal in SAD phasing. *Acta Crystallographica Section D Structural Biology*, 72(3):346–358, 2016.

[39] Thomas C. Terwilliger, Gábor Bunkóczi, Li-Wei Hung, Peter H. Zwart, Janet L. Smith, David L. Akey, Paul D. Adams, and IUCr. Can I solve my structure by SAD phasing? Planning an experiment, scaling data and evaluating the useful anomalous correlation and anomalous signal. *Acta Crystallographica Section D Structural Biology*, 72(3):359–374, 2016.

[40] Selamnesh Nida, Alexander Tsibizov, Thomas Ziemann, Judith Woerle, Andy Moesch, Clemens Schulze-Briese, Claude Pradervand, Salvatore Tudisco, Hans Sigg, Oliver Bunk, Ulrike Grossner, and Massimo Camarda. Silicon carbide x-ray beam position monitors for synchrotron applications. *J. Synchrotron Radiat.*, 26(Pt 1):28–35, 2019.

[41] U W Arndt and A J Wonacott. *The Rotation Method in Crystallography: Data Collection from Macromolecular Crystals*. North-Holland Publishing Company, 1977.

[42] Wayne A Hendrickson. Anomalous diffraction in crystallographic phase evaluation. *Q. Rev. Biophys.*, 47(1):49–93, 2014.

[43] A Meents, M O Wiedorn, V Srajer, R Henning, I Sarrou, J Bergtholdt, M Barthelmess, P Y A Reinke, D Dierksmeyer, A Tolstikova, S Schaible, M Messerschmidt, C M Ogata, D J Kissick, M H Taft, D J Manstein, J Lieske, D Oberthuer, R F Fischetti, and H N Chapman. Pink-beam serial crystallography. *Nat. Commun.*, 8(1):1281, 2017.

[44] Albert T Macrander and Xiangrong Huang. Synchrotron X-Ray optics. *Annu. Rev. Mater. Res.*, 47(1):135–152, 2017.

[45] Hiroo Tajiri, Hiroshi Yamazaki, Haruhiko Ohashi, Shunji Goto, Osami Sakata, and Tetsuya Ishikawa. A middle energy-bandwidth x-ray monochromator for high-flux synchrotron diffraction: revisiting asymmetrically cut silicon crystals. *J. Synchrotron Radiat.*, 26(Pt 3):750–755, 2019.

[46] P Oberta, Y Platonov, and U Flechsig. Investigation of multilayer x-ray optics for the 6 keV to 20 keV energy range. *J. Synchrotron Radiat.*, 19(Pt 5):675–681, 2012.

[47] A Snigirev, V Kohn, I Snigireva, and B Lengeler. A compound refractive lens for focusing high-energy x-rays. *Nature*, 384(6604):49–51, 1996.

[48] Matthew W Bowler, Didier Nurizzo, Ray Barrett, Antonia Beteva, Marjolaine Bodin, Hugo Caserotto, Solange Delagenière, Fabian Dobias, David Flot, Thierry Giraud, Nicolas Guichard, Mattias Guijarro, Mario Lentini, Gordon A Leonard, Sean McSweeney, Marcus Oskarsson, Werner Schmidt, Anatoli Snigirev, David von Stetten, John Surr, Olof Svensson, Pascal Theveneau, and Christoph Mueller-Dieckmann. MASSIF-1: a beamline dedicated to the fully automatic characterization and data collection from crystals of biological macromolecules. *J. Synchrotron Radiat.*, 22(6):1540–1547, 2015.

[49] Gavin B M Vaughan, Jonathan P Wright, Aleksei Bytchkov, Michel Rossat, Henri Gleyzolle, Irina Snigireva, and Anatoly Snigirev. X-ray transfocators: focusing devices based on compound refractive lenses. *J. Synchrotron Radiat.*, 18(Pt 2):125–133, 2011.

[50] Masaki Yamamoto, Kunio Hirata, Keitaro Yamashita, Kazuya Hasegawa, Go Ueno, Hideo Ago, and Takashi Kumasaka. Protein microcrystallography using synchrotron radiation. *IUCrJ*, 4(5):529–539, 2017.

[51] Kazuya Hasegawa, Keitaro Yamashita, Tomohiro Murai, Nipawan Nuemket, Kunio Hirata, Go Ueno, Hideo Ago, Toru Nakatsu, Takashi Kumasaka, and Masaki Yamamoto. Development of a dose-limiting data collection strategy for serial synchrotron rotation crystallography. *J. Synchrotron Radiat.*, 24(Pt 1):29–41, 2017.

[52] Sabine Botha, Karol Nass, Thomas R M Barends, Wolfgang Kabsch, Beatrice Latz, Florian Dworkowski, Lutz Foucar, Ezequiel Panepucci, Meitian Wang, Robert L Shoeman, Ilme Schlichting, and R Bruce Doak. Room-temperature serial crystallography at synchrotron x-ray sources using slowly flowing free-standing high-viscosity microstreams. *Acta Crystallogr. D Biol. Crystallogr.*, 71(Pt 2):387–397, 2015.

[53] Philip Roedig, Helen M Ginn, Tim Pakendorf, Geoff Sutton, Karl Harlos, Thomas S Walter, Jan Meyer, Pontus Fischer, Ramona Duman, Ismo Vartiainen, Bernd Reime, Martin Warmer, Aaron S Brewster, Iris D Young, Tara Michels-Clark, Nicholas K Sauter, Abhay Kotecha, James Kelly, David J Rowlands, Marcin Sikorsky, Silke Nelson, Daniel S Damiani, Roberto Alonso-Mori, Jingshan Ren, Elizabeth E Fry, Christian David, David I Stuart, Armin Wagner, and Alke Meents. High-speed fixed-target serial virus crystallography. *Nat. Methods*, 14(8):805–810, 2017.

[54] I Johnson, A Bergamaschi, H Billich, S Cartier, R Dinapoli, D Greiffenberg, M Guizar-Sicairos, B Henrich, J Jungmann, D Mezza, A Mozzanica, B Schmitt, X Shi, and G Tinti. Eiger: a single-photon counting x-ray detector. *J. Instrum.*, 9(05):C05032, 2014.

[55] A Mozzanica, M Andrä, R Barten, A Bergamaschi, S Chiriotti, M Brückner, R Dinapoli, E Fröjdh, D Greiffenberg, F Leonarski, C Lopez-Cuenca, D Mezza, S Redford, C Ruder, B Schmitt, X Shi, D Thattil, G Tinti, S Vetter, and J Zhang. The JUNGFRAU detector for applications at synchrotron light sources and XFELs. *Synchrotron Radiat. News*, 31(6):16–20, 2018.

[56] Florent Cipriani, Martin Röwer, Christophe Landret, Ulrich Zander, Franck Felisaz, and José Antonio Márquez. CrystalDirect: a new method for automated crystal harvesting based on laser-induced photoablation of thin films. *Acta Crystallogr. D*, 68(Pt 10):1393–1399, 2012.

[57] N Wright, F von Delft, P Collins, R Talon, E Nelson, and others. The Low-Cost, Semi-Automated shifter microscope stage transforms speed and robustness of manual protein crystal harvesting. *bioRxiv*, 2019.

[58] Fasséli Coulibaly, Elaine Chiu, Keiko Ikeda, Sascha Gutmann, Peter W Haebel, Clemens Schulze-Briese, Hajime Mori, and Peter Metcalf. The molecular organization of cypovirus polyhedra. *Nature*, 446(March):97–101, 2007.

[59] Adam Ben-Shem, Nicolas Garreau de Loubresse, Sergey Melnikov, Lasse Jenner, Gulnara Yusupova, and Marat Yusupov. The structure of the eukaryotic ribosome at 3.0 Å resolution. *Science*, 334(6062):1524–1529, 2011.

[60] Marcus Mueller, Meitian Wang, and Clemens Schulze-Briese. Optimal fine φ-slicing for single-photon-counting pixel detectors. *Acta Crystallogr. D Biol. Crystallogr.*, 68(Pt 1):42–56, 2012.

[61] Joshua L. Dickerson and Elspeth F. Garman. The potential benefits of using higher X-ray energies for macromolecular crystallography. *Journal of Synchrotron Radiation*, 26(4):922–930, 2019.

[62] Dorothee Liebschner, Yusuke Yamada, Naohiro Matsugaki, Miki Senda, and Toshiya Senda. On the influence of crystal size and wavelength on native SAD phasing. *Acta Crystallographica Section D Structural Biology*, 72(6):728–741, 2016.

[63] Hiroshi Kitano. Protein cryocrystallography using Laser-Processed crystal. http://dx.doi.org/10.1143/JJAP.44.L54. Accessed: 2019-2-21.

[64] Neil Thompson. The economic impact of moore's law: Evidence from when it faltered. *Available at SSRN 2899115*, 2017.

[65] John M Shalf and Robert Leland. Computing beyond moore's law. *Computer*, 48(SAND-2015-8039J), 2015.

[66] Filip Leonarski, Aldo Mozzanica, Martin Brckner, Carlos Lopez-Cuenca, Sophie Redford, Leonardo Sala, Andrej Babic, Heinrich Billich, Oliver Bunk, Bernd Schmitt, and Meitian Wang. Jungfrau detector for brighter x-ray sources: Solutions for it and data science challenges in macromolecular crystallography. *Structural Dynamics*, 7(1):014305, 2020.

[67] Neil Thompson and Svenja Spanuth. The decline of computers as a general purpose technology: Why deep learning and the end of moores law are fragmenting computing. *Available at SSRN 3287769*, 2018.

[68] T-W Ke, Aaron S Brewster, Stella X Yu, Daniela Ushizima, Chao Yang, and Nicholas K Sauter. A convolutional neural network-based screening tool for x-ray serial crystallography. *Journal of synchrotron radiation*, 25(3):655–670, 2018.

[69] X. Liang, S. Di, D. Tao, S. Li, S. Li, H. Guo, Z. Chen, and F. Cappello. Error-controlled lossy compression optimized for high compression ratios of scientific datasets. In *2018 IEEE International Conference on Big Data (Big Data)*, pages 438–447, 2018.

[70] Mark D Wilkinson, Michel Dumontier, IJsbrand Jan Aalbersberg, Gabrielle Appleton, Myles Axton, Arie Baak, Niklas Blomberg, Jan-Willem Boiten, Luiz Bonino da Silva Santos, and Philip E Bourne. The fair guiding principles for scientific data management and stewardship. *Scientific data*, 3, 2016.

[71] John R Helliwell, Wladek Minor, Manfred S Weiss, Elspeth F Garman, Randy J Read, Janet Newman, Mark J van Raaij, Janos Hajdu, and Edward N Baker. Findable accessible interoperable re-usable (fair) diffraction data are coming to protein crystallography, 2019.

[72] Herbert J. Bernstein, Andreas Förster, Asmit Bhowmick, Aaron S. Brewster, Sandor Brockhauser, Luca Gelisio, David R. Hall, Filip Leonarski, Valerio Mariani, Gianluca Santoni, Clemens Vonrhein, and Graeme Winter. Gold Standard for macromolecular crystallography diffraction data. *IUCrJ*, 7(5), 2020.

Chapter 16

microXAS 2.0 – a hierarchical, multimodal 4D chemical imaging beamline

D. Grolimund, D. F. Sanchez, C. Bostedt, B. Meyer, and M. Birri

In a nutshell

The visionary aim of the microXAS 2.0 Beamline project is to develop and provide unique capabilities for **Imaging Chemistry in Space and Time** in a wide range of reactive systems at relevant spatial and temporal length scales. The envisioned **In-situ 4D Chemical Imaging** allows diverse scientific communities to gain unrivaled insights into the chemical complexity of hierarchical, heterogeneous materials, including corresponding chemical reaction pathways and kinetics ('reactivity').
The superior brilliance of SLS 2.0 represents a true groundbreaking advance towards reaching this ultimate goal of microXAS. The spatial resolution will be enhanced by one order of magnitude (to below 100 nm), the total photon flux on the sample will increase by more than two orders of magnitude, along with an extension of the accessible energy range up to 40 keV. This direct impact of SLS 2.0 in combination with innovative methodological developments will reduce the experimental timescales dramatically. **4D Chemical Imaging** ('space-time') will become a most powerful analytical tool to investigate chemical reactions and biological processes under relevant conditions, covering relevant time frames, and matching the hierarchical length scales appropriate to probe these systems processes. As a long-term vision, we aim to pioneer technologies to add energy as a fifth imaging dimension. PSI and microXAS 2.0 will lead the invention of **5D Chemical Imaging** ('space-time-energy').

16.1 Upgrade motivation, goals, and designated impact

The chemical composition and reactivity of heterogeneous, hierarchical materials plays a most prominent role concerning the behavior of natural systems, functioning of organisms, as well as the performance of technical materials. The capability to study heterogeneous systems and linked chemical reactions in space and time under 'real-world' (native reactive) conditions is of high relevance for a broad range of chemical, physical, and/or biological processes and has consequently remarkable potential ramifications in almost all basic and engineering sciences.

To further advance our fundamental understanding of the chemical complexity of matter and related chemical transformations, it is necessary to develop and implement new methods which will push the resolution limits of current instrumentation concerning space and time as well as chemical sensitivity and contrast. Ideally, the advanced analytical methods provide chemical (and physical) information on all relevant length and time scales, are non-invasive/non-destructive, and are operating at conditions as close as possible to the real-world reactive environment. Further, the complexity and heterogeneity of hierarchical materials require a combination of techniques, ideally simultaneously operational (multimodal), with high repetition rates to capture dynamic (transient) processes.

We propose a hard x-ray based chemical imaging toolbox to answer the questions laid out above. We will combine multiple advanced, x-ray based analytical tools (e.g., XRF, XAS, XES, RIXS, XRD, PDF, etc.) with high (nanoscale) spatial and fast (μs) temporal resolution.

microXAS 2.0 corresponds to the 'revolutionary evolution' of the existing microXAS beamline. The existing beamline shall be transformed into a designated hard x-ray nanoprobe facility with the main scientific focus on ***high-resolution, dynamic, multimodal, 4D chemical imaging***. microXAS 2.0 will offer a unique combination of high resolution imaging techniques with several complementary methods delivering chemical (and physical) contrast accessible with a forefront temporal resolution.

While the vast majority of diffraction-limited storage ring (DLSR) based x-ray nanoprobe facilities strive to provide ultimate structural resolution ('physical imaging'), microXAS 2.0 is targeted to reveal spatially resolved chemical information, such as elemental composition, electronic structure, molecular speciation, phase and structure of crystalline materials, nature of amorphous material, and chemical reactivity. Precise energy tunability and bandwidth selection provide the mandatory spectroscopic power needed to deliver various advanced chemical contrasts, while dynamic focusing contributes to the ability to probe hierarchical length scales down to high spatial resolutions below (100 nm).

At the existing microXAS microprobe facility, XRF, XRD, and XAS can be routinely explored as chemical modalities, while transmission provides complementary structural information. While the vast majority of chemical imaging work performed at micro-focused beamlines around the globe is limited to 2D scanning, microXAS took a pioneering role in implementing 3D chemical tomography approaches. The penetration power of x-rays allows the investigation of intact, undisturbed systems and thus probing the 'natural' reactive environment. Additionally, tomographic chemical imaging further limits common 2D-scanning artefacts arising from sample deterioration during preparation (thin sectioning) or spatial blurring due to extended probing depth (averaging over the third dimension).

Ultimately we aim at chemical imaging on relevant time scales. However, the investigation of reaction dynamics based on multidimensional chemical imaging is currently still limited to rather slow processes (seconds to hours). However, very recently, breakthrough progress has been achieved for

Example of importance of hierarchical Chemical Imaging: Degradation of Solid Oxide Fuel Cell.

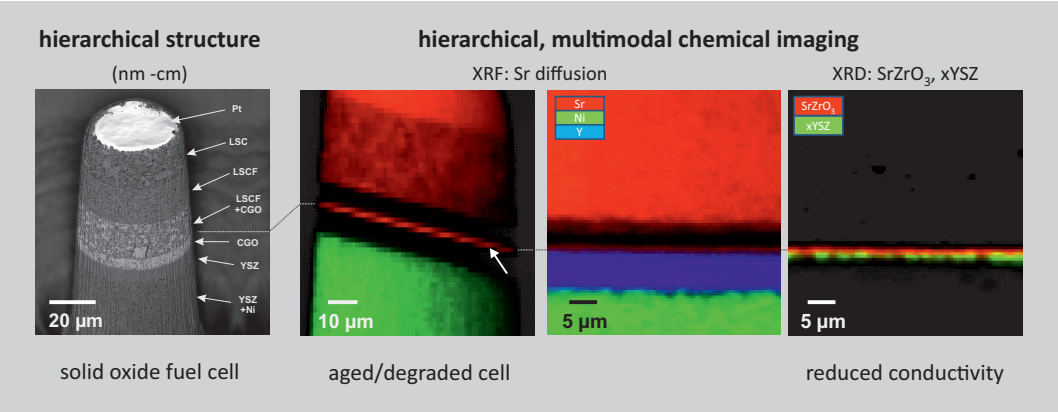

Figure 16.1: XRF based imaging identifies unexpected Sr-diffusion process. Simultaneous XRD imaging reveals $SrZrO_3$ precipitation and a linked chemical modification of YSZ at the electrolyte/diffusion barrier interface. These reaction products build a thin resistor layer, drastically reducing the device performance [1, 2].

1D in-situ chemical imaging of phase transformations during 3D metal printing with time resolution reaching 22 kHz (a collaboration with the Materials Science beamline at SLS and the Photons for Engineering and Manufacturing group (PEM) within the PSI Photon Science Division) [3]. In addition to increased detector speed, higher imaging dynamics can also be achieved by exploiting additional chemical contrast modes. Currently, for example, exploratory studies based on high-resolution XES as well as full-field 3D XANES tomography are underway, and PDF is being evaluated. Obviously, in all these scenarios, the available photon flux on the sample and complex motion control are additional and often primary determining factors concerning the ultimate temporal resolution of chemical imaging.

microXAS 2.0 will enable time-dependent studies of chemical reactions and processes under relevant conditions, covering appropriate time frames, and matching the hierarchical length scales. Such dynamical chemical nano/microtomography delivers fundamental scientific knowledge to understand chemical reactivities which are most elementary in various scientific fields such as chemistry, biology medicine, materials science. For numerous specific scientific challenges new opportunities will arise. Selected examples are given in the panel below.

Current and future scientific application fields of 4D Chemical Imaging:

Life Science and Health (3D cytometry in cancer research, dynamic biochemical composition of cells, cell metabolism of diseases, drug delivery and reaction pathways, biocompatible materials, implant-tissue interfaces, plant molecular biology, immune responses); Advanced Manufacturing (dynamic, in-situ process analysis of additive manufacturing techniques); Environmental Science (reactive transport in porous media, subsurface CO2 storage, geothermal energy, bioaccumulation, bioavailability and toxicity); Energy Research (in-situ electrochemical processes in batteries, solid oxide fuel cells, catalysis); Nanoscience and Nanotechnology (single particle reactivity in 3D, fate and reactivity of nanoparticles/wires/tubes, nanotoxicity, particle-support interactions); Functional Materials (tunable strain analysis, Mott insulators, nanoelectronic devices); Sustainable Technology and Engineering (corrosion, sustainable cement); Soft Matter (inclusions, crystallinity, single fiber analysis); Nuclear Materials (fusion reactor materials, irradiation-enhanced material degradation); Cultural Heritage (pigment degradation, ancient manufacturing techniques, corrosion).

16.1.1 Impact of new storage ring brilliance

DLSRs generally provide nominally the same total flux as present third-generation synchrotron light sources, but will nonetheless revolutionize chemical imaging capabilities due to their reduced horizontal emittance. SLS 2.0 will provide an approximately twentyfold improvement in horizontal emittance in the hard x-ray regime, in combination with new undulators it will also deliver up to a fourfold increase in spectral flux, thereby offering as much as a factor of 80 improvement in brightness. Consequently, SLS 2.0 as a DLSR will provide three main advancements for imaging beamlines: (i) brightness, (ii) coherence, and (iii) higher flux of high-energy photons.

Concerning the future performance of microXAS, the improved brilliance will have a seminal effect as the efficiency of focusing is strongly related to source brightness. A reduced source size and divergence result in smaller spot sizes, higher photon flux densities and enhanced total flux (due to an upgrade of the insertion device by a reduction in the undulator periodicity from 19 to 15 mm and increased total undulator length). While the superior brilliance has already a groundbreaking impact, new opportunities based on access to high-energy photons and the potential of the enhanced coherence are almost equally decisive. While the coherence will boost the performance and efficiency of the nanoImaging Module [4], access to high-energy photons will trigger a significant expansion of scientific fields and methods (e.g. buried systems, 3D cytometry, strain analysis, nuclear science).

16.1.2 Uniqueness compared to present and planned other BLs worldwide

Most other nano-beamlines under construction or consideration at DLSRs strive towards ultimate spatial resolution. Nearly all optical concepts are based on ultra-long beamlines with maximized mechanical stability (and consequently limited optical and experimental flexibility). Additionally, (all)

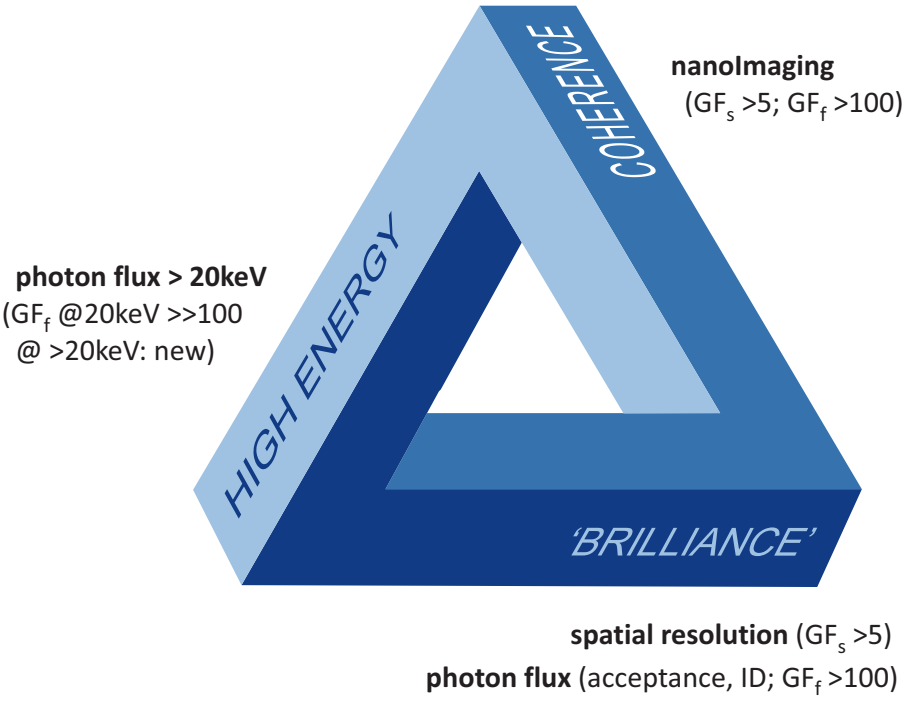

Figure 16.2: Main impact of new storage ring performance on microXAS 2.0. Corresponding gain factors are given in terms of spatial resolution (GF_s) and photon flux on sample (GF_f).

these projects set their main focus on exploring coherence-based methods to investigate structural features ($\rightarrow$ physical imaging). In contrast and rather uniquely, microXAS 2.0 is dedicated to hierarchical, multimodal **chemical imaging**. In a rather exceptional manner, the beamline concept is based on the following innovative key features: (i) dynamic focusing schemes, (ii) flexible and fast, but extremely precise wavelength tunability, (iii) active, feedback-controlled, pointing stability, and (iv) advanced detection schemes. Already at present, microXAS has demonstrated leadership in multimodal chemical tomography as a high level variant of chemical imaging. The SLS upgrade and the adapted beamline will establish the project in a prime position concerning dynamical chemical tomography – being unrivaled by any competing beamline project in terms of the number of simultaneous chemical modalities in combination with the provided spatial and temporal resolutions.

A unique feature of microXAS is its role as a hard x-ray microprobe for radioactive samples. Already the present status represents world-unique chemical imaging capabilities (effective micrometer spatial resolution) for active materials. Upgraded microXAS 2.0 features, in combination with recently implemented advanced sample preparation capabilities (e.g. the focused ion beam system for active samples in the PSI hotlab), will further increase, or at least secure, the present lead. In view of pressing nuclear challenges such as nuclear waste storage, or power plant decommissioning on the one hand, and nuclear research related to next-generation plants and fuel materials or fusion reactors on the other, a high potential impact can be assigned to the 'active nanoprobe' for the coming years.

16.1.3 Complementarity to other PSI beamlines

The microXAS Beamline Project is a complementary and integral part of the advanced hard x-ray imaging program at SLS. While cSAXS strives for ultimate spatial resolution and TOMCAT is dedicated to ultimate time resolution of physical imaging, the unique core competence of microXAS is in chemical contrast modalities in >3D imaging. The synergistic and effective collaboration is reflected by numerous joint scientific projects (in-house and user projects) and corresponding publications (e.g. [5–7]). Further, based on the broad range of x-ray techniques used in the multimodal chemical imaging approach of microXAS, numerous interactions with other beamlines are maintained (e.g. knowledge transfer and scientific collaborations with superXAS, PHOENIX, MS, and PX). As an example, most recently, a productive collaboration with MS was established to foster activities related to fast in-situ process analysis of advanced manufacturing methods [3,8]. In terms of chemical dynamics, microXAS 2.0 offers complementarities to the SwissFEL beamlines and related activities within LSF, already with numerous corresponding past and ongoing collaborations, see e.g. [9].

16.1.4 Impact on user community and industrial use

Access to microXAS 2.0 will definitely become more competitive. The upgraded beamline will attract new, high-impact science areas. Expected growth areas are: life sciences, industry-related materials science, nano-science and nano-technology, medical/pharmaceutical sciences, and energy research. Qualitative (scientific impact) growth areas are: environmental sciences, geochemistry, and nuclear sciences.

In the past, proprietary industrial R&D was performed at microXAS for a range of industries, including fine chemicals, nuclear power plants, nuclear fuel producer, cement industries, waste management organizations, and catalysis. With enhanced, dynamic in-situ 3D characterization capabilities of reactive materials, a noticeable growth of industry-related interest can be expected (catalysis, energy storage and conversion, medical/health as well as pharmaceutical). Based on proactive efforts (supported by park innovAare and ANAXAM [10]), the recognition of the potential of chemical imaging is already growing (e.g. sustainable cement, corrosion studies, drug application).

A large potential for interaction with industries is recognized in the area of advanced manufacturing, mainly triggered by our drastically improved and unique capabilities to detail in-situ processes during additive manufacturing (e.g. 3D metal/ceramics printing [in collaboration with PSD-PEM and ANAXAM]).

Once intracellular resolution is ‘routinely’ achieved even for trace elements, an enormous potential will arise in the fields of biomedical, pharmaceutical, and molecular biology.

16.2 Conceptual design

16.2.1 Floor location (sector X08)

Within the SLS 2.0 upgrade path the microXAS beamline is proposed to move from the long straight X05 to the short straight of Sector X08. A conceptual sketch of the proposed realization of the optics hutch, the experimental hutch, as well as the related infrastructure facilities such as control room

and preparation or engineering laboratories is illustrated in Figure 16.3. A realistic 3D representation of microXAS 2.0 to be built at Sector 08 is shown in Figure 16.4 and stresses the locally enhanced clustering of relevant general infrastructures such as SLS loading zone, main gangway ("passerelle"), and beamline essentials.

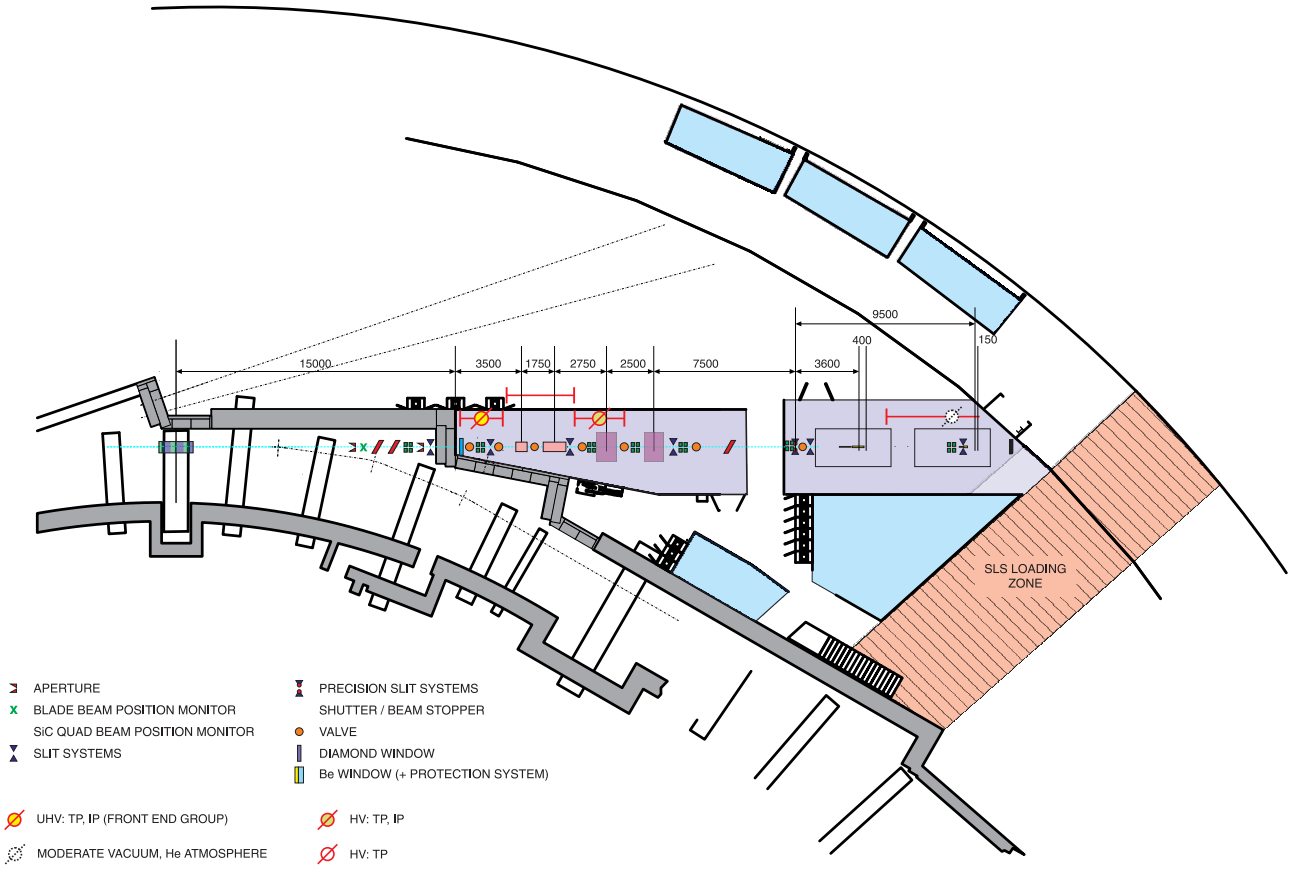

Figure 16.3: Proposed arrangement of the microXAS beamline after relocation to Sector X08. Light blue areas correspond to floor space assigned to the control room and preparation or engineering laboratories. Lead-shielded optical and experimental hutches are indicated by violet areas.

16.2.2 Source (machine and insertion device)

Taking advantage of the new 'optical' opportunities offered by the superior SLS 2.0 brightness, the replacement of the existing U19 and the installation of an advanced insertion device – a cryo-cooled permanent magnet undulator CPMU15 – is proposed. Compared to the present situation, the device length will be increased from 2 meters to 3 meters. First of all, this replacement of the radiation source will result in a gain in total photon flux by about factor of five at lower energies and a factor of more than 30 (!) at energies above 20 keV. Further, considering the gain based on acceptance and reflectivity, a total flux gain of more than 100 results at the presently accessible high-end energy range ($\sim$ 17 to 22 keV). Even more importantly, however, the scientific communities using chemical

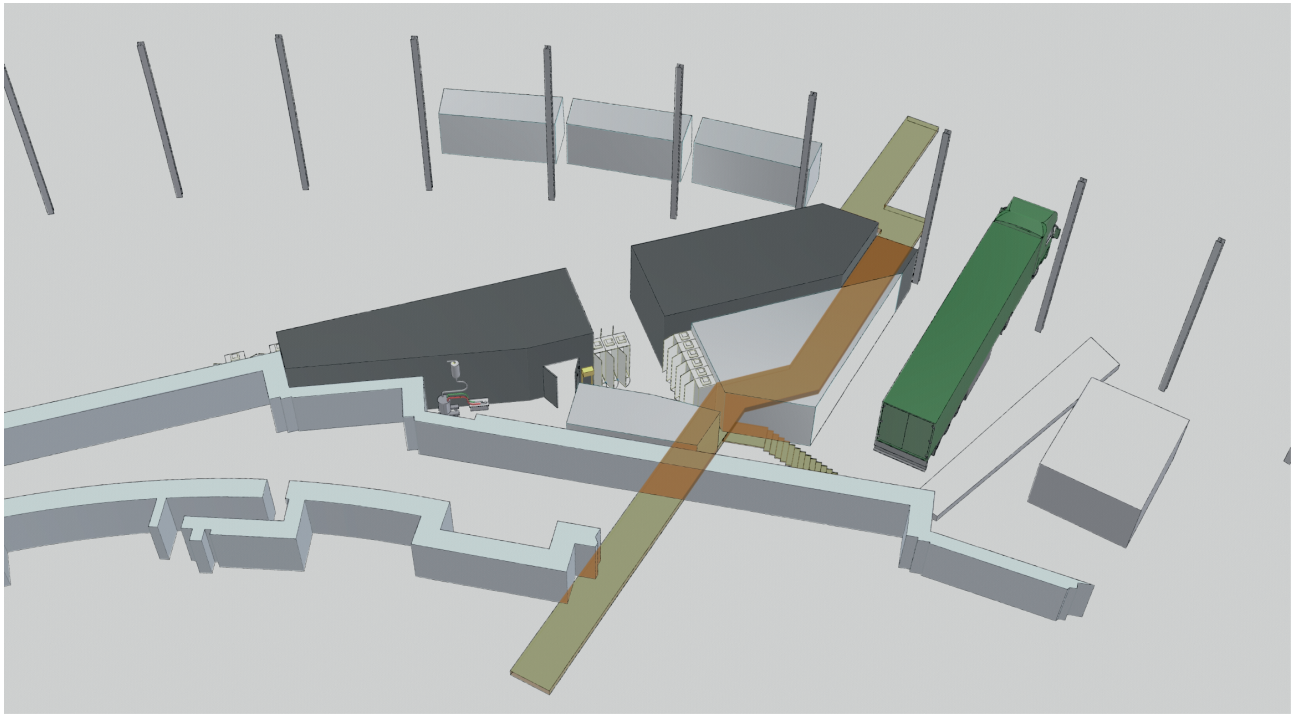

Figure 16.4: 3D representation of microXAS 2.0 to be built at Sector 08.

imaging will gain access to higher energy photons. As detailed in the previous section, high-energy photons are of utmost importance for a broad range of new imaging modes, concerning 'real-world' (in situ) measurements using containments or studying buried systems, as well as regarding nuclear chemistry. The remarkable improvements in terms of brightness, photon flux density, and photon flux are illustrated in Figure 16.5, comparing the present U19 (with two meters length, operated at 2.5 GeV) with the designated CPMU15 (three meters length, operated at 2.7 GeV).

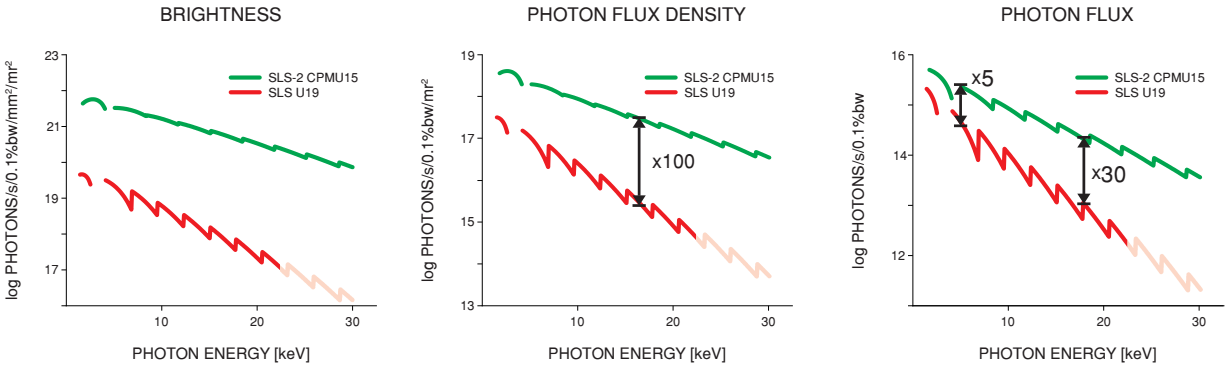

Figure 16.5: Resulting increase in brightness, photon flux density and total photon by the upgrade of the SLS machine (DLSR, 2.7 GeV) and insertion device replacement (CPMU15).

Further, in the context of white-light operation and the proposed 5D chemical imaging, first conceptual studies of a specialized U14/U15 operation mode have been conducted by the insertion-device group at PSI. A tilting option of the U14/U15 turns out to be very promising for the production of a continuous white light spectrum, highly beneficial for 5D chemical imaging. As shown in Figure 16.6, the width of an undulator harmonic can be broadened, resulting in a nearly constant intensity distribution over an extended energy range of ~ 200 eV. This potential feature opens interesting prospects for 3D/4D chemical imaging based on dispersive XAS by off-axis diffractive optics [11].

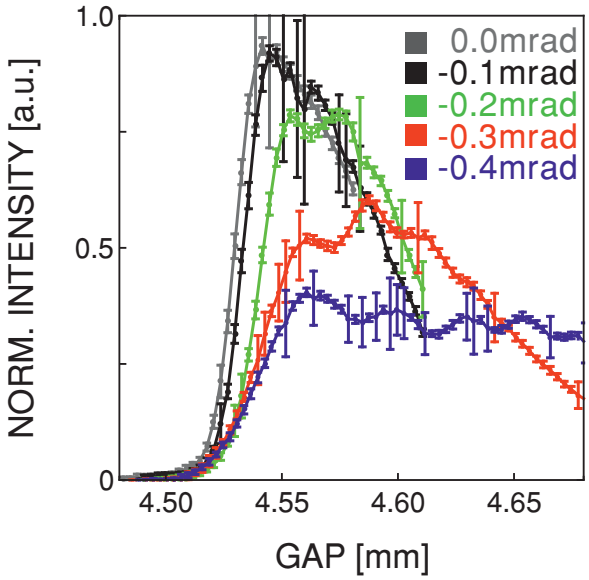

Figure 16.6: Insertion device tilting. Proof of principle towards pink beam light spectrum smoothing. (data courtesy of M. Calvi & Th. Schmidt, PSI)

The relevant source parameters [12] are listed in Table 16.1, while the corresponding phase space representations of the electron beam and the photon source point for photon energies of 5 keV and 25 keV are given in Figure 16.7. A comparison with the present source readily reveals the remarkable improvements. The source size (σ) is reduced from 95×5.5 μm^2 to 20×4.5 μm^2. Further, the vertical divergence is reduced from 11 to 3.5 μrad, while the horizontal divergence is significantly reduced from 56 to 7.9 μrad.

16.2.3 Front end

It is expected that a modular set of common, 'standard' front end components for most SLS 2.0 beamlines will be conceptualized and installed. For the microXAS 2.0 beamline the front end will include first a fixed beam mask, a blade, a transmission quadrant x-ray beam position monitor, a movable diaphragm, high heat load white beam slits, a combined heat absorber and photon shutter

Parameter	SLS X05	SLS 2.0 X08
hor. emittance [10^{-10} m rad]	56	1.56
vert. emittance [10^{-10} m rad]†	0.56	0.156
hor. e-beam size [σ μm]	215 [95‡]	11
vert. e-beam size [σ μm]	5.5	4.5
hor. e-beam divergence [σ μrad]	58	7.9
vert. e-beam divergence [σ μrad]	11	3.5
@ 5keV		
hor. photon beam size [σ μm]	215 [95‡]	20
vert. photon beam size [σ μm]	6	5.2
hor. photon beam divergence [σ μrad]	68	11
vert. photon divergence [σ μrad]	14	9.3
@ 25keV		
hor. photon beam size [σ μm]	215 [95‡‡]	20
vert. photon size [σ μm]	5.5	4.7
hor. photon beam divergence [σ μrad]	68	8.6
vert. photon divergence [σ μrad]	12	6.3

† 10% coupling ‡virtual source size

Table 16.1: Comparison of source parameters.

unit, and a final heat load filter ($\sim$ 200 μm CVD diamond). As alternative for the movable fixed-aperture diaphragm, a combination of two consecutive fixed-aperture diaphragms can be envisaged yielding a dynamic aperture diaphragm.

In addition to its radiation-safety-related functionality, the microXAS 2.0 front end concept has to be optimized towards minimal heat load transmission. Reducing the power leaving the front-end is crucial in minimizing the contributions of heat bumps developed on optical elements to the total figure error.

16.2.4 Optics

General optical concept

Exploiting the full potential of SLS 2.0 as a DLSR requires an adapted beamline to transfer and maintain the superior source qualities (flux, brilliance and coherence) to the sample. Each link of the instrumentation sequence thus has to be optimized. First, an optimized x-ray source (e.g., CPMU U15) has to be installed to maximize benefits from the new machine characteristics. Subsequently, near-perfect optical components are crucial. The pointing stability has to be guaranteed by innovative diagnostics and feedback control systems. Advanced experiments require dedicated samples environments and sample-manipulation capabilities.

In terms of beamline adaptation, the optical scheme is of central importance. A **dynamic optical**

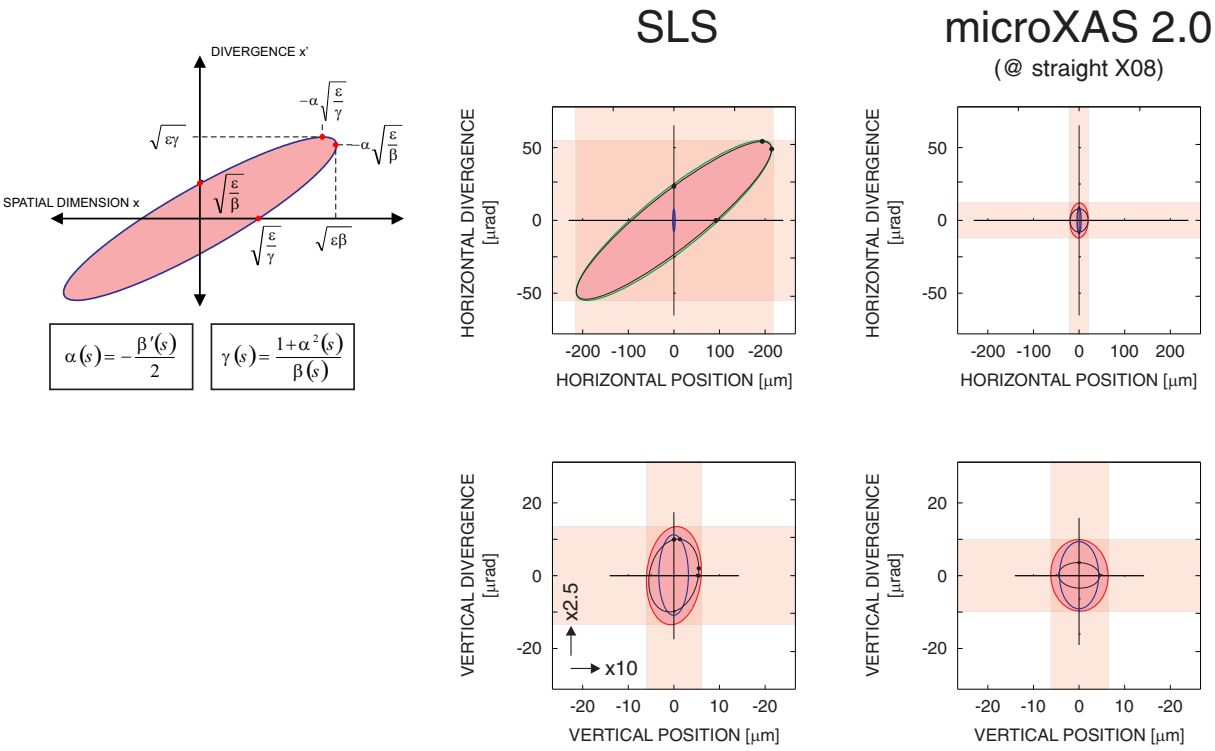

Figure 16.7: Phase space representation of the source characteristic. A comparison between the present situation at SLS-X05LA with expected conditions for SLS 2.0 are given for the lower energy limit of 5 keV. (Note the different scales for horizontal and vertical dimensions.)

scheme with high flexibility was conceptualized. Both the spatial as well as the spectral resolution can be dynamically adjusted to the requirements of the scientific question and/or system to be investigated. The spatial resolution dynamics allow for hierarchical imaging, while the spectral resolution dynamics open up opportunities for novel chemical imaging modes, as well as an improved temporal resolution.

With regards to the spectral resolution dynamics, the beamline concept includes flexible and fast wavelength selection by a 2-bounce, fixed-exit double crystal monochromator. Flexible tuning of the beam energy to and/or across various elemental resonances represents a fundamental prerequisite of chemical imaging. In addition to the high spectral resolution mode (monochromatic mode), two additional modes are proposed. Based on multilayer optics, the spectral bandwidth of the primary x-ray beam can be adjusted to capture a full width of a harmonic of the undulator (pink beam mode). The resulting remarkable gain in photon flux would enable a much enhanced acquisition speed in multimodal chemical imaging (e.g. based on XRF or XES chemical tomography). Finally, the microXAS beamline will continue to offer a white-light mode. This mode, in combination with new, energy-resolving pixel detector technologies, will lead in the near future to innovative chemical imaging concepts based on polychromatic Laue XRD. Such original imaging can be expected to change dramatically the analysis of single phase/multi grain/multi phase systems (e.g. defect location and evolution, grain orientation, strain and stress analysis, fast phase identification in complex systems,

etc.).

The dynamic optical scheme further results in advantageous spatial-resolution dynamics. First of all, a nearly instantaneous transition between focused beam and unfocused direct beam is feasible. This provides the unique opportunity to combine full-object 3D structural or chemical information (full-field mode) with high-resolution chemical tomography data [line tomography or spiral golden ratio tomography mode (combination of [13–15])]. Second, the optical concept strives for full flexibility of the nano-/micro-focusing. The foreseen dynamic focusing scheme will include the opportunity of a fast swap between two-step and one-step focusing. While one-step focusing minimizes the impact of imperfect optics (e.g. for coherence based high-resolution focusing by diffractive optics), the two-step approach offers a dynamic trade-off between flux and resolution. By implementing such a dual concept, the beamline can be optimized for either highest photon flux (and time resolution) or best spatial resolution. This strategy is further optimized by implementing two focusing modules based on achromatic reflective Kirkpatrick-Baez (KB) optics. One module is dedicated to the ultimate spatial resolution ($\leq$ 200 nm), but constricted by limited acceptance, reduced working distance and experimental flexibility. The second KB module represents the 'full-flux', sub-micron, focusing unit with large working distance, offering full experimental flexibility (e.g. for implementing exceptional experimental infrastructures such as in-situ 3D printing devices or picosecond pump-probe setups). The microXAS beamline has extensive experience in successfully operating such a dynamic modular optical infrastructure.

A schematic of the proposed optical layout of the new microXAS beamline is depicted in Figure 16.8 for the case of nanofocusing with the highest spatial resolution. As described above, a CPMU U15 minigap, in-vacuum undulator serves as the radiation source. The front end includes SLS 2.0 standard radiation safety equipment as well as an aperture system to reduce bremsstrahlung and the total radiation power. These apertures in the front end define the maximal angular extension of the photon beam to approximately $\pm 5\sigma$ in both, the horizontal and the vertical ($\sim 100 \times 100\ \mu\text{rad}^2$).

Pre-focusing mirror system

At a distance of roughly 20 m from the source point, the x-rays pass the first optical unit. This optical system is a set of two mirrors in the classical KB geometrical arrangement. The two flat mirrors can be dynamically bent, thus providing dynamic and independent horizontal and vertical focusing capabilities. The mirrors are operated at 2 mrad grazing-incidence angle and have three reflectivity stripes (Si, Pt, Rh). This configuration allows dynamic focusing of x-rays up to 40 keV without energy regions disturbed by absorption edges of the coating elements. The tunability of the mirror figure provides the capability to dynamically tune the prefocusing strength, with three main configurations: (i) prefocusing in both directions yielding an approximately 1:1 image of the source at the intermediate focus, (ii) 'perfectly' flat mirrors allowing for an undisturbed propagation of the beam, and (iii) collimated beam for high resolution spectroscopic applications. Additionally, the primary beam can be focused to about one to two times the original source size at any location within the experimental hutch, resulting in a unique flexibility regarding non-standard experiments, including their location. As can be recognized from Figure 16.8, both mirrors employ meridional focusing (elliptical cylinders). While this approach provides considerable advantages concerning dynamic focusing and selection of

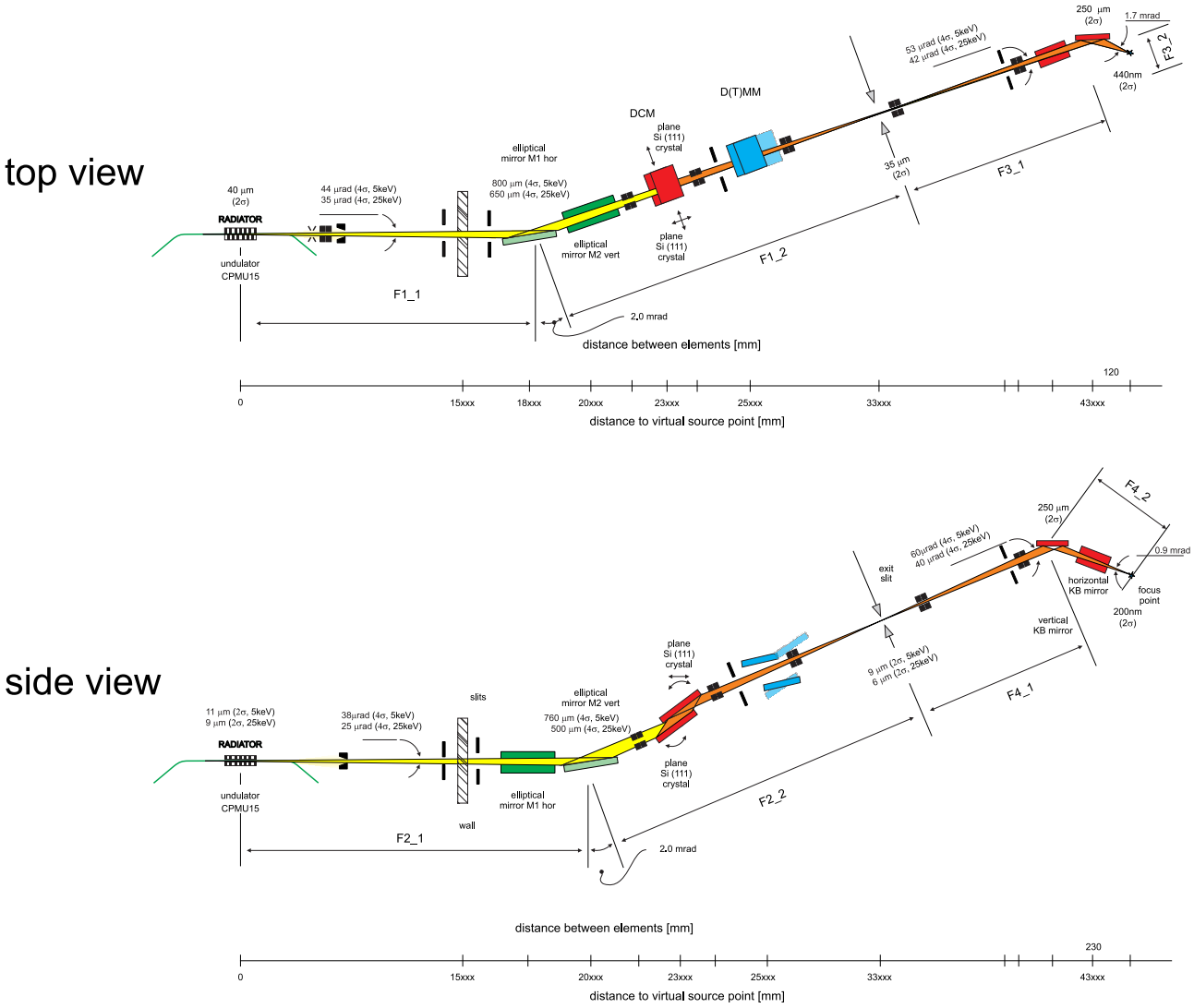

Figure 16.8: Schematic representation of the proposed optical scheme of the microXAS beamline at Sector X08. Depicted is the case of the achromatic nanofocusing with high spatial resolution based on an intermediate focus acting as a secondary source.

reflectivity stripes, slope errors have more severe deterioriation power in the meridional direction compared to sagittal focusing. This issue is accentuated for the vertical deflecting mirror for which gravity acts in the mirror meridional direction, potentially contributing to the total figure error. Consequently, these mirrors have to be of superior optical quality with final meridional figures of error of less than 0.2 μrad rms. Accordingly, the mirror length has to be optimized regarding the achievable figure error and maximized acceptance.

Spectrometer system

The modular spectrometer unit has to be installed in the closest possible proximity to the prefocusing system. The location is dictated by the strong preference for a larger beam extension to minimize the magnitude, spatial gradients and corresponding negative impact of the thermal bump developing on the first crystal or multilayer of the monochromator. The spectrometer unit consists of two main components: (i) a fixed-exit double-crystal monochromator (DCM) and (ii) a double- (or triple-) multilayer monochromator (DMM/TMM).

The DCM is equipped with three sets of monochromator crystals, namely Si(111), Si(220), and Si(311), and provides monochromatic radiation with selectable spectral resolution. The achievable energy resolution varies from $\Delta E/E$ of 2.5×10^{-4} for Si(111) crystals operated in vertical deflection in combination with a non-collimated beam, to 3×10^{-5} for a pair of Si(311) crystals illuminated by a collimated beam.

The DMM/TMM system serves multiple purposes. Firstly, the unit can be used to produce a high-intensity, polychromatic beam with a spectral bandwidth of approximately $\Delta E/E = 10^{-2}$. The corresponding increase in photon flux compared to monochromatic radiation offers novel opportunities for high-speed chemical imaging. Secondly, the same system can act as a **kick-back unit**, allowing to bring back the trajectory of the monochromatic beam to the pink beam pathway. The realization of a TMM would lend two additional main benefits. Firstly, the beam path of the monochromatic beam, that of the polychromatic radiation, as well as the pink beam, could be matched. Consequently, all three types of probe beams on a sample could be interchanged with minimal time delay. Secondly, the offset between monochromatic and polychromatic beam trajectory would vanish, allowing a considerable reduction in vacuum pipe diameter and related engineering and instrumentation costs.

The choice of deflection geometry of the DCM/D[T]MM is a serious optical design issue of the beamline upgrade. While a horizontally diffracting geometry would be favorable in terms of mechanical stability, the smaller vertical source size and the reduced vertical beam divergence provide an enhanced energy resolution in the case of vertical diffraction. Furthermore, due to the linear horizontal polarization of the CPMU15 radiation, the classical vertical geometry yields higher efficiencies of the DCM, in particular at lower energies (5 to 8 keV).

Achromatic focusing units

As a natural evolution of the successful present installation, two achromatic focusing units are foreseen. The first unit ('*microKB module*') is characterized by a large acceptance and therefore high total photon flux, as well as an extended working distance, allowing the installation of complex sample environments or detection schemes. The minimal spot size delivered by the reflective optic is of the order of 500 nm, but can be enlarged dynamically. The second achromatic focusing unit ('*nanoKB module*') strives for a minimal spot size of 100 to 200 nm, while nevertheless providing an experimentally useful working distance. Both units are operational up to 40 keV, due to an incidence angle of the mirrors of 2 mrad and three coating stripes (Si, Rh, Pt). For both units, the required elliptical shape of the two independent, orthogonal mirrors is achieved by means of dynamical bending. Mirror positioning and bender mechanics as well as the corresponding vacuum enclosure are integral (non-removable) parts of the beamline optics infrastructure.

As mentioned before, the designated microKB module has a spatial resolution target of 500 nm. A large working distance can be achieved by direct demagnification of the ID source point. For both dimensions, geometrical demagnification yields a spot size of $\leq$ 300 nm. However, due to the reduced numerical aperture of the vertical focusing mirror (with the more extended image distance), the achievable spot size will be enlarged at lower energies (5 to 10 keV), due to the corresponding diffraction limits. However, as the source is imaged directly, thee most crucial aspects concerning achievable spot sizes are the figure errors of the upstream optics (the two flat prefocusing mirrors and the first elements of the DCM or the DMM systems).

Extensive ray-tracing simulations [16] indeed indicate, as expected, that thermal deformations of the monochromator crystals/multilayers are the most critical potential contribution to beam-spot degradation ('blurring'). A corresponding ray-tracing realization is shown in Figure 16.9. For the represented simulation, both prefocusing mirrors as well as both 300-mm-long KB mirrors have average slope errors of 0.2 μrad rms, while the anticipated extension of the thermal bump on the first Si crystal of the monochromator results in a slope error of 0.5 μrad. While such beam simulations support the basic feasibility of the chosen optical concept, the central importance of the monochromator thermal bump and the figure error of the vertical KB mirror with its large image distance are clearly stressed. Obviously, heat-load management is a central concern in the final technical design of the beamline optics.

The nanoKB module is optimized towards minimal nanometric spot size. The chosen optical configuration represents the achievable optimum between numerical aperture (NA), working distance, and acceptance. A fixed defining parameter is the grazing angle of 2 mrad dictated by the design parameter of the upper energy cut-off of 40 keV.

A detailed evaluation process revealed that an optical concept using an intermediate focus is superior, in various aspects, to a focusing scheme without prefocusing. Briefly, the main advantages are acceptance, susceptibility to beam motion, dynamic source size definition, and rejection of harmonics. Further, the dynamic aperture defining the secondary source size extension is acting as a clean-up 'filter' for aberration effects of optical elements upstream of these slits. X-ray tracing simulations confirmed a reduced impact of the prefocusing mirror aberrations as well as of the thermal bump of the monochromator unit. The main limiting factors to achieving geometrical or diffraction-limited spot sizes are the figure errors by the nano-KB mirror.

Based on the chosen acceptance (200 μm based on a 100 mm long mirror at 2 mrad) and an effective working distance of 60 mm (with a focus distance of 120 mm of the last nanoKB mirror) the secondary source is demagnified by factors of 40 and 75, respectively. Accordingly, without any further aperturing at the intermediate focus, the nanoKB beam spot is 350×200 nm^2. At 5 keV, this beam would be already diffraction limited in the vertical direction (due to the limited numerical aperture). By trading in photon flux for enhanced resolution and limiting the horizontal secondary source size, the horizontal diffraction limit of 120 μm at 5 keV can be reached (assuming near perfect optical characteristics of the KB mirrors). With increasing beam energy, reducing the secondary source size in both directions can generate a diffraction-limited beam of $\sim 100 \times 100$ nm^2. Obviously, in order to reach such a challenging goal, the optical quality of the KB mirrors must be matched accordingly. As bendable mirrors are employed, an x-ray tracing simulation based on rather conservative figure-error assumptions (0.2 μrad for both nanoKB mirrors) was performed. As can be seen in Figure 16.9, the

final figure error has to be considerably below this value. This statement holds up in particular for the vertical focusing mirror with the more extended working distance. For the same optical geometry, improved figure errors of 0.1 μrad, as well as a reduced secondary source size of 10×5 μm^2, provide a nanoscopic spot of 100×150 nm^2. Clearly, a total figure error of 0.1 μrad represents extremely demanding optical specifications for dynamically bent mirrors. As an alternative to bendable KB mirrors, fixed-figured elliptical optics with figure errors as low as 0.03 μrad are nowadays provided by a limited number of commercial vendors. Nonetheless, based on the numerous advantages of dynamical focusing, there is a strong preference for bendable mirrors. Current progress in optics fabrication as well as bender engineering is closely followed by the microXAS project team and corresponding new advances are included in the continuous optimization of the nanoKB module.

NanoImaging Module

Based on the past successes of the hard x-ray nanofocussing activities at microXAS in terms of scientific results as well as impact on other SLS beamline facilities (e.g., [17, 18]), but also considering its future potential being leveraged by the advanced SLS 2.0 characteristics, it is imperative to transfer the nanoImaging module [4] activities as an innovative toolbox to the SLS 2.0 microXAS beamline. Complementing reflective optics schemes with diffractive optics allows one to extend the spatial resolution of a hard x-ray nanoprobe facility to its theoretical limits. Taking advantage of the superior coherence of the SLS 2.0 beam and the PSI-driven development of novel diffraction-based optics (high efficiency kinoform linear zone plate setup), one can obtain very high focused flux even for higher x-ray energies ($\sim$ 20 keV and higher) into a focal spot of 50 to 100 nm. In combination with the source characteristics of SLS 2.0, even the present system would deliver a spot size of 100 nm [4]. Considering a realistic progress in lens manufacturing, a target spot size of 50 nm appears feasible. It is foreseen to strengthen current efforts to achieve energy-scanning capabilities of such a linear zone plate setup (complex motion control of the two lenses with advanced real-time alignment feedback).

As an innovative strategy, the nanoImaging diffractive lens system in combination with polychromatic radiation and an area detector can act as an energy-dispersive setup by illuminating the diffractive optics only partially in an off-axis mode [11]. This would allow one to conduct XANES tomography in an energy dispersive mode with high spatial resolution without the need for technically challenging focusing by bent monochromator crystals [19].

16.2.5 Beam stabilization

Pointing stability in position and angle is absolutely crucial for multidimensional chemical imaging with (sub-)micron spatial resolution. Beam pointing stability will become an even more critical issue for the high brilliance beams of microXAS 2.0 compared to today's situation. As a strategic development, the microXAS beamline project is already contributing to an advanced and innovative beam-position feedback system [20]. microXAS entered a productive collaboration with the Laboratory for Micro- and Nanotechnology (LMN) to develop and implement a 'next generation' inline beam monitoring concept. In combination with an active, kHz feedback control loop linking the monitoring information to fast optical corrector actuators, an excellent beam pointing stability can be achieved, especially critical during spectroscopic activities involving energy scanning. A pilot instrumentation

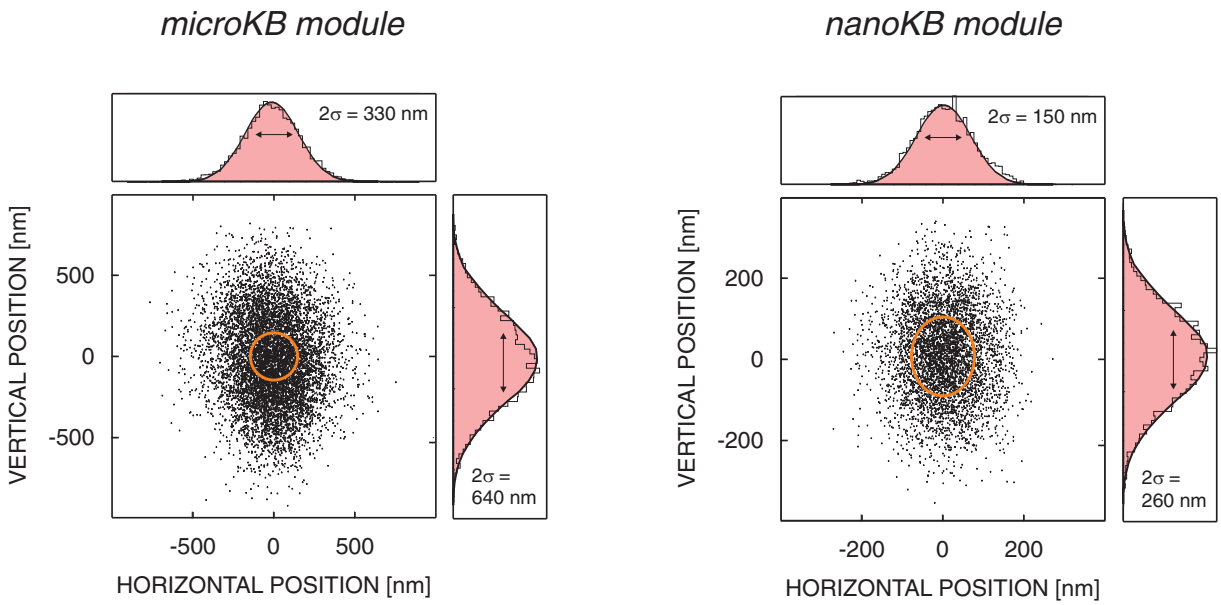

Figure 16.9: Optical feasibility studies for the *microKB* module (left) and the nanoKB module (right) by ray tracing [16], and employing realistic figure errors. In the case of the shown performance of the nanoKB module, the aperture at the intermediate focus was set to the geometrical focus spot size of 26×8 μm^2 (no reduction of secondary source size, only 'clean-up'). Red circular lines represent the 2σ beam extension for the case of optics without figure errors. Note the different scales in the left and right panels.

most recently installed at microXAS resulted in a pronounced reduction of pointing instabilities by more than an order of magnitude. For an extended energy scan of 800 eV (typical range for EXAFS scans) the total amplitude of the pointing instabilities for a micro-focused monochromatic beam was below 200 nm.

16.2.6 Experimental endstation modules

The strategy concerning endstations represents a derivative of the well-proven concept of microXAS based on three main experimental platforms. This allows one to maintain the highly appreciated level of experimental flexibility offered by the present experimental infrastructure. The three focusing modules *microKB*, *nanoKB*, and *nanoImaging*, in combination with the modular sample manipulator are the main endstation modules. There are two movable optical tables in the experimental hutch. The upstream table hosts the *microKB module* characterized by its large working distance. Accordingly, in-situ studies, user-engineered experimental setups, non-standard techniques but also time-resolved studies involving pump lasers are conducted within this area. Further, the nanoImaging module has to be placed on the upstream table while in use. The second, downstream optical table is mainly dedicated to experimental investigations involving the nanoKB module. This endstation module requires a much higher degree of mechanical and engineering stability to guarantee high spatial resolution on a routine

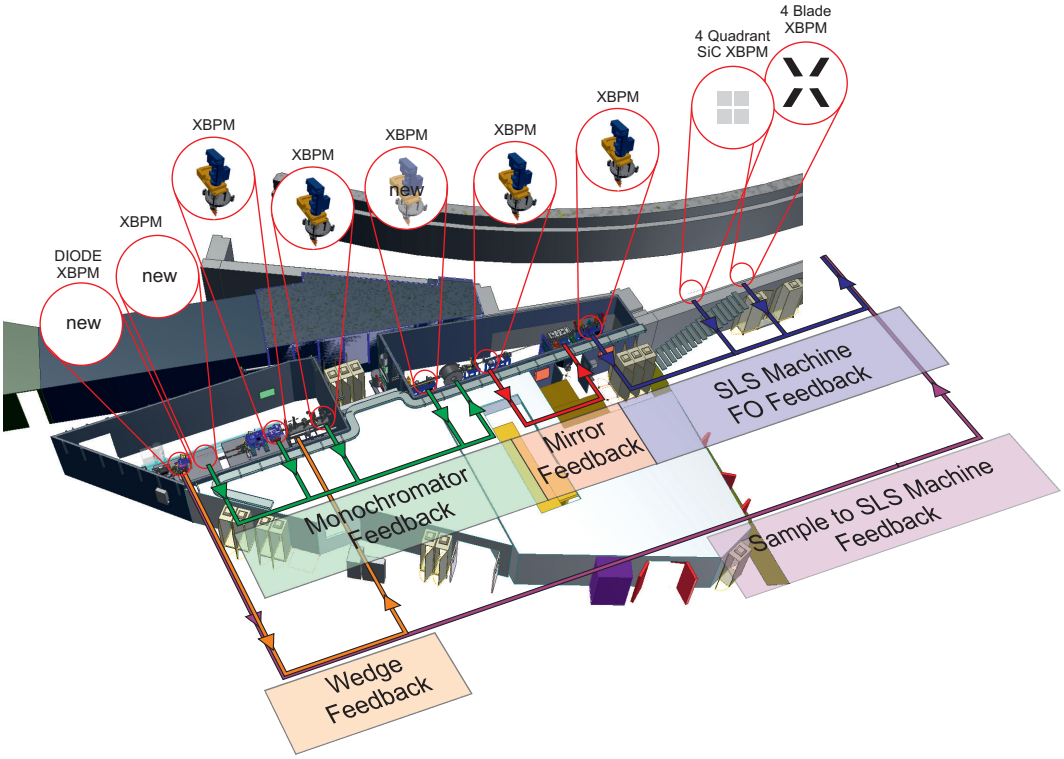

Figure 16.10: Existing pilot implementation and planned extension of an integrated fast x-ray beam position stabilization closed-loop system of the microXAS beamline.

level.

The measurements involving radioactive sample can be considered as an additional endstation module. However, based on the past years' experience, a new, modular concept will be negotiated with the Federal Office of Health (Bundesamt für Gesundheit, BAG). As a new strategy, different levels of mandatory (temporary) local shielding should be defined based on the radiation type and dose of the samples. Active samples exceeding the exemption limits are measured using the microKB module on the upstream experimental table. Samples with activity levels below the exemption limit can be analyzed using all endstation modules.

Sample positioning and environment

Parallel to the expected reduction in spot size, the sample position accuracy and stability has to kepp in step. A next-generation chemical tomography module has already been conceived by the microXAS project. The unit is soon ready for commissioning within the existing beamline infrastructure. The system allows for complex multi-dimensional motions based on the synchronized motion of several independent actuators. Furthermore, the design includes an integrated slip ring unit, providing the capability of fast and continuous rotation of the main axis. As a result, the overhead time can be dramatically reduced and, in addition, advanced data acquisition schemes such as spiral golden ratio

tomography can be implemented. The factory acceptance tests revealed a spatial stability of less than 25 nm run-out without any active correction employed, a value already compatible with the requirements for measurements based on the nanoKB endstation of the microXAS 2.0 beamline. The corresponding technical 3D model and experimental stability data are given in Figure 16.11.

The present manipulator system already fulfills the technical requirements of the designated microKB module and can simply be transferred without major adaptations.

Based on the observed trends concerning needs of the different user communities, cryogenic measurement conditions, as well as the implementation of various in-situ/operanto setups represent key aspects. Activities have been initiated to address the related instrumental upgrades.

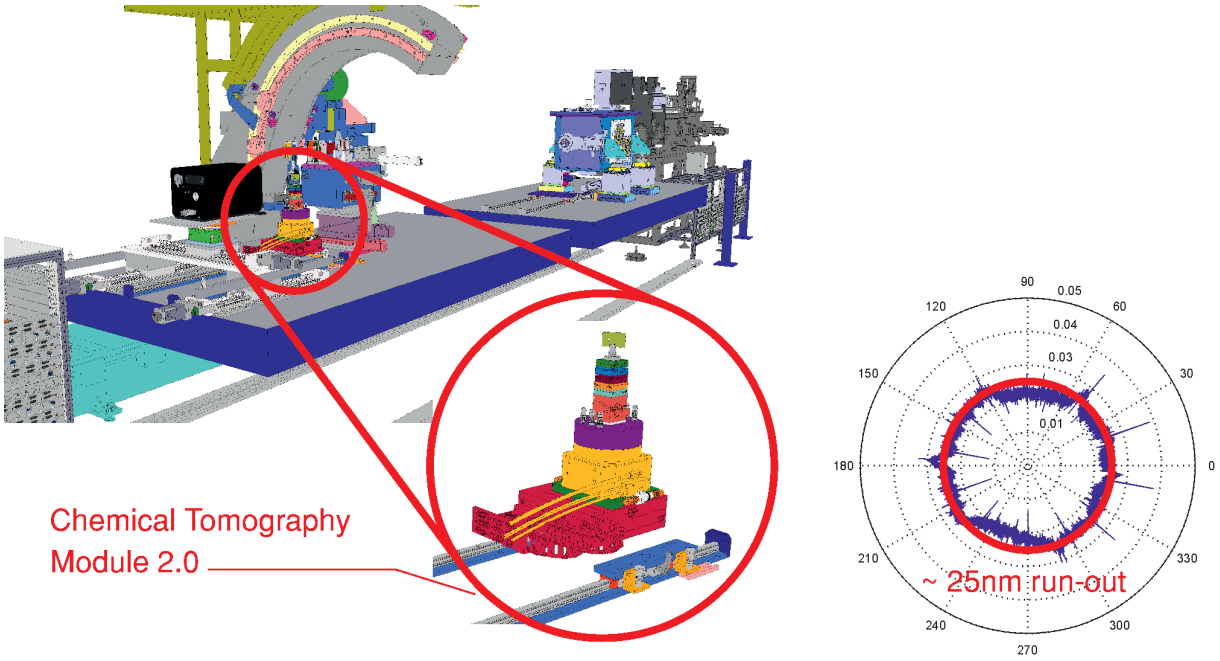

Figure 16.11: Ongoing development of a 'SLS 2.0-ready' chemical tomography sample manipulator module.

Detectors

microXAS just completed the (partially third-party funded) 'Factor X' detector upgrade program. Multiple state-of-the-art XRF detectors with modern pre-amplifiers coupled to high throughput readout electronics as well as a DECTRIS 4M EIGER system are now integral elements of the chemical imaging setup. Based on a PSI 500K EIGER and a third-party funded PSI 1M EIGER (in production), a MS/microXAS – detector-group joint initiative is currently pushing the limits of temporal resolution (operational frame rate of 22 kHz at present [3] and successful pilot studies with 70 kHz).

The midterm perspective includes 2D detector systems capable of even higher frame rates, as well as energy-resolving pixel detectors (such as MOENCH) as essential upgrades to extend the chemical imaging capabilities of microXAS 2.0 even further (towards *5D Chemical Imaging*).

As a part of our efforts to extend the number of parallel analytical modes applicable for chemical imaging at microXAS, considerable efforts are being made to include advanced spectrometer-based detection schemes in 2D chemical imaging (e.g., [21]) or even in 3D, such as XES tomography (work in progress). In addition, by the development of SiC based, miniaturized quadrant beam stop diodes, additional transmission modes are accessible.

16.2.7 Controls and data systems

To optimize the temporal resolution and minimize the radiation dose, innovative data collecting algorithms have to be developed to maximize the information content obtained per photon on the sample. Options to be considered include high-speed data acquisition with 'zero' motion overhead, optimized detection efficiency, energy resolving 2D pixel detectors, or minimal oversampling. Such innovative schemes will be especially beneficial for radiation-sensitive samples.

microXAS 2.0 strives to be a pioneering facility in terms of Industry 4.0 based operation and control concepts (IoT, digital beamline, complex motion control and real-time quality control feedback systems, machine-learning). The implementation of next-generation, etherCAT based beamline controls will enable original and/or highly efficient data acquisition schemes. In combination with a high throughput data collection/processing pipeline, this will result in a dramatic increase of scientific productivity and data quality.

In parallel with the prescient detector upgrade program (*Factor X*) currently implemented, the necessary adaptations and/or improvements of the data acquisition, storage, and processing strategies have been initiated. No major additional efforts or investments are currently anticipated.

16.3 IT requirements

Simultaneous to the Factor X 'Factor X' detector upgrade program, microXAS has already initiated the corresponding IT infrastructure upgrade program. High-end network switches, direct optical fiber connections to the data server, as well as large storage capacity have been purchased and implemented. Obviously, the corresponding technical infrastructure has to be reestablished after moving the micoXAS beamline to Sector X08. The higher photon flux of the new beamline, smart motion control, and higher frame rates of advanced area detectors will definitely lead to a continuous growth in terms of data volume produced per user day. Considering the recently realized upgrades, however, only moderate adaptations to the present IT infrastructure appear to be required, mainly a steady increase of the intermediate and long-term data storage volume.

The real-time pre-processing of the increasing raw data volume simultaneous to data collection requires attention. The possibility of prompt inspection of data quality is most crucial to successful experimental campaigns. However, considering the expected data production rates, no substantial investment in IT infrastructure is anticipated for 4D chemical imaging.

The situation will change, however, with the introduction of 5D chemical imaging based on fast, energy-resolving area detectors. First pilot studies using a single MOENCH module have revealed unambiguously the need for a dedicated server and high volume storage infrastructure for data collection as well as computing capacity for raw data processing.

16.4 Timeline

The microXAS project is not restricted by rigid constraints imposed by existing long-term industrial or scientific contracts. However, the relocation of the beamline project from a long straight to a standard short straight requires major redesign efforts and construction works. In principle, the adaptation of microXAS to SLS 2.0 has to be considered in effect to be the construction of a new beamline. This will lead to an extended upgrade period required to complete all the civil engineering works, installation of major optics elements, and endstation infrastructures. Although ostensibly an undesired aspect, one can make a virtue out of this necessity by allowing for additional flexibility in assigning planning and realization periods. The drawback of a slightly longer downtime will certainly be outweighed by the quality gain of the final realization. Further, this flexibility will be to the benefit of other beamlines with severe constraints. These projects can be assigned priority during peak times during the regular machine dark period.

Despite this planning flexibility, the major civil engineering work has to happen within the machine dark period. The installation of the lead shielded optics and experimental hutches and main heavy optical components has to be completed before the end of the shutdown period. As soon as light will be delivered by the upgraded SLS machine, commissioning of the new optics components must begin. Given the technically straightforward conversion of the exisiting FEMTO-KB system into the new microKB module, combined with the presently already available sample manipulator, the current user activities can be continued without further delay – with the significantly improved performance parameters.

In parallel with these immediate (expert) user activities, the final implementation and commissioning of the nanoKB module can occur. The nanoImaging module is available immediately after the start of SLS 2.0 operation with 100 nm spatial resolution. Further upgrades of this diffractive lens system, e.g. to 50 nm spatial resolution, active energy tracking, or off-axis dispersive XAS, are scheduled to take place subsequent to the resumption of full user operation.

16.5 Cost and funding program

At present, a reliable cost estimate is rather challenging for the specific case of the microXAS upgrade. For the microXAS beamline as a 'red-red-red' beamline, the required investments for beamline infrastructure can potentialy be close to the grand costs of a new beamline. At this stage it is in particular unsure to which extent the reuse of components (e.g. lead shielding, front-end components, supports and vacuum chambers, etc.) can contribute to the microXAS cost saving program. Obviously, major efforts are made to re-use existing, well-proven components such as vacuum components, XBPM units, microKB unit, or sample manipulator.

Inevitable beamline optics related investments include

i prefocussing: two dynamic 1D focusing mirrors in KB arrangement. Fully dynamic focusing but optimized for the three modes: (1) flat, (2) collimating, and (3) focusing. Elliptical figure. 2 mrad incidence angle. Multiple stripe coatings (Si, Rh, Pt).

ii monochromator, energy range $\sim$ 4 to 40 keV, multiple crystal pairs [Si(111), Si(220), Si(311)]. Either existing vertically diffracting fixed-exit DCM or new horizontally deflecting system with

reduced offset.

iii kickback system: double multilayer monochromator, cryo-cooled (on same cryo-cooler as DCM). Ideally triple multilayer monochromator.

iv microKB: full flux KB (existing FEMTO-KB bender system with new mirrors, 2 mrad incidence angle, multiple stripe coatings (Si, Rh, Pt).

v new high–performance nano–KB, 2 mrad incidence angle, limited working distance

A conceptual sketch of the hierarchical upgrade plan of the beamline optics is given in Figure 16.12.

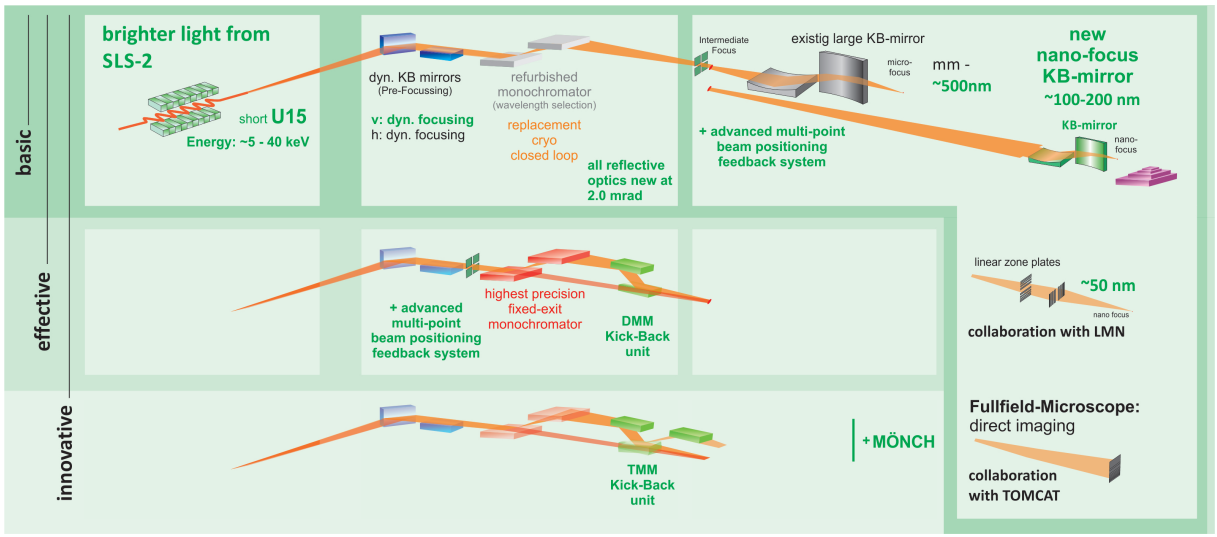

Figure 16.12: Conceptual sketch of the hierarchical upgrade plan .

microXAS has a recognized track record in obtaining funding for strategic instrumentation investments to continuously advance the facility. For example, recently, microXAS has initiated a strategic upgrade program related to advanced detection capabilities (EIGER 4M, FalconX). To match the advanced source quality and expected optical quality of the beamline, proposals for related innovative endstation instrumentations are already or will soon be submitted. At present, strategic areas are, among others, beam position feedback system (CROSS, ACCURAT; recently funded/submitted, collaboration with LMN), dynamic and non-equilibrium end systems (pump and heating lasers; R'Equip, considered), cryo-tomography (CROSS, pilot phase recently funded), computer-aided sample positioning (R'Equip, LEAPS, considered; collaboration with PX).

16.6 Concluding remarks

The clear ambition of microXAS is to have global leadership in imaging of chemical heterogeneity and reaction dynamics in hierarchical systems under real (undisturbed) conditions - in short in-situ 4D chemical imaging. This would allow a broad range of scientific communities to gain unrivaled insights into the chemical complexity of heterogeneous, hierarchical materials, the corresponding reactivity, and chemical transformations. The corresponding scientific knowledge is ideally obtained on all relevant

length and time scales. As an illustrative example, an as-yet elusive challenge is to image and rationale under physiological relevant conditions the action and response of a drug application - covering key processes such as the transport of the applied pharmaceutical compounds through tissue material, the uptake and distribution into individual cells, the possible metabolism (deactivation and side effects) or effect of the substance within intracellular compartments.

Going beyond 2035, we will leverage from new technologies that are under development now at PSI and add energy information as a 'fifth axis' to our instrument. New pixel detectors will yield energy-dispersive information and novel undulator operation modes will allow the creation of a broad energy continuum. Consequently, sequential 4D chemical imaging by energy scanning can be compressed in a single white light exposure with the energy information being provided by the pixel detector. Based on these unique opportunities, PSI and microXAS will lead the invention of 5D chemical imaging ('space - time – energy').

Bibliography

[1] N.-I. Khamidy, J. Laurencin, D.F. Sanchez, F. Monaco, F. Charlot, and E. Djurado. Durability of nanostructured $LaPrNiO_{4+\delta}$ electrode for solid oxide cells: electrochemical, microstructural, and structural investigation. *J. Power Sources*, 450:227724, 2020.

[2] J. Laurencin, M. Hubert, D.F. Sanchez, S. Pylypko, M. Morales, A. Morata, B. Morela, D. Montinaroe, F. Lefebvre-Jouda, and E Siebert. Degradation mechanism of $La_{0.6}Sr_{0.4}Co_{0.2}Fe_{0.8}O_{3-\delta}/Gd_{0.1}Ce_{0.9}O_{2-\delta}$ composite electrode operated under solid oxide electrolysis and fuel cell conditions. *Electrochimica Acta*, 241:459476, 2017.

[3] S. Hocine, H. Van Swygenhoven, S. Van Petegem, C.S.T. Chang, T. Maimaitiyili, G. Tinti, D.F. Sanchez, D. Grolimund, and N. Casati. Operando x-ray diffraction during laser 3D printing. *Materials Today*, in press.

[4] P. Karvinen, D. Grolimund, M. Willimann, B. Meyer, M. Birri, C. Borca, J. Patommel, G. Wellenreuther, G. Falkenberg, M. Guizar-Sicairos, A. Menzel, and C. David. Kinoform diffractive lenses for efficient nano-focusing of hard x-rays. *Optics Express*, 22/14:16676–16685, 2014.

[5] E.H.R. Tsai, J. Billaud, D.F. Sanchez, J. Ihli, M. Odstrcil, M. Holler, D. Grolimund, C. Villevieille, and M. Guizar-Sicairos. Correlated x-ray ptychographic nano-tomography and diffraction microscopy visualize hidden stress in lithium-rich cathode materials. *Optics Express*, 11:356365, 2019.

[6] J. Ihli, R.R. Jacob, M Holler, M. Guizar Sicairos, A. Diaz, J.C. da Silva, D.F. Sanchez, F. Krumeich, D. Grolimund, M. Taddai, W.C. Cheng, Y.Y. Shu, A. Menzel, and J.A. van Bokhoven. Three dimensional view of structural changes caused by deactivation of fluid catalytic cracking catalysts. *Nature Communications*, 8:809, 2017.

[7] J. Ihli, D.F. Sanchez, R.R. Jacob, V. Cuartero, O. Mathon, F. Krumeich, C. Borca, T. Huthwelker, W.C. Cheng, Y.Y. Shu, S. Pascarelli, D. Grolimund, A. Menzel, and J.A. van Bokhoven. Localization and speciation of iron impurities within a fluid catalytic cracking catalyst. *Angew. Chem. Int.*, 56/45:14031–14035, 2017.

[8] C. Kenel, D. Grolimund, X. Li, E. Panepucci, V.A. Samson, D.F. Sanchez, F. Marone, and C. Leinenbach. Mimicking additive manufacturing conditions combining laser melting of Ti-6Al-4V with in situ high-speed x-ray diffraction. *Sci. Rep.*, 7:16358, 2017.

[9] P. Beaud, S. L. Johnson, A. Streun, R. Abela, D. Abramsohn, D. Grolimund, F. Krasniqi, T. Schmidt, V. Schlott, and G. Ingold. Spatiotemporal stability of femtosecond hard x-ray undulator radiation studied by control of coherent optical phonons. *Physical Review Letters*, 99:174801, 2007.

[10] anaxam. ANAXAM: analytics for advanced manufacturing.

[11] P. Bougiatioti, A. Kubec, Doering F., V.A. Guzenka, B. Roesner, C. Milne, S. Reiche, and C. David. Towards single-shot xas on transition metals. In *PSI PSD-GFA cross-divisional science day*, 2019.

[12] A. Streun. SLS 2.0 baseline lattice. Technical report.

[13] K. Köhler. A projection access scheme for iterative reconstruction based on the golden section. *IEEE Nuclear Science Symp. Conf. Record*, 6:39613965, 2004.

[14] A. Kaestner, B. Munch, P. Trtik, and L. Butler. Spatiotemporal computed tomography of dynamic processes. *Optical Eng.*, 12:123201, 2011.

[15] B. Golosio, A. Somogyi, A. Simionovici, P. Bleuet, J. Susini, and L. Lemelle. Nondestructive three-dimensional elemental microanalysis by combined helical x-ray microtomographies. *Appl. Phys. Lett.*, 84:2199–2201, 2004.

[16] M. Sanchez del Rio, N. Canestrari, F. Jiang, and F. Cerrina. Shadow3: a new version of the synchrotron x-ray optics modelling package. *J. Synchrotron Rad.*, 18:708–716, 2011.

[17] S. Kapishnikov, D. Grolimund, G. Schneider, E. Pereiro, J. McNally, J. Als-Nielsen, and L. Leiserowitz. Unraveling heme detoxification and crystallization in the malaria parasite by correlative x-ray microscopy. *Sci. Rep.*, 7:7610, 2017.

[18] M Lebugle, F. Dworkowski, A. Pauluhn, V.A. Guzenko, N. Meier, D.F. Sanchez, D. Grolimund, M. Wang, and C. David. A high-intensity x-ray microbeam for macromolecular crystallography using silicon kinoform diffractive lenses. *Applied Optics*, 57/30:9032–9039, 2018.

[19] D.F. Sanchez, A.S. Simionovici, L. Lemelle, V.C. Cuartero Yague, O. Mathon, S. Pascarelli, A. Bonnin, R. Shapiro, K. Konhauser, D. Grolimund, and P. Bleuet. Microanalysis by energy dispersive x-ray absorption spectroscopy tomography. *Sci. Rep.*, 7:16453, 2017.

[20] M. Carulla, N. Selam, A. Tsibizov, T. Ziemann, M. Birri, B. Meyer, D. Grolimund, C. Pradervand, O. Bunk, U. Grossner, and M. Camarda. Systematic analysis and optimization of silicon carbide ultra-thin (< 2 μm) x-ray sensors for synchrotrons beam position monitors applications. In *ICSCRM Conference Proceedings*, 2019.

[21] F. Gervilla, M.P. Asta, Fanlo, D. I. Grolimund, D.F. Sanchez, V.A. Samson, D. Hunziker, V. Colas, J. M. Gonzlez-Jimnez, T.N. Kerestedjian, and I. Sergeeva. Monitoring the diffusion of Fe^{2+} and Fe^{3+} during the formation of ferrian chromite: a μxanes study. *Contributions to Mineralogy and Petrology*, 174/8:65:1–16, 2019.

Chapter 17

ADDAMS: ADvanced DiffrAction for Material Science

Nicola Casati, Antonio Cervellino, Dominik Meister, and Michael Lange

In a nutshell

The MS beamline scientific program spans many disciplines, including geology, chemistry, physics, and pharmacy. The beamline, operational for powder and surface diffraction, has successfully served over **400 academic and 150 industrial user projects** over the years. The SLS 2.0 upgrade will substantially improve all the basic characteristics of the present instrument. In particular, it will significantly expand its higher photon-energy capabilities, thus exploiting the present optics setup which is already designed for a higher accessible photon-energy range.

We propose a beamline dedicated to ADvanced DiffrAction for Material Science (ADDAMS), a medium-to-high photon-energy instrument with versatile experimental stations. It will be based on the novel superconducting undulator (or the refurbished U14, if the former is not available), making full use of the optics presently available and improving their capabilities. Three versatile experimental tables will be available to best address all experimental geometries. Such an instrument fits perfectly not only within the Swiss scientific community but, in particular, within PSI, having clear complementarities and added-value synergies with other local instruments, and being strongly related to the PSI spin-off Excelsus and the ANAXAM center.

We believe the upgrade will maintain the ADDAMS beamline among the best performing instruments in the field, being a world leader for **time-resolved** diffraction experiments and **high-quality measurements**, while expanding the scope and nature of our total-scattering and *in situ* capabilities.

17.1 Overview

X-ray diffraction is a mature technique, more than 100 years old; over the years its importance and capabilities have grown tremendously. Most solid-state laboratories in the world are equipped with diffractometers, at both industrial and academic institutions, as well as all the major synchrotron facilities in the world. The need for diffraction is in fact growing with the amount of materials being produced and tested, as a more rational design requires a deep understanding of structure/property relations.

Nowadays, synchrotron diffraction for materials is mostly devoted to high-quality or challenging measurements, complex experiments (*in situ*, *operando* etc.) and, more recently, high throughput. Demand in all these capabilities will keep growing in many different fields. In the pharmaceutical industry, for example, polymorphs and not compounds are typically patented, which means detection capability and observation/quantification of minor phases, related to the quality of measurements, are an increasingly strong motivation for industries to access ever better performing synchrotron facilities. As coatings, surfaces and interfaces are becoming increasingly technologically relevant, challenging measurements on thin, deposited layers, requiring a low-divergence source, will grow equally in importance. Disordered, deliberately-defective and amorphous materials are also becoming more and more relevant, as are the total-scattering methods (TS) used to study their structures [1–3]. These studies require the high-energy x-rays from synchrotron sources. Multi-wavelength experiments such as Diffraction Anomalous Fine Structure (DAFS), bridging the long-range order diffraction information and short-range order from spectroscopy, also require the tunable energy available at synchrotron sources [4]. Finally, *in situ* and *operando* experiments will compete with high-throughput measurements for the understanding and fine-tuning of materials. These two types of studies reflect the rational approach (understanding the structure-property relationship to achieve desired materials) and the combinatorial one (trying all possibilities and selecting the best), which are followed in different cases.

The Material Science beamline (MS), operational since 2001 [5, 6], is a versatile instrument for diffraction experiments, which provides structural information of crystalline and amorphous materials down to 10 fm resolution. Experiments are typically performed in transmission at the Powder Diffraction station (PD), or in reflection mode at the Surface Diffraction station (SD); these are operated in series. The large range of energies (5 to 38 keV) and the availability of several *in situ* and *operando* setups are mirrored by the large span of scientific areas to which the beamline has contributed, such as pharmaceutical studies, condensed-matter physics, chemistry, metallurgy, structural biology, electrochemistry, geology, and material science. The beamline was also the cradle of the photon-counting detectors. The first strip detector (Mythen) was developed and installed at the PD station more than 15 years ago [7, 8]; the SD station implemented and developed the first experiments using the Pilatus area detector [9–11]. This catapulted the beamline to the forefront of the synchrotron diffraction world, in particular with respect to time-resolved studies; its design has been replicated in several

facilities around the world (e.g. MSPD at Alba, I11 at Diamond, PD at ANSTO, BL02B at Spring8).

The beamline was upgraded in 2011, when the original wiggler source was replaced with an in-vacuum undulator (U14) and the optics entirely redesigned and commissioned [6]. Since then, on top of the many publications, the constantly growing industrial usage showcases the quality of the upgrade. In the last five years, industrial applications have been on average exceeding 10% of the academic user time, second only to protein crystallography within the SLS.

17.2 Proposed upgrade

17.2.1 Goals – opportunities from the SLS 2.0 machine

Within the SLS 2.0 upgrade we propose ADDAMS, an instrument delivering ADvanced DiffrAction for Material Science. The aim of the beamline is to address a wide range of diffraction experiments performed with monochromatic radiation, and be a world-leading instrument to probe materials in action with time-resolved and *in situ* experiments and highest-quality data. We would maintain the presently existing and developing framework of the endstations, which delivers a large flexibility in terms of diffraction experiment types and geometries. Upgrades, a constant process for any diffraction beamline, are in this sense already ongoing, not only in order to match the new machine capabilities, but also as a result of exploiting the latest experimental technologies. On the other hand, SLS 2.0 and related developments will deliver some unique features and the possibility for a radical improvement in several areas.

The improved coherence of the beam will allow the inclusion, in the longer term, of new techniques for ADDAMS. Bragg Coherent Diffraction Imaging is already actively pursued at other beamlines (cSAXS). Less explored and better matched to our strengths and working field is X-Ray Cross Correlation Analysis (XCCA), which can be regarded as an extension of TS methods, exploiting coherent radiation. XCCA methods can be applied to amorphous and liquid materials, as well as mesoscale disordered/partially ordered systems, such as colloids, liquid crystals, and interacting nanoparticle ensembles [12–14].

The increased brilliance of SLS 2.0 will benefit all experiments requiring a round beam or stronger focusing, without any further modifications. The small lateral size of the photon beam suggests also some modifications and additions to the optics that will improve performance and ease of operation, a very important point given the diverse nature of applications which require continuous change. It is worth noting, in this respect, some user beamtimes are limited to half a shift and in the future even faster access might be forecast. During the last beamline upgrade (2011) the design for the optics was forward-looking, being designed for energies up to 40 keV [6]. Due to a lack of competitive flux in the region above 27-30 keV, however, the full capability was seldom exploited.

Thanks to sharper harmonics from the undulator, the flux at higher energies is set to increase (see Figure 17.2), even without further upgrades, making TS experiments more efficient. A proposed new insertion device would significantly improve these capabilities. This means TS studies could be performed with application-relevant time resolutions (10 seconds or less) and/or in very low signal-to-noise-ratio conditions (very dilute specimens), opening up the possibility to compete in a rapidly growing field. Small additions to the optics (deposition of multilayers on existing elements and an

extra horizontal mirror) will also improve the flux for very fast experiments and improve the general ease of operation.

17.2.2 Comparison and complementarity to other instruments

The presence of simpler instruments at the laboratory level has created a large community of proficient diffraction users which understands synchrotron facilities as the ultimate location to perform more complex and high-quality experiments. In the future, synchrotron sources will certainly maintain this advantage from many points of view. Photon flux is certainly one of the main, but not only, motivation. It enables experiments at time resolutions not available to laboratory sources and brings the signal-to-noise ratio to unparalleled levels. Brilliance allows one to focus the flux into ever-smaller samples or into smaller *in situ* or *operando* setups. The development, realization and in most cases usage of such setups are in fact possible only at large-scale facilities. Another clear advantage is the wavelength tunability, which ensures not only the correct penetration, but also the possibility to work around elemental edges, to improve contrast or highlight specific elements within a structure. Despite the many improvements, therefore, diffraction laboratories should be considered useful partners and not competitors. In fact ADDAMS is complementary to laboratory diffractometers: a small-scale, fast-measurements and easy-access service called Mesquik is already operational, allowing users to consider the synchrotron source an extension of their laboratory, at least in simple cases.

Most synchrotron facilities include one or more material diffraction beamlines, which are pursuing similar strategies. While other beamlines offer typically one experimental endstation, we have the possibility to keep most options available, as we offer a variety of solutions for several types of experiments, including surface single crystal and powder diffraction, transmission single crystal and powder diffraction, time-resolved experiments (presently up to 22 kHz, soon to extend into the MHz region), on-edge diffraction, etc. Keeping a wide range of possibilities, though, will not result in a loss of competitiveness; although dedicated instruments delivering mainly one experiment type (TS beamlines, or extreme conditions ones) can concentrate their parameters exclusively for that technique, in many cases, the difference in quality compared to ADDAMS will be modest. The flexibility of ADDAMS will thus make it more attractive for many applications. The proposed SLS 2.0 beamline will maintain its edge in time-resolved experiments and further expand the successes achieved with TS and *in situ* capabilities, as well as reduce the price for such a wide range of experiments, by improving the ease of usage.

The beamline has been complementary and in many cases working in partnership with several instruments within PSI. The powder diffraction instrument has established an active collaboration with the SinQ comparable instruments, HRPT and DMC, and a joint call for x-rays and neutron joint experiments has been open to users for well over a decade; this will possibly be expanded to single crystal techniques at ZEBRA. A strong collaboration exists with the SwissFEL teams at Bernina and soon Cristallina stations, as the surface diffractometer mirrors local capabilities and is well suited for performing relevant preparatory measurements before challenging time-resolved experiments. This collaboration should become official in the near future, offering users the possibility to perform measurements at different time domains within a single proposal.

A strong collaboration has been ongoing for several years with the microXAS beamline and the

Photons for Engineering and Manufacturing groups at PSI, in particular in the fields of time-resolved diffraction and advanced manufacturing. In this respect, the two beamlines cover different beam sizes and energy domains, with microXAS devoted to micro or even single-grain diffraction and MS to a more averaged material response, including working at higher energies.

17.2.3 Industrial potential

As mentioned, the MS beamline has in the last few years the largest industrial access of any non-protein beamline at the SLS, see Figure 17.1. This trend mirrors the increasing popularity of diffraction and the

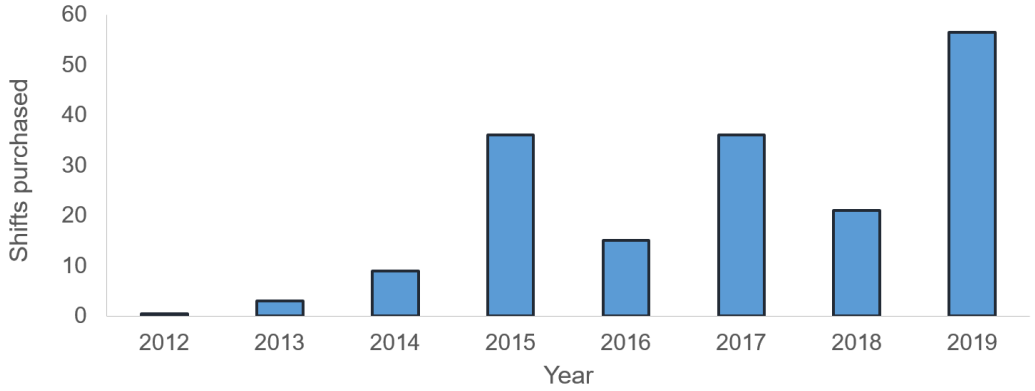

Figure 17.1: Number of shifts purchased per year by industrial partners; the period considered is after the MS upgrade in 2011.

constant growth in the number of synchrotron-aware scientists within industrial R&D departments. Moreover, this specific success was aided by a flexible access program, custom-tailored industrial developments, and the presence of an official PSI spin-off dedicated to powder diffraction for the pharmaceutical industry (Excelsus). In the technology adoption lifecycle of synchrotron diffraction, we are at the beginning of the "early adopters" phase, with several partners now considering synchrotron access as a continuous requisite rather than as a one-off event or highly intermittent requirement. In the next ten years, we expect the pharmaceutical industry to include it into its best practices, as well there being as a strong increment in access from companies with high added-value products in the chemical and technological sectors.

An untapped source of potential industrial revenue is that of high-throughput. Thanks to the top-quality infrastructure and high level of automation that has been implemented at the MS beamline, the price per sample of simple powder diffraction measurements (i.e. that could be performed in home laboratories) has dropped so strongly that synchrotron diffraction is not only limited to high-quality or complex experiments, but is also cheaper per sample compared to home laboratories. Laboratory-quality measurements can be performed in about 5 to 10 seconds and automated to the point that grinding, the lengthy process of reducing particles to microns in size, is no longer required. This was a major hurdle for high throughput in powder diffraction. Industries with combinatorial approaches, in the mining and raw-materials sectors are present or potential customers of these developments, for

which MS is a pioneer.

The recent approval of the ANAXAM center, devoted to support industrial partners using PSI large-scale facilities and in which the MS beamline plays a significant role, will surely contribute to increased industrial access, as Excelsus has done for the pharmaceutical sector.

The higher brilliance and flux that would be guaranteed by the proposed upgrade, play a significant role for most of the industrial activities, which are forecast to grow significantly, possibly more than at the present rate.

17.3 Conceptual design

The ADDAMS beamline will perform diffraction experiments in the 5 to 40 keV region, all of the initially forecast range being usable for time-resolved and high-quality experiments. At higher energies, this requires a sharp increase in photon flux, the most relevant parameter for diffraction. The ease of use of the optics should be improved, in particular for beam focusing and energy change, which is at present not automatic and too complex. A one-button operation, with automatic fine-tuning, should be fully automated for experiments across elemental edges. Moreover, increasing the operator-independence of optics tuning is a very relevant aspect for several industrial partners, which should be able to guarantee a high degree of reproducibility. ADDAMS should offer a variety of experimental geometries and setups. The former guarantee the ability to perform experiments and measurements in the best conditions, the latter that we can serve as wide a community as in the past, potentially further improving our experimental capabilities.

17.3.1 Source

The present cryogenically-cooled in-vacuum undulator (U14), which had a pioneering design and is equipped with NdFeB magnets [15], is an excellent source for low to middle energies (from 5 to approximately 20 keV) but fails to perform adequately at the highest energies, which are therefore seldom used at the beamline. The electron-beam characteristics of SLS 2.0, however, will provide sharper undulator harmonics even without any other changes, with a two or threefold increment in the photon flux available, see Figure 17.2(**a**). A simple upgrade to PrFeB magnets could bring a further similar improvement, resulting in almost an order of magnitude improvement in flux at higher energies, see Figure 17.2(**b**).

A short-period high-temperature superconducting undulator (SCU10) would be a real game changer [16], with combined gains at energies above 30 keV exceeding an increase in flux by two orders of magnitude compared to today, see Figure 17.2(**c**). Such a flux will enable ADDAMS to compete in time-resolved TS studies, high-pressure experiments in the Mbar region, and metallurgy, to name just three fields. Moreover, the penetration of the beam can significantly ease the requirements for several *in situ* setups. An SCU10 is presently under development. While it is not clear at present the timeline for this R&D project, which is of primary interest also for the I-TOMCAT beamline, this should become clearer well before the dark period. Should the installation of an SCU10 become unfeasible before the SLS 2.0 upgrade, this would not affect strongly our financial plans, although it would reduce the scientific aim and appeal. It would in that case be limited to an upgrade of the

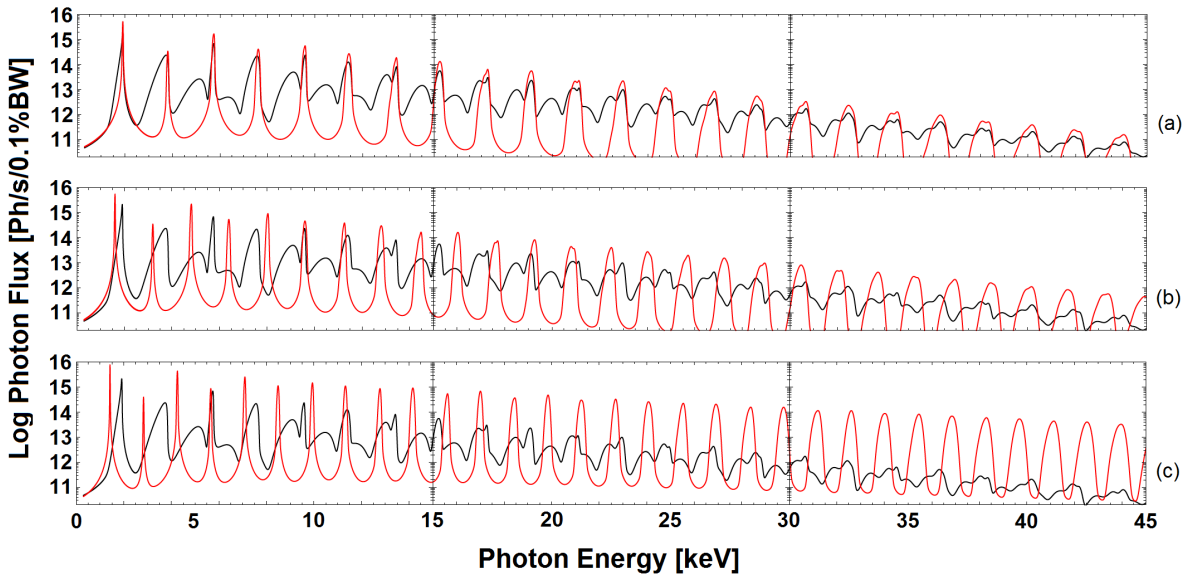

Figure 17.2: Flux comparison from different undulator sources at a 4.0-mm gap for SLS (black line) and SLS 2.0 (red line) machines. (a) present Nd based U14, (b) novel Pr-based U14 (c) superconducting U10

magnets, as mentioned above.

17.3.2 Front end

The front end will need several elements to be modified or changed. The biggest challenges will be given by the large thermal load of the SCU10, which is presently calculated to irradiate 12 kW. The front-end x-ray beam-position monitors (XBPMs) can be refurbished to keep them in operation, the photon shutter will need to be redesigned, and a new long tapered diaphragm should be placed in front of it to remove most of the thermal load. The design of such a diaphragm, with calculations of its cooling power, has shown the feasibility of this approach. All filters should be subject to a smaller heat load. The first optical element, the first crystal of the existing monochromatic, is already cryogenically cooled and should not be subject to much higher power than presently.

17.3.3 Optics

Most of the optics can be kept, as it has been designed for energies up to 40 keV. This includes a cryogenically cooled double-crystal monochromator (DCM), with a sagittally bendable crystal for horizontal focusing, and two vertical (normal to plane) mirrors, one of which bendable for vertical focusing. The weak point of the present system is the horizontal sagittal focusing. In particular, this focussing element has never exhibited high reproducibility of the motor settings required to obtain a given focus. Moreover, its operation is complex, requiring long experience. Lastly, the crystal is also at risk of rupture for the most extreme bendings. Given the laterally reduced beam size expected

in SLS 2.0, a horizontally focusing mirror, with a fixed reflection angle, would now be an option without the need for very long mirrors, see Figure 17.3. This creates the opportunity to produce small

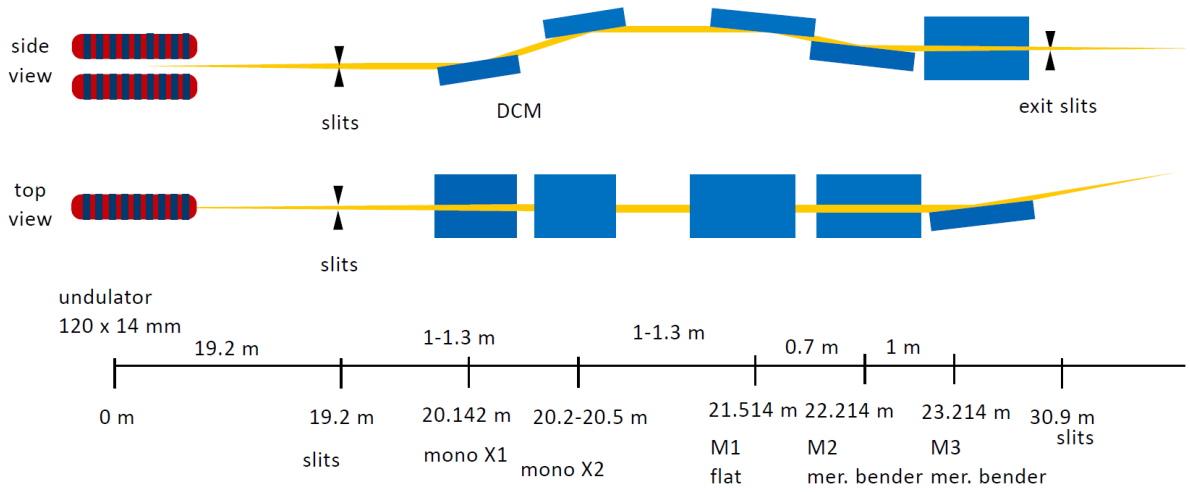

Figure 17.3: Schematic of operation including a horizontally focusing mirror M3. Distances are based on the present optics.

enough beam sizes and improves tremendously the ease of operation, given the higher quality in the motorization for bending a mirror compared to crystal flexure. It is technically possible to include such mirror in the present optics hutch, as space can be made at different locations. Its exact position will depend also on focusing performances and will therefore be finalized based on the exact source position.

The reduced lateral beam size will present a further opportunity: to deposit multilayer strips on the laterally non-occupied areas of our optical elements. By reflecting on multilayer-coated sides of the first crystal of the DCM and then on the first mirror, we will obtain a larger bandpass at selected fixed energies, see Figure 17.4. In this scenario, the energies will be fixed as the reflection angle of the beam is somewhat limited by the relative distances of the elements, which can translate laterally and vertically, but not along the beam direction. There could conceivably be two modes of operation: including or not the second mirror (and therefore including or not vertical focusing). These two modes have different angles of operation, with minor angular flexibility, and a combination of two multilayers on each element can therefore deliver up to 6 different energies. Preliminary calculations at fixed angles and with selected multilayer spacings show high potential in the region below 20 keV, while at higher energies the performances have still to be optimized, see Figure 17.5. The resulting sharp increase in photon flux from using multilayers (one to two orders of magnitude) comes at the expense of energy resolution. This and the small number of selected energies is still very acceptable for a number of highly time-resolved experiments, where improving signal to noise and not resolution is relevant. This development is considered also rather low cost, given the potential it brings.

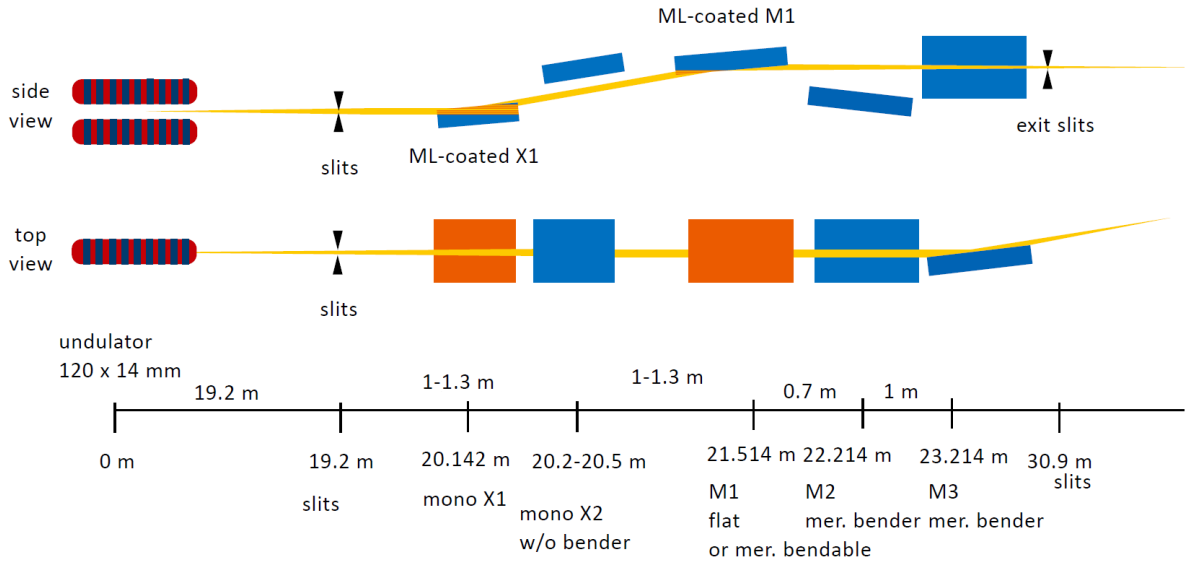

Figure 17.4: Schematic of operation, including multilayers deposited on a translating monochromator crystal X1 and mirror M1. Distances are based on the present optics. The novel beam path utilizing the multilayer would not include crystal X2, while mirror M2, not included in the picture, could in fact be operational if M1 goes to a higher position. Both schemes would still enable only few selected energies.

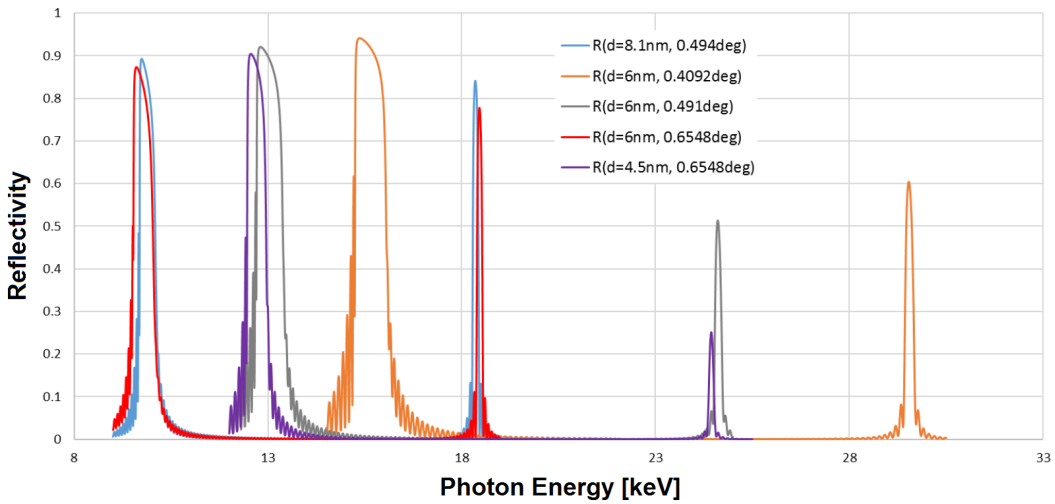

Figure 17.5: Calculated reflectivity of B_4C/Ni multilayer mirrors at fixed angles. 100 periods were considered with γ of 0.1/0.25/0.34 for the 8.1/6/4.5 nm periods respectively. Possible angle combinations include X1=M1=0.4092° or X1=0.492°/M1=0.6548°.

17.3.4 Endstations

While the infrastructure with two stations in series will be kept, its division into PD and SD will not. As a variety of end uses can be provided with each instrument, the stations and their experimental capabilities are in fact better described in terms of the specific geometry of the diffraction experiments that can be performed within them. For this reason, and to further integrate the operations in both stations, they will both be operated from the same control room, while the other will be transformed into a laboratory for sample preparation. A door change of the PD lead hutch is forecast for the beginning of 2020. It is worth noting in this context we plan to complete the upgrade of the stations before the beginning of the dark period of SLS 2.0, as it is incremental in nature and most of its costs are already allocated. During the dark period only slight movements of all main components, re-cabling and changes in the motion controls are forecast at the endstations. The plan is to include three experimental tables (1D, 2D and 3D), presently existing or under development.

The first instrument from the source is the high-resolution powder diffractometer. The geometry for such experiments is based on the Debye-Scherrer geometry, which is cylindrical around the sample axis. This is a very well described geometry, which can be treated by most programs in an exact manner and which provides resolution high enough for a full profile analysis. Samples are typically capillaries and the detector is a 1D microstrip, in this case the third generation of the Mythen detector [17], which will be completed and commissioned in 2020 as part of a financed REquip project (206021_183320). This novel detector, developed at PSI, has framerate capabilities up to 1 MHz and, importantly, a lower electronic noise. Such features will enable measurements on an elemental edge, without the non-statistical noise that presently affects them due to the high fluorescence. At the same time, the large angular range of the Mythen III (120°) ensures collecting a large enough Q-range even at moderate energies, in order to enable TS measurements. Developments are ongoing to substitute part of the modules with higher Z elements, to improve the detector efficiency at higher energies, and fully profit from the new source.

A second table is based on a large 2D detector, in frontal transmission diffraction, and placed on a heavy-duty optical table. This detector, presently a Pilatus 6M, complements the Mythen III system for SAXS measurements, with a maximum distance of 4 to 5 m from the sample. In additon, the Pilatus 6M operates as a standalone detector for powder and single crystal diffraction, or scientific problems at the border between these two conditions. The advantage for powder diffraction is the ability to improve both the signal-to-noise ratio and, by collecting full rings, also the particle statistics for non-representative samples, thereby improving phase quantification. Moreover XCCA entails the use of a 2-D detector. Exactly like TS, it demands a momentum-transfer range large enough to clearly define the interatomic (interparticle) vectors in the range of interest. Whilst TS only uses the radial intensity distribution (therefore, when a 2-D detector is used, a ring averaging is performed), XCCA uses the full 2-D pattern, by way of two-point intensity correlations – this enhances the coherent speckle pattern induced by a coherent beam [12, 18]. The main drawbacks of the 2D detector with respect to the Mythen III are the small accessible angular range, typically 30°, the lower intrinsic angular resolution, and the timeframe, which is limited to 20 Hz.

The third instrument is the multiaxis diffractometer presently in the SD hutch. With three rotational degrees of freedom for the detector, this instrument truly harnesses the full geometry of

diffraction in three dimensions. The detector is positioned at 1.2 m from the sample and, despite being an area detector (presently Pilatus 100K) it is used point to point to explore the sphere of diffraction around the sample. The possibility to insert a crystal between the scattered beam and the detector enables polarimetry measurements. The sample stage itself has 2 rotational degrees of freedom plus the ability to micro-position the samples themselves, provided by a high-precision heavy-duty hexapod. The instrument has been used in the past for x-ray reflectometry measurements, analysis of crystal truncation rods, and x-ray magnetic scattering. Due to its flexibility, it can serve a wide variety of experiments, such as grazing-incidence powder diffraction or high-resolution single-crystal diffraction in transmission. The presence of a further eulerian cradle may also enable azimuthal scans for magnetic x-ray scattering on chosen [hkl] planes. The main drawback of so many degrees of freedom is the small portion of the full Ewald sphere that is typically probed at any one time. This implies as well a rather large time for measurements and sample alignment, which is more critical too. To complete the station the addition of a fast Eiger detector (1 Megapixel, up to 22 kHz) closer to the sample position is planned, which will be commissioned by the end of 2020. At the closest distance it will cover an angular range of 45° (to be compared to 2° for the Pilatus). This new area detector will serve two purposes, namely to help in the alignment of samples, and to perform its own experiments, mainly for fast experiments with complex machinery that requires the precise alignment that can be delivered by the hexapod. It is forecast to be the main instrument for studies under the topic Advanced Manufacturing.

The three tables have different strengths and complementarities; they cover most of the possible ways experiments can be conducted. A one-fits-all approach, aside from being most likely significantly more expensive, would definitely not address all the different needs in such a simple and straightforward way.

17.3.5 IT requirements

The large amount of data coming from time-resolved and high-throughput measurements have to be handled and treated in real time, at least to provide users with a qualitative picture of the experiment/measurements as they are being performed. This increases significantly the success rate of proposed experiments. The forecast data volumes, with a maximum of few Tb per day, do not pose nowadays a significant technological problem. The IT infrastructure for ADDAMS will be operational by the beginning of the dark period.

17.3.6 Timeline

With the exception of the SCU10, most of the other developments are minor, although it is not yet clear how much the optics lead hutch will be impacted in the new machine design. The decision on whether or not to install directly the novel undulator can be postponed until it will be clear if this becomes available or not by first light at SLS 2.0, given the existence of a backup plan. The insertion device group is anyway confident an answer can be obtained at the end of 2020 on the timeline for this development, which we would install anyway as soon as it became available.

In the Gantt chart in Figure 17.6, an extended period for design and subsequent procurement is tentatively placed, although clearly it will depend on the availability of a superconducting, short-

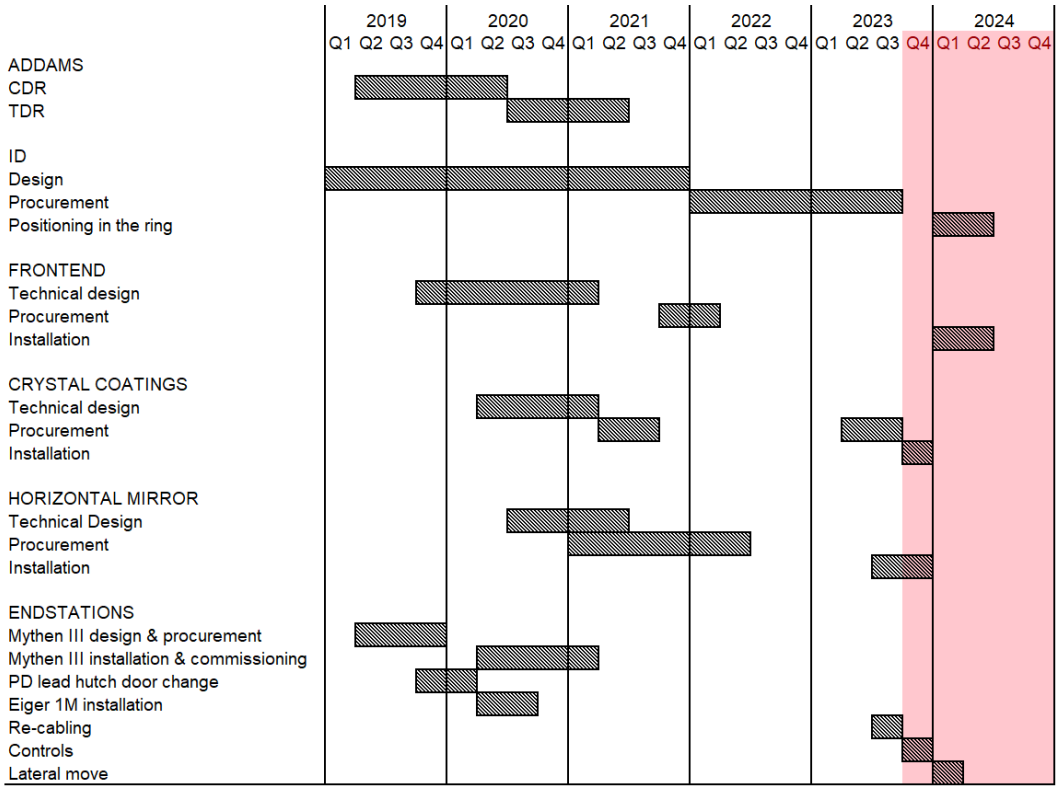

Figure 17.6: Gantt chart for the progress of the ADDAMS upgrade.

period undulator. At the same time, to make sure the design of the front end is appropriate for the characteristics of the new undulator, its design will be completed in 2020, although its final procurement will be postponed to the end of 2021, to leave some room for changes, in case characteristics of the source are modified or even improved.

17.3.7 Costs and funding program

The upgrades at endstations are coming from industrial partners, internal funds, and an SNF R'Equip project. The calculated manpower for moving the elements and installing new components is of 68.5 man-months, not including design of the different parts.

17.4 Concluding remarks

The improved brilliance, flux and general infrastructure is set to make ADDAMS a world leader among advanced diffraction beamlines. We expect to become competitive in TS studies as well as improve our efficiency for time-resolved experiments. Overall, our appeal for industrial applications is also set to increase even further, at a time when synchrotron diffraction is becoming more widely adopted.

Bibliography

[1] F. Bertolotti, D.N. Dirin, M. Ibanez, F. Krumeich, A. Cervellino, R. Frison, O. Voznyy, E. H. Sargent, M. V. Kovalenko, A. Guagliardi, and N. Masciocchi. Crystal symmetry breaking and vacancies in colloidal lead chalcogenide quantum dots. *Nat. Mater.*, 15(9):987–994, 2016.

[2] J. M. Delgado-Lopez, F. Bertolotti, J. Lyngso, J. S. Pedersen, A. Cervellino, N. Masciocchi, and A. Guagliardi. The synergic role of collagen and citrate in stabilizing amorphous calcium phosphate precursors with platy morphology. *Acta Biomater.*, 49:555–562, 2017.

[3] F. Bertolotti, G. Nedelcu, A. Vivani, A. Cervellino, N. Masciocchi, A. Guagliardi, and M. V. Kovalenko. Crystal structure, morphology, and surface termination of cyan-emissive, six-monolayers-thick cspbbr$_3$ nanoplatelets from x-ray total scattering. *ACS Nano*, *Articles ASAP*:*n.a.*, 2019. PMID: 31747248.

[4] T. Kawaguchi, K. Fukuda, K. Tokuda, K. Shimada, T. Ichitsubo, M. Oishi, J. Mizuki, and E. Matsubara. Revisit to diffraction anomalous fine structure. *J. Synchrotron Rad.*, 21(6):1247–1251, 2014.

[5] F. Gozzo, B. Schmitt, T. Bortolamedi, C. Giannini, A. Guagliardi, M. Lange, D. Meister, D. Maden, P. Willmott, and B.D. Patterson. First experiments at the Swiss Light Source Materials Science beamline powder diffractometer. *J. Alloys Compd.*, 362(1-2):206–217, 2004. 6th International School and Symposium on Synchrotron Radiation in Natural Science, Ustron Jaszowiec, Poland, Jun 17-22, 2002.

[6] P. R. Willmott, D. Meister, S. J. Leake, M. Lange, A. Bergamaschi, M. Böge, M. Calvi, C. Cancellieri, N. Casati, A. Cervellino, Q. Chen, C. David, U. Flechsig, F. Gozzo, B. Henrich, S. Jäggi-Spielmann, B. Jakob, I. Kalichava, P. Karvinen, J. Krempasky, A. Lüdeke, R. Lüscher, S. Maag, C. Quitmann, M. L. Reinle-Schmitt, T. Schmidt, B. Schmitt, A. Streun, I. Vartiainen, M. Vitins, X. Wang, and R. Wullschleger. The Materials Science beamline upgrade at the Swiss Light Source. *J. Synchrotron Rad.*, 20(5):667–682, 2013.

[7] B. Schmitt, C. Bronnimann, E. F. Eikenberry, F. Gozzo, C. Hormann, R. Horisberger, and B. Patterson. Mythen detector system. *Nucl. Instrum. Meth. A*, 501(1):267–272, 2003. 10th International Workshop on Vertex Detectors, Brunnen, Switzerland, Mar 21 2001.

[8] A. Bergamaschi, A. Cervellino, R. Dinapoli, F. Gozzo, B. Henrich, I. Johnson, P. Kraft, A. Mozzanica, B. Schmitt, and X. Shi. The MYTHEN detector for X-ray powder diffraction experiments at the Swiss Light Source. *J. Synchrotron Rad.*, 17(5):653–668, 2010.

[9] B. Henrich, A. Bergamaschi, C. Broennimann, R. Dinapoli, E. F. Eikenberry, I. Johnson, M. Kobas, P. Kraft, A. Mozzanica, and B. Schmitt. PILATUS: A single photon counting pixel detector for X-ray applications. *Nucl. Instrum. Meth. A*, 607(1):247–249, 2009. 10th International Workshop on Radiation Imaging Detectors, Helsinki, Finland, Jun 29-Jul 03, 2008.

[10] P. Kraft, A. Bergamaschi, Ch. Broennimann, R. Dinapoli, E. F. Eikenberry, B. Henrich, I. Johnson, A. Mozzanica, C. M. Schlepütz, P. R. Willmott, and B. Schmitt. Performance of single-photon-counting PILATUS detector modules. *J. Synchrotron Rad.*, 16(3):368–375, 2009.

[11] C. M. Schlepütz, P. R. Willmott, S. A. Pauli, R. Herger, D. Martoccia, M. Bjorck, D. Kumah, R. Clarke, and Y. Yacoby. Surface xray diffraction of complex metal oxide surfaces and interfacesa new era. *AIP Conference Proceedings*, 1092(1):9–12, 2009.

[12] P. Wochner, C. Gutt, T. Autenrieth, T. Demmer, V. Bugaev, A. D. Ortiz, A. Duri, F. Zontone, G. Gruebel, and H. Dosch. X-ray cross correlation analysis uncovers hidden local symmetries in disordered matter. *PNAS*, 106(28):11511–11514, 2009.

[13] I. Lokteva, M. Koof, M. Walther, G. Gruebel, and F. Lehmkuehler. Monitoring nanocrystal self-assembly in real time using in situ small-angle x-ray scattering. *Small*, 15(20), 2019.

[14] F. Lehmkuehler, B. Fischer, L. Mueller, B. Ruta, and G. Gruebel. Structure beyond pair correlations: X-ray cross-correlation from colloidal crystals. *J. Appl. Crystallogr.*, 49(6):2046–2052, 2016.

[15] M. Calvi, T. Schmidt, A. Anghel, A. Cervellino, S. J. Leake, P. R. Willmott, and T. Tanaka. Commissioning results of the U14 cryogenic undulator at SLS. *J. Phys. Conf. Ser.*, 425(032017), 2013.

[16] I. Kesgin, M. Kasa, Q. Hasse, Y. Ivanyushenkov, Y. Shiroyanagi, J. Fuerst, E. Barzi, D. Turrioni, A. V. Zlobin, and E. Gluskin. Development of short-period Nb_3Sn superconducting planar undulators. *IEEE T. Appl. Supercon.*, 29(5):1–4, 2019.

[17] M. Andra, R. Dinapoli, A. Bergamaschi, R. Barten, M. Bruckner, S. Chiriotti Alvarez, E. Frojdh, D. Greiffenberg, C-Lopez-Cuenca, D. Mezza, A. Mozzanica, S. Redford, C. Ruder, B. Schmitt, X. Shi, D. Thattil, G. Tinti, S. Vetter, and J. Zhang. Towards MYTHEN 3: Characterization of prototype chips. *Nucl. Instrum. Meth. A*, 936:383–385, 2019.

[18] R. P. Kurta, M. Altarelli, and I. A. Vartanyants. X-ray cross-correlation analysis of disordered ensembles of particles: Potentials and limitations. *Adv. Cond. Matter Phys.*, (959835), 2013.

Chapter 18

"Coherent small-angle x-ray scattering" cSAXS

A. Diaz, X. Donath, M. Guizar-Sicairos, and A. Menzel

In a nutshell

One of the characteristic features of new light sources such as SLS 2.0 is the increase of brilliance. To take optimal advantage of this property for high-resolution x-ray imaging and other coherence-based techniques, we propose a new beamline. Compared to the performance of today's cSAXS beamline, usable flux will increase by several orders of magnitude, allowing larger and more representative sample volumes and numbers to be characterized, imaging performance to increase, and coherence-based experiments to be conducted at higher photon energies, thereby reducing many samples' susceptibility to radiation damage.
While offering highly optimized conditions for a variety of experimental techniques, including ptychography and small-angle x-ray scattering with high spatial and/or temporal resolution, the beamline design shall also allow for flexible setups to account for techniques not yet foreseen and to facilitate future upgrades.

The main design tasks for cSAXS at SLS 2.0 can be summarized:

- To extract and deliver efficiently coherent flux to the experiment.
- To allow for cutting-edge microscopy and scattering studies while maintaining the faculty for unique and still-to-be-developed techniques.
- To allow for efficient change between experimental techniques.

Characteristic features include a modular optical setup that allows for almost all optics components to be easily replaced, a common beam path for both broad- and narrow-band illumination, and a massive 200 Megapixel detector that leverage PSI's state-of-the-art detectors for the most demanding experiments. This new instrument will allow PSI to remain at the forefront of high-resolution x-ray imaging for the materials and life sciences.

18.1 Overview

18.1.1 Mission

Structural investigations in the nano- to micrometer regime frequently require techniques that exploit both imaging and scattering characteristics. Often, such techniques amplify weak signals by measuring in parallel multiple copies of nominally identical samples or by imposing order constraints on the sample as in crystallography. An alternative approach exploits the illumination source's brightness, which gives rise to coherence, i.e., to statistical sparsity of the illumination, which allows for detailed and precise inferences about the sample.

In coherent diffraction imaging (CDI) for instance, coherent scattering patterns are used to computationally reconstruct 2D or 3D images [1], exceeding the resolving power of "classical" x-ray microscope techniques. Significant progress was made when measurement diversity could be brought to bear, most remarkably in "ptychography" [2]. cSAXS has been at the forefront of this technique's development [3–5] and application to the life [6] and materials sciences [7] including *in situ* sample manipulation [8], weak magnetic contrast [9–11], and sample dynamics [11].

Quantifying abundance, shape, orientation, etc. of nanoparticles, small-angle x-ray scattering (SAXS) can similarly be enhanced by coherent techniques, e.g., in x-ray photon correlation spectroscopy (XPCS) [12] or exploiting angular (cross-)correlations [13, 14].

An important figure of merit is "coherent flux," which can be defined as the number of photons in a single coherent mode. It is a measure of photon density in phase space, proportional to the intensity that can be confined simultaneously both in the terms of spatial extent and divergence. This gives rise to ever smaller sample sizes for spatially resolved (SAXS) [15], faster time-resolved measurements [16, 17], and small-angle scattering (SAS) tensor tomography [18, 19].

We intend to further expand our expertise in analytic techniques [20–22] and instrumentation [23–25] to offer unique imaging capabilities and increase measurement speed such that ptychographic imaging, for instance, becomes economically more approachable for proprietary use. Imaging activities at cSAXS will thus complement activities at TOMCAT, where one can access higher energies, dynamics, and throughput, microXAS with its focus on chemical imaging, and PolLux, SIM, and PHOENIX, all offering imaging at lower energies. For small-angle scattering, cSAXS will be similarly be complemented by PHOENIX at lower and MS at higher energies.

Most specifically, cSAXS shall remain the premier facility at SLS to make direct use of x-ray coherence properties in the energy range of $\sim 5\,\mathrm{keV}$ to $\sim 20\,\mathrm{keV}$ and beyond, which includes future additions to the supported techniques, such as Bragg coherent diffractive imaging (CDI) [26], Bragg ptychography [27], and correlation-based techniques [12–14], but also techniques that are yet to emerge.

18.1.2 Impact of SLS 2.0 and Conceptual Design

The increased brightness at SLS 2.0 allows us to extend the range of operation from a current "sweet spot" at 6.2 keV for coherence applications toward a range around 12.4 keV and beyond. This will make possible the imaging of larger samples and reduce radiation damage inflicted to the samples. For some experiments, a broad bandwidth option, will increase available flux by approx. 4 orders of magnitude. This will allow for even higher resolving power, it will render weak-contrast measurements,

e.g., on magnetic samples, more feasible, and will increase throughput of samples to a degree that ptychographic microscopy can contribute in statistically significant ways to demanding comparative studies [28, 29].

We aim to continue the dual strategy of offering both state-of-the-art instrumentation, e.g., dedicated to high-resolution microscopy and various forms of SAXS mapping, and the ability to conduct one-of-a-kind experiments, proofs of concept, and pre-characterisations for subsequent FEL experiments. In fact, the ability to test and perfect over time various measurement schemes and sample environments has proven crucial for the success of cSAXS.

Whereas coherence is directly related to source brightness, its preservation and usability for an experiment require beamline optics of high quality and high stability [30]: Static aberrations give rise to unwanted variations in the illumination, be it on the sample or as broadened point spread on the detector. Dynamic fluctuations and drifts in turn reduce the degree of coherence and increase sampling requirements in techniques such as ptychography [20] or x-ray photon correlation spectroscopy (XPCS) [12]. These demands are intimately coupled: The more inhomogeneous an intensity distribution, the more detrimental the effects of any instabilities and the more costly is any attempt to compensate for this. Accordingly, the beamline design pays particular attention to optics quality and stability.

18.1.3 Position/floorplan

cSAXS is located at the twelfth straight section of the SLS ring. The construction of an additional entrance to the SLS hall in this section close to columns $19-21$ offers the opportunity to extend cSAXS beyond the current experimental floor. Large distances of the sample from the source allow for large working distances of optics and offer more convenient opportunities to define beam properties, including bandwidth, spatial coherence, and divergence. Increasing the distance between sample and detector, in turn, facilitates sampling in reciprocal and real space [31] and thus helps to increase data acquisition speed and sample throughput. Additionally, the high intensities present in scattering patterns (e.g., close to the direct beam, but also in speckles or Bragg peaks) can be more easily measured accurately at large distances. Lastly, the ability to distribute the beam over a large area/volume of the sample helps to mitigate detrimental effects of the radiation.

The sample distance from the source will be limited to $\sim 40\,\mathrm{m}$ by the demand that it should remain reachable by the hall crane. This sample position is located on the high-stability experimental floor of the SLS, whereas the detector, which will be up to $\sim 12\,\mathrm{m}$ from the sample, will be the only equipment interacting with the x-ray beam that will be outside the experimental floor.

Figure 18.1 shows the approximate floorplan. The experimental hutch will exceed the current SLS building between columns 20 and 21. Still, thanks to the gained area of the entrance, people and equipment can move around the beamline.

For a later stage of beamline development, we plan to accommodate experiments on Bragg reflections. Besides a high-stability cradle to complement current setups, such as our current instruments for ptychographic microscopy: flOMNI [23], OMNY [24], and LaMNI [25], a robot arm shall be installed to position a small single-module detector at reasonably large distances of $2-3\,\mathrm{m}$ over an octant of a sphere.

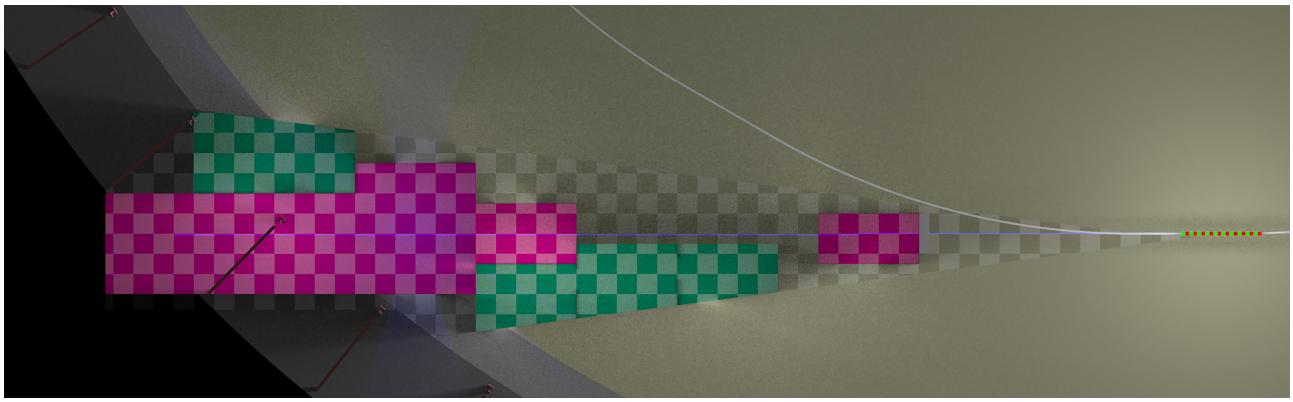

Figure 18.1: Approximate floorplan including the beamline extension beyond the experimental floor of SLS. The low-vibration experimental floor is marked in light grey. The color yellow indicates accessibility by the hall crane. Dark grey marks the present walkway. The beam position is marked by a blue line. Optics and experimental hutch are marked in red, user support rooms, lab space and working areas are marked in green. The square pattern marks meters.

From the beginning, beamline infrastructure, in particular the experimental hutch, shall be designed to allow for such later-stage extensions of the beamline’s portfolio.

18.2 Source

The beamline shall operate between $\sim 5\,\mathrm{keV}$ and $\sim 30\,\mathrm{keV}$ photon energy. A summary of source properties is provided in Table 18.1. The center of this range will allow for efficient use of ptychography and other coherent imaging techniques for samples in excess of $100\,\mu\mathrm{m}$ projected thickness. Lower energies remain attractive for thinner, less absorbing samples, whereas the high-energy range will be used primarily for SAXS etc. on extended dense samples, including metals, ceramics, and hard biological tissue.

Combined with the storage ring energy of 2.7 GeV, an undulator with 14 mm period will restrict the beamline’s low-energy limit to $\sim 5\,\mathrm{keV}$. Compared to today’s performance, however, total flux is about an order of magnitude higher (e.g. at 12.4 keV) and coherent flux increases by ca. two orders of magnitude (at the current “sweet spoot” at 6.2 keV), Figure 18.2.

As a future upgrade, in particular when ptychography and SAXS capabilities at PHOENIX will have

6.2 keV				12.4 keV				18.6 keV			
Σ_x	$12.47\,\mu\mathrm{m}$	$\Sigma_{x'}$	$35.50\,\mu\mathrm{rad}$	Σ_x	$12.38\,\mu\mathrm{m}$	$\Sigma_{x'}$	$48.94\,\mu\mathrm{rad}$	Σ_x	$12.34\,\mu\mathrm{m}$	$\Sigma_{x'}$	$59.42\,\mu\mathrm{rad}$
Σ_y	$3.13\,\mu\mathrm{m}$	$\Sigma_{y'}$	$7.64\,\mu\mathrm{rad}$	Σ_y	$2.72\,\mu\mathrm{m}$	$\Sigma_{y'}$	$13.18\,\mu\mathrm{rad}$	Σ_y	$2.57\,\mu\mathrm{m}$	$\Sigma_{y'}$	$19.13\,\mu\mathrm{rad}$

Table 18.1: Source size $\Sigma_{x,y}$ and divergence $\Sigma_{x',y'}$ (x horizontal, y vertical). Optical elements will increase the phase space volume mostly by increasing the size of the beam; the effective source size can be approximated by $\Sigma_j^{\mathrm{eff}} \sim \sqrt{\Sigma_j^2 + (2\sigma_{\mathrm{se}} d)^2}$, where σ_{se} represents a slope error of a mirror and d the distance from the source.

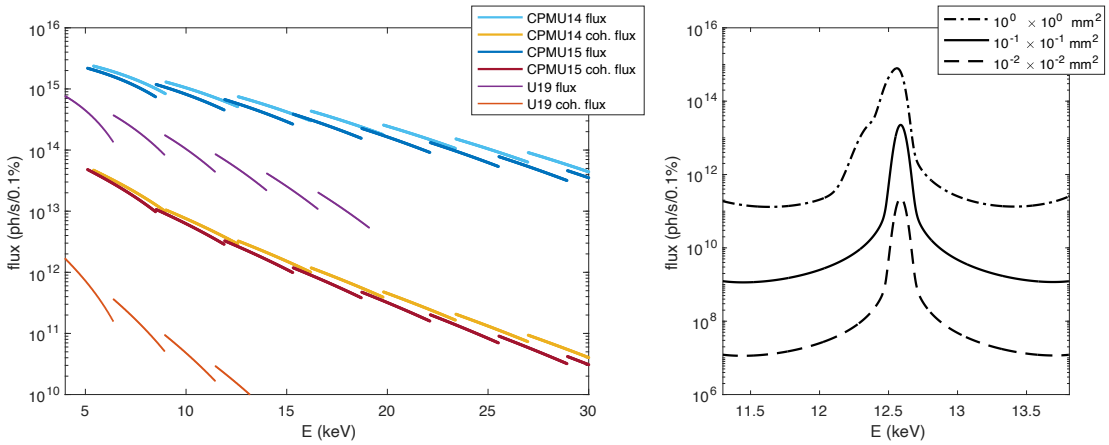

Figure 18.2: **Left:** Expected total and coherent flux of CPMU 14 and CPMU 15 at SLS 2.0. As reference, the performance of the current cSAXS insertion device, U19, at SLS is also shown, indicating the approximately 100-fold increase in coherent flux or the extension of energy range up to $\sim 20\,\text{keV}$, for which the same coherent flux is expected as currently at cSAXS's "sweet spot" at 6.2 keV. **Right:** Spectra on 7^{th}-harmonic peaks for various sizes of apertures $\sim 17\,\text{m}$ from the source. See Subsection 18.3.2.

been established, the accessible energy range at cSAXS may be further reduced in favor of increased flux at high energies by using an insertion device with even shorter period. Another upgrade option currently being discussed with the PSI Insertion Device Group, would be an additional, highly optimized insertion device with drastically suppressed low-energy and broadband contributions. Such advancements should require only minimal changes along the beamline. To this end, beamline optics shall be designed, wherever possible, to be flexible with regard to the exact source point along the beamline axis.

18.3 Beam delivery

We propose a beamline design with fixed exit for both broadband and narrow-band illumination. Particular importance shall be put on the stability of all optical elements. This demand leads us to favor, as detailed in the following, a horizontally shifting broadband monochromator, channelcuts for the narrow-band monochromator, and diffractive and refractive optics for variable focusing. We are investigating and developing compact means of wavefront sensing in order to characterize potential aberrations and quantify coherence without the need for any specific setup in the experimental hutch.

A high degree of modularity shall allow in the long term for beamline components to be replaced after degradation due to usage or for purposes of future upgrades. Table 18.2 provides an overview of the foreseen elements and their distribution along the beamline.

front end $0 - 15\,\mathrm{m}$	OP1 $15 - 20\,\mathrm{m}$	OP2 $32 - 37\,\mathrm{m}$	close to the sample $40\,\mathrm{m}$
• basic beam conditioning • removal of off-axis radiation • slits	• beam position monitor • DMLM • attenuators • first focusing unit • corrective optics • wavefront sensor • slits	• beam position monitor • DCCM • attenuators • second focusing unit • corrective optics • wavefront sensor • slits	• beam position monitor • final beam conditioning and focusing • fast shutter • slits

Table 18.2: Summary of optical elements and their location. The double-multilayer monochromator (DMLM) and double-channelcut monochromator (DCCM) are discussed in Section 18.3.2, the focusing strategy in Section 18.3.3, and beam metrology in Section 18.3.5.

18.3.1 Front end

The main task of front end components at cSAXS is the removal of unwanted off-axis synchrotron radiation from the desired "coherent" contribution, which is narrow band and rather compact. The maximal expected divergence will not exceed $76\,\mu\mathrm{rad} \times 31\,\mu\mathrm{rad}$ (h × v), sufficient for extraction of up to 30 keV radiation. Since these demands are similar to other hard-x-ray beamlines at SLS and do not require dedicated hardware development, the front end for the cSAXS beamline should be of a standard windowless design.

18.3.2 Monochromators

Experience at cSAXS has shown that many experiments do not require the narrow bandwidth defined by its double-Si(111)-crystal monochromator. A broadband option is therefore envisioned, not only for time-resolved experiments [16, 17] but also for many ptychographic-imaging activities, for which suitable bandwidth-related correction techniques have been developed [20,32,33]. The design therefore foresees both narrow-band and broadband options at the same beam position.

The double-multilayer monochromator, which extracts a single undulator harmonic, will be horizontal, and the narrow-band illumination will be provided by a removable double-channelcut monochromator, making use of the inherent stability offered by channelcuts and the already reduced heatload. This monochromatization strategy (Figure 18.3) shares many similarities with Ref. [34] with the main difference that instead of total-reflection mirrors, a multilayer monochromator will be used to extract only a single undulator harmonic.

Broadband monochromator

The insertion device CPMU 14 will feature $N = 212$ periods and a fundamental at $\sim 1.8\,\mathrm{keV}$. Extracted will be odd-numbered harmonics of order $n \geq 3$. We can thus expect on-axis a bandwidth of $\frac{\Delta E}{E} < 1\,\%$, broadened mostly on the low-energy side as a function of chosen aperture. Slits in OP1, i.e. approx. 17 m from the source can be used to efficiently choose a bandwidth that is sufficiently narrow for small-angle scattering experiments and advantageous even for some coherent diffractive imaging

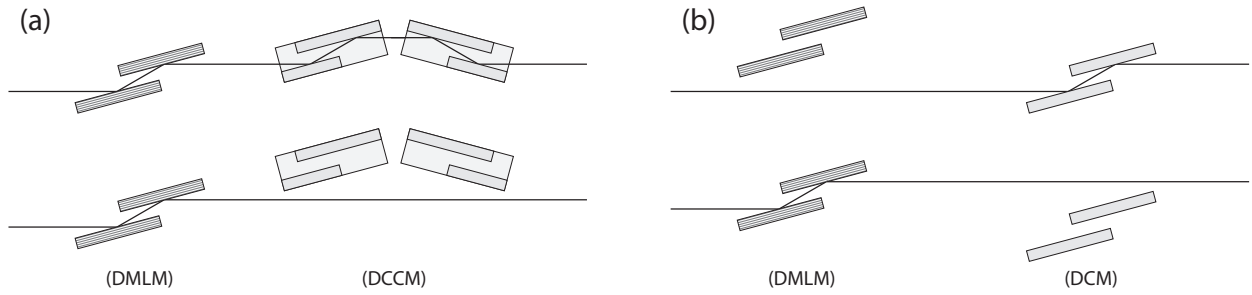

Figure 18.3: **(a)** Schematics of the desired monochromator arrangement, of a double multilayer monochromator (DMLM) and a double channelcut monochromator (DCCM). Here, the DMLM is constantly in the beam while the DCCM is removable to switch between narrow-band (top) and broadband illumination (bottom). Note that the DMLM is envisioned to provide a horizontal shift, whereas the DCCM scatters vertically. **(b)** Backup option, in case no multilayer monochromator of sufficient quality and reliability is available in time: Either double-multilayer or double-crystal monochromator (DCM) will be employed.

applications. Table 18.3 summarizes estimates based on the calculations [35] shown in Figure 18.2.

A fixed-exit double-multilayer monochromator shall be used to extract a single harmonic of the undulator spectrum. It will further help in reducing the heatload on the subsequent narrow-band monochromator. Of major concern, of course, are effects of figure errors and roughness on the wavefront in case of a device permanently in the beam [36]. However, such devices have been successfully deployed elsewhere [37, 38], and some constant wavefront distortions can be corrected for [39].

Narrow-band monochromator

The narrow-band monochromator shall consist of a pair of plasma-chemical-vaporization-machined (PCVM) channelcut crystals. This treatment has been shown to result in close to damage-free optics for optimal wavefront preservation [34, 40]. A (+,–,–,+) geometry [Figure 18.3(a)] has been shown to be highly stable and does not alter the beam position.

Aperture	FWHM	Integ. flux
$0.01 \times 0.01\,\mathrm{mm}^2$	0.6%	$1.7 \times 10^{13}\,\mathrm{ph/s}$
$0.1 \times 0.1\,\mathrm{mm}^2$	0.6%	$1.7 \times 10^{15}\,\mathrm{ph/s}$
$1 \times 1\,\mathrm{mm}^2$	0.9%	$9.2 \times 10^{16}\,\mathrm{ph/s}$

Table 18.3: Variation of beam spectrum as a function of an aperture $\sim 17\,\mathrm{m}$ from the source by example of the 7^{th} harmonic at a photon energy of 12.56 keV. Below $\sim 0.1 \times 0.1\,\mathrm{mm}^2$ the spectrum barely changes but flux simply scales with aperture area. Larger apertures start to increase the bandwidth.

	OP1	OP2	sample	detector	
Application	$15 - 20\,\mathrm{m}$	$32 - 37\,\mathrm{m}$	$40\,\mathrm{m}$	$52\,\mathrm{m}$	Comments
high-res. SAXS	$\lesssim 900 \times 250\,\mu\mathrm{m}^2$		$\sim 400 \times 170\,\mu\mathrm{m}^2$	$26 \times 10\,\mu\mathrm{m}^2$	sufficient for
(@ 12.4 keV)	$f \sim 11.6\,\mathrm{m}$			$\lesssim 39 \times 16\,\mu\mathrm{rad}^2$	$q_{\mathrm{min}} \sim 10^{-4}\,\mathrm{Å}^{-1}$
scanning SAXS	$\lesssim 1200 \times 450\,\mu\mathrm{m}^2$		$16 \times 3\,\mu\mathrm{m}^2$	$\sim 280 \times 100\,\mu\mathrm{m}^2$	sufficient for
(@ 24.8 keV)	$f \sim 9.8\,\mathrm{m}$		$\lesssim 53 \times 20\,\mu\mathrm{rad}^2$		$q_{\mathrm{min}} \sim 2 \times 10^{-3}\,\mathrm{Å}^{-1}$
secondary source	$\lesssim 1.4 \times 0.6\,\mathrm{mm}^2$	$\lesssim 13 \times 3\,\mu\mathrm{m}^2$	$\lesssim 185\,\mu\mathrm{m}$		
($\sim 1:1$)	$f \sim 8.6\,\mathrm{m}$	$\lesssim 78 \times 32\,\mu\mathrm{rad}^2$			

Table 18.4: Overview of focusing options using the focusing unit in the optical hutch OP1. The beam size on the focusing optics for the specified application and the focal length is shown. Highlighted in grey is the location onto which the source is imaged. Focusing onto a plane in the second optics hutch OP2 is used to define a secondary source. The parameters given for this case hold for all energies. The beam size given at the sample position in this case reflects the maximum size of further optical elements that can be fully illuminated. With the exception of the “comments,” where rather conservative safety margins have been applied, these numbers do not take into account figure errors in reflecting surfaces or lens aberrations.

Si(111) and Si(333) reflections can be used in a single pair of channelcuts and are suitable to cover the entire energy range.

In case we do not have sufficient confidence in the available multilayer monochromators when the technical design is finalized, we will consider as fallback option a beamline layout with double-multilayer monochromator and double-crystal monochromator in a row. The design task of a fixed exit for both broad- and narrow-band beam will be hard to realize under these circumstances, however, precluding easy changes in techniques such as ptychographic tomography, which require the most careful alignment of optics, sample, rotation axis, and detector axes.

Both options are schematically shown in Figure 18.3.

18.3.3 Focusing

Table 18.4 summarizes various applications for a focusing unit in the first optical hutch OP1. They include focusing onto the detector, onto the sample, and onto a slit system in the second optical hutch OP2. Such a secondary source can be used for coherence filtering and further demagnification onto the sample.

Currently, we foresee a combination of diffractive and refractive optics for focusing. Efficiencies of approximately 50 % seem feasible over the energy range of the beamline. Such focusing elements are highly reproducible, are easily exchanged if necessary, and their aberrations can be well characterized and corrected for [39]. Since such focusing elements are highly chromatic, they may also be employed to suppress undulator harmonics that may not be fully removed by the monochromators.

Additionally, the suitability of reflective optics as an alternative approach is being evaluated. For all focusing elements being considered, the scattering background will be evaluated, not least by polling similar beamlines at ALS, APS, Max IV, NSLS-II, Petra-III, Spring-8, etc.

Both OP2 and the experimental station ES1 will host further focusing optics to demagnify the

(secondary) source. In some instances, such as flOMNI etc., they are incorporated in dedicated instruments. For other applications, large working distances are beneficial, for instance in order to reduce the spot size on the sample without increasing beam divergence or when, as for SAXS applications, slits have to be employed between the last beam-defining optical element and the sample.

In general, both modularity and the compatibility with/for future upgrades will inform the choice of diffractive, refractive and reflective optics as well as their location.

18.3.4 Coherence filtering

As indicated in Figure 18.2, at the energies relevant for cSAXS, SLS 2.0 is still a rather incoherent source and slits will have to be used to increase spatial coherence. Slits, as close to the source point as feasible, have been found advantageous for such "coherence filtering," i.e. the lossy decrease of source size, and will be used in case of an unfocused beam.

However, the proposed combination of focusing optics, close to which slits are employed, in OP1 and a "secondary source" in OP2, also defined by slits, offers the ability to increase coherence independent of the divergence of the beam. Thus, the illumination of downstream optics, for instance, can be tailored independently of the chosen degree of coherence.

As any beam-defining element, slits are required to satisfy stringent stability requirements, wherever possible their positions should be readable using encoders, and the resultant beam subjected to detailed characterization.

18.3.5 Beam characterization

Pointing stability requirements for coherent diffractive imaging in the forward direction or small-angle scattering scales with the ratio of detector pixel size to source-to-detector distance. Since for many other diffraction-based techniques the relevant ratio is rather the pixel size to the sample-to-detector distance, pointing stability requirements are here $\gtrsim 20$ times more stringent. Consequently, beam position and direction shall be monitored using real-time information from electron-beam diagnostics, incorporating encoder feedback from any beam-defining aperture and using x-ray beam position monitors in the front end, at the double-multilayer monochromator (OP1), at the double-channelcut monochromator (OP2), and close to the sample position (ES). This multitude of diagnostic tools will not only facilitate the commissioning and alignment of x-ray optical elements, but shall also enable fast determination of stability- or coherence-limiting factors during operation. To this end, beam position and intensity monitoring shall be conducted with at least the foreseen rate of pixel detector readout, i.e., 2 kHz.

As important as monitoring beam intensity and position is the ability to reliably quantify coherence properties of the beam and compare it with established values. With this in mind, dedicated modules shall be installed in both optics hutches that are easily inserted into the beam for baseline measurements. Techniques may include Shack-Hartmann sensors [41], Talbot interferometry [42, 43] and other interference-based techniques [44, 45], and/or near-field speckle metrology [46]. High-frequency fluctuation measurements shall be conducted by measuring speckle fluctuations and form a part of the coherence measurements that can take place even during the experiment.

18.4 Endstation

Next to relatively small setups, e.g., for scanning SAXS, SAXS from microfluidic devices etc., and SAS tensor tomography, several highly specialized systems will be used at cSAXS, such as flOMNI [23], OMNY [24] and LaMNI [25]. In order to host such a variety of devices, a large fraction of the infrastructure at the sample position shall be removable and exchangeable.

A number of "standard" experiments uses a mineral cast table of $1.1 \times 1.1\,\mathrm{m}^2$ 550 mm underneath the x-ray beam. It is situated on a girder with five degrees of freedom (i.e. all three angles and two translations, perpendicular to the beam). This table can be removed and exchanged, for instance, with OMNY. This arrangement has proven quite successful and shall be maintained, and only two changes from the current state are foreseen: Firstly, the range of the girder mover needs to be increased to a few centimeters. And secondly, it will be advantageous if even heavy equipment, such as the table (weight: $\sim 2\,\mathrm{t}$) and OMNY ($\sim 4\,\mathrm{t}$), could be moved without the need of the SLS crane. The option of air cushion carriers, as have been used for SwissFEL undulators, shall be foreseen. The same technology should be used to move the detector and flight tube.

An evacuated flight tube is used to prevent unwanted scattering and absorption between the sample and the detector. It will contain the in-vacuum detector(s) as well as an array of beamstops equipped with beam intensity — and possibly even beam position — monitors. Since we foresee a sample-to-detector distance of 12 m, this will be a long and heavy device that ought to be movable with six degrees of freedom, once positioned approximately to its in-experiment position. In the rare instances where the flight tube will not be in use, it needs to be parked inside the experimental hutch, and a place toward the outside wall is reserved for this purpose.

While it would be advantageous if the experimental hutch were not partially obstructed by any columns, both beamline operation with a flight tube and with the flight tube in a parking position are compatible with both parts of Column 20 remaining: The flight tube at either position fits underneath the angle spanned by the load-bearing and support column 20, as shown in Figure 18.4. The beam would pass ca. 60 cm from the center of the load-bearing column.

Space shall be reserved for a future upgrade for coherent imaging on Bragg peaks. Whereas the sample orientation shall be established by a dedicated cradle to be located on the girder/table, a detector needs to be movable over approximately an spherical octant of at least 2 m radius. The height of the experimental hutch, limited by the hall crane, will set the upper bound. This detector shall be mounted on a robotic arm on the inside side of the beam, i.e., toward the synchrotron ring. This detector, suitable also for SAXS, XPCS etc. and located high above the sample, can then also be used for demanding rheology experiments that require a vertical beam.

cSAXS has profited from its air conditioning unit being spatially separated from the experimental and optical hutches. This should be maintained, albeit scaled for the increased hutch volume. Furthermore, ventilation requirements for experiments involving gases or cryogenics should be readily met, and the hutch shall be equipped with the necessary laser safety features for experiments involving class 4 lasers.

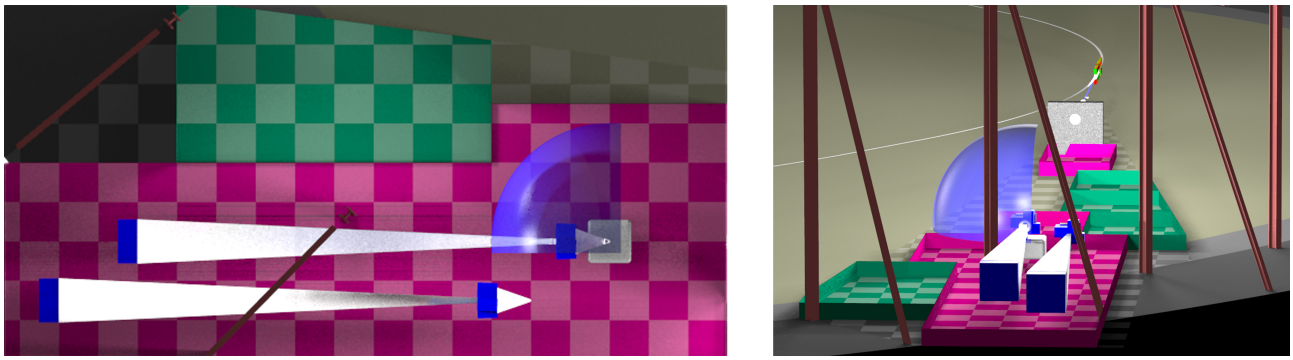

Figure 18.4: **Left:** The experimental hutch with two positions for the flight tube/detector system: one for experiments, the other one as parking position when the flight tube is not in use. Indicated in blue is a 3 m octant to be reachable in future experiments on Bragg peaks. **Right:** The beamline as seen from downstream, illustrating the SLS column structure. Beamline equipment can reasonably fit underneath the angle spanned by the main and supporting columns, which are visible also in the top view as brown H's and lines, respectively

18.5 Detectors

18.5.1 Small-angle x-ray scattering detector

As primary detector, we plan to construct and install a 200 Megapixel in-vacuum detector. It shall be likely based on the charge-integrating Jungfrau detector, possibly on a photon-counting Eiger-II detector, both of which feature 75 μm pixels [47] and sustained readout rates of up to 2 kHz, Table 18.5. Such a large detector removes the need to be moved along the beam. It can serve simultaneously high resolution tasks resolving 5 nm at 1 Å wavelength and sample accurately over 8 μm illumination at that wavelength. Large illumination footprints on the sample are beneficial for reducing radiation effects, not only in imaging applications but also in the case of SAXS, where the beam can easily locally change the temperature and/or chemistry; or XPCS, where it can alter the very dynamics to be studied.

This detector has to be equipped with on-board "intelligence" to make manageable the massive data flow through data mining and compression. While the choice of detector is guided by three demands, i.e., small pixels, large area, and rapid readout, rarely if ever will all these three demands be satisfied simultaneously, as illustrated in Table 18.6.

18.5.2 Wide-angle x-ray scattering detector

The SAXS detector will be complemented by a wide-angle x-ray scattering (WAXS) detector located around the SAXS "cone." The basic geometry is illustrated in Figure 18.5. The detector shall cover at least up to 2 Å^{-1} at 12.4 keV for the entire azimuth such that it can be used for scanning WAXS measurements. For normalization on the water peak and measurements of the local sample temperature, access to 3 Å^{-1} at 12.4 keV is required in at least one direction. Angular overlap between SAXS and WAXS detectors can be achieved by tilting the flight tube/detector setup slightly away from the beam.

For most applications, including both scattering and imaging experiments, small pixels will be

	Jungfrau	Eiger-II	MOENCH
Detection mode	Integrating possibly switchable to counting	Photon counting	Integrating
Pixel size	75 μm	75 μm	25 μm sub-pixel resolution possible
Max. count rate	$>$ 100 MHz	$\gg$ 1 MHz	t.b.d.
Readiness	in use at SwissFEL limited expertise at synchrotrons	upgrade from existing EIGER	the most unknown of the three

Table 18.5: An overview of available detector technologies at PSI. Considering the foreseeable gain in flux, the charge-integrating Jungfrau detector is most likely central to the SAXS detector suite. Its usage at synchrotrons needs to be established and fast and efficient data reduction schemes need to be developed. Similarly, the performance of Eiger-II and MOENCH will have to be determined in order to inform a final decision.

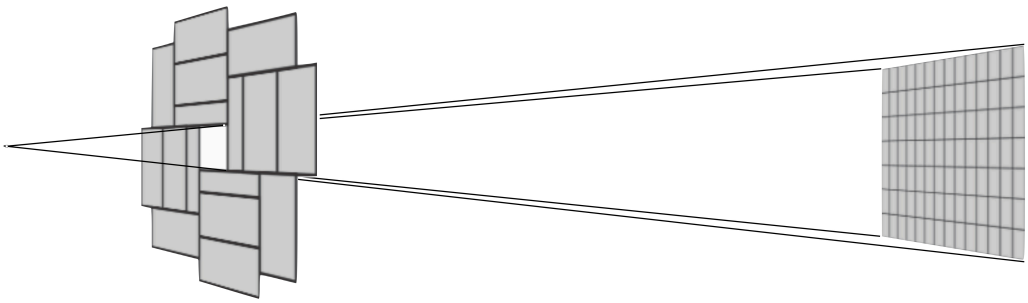

Figure 18.5: A sketch of the SAXS/WAXS detector geometry. For clarity, the displayed number of detector modules is smaller by a factor of 4 than necessary for the 200M detector, which comprised 28×14 modules.

useful. We therefore consider the MOENCH technology for the WAXS detector. It has a physical pixel size of 25 μm [47] but can, when sparsely illuminated, interpolate toward even smaller pixels [48].

18.5.3 Fluorescence detectors

Increasingly, imaging activities at cSAXS are accompanied by fluorescence mapping. Since sample environments or variable instrumentation often occlude access, a fluorescence detector cannot be permanently installed. Energy-resolving detectors capable of high count rates are therefore to be installed on a case-by-case basis or will be part of instrumentation modules, such as OMNY.

18.5.4 Support infrastructure

Directly adjacent to the beamline will be three user rooms (Figure 18.1). Listing them in direction of x-ray beam propagation: A "lounge," in which users can take breaks and eat or drink without removing

themselves entirely from the experiment, analysis, discussion, etc. The control room, from where the experiment is typically controlled and supervised and where data analysis can be initiated. The experimental hutch shall be reachable through a laboratory room, for last-minute sample preparation, purification, etc. It will allow for work with cryogenic liquids, basic wet chemistry with acids and bases, and biosafety level 1.

Additional to these rooms which are accessible to users, a workshop/laboratory reserved for beamline staff is foreseen for maintenance and storage of sensitive equipment.

18.6 IT requirements

Information technology forms an integral component of any modern beamline. Ptychography is very demanding in terms of computing power. These demands will increase when advanced analysis techniques (such as multi-mode [20], orthogonal probe relaxation [21], multi-slice [49], non-rigid registration [50] etc.) are employed, as increasingly necessary when data acquisition conditions become less ideal, e.g. through partial coherence, exceeding the depth of field, misalignment, on-the-fly scans, or sample dynamics due to radiation damage. Simultaneously, data volume is expected to increase towards teravoxel tomograms, for instance.

It seems rather clear that current analysis methods will not scale sufficiently. Alternative analysis schemes are being investigated, including analytic low-resolution solutions as good initial guesses to the computationally expensive iterative algorithms and machine learning, where the burden is shifted to a "training" period but which can be highly efficient afterwards.

At the present stage it seems impossible to predict where the compromises between experimental requirements and computational resources will be. What seems clear, though, is that computational resources should be sufficient to provide some sort of feedback to the user within seconds in order for ptychography to be accepted as "normal" microscopy technique. We are investigating whether and to what extent the Swiss National Supercomputing Center (CSCS) can be utilized to this task. The outcome of this study, called SELVEDAS, will inform the strategic decision how computing resources are to be allocated amongst beamlines, a centralized shared facility at PSI, and CSCS.

18.7 Timeline

The proposed beamline is a complete redesign of cSAXS. While single elements can be reused, some others that define the beam position and direction cannot. This leads us to believe that it will be rather impractical to move from the current beamline to the new beamline without significant interruption of availability to users. Ideally, this period should coincide with the dark period due to the machine upgrade, 2023–2024.

A decision is therefore sought in 2020 whether, for "first light" at cSAXS @ SLS 2.0, which is planned for early 2025, the present-day cSAXS shall be moved to the slightly shifted source point or if the beamline shall be decommissioned 2023 and replaced by a new instrument, as proposed herein. In the first case, one would either be willing to incur two extended dark periods within a few years or postpone, forego completely, or reduce the upgrade in such a way that it is achievable with only short

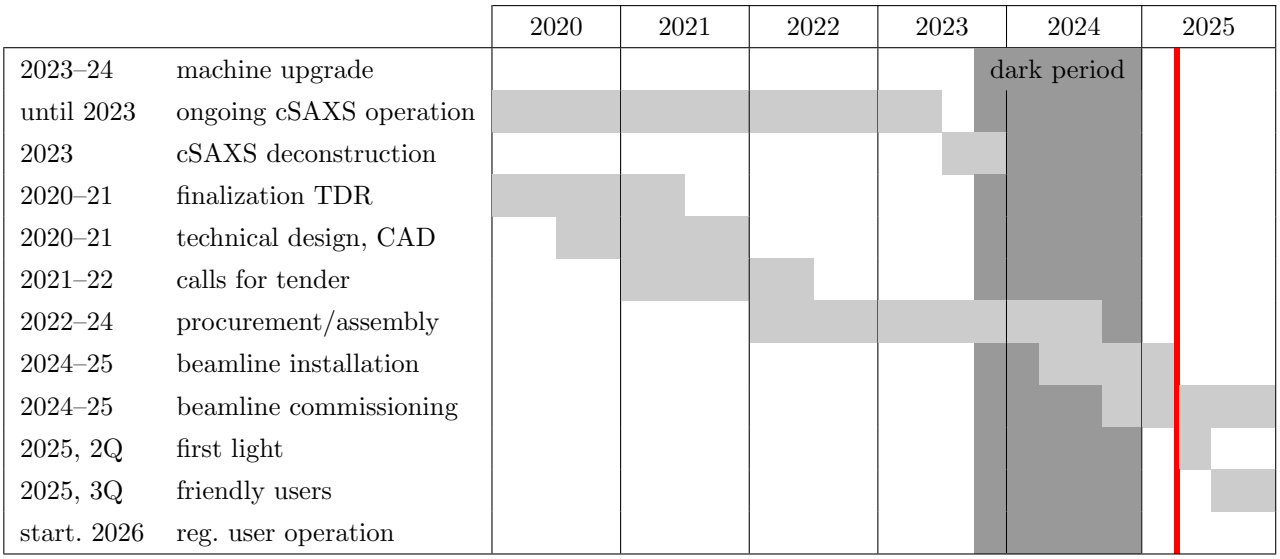

Figure 18.6: Timeline for further planning, design, construction, and commissioning of cSAXS at SLS 2.0. We expect an interruption of two and a half years of regular user operation (two years for friendly “expert” users).

interruptions of service. For the case of a new beamline, as proposed here, about five years remain to accomplish

- finalization of planning and technical design,
- fabrication, procurement, and assembly of components,
- commissioning without and with x-rays, and
- start-up of user operation.

A rough timeline is shown in Figure 18.6, assuming sufficient availability of support personnel, craftspeople, etc.

18.7.1 Preparatory work

In 2020 the design phase will continue and shall become increasingly precise. For detailed technical drawings, we are considering hiring an extra engineer on a project basis. Their task would be to support the technical design phase and/or support the beamline technician in preparing for moving the current instrument, should this indeed be necessary.

Several small items that need to be designed, assembled and commissioned lend themselves to be addressed early through independent funding. One example is the optical layout, including detailed specifications of the focusing optics. Refractive optics could then be ordered and financed via R’Equip or related means. Diffractive optics will likely be produced locally at PSI. Wavefront sensing modules shall be developed, constructed, and commissioned in the format of a scientific research-&-development project. Funding through SNF project funds will be sought.

Loose contact with potential suppliers of (PCVM) channel-cuts in Japan has been initiated. Manufacturers of multilayers will be contacted over the course of 2020. In general, detailed discussions

with beamline scientists at ALS, APS, Max IV, NSLS-II, Petra-III, and Spring-8 are ongoing to profit from practical experiences gained with technologies and methods that are, thus far, rarely used at PSI, if at all.

IT demands are constantly growing. In fact, it can be argued that we are already IT-limited in performance at cSAXS, for scan parameters such as speed are frequently adapted such that "online" processing (i.e. processing for immediate feedback) can keep up with data acquisition. This results in continuous upgrades, be it by increasing infrastructure quantitatively (i.e. more, faster CPUs for instance) or qualitatively (such as the recent adaptation of GPUs into normal processing pipelines). Here we profit from a long-standing and close collaboration with PSI's Scientific Computing Group. Most recently, we got involved collaboratively in the SELVEDAS project with the aim to develop means to use the Swiss National Supercomputing Center CSCS for online ptychography reconstruction. Of particular interest is the feasibility of a strict limitation on latency, such that the data can be transferred to CSCS, processed and returned to PSI in time to provide feedback to ongoing experiments. The outcome of this project will inform strategic decisions how much and what type of computing infrastructure is required to be located at PSI and how much can be outsourced to CSCS.

18.7.2 Interruption and resumption of service

In order to gain space for construction and assembly, we propose to decommission cSAXS after the first semester of 2023, i.e., three months prior to the dark period as defined by the machine shutdown. Removing the current hutches will remove obstacles for the transfer of material from and into the SLS through the new entrance, which will be located exactly opposite the beamline. The gained space shall also be used to assemble beamline components when possible. However, installation of the experimental hutch will have to wait for the construction entrance to be cleared, which is why first light at cSAXS is not expected directly after conclusion of the machine "dark period."

After an interruption of two years in the second semester of 2025, user operation is planned to resume for friendly "expert" users, who volunteer their experiments to be used as early test cases for ongoing commissioning and/or who are willing to work with not fully commissioned equipment and software. Regular user operation shall proceed beginning 2026.

18.8 Concluding remarks

We described in this document a beamline which shall replace the current cSAXS beamline and which shall allow highly optimized conditions for coherence-based techniques in the hard x-ray range from $\sim 6\,\mathrm{keV}$ to $\sim 30\,\mathrm{keV}$ photon energy. Its most characteristic features are stable, yet flexible beam delivery optics and a 200 Megapixel detector, which will allow highly efficient sampling while mitigating some of the adverse effects of the high flux density. The beamline design is modular, such that it is able to accommodate future upgrade needs, both with regard to the x-ray optical setup and to the infrastructure in the experimental hutch. However, we do not see a "smooth transition" between the current and the future instrument: The former has to be disassembled to make room for the latter.

The instrument as described here will allow researchers at PSI to further build on and develop their leading expertise in various forms of ptychographic imaging and on novel high-brilliance applications

of SAXS. Both Swiss and international researchers will be thereby offered uniquely suitable conditions for the most demanding imaging and scattering measurements.

Application	Small pixels	Large area	Rapid readout
Ptychography	• facilitating sampling in q-space • reducing the number of scan positions	• high spatial resolution (even if frequently limited by other factors than detector size)	• reducing detector overhead • many low-SNR measurements often preferable to few high-SNR measurements
SAXS	• extending the length scale	• high spatial resolution	• extending time resolution • allowing high-rep.-rate experiments

Table 18.6: Importance of detector geometry and readout rate for two representatives for the main activities at cSAXS. Advantages of rapid readout affect any scanning microscopy technique, i.e., hold equally for scanning SAXS etc. and ptychography.

Bibliography

[1] J. Miao, T. Ishikawa, I. K. Robinson, and M. M. Murnane. Beyond crystallography: Diffractive imaging using coherent x-ray light sources. *Science*, 348(6234):530–535, 2015.

[2] F. Pfeiffer. X-ray ptychography. *Nat. Photonics*, 12(1):9–17, 2018.

[3] J. M. Rodenburg, A. C. Hurst, A. G. Cullis, B. R. Dobson, F. Pfeiffer, O. Bunk, C. David, K. Jefimovs, and I. Johnson. Hard-x-ray lensless imaging of extended objects. *Phys. Rev. Lett.*, 98(3), 2007.

[4] P. Thibault, M. Dierolf, A. Menzel, O. Bunk, C. David, and F. Pfeiffer. High-resolution scanning x-ray diffraction microscopy. *Science*, 321(5887):379–382, 2008.

[5] M. Dierolf, A. Menzel, P. Thibault, P. Schneider, C. M Kewish, R. Wepf, O. Bunk, and F. Pfeiffer. Ptychographic x-ray computed tomography at the nanoscale. *Nature*, 467(7314):436–439, 2010.

[6] S. H. Shahmoradian, E. H. R. Tsai, A. Diaz, M. Guizar-Sicairos, J. Raabe, L. Spycher, M. Britschgi, A. Ruf, H. Stahlberg, and M. Holler. Three-dimensional imaging of biological tissue by cryo x-ray ptychography. *Sci. Rep.*, 7(1):6291, 2017.

[7] M. Holler, M. Guizar-Sicairos, E. H. R. Tsai, R. Dinapoli, E. Müller, O. Bunk, J. Raabe, and G. Aeppli. High-resolution non-destructive three-dimensional imaging of integrated circuits. *Nature*, 543(7645):402–406, 2017.

[8] M. Esmaeili, J. B. Fløystad, A. Diaz, K. Høydalsvik, M. Guizar-Sicairos, J. W. Andreasen, and D. W. Breiby. Ptychographic x-ray tomography of silk fiber hydration. *Macromolecules*, 46(2):434–439, 2013.

[9] C. Donnelly, V. Scagnoli, M. Guizar-Sicairos, M. Holler, F. Wilhelm, F. Guillou, A. Rogalev, C. Detlefs, A. Menzel, J. Raabe, and L. J. Heyderman. High-resolution hard x-ray magnetic imaging with dichroic ptychography. *Phys. Rev. B*, 94(6):064421, 2016.

[10] C. Donnelly, M. Guizar-Sicairos, V. Scagnoli, S. Gliga, M. Holler, J. Raabe, and L. J. Heyderman. Three-dimensional magnetization structures revealed with x-ray vector nanotomography. *Nature*, 547(7663):328–331, 2017.

[11] C. Donnelly, K. L. Metlov, V. Scagnoli, M. Guizar-Sicairos, M. Holler, N. S. Bingham, J. Raabe, L. J. Heyderman, N. R. Cooper, and S. Gliga. Experimental observation of vortex rings in a bulk magnet. *Nat. Phys.*, pages 1–6, 2020.

[12] O. G. Shpyrko. X-ray photon correlation spectroscopy. *J. Synchrotron Radiat.*, 21(5):1057–1064, 2014.

[13] P. Wochner, C. Gutt, T. Autenrieth, T. Demmer, V. Bugaev, A. Díaz Ortiz, A. Duri, F. Zontone, G. Grübel, and H. Dosch. X-ray cross correlation analysis uncovers hidden local symmetries in disordered matter. *Proc. Natl. Acad. Sci. U.S.A.*, 106(28):11511–11514, 2009.

[14] I. A. Zaluzhnyy, R. P. Kurta, M. Scheele, F. Schreiber, B. I. Ostrovskii, and I. A. Vartanyants. Angular x-ray cross-correlation analysis (AXCCA): Basic concepts and recent applications to soft matter and nanomaterials. *Materials*, 12(21):3464, 2019.

[15] O. Bunk, M. Bech, T. H. Jensen, R. Feidenhans'l, T. Binderup, A. Menzel, and F. Pfeiffer. Multimodal x-ray scatter imaging. *New J. Phys.*, 11(12):123016, 2009.

[16] S. Westenhoff, E. Malmerberg, D. Arnlund, L. C. Johansson, E. Nazarenko, M. Cammarata, J. Davidsson, V. Chaptal, J. Abramson, G. Katona, A. Menzel, and R. Neutze. Rapid readout detector captures protein time-resolved WAXS. *Nat. Methods*, 7(10):775–776, 2010.

[17] S. Ibrahimkutty, P. Wagener, T. dos Santos Rolo, D. Karpov, A. Menzel, T. Baumbach, S. Barcikowski, and A. Plech. A hierarchical view on material formation during pulsed-laser synthesis of nanoparticles in liquid. *Sci. Rep.*, 5:16313, 2015.

[18] M. Liebi, M. Georgiadis, A. Menzel, P. Schneider, J. Kohlbrecher, O. Bunk, and M. Guizar-Sicairos. Nanostructure surveys of macroscopic specimens by small-angle scattering tensor tomography. *Nature*, 527(7578):349–352, 2015.

[19] F. Schaff, M. Bech, P. Zaslansky, C. Jud, M. Liebi, M. Guizar-Sicairos, and F. Pfeiffer. Six-dimensional real and reciprocal space small-angle X-ray scattering tomography. *Nature*, 527(7578):353–356, 2015.

[20] P. Thibault and A. Menzel. Reconstructing state mixtures from diffraction measurements. *Nature*, 494(7435):68–71, 2013.

[21] M. Odstrčil, P. Baksh, S. A. Boden, R. Card, J. E. Chad, J. G. Frey, and W. S. Brocklesby. Ptychographic coherent diffractive imaging with orthogonal probe relaxation. *Opt. Express*, 24(8):8360–8369, 2016.

[22] K. Wakonig, H.-C. Stadler, M. Odstrčil, E. H. R. Tsai, A. Diaz, M. Holler, I. Usov, J. Raabe, A. Menzel, and M. Guizar-Sicairos. PtychoShelves, a versatile highlevel framework for highperformance analysis of ptychographic data. *J. Appl. Crystallogr.*, 53(2):574–586, 2020.

[23] M. Holler, A. Diaz, M. Guizar-Sicairos, P. Karvinen, E. Farm, E. Härkönen, M. Ritala, A. Menzel, J. Raabe, and O. Bunk. X-ray ptychographic computed tomography at 16 nm isotropic 3D resolution. *Sci. Rep.*, 4:3857, 2014.

[24] M. Holler, J. Raabe, A. Diaz, M. Guizar-Sicairos, R. Wepf, M. Odstrčil, F. R. Shaik, V. Panneels, A. Menzel, B. Sarafimov, S. Maag, X. Wang, V. Thominet, H. Walther, T. Lachat, M. Vitins, and O. Bunk. OMNY - A tOMography Nano crYo stage. *Rev. Sci. Instrum.*, 89(4):043706, 2018.

[25] M. Holler, M. Odstrčil, M. Guizar-Sicairos, M. Lebugle, E. Müller, S. Finizio, G. Tinti, C. David, J. Zusman, W. Unglaub, O. Bunk, J. Raabe, A. F. J. Levi, and G. Aeppli. Three-dimensional imaging of integrated circuits with macro- to nanoscale zoom. *Nat. Electron.*, 2(10):464–470, 2019.

[26] I. K. Robinson and R. Harder. Coherent x-ray diffraction imaging of strain at the nanoscale. *Nat. Mater.*, 8(4):291–298, 2009.

[27] S. O. Hruszkewycz, M. Allain, M. V. Holt, C. E. Murray, J. R. Holt, P. H. Fuoss, and V. Chamard. High-resolution three-dimensional structural microscopy by single-angle Bragg ptychography. *Nat. Mater.*, 16(2):244–251, 2017.

[28] K. Mader, F. Marone, C. Hintermüller, G. Mikuljan, A. Isenegger, and M. Stampanoni. High-throughput full-automatic synchrotron-based tomographic microscopy. *J. Synchrotron Radiat.*, 18(Pt 2):117–24, 2011.

[29] K. S. Mader, L. R. Donahue, R. Müller, and M. Stampanoni. High-throughput phenotyping and genetic linkage of cortical bone microstructure in the mouse. *BMC Genom.*, 16(1):493, 2015.

[30] M. Yabashi, K. Tono, H. Mimura, S. Matsuyama, K. Yamauchi, T. Tanaka, H. Tanaka, K. Tamasaku, H. Ohashi, S. Goto, and T. Ishikawa. Optics for coherent x-ray applications. *J. Synchrotron Radiat.*, 21(5):976–985, 2014.

[31] J. C. da Silva and A. Menzel. Elementary signals in ptychography. *Opt. Express*, 23(26):33812–33821, 2015.

[32] B. Enders, M. Dierolf, P. Cloetens, M. Stockmar, F. Pfeiffer, and P. Thibault. Ptychography with broad-bandwidth radiation. *Appl. Phys. Lett.*, 104(17):171104, 2014.

[33] M. Odstrčil, P. Baksh, H. Kim, S. A. Boden, W. S. Brocklesby, and J. G. Frey. Ultra-broadband ptychography with self-consistent coherence estimation from a high harmonic source. *Proc. of SPIE*, 9589:958912, 2015.

[34] T. Katayama, T. Hirano, Y. Morioka, Y. Sano, T. Osaka, S. Owada, T. Togashi, and M. Yabashi. X-ray optics for advanced ultrafast pump–probe x-ray experiments at SACLA. *J. Synchrotron Radiat.*, 26(2):333–338, 2019.

[35] T. Tanaka and H. Kitamura. SPECTRA: a synchrotron radiation calculation code. *J. Synchrotron Radiat.*, 8(6), 2001.

[36] A. Rack, T. Weitkamp, M. Riotte, D. Grigoriev, T. Rack, L. Helfen, T. Baumbach, R. Dietsch, T. Holz, M. Krämer, F. Siewert, M. Meduna, P. Cloetens, and E. Ziegler. Comparative study of multilayers used in monochromators for synchrotron-based coherent hard X-ray imaging. *J. Synchrotron Radiat.*, 17(4):496–510, 2010.

[37] S. J. Leake, G. A. Chahine, H. Djazouli, T. Zhou, C. Richter, J. Hilhorst, L. Petit, M. I. Richard, C. Morawe, R. Barrett, L. Zhang, R. A. Homs-Regojo, V. Favre-Nicolin, P. Boesecke, and T. U.

Schülli. The nanodiffraction beamline ID01/ESRF: a microscope for imaging strain and structure. *J. Synchrotron Radiat.*, 26(2):571–584, 2019.

[38] Christian Morawe. Multilayer based X-ray optics at the ESRF. *AIP Conf. Proc.*, page 060002, 2019.

[39] F. Seiboth, A. Schropp, M. Scholz, F. Wittwer, C. Rödel, M. Wünsche, T. Ullsperger, S. Nolte, J. Rahomäki, K. Parfeniukas, S. Giakoumidis, U. Vogt, U. Wagner, C. Rau, U. Boesenberg, J. Garrevoet, G. Falkenberg, E. C. Galtier, H. J. Lee, B. Nagler, and C. G. Schroer. Perfect X-ray focusing via fitting corrective glasses to aberrated optics. *Nat. Commun.*, 8:14623, 2017.

[40] T. Hirano, T. Osaka, Y. Sano, Y. Inubushi, S. Matsuyama, K. Tono, T. Ishikawa, M. Yabashi, and K. Yamauchi. Development of speckle-free channel-cut crystal optics using plasma chemical vaporization machining for coherent x-ray applications. *Rev. Sci. Instrum.*, 87(6):063118, 2016.

[41] G. E. Artzner. Microlens arrays for Shack-Hartmann wavefront sensors. *Opt. Eng.*, 31(6):1311–1322, 1992.

[42] Y. Kayser, C. David, U. Flechsig, J. Krempasky, V. Schlott, and R. Abela. X-ray grating interferometer for in situ and at-wavelength wavefront metrology. *J. Synchrotron Radiat.*, 24(1):150–162, 2017.

[43] M. Seaberg, R. Cojocaru, S. Berujon, E. Ziegler, A. Jaggi, J. Krempasky, F. Seiboth, A. Aquila, Y. Liu, A. Sakdinawat, U. Lee, H. J. Flechsig, L. Patthey, F. Koch, G. Seniutinas, C. David, D. Zhu, L. Mikeš, M. Makita, T. Koyama, A. P. Mancuso, H. N. Chapman, and P. Vagovič. Wavefront sensing at X-ray free-electron lasers. *J. Synchrotron Radiat.*, 26(4):1115–1126, 2019.

[44] W. Hua, G. Zhou, Y. Wang, P. Zhou, S. Yang, C. Peng, F. Bian, and X. Li. Measurement of the spatial coherence of hard synchrotron radiation using a pencil beam. *Chin. Opt. Lett.*, 15(3):033401–33405, 2017.

[45] M. Lyubomirskiy, I. Snigireva, and A. Snigirev. Lens coupled tunable Young's double pinhole system for hard X-ray spatial coherence characterization. *Opt. Express*, 24(12):13679–13686, 2016.

[46] Y. Kashyap, H. Wang, and K. Sawhney. Two-dimensional transverse coherence measurement of hard-x-ray beams using near-field speckle. *Phys. Rev. A*, 92(3):033842, 2015.

[47] P. Denes and B. Schmitt. Pixel detectors for diffraction-limited storage rings. *J. Synchrotron Radiat.*, 21(5):1006–1010, 2014.

[48] S. Cartier, M. Kagias, A. Bergamaschi, Z. Wang, R. Dinapoli, A. Mozzanica, M. Ramilli, B. Schmitt, M. Brückner, E. Fröjdh, D. Greiffenberg, D. Mayilyan, D. Mezza, S. Redford, C. Ruder, L. Schädler, X. Shi, D. Thattil, G. Tinti, J. Zhang, and M. Stampanoni. Micrometer-resolution imaging using MÖNCH: towards G_2-less grating interferometry. *J. Synchrotron Radiat.*, 23(6):1462–1473, 2016.

[49] P. Li and A. Maiden. Multi-slice ptychographic tomography. *Sci. Rep.*, 8(1):2049, 2018.

[50] M. Odstrčil, M. Holler, J. Raabe, A. Sepe, X. Sheng, S. Vignolini, C. G. Schroer, and M. Guizar-Sicairos. Ab initio nonrigid X-ray nanotomography. *Nat. Commun.*, 10(1):2600, 2019.

Chapter 19

TOMCAT 2.0: Multiscale - Multimodal - Dynamic Tomographic X-ray Microscopy

F. Marone, A. Bonnin, C. M. Schlepütz, G. Mikuljan, P. Zuppiger, and M. Stampanoni

In a nutshell

In the last decade, TOMCAT has been providing cutting-edge tomographic microscopy to a heterogeneous international scientific community and has generated seminal contributions in key areas like (bio-)medical research, material science, energy, geoscience, and paleontology, to cite just a few. Internationally, TOMCAT is considered a benchmark and is presently driving the developments of dynamical tomographic microscopy. To maintain and strengthen our leading role in the field, we plan to capitalise on our expertise in multiscale, multimodal dynamic tomographic microscopy and propose to deploy the TOMCAT 2.0 upgrade on two beamlines, dubbed **I-TOMCAT**, a brand-new instrument based on an insertion device of the latest generation (see Section 2.2), and **S-TOMCAT**, powered by a new high-field superconducting bending magnet. The embedment of SLS 2.0 within PSI will allow the implementation of innovative technical solutions in a very short time: at a pace that competitors will not be able to follow. TOMCAT 2.0 will be unique in offering one entry point for complex dynamical, high-throughput multidimensional imaging tasks requiring a spatial resolution ranging from 100 nm up to 10 μm and energies from 8 up to 80 keV. TOMCAT 2.0 on SLS 2.0 will provide images of increased quality, boosted by the smaller source size and higher photon flux at most energies. The upgrade will lead to better and novel characterization techniques, with simultaneously higher spatial and temporal resolution, pushing dynamic tomographic imaging towards unexplored frontiers. Extensive capabilities for *in-situ, operando, in-vivo* and *in-fieri* experiments will be offered to broad academic and industrial communities addressing grand challenges in medical, energy and the material sciences. The TOMCAT 2.0 upgrade will enduringly establish PSI on the map as one of the best imaging facilities worldwide for the next 20 years.

19.1 Upgrade motivation – goals – expected impact

X-ray tomographic microscopy provides quantitative volumetric information on a large variety of opaque samples in a fast and non-destructive manner with micrometer spatial resolution for samples of a few millimetres in diameter. The high brightness of synchrotron radiation sparked the development of multi-modal imaging techniques, including phase contrast, dark-field imaging, and diffraction CT. Over the last few years, new fast camera and readout systems [1] have triggered the advance of dynamic tomographic studies, to a point where processes can be followed in 3D up to speeds of 20 tomograms (i.e., 3D volumes) per second at a few microns spatial resolution. TOMCAT has been at the forefront from the very early days of synchrotron-based tomography, both for fast tomographic measurements and for multi-modal imaging. In the last decade, TOMCAT has been providing cutting-edge tomographic microscopy in different flavours to a heterogeneous international scientific community and has generated seminal contributions in key areas like (bio-)medical research [2], material science [3], energy [4], geoscience [5], and paleontology [6], to cite but a few.

In addition to a significant overall increase in image quality boosted by the higher photon flux at most energies, the unprecedented beam properties of SLS 2.0 will lead to better and novel characterization techniques, with simultaneously higher spatial and temporal resolution, pushing *dynamic tomographic imaging towards unexplored frontiers*. We plan to capitalize on our expertise in multiscale, multimodal, dynamic tomographic microscopy and propose to deploy the TOMCAT 2.0 upgrade at *two* beamlines, dubbed I-TOMCAT a brand-new instrument based on an insertion device of the latest generation, and S-TOMCAT powered by a high-field superconducting bending magnet. With two beamlines, TOMCAT 2.0 will offer a unique and comprehensive imaging portfolio at energies ranging from 8 up to 80 keV. In Annex 19.5.1, we briefly discuss the impact of the TOMCAT 2.0 upgrade on the science carried out by current and future users, while Figure 19.1 illustrates the expected improvement in tomographic capabilities at TOMCAT 2.0 compared to the present status. The figure shows the time needed to acquire a 3D volume at a given 3D resolution for different instruments and techniques.

TOMCAT 2.0 will enable the study of dynamic processes over an unparalleled length scale range (100 nm up to 10 μm), to some extent even in a simultaneous manner, an important aspect for processes with hierarchical structures. We foresee up to three orders of magnitude increase in time resolution for the Transmission X-ray Microscopy (TXM) instrument with a target spatial resolution of at least 100 nm and almost a doubling of the operating energy range. The full-field instrument will experience almost two orders of magnitude improvement in speed and up to one order of magnitude better spatial resolution for the same energy. For the same time and spatial resolution, it will be possible to double (!) the probing energy, enabling the investigation of significantly thicker and heavier samples compared to now. Similar arguments hold for the fast instrument. Its time-resolution will be pushed to the physical barrier imposed by centrifugal forces acting during sample rotation. Overcoming this barrier means entering the domain of single-shot kHz (and above) 3D imaging, which will require illuminating the sample *simultaneously* from multiple directions under limited — or eventually even no — specimen rotation[a].

The higher flux and larger fraction of coherent photons at higher energies as well as a palette of

[a] Time resolutions in the kHz regime have been achieved already thanks to post-gating techniques

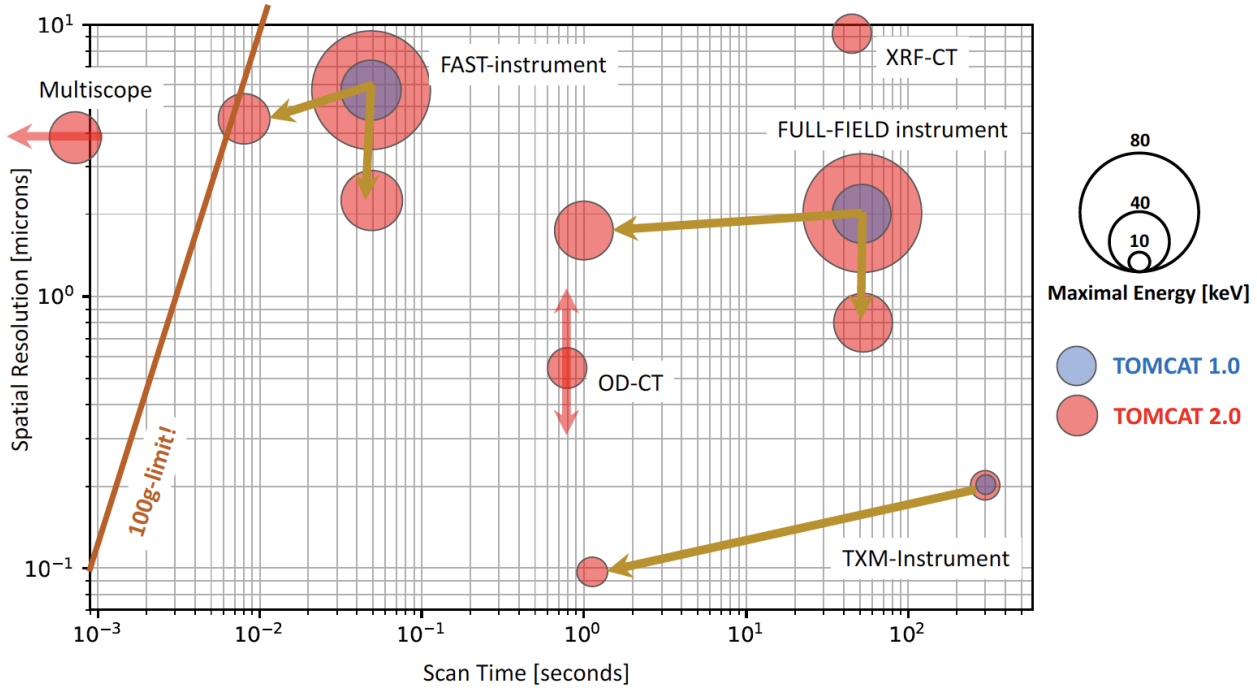

Figure 19.1: Expected development of tomographic microscopy capabilities on TOMCAT 2.0. The performance of TOMCAT at the current SLS is marked in light-blue, while TOMCAT 2.0 features at SLS 2.0 are given in light-red. Brown arrows indicate expected orders-of-magnitude sized improvement of our core instruments: a transmission x-ray microscope, a parallel-beam full-field device and a fast-imaging instrument. Expected performances of full-field x-ray fluorescence (XRF-CT) and omnidirectional computed tomography (OD-CT) are indicated as well. Light-red arrows show future extension of the techniques. The 100 g centrifugal force barrier marked on the left indicates the physical limit for the transition from rotating to non-rotating sample environments.

specialized *in-situ, operando, in-vivo*, and *in-fieri* sample environments will be instrumental for the investigation of dynamic phenomena under realistic conditions (e.g., less boundary effects) and will expand the scope of current high-speed capabilities to new systems and scientific questions. Low-dose *in-vivo* studies on small and larger organisms will also strongly benefit from the unrivalled beam properties at SLS 2.0. The investigation of large volumes at high resolution — stitched teravoxel tomography [7] — will become routine. TOMCAT 2.0 dynamic aspects will be complemented by 3D multimodal capabilities revealing, in addition to the 3D microstructural evolution, information on the elemental distribution (full-field x-ray fluorescence tomography), crystallographic orientations (white-beam diffraction contrast tomography) and structural anisotropy (omnidirectional Talbot interferometry).

19.1.1 Uniqueness compared to other present and planned beamlines worldwide

Essentially all synchrotron facilities worldwide operate or plan a hard x-ray TXM or a full-field tomography beamline. Consequently, both new and currently upgrading facilities all have a strong imaging program in their refurbishment portfolio. TOMCAT is internationally considered a benchmark; it has established itself as a world reference for tomographic imaging performed at energies between 8 and 30 keV, making very good use of the excellent performances of the SLS machine in that particular energy range. The documented great success of the beamline with more than 600 papers published so far and a ten-years average overbooking factor of 1.6 — and this, despite data acquisition becoming more than ten times faster during the last few years — clearly places TOMCAT at the forefront of the synchrotron imaging community. Several facilities have plans to build imaging beamlines inspired by TOMCAT (AS in Melbourne, PAL in Pohang, SSRF in Shanghai, ALBA in Barcelona, HEPS in Beijing, MOGNO in Campinas, BEATS in Amman), while others have clearly identified (full-field) imaging as their "raison d' être" for their upgrade programs (ESRF and APS in particular).

The proposed TOMCAT 2.0 upgrade foresees the implementation of a number of high-potential technical innovations which will guarantee us a leading position in the imaging community for the next two decades. We are not aware of any other institution able to design, construct, install, and commission a superconducting short-period undulator and a superconducting high-field longitudinally-graded bending magnet, while simultaneously offering access to resources conceiving and fabricating both novel optics and detectors: such a synergetic effort is only possible at PSI and will enable an efficient implementation of innovative ideas at a pace that competitors will not be able to keep. No one worldwide can/will offer such a flexible operative range as TOMCAT 2.0 will be able to do, as most of the competitors usually run full-field and TXM endstations with independent, often not even collaborating, teams. Our crew will share knowledge and distribute it on either I-TOMCAT or S-TOMCAT ensuring the latest developments and protocols are implemented and exploited.

19.1.2 Impact of the new ring brilliance

At SLS 2.0, we expect a significantly larger horizontal transverse coherence length compared to SLS today, given by the much-improved horizontal emittance properties of the SLS 2.0 machine. This will lead to an almost isotropic transverse coherence function — for S-TOMCAT the source actually becomes slightly smaller and round, while now we have roughly a 7:1 (H:V) ratio — which will translate into a generally improved image quality for all phase-contrast techniques implemented at TOMCAT 2.0: propagation-based, grating interferometry, Zernike and, in the long term, single-shot. In its simplest form, phase-contrast imaging relies on the detection of interference fringes arising from a subtle refraction of the x-ray beam at interfaces between materials with slightly different refractive indices. In the current SLS, the horizontal fringe visibility is significantly reduced due to source size blurring, an effect which is exacerbated by increasing the propagation distance (and hence reducing the source demagnification ratio of the imaging system). Much sharper fringe patterns — resulting from the increased SLS 2.0 brilliance — will dramatically boost phase-contrast sensitivity. New phase-reconstruction algorithms to take optimal advantage of that situation are already under development in the community [8]. This will be particularly important for coarse resolution scans in multiscale imaging and high-energy experiments, both of which require larger propagation distances; and for

high-speed measurements, where the enhanced fringe visibility will allow feature detection even at very low signal to noise ratios.

It has to be pointed out that not only phase-sensitive techniques will profit from the improved ring brilliance. One advantage of SLS 2.0 (compared to other – larger – rings) is that due to its small dimension it is actually possible to install optical components very close to the source. For a 2 m short-straight undulator and a predicted machine emittance reduction of 30× along the horizontal direction, we expect a significant reduction of horizontal source size and divergence compared to TOMCAT. We calculated that a refractive axicon [9] placed at 15 m from the source will collect the full undulator beam with a transmission efficiency higher than 97% at 12 keV. This will allow us to efficiently operate the TXM at 400× magnification with a working distance of 50 mm. In combination with a MOENCH detector, this will result in a pixel size of 65 nm and we expect to collect about 4000 photons/pixel/frame at 1000 frames/s[b]. This means an improvement in speed of about 2000× compared to what we can do now on TOMCAT, see Figure 19.1. More details are provided in Section 19.2.

19.1.3 Complementarity to other PSI BLs

TOMCAT 2.0 will focus mainly on the dynamic multi-modal aspects of tomographic microscopy. Our goal will be to provide time-resolved image volumes of evolving samples, *in situ, in vivo, operando*, or *in fieri*. We target a maximum spatial resolution of 100 nm, while chemical discrimination will be in the order of 600 to 900 eV. In this sense, TOMCAT 2.0 will be complementary to cSAXS (where spatial resolution is pushed to the physical limits) and microXAS (where chemical imaging is the daily business and can be performed at higher spatial resolution). We are and will continue cooperating with the cSAXS and microXAS teams, for instance in the development of ptychographic methods as well as full-field XRF-CT and WB-DCT. Other beamlines are planning to reinforce their imaging portfolio (Phoenix, PolLux, and SIM in particular) and we will be very happy to share our knowledge in tomographic imaging with them.

19.1.4 Size and impact of community – potential increase through the upgrade

TOMCAT's 10 years average overbooking factor is 1.6, while during the last five years, it risen to 1.8. These can be considered healthy numbers and they confirm a sustained interest in the beamline, which has been fully booked for more than a decade. In view of the SLS 2.0 upgrade, we organized a workshop in November 2016[c], where we invited key opinion leaders (KOLs) from our broad user community to brainstorm on the mission of TOMCAT 2.0. Physical limitations of the current TOMCAT beamline were discussed and game-changers as well as new science enablers were identified in

- the capability to dynamically resolve 3D morphological details down to 100 nm (*in situ, in fieri, operando, in vivo*);

[b] The present MOENCH0.3 design can handle a maximum of 1000 photons/pixel/frame. Future designs might perform better in this respect and will further contribute towards better image quality.

[c] "Towards TOMCAT 2.0: selected scientific cases and preliminary specifications", PDF Report sent to SLS management on November 7th, 2016.

- in the ability to visualize sub-micron functional features (like fiber orientation in a polymer material) on large areas;
- in the implementation of correlative microscopy options (fluorescence information on top of structural details).

These are features which can only be successfully implemented on an undulator beamline, as proposed for I-TOMCAT. Last, but not least, imaging up to 80 keV has been identified as a key functionality to extend significantly TOMCAT 2.0 capabilities and its user portfolio. This feature can only be provided on SLS 2.0 by using a high-field superconducting bending magnet, as suggested for S-TOMCAT. The proposed conceptual design for TOMCAT 2.0 has thus been driven by the imaging needs dictated by the science carried out by world-leading scientists. A letter of support in this sense signed by 12 KOLs was attached to the November 2016 report. With a real-time hard x-ray TXM operated synergistically with a high-energy full-field imaging setup, TOMCAT 2.0 will capitalize on a decade of cutting-edge tomographic microscopy expertise and attract a plethora of new users fully exploiting the new opportunities.

19.1.5 Industrial potential

TOMCAT is being regularly booked by industrial customers and their interest in multiscale, dynamical tomographic imaging is constantly growing. Our proprietary research reflects the flexibility of the TOMCAT instrument and our industrial requests come from very different areas (like pharmaceutical, energy or space technology). We do not offer a standardized product, but rather a customized service to target specific problems. We advise customers on how to design their synchrotron experiment and we help them during the beamtime and whenever possible in the quantification of the generated data: this comprehensive service package is a very much appreciated asset. A successful industrial beamtime requires a significant effort from the local team, before, during and after a proprietary beamtime. In March 2019, we hired an industrial liaison scientist, dedicated to this task and with the charge to develop an even more complete and competitive industrial program on TOMCAT 2.0. The flexibility of our technology is mirrored by the heterogeneity of our industrial community. Within the context of a EU-funded project proposal, we recently asked for Letters of Support (LOSs) and the response from industry was enthusiastic, with supportive statements from ABB, Novartis, Toyota, Shell, TyssenKrupp, Lument and SAFT[d]. Although it might be difficult to group all those companies into a consortium willing to co-fund a complete beamline, we think that such a strong interest from a broad variety of companies is actually a very healthy operational context as our industrial income is diversified and hence does not depend on a single industrial area.

19.2 Conceptual design

The TOMCAT 2.0 upgrade will be deployed on *two* beamlines: (i) I-TOMCAT, based on a superconducting, short-period undulator (SCU10) and (ii) S-TOMCAT, powered by a superconducting high-field longitudinally graded bending magnet.

[d] Letters of support can be made available.

I-TOMCAT will be installed at Sector 2, and will not interfere[e] with potential EEHG plans at ADRESS (RIXS). As for any new beamline, I-TOMCAT will require a new front-end, an optical and an experimental hutch, as well as dedicated control rooms and sample preparation areas. We do not plan to exit the WSLA building and foresee a maximum beamline length of 40 m. The proximity to S-TOMCAT will allow us to synergistically share the location of control racks, existing specialized labs, as well as mitigate shielding costs. For S-TOMCAT, we foresee the construction of a small optics hutch to host a ML-monochromator (now in the front-end) and a Bent-Laue high energy monochromator/beam-expander. Beamline repositioning following the displacements of the source-point has been considered and related costs included in the budget request. Figure 19.2 presents the first conceptual layout of TOMCAT 2.0, with I-TOMCAT adjacent to S-TOMCAT.

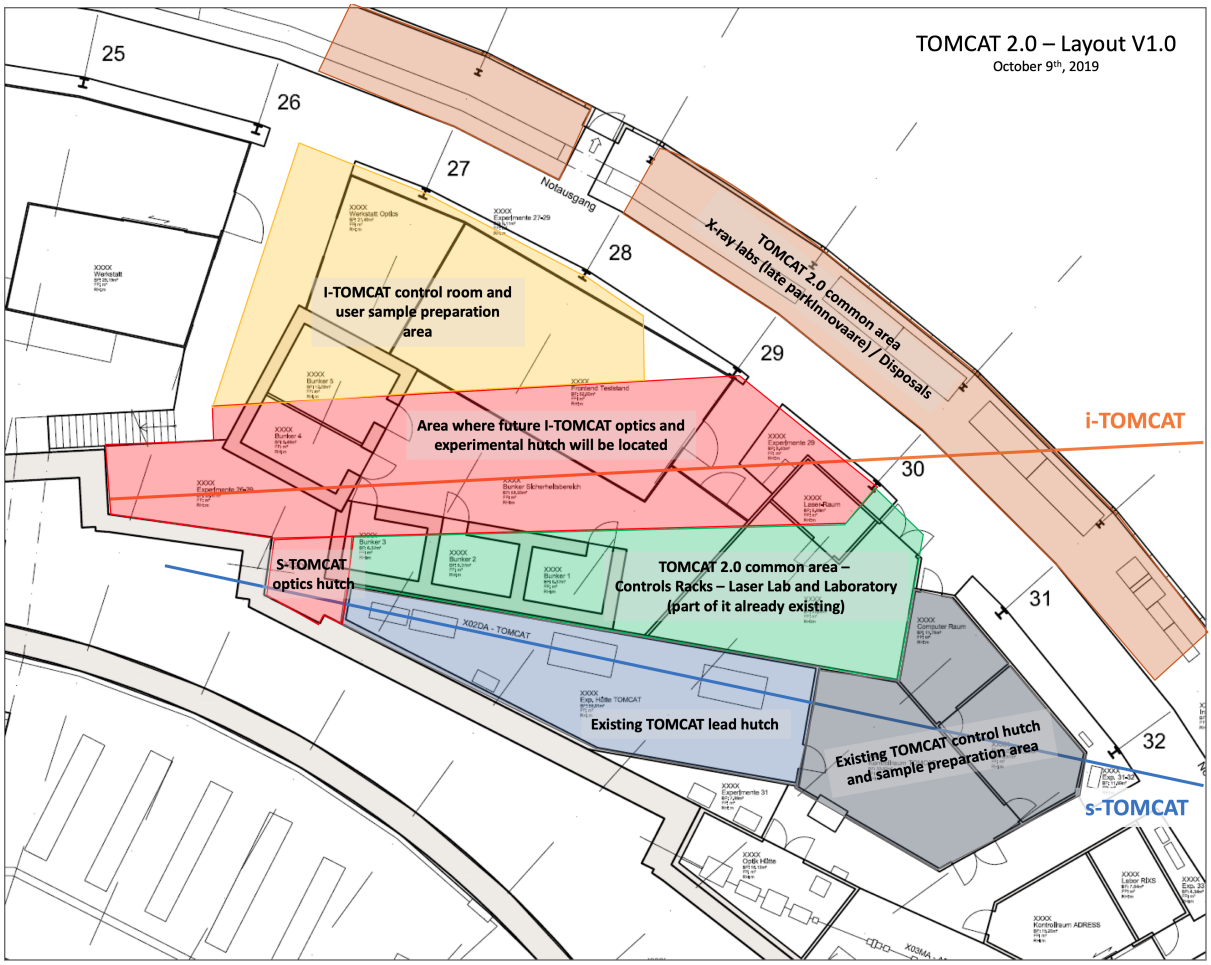

Figure 19.2: TOMCAT 2.0 conceptual layout. I-TOMCAT and S-TOMCAT will occupy Sector 2, extending from Pillar 26 to Pillar 32 (Pillars 29–32 already occupied by TOMCAT now).

S-TOMCAT will deliver energies potentially up to 80 keV and accommodate samples up to 50 mm

[e]Based on the slides shown by P. Willmott at the Laboratory Meeting on September 24th, 2019.

in diameter. I-TOMCAT will provide photons up to 45 keV (60 keV for the SCU10) for samples up to 1 mm diameter and will be optimized for high-speed TXM imaging. Some methods and end-stations will be interchangeable between S-TOMCAT and I-TOMCAT, as summarized in Table 19.1.

	S-TOMCAT	**I-TOMCAT**
Source	Superbend 4T (6T)	U14 (SCU10)
Energy range	10–50 keV (10–80 keV)	8–45 keV (8–60 keV)
Optics	Multilayer monochromator (MLM) Bent Laue (magic condition)	Channel-cut MLM-based harmonic suppression
Broad-band option	White beam (filtered)	Pink beam (single harmonic)
Sample diameter	< 50 mm @ 25 m	< 1 mm @ 30 m
Techniques	Enhanced absorption and propagation-based phase contrast imaging Dynamic tomographic imaging (4D)	
	WB-DCT OD-Talbot interferometry Wide-field tomography	TXM Zernike phase contrast Fourier ptychography XRF-CT
Detectors	20 kPix horizontal High-NA optical coupling GigaFRoST2.0	MOENCH(s) High-NA optical coupling GigaFRoST2.0
Endstations	Interchangeable sample holders compatible with both branches Versatile sample manipulators Generous in-situ, operando and in-vivo capabilities	

Table 19.1: Most relevant aspects related to the TOMCAT 2.0 upgrade.

19.2.1 Sources

The SLS 2.0 machine will be a game-changer for dynamic tomographic microscopy: a rounder source will intrinsically improve the quality of every phase-contrast-based imaging technique, while the improved emittance figures will permit the installation of insertion devices of the latest generation. Figure 19.3 illustrates the expected flux for different superbend and ID options on SLS 2.0, while Figure 19.5 provides a first estimation of the spectral flux densities at sample position for two high-field bending magnets options (4-T and 6-T peak fields) compared to TOMCAT on SLS (2.9-T peak field), as well as two undulator options (U14 and SCU10) for the new I-TOMCAT beamline.

- **I-TOMCAT with SCU10**: Compared to TOMCAT today, a superconducting U10 insertion device operated at K=2.4, will provide an increase in spectral flux between 1000× up to 10000× for energies between 40 keV and 10 keV with a corresponding gain in photon flux between 200× and 2000× for a bandwidth of 0.5%. Significant flux is expected above 40 keV as well, exact calculations are pending, see Figure 19.5. The SCU10 is *the* ID which will make TOMCAT 2.0 unique and the novel technology required for the development of the SCU10 would be directly applicable for the design and implementation of the PORTHOS beamline at SwissFEL. The PSI

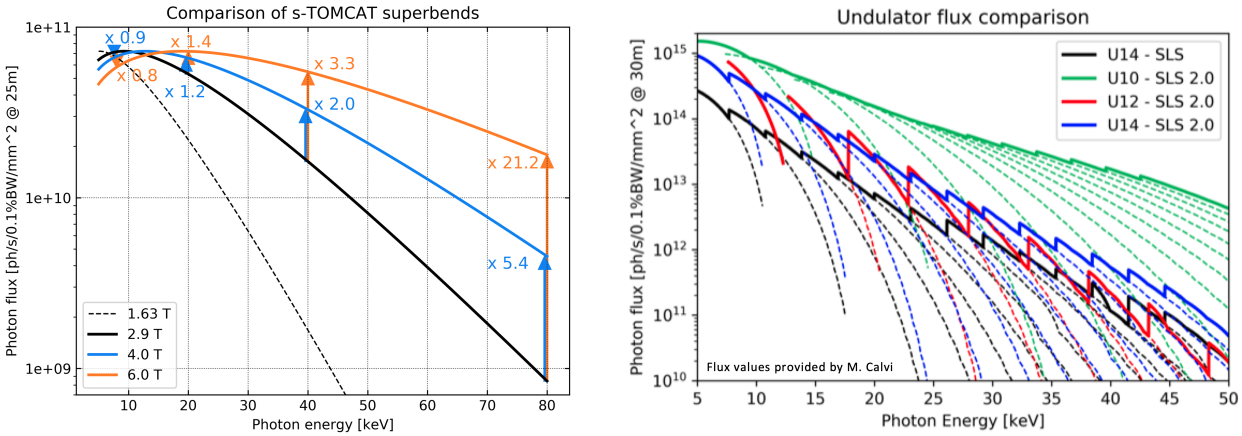

Figure 19.3: Expected photon flux as provided by different high-field superconducting magnets on S-TOMCAT (2.9 T corresponds to TOMCAT on SLS) as well as I-TOMCAT undulators, including a commercially available U14 as well as the proposed superconducting U10 presently under development.

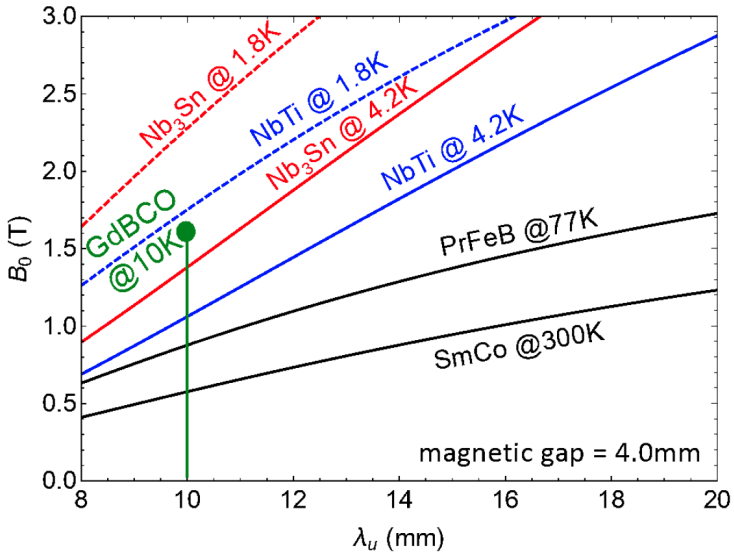

Figure 19.4: The scaling laws published in the literature are presented in the undulator field B_0 versus the undulator period λ_u plane at 4 mm magnetic gap for permanent magnets (SMCo), cryogenic permanent magnets (PrFeB) and low temperature superconductors (NbTi and Nb_3Sn). The highest value for GdBCO has been plotted after applying a geometrical scaling factor from 6 mm to 4 mm magnetic gap.

Insertion Device group has started an R&D program on HTS undulators aiming at reducing the period length and increasing the undulator's magnetic field well beyond the present capability. Simulation results for a 10 mm period and 4 mm magnetic gap staggered array of GdBCO bulks

Spectral flux in 1 mm^2 [photons/sec/0.1% BW]

Beamline	TOMCAT	S-TOMCAT				I-TOMCAT			
Machine	SLS	SLS-2				SLS-2			
Source	2.9T @ 25m	*4.0 T SB @ 25m*		*6.0 T SB @ 25m*		U-14 @ 30m		SCU-10 @ 30m	
	Flux	Flux	Factor vs. TOMCAT	Flux	Factor vs. TOMCAT	Flux	Factor vs. TOMCAT	Flux	Factor vs. TOMCAT
10 keV	*7.20E+10*	7.06E+10	0.98	6.35E+10	0.88	2.60E+14	3'611	7.84E+14	10'889
20 keV	*5.30E+10*	6.57E+10	1.24	7.21E+10	1.36	2.84E+13	536	1.54E+14	2'905
30 keV	*3.09E+10*	4.87E+10	1.58	6.57E+10	2.12	3.51E+12	114	4.57E+13	1'479
40 keV	*1.63E+10*	3.27E+10	2.01	5.46E+10	3.34	5.37E+11	33	1.69E+13	1'036
60 keV	*3.89E+09*	1.28E+10	3.22	3.28E+10	8.43	-	-	*	-
80 keV	*8.43E+08*	4.54E+09	5.39	1.78E+10	21.1	-	-	*	-

Flux in 1 mm^2 [photons/sec]

Beamline	TOMCAT	S-TOMCAT				I-TOMCAT			
Machine	SLS	SLS-2				SLS-2			
Source	2.9T	4.0 T SB @ 25m		6.0 T SB @ 25m		U-14 @ 30m		SCU-10 @ 30m	
Optics	MML 2%	MML 2% (<45keV)		MML 2% (<45keV)		MML (full ~0.5% BW FWHM of undulator)			
	Flux	Flux	Factor vs. TOMCAT	Flux	Factor vs. TOMCAT	Flux	Factor vs. TOMCAT	Flux	Factor vs. TOMCAT
10 keV	1.44E+12	1.41E+12	0.98	1.27E+12	0.88	1.04E+15	722	3.13E+15	2174
20 keV	1.06E+12	1.31E+12	1.24	1.44E+12	1.36	1.14E+14	107	6.16E+14	581
30 keV	6.17E+11	9.74E+11	1.58	1.31E+12	2.12	1.41E+13	22.9	1.83E+14	297
40 keV	3.25E+11	6.54E+11	2.01	1.09E+12	3.34	2.15E+12	6.6	6.76E+13	208
60 keV	X	**	-	**	-	-	-	*	-
80 keV	X	**	-	**	-	-	-	*	-

Figure 19.5: Spectral flux (top) and flux (bottom) density incident upon 1 mm^2 estimated at the sample position (25 m for S-TOMCAT and 30 m for I-TOMCAT). Note that all numbers will be recalculated as soon as the lattice design will be frozen and will be refined at the TDR stage, including proper ray-tracing.

predict a peak magnetic field greater than 2 T. A first measurement campaign, see Figure 19.4, confirmed the high-potential of GdBCO bulks compared to permanent magnets and low temperature superconductors. Even higher performances are expected with reinforced bulk supports

to avoid quenches. As a next step, a standard 10-period short undulator will be assembled and tested at the nominal gap of 4 mm. The team aims to deliver a final design of a full-scale undulator in 2021[f]. This timeline is well aligned with our project, which foresees the order of a commercially available U14 (as a risk mitigation option) at latest in mid 2021, to guarantee on-time delivery, commissioning and installation.

- **S-TOMCAT with high-field superconducting bending magnet**: Following our TOMCAT 2.0 workshop in November 2016, we identified a 6 T superconducting bending magnet to be the ideal source to address the growing demand of high-energy applications. Intense discussions involving machine, magnet and vacuum experts have shown that the technology required to reach such high fields under the constraints imposed by the SLS 2.0 lattice is not mature yet. It was therefore decided to defer the R&D related to the 6 T (or even higher!) magnets to the CHART[g] initiative, in which PSI has a leading role. At the time of writing, the most promising solution for S-TOMCAT seems to be an H-shape in-vacuum design, see Figure 19.6, potentially reaching a peak field of 5 T.

  Compared to the originally proposed C-shape, the "H" design is preferred, as it is more stable, easier to design, cheaper and can provide higher fields. It will require additional gate valves to guarantee a smooth installation, though. A 5 T superbend would be an acceptable solution for S-TOMCAT, providing a significant improvement compared to TOMCAT and being aligned with future developments within the CHART program.

We would like to emphasise that, while we fully understand that the machine team would like to start up SLS 2.0 without superbends, S-TOMCAT will significantly underperform compared to now if operated on the SLS 2.0 normal bend.

19.2.2 Front end

I-TOMCAT will require a new front end, including diaphragm, absorber, CVD window, slits pairs, filter battery, beam position monitors, and safety shutter (with bremsstrahlung blocker). The design of a high-power diaphragm and high-power slits pair able to cope with the intense emission of the SCU10 is well advanced. The S-TOMCAT front-end components will be partially refurbished and relocated, while the DMM/DCM monochromator will be decommissioned in favor of a significantly improved new design. The exact location of each component will be determined once the lattice will be fixed.

19.2.3 Optics

This section discusses the design concepts of key optical components currently under consideration for the TOMCAT 2.0 upgrade.

- **Double Multilayer Monochromator** (S-TOMCAT, < 40 keV): We foresee an upgrade of the TOMCAT monochromator [DMM only, no Si(111)]. It will be designed to accept the full beamline divergence (expected to be 2 mrad, as defined by the diaphragm) at about 10 m distance from the source. Note that the DMM will be located *outside* the front-end in a dedicated optics

[f] Internal communication by Dr. M. Calvi, PSI Insertion Device group.
[g] CHART: Swiss Accelerator Research and Technology

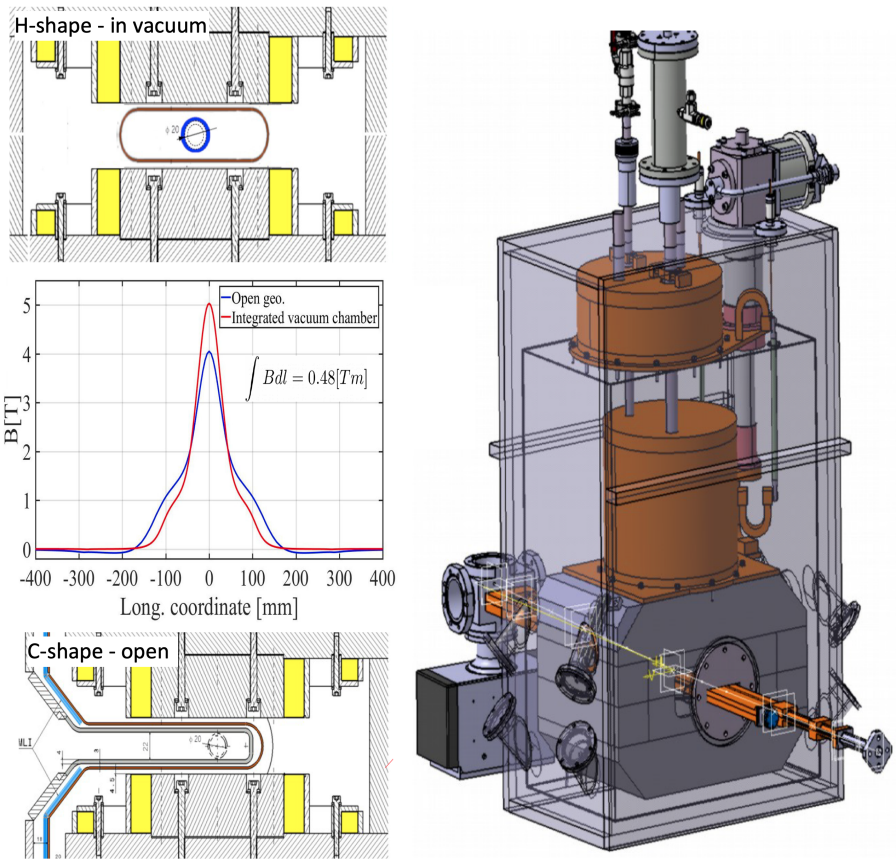

Figure 19.6: Currently proposed designs for an in-vacuum H-shape superconducting longitudinally graded (above left) and C-shape in-air bending magnet (below left). The in-vacuum solution allows the reduction of the magnetic gap down to 35 mm (compared to 46 mm for the C-shape). Consequently, a peak field up to 5 T will be reachable with established Ni-Ti superconducting technology.

hutch, see Figure 19.2. Several multilayer (ML) coatings are currently under investigation, see Figure 19.7.

- **Vertical beam expansion** (S-TOMCAT, > 40 keV): A Bent-Laue monochromator can be operated in the so-called magic condition (coincident geometrical and spectral foci), to perform (phase-preserving) beam expansion in the vertical direction [10]. A post-doc (member of the team who first proposed this method) has been hired to investigate and ray-trace this particular optical component.
- **Artificial Channel Cut** (I-TOMCAT): A fixed-exit monochromator based on an off-surface rotation center geometry (artificial channel cut) is currently considered as a compact and fast wavelength selector and harmonic suppressor.
- **Axicon-TXM** (I-TOMCAT): A refractive axicon lens shall be used to prepare the illumination of a diffractive beamshaper in TXM configuration. This approach will make full use of the SLS 2.0 improved emittance by distributing the full (transmission >97% for energies higher

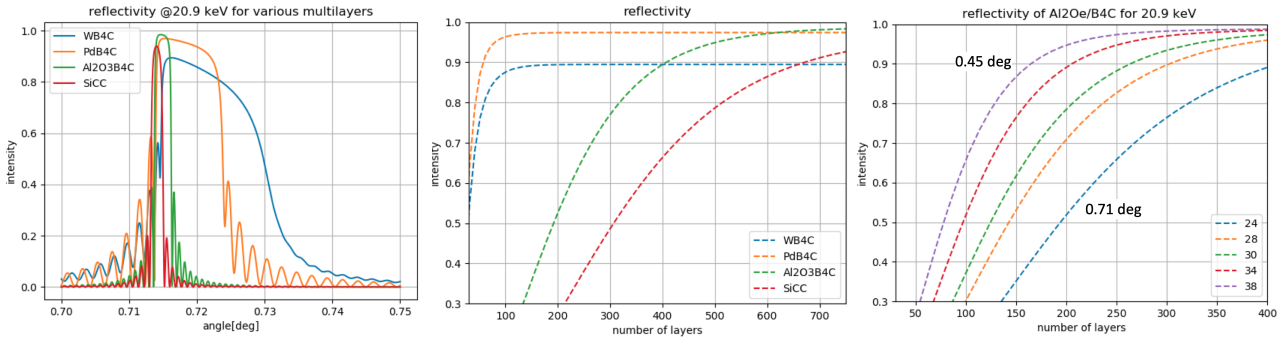

Figure 19.7: Left: Reflectivity curves at 20.9 keV for different ML materials: Al_2O_3/B_4C with a bandwidth significantly narrower than W/B_4C (layer thickness ratio optimised for reflectivity). Middle: Peak reflectivity as a function of the number of layers. Right: optimization of d-spacing to further maximize reflectivity (has an effect on the geometry!).

than 12 keV) beam from the ID-source in an annular area onto the beamshaper, making the use of a classical beamstopper unnecessary, see Figure 19.8.

- **High-NA optical coupling** (I-TOMCAT and S-TOMCAT): We recently introduced [11] a specially designed large numerical aperture optical coupling (4×) at TOMCAT, which leads to a system with a significantly improved modulation transfer function (MTF) and efficiency and has been a game-changer for essentially all users working at this magnification, and in particular for the dynamic applications. We foresee similar optics for higher magnifications to be installed on both branches.

19.2.4 Operation modes

Figure 19.9 sketches the top views of the proposed beamline designs for the TOMCAT 2.0 upgrade.

- **S-TOMCAT**: The layout corresponds essentially to TOMCAT at SLS. The main difference is the location of the DMM (5) outside the front-end tunnel as well as an optional Bent-Laue monochromtator (6) which can be inserted on demand (current idea). Secondary slits (7) are located in the existing TOMCAT experimental hutch. The sample (8) is placed for illustration at 25 m from the source. S-TOMCAT will be offering omnidirectional Talbot interferometry capabilities, a method we have recently introduced [12] and are constantly improving. This approach allows for an efficient measure of anisotropy distributions in 3D and 4D across several length-scales. This method could be implemented on I-TOMCATfull-field mode as well.
- **I-TOMCAT full-field**: This configuration will provide ultra-fast structural information at about 1 μm spatial resolution. An artificial ML channel-cut monochromator (5) will guarantee fast monochromatization and harmonic rejection. Secondary slits (6) will be installed in the first part of the experimental hutch. Samples with a diameter up to 600 μm and up to 1200 μm can be measured by positioning the specimen at 25 m (7) and 38 m (8) from the source, respectively[h].

[h]These values have been calculated assuming a diaphragm aperture of 25 μrad, which seems to be a realistic source divergence when the ID is operated in combination with a multilayer optics.

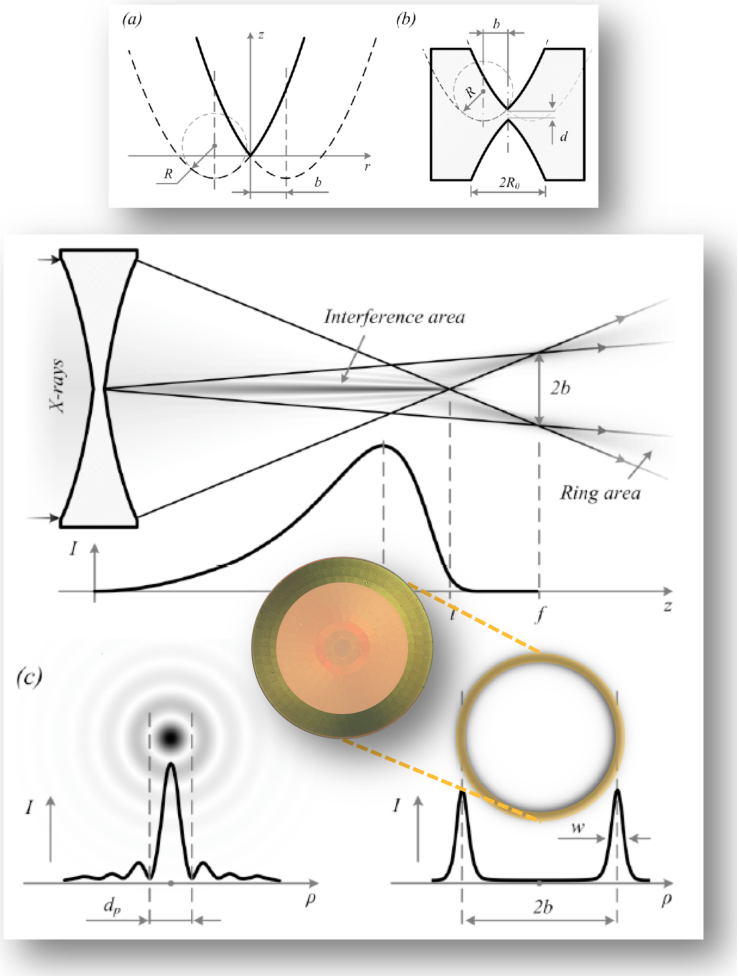

Figure 19.8: A parabolic axicon refractive surface can be used as a lens in order to distribute the incoming intensity into a ring area in the far field [9]. A beamshaper positioned on-axis at that location will be illuminated accordingly, exploiting the full beam of the ID and making the need for a beamstopper obsolete.

Further, using two MOENCH detectors placed at 90° from the optical axis (10) combined with two 10 μm pinholes, it will be possible to provide 3D elemental mapping at around 10 μm spatial resolution and 600 – 900 eV energy resolution, without the need of microbeams, or scanning. The full-field detector (9) is illustratively placed at 40 m.

- **I-TOMCAT axicon TXM**: By inserting an axicon (6) right after the monochromator, the beam can be shaped (see Figure 19.8) in order to optimally illuminate a structured condenser (8) as originally proposed by Stampanoni [13] and refined by Vartiainen [14]. By appropriate manipulation of the wavefront with phase modulators ("rings") placed in the back-focal plane of the zone plate (10), the TXM can be operated in Zernike phase-contrast mode. Assuming the

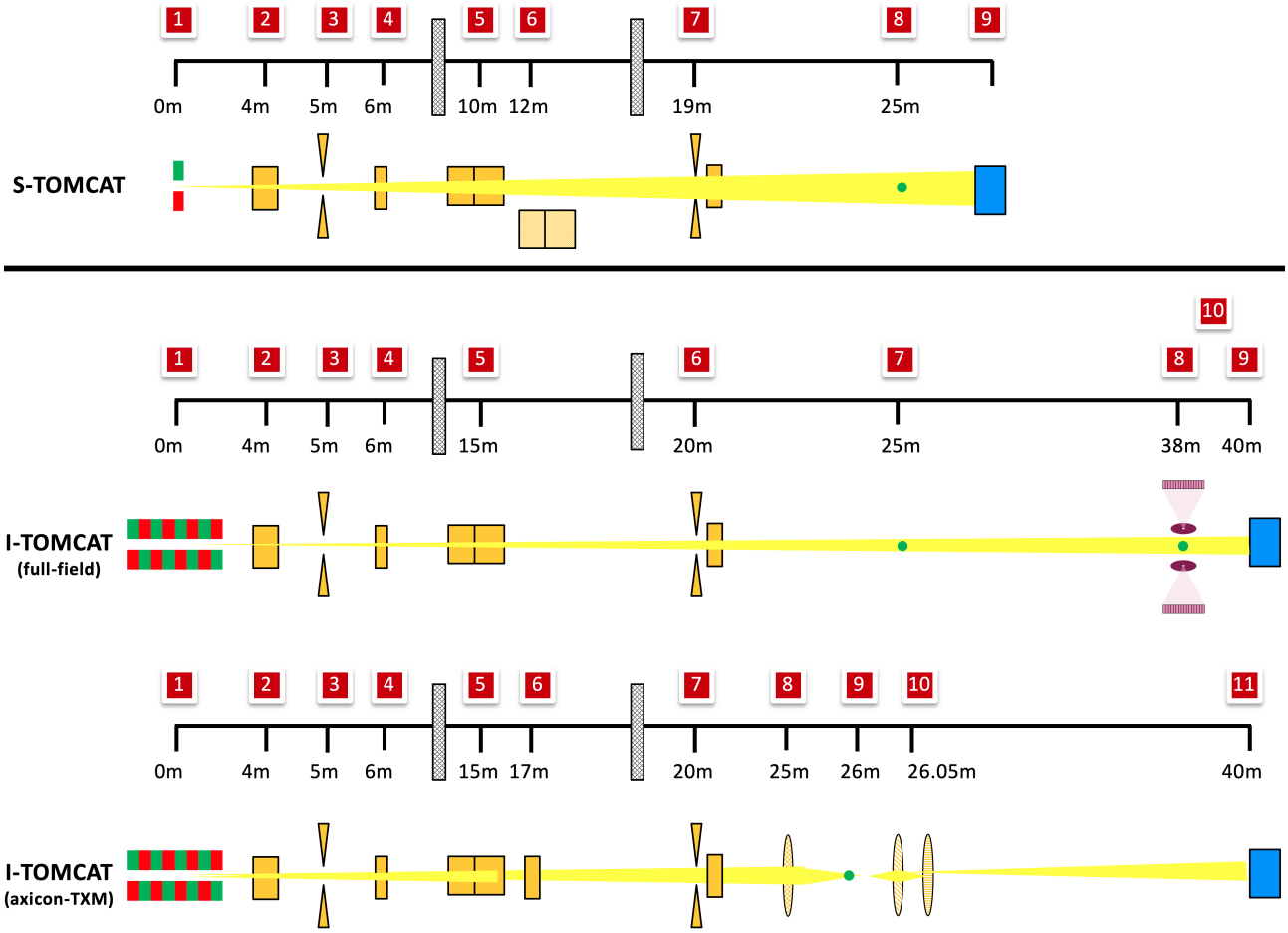

Figure 19.9: TOMCAT 2.0 top views. Upper panel: S-TOMCAT in full field mode. Middle panel: I-TOMCAT in full field (with XRF-CT add-on). Bottom panel: I-TOMCAT in axicon-TXM mode. In all panels: 1 = source, 2 = aperture, 3 = primary slits, 4 = primary filters. The sample location is marked with a green dot. The exact on-axis location of the front-end components is still open and will be finalized as soon as the lattice is fixed.

SCU10 as a source, an axicon efficiency larger than 97%, a condenser and zone-plate efficiency of about 10% as well as a MOENCH operated in 2× pixel virtualization mode (11), a first back-of-the envelope calculation made for 12 keV photon energy shows that it should be possible to achieve a frame rate of 1000 frames-per-second with the TXM operated at 400× (theoretical pixel size of 65 nm) and a working distance of 50 mm[i].

The axicon-TXM can be naturally extended into a Fourier-ptychography x-ray microscope (pioneered by cSAXS/TOMCAT [15]) for even further improved spatial resolution and quantitative phase retrieval. To optimally exploit this new method, multiplexed zone-plates as well as a large area MOENCH (2×3 cm^2) will be needed.

[i]Here we assumed a large area MOENCH (at least 1000x1000 pixels) to be available at the time of operation.

On a longer time perspective, i.e., after the consolidation of TOMCAT 2.0 we are considering investigating the potential of some ideas for future method developments, as summarized in Section 19.5.2.

19.2.5 IT requirements and controls

The higher brilliance provided by the new machine and the proposed expansion of the dynamic imaging program at TOMCAT 2.0 will lead to the generation of data with a rate in excess of tens of TB per day. We have estimated that each branch could routinely deliver 16 TB of raw data per day at the start of SLS 2.0 and that the corresponding derived data (tomographic reconstructions) could amount to 50 TB/day[j]. For an efficient user operation, each branch will need 400 dedicated online CPU cores and access to an HPC infrastructure (typically requesting 400 CPU cores per job). Management of these large data, including streaming, reconstruction, analysis, and archiving, is a big challenge. As one of the beamlines at SLS currently producing the largest amount of data, we are strongly involved in the discussions with the IT section for the development of scalable and sustainable solutions for SLS 2.0. Approaches allowing an active control of this data deluge are currently being developed: for instance, we have identified several intervention opportunities for data reduction along the entire data chain including classical lossy compression and smart data acquisition. Strategically, we are considering filling one of the 3 FTEs budgeted for the TOMCAT 2.0 upgrade with a computer scientist profile, i.e. a dedicated resource within the group who will actively contribute to the developments of computational solutions to address our imaging challenges with potential benefit also for other beamlines such as PX or cSAXS.

19.3 Timeline

From an infrastructural and logistical point of view, the SLS 2.0 upgrade is a significant challenge. In this context, the TOMCAT 2.0 project offers the unique opportunity to distribute some of the working load (in particular the matrix pull) over a period preceding the dark-time. In fact, I-TOMCAT shall be installed on Sector 2 — presently not in use — and therefore can be realized to a great extent well *before* the expected downtime.

Assuming appropriate funding will be available we laid out a timeline aiming at designing, procuring, installing and commissioning most of the I-TOMCAT components during the 2020-2023 period (see Figure 19.10), while guaranteeing full operation of TOMCAT on SLS at the same time (see Figure 19.11). At the time of writing this CDR, we already started working on our TDR and plan to be ready to place first purchase orders by Fall 2020.

19.3.1 Risk mitigation: SCU10 vs U14

The SCU10 might not be ready by the SLS 2.0 restart and an exact timeline (including costs) for its development are still undefined. Therefore, we have budgeted a commercially available U14 (2 MCHF) and plan to order it as a contingency at the latest in Q1-2021, i.e., about two years before the beginning of the dark-time. At the latest by that time-point, we expect the ID-team to be able to provide a

[j]Data presented by G. Mann (Head of IT) at the Pre-CDR Workshop in April 2019.

binding timeline for the design, construction and installation of the SCU10 on SLS 2.0. Therefore, we will be able to assess whether it will be realistic to expect an SCU10 on I-TOMCAT at the time SLS 2.0 is scheduled to start up. If not, we will have to opt for a risk mitigating decision, i.e., order and temporarily install the U14 (either in the first or second half of the Sector 2 straigh) to guarantee user operation. Obviously, the U14 is a back-up solution as it will clearly underperform compared to the SCU10. Therefore, once the SCU10 will be ready, it shall be immediately installed in the free half of the Sector-2 straight. It should be possible to commission it with minimal effects on the I-TOMCAT user operation. After a successful SCU10 commissioning, the U14 can be removed. We understood that the U14 can be kept as a spare ID for other SLS 2.0 beamlines or we can consider reselling it to other facilities.

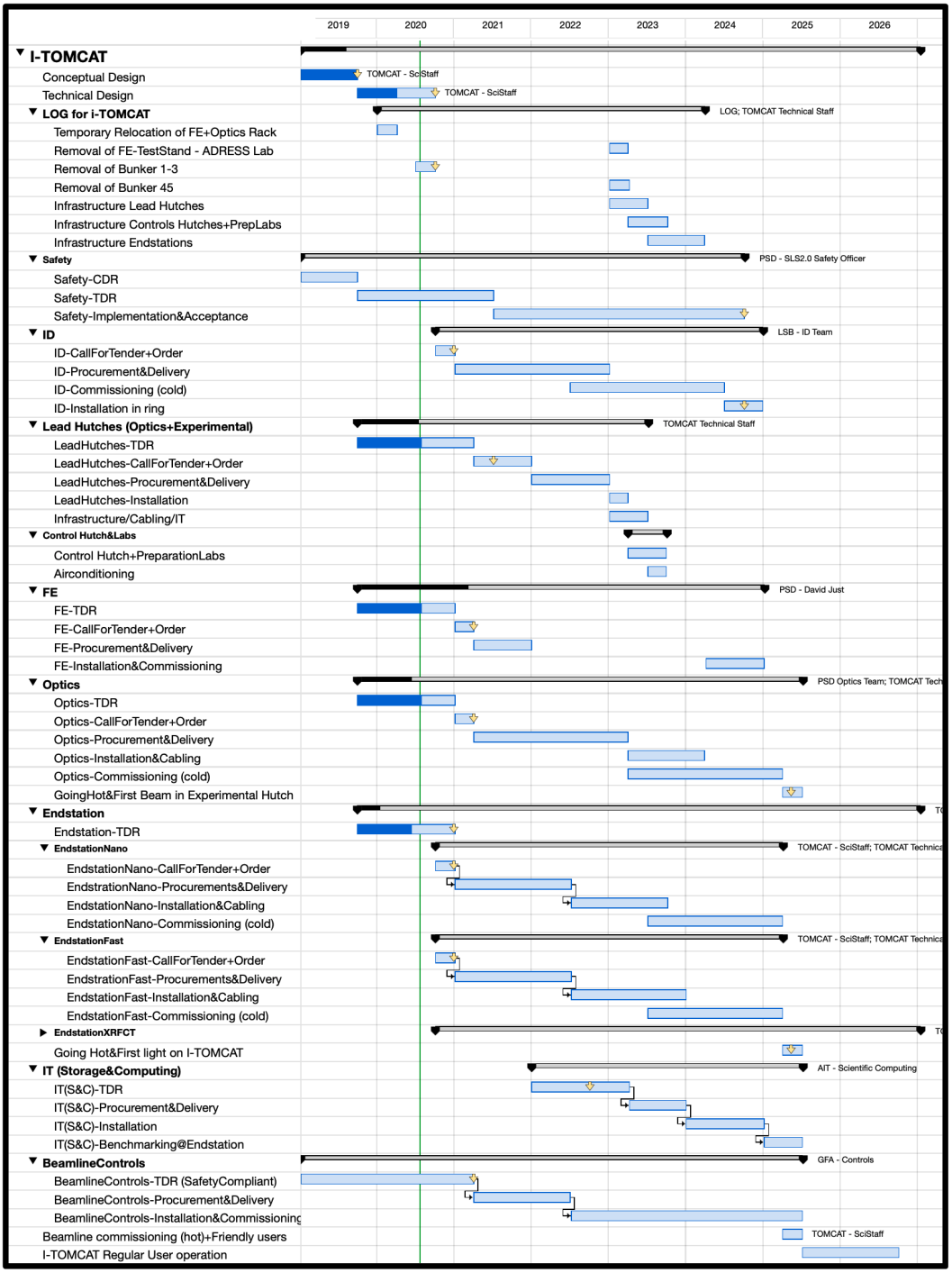

Figure 19.10: I-TOMCAT Gantt chart: Most of the installation work is scheduled to take place before the dark period.

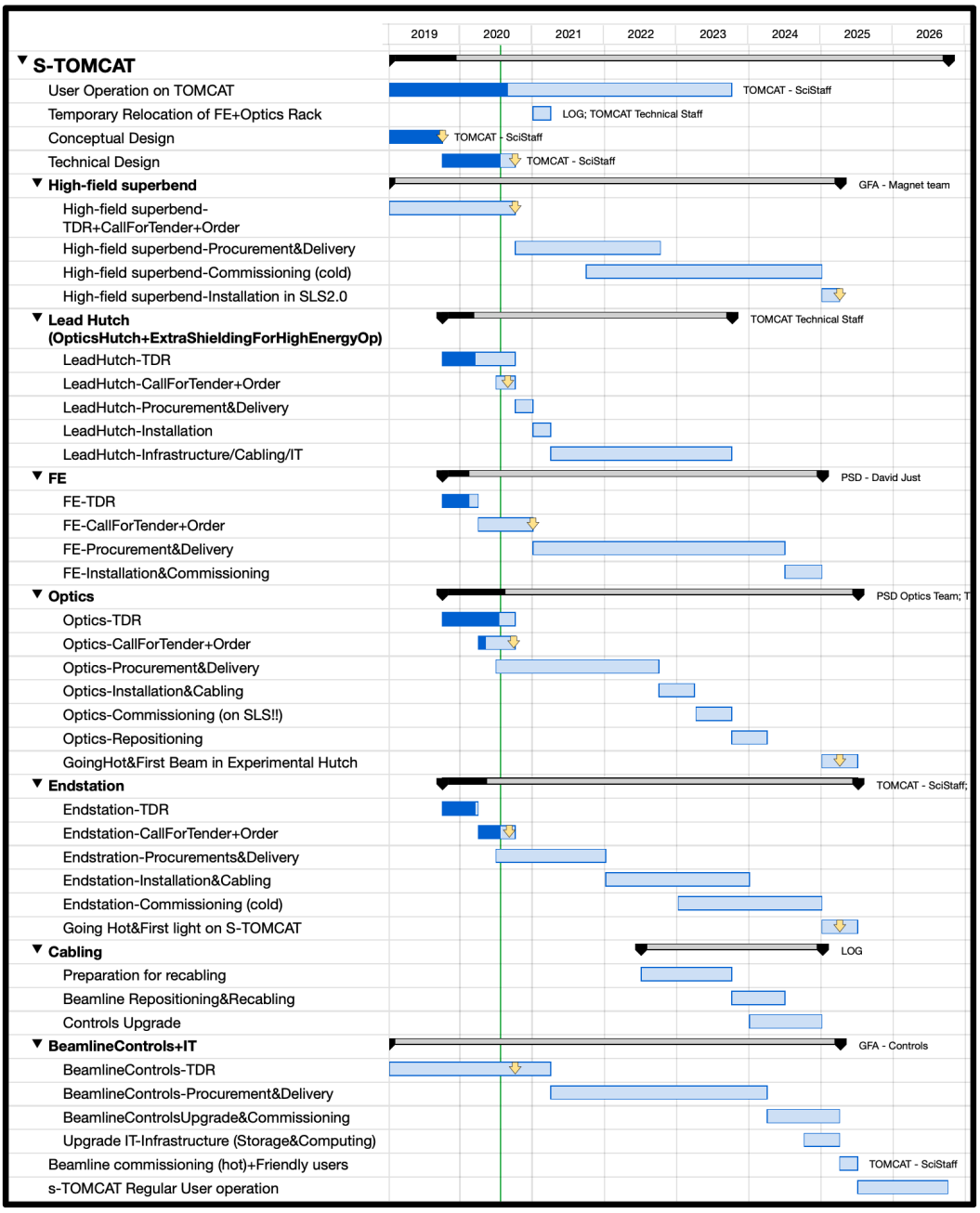

Figure 19.11: S-TOMCAT Gantt chart: User operation on TOMCAT will be maintained until the beginning of the dark period and will resume immediately when SLS 2.0 becomes operational.

19.4 Concluding remarks

The TOMCAT 2.0 upgrade relies on the SCU10 and the 5 T (or above) superconducting magnet as sources: both components are pushing the limit of the involved technologies towards new frontiers

and there is a certain risk involved. This is not new to PSI though, where very ambitious projects have notably been carried out successfully. For over a decade, TOMCAT has been running smoothly and at very high performance level, with hundreds of really very happy users. While being a bit worried about the very sporty SLS upgrade schedule, the user community welcomes the SLS upgrade enthusiastically and is very much eager to be back in operation as soon as the new machine resumes, expecting and relying on a significantly improved performance. This is a much higher expectation compared to starting up a greenfield machine: SLS (and PSI) reputation is at stake and we must therefore guarantee a timely return-to-operation within specifications. If successful, the TOMCAT 2.0 upgrade, with the I-TOMCAT and S-TOMCAT branches, will enduringly establish PSI on the map as one of the best imaging facilities worldwide for the next 20 years. Multiscale, multimodal, dynamic tomographic microscopy for better and novel characterization techniques, with simultaneously higher spatial and temporal resolution, will push dynamic tomographic imaging towards unexplored frontiers. Extensive capabilities for *in-situ, operando, in-vivo* and *in-fieri* experiments will be offered to broad academic and industrial communities addressing grand challenges in medicine, energy, and the material sciences.

19.5 Annex I: Vision 2035 - Science and technology

19.5.1 Science

The realisation of the TOMCAT 2.0 upgrade will firmly establish PSI on the map as one of the best imaging facilities worldwide for the next 20 years. In the following, we provide a brief summary of long term visions in three representative areas selected from our research portfolio.

Optogenetically stimulated cardiac x-ray microscopy imaging

The description of the complex (micro)-structure of the heart is nowadays accessible via diverse techniques, including phase-contrast tomographic microscopy. The link between microstructure and heart function stills remains an open and highly debated scientific challenge. Recently, optogenetics [16] has been suggested as a powerful method for precise, genetically engineered, excitation of the cardiac muscle at the cellular level. This technique brings new insights on the cell-type-specific activation mechanism, facilitating the control of cardiac rhythm. Optogenetics is currently mainly combined with optical imaging. If associated with x-ray tomographic microscopy as performed on TOMCAT 2.0 this could open the door to better spatially and temporally controlled *in-vivo* experiments. An improved understanding of how cardiac cells behave in 3D during a heartbeat is of prime interest for cardiology. It will contribute to more reliable computer models and eventually improved clinical practice, such as the development of pain-free implantable devices to treat arrhythmias.

Unveiling the relationships between different levels of the brain organization

The human brain participates in every human emotion, every human feeling, every human thought and every human decision. No other natural or engineered system can match its ability to adapt to novel challenges, to acquire new information and skills, to take complex decisions and to work reliably for decades on end. And despite its many diseases, no other system can match its robustness in the face of severe damage or match its amazing energy efficiency. Our brain consumes about 30 W, the same as an electric light bulb, thousands of times less than a small cluster. The human brain is a massively complex information-processing system with a hierarchy of different yet tightly integrated levels of organization: from genes, proteins, synapses and cells to microcircuits, brain regions, and the whole brain. Today, we know a lot about the individual levels. What we do not have is a causal understanding of the way events at the lowest level in the hierarchy cascade through the different levels to produce human cognition and behavior. For example, more than a hundred years of research have yet to give us a proper understanding of the link from synaptic plasticity to learning and memory, or of the way a gene defect works through the different levels to produce disease. Achieving this kind of understanding is a major challenge for neuroscience with implications that go far beyond research: if we could understand the brain, we might prevent or cure brain diseases such as autism, depression and Alzheimer's; we could also produce new computing technologies that share the brain's ability to operate reliably on very little power, and its ability to learn. PSI large-scale facilities like SLS 2.0 and SwissFEL will contribute to answering key questions[k] concerning the relationships between different

[k] "PSI Neuroscience Strategy Paper", submitted to SLS management on January 25th, 2015.

levels of the brain organization. How many and what types of cells are present in different regions of the brain? What are their morphologies? What are the relationships between genetic mutations, gene expression and morphology? How do neurons, glia and blood vessels interact? What is the detailed architecture of the vasculature that directs blood within the brain? What is the structural relationship between neurons, glia and vessels? How do changes in neurons alter the properties of vessels and vice-versa? With its high-throughput, high-resolution multiscale dynamic tomographic capabilities, TOMCAT 2.0 will be able to provide seminal contributions towards the answers to these questions.

Active-feedback x-ray microscopy for additive manufacturing

The current widespread ongoing digitalization has sparked renewed interest in additive manufacturing (AM), a promising technology showing high potential in particular in industrial areas where production of complex parts, with a complicated geometry or surface topography is key. AM uses, e.g., design software to control the layer-by-layer material deposition in arbitrarily complex shapes. A laser or electron beam selectively (partially) melts the deposited material, which as it cools fuses to form a 3D object. The exact interplay between processing parameters like spot size and displacement speed, beam power and the overall final object performance such as 3D microstructure, 3D phase distribution, residual stresses and textures is key to the advancement of AM. Ultrafast multi-projection single-shot tomographic imaging (see below) will be instrumental in moving away from a trial-and-error, post-mortem approach. Single-shot tomographic imaging will eliminate the necessity to spin the specimen and thereby will support (more) realistic production conditions *in situ* at the beamline. It will enable one to unravel the details of the highly dynamic and transient physical phenomena occurring at the beam-material interaction point as well as the pore and 3D microstructure formation process, *in fieri*. Active feedback from key object performance values evaluated in real-time from the tomographic volumes back to the processing parameters will pave the way to new production optimization strategies.

19.5.2 Methods developments

3D scattering imaging

The same instrument we will develop for full field XRF-CT can be used to implement a simple, rotation-free 3D scattering imaging setup. Placed at a small angle with respect to the (vertically collimated) direct beam, the pinhole + MOENCH ensemble can be used to collect the 3D volume of a sample without the need of rotating it, following the old principle of the camera obscura.

Stereo x-ray microscope

At 25 m from the source, S-TOMCAT will provide a 50 mm wide beam. With a pair of crystals positioned about 20 mm off-axis, it will be possible to create a stereo illumination of a sample placed downstream. The longitudinal position of the crossing beams (i.e., the sample position) will depend on the energy and selected crystal reflection. For a Si(220) crystal pair at 40 keV, the two beams will cross 122 mm downstream, each at an angle of 4.6° with respect to the optical axis. The two independent projections (9.2° apart) will be recorded with MOENCHs in virtual pixelization mode to compensate

for the reduced crystal bandwidth. Multilayers – instead of crystals – could overcome the bandwidth limitation and significantly improve the efficiency of this design. The stereo x-ray microscope will mitigate the lack of 3D information in dynamical experiments that cannot accommodate a rotating sample.

Optical klystron as an x-ray Michelson interferometer

We are considering using the SCU10 phase matcher to produce a phase-shifted, canted beam to emerge from the undulator. While the direct beam will travel through the sample, the canted one will be used as a reference to interferometrically directly recover the phase shift of the specimen in a quantitative way. It will be possible to tune the phase shift between the two beams very quickly and adapt it to the sample refractive characteristics, which might also vary quickly over time. This approach will fully exploit the high-brightness properties of the SLS 2.0 machine together with the unique features of the SCU10 device, providing a simple, powerful imaging tool.

Axicon-multiscope

Inspired by our recent work on hard x-ray multi-projection imaging for single-shot approaches [17], we can imagine a beam splitter based on the combination of an axicon with a battery of crystals/multilayers into a multiscope which should provide simultaneous illumination of a sample from multiple directions. Depending on the number of usable illuminations it will be possible to achieve and use, we aim at eliminating the necessity to rotate the sample during the acquisition of a tomographic scan. If successful, this will open the door to fully 3-dimensional ultrafast imaging. This approach could be complementary to SwissFEL, where a similar multiscope could be implemented and operated at a lower pulse rate but with at significantly higher brilliance.

Compton x-ray microscopy

Recently, Villanueva [18] presented a sketch for a scanning x-ray microscope based on Compton (inelastic) x-ray scattering for high-resolution cellular imaging. Their estimates predict a minimal dose per imaging signal to be obtained at 64 keV. This corresponds to a short enough wavelength to provide nanometer transverse resolution and micrometer depth of field for tomographic imaging of whole cells. In the presented sketch, the authors aim at reaching resolution via a scanning protocol: this requires focusing high-energy photons to a few nm (potentially feasible with MLL of the future generation [19]) in combination with a detector (not clear of which type!) covering essentially a cylindrical space along the optical axis around the sample. This is a very interesting proposal which we will keep on our radar. I-TOMCAT, thanks to the unique high-energy emission characteristics of its SCU10, will be the best option on SLS 2.0 to implement Compton x-ray microscopy, which could develop into a dose-efficient alternative to ptychography.

Bibliography

[1] R. Mokso, C. M. Schlepütz, G. Theidel, H. Billich, E. Schmid, T. Celcer, G. Mikuljan, L. Sala, F. Marone, N. Schlumpf, and M. Stampanoni. Gigafrost: the gigabit fast readout system for tomography. *Journal of Synchrotron Radiation*, 24:1250–1259, 2017.

[2] A. Lathuiliere, V. Laversenne, A. Astolfo, E. Kopetzki, H. Jacobsen, M. Stampanoni, B. Bohrmann, B. L. Schneider, and P. Aebischer. A subcutaneous cellular implant for passive immunization against amyloid-beta reduces brain amyloid and tau pathologies. *Brain*, 139:1587–1604, 2016.

[3] L. K. Aagesen, A. E. Johnson, J. L. Fife, P. W. Voorhees, M. J. Miksis, S. O. Poulsen, E. M. Lauridsen, F. Marone, and M. Stampanoni. Universality and self-similarity in pinch-off of rods by bulk diffusion. *Nature Physics*, 6(10):796–800, 2010.

[4] Patrick Pietsch, Daniel Westhoff, Julian Feinauer, Jens Eller, Federica Marone, Marco Stampanoni, Volker Schmidt, and Vanessa Wood. Quantifying microstructural dynamics and electrochemical activity of graphite and silicon-graphite lithium ion battery anodes. *Nature Communications*, 7:12909, 2016.

[5] D. R. Baker, F. Brun, C. O'Shaughnessy, L. Mancini, J. L. Fife, and M. Rivers. A four-dimensional X-ray tomographic microscopy study of bubble growth in basaltic foam. *Nature Communications*, 3, 2012.

[6] D. J. E. Murdock, X. P. Dong, J. E. Repetski, F. Marone, M. Stampanoni, and P. C. J. Donoghue. The origin of conodonts and of vertebrate mineralized skeletons. *Nature*, 502(7472):546–+, 2013.

[7] A. Miettinen, A Bonnin, A. Patera, F. Marone, and Stampanoni M. Non-rigid stitching of teravoxel-scale volumetric images. *Bioinformatics*, 2019.

[8] J. Villanova, R. Daudin, P. Lhuissier, D. Jauffres, S. Y. Lou, C. L. Martin, S. Laboure, R. Tucoulou, G. Martinez-Criado, and L. Salvo. Fast in situ 3D nanoimaging: a new tool for dynamic characterization in materials science. *Materials Today*, 20(7):354–359, 2017.

[9] D. Zverev, A. Barannikov, I. Snigireva, and A. Snigirev. X-ray refractive parabolic axicon lens. *Optics Express*, 25(23):28469–28477, 2017.

[10] M. Martinson, N. Samadi, B. Bassey, A. Gomez, and D. Chapman. Phase-preserving beam expander for biomedical X-ray imaging. *Journal of Synchrotron Radiation*, 22(3):801–806, 2015.

[11] Minna Bührer, Marco Stampanoni, Xavier Rochet, Felix Buchi, Jens Eller, and Federica Marone. High-numerical-aperture macroscope optics for time-resolved experiments. *Journal of Synchrotron Radiation*, 26(4, SI):1161–1172, 2019. 10th International Workshop on X-Ray Radiation Damage to Biological Crystalline Samples, Brookhaven Natl Lab, Natl Synchrotron Light Source II, Upton, NY, SEP 13-14, 2018.

[12] M. Kagias, Z. Wang, P. Villanueva-Perez, K. Jefimovs, and M. Stampanoni. 2D-omnidirectional hard-x-ray scattering sensitivity in a single shot. *Physical Review Letters*, 116(9):093902, 2016.

[13] M. Stampanoni, R. Mokso, F. Marone, J. Vila-Comamala, Sergey G., K. Trtik, P.and Jefimovs, and C. David. Phase-contrast tomography at the nanoscale using hard x rays. *Physical Review B*, 81(14), 2010.

[14] I. Vartiainen, R. Mokso, M. Stampanoni, and C. David. Halo suppression in full-field x-ray Zernike phase contrast microscopy. *Optics Letters*, 39(6):1601–1604, 2014.

[15] K. Wakonig, A. Diaz, A. Bonnin, M. Stampanoni, A. Bergamaschi, J. Ihli, M. Guizar-Sicairos, and A. Menzel. X-ray fourier ptychography: A method for quantitative phase contrast and high-resolution x-ray microscopy. *Accepted in Science Advances*, 2018.

[16] T. Bruegmann, T. Beiert, C. C. Vogt, J. W. Schrickel, and P. Sasse. Optogenetic termination of atrial fibrillation in mice. *Cardiovascular Research*, 114(5):713–723, 2018.

[17] P. Villanueva-Perez, B. Pedrini, R. Mokso, P. Vagovic, V. Guzenko, S. J. Leake, P. R. Willmott, P. Oberta, C. David, H. N. Chapman, and M. Stampanoni. Hard x-ray multi-projection imaging for single-shot approaches. *Optica*, 5(12):1521–1524, 2018.

[18] P. Villanueva-Perez, S. Bajt, and N. Chapman. Dose efficient Compton x-ray microscopy. *Optica*, 5(4):450–457, 2018.

[19] S. Bajt, M. Prasciolu, H. Fleckenstein, M. Domaracky, H. N. Chapman, A. J. Morgan, O. Yefanov, M. Messerschmidt, Y. Du, K. T. Murray, V. Mariani, M. Kuhn, S. Aplin, K. Pande, P. Villanueva-Perez, K. Stachnik, J. P. J. Chen, A. Andrejczuk, A. Meents, A. Burkhardt, D. Pennicard, X. J. Huang, H. F. Yan, E. Nazaretski, Y. S. Chu, and C. E. Hamm. X-ray focusing with efficient high-NA multilayer Laue lenses. *Light-Science and Applications*, 7, 2018.